



Mathematical Modeling of Electro-osmotic Flow and Heat Transfer in the Rough Micro-channels

Amalendu Rana

Mathematical Modeling of Electro-osmotic Flow and Heat Transfer in the Rough Micro-channels

*Thesis submitted
for the award of the degree
of*

Doctor of Philosophy

by

Amalendu Rana

Index No: 71/21/Maths./27 dated 08.04.2021

Under the supervision of

Prof. Gopal Chandra Shit

and

Prof. Motahar Reza



Department of Mathematics


Jadavpur University

Kolkata-700032, India

June, 2024


CERTIFICATE FROM THE SUPERVISOR(S)

This is to certify that the thesis entitled "**Mathematical Modeling of Electro-osmotic Flow and Heat Transfer in the Rough Micro-channels**", submitted by **Sri Amalendu Rana** who got his name registered on 08.04.2021 for the award of **Ph.D. (Science)** degree of **Jadavpur University**, is absolutely based upon his own work under the supervision of ourselves and that neither this thesis nor any part of it has been submitted for either any degree / diploma or any other academic award anywhere before.


05.06.2024
Prof. Motahar Reza

Associate Professor and HOD
Department of Mathematics
GITAM Deemed to be University
Hyderabad-502329

Dr. Motahar Reza
Associate Professor
Department of Mathematics
School of Science
GITAM (Deemed to be University)
Hyderabad


5.6.2024
Prof. Gopal Chandra Shit

Professor
Department of Mathematics
Jadavpur University
Kolkata-700032

Dr. Gopal Chandra Shit
Professor
Department of Mathematics
Jadavpur University
Kolkata - 700 032. (India)

Dedicated to
All My Revered Teachers

Acknowledgments

Writing a doctoral thesis is a challenging and often solitary endeavor, requiring support from a variety of individuals. I am fortunate to have received such support from many people, and I am grateful for the opportunity to acknowledge their contributions.

First and foremost, I express my deepest gratitude to my research supervisors, Prof. Gopal Chandra Shit from the Department of Mathematics at Jadavpur University, Kolkata, India, and Prof. Motahar Reza from the Department of Mathematics at GITAM Deemed to be University, Hyderabad, India. Throughout my doctoral research, Prof. Shit and Prof. Reza have provided continuous encouragement, detailed feedback, and invaluable guidance. Their passion for improving my language skills has been instrumental in my development as a researcher, and I am truly grateful for their unwavering support.

I am deeply grateful for the invaluable collaboration and mentorship provided by Prof. G. P. Raja Sekhar from the Department of Mathematics at the Indian Institute of Technology, Kharagpur, India, and Prof. Klaus Stefan Drese from the Institute for Sensor and Actuator Technology at Coburg University of Applied Sciences and Arts, Germany. Working with them during my PhD has been a tremendous privilege and has greatly enriched my research experience. Their guidance and expertise have been instrumental in shaping my academic journey.

I want to acknowledge the Department of Mathematics, Jadavpur University, and the Department of Mathematics, GITAM Deemed to be University, Hyderabad, for providing an outstanding research environment. I am grateful for the financial assistance provided by the Govt. of West Bengal, India, through the Swami Vivekananda Merit Cum Means fellowship with Grant number: WBP211640929362.

I would also like to thank Prof. Sagnik Sinha (present), Prof. Sudeshna Banerjea (former), and Prof. Swapna Debnath (former), Heads of the Department, for their support and for providing the necessary facilities for my research. Additionally, I am grateful to Prof. Alaka Das, Prof. Subhas Chandra Mandal, Prof. Farook Rahaman, Prof. Anup Bandyopadhyay, and all other faculty members of the Department of Mathematics for their valuable suggestions and support. I am thankful to the office staff and authorities of Jadavpur University for their assistance during my stay and thesis work.

I wish to take this opportunity to express my sincere gratitude to all my teachers from primary to postgraduate level for all their support to reach this stage. Specially, I would like to acknowledge the affection and inspiration of Dr. Himadri Shekhar Mondal, Department of Mathematics, Midnapore College, who was the first person to grow my interest in Mathematics research.

Special thanks are due to my friends, who have provided a stimulating and enjoyable environment, making each day at Jadavpur University a new experience. I am especially grateful to Dwaipayan da, Kausik da, Swarup da, Biswajit da, Subrata da, Mansur, Nripendu, Pintu, Tanmay and many more, who helped me a lot at various stages of my Ph.D. life. I would like to express my gratitude to Suman, Anirban, Biswarup, Gour, Prasanta, Subhara, Shreya didi and many others for

their support at Jadavpur University. I am also thankful to my friends Gopal, Mohanlal, Shreyashri, Sumita, Srivally, Pranava Sree, Pranavi, Sivasakthi, Aswathi, Rohan, Sujith, Chaitanya, Jayhind for their encouragement and support. I am also thankful to some of my school friends Jagadish, Kunal, Ranjan, and Gautam for their purposeless help and mental support to me.

My deepest gratitude goes to my family members, my father Sri Joyjiban Rana, my mother Smt. Basanti Rana, for their unwavering love and support throughout my life. I would also like to thank my sister Smt. Moupiya Rana, as well as my brothers-in-law Sri Sanjit Rana, for their constant support. My heartfelt appreciation extends to my maternal uncle, Sri Harekrishna Rana, and my maternal aunt, Smt. Sumati Rana, for their enduring love and unwavering support that have been constants in my life. I am profoundly grateful to my uncle Dr. Dilip Kumar Ghosh and my aunt, Smt. Dipa Ghosh, whose unwavering support and guidance have been a beacon of light in my life. My grandmother Srimatya Shradhamoyi Rana has also played a significant role in shaping my life, and I am grateful for her teachings. I express my gratefulness for the loving presence of my niece, Divyanshi. Also, I received comfort, companionship, and support throughout the entire research journey from my closest confidante, Sudeshna.

Finally, I wish to express my deepest appreciation to the members of Akhil Bharat Vivekananda Yuva Mahamandal. Their motivational ideas and life teachings have been invaluable to me, guiding me on my journey.

Jadavpur
June, 2024

Amalendu Rana
Amalendu Rana 05.06.2024

Declaration

I certify that

1. The work contained in the thesis is original and has been done by myself under the general supervision of my supervisor.
2. The work has not been submitted to any other Institute for any degree or diploma.
3. I have followed the guidelines provided by the Institute in writing the thesis.
4. I have conformed to the norms and guidelines given in the Ethical Code of Conduct of the Institute.
5. Whenever I have used materials (data, theoretical analysis, and text) from other sources, I have given due credit to them by citing them in the text of the thesis and giving their details in the references.
6. Whenever I have quoted written materials from other sources, I have put them under quotation marks and given due credit to the sources by citing them and giving required details in the references.

Jadavpur
June, 2024

Amalendu Rana,
Amalendu Rana 05.06.2024

Mathematical Modeling of Electro-osmotic Flow and Heat Transfer in the Rough Micro-channels

Index no: 71/21/Maths/27 Dated-08/04/2021

Abstract

This thesis investigates the mathematical modeling of electroosmotic flow and heat transfer in microchannels and microtubes, especially focusing on how surface roughness affects these processes. It also examines the impact of magnetic fields, system rotation, and porous media on electroosmotic flow behavior, considering their interaction with surface roughness. This research study is motivated by the increasing importance of microfluidic systems, especially in applications like micro-heat exchangers, microreactors, micropumps, and lab-on-a-chip devices.

The thesis comprises an introductory chapter (**Chapter 1**) that explains microfluidics and electrokinetic phenomena. Subsequently, six main chapters explore various aspects of the new research findings, giving a detailed analysis of the problem.

In **Chapter 2**, the combined effects of electroosmosis and surface roughness on rotating electrothermal flow in a microchannel under a magnetic field are studied. The governing equations, including the Navier-Stokes equations, energy equation, and the Poisson-Boltzmann equation for EDL potential, are formulated. The analytical solutions are obtained using the separation of variables method combined with cosine Fourier series expansion. The analysis shows that surface roughness significantly affects flow patterns by increasing wall shear stress and friction, leading to a higher Poiseuille number. The Coriolis force from rotation increases entropy generation, causing more internal irreversibilities.

Chapter 3 investigates the electromagnetohydrodynamic flow of two immiscible fluids in a hydrophobic microchannel with a topographically charged rough surface. The mathematical model includes the Navier-slip and the changing zeta potential at the fluid-solid interface. It also considers the balance of viscous stress and zeta potential jump at the liquid-liquid interface. Analytical solutions are obtained using the perturbation technique. The investigations show that surface roughness intensifies flow disturbances, leading to the formation of microfluidic droplets. The zeta potential difference at the fluid-fluid interface can cause one layer to move faster than the other. Increased surface roughness intensifies flow disturbances, leading to microfluidic droplet formation.

In **Chapter 4**, the heat transfer characteristics associated with combined electromagnetohydrodynamic flow in a microchannel with regular wavy rough walls through a porous medium are examined. The solutions for the velocity and potential distribution equations are obtained using

Dr. Mohan Reddy
Department of Mathematics
School of Science
GITAM (Deemed to be University)
Hyderabad

the perturbation technique. The analytical solution for temperature distribution, considering Joule heating, is derived to study the thermal characteristics. The study reveals that the mean velocity decreases with increasing Darcy number but has an enhancing effect on the applied magnetic field, while the rate of heat transfer increases with an increase in Joule heating effects and Hartmann number.

Chapter 5 examines how complex wavy rough walls affect thermo-fluidic transport with combined electromagnetohydrodynamic flow in a porous microchannel. The governing equations for thermo-fluidic transport are solved analytically using the perturbation technique, with the volumetric flow rate derived analytically and the Nusselt number computed numerically. The study shows that the velocity profiles become fully developed in a transverse electric field, and the rate of heat transfer enhances with an increase in the roughness of the microchannel surface.

In **Chapter 6**, the thermal transport characteristics of nanofluid through a wavy microchannel with anisotropic porous medium under electromagnetohydrodynamic effects are analyzed. The governing equations for the electric double layer (EDL) potential, velocity, and temperature distributions are solved using numerical methods. The results are validated against analytical asymptotic solutions. The study reveals that anisotropy and permeability ratio of the porous medium significantly affect flow and temperature profiles, with Forchheimer inertial effect generating frictional heating and slug flow behavior.

Chapter 7 studies the electromagnetohydrodynamic pumping in a fluid-saturated anisotropic porous microtube with a rough surface. The analytical solutions are found to solve the governing equations, including the linearized Poisson-Boltzmann and Navier-Stokes equations, for this problem at low Reynolds numbers. The analysis reveals that the EMHD pumping rate is affected by a second-order term ($-\varepsilon^2\eta$), where $\eta = \eta_1 + \eta_2$, indicating the effect of roughness on the mean pumping rate. The study shows that surface roughness alters the boundary layer near the microtube wall, leading to a thinner boundary layer and increased pumping rate, and higher anisotropic permeability introduces uneven resistance forces, leading to the formation of smaller eddies and boluses.

In the concluding **Chapter 8**, the thesis provides a concise summary of the important findings, emphasizing the influence of surface roughness on electroosmotic flow and heat transfer. The practical implications for lab-on-a-CD applications are highlighted, and avenues for future research, including further exploration of rough microchannels and microtubes, are outlined.

Amalendu Rame,
05.06.2024

Motahar R.
05.06.2024

Dr. Motahar Reza
Associate Professor
Department of Mathematics
School of Science
GITAM (Deemed to be University)
Hyderabad

Gopal Ch. Shit
5.6.2024

Dr. Gopal Chandra Shit
Professor
Department of Mathematics
Jadavpur University
Kolkata - 700 032. (India)

Contents

Acknowledgments	vii
Declaration	ix
Abstract	xi
1 Introduction	1
1.1 Microfluidics and micro-scale systems: An overview	1
1.1.1 Scaling laws in microfluidics	2
1.1.2 Microfluidics Versus Traditional Fluidics	2
1.1.3 Classification and Characteristics of Microchannels	3
1.1.4 Modeling of Microflows	4
1.2 Recapitulation of fluid mechanics	4
1.2.1 Conservation of mass	5
1.2.2 Conservation of momentum	5
1.2.3 Conservation of Energy	6
1.2.4 Mass Transfer Equation	7
1.3 Electrokinetic phenomena	7
1.3.1 Electroosmotic Flow	8
1.3.2 Electrical double layer (EDL)	8
1.3.3 Governing equations for electrokinetic phenomena	9
1.4 Magnetohydrodynamics	10
1.4.1 Maxwell's Equations	10
1.4.2 Electromagnetohydrodynamic flow	11
1.5 Rotationally Actuated Microflows	11
1.5.1 Governing equations for flow in rotating frame	12
1.6 Introduction to Porous Media	12
1.6.1 Porosity and Permeability	12
1.6.1.1 Darcy's Equation	12
1.6.2 Anisotropic porous media	13
1.7 Heat Transfer	14
1.7.1 Temperature distribution in Electromagnetic Scenarios	14
1.7.1.1 Viscous dissipation	15
1.7.1.2 Joule heating	16
1.8 Entropy generation	16
1.9 Boundary conditions	17
1.9.1 Boundary conditions for the electroosmotic flow	17

1.9.1.1	Slip boundary condition	17
1.9.1.2	Fluid-fluid interfacial boundary conditions for two immissible electrolytes	18
1.9.2	Boundary conditions for the electrostatic potential	18
1.9.2.1	Fluid-solid interfacial boundary condition	18
1.9.2.2	Interfacial potential jump condition	19
1.9.2.3	Charge Neutrality condition at fluid-fluid interface	19
1.9.3	Boundary conditions for temperature distribution	19
1.10	Microchannel roughness and applications in microfluidics	19
1.10.1	Lab-on-a-chip technology	20
1.10.2	Mixing and Seperation process	21
1.10.3	Micro-heat Exchangers	22
1.10.4	Microreactors	22
1.10.5	Micropumps	22
1.11	Brief review of existing literarures	23
1.12	Objectives of the Thesis	28
1.13	Overview of the thesis	29
2	Rotation Induced Electrothermal MHD Flow in a Rough Surface Microchannel	33
2.1	Introduction	33
2.2	Physical paradigm and mathematical formulation	35
2.2.1	Description of the problem	35
2.2.2	Governing equations for velocity distribution	37
2.2.3	Thermal energy	40
2.3	Analytical solution	41
2.3.1	Analytical solution for velocity distribution	41
2.3.2	Volumetric flow rate	43
2.3.3	Analytical solution for temperature distribution	43
2.3.4	The Nusselt number	45
2.4	Validation of results	45
2.4.1	Limiting case: Transient heat transfer in non-rotating microchannel with roughness	46
2.5	Results and Discussion	48
2.5.1	Rotation induced EMHD flow analysis	48
2.5.2	Flow rate analysis	55
2.5.3	Analysis of wall shear stress and Poiseuille number	56
2.5.4	Temperature distribution	60
2.5.5	Rate of heat transfer analysis	61
2.5.6	Entropy generation	62
2.6	Conclusions	63
	Appendix	65
2.A	Mathematical expressions in temperature distribution	65
3	Two-layer Electroosmotic Flow in a Rough Surface Microchannel	67
3.1	Introduction	67
3.2	Mathematical modeling and solution	70
3.2.1	Problem description	70
3.2.2	Governing equation for Potential distribution	71

3.2.2.1	Laplace equation for applied potential	71
3.2.2.2	Poisson equation for EDL potential	72
3.2.3	Governing equations for fluid flow	73
3.3	Analytical solution: Perturbation analysis	76
3.3.1	Effect of wave amplitude on applied potential	76
3.3.2	Effect of wave amplitude on EDL potential	77
3.3.3	Effect of wave amplitude on two-layered flow	79
3.4	Validation of Results	82
3.5	Results and Discussion	84
3.5.1	Two layered electromagnetohydrodynamic flow analysis	84
3.5.2	Streamline analysis	88
3.5.3	Volumetric flow rate	91
3.5.4	Estimation of boundary layer thickness	95
3.6	Concluding remarks	96
Appendices		100
3.A	Mathematical expressions in connection with the applied potential	100
3.B	Mathematical expressions in connection with the EDL potential	100
3.C	Mathematical expressions in connection with the transverse electric field	100
3.D	Mathematical expressions in connection with the velocity distribution	101
3.E	Mathematical expressions for the mean velocity	102
4	EMHD Flow and Heat Transfer in Porous Microchannel with Surface Corrugation	105
4.1	Introduction	105
4.2	Mathematical Model and Problem Description	108
4.3	Electrical potential distribution	108
4.4	Velocity distribution	110
4.5	Temperature distribution and Nusselt number	113
4.6	Results and Discussion	116
4.6.1	Effect of wall roughness on flow velocity	118
4.6.2	Effect of electromagnetic field on flow velocity	120
4.6.3	Effect of porosity on flow velocity	122
4.6.4	Effects on mean velocity	124
4.6.5	EMHD thermal characteristics: temperature variation	128
4.6.6	EMHD thermal characteristics: Nusselt number	129
4.7	Conclusions	133
5	Surface Roughness on EMHD thermo-fluidic transport in a porous microchannel	135
5.1	Introduction	135
5.2	Problem statement and Mathematical Formulation	138
5.3	Electrical potential distribution	139
5.3.1	The effects of roughness on the applied potential distribution	139
5.3.2	The effects of roughness on the EDL potential distribution	141
5.4	Velocity distribution	144
5.5	Thermal behaviour	148
5.6	Results and Discussion	151
5.6.1	Validation of the result	153
5.6.2	Analysis of electric field on rough surface	154
5.6.3	Analysis of flow transport characteristics	154

5.6.4	Analysis of volumetric flow rate	158
5.6.5	Analysis of thermal characteristics	161
5.6.6	Analysis of heat transfer rate: Nusselt number	166
5.7	Conclusions	167
6	Role of Anisotropic Permeability on EMHD Heat Transfer in a Rough Microchannel	169
6.1	Introduction	169
6.2	Mathematical formulation and problem description	171
6.2.1	Flow transport phenomena	174
6.2.2	Thermal transport phenomena	177
6.2.3	Mass transfer phenomena	179
6.3	Results and Discussion	180
6.3.1	Electromagnetohydrodynamic flow analysis	181
6.3.2	Pressure gradient analysis	185
6.3.3	Thermal characteristics analysis	185
6.3.4	Rate of heat transfer analysis	188
6.3.5	Volume fraction analysis	190
6.4	Asymptotic analysis for velocity distribution in a nano-particle free context	192
6.4.1	Case-I: For large Darcy number	192
6.4.2	Case-II: For small Darcy number	193
6.5	Conclusions	195
Appendix		196
6.A	Mathematical expressions connected with the asymptotic solution for velocity distribution	196
7	Electroosmotic flow in anisotropic porous microtube with rough surface	197
7.1	Introduction	197
7.2	Mathematical modeling of the Problem	200
7.2.1	Problem description	200
7.2.2	Governing equations	200
7.3	Perturbation analysis due to roughness	204
7.3.1	Effect of roughness on the applied electric field	204
7.3.2	Effect of roughness on Potential Distribution and Electric Double Layer	206
7.3.3	Effect of roughness on EMHD flow	208
7.3.4	EMHD pumping rate	211
7.4	Results and Discussions	215
7.4.1	Variability in η and its influence on EMHD pumping rate	215
7.4.2	Flow reversal and bolus formation: surface roughness and anisotropic permeability perspectives	221
7.4.3	Radial Pressure gradient	223
7.4.4	Wall shear stress distribution	226
7.5	Conclusions	228
8	Conclusions and Future scope of work	231
8.1	Major contributions and conclusions	231
8.2	Future scope of study	233
8.2.1	Microtube with random roughness	233
References		235

Contents

List of Publications	255
Conferences & Workshops	257

1

Introduction

This thesis focuses the interesting field of electroosmotic flow in microchannels. It examines how momentum and heat transfer occur when incompressible, viscous fluids move through rough microchannels. The effects of varying roughness on the microchannel surface, applied magnetic fields, rotational system and porous media on these transport phenomena are examined in detail. Additionally, the influence of surface topography on the complex dynamics of electromagnetohydrodynamic (EMHD) flow in both microchannels and microtubes is studied within anisotropic porous media. Before exploring the motivations and scope of these problems, a basic understanding of microfluidics, micro-scale systems, fluid mechanics, and electrokinetic phenomena is established in this chapter. The governing equations of mathematical model and a review of relevant literature are also covered to provide a strong foundation for this research.

1.1 Microfluidics and micro-scale systems: An overview

Micro-scale flow physics studies how fluids behave at very small scales, usually within the micrometer range. This field is crucial for understanding and designing microfluidic devices that handle small volume of fluids for various uses. Unlike traditional methods that rely on pressure gradients or gravity, microfluidic devices work at a scale where surface effects are more important than bulk effects. At the micro-scale, the interaction between the fluid and the channel walls becomes very important. Surface tension and electrokinetic effects, which are usually insignificant in larger systems, become dominant. These effects can be used to precisely control fluids in microchannels, allowing for accurate manipulation of small amount of fluid. Micro-scale flow physics combines knowledge from various fields, including fluid mechanics and its uses in surface science, physics, chemistry

and biology. This interdisciplinary approach reflects the complexity of microfluidic systems and their wide range of applications.

The main motivation for studying micro-scale flow physics is to develop microfluidics technology. Microfluidics deals with controlling fluids in channels that are only a few micrometers wide. Advances in micro and nano-fabrication technologies have enabled the creation of complex microfluidic devices for various applications, including biomedical engineering and electronics cooling. Understanding the basic principles of micro-scale flow physics is crucial for advancing these applications and expanding the possibilities in microfluidics ([Chakraborty \[2010\]](#)).

1.1.1 Scaling laws in microfluidics

Scaling laws are essential for understanding the physical properties of microsystems. They explain how physical quantities change with the size of the system while keeping other factors constant. For example, when comparing volume forces (like gravity and inertia) to surface forces (like surface tension and viscosity), the ratio between them scales with the inverse of the system size cubed. This means that as we move to the microscale, volume forces become less important compared to surface forces. ([Bruus \[2008\]](#)).

The basic scaling law for the ratio of these two types of forces can be generally expressed as

$$\frac{\text{surface forces}}{\text{volume forces}} \propto \frac{l^3}{l^2} = l^{-1} \rightarrow \infty \text{ as } l \rightarrow 0.$$

Here l typically represents the size of a system or object relative to some reference scale. This scaling law means that when we scale down to the microscale in lab-on-a-chip systems, the volume forces that are significant in everyday life become much less important. Instead, surface forces become dominant. As a result, we need to adjust our understanding and be ready for some surprises.

1.1.2 Microfluidics Versus Traditional Fluidics

Microfluidics is a branch of fluid mechanics that studies the behavior of fluids at very small scales, typically micrometers or nanometers. This contrasts with traditional fluid mechanics, which deals with larger, visible scales. In traditional fluid mechanics, forces like inertia and pressure-driven flow dominate fluid motion. However, in microfluidics, the higher surface area to volume ratio makes surface effects like viscosity, electrostatic forces, and surface tension more important. ([Chakraborty \[2010\]](#)).

One major difference between traditional fluidics and microfluidics is how they control flow. Traditional systems use pumps, valves, and pipes to handle large volumes of fluid. Microfluidic devices, on the other hand, use microchannels, electric fields, and surface tension to control and manipulate small volumes of fluid accurately. Also, traditional methods usually depend on turbulence for mixing efficiently, while microfluidic mixing relies mainly on diffusion because of the low Reynolds number (which measures inertia versus viscosity) in microchannels. At the microscale, how fluids act does not match what traditional fluid mechanics expects. In traditional fluid me-

chanics, we see fluids as smooth and consistent, with clear properties. But at the microscale, things change. The interactions between molecules become really important, and it is hard to pin down exactly what the fluid is like. ([Chakraborty \[2010\]](#)).

In microfluidics, when the channels get smaller, the way the fluid and the channel walls interact becomes more important. These interactions involve forces like van der Waals forces, electrostatic forces, and surface tension. They can really change how the fluid acts near the walls of the channel. This is called interfacial phenomena. It is not as big a deal in traditional fluid mechanics, where the walls of the channel do not affect the flow much. But in microfluidics, this interfacial phenomenon is important. We need to understand and control these effects to design and make microfluidic devices that work well for various applications.

1.1.3 Classification and Characteristics of Microchannels

Microchannels can be classified based on several characteristics, including shape (straight or curved), cross-sectional profile, size, wall material, wall roughness, and presence of holes in the walls. Various cross-sectional shapes, such as circular, square, rectangular, or tapered, are used. The channel walls can be made of materials like silicon, glass, quartz, metals, or polymers. In most experiments, we use gas, liquid, or nanofluid, and we see the same laminar or turbulent flow patterns as in macrochannels.

[Kandlikar \[2003\]](#) proposed a classification of microchannels based on size:

- Conventional channels: $D > 3 \text{ mm}$
- Minichannels: $3 \text{ mm} \geq D > 200 \text{ }\mu\text{m}$
- Microchannels: $200 \text{ }\mu\text{m} \geq D > 10 \text{ }\mu\text{m}$
- Transitional channels: $10 \text{ }\mu\text{m} \geq D > 0.1 \text{ }\mu\text{m}$
- Transitional microchannels: $10 \text{ }\mu\text{m} \geq D > 1 \text{ }\mu\text{m}$
- Transitional nanochannels: $1 \text{ }\mu\text{m} \geq D > 0.1 \text{ }\mu\text{m}$
- Molecular nanochannels: $0.1 \text{ }\mu\text{m} \geq D$

Here, D is the hydraulic diameter of the channel, calculated as $D = \frac{4S}{P}$ (where S is the cross-sectional area, and P is the channel perimeter). However, this classification based solely on size may not be entirely effective, and using specific features of physical processes in fluid flow as criteria could be more appropriate. Nonetheless, due to a lack of systematic theoretical and experimental investigations, this size-based classification is used for discussing flows in microchannels and transitional microchannels in this context.

1.1.4 Modeling of Microflows

Modeling microflows presents unique challenges due to the small length scales involved. In larger scales, such as mesoscopic scales, a continuum description is often sufficient. However, when we start looking at sizes smaller than a micron, we need atomistic modeling to really understand how things behave.

In microfluidics, understanding slip phenomena, wetting, adsorption, and electrokinetics is crucial. Slip phenomena refer to the behavior of fluids near a solid boundary, where the fluid velocity is higher than expected due to the presence of a thin layer of fluid in direct contact with the surface. Wetting describes how a liquid spreads over a solid surface. This is important for controlling fluid flow in microchannels. Adsorption refers to the adherence of molecules from a gas or liquid onto a solid surface, affecting the flow behavior. Electrokinetics, on the other hand, involves the movement of fluid induced by an applied electric field, which is particularly significant in microfluidic devices (Chakraborty [2010]).

One important effect in electrokinetics is electrophoresis. This is when charged particles in a fluid move because of an electric field. Electrophoresis is used to separate and analyze particles in microfluidic systems. Reuss [1809] observed in experiments with porous clay, these effects involve the interaction of ionized solutions with static charges on insulating surfaces. This interaction causes high ion concentrations near the walls, creating strong electrostatic forces. When a voltage is applied along a microchannel, it causes flow near the wall, which can be modeled with a slip velocity proportional to the electric field. A continuum approach is often suitable for describing these flows. Another important aspect of modeling microflows is understanding how different forces, such as viscous forces and electromagnetic forces, interact. These interactions can significantly affect the flow behavior, leading to complex flow patterns and phenomena.

Overall, modeling microflows requires a multi-faceted approach that considers the unique physics at play in these small-scale systems. From slip phenomena to electrokinetics, understanding these phenomena is crucial for designing and optimizing microfluidic devices for various applications.

1.2 Recapitulation of fluid mechanics

Fluid mechanics is the study of how fluids, like liquids and gases, behave and move. It mainly looks at large-scale phenomena, treating fluids as continuous substances where each small volume contains many particles. Instead of focusing on individual particles, it examines the movement of these small volumes. There are two main ways to describe fluid motion mathematically: the Lagrangian method and the Eulerian method. The Lagrangian approach tracks the movement of individual fluid particles over time, describing properties like position and velocity as they change. This method is like observing the flow of a river while drifting on a boat. In contrast, the Eulerian approach focuses on a fixed volume in space, examining fluid properties like velocity and pressure as they pass through this stationary area, similar to watching the flow of a river from a bridge. While the Lagrangian method provides detailed information about individual particles, solving its complex equations can be difficult. Therefore, the Eulerian method is more commonly used in fluid

mechanics because it is more practical.

A crucial concept in fluid mechanics is the material derivative, which quantifies the motion of a fluid element. It is defined as:

$$\frac{D}{Dt} \equiv \frac{\partial}{\partial t} + (\mathbf{V} \cdot \nabla) \quad (1.1)$$

where \mathbf{V} denotes the velocity vector, $\nabla \equiv \hat{i} \frac{\partial}{\partial x} + \hat{j} \frac{\partial}{\partial y} + \hat{k} \frac{\partial}{\partial z}$ in Cartesian coordinates. $\frac{D}{Dt}$ represents the material derivative, which indicates the Lagrangian rate of change, $\frac{\partial}{\partial t}$ denotes the Eulerian rate of change, and $(\mathbf{V} \cdot \nabla)$ is the convective rate of change.

The physics of fluid dynamics is based on fundamental equations derived from three core principles: conservation of mass, momentum, and energy. These principles are the foundation of fluid mechanics, helping us to understand and analyze the complex behavior of fluid motion.

1.2.1 Conservation of mass

The conservation of mass in fluid mechanics means that the total mass of a closed system stays the same over time unless mass is added or removed. The equation of continuity is the mathematical expression of this principle. In an isolated system, the equation of continuity can be written as:

$$\frac{D\rho}{Dt} + \rho \nabla \cdot \mathbf{V} = 0, \quad (1.2)$$

where \mathbf{V} and ρ are the velocity vector and the density of the fluid respectively. For incompressible flow, where the density of the fluid is constant, the equation of continuity simplifies to:

$$\nabla \cdot \mathbf{V} = 0. \quad (1.3)$$

1.2.2 Conservation of momentum

The conservation of momentum in fluid mechanics is described by Euler's equation for inviscid fluid flows, given by

$$\rho \frac{D\mathbf{V}}{Dt} = -\nabla p + \mathbf{F}, \quad (1.4)$$

where \mathbf{F} represents the body force. The Navier-Stokes equation, derived independently by Navier [1823] and Poisson in 1831, and later refined by Barre de Saint Venat and Stokes [1845], extends Euler's equations to include viscous effects. Based on Newton's law of motion, these equations modify Euler's equation to incorporate viscosity. According to Reynolds transport theorem, the momentum equation can be written as

$$\frac{\partial}{\partial t}(\rho \mathbf{V}) + \nabla \cdot (\rho \mathbf{V} \otimes \mathbf{V}) = \nabla \cdot \boldsymbol{\sigma} + \mathbf{F}, \quad (1.5)$$

where, $\boldsymbol{\sigma} = -p\mathbf{I} + \boldsymbol{\tau}$ denotes the stress tensor and $\boldsymbol{\tau} = \mu[(\nabla \mathbf{V}) + (\nabla \mathbf{V})^T - \frac{2}{3}(\nabla \cdot \mathbf{V})\mathbf{I}]$ represents the viscous stress. \mathbf{F} represents the collective influence of body forces acting within the system, encompassing the electroosmotic force, Lorentz force, Coriolis force, and resistance force due to the porous medium. Each of these forces plays a distinct role in the system dynamics: the elec-

osmotic force, discussed in Section 1.3, arises from the interaction between the electric field and the electrolyte fluid in the microchannel; the Lorentz force, detailed in Section 1.4, results from the interaction between the magnetic field and the electric current in the fluid; the Coriolis force, explained in Section 1.5, emerges due to the rotation of the system; and the resistance force due to the porous medium, outlined in section 1.6, is a consequence of the fluid flow through the porous structure. Understanding these forces is essential for understanding the complex behavior of fluid flow in microchannels

For incompressible flow, the Navier-Stokes equation is expressed as (Milne-Thomson et al. [1949])

$$\rho \left[\frac{\partial \mathbf{V}}{\partial t} + (\mathbf{V} \cdot \nabla) \mathbf{V} \right] = -\nabla p + \mu \nabla^2 \mathbf{V} + \mathbf{F}, \quad (1.6)$$

where μ is the dynamic viscosity of the fluid, $\mathbf{V} \cdot \nabla$ represents the inertial term, and $\nabla^2 \mathbf{V}$ is the viscous term characterizing fluid-fluid interactions.

In addition to these equations, the Reynolds number (Re) is essential for analyzing fluid flow and determining the relative importance of inertial and viscous forces. The Reynolds number (Reynolds [1883]) is a dimensionless quantity used in fluid mechanics to predict flow patterns in various fluid flow scenarios. It is defined as the ratio of inertial forces to viscous forces within a fluid and it is written as

$$Re = \frac{\text{Inertial forces}}{\text{Viscous forces}} = \frac{\rho U L}{\mu}, \quad (1.7)$$

where U and L denote the characteristic velocity and length scale respectively. The Reynolds number helps to predict flow patterns in different fluid flow situations. When the Reynolds number is small ($Re \ll 1$), viscous forces dominate over inertial forces, and the flow is typically smooth and laminar. Conversely, when the Reynolds number is large ($Re \gg 1$), inertial forces dominate, and the flow is turbulent.

At very low Reynolds numbers, the inertial term in the Navier-Stokes equation (1.6) can be neglected, particularly under steady-state conditions. Consequently, the equation reduces to the Stokes equation (Stokes [1845]), expressed as

$$-\nabla p + \mu \nabla^2 \mathbf{V} = 0. \quad (1.8)$$

1.2.3 Conservation of Energy

The principle of conservation of energy states that the total energy of an isolated system stays constant over time, meaning energy cannot be created or destroyed, only transformed. This principle comes from the first law of thermodynamics, which says that the heat added to a system, dQ , equals the increase in internal energy, dE_T , plus the work done by the system, dW . Mathematically, this is expressed as:

$$\frac{dQ}{dt} = \frac{dE_T}{dt} + \frac{dW}{dt}. \quad (1.9)$$

In simple terms, this means that the rate at which heat flows into a system equals the rate of

increase in its internal energy minus the rate at which work is done by surface forces. For a viscous, incompressible fluid, the energy equation is given by (Bird et al. [2002])

$$\rho C_p \left(\frac{\partial T}{\partial t} + \mathbf{V} \cdot \nabla T \right) = k_{th} \nabla^2 T + \tau : \nabla \mathbf{V} \quad (1.10)$$

where T is the local temperature, (ρC_p) is the heat capacitance of fluid, k_{th} represents the thermal conductivity of fluid. The last term $(\tau : \nabla \mathbf{V})$ of Eq. (1.10) indicate the heat generation due to the viscous dissipation, where $\tau = \mu(\nabla \mathbf{V} + \nabla \mathbf{V}^T)$.

1.2.4 Mass Transfer Equation

Mass transfer involves the transport of a substance within a fluid as a component or species. The average velocity of each species in a mixture can be determined based on their individual velocities and densities. The steady-state mass transfer equation for a three-dimensional Cartesian coordinate system, considering a first-order reaction term, is given by (Bird et al. [2002])

$$\frac{\partial C}{\partial t} + (\mathbf{V} \cdot \nabla)C = D_B \nabla^2 C + \frac{D_T}{T} \nabla^2 T, \quad (1.11)$$

where C denotes the concentration of the fluid, D_B denotes the effective Brownian diffusion coefficient, D_T take into account the effective thermophoresis coefficient. This equation describes how the concentration of a species changes due to diffusion and reaction processes within the fluid.

1.3 Electrokinetic phenomena

Electrokinetic effects refer to the relationship between the electrical properties at the boundary between two phases (usually a liquid and a solid) and their movement relative to each other. These effects are very important in microfluidics because controlling how fluids behave precisely is really important. These effects can be classified into four types. (Karniadakis et al. [2005]):

- **Electroosmosis:** This is an interesting concept in electrokinetic theory. It explains how a liquid moves along a charged solid surface when an electric field is applied. The electric field interacts with the charges on the surface, forming an electrical double layer. Ions moving within this layer pull the surrounding liquid, causing a flow in the direction of the electric field. This phenomenon is used in many ways in microfluidics to control small amounts of fluid precisely without needing pumps. It is important for tasks like bioanalysis, drug discovery, and environmental monitoring.
- **Electrophoresis:** Charged particles, like biomolecules or colloids, suspended in a fluid migrate towards the oppositely charged electrode when an electric field is applied. This phenomenon, known as electrophoresis, allows for the separation and analysis of particles based on their size and charge, finding applications in techniques like gel electrophoresis for DNA and protein analysis.

- **Streaming potential:** When a fluid flows past a charged stationary surface, the movement of charges within the electrical double layer creates a potential difference between the bulk fluid and the surface. This phenomenon, termed streaming potential, provides insights into surface properties and fluid flow behavior in microfluidic devices and porous media.
- **Sedimentation potential:** This occurs when charged particles move vertically under gravitational or centrifugal forces within a stationary liquid. This movement creates a potential difference between particles at different positions, leading to an additional electric force.

1.3.1 Electroosmotic Flow

Electroosmotic flow (EOF) refers to the movement of ionized liquid induced by an applied electric potential across porous materials, capillary tubes, membranes, or microchannels. This phenomenon is particularly significant in small channels, where velocities remain independent of conduit size, provided the electrical double layer is much smaller than the characteristic length scale of the channel. EOF plays a crucial role in various chemical separation techniques, notably capillary electrophoresis. It can occur in natural water as well as buffered solutions. The performance of EOF devices depends on the formation of the electric double-layer (EDL) near the channel walls or electrode surfaces and the electric potential difference between the inlet and outlet of the microchannel. Unlike pressure-driven flow, EOF does not require any moving parts, making it noise-free and easy to fabricate. Moreover, it offers highly efficient and multipurpose fluid flow control, leading to a plug-like velocity profile that reduces fluid sample dispersion along the microchannel. Consequently, Electroosmotic flow is considered as a preferred method for pumping fluids in biomicrofluidic lab-on-a-chip devices.

1.3.2 Electrical double layer (EDL)

An electrical double layer (EDL) ([Karniadakis et al. \[2005\]](#)) is a very thin region near the surface of a solid where there is a net charge. It forms because charged particles stick to or detach from the surface, causing nearby ions in the liquid to rearrange. When a liquid with electrolytes touches a non-conductive wall, it causes a split in charge near the surface. This split draws ions with opposite charges (counter-ions) close to the wall and pushes ions with the same charge (co-ions) away from it. The schematic diagram (Fig. 1.1) shows how free ions are arranged near a negatively charged wall. However, the total charge distribution is less than the charge of the wall because ions move around randomly due to heat. This thin layer is called the Stern layer, but it is also called the compact layer or Helmholtz layer. Next to the Stern layer, another layer of mobile counter-ions formed which termed as diffusion layer, or Gouy-Chapman layer, in which a shear plane separates these two layers.

The EDL plays a crucial role in electrokinetic phenomena, arising from the interaction of an ionized solution with static charges on dielectric surfaces. Theoretical investigations and models have been developed to elucidate ion distribution near the channel surface. The earliest model,

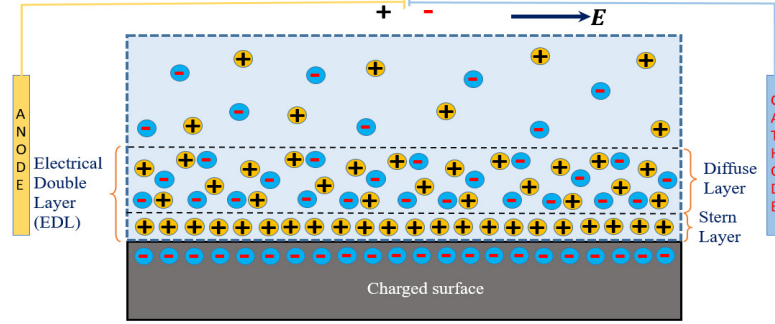


Figure 1.1: Electric double layer

the Helmholtz Double Layer model (Helmholtz [1879]), describes electrokinetic phenomena by assuming that electrically balanced counter ions are concentrated on a plane parallel to the uniformly charged surface. Gouy [1910] and Chapman [1913] expanded on this by considering the influence of the mobile layer of counter ions in the bulk fluid, leading to the Gouy-Chapman Diffuse Double Layer model. Stern [1924] made corrections to this model, proposing that the EDL consists of two layers: the Stern layer, where ions adhere tightly to the charged surface, and the Gouy-Chapman Diffuse Double layer, where ions are distributed by interparticle forces. The Stern layer is densely packed with counter ions and has a thickness roughly equivalent to one ionic diameter. The interface between fixed and mobile ions is known as the slipping plane (shear plane), and the potential at the edge of the slipping plane is termed the zeta potential (Karniadakis et al. [2005]).

1.3.3 Governing equations for electrokinetic phenomena

The characterization of ion distribution in the EDL relies on the electrokinetic potential, denoted as ψ . Due to the presence of oppositely charged ions in the Stern layer, which shield surface charges, the electrokinetic potential experiences a rapid decline across this region. At the boundary of the Stern layer, the electrokinetic potential is referred to as the zeta potential, represented by ζ . In practical scenarios, describing electrokinetic flows often involves utilizing the zeta potential rather than the wall potential, denoted as ψ_0 . The distribution of ions in the diffuse layer results in a net electric charge, expressed by the equation:

$$\nabla^2 \psi = -\frac{\rho_e}{\varepsilon}, \quad (1.12)$$

where ε is dielectric constant. The electric charge density ρ_e is determined by the equation:

$$\rho_e = \sum_i z_i e n_i \exp\left(-\frac{z_i e \psi}{k_B T_{av}}\right), \quad (1.13)$$

where n_i , e , z_i , k_B denote ion density, electronic charge, the valance, the Boltzmann constant respectively. Here T_{av} and ε represent the absolute temperature, the permittivity constant of the solution.

For sufficiently small values of $\frac{ez_i}{k_B T_{av}} \psi$, one may approximate $\sinh\left(\frac{ez_i}{k_B T_{av}} \psi\right)$ as $\frac{ez_i}{k_B T_{av}} \psi$, known as the Debye–Hückel approximation (Masliyah and Bhattacharjee [2006]). Therefore, the linearized Poisson-Boltzmann Equation (1.12) reduces to

$$\nabla^2 \psi = \kappa^2 \psi, \quad (1.14)$$

where $\kappa^{-1} = \left(\epsilon k_B T_{av} / e^2 \sum_i z_i^2 n_i\right)^{\frac{1}{2}}$ is called as Debye length.

When an external electric field is applied to an electrolyte solution, the charged particles within the electrical double layer (EDL) near the channel walls interact with this field. This interaction results in an electroosmotic force, denoted by $\rho_e \mathbf{E}$, which induces fluid motion. This motion is then transmitted to the adjacent fluid layers through viscous drag. Incorporating this electroosmotic force term into the Navier-Stokes equation yields:

$$\rho \left[\frac{\partial \mathbf{V}}{\partial t} + (\mathbf{V} \cdot \nabla) \mathbf{V} \right] = -\nabla p + \mu \nabla^2 \mathbf{V} + \rho_e \mathbf{E}. \quad (1.15)$$

1.4 Magnetohydrodynamics

Magnetohydrodynamics (MHD) is the study of how electrically conducting fluids, like plasmas, behave when there are magnetic fields around. It uses ideas from both fluid dynamics and electromagnetism to explain how these fluids work. The main equations of MHD come from rules about how mass, momentum, and energy are conserved, along with Maxwell's equations for electromagnetism. These equations are put together to make the MHD equations, which tell us how the fluid moves in presence of magnetic field. One important thing about MHD is how the fluid's movement and the magnetic field are connected. This connection leads to some big things happening, like electric currents forming in the fluid (called induction), magnetic fields forming because of moving fluids (called dynamo action), and the way magnetic fields and fluid flows interact (called magnetic reconnection).

1.4.1 Maxwell's Equations

In the context of MHD, Maxwell's equations are often combined with the MHD equations to form a complete set of equations that describe the behavior of magnetized fluids. This combined set of equations governs phenomena such as magnetic confinement in fusion plasmas, the dynamics of solar and planetary magnetospheres, and the behavior of astrophysical plasmas in stars and galaxies. Maxwell's equations, which describe the behavior of electromagnetic fields, play a crucial role in

magnetohydrodynamics (MHD). They are given by:

$$\nabla \cdot \mathbf{E} = \frac{\rho}{\epsilon_0}, \quad (1.16)$$

$$\nabla \cdot \mathbf{B} = 0, \quad (1.17)$$

$$\nabla \times \mathbf{E} = -\frac{\partial \mathbf{B}}{\partial t}, \quad (1.18)$$

$$\nabla \times \mathbf{B} = \mu_0 \mathbf{J} + \mu_0 \epsilon_0 \frac{\partial \mathbf{E}}{\partial t}, \quad (1.19)$$

where \mathbf{E} is the electric field, \mathbf{B} is the magnetic field, ρ is the charge density, ϵ_0 is the permittivity of free space, μ_0 is the permeability of free space, and \mathbf{J} is the current density.

1.4.2 Electromagnetohydrodynamic flow

Electromagnetohydrodynamics (EMHD) is a combination electroosmosis and magnetohydrodynamics (MHD), in which both of the electric field and magnetic field are applied. So, Electromagnetohydrodynamic flow or EMHD flow is the motion of liquid induced by a combined effect of applied electric field and magnetic field. In EMHD flow is happened due to the Lorentz force and the electroosmotic force, where the interaction between the induced magnetic field and applied electric field makes a continuous flow.

The electromagnetohydrodynamic (EMHD) body force, denoted as \mathbf{F} , is a critical component in understanding the dynamics of EMHD flows. It comprises two main forces: the electroosmotic body force, represented by $(\rho_e \mathbf{E})$, and the Lorentz force, represented by $\mathbf{J} \times \mathbf{B}$. Therefore, one can write

$$\mathbf{F} = \rho_e \mathbf{E} + \mathbf{J} \times \mathbf{B}. \quad (1.20)$$

Regarding the electroosmotic force $(\rho_e \mathbf{E})$, which was previously discussed, the last term of Eq. (1.20) signifies the Lorentz force. This force emerges from the interaction between fluid flow and an externally applied magnetic field. The expression for the current density is given by $\mathbf{J} = \sigma_e (\mathbf{E} + \mathbf{V} \times \mathbf{B})$, where σ_e represents the electrical conductivity of the medium.

1.5 Rotationally Actuated Microflows

Microflows can be controlled using spinning forces like centrifugal and Coriolis forces on a spinning disc that has tiny fluid networks. This method, often called CD-based microfluidics because it looks like Compact Discs (CDs), is getting attention because it is really useful for bio-microfluidic analysis. Using the benefits of being portable and doing quick analysis, CD-based microfluidics is a cheap way to do chemical analysis and biomedical diagnostics. It is good at dealing with different types of samples, controlling how fluids move, and doing lots of fluidic tasks at the same time. Even though the spinning forces get stronger as the size increases, CD-based microfluidics is still a popular way to do lots of tests at once.

1.5.1 Governing equations for flow in rotating frame

The momentum conservation in rotating frame is expressed by the modified Navier-Stokes equation

$$\rho \left[\frac{\partial \mathbf{V}}{\partial t} + (\mathbf{V} \cdot \nabla) \mathbf{V} + 2\boldsymbol{\Omega} \times \mathbf{V} \right] = -\nabla \tilde{p} + \mu \nabla^2 \mathbf{V} + \mathbf{F}, \quad (1.21)$$

where ρ , μ and \mathbf{V} respectively denote the density, viscosity, and velocity vector and $\boldsymbol{\Omega}$ denotes the angular velocity due to the rotation of the system. Here the term $2\boldsymbol{\Omega} \times \mathbf{V}$ is defined as coriolis force due to the rotation of the system, $\tilde{p} = p - \frac{\rho}{2} |\boldsymbol{\Omega} \times \mathbf{r}|^2$ is denoted by the modified pressure due to the centrifugal force in the rotating channel and \mathbf{F} is the body force.

1.6 Introduction to Porous Media

A porous material has tiny holes called pores, with the solid part often called the matrix. The matrix is either stiff or slightly bent. If the matrix is stiff, it is called a stiff porous material. If it can bend, it is called a bendable porous material. The holes let fluids flow through, either one kind of fluid or many. Natural porous materials, like beach sand, wood, or the human lung, have holes scattered in different ways. At the tiny level, the flow changes a lot in where it goes and when. To make sense of this, we need to measure a big area with lots of holes (macroscopic scale) to see how the flow changes over space and time.

1.6.1 Porosity and Permeability

The porosity of a porous medium refers to the extent to which pores or spaces exist within the solid. Very often, porosity is defined as the ratio of the volume occupied by the void space to that of the total volume. If ϕ_p is the porosity of a porous medium, then $(1 - \phi_p)$ is the fraction that is occupied by the matrix. For natural porous media, the porosity does not exceed 0.6.

Permeability is the measure of the ease at which a fluid can penetrate inside a porous medium. Generally, higher porosity amounts to high permeability. However, if the pores are not well connected, then even though the porosity is large, permeability may be very low.

For the case of granular or fibrous porous medium, if the grain diameter is D_p , then the Carman-Kozney hydraulic radius theory leads to the relationship (Nield and Bejan [2006]):

$$K = \frac{D_p^2 \phi_p^3}{180(1 - \phi_p)^2}, \quad (1.22)$$

where ϕ_p is the porosity and K is the permeability of the porous medium.

1.6.1.1 Darcy's Equation

The Darcy equation, formulated by Henry Darcy based on his experiments on water flow through sand beds, describes flow through a porous medium (Darcy [1856]). It is an empirical relationship

that correlates the pressure gradient with the flow velocity. This equation is expressed as:

$$\nabla p = -\mu K^{-1} \mathbf{V}, \quad (1.23)$$

where μ is the dynamic viscosity of the fluid, ∇p denotes the pressure gradient in the flow direction. K is the permeability of the porous medium, which may be a scalar or a tensor depending on the properties of the porous medium. For an isotropic porous medium, K is a scalar, while for an anisotropic porous medium, it is a tensor. For a three-dimensional situation, permeability is a third-order symmetric matrix given by (Nield and Bejan [2006]):

$$K = \begin{pmatrix} K_{xx} & K_{xy} & K_{xz} \\ K_{xy} & K_{yy} & K_{yz} \\ K_{xz} & K_{yz} & K_{zz} \end{pmatrix}. \quad (1.24)$$

Here, K_{ij} refers to the permeability along the i -th plane and j -th direction.

1.6.2 Anisotropic porous media

Anisotropic porous media have different properties in different directions, unlike isotropic materials, which have the same properties in all directions. For example, wood splits more easily along its grain because of its anisotropic properties. In porous materials, isotropic porous media have the same permeability in all directions, while anisotropic porous media have different permeability in different directions. Heterogeneous porous media have permeability that varies with position, while homogeneous porous media have uniform permeability. Anisotropy in porous media can arise from arbitrary pore distribution in granular media or fiber orientation in fibrous media. Anisotropic porous materials include stratified rocks, seabeds, solidifying alloys, glass wool, the human lung, and articular cartilage.

Various systems in industry and nature can be modeled as anisotropic porous media, where permeability depends on microstructure. The orientation of fibers creates anisotropic networks, leading to different permeability for porous media with the same porosity. Industrial materials like those used in filtration systems often exhibit anisotropic properties. For example, flow across an assembly of circular cylinders demonstrates anisotropic porous behavior, while flow across a regular assembly of spheres is isotropic. The orientation of cylinders can affect permeability, with horizontally oriented cylinders having different permeability in the horizontal and vertical directions. In contrast, the orientation of spheres does not affect permeability, allowing flow in all directions equally. In granular or stratified media, permeability varies only along principal axes, but in fibrous media, fiber orientation creates anisotropy.

Consider a channel blocked by an arrangement of circular cylinders, allowing flow through the gaps between them. If the cylinders are staggered and tilted at an angle φ to the horizontal direction, we simplify the flow to be horizontal. Let K_1 and K_2 represent the permeabilities parallel and perpendicular to the cylinders, respectively. This flow scenario is analogous to a porous medium where the principal axis with permeability K_2 is inclined at an angle φ to the horizontal direction.

The corresponding permeability matrix K in two dimensions is given by (Degan et al. [2002]):

$$\begin{aligned} K &= \begin{pmatrix} \cos \varphi & -\sin \varphi \\ \sin \varphi & \cos \varphi \end{pmatrix} \begin{pmatrix} K_2 & 0 \\ 0 & K_1 \end{pmatrix} \begin{pmatrix} \cos \varphi & \sin \varphi \\ -\sin \varphi & \cos \varphi \end{pmatrix} \\ &= \begin{pmatrix} K_2 \cos^2 \varphi + K_1 \sin^2 \varphi & (K_2 - K_1) \sin \varphi \cos \varphi \\ (K_2 - K_1) \sin \varphi \cos \varphi & K_1 \cos^2 \varphi + K_2 \sin^2 \varphi \end{pmatrix}. \end{aligned} \quad (1.25)$$

Here, φ represents the anisotropic angle. The ratio K_1/K_2 (or K_2/K_1) is known as the anisotropic ratio. For an isotropic porous medium, $K_1 = K_2$, resulting in an anisotropic ratio of 1. Therefore the distinction between isotropic and anisotropic porous media lies in the uniformity or variability of their permeability properties with direction. Isotropic media have uniform permeability in all directions, while anisotropic media exhibit directional variability in permeability.

1.7 Heat Transfer

In microfluidics, heat transfer primarily occurs through conduction, especially across the membranes and walls of microchannels. Due to the small scale, microfluidic systems exhibit unique heat transfer characteristics compared to macroscale systems.

Heat transfer in microfluidics finds applications in diverse fields. For example, precise temperature control is essential for reactions or sample preparation in lab-on-a-chip devices. Microfluidic heat exchangers enable efficient heat exchange between fluids with minimal mixing, proper for thermal management in electronics cooling or microreactors. In drug delivery systems, precise temperature control is crucial for maintaining the effectiveness of certain drugs.

In microfluidics, heat transfer is significantly influenced by surface roughness. The roughness elements, such as microfine or ribs, within microchannels can enhance heat transfer by promoting turbulence and increasing the surface area available for heat exchange. This can lead to more efficient heat transfer and improved thermal performance in microfluidic devices. Additionally, the shape and arrangement of these roughness elements can further impact heat transfer and friction characteristics, highlighting the importance of careful design considerations in microfluidic heat transfer applications.

1.7.1 Temperature distribution in Electromagnetic Scenarios

The governing equation for temperature distribution including the heat generation due to electromagnetic interaction, joule heating and viscous dissipation can be expressed as

$$\rho C_p \left(\frac{\partial T}{\partial t} + \mathbf{V} \cdot \nabla T \right) = k_{th} \nabla^2 T + \Phi + \frac{1}{\sigma_e} \mathbf{J} \cdot \mathbf{J}, \quad (1.26)$$

where T is the local temperature, (ρC_p) is the heat capacitance of fluid, k_{th} represents the thermal conductivity of fluid. The last two terms Φ and $\frac{1}{\sigma_e} \mathbf{J} \cdot \mathbf{J}$ of Eq. (1.26) indicate respectively the heat generation due to the viscous dissipation and electromagnetic interaction due to joule heating effect.

1.7.1.1 Viscous dissipation

The dissipation function is calculated from $\Phi = \tau : \nabla \mathbf{V}$, where $\tau = \mu_{eff}(\nabla \mathbf{V} + \nabla \mathbf{V}^T)$. For Newtonian fluid, it can be expressed as (Winter [1977])

$$\Phi = \mu_{eff} \left[2 \left(\frac{\partial u}{\partial x} \right)^2 + 2 \left(\frac{\partial v}{\partial y} \right)^2 + 2 \left(\frac{\partial w}{\partial z} \right)^2 + \left(\frac{\partial u}{\partial y} + \frac{\partial v}{\partial x} \right)^2 + \left(\frac{\partial u}{\partial z} + \frac{\partial w}{\partial x} \right)^2 + \left(\frac{\partial v}{\partial z} + \frac{\partial w}{\partial y} \right)^2 \right]. \quad (1.27)$$

When fluid flow in a porous medium adheres to Darcy's law, the heat-source term modeling viscous dissipation in the thermal energy equation is precisely described by Eq. (1.26). However, this equation is applicable only under conditions where the flow is primarily unidirectional or predominantly in a single direction, such as in boundary-layer flows. For a more comprehensive description, the complete expression for Φ can be expressed as (Nield and Bejan [1999])

$$\Phi = \frac{\mu}{K}(u^2 + v^2 + w^2). \quad (1.28)$$

When the microscopic Reynolds number exceeds approximately unity, the momentum equation typically includes an additional quadratic nonlinear term, known as the Forchheimer term, to account for form drag within the medium. Initially, it was believed that form drag did not impact viscous dissipation, as the coefficient of $|v|v$, represented by $c_f \rho K^{-1/2}$, does not include viscosity (Nield and Bejan [1999]). However, Nield [2002] proposed, using the drag force concept, that the term Φ should be written as

$$\Phi = \frac{\mu}{K} \mathbf{v} \cdot \mathbf{v} + c_f \rho \frac{K^{1/2}}{|v|} \mathbf{v} \cdot \mathbf{v} \quad (1.29)$$

While the expression for Φ provided by Eq. (1.29) is generally accepted for Darcy–Forchheimer flow, it may not be suitable for situations where boundary effects, represented by the Brinkman terms, play a significant role. The formulation by Nield [2002] based on drag force leads to the expression for Φ as

$$\Phi = \frac{\mu}{K} \mathbf{v} \cdot \mathbf{v} - \mu_{eff} \mathbf{v} \cdot \nabla^2 \mathbf{v} \quad (1.30)$$

where μ_{eff} is an effective viscosity, while Al-Hadhrami et al. [2003] use an argument based on the work done by frictional forces to obtain,

$$\Phi = \frac{\mu}{K}(u^2 + v^2 + w^2) + \mu_{eff} \left[2 \left(\frac{\partial u}{\partial x} \right)^2 + 2 \left(\frac{\partial v}{\partial y} \right)^2 + 2 \left(\frac{\partial w}{\partial z} \right)^2 + \left(\frac{\partial u}{\partial y} + \frac{\partial v}{\partial x} \right)^2 + \left(\frac{\partial u}{\partial z} + \frac{\partial w}{\partial x} \right)^2 + \left(\frac{\partial v}{\partial z} + \frac{\partial w}{\partial y} \right)^2 \right]. \quad (1.31)$$

Both formulations yield the correct form for Φ in the limit of small permeability. However, as the porosity approaches unity, only the formula proposed by Al-Hadhrami et al. [2003] matches that for a clear fluid.

1.7.1.2 Joule heating

Joule heating in microfluidics is a critical consideration due to its potential impact on device performance. This phenomenon occurs when electrical energy is converted into thermal energy, leading to temperature increases within the microfluidic channels. The rate of heat generation, Q_j , is governed by the formula $Q_j = \frac{1}{\sigma_e} \mathbf{J} \cdot \mathbf{J}$, where σ_e represents the electrical conductivity of the fluid and \mathbf{J} is the current density.

For cartesian co-ordinate system, the heat generation due to the joule heating can be expressed as

$$Q_j = \sigma_e \left\{ E_x^2 + E_y^2 + E_z^2 + u^2 B_x^2 + v^2 B_y^2 + w^2 B_z^2 - 2(uv B_x B_y + uw B_x B_z + vw B_y B_z) \right\}, \quad (1.32)$$

where u , v and w represent the velocity components along the coordinate axes. E_x , E_y , E_z denote the electric field components and B_x , B_y and B_z stand for the magnetic field components along the same axes.

Joule heating can have several consequences, including changes in fluid viscosity, bubble formation, and potential degradation of biomolecules. To mitigate these effects, designers can employ various strategies such as using lower conductivity buffer solutions, optimizing channel geometries to enhance heat dissipation, and utilizing pulsed electric fields instead of continuous operation. Understanding the relationship between electrical conductivity, electric field strength, and heat generation is crucial for designing microfluidic devices that minimize Joule heating and maximize performance.

1.8 Entropy generation

Entropy generation is crucial in engineering heat transfer processes because it indicates the loss of energy quality during a real process. While the first law of thermodynamics ensures energy conservation, the second law states that energy quality always decreases, measured by entropy. Minimizing entropy generation is essential to maintain energy quality in fluid flow problems. Understanding how entropy generation is distributed within a flow volume is key to improving system performance. The second law of thermodynamics links the irreversibility of a thermal engineering process to the amount of useful work lost. Analyzing the second law involves determining the rate of entropy generation and using entropy minimization techniques to understand irreversibilities in heat and mass transport processes.

The local volumetric rate of entropy generation, denoted as E_{gen} , is mathematically described as (Bejan and Kestin [1983])

$$E_{\text{gen}} = \frac{1}{T} \boldsymbol{\tau} \cdot \nabla \mathbf{V} + \frac{k_{th}}{T^2} (\nabla T)^2, \quad (1.33)$$

where T is the temperature of the medium, k is the thermal conductivity, μ is the viscosity of the fluid and $\boldsymbol{\tau} = \mu(\nabla \mathbf{V} + \nabla \mathbf{V}^T)$. Each term in Eq. (1.33) represents a specific source of entropy generation, with the first term describing entropy production due to irreversibility associated with

viscous dissipation and the second term expressing the entropy production due to heat transfer.

For a flow under electromagnetic environment, the entropy generation rate per unit volume is given by

$$E_{\text{gen}} = \frac{1}{T} \boldsymbol{\tau} \cdot \nabla \mathbf{V} + \frac{k_{th}}{T^2} (\nabla T)^2 + \frac{1}{\sigma_e T} \mathbf{J} \cdot \mathbf{J}, \quad (1.34)$$

where the last term indicates the Joule heating irreversibility.

In the case of Newtonian fluid under electromagnetic environment, the local volumetric entropy generation is expressed as

$$\begin{aligned} E_{\text{gen}} = \frac{\mu}{T} & \left[\left(\frac{\partial u}{\partial y} + \frac{\partial v}{\partial x} \right)^2 + \left(\frac{\partial u}{\partial z} + \frac{\partial w}{\partial x} \right)^2 + \left(\frac{\partial v}{\partial z} + \frac{\partial w}{\partial y} \right)^2 \right. \\ & \left. + 2 \left\{ \left(\frac{\partial u}{\partial x} \right)^2 + \left(\frac{\partial v}{\partial y} \right)^2 + \left(\frac{\partial w}{\partial z} \right)^2 \right\} \right] \\ & + \frac{k_{th}}{T^2} \left\{ \left(\frac{\partial T}{\partial x} \right)^2 + \left(\frac{\partial T}{\partial y} \right)^2 + \left(\frac{\partial T}{\partial z} \right)^2 \right\} \\ & + \frac{\sigma_e}{T} \left\{ E_x^2 + E_y^2 + E_z^2 + u^2 B_x^2 + v^2 B_y^2 + w^2 B_z^2 \right. \\ & \left. - 2(uv B_x B_y + uw B_x B_z + vw B_y B_z) \right\}, \end{aligned} \quad (1.35)$$

where u , v and w represent the velocity components along the coordinate axes. E_x , E_y , E_z denote the electric field components and B_x , B_y and B_z stand for the magnetic field components along the same axes.

1.9 Boundary conditions

Boundary conditions are crucial in fluid flow problems because they define the interactions between the fluid and its surroundings at the domain's edges. These conditions determine how the fluid behaves at the boundaries, influencing the overall flow pattern and solution. For example, at a solid boundary, the condition might specify the velocity of fluid, affecting how it flows past the boundary. Similarly, at the interface between two fluids, the condition could describe how momentum is transferred between them. Boundary conditions can also capture important physical phenomena like heat transfer, mass transfer, and chemical reactions at the boundaries. They are essential for accurately simulating complex flow behaviors such as boundary layer formation, separation, and recirculation zones.

1.9.1 Boundary conditions for the electroosmotic flow

1.9.1.1 Slip boundary condition

In channel flow, slip velocity refers to the phenomenon where a thin layer of fluid adjacent to the channel wall exhibits a different velocity compared to the bulk flow in the center of the channel.

While often neglected in macroscopic flows, slip velocity becomes significant in microfluidic applications where channel dimensions are on the order of micrometers. In these regimes, the ratio of surface area to volume becomes large, and the behavior of the fluid near the wall becomes more influential. Accounting for slip velocity in microfluidic design and analysis is crucial for accurate predictions of flow behavior. The velocity slip boundary conditions at the fluid-solid interface is defined as

$$\mathbf{V} + \beta \nabla \mathbf{V} \cdot \hat{n} = 0, \quad (1.36)$$

where β is called the slip length. This condition is also known as Rabin's boundary conditions. If $\beta = 0$, then the boundary condition reduces to the Dirichlet boundary condition $\mathbf{V} = 0$, which is known as the no-slip boundary condition.

1.9.1.2 Fluid-fluid interfacial boundary conditions for two immiscible electrolytes

At the boundary between two immiscible electrolytes, unique conditions arise due to the interaction of electrical and interfacial phenomena. These conditions are important for understanding and modeling mass and charge transport across this boundary, often referred to as the interface between two immiscible electrolyte solutions.

The fluid-fluid interfacial boundary conditions are defined as

$$\mathbf{V}_1 = \mathbf{V}_2, \quad (1.37)$$

$$-\mu_1 \nabla \mathbf{V}_1 \cdot \hat{n}_1 + \varepsilon_1 \mathbf{E} \nabla \psi_1 \cdot \hat{n}_1 = -\mu_2 \nabla \mathbf{V}_2 \cdot \hat{n}_2 + \varepsilon_2 \mathbf{E} \nabla \psi_2 \cdot \hat{n}_2, \quad (1.38)$$

Here subscript 1 and 2 indicate the fluid-1 and fluid-2.

1.9.2 Boundary conditions for the electrostatic potential

1.9.2.1 Fluid-solid interfacial boundary condition

In the context of a charged surface in an electrolyte solution, the zeta potential (ζ_w) defines the boundary condition for the electrostatic potential (ψ). Zeta potential is the electrical potential difference between the shear plane and the bulk electrolyte solution, indicating the strength of electrical repulsion between the charged surface and ions in the electrolyte. It influences the thickness and structure of the electrical double layer (EDL). In this case, the boundary condition is expressed as:

$$\psi = \zeta_w, \quad (1.39)$$

where ζ_w is the constant zeta potential or variable zeta potential which depends on surface roughness.

1.9.2.2 Interfacial potential jump condition

The electric double layer (EDL) potential (ψ), may exhibit a jump at the interface. Although the overall potential must remain continuous, a slight jump in the EDL potential can occur due to factors such as surface charge densities and ion specificity. This behavior can be described by the following Choi et al. [2011]:

$$\psi_2 - \psi_1 = \delta_\zeta, \quad (1.40)$$

where δ_ζ denotes the zeta potential difference at the interface of two fluids. Here subscript 1 and 2 indicate the fluid-1 and fluid-2.

1.9.2.3 Charge Neutrality condition at fluid-fluid interface

In systems with two immiscible electrolytes, the discontinuity of ionic flux boundary condition refers to the abrupt change in the flow of ions at the interface between the two electrolytes. This phenomenon is crucial for understanding the behavior of ions near interfaces and has significant implications for various fields, including electrochemistry, microfluidics, and colloid science. The forces acting on ions differ between the EDLs and the bulk. In the EDLs, electrical attraction from the opposing surface significantly influences ion movement, while in the bulk, the main driving force is the bulk flow of the electrolyte solution. The following boundary conditions for potential distribution are introduced at the fluid-fluid interface (Choi et al. [2011]):

$$\varepsilon_1 \nabla \psi_1 \cdot \hat{n}_1 - \varepsilon_2 \nabla \psi_2 \cdot \hat{n}_2 = -Q_d, \quad (1.41)$$

where Q_d , and δ_ζ respectively denote the charge jump and zeta potential difference at the interface of two fluids. Here subscript 1 and 2 indicate the fluid-1 and fluid-2.

1.9.3 Boundary conditions for temperature distribution

In fluid mechanics, temperature slip boundary conditions describe the behavior of temperature at the interface between a solid wall and a flowing fluid. Unlike the no-slip condition, which assumes zero velocity at the wall, temperature slip acknowledges that the fluid temperature might not be identical to the wall temperature.

The temperature slip boundary condition can be expressed mathematically using the following equation:

$$T + \tau_s \nabla T = T_w, \quad (1.42)$$

where τ_s is the teperature slip length, T_w stands for the wall temperature.

1.10 Microchannel roughness and applications in microfluidics

Electroosmotic flow is commonly used in microfluidic devices, soil analysis, and chemical analysis, often involving systems with highly charged oxide surfaces. One example is capillary electrophore-

sis, where electric fields separate chemicals based on their electrophoretic mobility by applying an electric field to a narrow silica capillary. In electrophoretic separations, electroosmotic flow affects the elution time of the analytes.

Microfluidic devices using electroosmotic flow are expected to have significant applications in medical research. Once we better understand and control this flow, separating fluids at the atomic level will become crucial for drug delivery systems. Currently, mixing fluids at the microscale is challenging. It is believed that electrically controlling fluids can be used for mixing small fluid volumes.

Electromagnetohydrodynamic (EMHD) microdevices are widely used to create small-scale systems in modern science and technology. They play an essential role in many scientific devices involved in heat and mass transfer. EMHD microdevices are used in various fields, including chemical transport, biomedical devices, lab-on-chip devices, EMHD micropumps, sample separation, magnetohydrodynamic (MHD) micropumps, heat transfer in micro-electro-mechanical systems (MEMS), and thermal transport in micro-electronic devices.

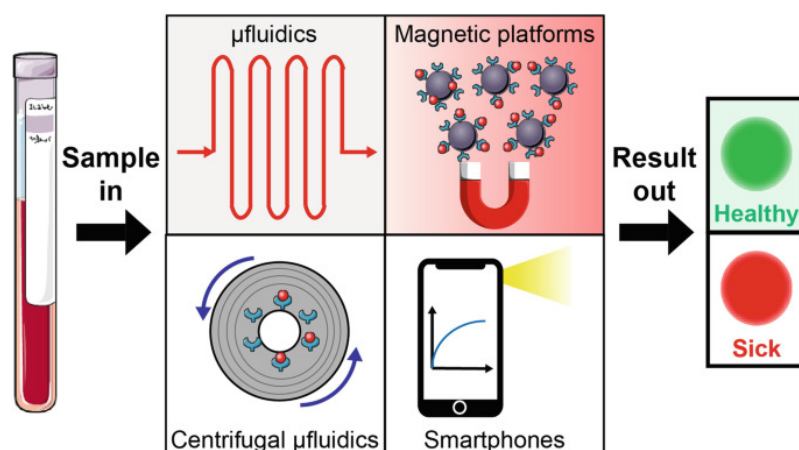


Figure 1.2: Lab-on-a-chip (Arshavsky-Graham and Segal [2020])

1.10.1 Lab-on-a-chip technology

Lab-on-a-chip (LOC) technology offers several advantages by scaling down laboratory setups to the microscale. One major benefit is the significant reduction in sample volume required, enabling fast analysis and efficient detection even with minimal sample amounts. Additionally, the small volumes allow for the development of compact and portable systems, making bio/chemical handling and analysis more convenient. Mass production of LOC systems also promises to make them very affordable. LOC systems extend the concepts of electronic integrated circuits and microelectromechanical systems (MEMS) into biology and chemistry. These systems can integrate optical, chemical, and electronic components, effectively miniaturizing an entire laboratory onto a chip. LOC technology has potential applications in biotechnology, pharmacology, medical diagnostics, forensics, environmental monitoring, and basic research. While the fundamental laws of physics

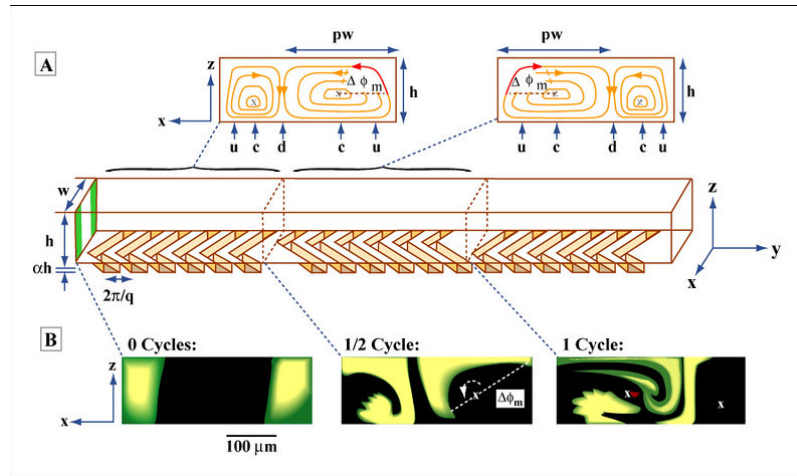


Figure 1.3: An illustrative example of Mixing (Stroock et al. [2002])

governing LOC systems are well understood, the interplay of different forces and their relative importance change as we move from macro- to micro- and nanosystems, presenting new challenges and opportunities in microfluidics.

1.10.2 Mixing and Separation process

In microfluidics, mixing and separation processes are crucial for applications like chemical analysis, drug delivery, and biological assays. Due to the small length scales and low Reynolds numbers in microchannels, conventional methods like diffusion are slow and inefficient. Microfluidic devices use techniques such as chaotic advection, flow focusing, and passive mixing structures to improve mixing efficiency. For separation, they utilize principles like electrophoresis, chromatography, and filtration in miniaturized formats to achieve rapid and efficient component separation in a sample.

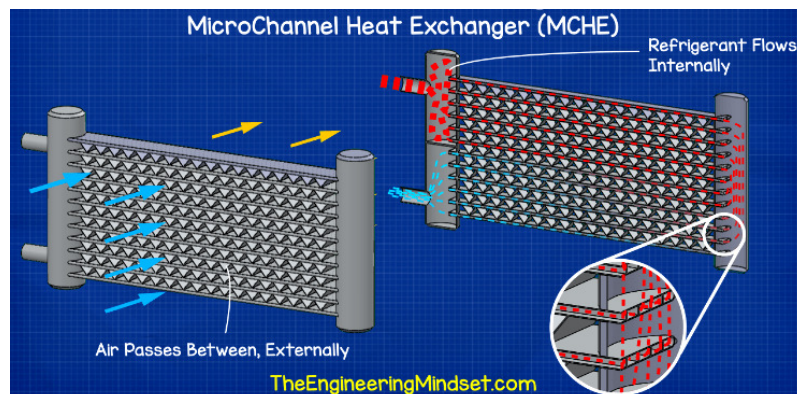


Figure 1.4: A typical example of Micro-heat exchanger
(<https://theengineeringmindset.com/hvac-heat-exchangers-explained/>)

1.10.3 Micro-heat Exchangers

Micro-heat exchangers are designed to efficiently transfer heat between two fluids in microscale devices. These exchangers are essential for thermal management in microfluidic systems, where heat dissipation and temperature control are critical for device performance. Micro-heat exchangers use techniques like microchannels with enhanced surface area, microfabricated fins, and integrated temperature control mechanisms to achieve efficient heat transfer in a compact form.

1.10.4 Microreactors

Microreactors, also known as microreactor systems or microchemical systems, are devices that enable chemical reactions to occur in a controlled and efficient manner on a microscale. These devices offer advantages such as improved reaction kinetics, enhanced heat and mass transfer, and reduced reaction volumes compared to traditional batch reactors. Microreactors find applications in organic synthesis, pharmaceutical manufacturing, and chemical analysis, where precise control over reaction conditions and rapid reaction times are crucial.

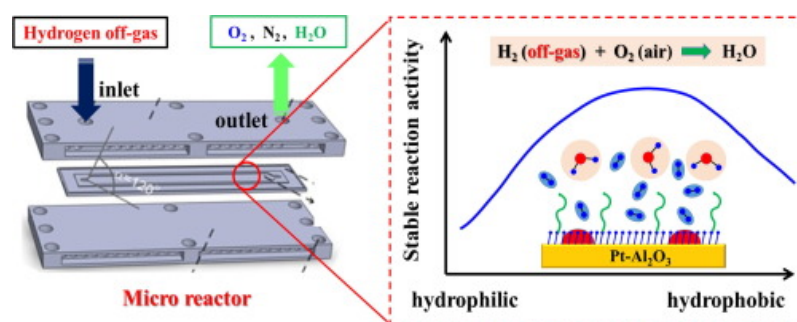


Figure 1.5: An example of Micro-reactor (Yu et al. [2017])

1.10.5 Micropumps

Micropumps are miniature devices used to generate fluid flow in microfluidic systems. These pumps are essential for controlling the movement of fluids in microchannels for various applications, including drug delivery, chemical analysis, and lab-on-a-chip systems. Micropumps can be based on different principles, such as electroosmosis, piezoelectric actuation, and membrane deformation, providing options for tailored pumping solutions based on the specific requirements of the application.

1.11 Brief review of existing literatures

The study of electroosmotic flow and heat transfer has gained increasing interest among researchers due to its relevance in biological processes and potential applications in industrial processes, medical diagnostics, and lab-on-chip technologies. In practical microchannels, surface roughness is unavoidable due to manufacturing limitations. Therefore, understanding electroosmotic flow through rough surfaces has become a significant focus in the literature. Numerous theoretical and experimental studies have been conducted to elucidate the transport phenomena associated with electrokinetic effects. The pioneering experiments of [Reuss \[1809\]](#) marked the beginning of investigations into electroosmotic flow, laying the foundation for subsequent research in this field. [Helmholtz \[1879\]](#) introduced the concept of electrical double layers formed at the interface between a charged metal surface and an electrolyte solution, providing insights into flow velocities under the electrokinetic effect in capillary tubes. [Smoluchowski \[1921\]](#) further developed the work of [Helmholtz \[1879\]](#) to investigate the speed of electroosmotic flow. [Gouy \[1910\]](#) and [Chapman \[1913\]](#) contributed by introducing diffusive double layers on flat surfaces, where ions accumulate according to the Boltzmann distribution, extending outwards from the solid surface. [Stern \[1924\]](#) later proposed a model that integrated Helmholtz's and Gouy-Chapman's diffusive layers at the solid-fluid interface.

Magnetohydrodynamic (MHD) flow, which describes the behavior of electrically conducting fluids under external magnetic fields, has attracted significant attention across various disciplines. Researchers have investigated a wide range of MHD flow phenomena, including mixed convection, electroosmotic flow, and heat transfer, in microchannels and other microfluidic systems ([Abdulahameed et al. \[2019\]](#); [Wang et al. \[2020\]](#); [Rashid and Nadeem \[2019\]](#); [Buren et al. \[2017\]](#); [Li et al. \[2019\]](#); [Ranjit and Shit \[2017\]](#)). For instance, [Sarkar et al. \[2016\]](#) studied hydro-electric energy conversion in EMHD flow through microchannels, aiming to optimize energy transfer in microfluidic systems. They presented analytical and numerical results to assess energy transfer in microscale systems. [Yang et al. \[2019\]](#) analyzed MHD electroosmotic flow and heat transfer in microchannels, considering factors such as viscous dissipation, Joule heating, and heat generation due to electromagnetic forces. They solved the governing equations using the method of separation of variables. [Rashid and Nadeem \[2019\]](#) developed a mathematical model to investigate the impact of nanoparticles on EMHD flow through corrugated microchannels using the perturbation method. They discussed how wall waviness affects velocity and temperature distributions, noting that an increase in wave number enhances corrugation and alters flow characteristics. [Noreen et al. \[2021\]](#) studied entropy generation in EMHD flow through porous asymmetric microchannels using water-based nanofluids, considering applications in nano-medicine technology. [Buren et al. \[2017\]](#) examined the effect of combined EMHD flow in a corrugated microchannel, observing that wall roughness reduces mean velocity. [Li et al. \[2019\]](#) investigated three-dimensional surface corrugations on EMHD flow, finding that flow rate can be maximized by increasing the strength of the magnetic field. [Ranjit and Shit \[2017\]](#) estimated entropy generation of a couple stress fluid in a narrow confinement with asymmetric porous surfaces, aiming to develop microfluidic devices for

biomedical and industrial applications.

In electromagnetohydrodynamic (EMHD) micropumps, flow is driven by the Lorentz force resulting from the interaction between magnetic and electric fields, enabling continuous flow in the pump. This research contributes to the development of devices such as micro coolers and addresses complex flow phenomena in fluidic networks, mixing, and stirring (Bau et al. [2001]; Shojaeian and Shojaeian [2012]; Bau et al. [2003]; Gao et al. [2005]; Gleeson et al. [2004]). EMHD flow in microchannels has been extensively studied by researchers, with various theoretical and experimental investigations conducted (Das et al. [2012]; Sinha and Shit [2015]; Sarkar et al. [2017b]; Wang et al. [2016]; Sarkar et al. [2017a]; Vargas et al. [2017]; Xie and Jian [2017]; Sarkar et al. [2016]). Chakraborty and Paul [2006] studied EMHD flow in parallel plate microchannels and further, Chakraborty et al. [2013] analyzed thermo-fluidic transport phenomena. Liu et al. [2018] analyzed EMHD flow through a curved rectangular microchannel, discussing analytical solutions for velocity and entropy generation rate. Researchers have also studied EMHD flow with different fluids, including Newtonian and non-Newtonian fluids, as working fluids in microchannels. Liu and Jian [2019] investigated the electroviscous effects on EMHD flow of Maxwell fluids in microchannels, discussing flow transport characteristics influenced by streaming potential and electroviscous effects. Zhao et al. [2017] examined thermal transport of nanofluids in parallel plate microchannels, considering the influence of electromagnetohydrodynamic effects.

The study of flow transport and heat transfer in rough microchannels has garnered significant attention due to its relevance in cooling systems, computational biology, and other applications (Yang and Liu [2008]; Hitt and McGarry [2004]; Hadigol et al. [2011]; Shit et al. [2016b]; Yang et al. [2021]; Shit et al. [2016c]; Vasista et al. [2021]; Jimenez et al. [2019]; Deng et al. [2021]). Cakir and Akturk [2021] investigated heat transfer characteristics of nanofluids in wavy microchannels computationally, analyzing thermal conductivity efficiency and convective heat transfer coefficients for different Reynolds numbers and nanoparticle ratios. Tiwari and Moharana [2021] conducted a three-dimensional numerical investigation of two-phase boiling flow in wavy microchannels, comparing boiling instability and bubble behavior in single and two-phase flow in straight and wavy microchannels. Saleem et al. [2021] proposed a mathematical model for peristaltic electroosmotic flow of micropolar Bingham viscoplastic fluid using lubrication theory, noting changes in flow characteristics with varying electric field strength. The study of roughness in microfabricated surfaces is crucial, as it can impact friction, wear, and overall efficiency (Kang and Suh [2009]; Cho et al. [2013]; Keramati et al. [2016]). Tripathi et al. [2018] analyzed electroosmotic flow transport of nanofluids in a complex wavy microchannel, observing significant impacts on flow patterns. Banerjee and Nayak [2019] investigated isothermal micromixing in a wavy patterned microchannel, revealing enhanced mixing compared to straight channel flow. Asghar et al. [2020] discussed the collective self-propulsion of unicellular organisms in non-Newtonian fluids, showcasing the resistance of microorganisms to movement in non-Newtonian fluids. Reza et al. [2021] analyzed thermal characteristics in a porous microchannel with a rough wall under combined EMHD effect, revealing effects on velocity and temperature profiles. Gao et al. [2023] proposed a numerical model to investigate thermal performance in a microchannel heat sink with secondary branches, showing

enhanced mixing efficiency and thermal performance.

The presence of secondary velocity in a rotating system plays an important role in achieving efficient mixing, especially in microfluidic devices. This enhanced mixing capability is valuable for various processes that require effective blending of reactants, sample preparation, or analysis in microscale systems. The secondary velocity-driven mixing mechanism in a rotating system offers a promising solution to achieve rapid and uniform mixing in microfluidic devices ([Leung and Ren \[2014\]](#); [Verma and Kumaran \[2013\]](#); [Jalali et al. \[2015\]](#)). [Chang and Wang \[2011\]](#) were the first to demonstrate the existence of secondary velocities theoretically. Subsequently, the effect of rotation on fluidic systems has been extensively investigated through theoretical and numerical studies, focusing on understanding how rotation influences flow behavior and leads to the generation of secondary velocities ([Takashima \[1976\]](#); [Ruo et al. \[2010\]](#); [Othman \[2004\]](#)). Additionally, researchers have explored the use of electro-osmotic force to enhance the velocities of non-Newtonian fluids in rotational microflows, offering potential advantages for various applications by improving fluid mixing, transport, and manipulation in microscale systems ([Ng and Qi \[2015\]](#); [Xie and Jian \[2014\]](#)). A comprehensive investigation into transient electroosmotic flow dynamics has been conducted by [Gheshlaghi et al. \[2016\]](#), revealing the oscillatory behavior exhibited by flow velocity. [Sun et al. \[2019\]](#) focused on analyzing thermal transport through a rectangular microchannel with a rotating environment under fully-developed electroosmotic flow, offering insights for designing energy-efficient micro-systems. The impact of slip on the behavior of rotating electroosmotic flow in a non-uniform micro-channel was investigated by [Shit et al. \[2016a\]](#), highlighting the significance of slip velocity in reducing effective viscosity and wall shear stress.

The impact of rotational force on viscoelastic fluid flow in a microchannel with a polymeric layer has been numerically investigated by [Balasubramanian et al. \[2020\]](#), providing insights for the design of microfluidic devices. [Kaushik et al. \[2022\]](#) investigated the enhancement of mixing functionality in a lab-on-chip device embedded in a rotating disk, demonstrating that rotational force and molecular diffusion impact mixing, with strong advective transport leading to enhanced mixing at short distances from the channel entry. Recently, [Gandharva and Kaushik \[2022\]](#) studied the transient flow velocities in rotating microchannels with a polyelectrolyte layer, revealing critical roles of the polyelectrolyte layer size in controlling flow velocities and oscillations, offering potential benefits for managing mass and momentum transport in Lab-on-CD.

The study of two-layer flow through microchannels has attracted considerable attention due to its relevance in various applications, such as microreactors, microelectronic cooling systems, and micro energy systems ([Wang et al. \[2009\]](#)). [Gu and Lawrence \[2005\]](#) presented a one-dimensional analytical solution to the fully nonlinear problem of two-layer frictional exchange, comparing their results with experimental data to highlight the role of interfacial and bottom friction in flow rate exchange. [Lenz and Kumar \[2007\]](#) investigated the steady-state behavior of the interface between two immiscible liquids flowing in a channel with one fixed wall and one topographically microstructured wall, noting cases where interfacial features can be suppressed by large pressure gradients. [Gaurav \[2010\]](#) studied the effect of free surface on interfacial instabilities of gravity-driven flow of two superposed Newtonian liquid layers down an inclined wall, identifying stabilizing effects

of surface variation on certain interfaces. Samanta [2013] examined the effect of surfactants on interfacial waves in a two-layer channel flow at low to moderate Reynolds numbers, focusing on linear stability analysis. Dubrovina et al. [2017] investigated streamwise pressure-driven flow of two stratified viscous immiscible fluids with different electric properties in a channel with topographically structured walls, noting the emergence of nonlinear structures in the linearly unstable regime. Mohammadi and Smits [2017] studied the stability of two-layer Couette flow considering variations in viscosity ratio, thickness ratio, interfacial tension, and density ratio, observing a new interfacial mode at low viscosity ratios and the stabilizing effect of interfacial tension.

In the context of electroosmotic flow (EOF), two-layer flow plays a significant role in various microfluidic systems. Su et al. [2013] discussed transient electroosmotic flow of two immiscible fluids through a slit microchannel, focusing on velocity distribution and concluding that velocity magnitude is enhanced with the zeta potential difference at the fluid-fluid interface. Das and Hardt [2011] obtained an analytical result for electrostatic potential distribution, highlighting the influence of electric double layers and potential jump at the liquid-liquid interface. Huang et al. [2014] studied electroosmotically driven flow of two immiscible fluids, considering one layer as a non-Newtonian power-law fluid driven by electroosmotic force and the other as a Newtonian fluid driven by interfacial shear stress. Demekhin et al. [2016a] investigated the stability analysis of two-layer electrolyte fluids in the presence of an electric field, with computed results agreeing well with experimental data. Shit et al. [2016d] analyzed the heat transfer in two-layer electroosmotic flow, obtaining analytical solutions for velocity and temperature distribution. Ranjit et al. [2021] performed an electrothermal pumping analysis of peristaltic flow of two-layer couple stress fluids in an asymmetric microchannel without considering a magnetic field. Wang et al. [2005] conducted an experimental investigation of electroosmotically and pressure-driven flow of two fluids. Gao et al. [2007] conducted a comparative study with experimental and theoretical investigation of electroosmotic two-layered flow to control the fluid-fluid interface using an external electric field. However, previous investigations are limited to the study of electroosmotic two-layered flow through a smooth narrow confinement.

Flow transport and heat transfer through saturated porous media are crucial in modern science and technology, captivating researchers for decades due to their diverse applications. These include petroleum exploration, electronic component cooling, pressurized water reactors, transpiration cooling, and oil recovery, as well as processes involving porous insulation, heat pipe wicking structures, packed-bed catalytic nuclear reactors, chemical catalytic reactors, and thermal insulation. These processes also play a role in the flow of liquids in various physiological and biological processes. Researchers have extensively studied heat transfer phenomena through porous media. For example, Biswas et al. [2021a] investigated MHD thermal convection flow of hybrid nanofluids to enhance thermal transport in porous media under non-uniform heating. Krishna et al. [2020] studied unsteady MHD free convective rotating flow over an exponentially accelerated inclined plate through a saturated porous medium, analyzing the effects of Hall current and ion slip on the transport of rotating flow with varying temperature and concentration. Ghalambaz et al. [2020] simulated free convection heat transfer of a suspension of NEPCMs in an inclined porous cavity

using the finite volume method. [Nield and Bejan \[2006\]](#) conducted numerical and experimental studies on flow patterns within porous channels. [Marzougui et al. \[2021\]](#) investigated mixed convection flow and heat transport in a channel with a uniform magnetic field using the generalized Brinkman-extended Darcy model and COMSOL Multiphysics. [Alhajaj et al. \[2020\]](#) validated hybrid nanofluidic flow and heat transport through a porous channel with experimental and numerical comparisons. [Degan et al. \[2016\]](#) studied radiation-mixed convection flow in a vertical channel with an anisotropic porous medium, revealing the effects of thermal radiation and anisotropic permeability. [Neffah et al. \[2018\]](#) explored thermo-fluidic transport of a non-Newtonian power-law fluid in an anisotropic porous channel under chemical reactions. [Malashetty et al. \[2005\]](#) analyzed the linear stability of horizontally flowing fluid in an anisotropic porous medium, investigating thermal non-equilibrium and permeability effects on convection onset. [Kameswaran et al. \[2016\]](#) examined the melting effect on mixed convection flow over a variable permeability vertical plate, finding enhancements in heat and radiative heat transfer. [Degan et al. \[2002\]](#) provided an exact solution for fully developed forced convection flow in a horizontal channel with an anisotropic porous medium, highlighting the impact of porous matrix orientation, permeability ratio, and angle on thermal convection.

Now a days, there has been increasing interest in the transport phenomena of porous microchannels, driven by their applications in emerging fields of microscale heat transfer ([Karniadakis et al. \[2005\]](#); [Nield and Bejan \[1999\]](#)). Porous microchannels are instrumental in the development of advanced microfluidic devices across various industries and applications. [Zhou et al. \[2022\]](#) discussed electrochemical reactions in microreactor flow through an anisotropic porous microchannel. They numerically simulated three-dimensional flow fields under low pressure, optimizing the anisotropic porous media.

1.12 Objectives of the Thesis

Electroosmotic flow and heat transfer have received significant attention due to their wide-ranging applications in engineering, biology, and various industrial processes. Although modeling of electroosmotic flow began almost a century ago, much of the existing research focuses on smooth microchannels. However, manufacturing limitations often result in microchannels with inherent surface roughness. While some studies have explored the impact of roughness on thermo-fluidic transport in microchannels, there is still a gap in understanding these effects in various microchannels and microtubes. This thesis aims to investigate the effect of surface roughness on electroosmotic flow and heat transfer in different types of microchannels, including wavy microchannels, complex wavy microchannels, and rough microtubes.

This thesis involves the mathematical modeling of electroosmotic flow through various types of microchannels and microtubes, considering different wall roughness conditions. The primary goal is to derive analytical solutions for thermo-fluidic transport phenomena in electroosmotic flow through rough microchannels. Additionally, the study aims to investigate the influence of external forces, such as the Lorentz force, resistance force due to a porous medium, and the Coriolis force, in conjunction with surface roughness. Analytical solutions will be primarily obtained using the perturbation technique, while numerical solutions will be obtained using the shooting technique based on the Runge-Kutta method. The NDSolve and NIntegrate algorithms in Mathematica will be used for numerical solutions. The analytical solutions will be cross-validated with existing literature to ensure their accuracy.

The objectives of this thesis are as follows:

- Investigate how surface waviness (roughness) impacts electroosmotic flow and heat transfer in a wavy microchannel, particularly in the presence of a magnetic field. This study aims to understand how the irregularities on the surface of the channel affect the flow behavior and heat transfer characteristics.
- Explore the influence of surface roughness on electroosmotic flow within a microchannel filled with porous material. This investigation will provide insights into how the combined effects of surface roughness and porous media affect fluid flow and heat transfer, which is crucial for applications involving porous microchannels.
- Analyze the effect of system rotation on electrothermal magnetohydrodynamic (MHD) flow in a rough microchannel. By studying how the rotational motion of the system affects the MHD flow behavior, this research aims to enhance our understanding of the complex fluid dynamics in such systems.
- Evaluate the impact of surface roughness on the boundary layer thickness of electroosmotic flow with electromagnetohydrodynamic (EMHD) effects, particularly in the context of two immiscible electrolytes. This study aims to understand how surface roughness influences the boundary layer characteristics, which is vital for optimizing the design and performance of microfluidic devices.
- Examine the effect of anisotropic permeability on EMHD heat transfer in rough microchannels

and microtubes. This investigation will focus on understanding how the directional variation in permeability affects the heat transfer characteristics, which is essential for designing efficient heat transfer systems involving microchannels and microtubes with irregular surfaces.

1.13 Overview of the thesis

This thesis mainly focuses on the analysis of mathematical models for electroosmotic flow and heat transfer in different types of microchannels and microtubes with various wall roughness conditions. These shapes are studied for specific uses. The thesis comprises six main chapters (**Chapter 2-Chapter 7**), along with an introductory chapter (**Chapter 1**) and a concluding chapter (**Chapter 8**) describing the overall conclusions and future directions of the research. In the introductory section of each main chapter (**Chapter 2-Chapter 7**), this thesis addresses the problem description, provides a brief literature review, explains the motivation behind the study, and discusses the applicability of the research. It then outlines the mathematical formulation and the solution procedure. Finally, the results and discussions are presented, along with comparisons to existing literature to validate the study.

Chapter 1 serves as the introduction to the thesis. It begins with a discussion on the fundamental concepts of microfluidics and microscale systems. The chapter then provides a brief overview of basic fluid mechanics, covering the governing equations such as conservation of mass, momentum, and energy. It also introduces electrokinetic phenomena, magnetohydrodynamic flow, flow through rotating systems, and porous media. The chapter presents the equations governing flow in electromagnetic environments. Additionally, it discusses surface roughness and its relevance to microfluidic applications, including lab-on-a-chip devices. A brief literature review on anisotropy is included, along with a discussion on the practical applications of rough microchannels in real-life problems.

In **Chapter 2**, we investigate the combined effects of electroosmosis and surface roughness on rotating electrothermal flow in a microchannel under the presence of a magnetic field. We present a mathematical model considering variable zeta potential, heat transfer characteristics and entropy generation within the microchannel. We obtain analytical solutions using the separation of variables method in combination with cosine Fourier series expansion. The study shows the interplay between microchannel roughness and rotation significantly influences the flow patterns. Surface roughness causes increasing wall shear stress and friction factor, resulting in a higher Poiseuille number. The Coriolis force due to rotation enhances the entropy generation thereby increasing internal irreversibilities.

We investigate a mathematical model in **Chapter 3** to analysis the interaction of electromagnetohydrodynamic (EMHD) flow of two immiscible fluids in a hydrophobic microchannel with topographically charged rough surface. We consider the Navier-slip and the variable zeta potential at the fluid-solid interface, and the equality of viscous stress and zeta potential jump at the liquid-liquid interface. Employing the perturbation technique, we obtain the analytical solution of the governing equations to shed light on the transport characteristics of the flow in the two-layer

microchannel. We estimate the boundary layer thickness to predict its behavior in the presence of a magnetic field and the amplitude of surface waviness for the first time in this context. Our findings reveal that increased surface roughness intensifies flow field disturbances in both layers, leading to microfluidic droplet formation. Adjusting the zeta potential difference at the fluid-fluid interface can cause one layer to move faster than the other. By managing surface roughness, zeta potential difference, and electromagnetic fields, we can optimize the transport efficiency of ionic liquids and enhance microfluidic device performance.

In **Chapter 4**, the heat transfer characteristics associated with the impact of combined electromagnetohydrodynamic flow in a microchannel with the regular wavy rough wall through a porous medium have been investigated. The approximate analytical solutions for the velocity and potential distribution are obtained using the perturbation technique. To study the thermal characteristics, the analytical solution for temperature distribution in the presence of Joule heating is obtained. Impressive results are obtained to examine the behavior of velocity and temperature due to the rough wavy wall in the presence of applied magnetic field and transverse electric field. The significant effects on velocity and heat transport within the corrugated microchannel for various combination of pertinent parameters such as Hartmann number, Darcy number and transverse electric field are elaborated. Furthermore, variation of the mean velocity and the rate of heat transfer characteristic due to wavy roughness and the magnetic field has been studied. The study shows that the mean velocity decreases with Darcy number and has enhancing effect on applied magnetic field, whereas the trend is reversed in the case of applied electric field. The rate of heat transfer increases with an increase in Joule heating effects, Hartmann number and permeability of the porous medium.

The **Chapter 5** aims to estimate such disturbances on the thermo-fluidic transport with combined electromagnetohydrodynamic (EMHD) flow in a porous microchannel having complex wavy roughness walls. The governing equations for thermo-fluidic transport are solved analytically by employing the perturbation technique. The volumetric flow rate is derived analytically and the Nusselt number is computed numerically. The velocity and temperature distribution are interpreted graphically and discussed the importance of different pertinent parameters. The changes in the flow pattern and the disturbance in heat transfer performance are examined properly for different degrees of roughness (wave amplitude ratio). The velocity profiles become fully developed in a transverse electric field and the disturbance is shown at the boundary layers. Furthermore, the higher permeability of the porous medium and roughness of the microchannel reduces the volume flow rate, but the roughness of the surface of the microchannel enhances the rate of heat transfer.

In **Chapter 6**, the thermal transport characteristics of nanofluid through a wavy microchannel with anisotropic porous medium is analyzed under electromagnetohydrodynamic (EMHD) effect and constant pressure gradient. Assumed that the permeability of the porous medium is varying along all the directions. The solution for the EDL potential, velocity and temperature distributions have been obtained by employing the numerical methods. Further, the results are validated with the analytical asymptotic solution. The variations of pertinent parameters such as Hartmann number, Darcy number, Casson parameter, volume friction parameter of nanoparticles, joule heating parameter on the nanofluidic flow are delineated graphically and discussed in details. It can be observed

that the anisotropic permeability ratio and angle both make the diversity on the flow profiles as well as the temperature profiles. The Forchheimer inertial effect makes a frictional heating which enhances the temperature and it generates the slug flow behavior for low Darcy number. Notably, the retarding effect of electromagnetic force and the Hall current both are reduced the flow velocity. Further, the Nusselt number becomes maximum for low Darcy number and $\varphi = \pi/2$ and it becomes minimum in low inertial environment with $\varphi = 0$.

Chapter 7 examines electromagnetohydrodynamic (EMHD) pumping in a fluid-saturated anisotropic porous microtube with a rough surface, which is more applicable for microfluidic systems than EMHD flow through rough microchannels. Using boundary perturbations and assumptions of low Reynolds numbers, the study derives analytical solutions for the governing equations, considering linearized Poisson-Boltzmann and Navier-Stokes equations. The analysis reveals that the EMHD pumping rate is affected by a second-order term ($-\varepsilon^2\eta$), where $\eta = \eta_1 + \eta_2$, which indicate the effect of roughness on the mean pumping rate. Here, η_1 represents a pure gain (with $\eta_1 < 0$), while η_2 is influenced by the applied magnetic field, transverse electric field, and anisotropic porous medium. Notably, the changes in η_2 are minimal for $\varphi = 0$ and a low Darcy number but are maximal for $\varphi = 0$ and a large Darcy number with $Ha < 1$. The maximum pumping rate is achieved with an isotropic porous medium ($\varphi = 0$). Surface roughness alters the boundary layer near the microtube wall, leading to a thinner boundary layer and increased pumping rate. Additionally, higher anisotropic permeability introduces uneven resistance forces along the radial and axial directions, leading to the formation of smaller eddies and boluses. Radial pressure gradients decrease for $K < 1$ due to increased resistance along the radial direction and increase for $K > 1$ as higher permeability reduces resistance. The study also highlights that surface roughness enhances the friction factor ratio between a rough microtube and a smooth microtube due to increased surface area and irregularities, leading to higher frictional resistance.

In **Chapter 8**, we provide a concise summary of the important findings in this thesis. We conclude the influence of surface roughness on electroosmotic flow and heat transfer in microchannels. Additionally, we summarize the intricate interplay of magnetic fields, system rotation, and porous media with surface roughness, dissecting their combined effects on electroosmotic flow dynamics. We also highlight the practical implications of our research and its potential applications. Finally, we outline avenues for future research, suggesting further exploration of rough microchannels and microtubes.

2

Rotation Induced Electrothermal MHD Flow in a Rough Surface Microchannel

2.1 Introduction

Microfluidic devices with electroosmotically driven flow play an important role in manipulating and transporting small volumes of fluids and particles or cells. Several researchers have been drawn to the study of electroosmotic flow (EOF) due to its diverse applications in biomedical engineering and chemical analysis, particularly its role in micromixing ([Aoki and Mae \[2006\]](#); [Maadi and Goltmarz \[2014\]](#); [Chen et al. \[2016\]](#); [Das et al. \[2024\]](#)). For mixing, rough surfaces in microchannels remained relatively understudied, as highlighted by Gloss and Herwig ([Gloss and Herwig \[2009\]](#)). However, numerous researchers ([Chang and Wang \[2011\]](#); [Gheshlaghi et al. \[2016\]](#); [Sun et al. \[2019\]](#); [Kaushik et al. \[2022\]](#)) have explored fluid flow in microchannels without explicitly focusing on surface roughness. Despite substantial research on fluid flow in microchannels, particularly under low Reynolds numbers ([Mautner \[2004\]](#); [Sochol et al. \[2014\]](#); [Nimmagadda and Venkatasubbaiah \[2017\]](#); [Mehboudi and Yeom \[2019\]](#); [Madana and Ali \[2020\]](#); [Hsieh et al. \[2021\]](#); [Alizadeh et al. \[2021\]](#)), investigations into the influence of surface roughness remain relatively limited. A significant challenge in microfluidics involves the high pumping power required to drive fluid flow through the microchannel ([Yang and Li \[1997\]](#); [Kar et al. \[1998\]](#)). To address this issue, [Yang et al. \[2001\]](#) investigated the use of electroosmotic actuation for flow control in the microchannels. By

The content of this chapter has been communicated to Physics of Fluids (AIP).

applying an electric field, electroosmosis enables efficient flow manipulation and actuation. In the context of biomedical applications, the achievement of effective flow mixing remains challenging, particularly under laminar flow conditions. [Kurzthaler et al. \[2024\]](#) considered the pressure-driven flow in a microfluidic channel and introduced a helical flow to enhance mixing. Microfluidic devices like Lab-on-CD ([Sengupta et al. \[2019\]](#)) utilize Coriolis force, operating at a consistent rotational speed, which induces secondary flows. Such secondary flows are important in designing rotational microfluidic systems, ensuring effective mixing and fluid transport within the microchannels.

This enhanced mixing capability is useful in various processes that require effective blending of reactants, sample preparation, or analysis in microscale systems ([Maadi and Golmarz \[2014\]](#); [Das et al. \[2024\]](#)). A secondary velocity-driven mixing mechanism in a rotating system provides a promising solution to achieve rapid and uniform mixing in microfluidic devices ([Leung and Ren \[2014\]](#); [Verma and Kumaran \[2013\]](#); [Jalali et al. \[2015\]](#)). [Chang and Wang \[2011\]](#) demonstrated the existence of secondary velocities in the rotating electroosmotic flow through a straight channel. These studies have focused on understanding how rotation influences flow behaviour and leads to the generation of secondary velocities ([Takashima \[1976\]](#); [Ruo et al. \[2010\]](#); [Othman \[2004\]](#)). [Kumar et al. \[2023\]](#) explored the swirling flow phenomena in the microfluidic channel to enhance efficient mixing. The combination of rotation and electro-osmotic force offers potential advantages for various applications by improving fluid mixing, speedy transport and manipulation in microscale systems ([Ng and Qi \[2015\]](#); [Xie and Jian \[2014\]](#)). [Gheshlaghi et al. \[2016\]](#) investigated the transient electroosmotic flow and heat transfer through a straight microchannel by paying due attention to the time evolution of velocity and temperature. [Sun et al. \[2019\]](#) focused on analyzing thermal energy transport through a rectangular microchannel in a rotating system under the assumption of a fully developed electroosmotic flow. Their findings reported that the performance of the systems can be increased by minimizing entropy generation with a suitable aspect ratio. [Shit et al. \[2016a\]](#) examined the effect of slip velocity on electroosmotic flow in a non-uniform rotating microchannel, highlighting its significance in optimizing the characteristics of electroosmotic flow. [Balasubramanian et al. \[2020\]](#) numerically investigated the impact of rotational force on viscoelastic fluid flow in a microchannel with a polymeric layer for understanding the design of microfluidic devices. [Kaushik et al. \[2022\]](#) investigated the enhancement of mixing functionality in a rotating lab-on-chip disk type device. [Gandharva and Kaushik \[2022\]](#) studied the transient flow velocities in rotating microchannels having a polyelectrolyte layer, wherein they revealed that the size of the polyelectrolyte layer plays a critical role in controlling flow velocities and oscillations, offering potential benefits for managing mass and momentum transport in the Lab-on-CD. However, all of these studies are limited to the consideration of the roughness of the microchannel.

The roughness of the surfaces in microfabrication may be focused on various factors, including lithography techniques, 3D printing technology, deposition methods, and manufacturing processes ([Kang and Suh \[2009\]](#); [Cho et al. \[2013\]](#); [Keramati et al. \[2016\]](#); [Waheed et al. \[2016\]](#); [Lade et al. \[2017\]](#); [Zhang et al. \[2020\]](#); [Nadarajah et al. \[2024\]](#)). [Banerjee and Nayak \[2019\]](#) investigated isothermal micromixing in a wavy-patterned microchannel using an induced charge mechanism. They reported that the sinusoidal charged surface enhances interfacial contact area, contradicting

conventional beliefs that led to effective mixing compared to straight channel flow. [Reza et al. \[2021\]](#) conducted thermal characteristics in a porous microchannel with a rough wall under the combined electromagnetohydrodynamic (EMHD) effect. [Gao et al. \[2023\]](#) introduced a numerical model and examined the thermal performance of a microchannel heat sink with secondary branches employing two parallel sinusoidal channels. The investigation into the effects of roughness on fluid flow in microchannels is propelled by its significance in diverse engineering applications, including microfluidics and heat transfer ([Krogstad et al. \[2005\]](#); [Hall \[2020\]](#)). Understanding the impact of surface roughness on friction factors and entropy generation is vital for optimizing microchannel system design. [Herwig et al. \[2010\]](#) investigated the effects of friction factors and entropy generation in pipe and channel flow with arbitrarily shaped wall roughness. [Gloss and Herwig \[2009\]](#) further explored this topic, focusing on micro-sized channel flow geometry and highlighting wall roughness effects on the local skin-friction and entropy production. [Gamrat et al. \[2008\]](#) conducted experimental research on microchannel flow to assess the impact of roughness. They developed a one-dimensional rough-layer model using a discrete-element approach and volume-averaging technique. [Liu et al. \[2019\]](#) numerically investigated the effects of rectangular rib roughness on frictional drag and pressure drop in microchannel flow, revealing a strong dependence on relative roughness at low Reynolds numbers. These studies have not investigated the influence of surface roughness on electroosmotic flow (EOF) in microchannels under rotation-induced secondary velocity.

Owing to the studies mentioned above, a research gap arises concerning the analysis of rotation-induced thermal behaviour and entropy generation in a rough surface microchannel under the influence of electromagnetic force. Therefore, we investigate the transient thermo-fluidic behaviour of the electromagnetohydrodynamic (EMHD) flow through a rough surface microchannel under a rotational environment. The flow is driven solely by electroosmotic flow (EOF) and the rotation-induced Coriolis force. We solve the governing partial differential equations for momentum and heat transfer analytically using the separation of variables method. Our study aims to explore the behaviours of the secondary flow induced by rotation and surface roughness as well as their impact on thermal energy and entropy generation within the system. Further, we determine the friction factor in terms of Poiseuille number and the heat transfer rate for the design of micromixer and micro heat exchanger devices.

2.2 Physical paradigm and mathematical formulation

2.2.1 Description of the problem

We aim to focus on the investigation of electromagnetohydrodynamic flow and thermal behaviour of an electrolyte solution through a sinusoidally varying rough microchannel under the influence of rotation. The laminar flow regime under examination is treated as incompressible and viscous, with the microchannel featuring a sinusoidal roughness pattern. The mathematical representation of the

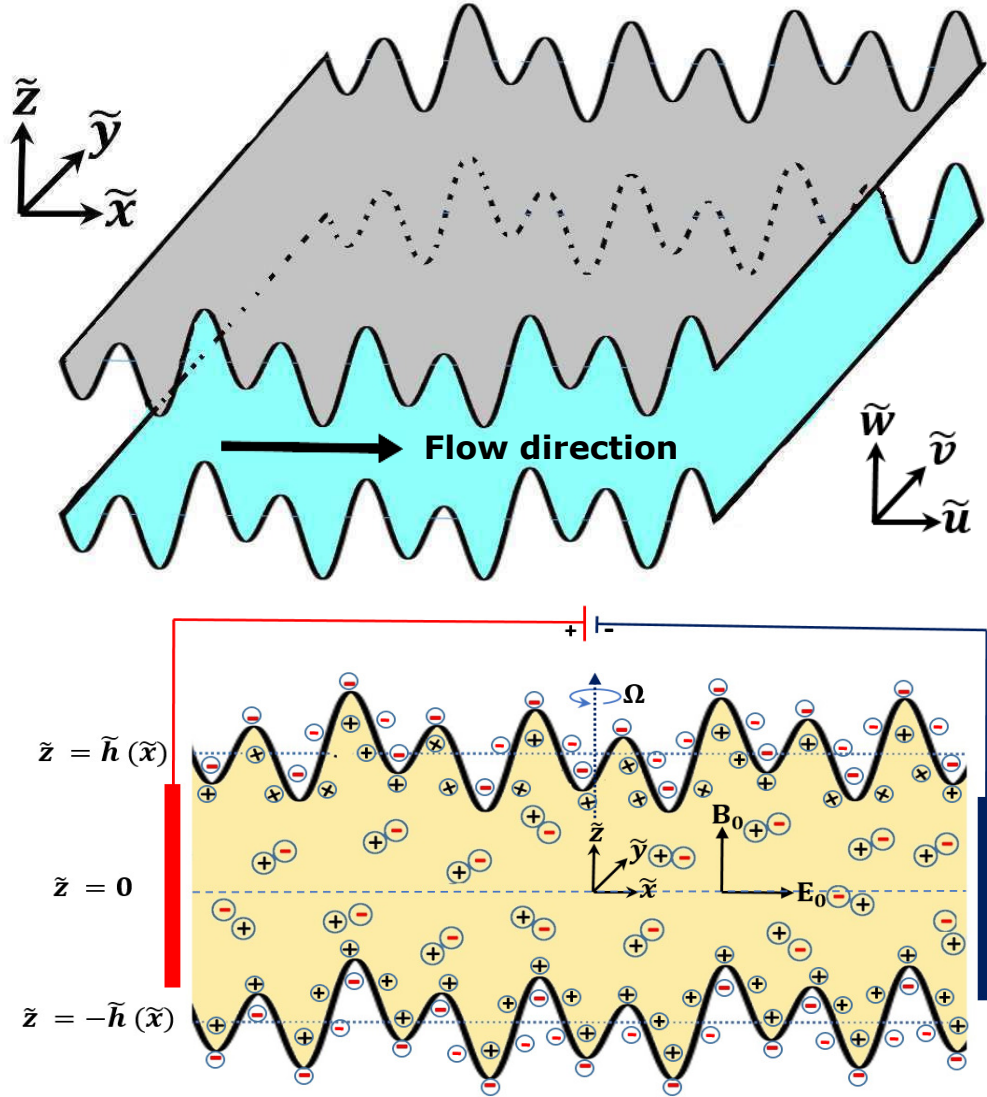


Figure 2.1: The schematic diagram of the microchannel with sinusoidal roughness, where the walls are represented by $\tilde{z} = \pm \tilde{h}(\tilde{x})$. The flow takes place in the streamwise direction \tilde{x} and the entire channel is rotating with an angular velocity Ω about the spanwise direction \tilde{z} . Due to rotation, secondary flow induces in the wall-normal direction \tilde{y} . The uniform magnetic field of strength B_0 is applied along the perpendicular direction of the primary flow. The electric field of strength E_0 is imposed along the axial direction.

rough walls that follow $\tilde{z} = \pm \tilde{h}(\tilde{x})$ is sketched in Fig. 2.1, has the expression

$$\pm \tilde{h}(\tilde{x}) = \pm \left\{ \tilde{H} + \tilde{\alpha}_1 \sin\left(\frac{\beta_1 \tilde{x}}{\tilde{H}}\right) + \tilde{\alpha}_2 \sin\left(\frac{\beta_2 \tilde{x}}{\tilde{H}}\right) + \tilde{\alpha}_3 \sin\left(\frac{\beta_3 \tilde{x}}{\tilde{H}}\right) \right\}, \quad (2.1)$$

where \tilde{H} indicates the constant average half height of the channel, α_j ($j = 1, 2, 3$) the amplitude of the different waves of sinusoidal roughness and β_j denote the wave numbers.

We assume that an applied electric field exerts its effect in the flow direction \tilde{x} , while a magnetic field \mathbf{B} influences the flow in the \tilde{z} -direction. Furthermore, the entire system rotates steadily at a constant angular speed Ω , as depicted in Fig. 2.1. The roughness of the microchannel walls plays an important role in the consideration of variable zeta potential. The variable zeta potential is taken to capture the intricate interplay between surface roughness, rotation and fluid behaviour. Due to the rotation and roughness of the surface, the secondary flow induces in the \tilde{y} direction. To explore the thermal energy aspects, a constant heat flux denoted as \tilde{q}_w is applied to the rough wall of the microchannel.

2.2.2 Governing equations for velocity distribution

The flow of an incompressible, laminar, Newtonian fluid through a rotating microchannel under the influence of EMHD is assumed to be described by two fundamental governing equations. The first equation is the continuity equation, which ensures mass conservation and it is given by

$$\tilde{\nabla} \cdot \tilde{\mathbf{U}} = 0, \quad (2.2)$$

and the momentum conservation is expressed by the modified Navier-Stokes equation

$$\rho \left[\frac{\partial \tilde{\mathbf{U}}}{\partial \tilde{t}} + (\tilde{\mathbf{U}} \cdot \tilde{\nabla}) \tilde{\mathbf{U}} + 2\tilde{\Omega} \times \tilde{\mathbf{U}} \right] = -\tilde{\nabla} \tilde{p} + \mu \tilde{\nabla}^2 \tilde{\mathbf{U}} + \mathbf{F}, \quad (2.3)$$

where ρ , μ and $\tilde{\mathbf{U}}$ respectively denote the density, dynamic viscosity, and velocity vector and $\tilde{\Omega}$ denotes the angular velocity due to the rotation of the system. Here $\tilde{p} = p - \frac{\rho}{2} |\tilde{\Omega} \times \mathbf{r}|^2$ is the modified pressure that exhibits centrifugal force in the rotating microchannel and \mathbf{F} is the EMHD force, is the combined effects of electroosmotic force and Lorentz force. Therefore, one may write

$$\mathbf{F} = \rho_e \mathbf{E} + \mathbf{J} \times \mathbf{B}, \quad (2.4)$$

where \mathbf{E} is the electric field, ρ_e denotes the net charge density and the current density \mathbf{J} expressed as $\mathbf{J} = \sigma_e(\mathbf{E} + \mathbf{U} \times \mathbf{B})$ is due to Ohm's law. Here, \mathbf{B} indicates the applied magnetic field and σ_e represents the electrical conductivity of the fluid.

The presence of the Coriolis force $2\rho\tilde{\Omega} \times \tilde{\mathbf{U}}$ in the flow of a rotating microchannel induces a secondary flow along the \tilde{y} -direction. Therefore, the velocity vector in two-dimensional flow is $\tilde{\mathbf{U}} = (\tilde{u}, \tilde{v}, 0)$, the angular velocity $\tilde{\Omega} = (0, 0, \Omega)$ is imposed along \tilde{z} direction as the axis of rotation and the axial electric field (\mathbf{E}) with strength E_0 is in the \tilde{x} direction. Further, the magnetic field

component B_0 is imposed transverse to the flow direction, i.e., the direction of \tilde{z} . We assume that the length is much greater than the height and width of the microchannel. For low Reynolds number flow, the convective term $(\tilde{\mathbf{U}} \cdot \tilde{\nabla})\tilde{\mathbf{U}}$ is neglected (Gheshlaghi et al. [2016]) as dominated by the viscous force and the flow is purely driven by the electric field in the microchannel. Based on these assumptions, the governing Eq. (2.3) for transient EMHD flow through a rotating microchannel can be written as

$$\rho \left(\frac{\partial \tilde{u}}{\partial \tilde{t}} - 2\Omega \tilde{v} \right) = -\frac{\partial \tilde{p}}{\partial \tilde{x}} + \mu \frac{\partial^2 \tilde{u}}{\partial \tilde{z}^2} + \rho_e E_0 - \sigma_e B_0^2 \tilde{u}, \quad (2.5)$$

$$\rho \left(\frac{\partial \tilde{v}}{\partial \tilde{t}} + 2\Omega \tilde{u} \right) = -\frac{\partial \tilde{p}}{\partial \tilde{y}} + \mu \frac{\partial^2 \tilde{v}}{\partial \tilde{z}^2} - \sigma_e B_0^2 \tilde{v}, \quad (2.6)$$

$$\frac{\partial \tilde{p}}{\partial \tilde{z}} = 0. \quad (2.7)$$

In this study, we investigate a scenario in which no external pressure gradient is applied. This implies that (Gupta et al. [2003])

$$\frac{\partial \tilde{p}}{\partial \tilde{x}} = 0 \text{ and } \frac{\partial \tilde{p}}{\partial \tilde{y}} = 0. \quad (2.8)$$

Therefore, the Eqs. (2.7) and (2.8) renders that the modified pressure \tilde{p} (which we call now centrifugal force) can be considered as a function of time only (Gupta et al. [2003]) or constant (Chang and Wang [2011]; Gheshlaghi et al. [2016]; Abhimanyu et al. [2016]).

Now we propose to solve the Eqs. (2.5) and (2.6) along with the no-slip boundary conditions at the rough wall and initial condition at $\tilde{t} = 0$, which are defined as

$$\tilde{u}(\pm \tilde{h}, \tilde{t}) = 0, \quad \tilde{v}(\pm \tilde{h}, \tilde{t}) = 0, \quad (2.9)$$

$$\tilde{u}(\tilde{z}, 0) = 0, \quad \tilde{v}(\tilde{z}, 0) = 0. \quad (2.10)$$

Next, we calculate the electric potential distribution to obtain the electroosmotic body force term ($\rho_e E_0$) in Eq. (2.4). The electroosmotic force is a result of the interaction between the electric field and the electrical double layer (EDL) near the surface of the channel. The EDL plays an important role in determining the magnitude of the electroosmotic force through the zeta potential at the surface of the channel. The EDL consists of an inner layer of ions of the opposite charge to that of the surface, called counter-ions, and an outer layer of ions of the same charge as the surface, called co-ions. Using the simplified Poisson-Boltzmann equation, the EDL potential ($\tilde{\psi}$) is taken as (Masliyah and Bhattacharjee [2006])

$$\frac{\partial^2 \tilde{\psi}}{\partial \tilde{z}^2} = -\frac{\rho_e}{\varepsilon}, \quad (2.11)$$

where ε is the dielectric permittivity constant of the electrolyte solution. The net charge density (ρ_e) has the expression of the form (Sadeghi et al. [2012])

$$\rho_e = 2n_0 e z_0 \sinh\left(\frac{e z_0}{k_B T_{av}} \tilde{\psi}\right), \quad (2.12)$$

where n_0 is the number of positive and negative ions (in molar unit), e is denoted by the charge of an electron, z_0 indicates the valence, k_B is the Boltzmann constant, and T_{av} denotes the absolute average temperature.

For sufficiently small values of $\frac{ez_0}{k_B T_{av}} \tilde{\psi}$, one may approximate $\sinh\left(\frac{ez_0}{k_B T_{av}} \tilde{\psi}\right)$ as $\frac{ez_0}{k_B T_{av}} \tilde{\psi}$, known as the Debye–Hückel approximation (Masliyah and Bhattacharjee [2006]). The surface charge density in terms of zeta potential due to the Gouy–Chapman model, given by $\sigma = 2\sqrt{2}\epsilon\Phi/\tilde{\kappa} \sinh(\zeta/2\phi)$, (Ganchenko et al. [2015]; Demekhin et al. [2016b]) allows us to calculate the zeta potential ($\tilde{\zeta}_0$) for specific conditions. For example, for a surface charge density of $\sigma = 10^{-3} \text{ C m}^{-2}$ in the case of glass substrate, using the values $\Phi = 25 \text{ mV}$ and $\tilde{\kappa}^{-1} = 200 \text{ nm}$, we obtain approximately the value of $\tilde{\zeta}_0 = 0.012 \text{ mV}$, which is much less than the threshold value. This suggests the applicability of the Debye–Hückel approximation in this analysis (Masliyah and Bhattacharjee [2006]). Therefore, the linearized Poisson-Boltzmann Eq. (2.11) reduces to

$$\frac{\partial^2 \tilde{\psi}}{\partial \tilde{z}^2} = \tilde{\kappa}^2 \tilde{\psi}, \quad (2.13)$$

with inverse Debye length $\tilde{\kappa} = \frac{1}{ez_0} \sqrt{\frac{\epsilon k_B T_{av}}{2n_0}}$. We consider the boundary conditions for $\tilde{\psi}$ as

$$\tilde{\psi} = \tilde{\zeta}_w \text{ on } \tilde{z} = \pm \tilde{h}, \quad (2.14)$$

where $\tilde{\zeta}_w$ represents the scaled zeta potential at the rough surface of the microchannel and has the form $\tilde{\zeta}_w = \tilde{\zeta}_0 \left\{ 1 + \sin\left(\beta_1 \frac{\tilde{x}}{\tilde{H}}\right) + \sin\left(\beta_2 \frac{\tilde{x}}{\tilde{H}}\right) + \sin\left(\beta_3 \frac{\tilde{x}}{\tilde{H}}\right) \right\}$. The variation in zeta potential at the rough wall, represented by sinusoidal functions in the equations, ensures that the electric field strength varies periodically along the rough surfaces (Banerjee and Nayak [2019]).

To scale the equations, we use the following dimensionless variables:

$$x = \frac{\tilde{x}}{\tilde{H}}, \quad z = \frac{\tilde{z}}{\tilde{H}}, \quad \psi = \tilde{\psi} \frac{ez_0}{k_B T_{av}}, \quad \zeta_w = \tilde{\zeta}_w \frac{ez_0}{k_B T_{av}}, \quad \zeta_0 = \tilde{\zeta}_0 \frac{ez_0}{k_B T_{av}}, \quad h = \frac{\tilde{h}}{\tilde{H}}, \quad \alpha_i = \frac{\tilde{\alpha}_i}{\tilde{H}} \quad (j = 1, 2, 3). \quad (2.15)$$

By employing these dimensionless variables, we can solve the transformed Eq. (2.13) while imposing the boundary condition $\psi(\pm h) = \zeta_w$. This enables us to obtain a solution for the distribution of the EDL potential as

$$\psi = \frac{\zeta_w \cosh(\kappa z)}{\cosh(\kappa h)}, \quad (2.16)$$

where $\zeta_w = \zeta_0 \{1 + \sin(\beta_1 x) + \sin(\beta_2 x) + \sin(\beta_3 x)\}$, $h = 1 + \alpha_1 \{\sin(\beta_1 x) + \frac{\alpha_2}{\alpha_1} \sin(\beta_2 x) + \frac{\alpha_3}{\alpha_1} \sin(\beta_3 x)\}$ and $\kappa = \tilde{\kappa} \tilde{H}$ is called electroosmotic parameter. Here, α_1 is called the roughness parameter as introduced by Herwig et al. [2008].

To combine the Eqs. (2.5) and (2.6) in a single equation, let us introduce a complex velocity distribution function $\tilde{\xi}(\tilde{z}, \tilde{t}) = \tilde{u}(\tilde{z}, \tilde{t}) + i\tilde{v}(\tilde{z}, \tilde{t})$. Then the combined form of Eqs. (2.5) and (2.6) can be expressed as

$$\rho \left(\frac{\partial \tilde{\xi}}{\partial \tilde{t}} + 2i\Omega \tilde{\xi} \right) = \mu \frac{\partial^2 \tilde{\xi}}{\partial \tilde{z}^2} + \rho_e E_0 - \sigma_e B_0^2 \tilde{\xi}. \quad (2.17)$$

To obtain the dimensionless form of the Eq. (2.17), we use the following scaling variables and non-dimensional parameters:

$$\xi = \frac{\tilde{\xi}}{u_{HS}}, t = \frac{\tilde{t}\mu}{\rho\tilde{H}^2}, u_{HS} = \frac{-\epsilon k_B T_{av} E_0}{e z_0 \mu}, Ha = B_0 \tilde{H} \sqrt{\frac{\sigma_e}{\mu}}, \omega = \frac{\Omega \rho \tilde{H}^2}{\mu}, \quad (2.18)$$

where u_{HS} represents Helmholtz-Smoluchowski velocity, ω and Ha are denoted by rotation number, Hartmann number respectively.

The dimensionless form of Eq. (2.17) can be written as

$$\frac{\partial \xi}{\partial t} + 2i\omega\xi = \frac{\partial^2 \xi}{\partial z^2} + \frac{\partial^2 \psi}{\partial z^2} - Ha^2 \xi. \quad (2.19)$$

The boundary conditions (2.9) and initial condition (2.10) reduce to the dimensionless complex form as

$$\xi(\pm h, t) = 0, \quad \xi(z, 0) = 0. \quad (2.20)$$

2.2.3 Thermal energy

The governing equation for temperature distribution, incorporating heat generation from electromagnetic interaction, viscous dissipation and Joule heating is formulated as (Jian [2015])

$$\rho C_p \left(\frac{\partial \tilde{T}}{\partial \tilde{t}} + \tilde{\mathbf{U}} \cdot \tilde{\nabla} \tilde{T} \right) = k_{th} \tilde{\nabla}^2 \tilde{T} + \tau \cdot \tilde{\nabla} \tilde{\mathbf{U}} + \frac{1}{\sigma_e} \mathbf{J} \cdot \mathbf{J}, \quad (2.21)$$

where \tilde{T} is the temperature, (ρC_p) the heat capacitance of fluid at constant pressure and k_{th} represents the thermal conductivity of fluid. The last two terms $(\frac{1}{\sigma_e} \mathbf{J} \cdot \mathbf{J})$ and $(\tau \cdot \tilde{\nabla} \tilde{\mathbf{U}})$ of Eq. (2.21) indicate the heat generation due to joule heating and viscous dissipation, with $\tau = \mu(\tilde{\nabla} \tilde{\mathbf{U}} + \tilde{\nabla} \tilde{\mathbf{U}}^T)$.

Considering the physical characteristics of the problem, the temperature distribution in the EMHD flow through a rotating microchannel with sinusoidal roughness is described. Hence, the thermal energy equation is formulated as

$$\rho C_p \left(\frac{\partial \tilde{T}}{\partial \tilde{t}} + \text{Re}[\tilde{\xi}] \frac{\partial \tilde{T}}{\partial \tilde{x}} + \text{Im}[\tilde{\xi}] \frac{\partial \tilde{T}}{\partial \tilde{y}} \right) = k_{th} \frac{\partial^2 \tilde{T}}{\partial \tilde{z}^2} + \mu \left\| \frac{\partial \tilde{\xi}}{\partial \tilde{z}} \right\|^2 + \sigma_e \left(E_0^2 + B_0^2 \|\tilde{\xi}\|^2 \right). \quad (2.22)$$

We solve the Eq. (2.22) subject to the constant wall temperature and the initial condition at $\tilde{t} = 0$,

$$\tilde{T}(\pm \tilde{h}, \tilde{t}) = \tilde{T}_w, \quad \tilde{T}(\tilde{z}, 0) = 0, \quad (2.23)$$

where \tilde{T}_w denotes the temperature at the wall.

In the scenario of thermally fully developed flow with a constant wall heat flux (\tilde{q}_w) , we can formulate as (Liu et al. [2018])

$$\frac{\partial \tilde{T}}{\partial \tilde{x}} = \frac{\partial \tilde{T}_b}{\partial \tilde{x}} = \tilde{\gamma}_1, \quad \text{and} \quad \frac{\partial \tilde{T}}{\partial \tilde{y}} = \frac{\partial \tilde{T}_b}{\partial \tilde{y}} = \tilde{\gamma}_2, \quad (2.24)$$

2.3. Analytical solution

where $\tilde{\gamma}_1$ and $\tilde{\gamma}_2$ are two constants, \tilde{T}_b stands the bulk mean temperature which can be defined as $\tilde{T}_b = (\int_{-\tilde{h}}^{\tilde{h}} \tilde{\xi} \tilde{T} d\tilde{z}) / (\int_{-\tilde{h}}^{\tilde{h}} \tilde{\xi} d\tilde{z})$.

By employing the Eq. (2.24) and using the dimensionless temperature $\theta = \frac{k_{th}(\tilde{T} - \tilde{T}_w)}{\tilde{q}_w \tilde{H}}$ in Eq. (2.22), we derive the thermal energy equation in non-dimensional form as

$$Pr \frac{\partial \theta}{\partial t} + Pe \left\{ \gamma_1 \text{Re}[\xi] + \gamma_2 \text{Im}[\xi] \right\} = \frac{\partial^2 \theta}{\partial z^2} + Br \left\| \frac{\partial \xi}{\partial z} \right\|^2 + Ha^2 \|\xi\|^2 + \gamma_j, \quad (2.25)$$

where $Pr = C_p \mu / k_{th}$ is the Prandtl number, $Pe = \rho C_p u_{HS} \tilde{H} / k_{th}$ is called thermal Peclet number, $\gamma_1 = k_{th} \tilde{\gamma}_1 / \tilde{q}_w$, $\gamma_2 = k_{th} \tilde{\gamma}_2 / \tilde{q}_w$ are the heat generation constants, $Br = (u_{HS}^2 \mu) / (\tilde{H} \tilde{q}_w)$ is the Brinkman number (the ratio of heat production by viscous dissipation and heat transport by molecular conduction), and $\gamma_j = \sigma_e E_0^2 \tilde{H} / \tilde{q}_w$ is the measure of the joule heating due to heat conduction. The dimensionless form of the boundary conditions (2.23) and the initial condition are given by

$$\theta(\pm h, t) = 0, \quad \theta(z, 0) = 0. \quad (2.26)$$

2.3 Analytical solution

This section focuses on the analytical solution for velocity and temperature distributions. The dimensionless partial differential equations for reduced momentum equation (2.19) and the thermal energy equation (2.25) with the boundary conditions (2.20) and (2.26) are solved using the separation of variables method in conjunction with Fourier series expansion. Furthermore, the volumetric flow rate, the Nusselt number and entropy generation are computed analytically to provide a quantitative measure of the effect of rough microchannel.

2.3.1 Analytical solution for velocity distribution

Here, we present an analytical solution of the complex partial differential equation [Eq. (2.19)]. The solution, according to the superposition property one may write

$$\xi(z, t) = \xi_1(z) + \xi_2(z, t), \quad (2.27)$$

where $\xi_1(z)$ states the steady state component and $\xi_2(z, t)$ is the transient component of the velocity distribution. Introducing Eq. (2.27) in Eq. (2.19) one can easily obtain the set of differential equations for $\xi_1(z)$ and $\xi_2(z, t)$, are such that

$$\frac{\partial^2 \xi_1}{\partial z^2} - 2i\omega \xi_1 + \frac{\partial^2 \psi}{\partial z^2} - Ha^2 \xi_1 = 0, \quad (2.28)$$

$$\frac{\partial^2 \xi_2}{\partial z^2} - \frac{\partial \xi_2}{\partial t} - 2i\omega \xi_2 - Ha^2 \xi_2 = 0. \quad (2.29)$$

The initial and boundary condition (2.20) reduces to

$$\xi_2(z, 0) = -\xi_1(z), \quad \xi_1(\pm h) = 0, \quad \xi_2(\pm h, t) = 0. \quad (2.30)$$

Using the boundary condition $\xi_1(\pm h) = 0$ into Eq. (2.28) gives the solution of the steady velocity profile as

$$\xi_1(z) = \frac{\zeta_w \kappa^2 \cosh(\kappa z)}{(Ha^2 - \kappa^2 + 2i\omega) \cosh(\kappa h)} - \frac{\zeta_w \kappa^2 \cosh(z\sqrt{Ha^2 + 2i\omega})}{(Ha^2 - \kappa^2 + 2i\omega) \cosh(h\sqrt{Ha^2 + 2i\omega})}. \quad (2.31)$$

Utilizing the separation of variables method in conjunction with cosine Fourier series expansion, the solution of Eq. (2.29) for $\xi_2(z, t)$ subject to the boundary condition (2.30), is obtained as

$$\xi_2(z, t) = \sum_{n=0}^{\infty} A_n \cos(\lambda_n z) e^{-(2i\omega + Ha^2 + \lambda_n^2)t}, \quad (2.32)$$

where $\lambda_n = (2n + 1)\frac{\pi}{2h}$.

Again using the initial condition $\xi_2(z, 0) = -\xi_1(z)$, the coefficient A_n can be determined as

$$\begin{aligned} A_n = & \frac{8h}{(\pi + 2n\pi)^2 + 4h^2(Ha^2 + 2i\omega)} \left[-\frac{2h(1 + 2n)\pi \zeta_w \kappa^2}{(\pi + 2n\pi)^2 + 4h^2 \kappa^2} \cos(n\pi) \right. \\ & \left. - \frac{\sin(n\pi) \tanh(h\sqrt{Ha^2 + 2i\omega})}{\sqrt{Ha^2 + 2i\omega}(Ha^2 - \kappa^2 + 2i\omega)} \left(Ha^2 \zeta_w \kappa^2 + 2i\zeta_w \kappa^2 \omega \right) \right] \\ & + \frac{8h \zeta_w \kappa^3 \sin(n\pi) \tanh(\kappa h)}{\{(\pi + 2n\pi)^2 + 4h^2 \kappa^2\}(Ha^2 - \kappa^2 + 2i\omega)}. \end{aligned} \quad (2.33)$$

Combining $\xi_1(z, t)$ and $\xi_2(z, t)$ from Eqs. (2.31) and (2.32), one can easily obtain the final solution for $\xi(z, t)$, which exhibits three distinct stages of development. During the initial stage, characterized by the condition $\omega t \ll 1$, the influence of the Coriolis force in Eq. (2.19) is relatively insignificant compared to the stress gradient. In this regime, the flow behaviour is primarily determined by the stress gradient, while the effect of the Coriolis force can be considered negligible. In this stage, the solution can be simplified by using the relationship $e^{i\omega t} = \cos(\omega t) + i \sin(\omega t)$. Use of this, the solution is now expressed as

$$\xi(z, t) = \xi_1(z) + \sum_{n=0}^{\infty} A_n \cos(\lambda_n z) e^{-(Ha^2 + \lambda_n^2)t}. \quad (2.34)$$

Here, the solution represents a transport process without rotation that experiences acceleration due to constant stress. The velocity profile is primarily determined by the stress gradient, and the flow behavior resembles that of a non-rotating system. In the next stage, as time progresses and ωt increases, the Coriolis force becomes more significant and starts to influence the flow. The flow is gradually deflected towards steady-state conditions under the combined effects of the stress gradient and the Coriolis force. The oscillations arise due to the interplay between the applied stress and the rotational effects. In the final stage, after a long period of time where $\omega t \gg 1$, the momentum within the flow has fully diffused and the flow has reached a quasi-steady state. At this point, the initial conditions and the influence of rotation become less significant. The flow behaviour is dominated by diffusion and approaches a stable, steady-state profile.

2.3.2 Volumetric flow rate

The integration of velocity distribution $\xi(z, t)$ with respect to z , yields a comprehensive measure of the flow rate, taking into account the spatial variation of velocity along the vertical direction within the microchannel. By performing this integration, we able to quantify the overall volumetric flow which can be obtained as

$$\begin{aligned} Q(x, t) &= Q_x(x, t) + iQ_y(x, t) = \int_{-h}^h \xi(z, t) dz \\ &= \frac{2\zeta_w \kappa}{(Ha^2 - \kappa^2 + 2i\omega)} \left\{ \tanh(\kappa h) - \frac{\kappa \tanh(h\sqrt{Ha^2 + 2i\omega})}{\sqrt{Ha^2 + 2i\omega}} \right\} \\ &\quad + \sum_{n=0}^{\infty} \frac{4hA_n}{(\pi + 2n\pi)} \cos(n\pi) e^{-(2i\omega + Ha^2 + \lambda_n^2)t}. \end{aligned} \quad (2.35)$$

The terms $Q_x(x, t)$ and $Q_y(x, t)$ correspond to the time-varying volume flow rates along the x and y directions, respectively. These quantities describe the rate at which fluid flowing in the corresponding directions and vary with respect to the position x and time t .

Taking the average over one wavelength of the volume flow rate in the rough microchannel leads to the following expression:

$$q(t) = q_x(t) + iq_y(t) = \int_0^1 Q(x, t) dx. \quad (2.36)$$

2.3.3 Analytical solution for temperature distribution

By utilizing the separation of variables method in combination with cosine Fourier series expansion, one can also derive an analytical solution for the temperature profile. Similarly, the analytical solution of Eq. (2.25) can be expressed as

$$\theta(z, t) = \Theta_1(z) + \Theta_2(z, t), \quad (2.37)$$

where $\Theta_1(z)$ states the steady state component and $\Theta_2(z, t)$ is the transient component of the temperature distribution. Introducing Eq. (2.37) in Eq. (2.25), we can obtain the set of differential equations for $\Theta_1(z)$ and $\Theta_2(z, t)$, yielding

$$\frac{\partial^2 \Theta_1}{\partial z^2} - Pe \left\{ \gamma_1 \text{Re}[\xi_1] + \gamma_2 \text{Im}[\xi_1] \right\} + Br \left\| \frac{\partial \xi_1}{\partial z} \right\|^2 + Br Ha^2 \|\xi_1\|^2 + \gamma_j = 0, \quad (2.38)$$

$$\frac{\partial^2 \Theta_2}{\partial z^2} - Pr \frac{\partial \Theta_2}{\partial t} - Pe \left\{ \gamma_1 \text{Re}[\xi_2] + \gamma_2 \text{Im}[\xi_2] \right\} + Br \left\| \frac{\partial \xi_2}{\partial z} \right\|^2 + Br Ha^2 \|\xi_2\|^2 = 0. \quad (2.39)$$

The corresponding boundary condition (2.20) reduces to

$$\Theta_1(\pm h) = 0, \quad \Theta_2(\pm h, t) = 0, \quad \Theta_2(z, 0) = -\Theta_1(z). \quad (2.40)$$

Using the boundary condition $\Theta_1(\pm h) = 0$ in Eq. (2.38), we obtain the solution of the steady

temperature profile as

$$\begin{aligned}
 \Theta_1(z) = & \frac{A_1 Pe \gamma_2 \cosh(z\kappa)}{\kappa^2} - \frac{\gamma_j z^2}{2} + \frac{Pe \gamma_2}{(\phi_1^2 + \phi_2^2)^2} \left\{ (2A_5 \phi_1 \phi_2 + A_4 \phi_2^2) \sin(z\phi_1) \sinh(z\phi_2) \right. \\
 & - A_2 \left(\frac{A_5 \phi_1^2 + 2A_4 \phi_1 \phi_2 - A_5 \phi_2^2}{\phi_1^2 - A_4 \phi_1^2 + \phi_2^2} \right) \cos(z\phi_1) \cosh(z\phi_2) \left. \right\} + \frac{Pe(A_6 \gamma_1 + A_1 \gamma_2) \cosh(h\kappa)}{\kappa^2} \\
 & + \frac{Pe \gamma_1 A_6 \cosh(z\kappa)}{\kappa^2} + \frac{Pe \gamma_1}{(\phi_1^2 + \phi_2^2)^2} \left\{ A_2 (2A_5 \phi_1 \phi_2 + A_4 (\phi_2^2 - \phi_1^2)) \cos(z\phi_1) \cosh(z\phi_2) \right. \\
 & + (2A_4 \phi_1 \phi_2 + A_5 (\phi_1^2 - \phi_2^2)) \sin(z\phi_1) \sinh(z\phi_2) \left. \right\} + \frac{A_2 Pe}{(\phi_1^2 + \phi_2^2)^2} \left[- \left(\frac{(A_4 \gamma_1 + A_5 \gamma_2) \phi_1^2}{(\phi_1^2 + \phi_2^2)} \right) \right. \\
 & + 2 \left(\frac{(A_5 \gamma_1 - A_4 \gamma_2) \phi_1 \phi_2}{(\phi_1^2 + \phi_2^2)} \right) + \left. \left(\frac{(A_4 \gamma_1 + A_5 \gamma_2) \phi_2^2}{(\phi_1^2 + \phi_2^2)} \right) \right] \cos(h\phi_1) \cosh(h\phi_2) \\
 & + \left\{ \left(\frac{(A_5 \gamma_1 - A_4 \gamma_2) \phi_1^2}{(\phi_1^2 + \phi_2^2)} \right) + 2 \left(\frac{(A_4 \gamma_1 + A_5 \gamma_2) \phi_1 \phi_2}{(\phi_1^2 + \phi_2^2)} \right) \right\} \sin(h\phi_1) \sinh(h\phi_2) \\
 & + \left(\frac{(-A_5 \gamma_1 + A_4 \gamma_2) \phi_2^2}{(\phi_1^2 + \phi_2^2)} \right) \sin(h\phi_1) \sinh(h\phi_2) + \Gamma(z), \quad (2.41)
 \end{aligned}$$

where the mathematical expressions for ϕ_1 , ϕ_2 , A_j ($j = 1, 2, \dots, 6$) and $\Gamma(z)$ are given in Appendix 2.A.

The solution of Eq. (2.39) by employing the separation of variables method in conjunction with cosine Fourier series expansion subject to the boundary condition (2.40), is obtained as

$$\Theta_2(z, t) = \sum_{n=0}^{\infty} B_n(t) \cos(\lambda_n z), \quad (2.42)$$

where $B_n(t) = e^{-\frac{\lambda_n^2}{Pr} t} \int e^{\frac{\lambda_n^2}{Pr} t} P_n(t) dt + C_n e^{-\frac{\lambda_n^2}{Pr} t}$, and the time-dependent Fourier coefficient can be obtained as

$$P_n(t) = \frac{\int_0^h P(z, t) \cos(\lambda_n z) dz}{\int_0^h \cos^2(\lambda_n z) dz}, \quad (2.43)$$

where

$$P(z, t) = \left[Pe \left\{ \gamma_1 \text{Re}[\xi_2] + \gamma_2 \text{Im}[\xi_2] \right\} - Br \left\| \frac{\partial \xi_2}{\partial z} \right\|^2 - Br Ha^2 \|\xi_2\|^2 \right].$$

Using the initial condition $\Theta_2(z, 0) = -\Theta_1(z)$, the coefficient C_n can be determined as

$$C_n = - \frac{\int_0^h \Theta_1(z) \cos(\lambda_n z) dz}{\int_0^h \cos^2(\lambda_n z) dz}. \quad (2.44)$$

2.3.4 The Nusselt number

After having determined the velocity and temperature distributions, the dimensionless temperature averaging over one wavelength is expressed as

$$T_b(t) = \frac{k_{th}(\tilde{T}_b - \tilde{T}_w)}{\tilde{q}_w \tilde{H}} = \frac{\int_0^1 \int_{-h}^h \xi(z, t) \theta(z, t) dz dx}{\int_0^1 \int_{-h}^h \xi(z, t) dz dx}. \quad (2.45)$$

The rate of heat transfer at the surface of the microchannel is represented by the Nusselt number, which is defined by

$$Nu(t) = \frac{2\tilde{H}\tilde{q}_w}{k_{th}(\tilde{T}_w - \tilde{T}_b)} = -\frac{2}{T_b(t)}. \quad (2.46)$$

2.4 Validation of results

In the present study, we have obtained an analytical solution of complex velocity profile $\xi(z, t)$ for unsteady EMHD flow through a rotating microchannel with sinusoidal surface roughness, where $\xi(z, t)$ is the combination of steady component ($\xi_1(z)$) and unsteady component ($\xi_2(z, t)$). In the case of rotating electroosmotic flow through a smooth microchannel (when $\alpha_j = 0$ with $\zeta_w = 1$ and $Ha = 0$), the solution to the steady component ($\xi_1(z)$) yields

$$\xi_1(z) = \frac{\kappa^2}{(\kappa^2 - 2i\omega)} \left[\frac{\cosh(z\sqrt{2i\omega})}{\cosh(\sqrt{2i\omega})} - \frac{\cosh(\kappa z)}{\cosh(\kappa)} \right]. \quad (2.47)$$

This expression exhibits perfect consistency and conformity with the results obtained by [Chang and Wang \[2011\]](#).

To ensure the validity of our current analytical investigation, we have conducted a comparative analysis between our results and the results obtained by [Gheshlaghi et al. \[2016\]](#). Their study involved an analytical examination of time-dependent electroosmotic flow through a rotating microchannel, specifically focusing on the impact of frame rotation on the flow. However, in our present investigation, we have expanded based on their work by considering a sinusoidal rough microchannel with varying wave amplitudes (α_j , where $j = 1, 2, 3$) and wave numbers (β_j , where $j = 1, 2, 3$). Our analysis also incorporates the scenario where the microchannel becomes smooth, represented by $\alpha_j = 0$. By fixing $\alpha_j = 0$, $Ha = 0$ in the present results, we have incorporated the transient velocity profiles versus time for different values of rotation number (ω), which is depicted in Fig. 2.2. Thus the present results are strongly agreed with the analysis of [Gheshlaghi et al. \[2016\]](#), where the effect of the applied magnetic field and transverse electric field was neglected, and assuming a constant zeta potential. In Fig. 2.2(a), the increasing rotation number ω , contributes to the higher oscillations in the central line velocity. Similar oscillatory velocity profiles are observed in Fig. 2.2(b) in the transverse centre line velocity (v_c), as displayed. For both velocity profiles, the present results have a strong alignment with the results of [Gheshlaghi et al. \[2016\]](#). This oscillation of flow is only due to the flow development in time and the flow becomes steady-state after a certain period of time, hence for $t = 2$.

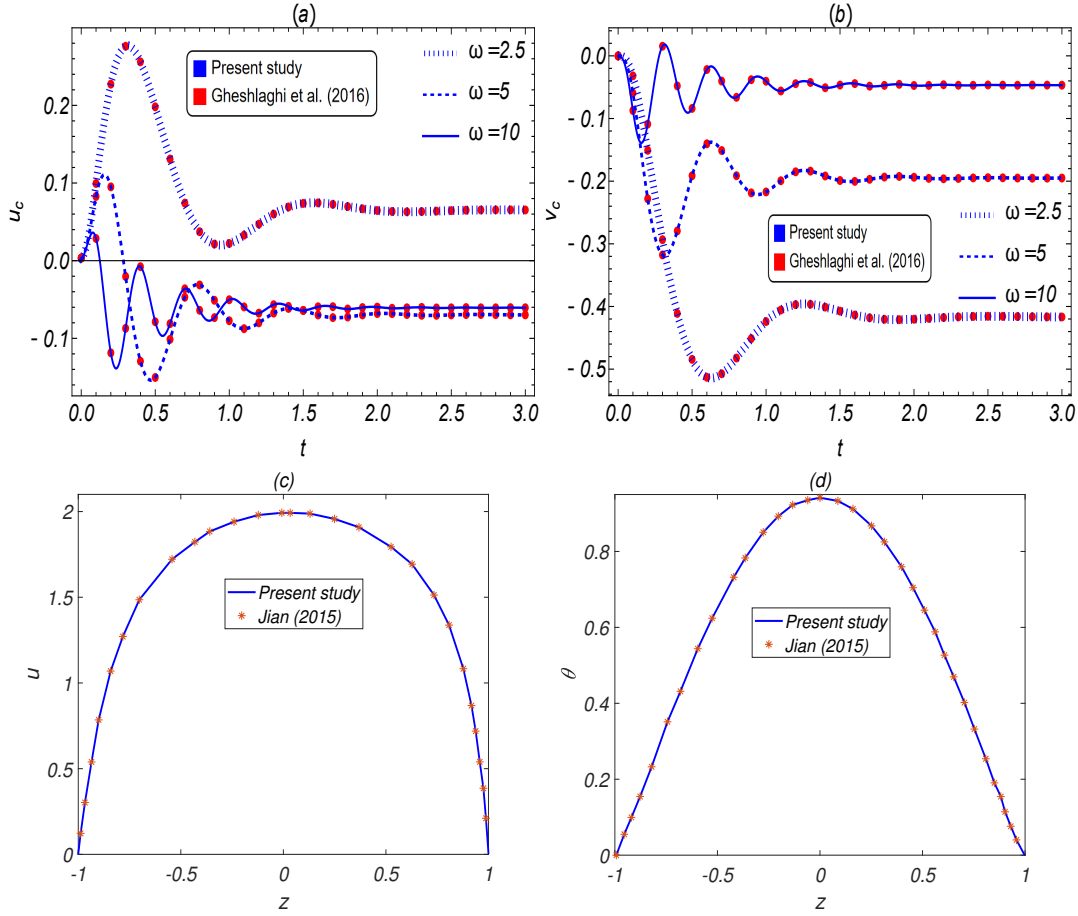


Figure 2.2: Comparison of center-line velocity components with the results of Gheshlaghi et al. [2016] for $\kappa = 5$, $\zeta_w = 1$, $Ha = 0$, $\alpha_1 = 0$, $\alpha_2 = 0$, $\alpha_3 = 0$, where (a) displays the variation of center-line primary velocity u_c and (b) shows the center-line secondary velocity v_c for different values of ω . In the limiting case, comparison of (c) axial velocity (u) and (d) temperature distribution (θ) for the non-rotating case ($\omega = 0$) with the results of Jian [2015] when we set $\kappa = 10$, $Ha = 1$, $t = 0.4$, $\alpha_1 = \alpha_2 = \alpha_3 = 0$.

2.4.1 Limiting case: Transient heat transfer in non-rotating microchannel with roughness

If the micro-channel is in non-rotating frame ($\omega = 0$), then the dimensionless axial momentum equation can be governed from Eq. (2.17) and it can be written as

$$\frac{\partial u}{\partial t} = \frac{\partial^2 u}{\partial z^2} + \frac{\partial^2 \psi}{\partial z^2} - Ha^2 u, \quad (2.48)$$

with dimensionless boundary conditions

$$u(\pm h, t) = 0, \quad u(z, 0) = 0. \quad (2.49)$$

Hence the solution for velocity distribution is obtained as

$$u(z, t) = \frac{\zeta_w \kappa^2 \cosh(\kappa z)}{(Ha^2 - \kappa^2) \cosh(\kappa h)} - \frac{\zeta_w \kappa^2 \cosh(zHa)}{(Ha^2 - \kappa^2) \cosh(hHa)} + \sum_{n=0}^{\infty} H_n \cos(\lambda_n z) e^{-(Ha^2 + \lambda_n^2)t}, \quad (2.50)$$

where

$$H_n = \left\{ D_n + \frac{8h\zeta_w \kappa^3 \sin(n\pi) \tanh(\kappa h)}{\{(\pi + 2n\pi)^2 + 4h^2 \kappa^2\} (Ha^2 - \kappa^2)} \right\}, \quad \lambda_n = (2n + 1) \frac{\pi}{2h},$$

$$D_n = \frac{8h}{(\pi + 2n\pi)^2 + 4h^2 Ha^2} \left[-\frac{2h(1 + 2n)\pi \zeta_w \kappa^2}{(\pi + 2n\pi)^2 + 4h^2 \kappa^2} \cos(n\pi) - \frac{Ha \zeta_w \kappa^2 \sin(n\pi) \tanh(hHa)}{(Ha^2 - \kappa^2)} \right].$$

With this assumption, the temperature equation can be modelled from Eq. (2.25), which reduces to

$$Pr \frac{\partial \theta}{\partial t} + Pe \gamma_1 u = \frac{\partial^2 \theta}{\partial z^2} + Br \left(\frac{\partial u}{\partial z} \right)^2 + Ha^2 u^2 + \gamma_j, \quad (2.51)$$

with the boundary conditions

$$\theta(\pm h, t) = 0, \quad \theta(z, 0) = 0. \quad (2.52)$$

The analytical solution of the temperature distribution is obtained by solving Eq. (2.51) along with the boundary conditions (2.52) in the form

$$\theta(z, t) = \Upsilon(z) - \Upsilon(h) + \sum_{n=0}^{\infty} E_n(t) \cos(\lambda_n z), \quad (2.53)$$

where,

$$\begin{aligned} \Upsilon(z) &= \iint \left[Pe \gamma_1 u - Br \left(\frac{\partial u}{\partial z} \right)^2 + Ha^2 u^2 - \gamma_j \right] dz dz, \\ E_n(t) &= e^{-\frac{\lambda_n^2}{Pr} t} \int e^{\frac{\lambda_n^2}{Pr} t} F_n(t) dt + G_n e^{-\frac{\lambda_n^2}{Pr} t}, \\ F_n(t) &= \frac{1}{\int_0^h \cos^2(\lambda_n z) dz} \left[\int_0^h \left\{ Pe \gamma_1 u - Br \left(\frac{\partial u}{\partial z} \right)^2 + Ha^2 u^2 \right\} \cos(\lambda_n z) dz \right], \\ G_n &= -\frac{\int_0^h \{ \Upsilon(z) - \Upsilon(h) \} \cos(\lambda_n z) dz}{\int_0^h \cos^2(\lambda_n z) dz}. \end{aligned}$$

Further, one can easily evaluate the transient rate of heat transfer in a similar process, which is already discussed above.

To validate our findings in the limiting case, we compared our results with those of Jian [2015], who discussed transient electromagnetic hydrodynamic (EMHD) flow and heat transfer through a smooth microchannel. Specifically, when the parameters α_j (where $j = 1, 2, 3$) are set to zero, our solution for the non-rotating EMHD flow aligns with the results presented by Jian [2015]. This

comparison provides a confirmation of the accuracy and consistency of our obtained solution for the specific limiting case, which is delineated in Figs. 2.2(c)-2.2(d).

2.5 Results and Discussion

The analytical investigation was conducted to observe the transient flow transport through a sinusoidal rough microchannel under an electromagnetic environment, in the presence of the Coriolis force. To obtain the numerical results for graphical representation, we use the values of the following physical variables to calculate the reference parameters of the present study: the half-height of the microchannel (\tilde{H}) ranges in $10 - 40\mu m$ (Rana et al. [2022]) with wave amplitude $\alpha_j \sim 0 - 0.1$ (up to 10% roughness of the channel) and wave number $\beta_j \sim 0 - 20$ for sinusoidal rough surface (Cho et al. [2013]; Keramati et al. [2016]; Rana et al. [2022]), EDL thickness ($\tilde{\kappa}$) varies $0.25\mu m - 1\mu m$ (Shit et al. [2016a]; Gheshlaghi et al. [2016]). Hence, the electroosmotic parameter is calculated to be $\kappa \sim 10 - 100$. The strength of the electric field along the axial direction is imposed as $E_0 \sim 0 - 2 \times 10^4 V/m$ (Chang and Wang [2011]; Shit et al. [2016a]). The uniform magnetic field strength $B_0 \sim 1 - 10T$, (Jang and Lee [2000]; Rana et al. [2022]) gives the range of the Hartmann number as $Ha \sim 0 - 2$. We impose the zeta potential in the range of $\tilde{\zeta}_0 \sim (-18)mV - (-12.5)mV$ (Banerjee et al. [2022]). Further, the rotation number varies from $\omega \sim 0 - 10$, where the range of the angular velocity $\Omega \sim 0 - 1000 rps$ (Chang and Wang [2011]; Gheshlaghi et al. [2016]). The constant heat flux $q_w = 1500W/m^2$, gives the joule heating parameter in the range $\gamma_j \sim 1 - 10$ (Banerjee and Nayak [2019]). The range of Peclet number is $Pe \sim 0.26 - 19$, the Prandtl number varies from $Pr \sim 5 - 10$ according to the study conducted by Horiuchi and Dutta [2006] and the Brinkman number Br varies in $\sim 0 - 1$, as per the existing literature (Jian [2015]; Avramenko et al. [2017]; Horiuchi and Dutta [2004]).

2.5.1 Rotation induced EMHD flow analysis

This subsection demonstrates the characteristics of the analytical solution for rotation-induced EMHD velocity profiles through the Figs. 2.3-2.7. Specifically, contour plots and 2D velocity profiles for the primary velocity component (streamwise velocity) and secondary velocity component (wall-normal velocity) are illustrated to depict the effects of different values of the rotation number (ω), Hartmann number (Ha), electroosmotic parameter (κ) and roughness parameter (α_1).

Figure 2.3 depicts the velocity profiles as a function of z at a location of $x = 0.2$. The velocity profiles are significantly affected by the system rotation. Figure 2.3(a) shows an increase in the rotation number ω reduces the primary velocity, as the rotational effect is caused by the Coriolis force, which counteracts the flow motion. This force acts perpendicular to the direction of fluid motion and the axis of rotation. As the fluid moves along the streamwise direction, the Coriolis force introduces additional resistance, effectively reducing the flow velocity at the central region of the channel. It is interesting to note from Fig. 2.3(a) that two minima exist in the velocity profiles at high rotation speeds. These minima ensure the presence of velocity gradients, enhancing molecular diffusion, especially for low Reynolds number flows. As the fluid moves from higher velocity to lower velocity,

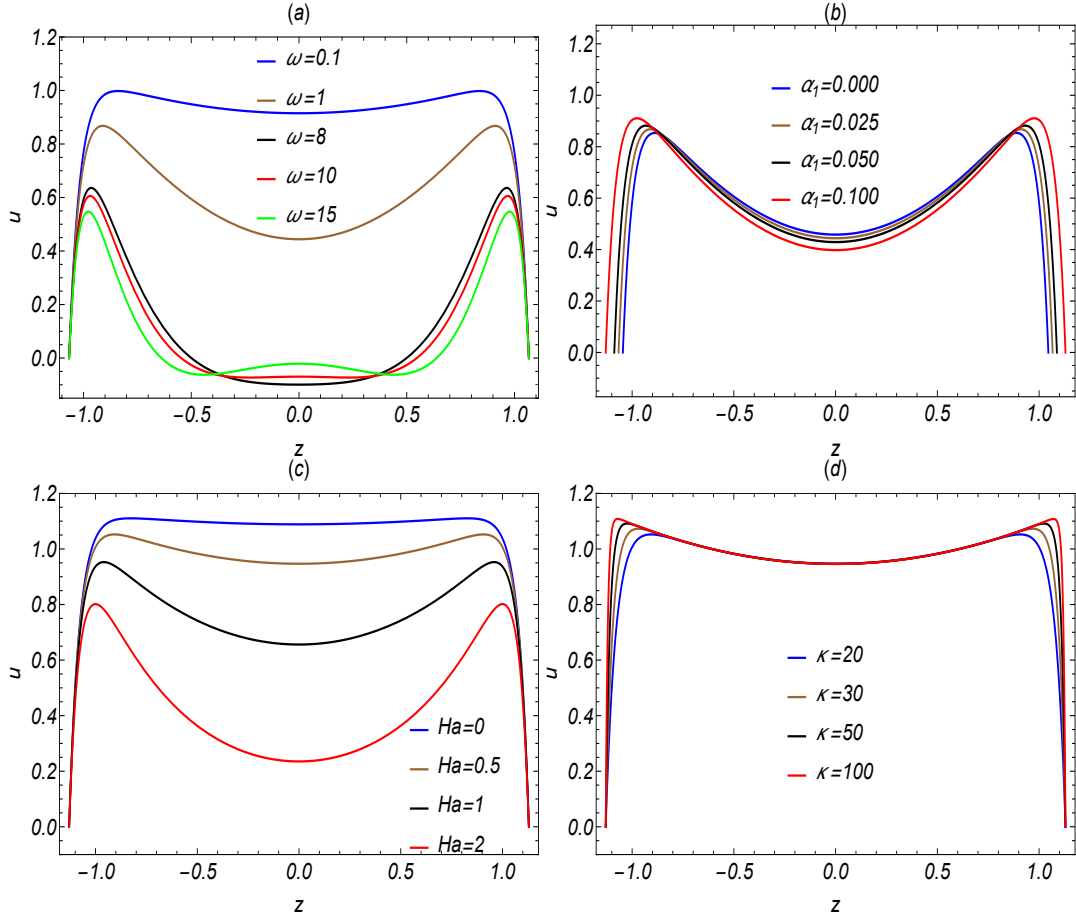


Figure 2.3: Variation of primary velocity profiles (u) at $x = 0.2$, while varying parameters ω , α_1 , Ha , and κ . Subfigure (a) examines the influence of different rotation ω on the axial velocity profiles when $\alpha_1 = 0.025$. Subfigure (b) explores the impact of different roughness α_1 on the velocity profiles, when $\omega = 1$. Subfigure (c) shows the effect of Ha , when $\omega = 0.1$ and $\alpha_1 = 0.1$. Subfigure (d) displays the effect of varying κ on the velocity profile, with fixed $\omega = 0.1$ and $\alpha_1 = 0.1$. These profiles are computed for specific values of $\kappa = 20$, $Ha = 0.5$, $\alpha_2 = 0.04$, $\alpha_3 = 0.03$, $\beta_1 = 5$, $\beta_2 = 4$, and $\beta_3 = 2$ at $t = 2$.

the diffusion process is accelerated, leading to enhanced micromixing. Moreover, the presence of velocity gradients can result in Taylor dispersion, a phenomenon where fluid molecules experience dispersion due to the variation in flow velocities along the channel length. However, the maximum velocity exists near the boundary layers, where the fluid particles aggregate. The influence of surface roughness on the velocity profile is displayed in Fig. 2.3(b). The increase in the roughness parameter enhances the flow velocity near the boundary layers but reduces it in the middle layer of the flow when the system undergoes rotation. This effect can be attributed to the increased surface area and friction factor caused by the roughness elements. Near the boundary layers, the rough surface disrupts the flow, creating eddies that can increase the velocity locally. However, in the middle layer of the channel, the roughness elements disturb the flow more uniformly, leading to an overall reduction in velocity. Fig. 2.3(c) illustrates the effect of the magnetic field on the velocity

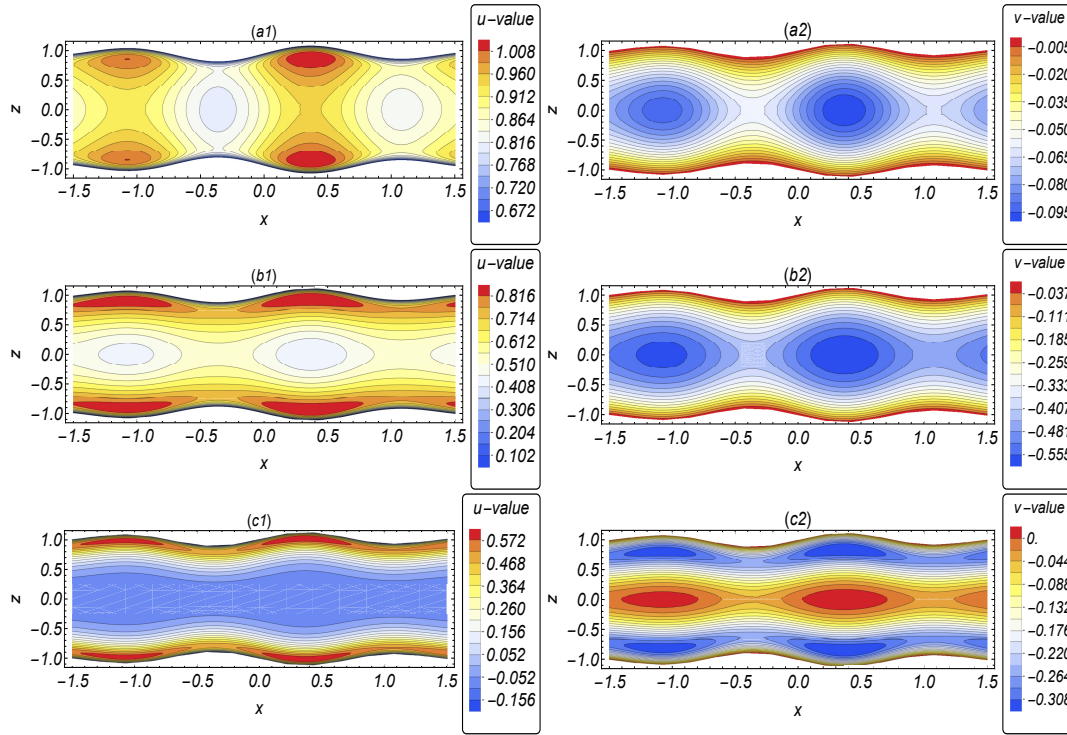


Figure 2.4: The velocity contours for primary velocity component (u) in the left panel and secondary velocity component (v) in the right panel for (a) $\omega = 0.1$, (b) $\omega = 1$, (c) $\omega = 10$, when $\kappa = 20$, $Ha = 0.5$, $t = 2$, $\alpha_1 = 0.05$, $\alpha_2 = 0.04$, $\alpha_3 = 0.03$, $\beta_1 = 5$, $\beta_2 = 4$ and $\beta_3 = 2$. The development of secondary flow due to the rotation modifies the primary velocity and the maximum velocity shifted toward the surface of the channel.

profile with 10% surface roughness of the channel half-height. We observe that with an increase in the Hartmann number (Ha), the flow velocity decreases, which agrees with the well-established results (Chakraborty and Paul [2006]). This phenomenon is attributed to the Lorentz force, which acts as a retarding force. Fig. 2.3(d) demonstrates the variation of axial velocity with varying electroosmotic parameter (κ). The increase in the electroosmotic parameter enhances the flow velocity in the boundary layer due to the electric potential at the EDL, where the counter-ions move towards the surface and the bulk fluid motion takes place in the central region. In the boundary layer, where the fluid interacts more closely with the solid surface, and the effects of the electric potential are significant. The electrical double layer creates a net flow of the fluid, known as the electroosmotic flow, which enhances the velocity near the walls.

Figure 2.4 illustrates the velocity contours for primary and secondary flows with varying rotation numbers. Velocity contours provide quantitative flow structure and the magnitude of the velocity. The fluid boluses (referred to concentrated volume of fluids that moves through the channel) with different structures are formed for different rotation numbers. In Fig. 2.4, the left panel indicates contour plots of primary velocity components with a region of higher velocity that moves faster than the region of minimum velocity. The right panel represents the corresponding development of secondary flow induced in the wall-normal direction due to the rotation. In Fig. 2.4(a), for

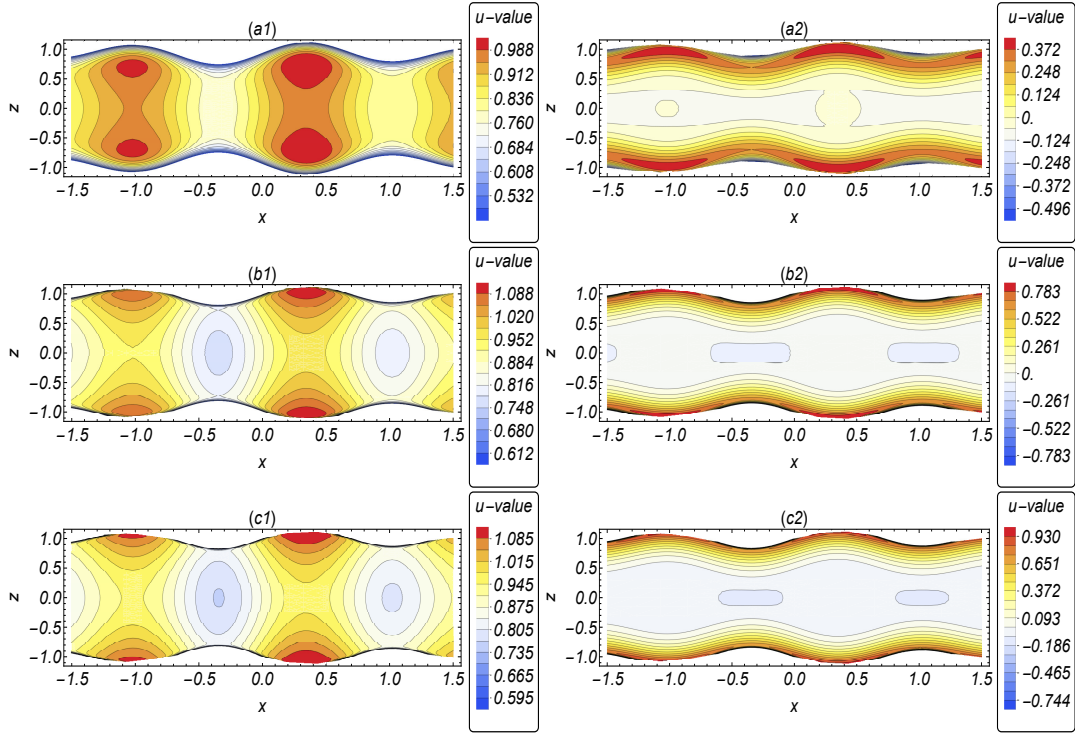


Figure 2.5: Velocity contour for primary flow (u) when (a) $\kappa = 10$, (b) $\kappa = 50$, (c) $\kappa = 100$ and setting $Ha = 0.5$, $t = 2$, $\alpha_1 = 0.1$, $\alpha_2 = 0.04$, $\alpha_3 = 0.03$, $\beta_1 = 5$, $\beta_2 = 4$ and $\beta_3 = 2$. The figures in the left panel represent without rotation ($\omega = 0$), while the figures in the right panel correspond to the rotation ($\omega = 10$).

$\omega = 0.1$, primary flow circulations are formed with the highest velocity near the boundary, while the secondary flow circulation exists in the middle layers. As the rotation speed increases, the secondary flow strongly develops in the middle of the channel and pushes back the primary velocity to exist at the boundary layer. Similar observation is noticed for $\omega = 1$ in Fig. 2.4(b), as depicted in Fig. 2.4(a). However, for higher rotation numbers as shown in Fig. 2.4(c), with $\omega = 10$, the velocity decreases, and the primary flow circulation shifts towards the surface of the channel. Interestingly, in the case of secondary flow, some additional flow circulation appears within the boundary layers due to the interaction of Coriolis and viscous forces. The occurrence of maximum velocity at the boundary layer for primary flow can be attributed to the effect of the Coriolis force. The boundary layer experiences more friction with the solid surface, which enhances the velocity gradient near the walls. For the secondary flow, the rotation of the system introduces centrifugal force, pushing the fluid towards the centre and resulting in higher velocities in the middle layers. But for higher rotation numbers, the secondary flow velocity is minimum at the middle layers and some small flow circulations are formulated at the boundary layers where the velocity magnitude of the secondary flow is maximum (cf. Fig. 2.4(a)-Fig. 2.4(b)). The interplay between centrifugal and viscous forces results in a complex flow pattern where the maximum velocity of the secondary flow occurs at the boundary layers, and the eddies are formed, while the velocity decreases at the middle layers (Fig. 2.4(c)).

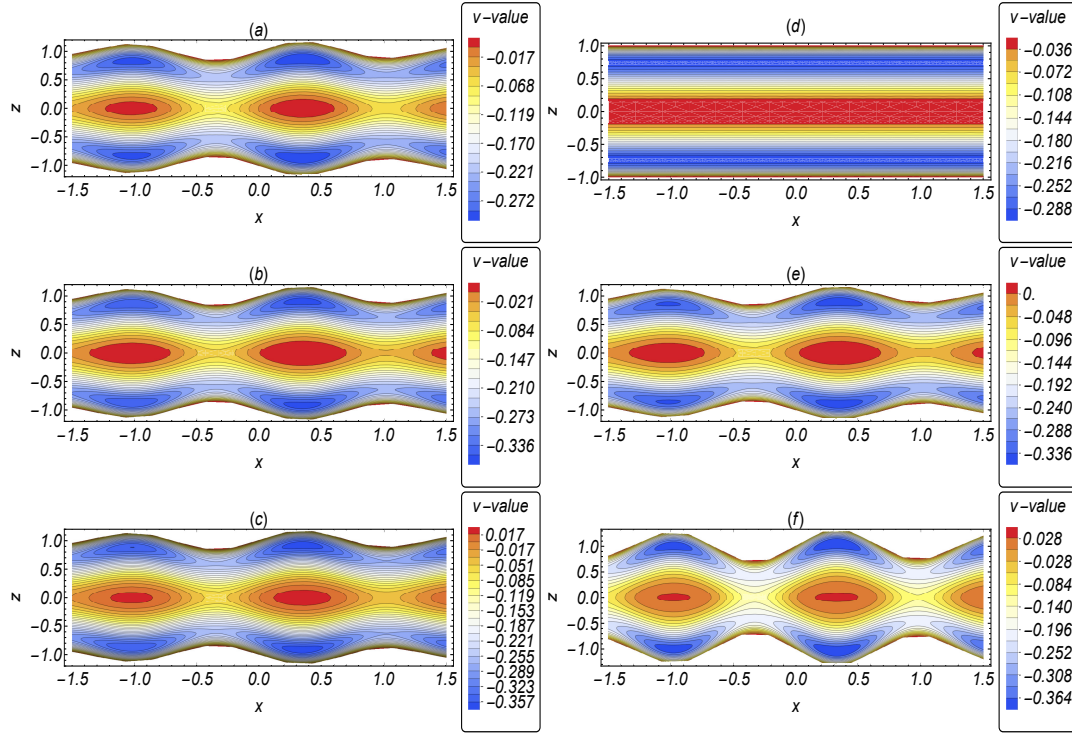


Figure 2.6: Velocity contours for secondary flow (v) in the left panel when (a) $\kappa = 10$, (b) $\kappa = 50$, (c) $\kappa = 100$ with fixed values $Ha = 0.5$, $\omega = 10$, $t = 2$, $\alpha_1 = 0.1$, $\alpha_2 = 0.04$, $\alpha_3 = 0.03$, $\beta_1 = 5$, $\beta_2 = 4$ and $\beta_3 = 2$. Velocity contours for secondary flow (v) in the right panel for a smooth and rough surface channel when (d) $\alpha_1 = 0$, (e) $\alpha_1 = 0.1$, (f) $\alpha_1 = 0.25$ with fixed values $\kappa = 20$, $\omega = 10$, $Ha = 0.5$, $t = 2$, $\alpha_2 = 0.04$, $\alpha_3 = 0.03$, $\beta_1 = 5$, $\beta_2 = 4$ and $\beta_3 = 2$.

The velocity contours in Fig. 2.5 illustrate the complex interplay between the electroosmotic effects, surface roughness, and Coriolis force in the microchannel flows. In the absence of rotation ($\omega = 0$), surface roughness induces the formation of two distinct flow circulations (cf. Fig 2.5(a)), one characterizing with positive values and the other for negative values. However, when rotation is introduced ($\omega = 10$), flow reversal emerges for low electroosmotic parameters (large EDL thickness). For higher values of κ (Figs. 2.5(b) and 2.5(c)), the influence of rotation ($\omega = 10$) becomes more pronounced, leading to a more intricate flow pattern that intensifies the backflow. These observations highlight the importance of considering rotational effects in micro-scale flows, as they can significantly alter the flow behaviour and mixing characteristics. The electric double layer near the solid surfaces induces an electroosmotic flow, which drives fluid motion towards the walls, resulting in higher velocities. This effect is more pronounced in the boundary layers due to the closer proximity to the solid surfaces, where the influence of the electric double layer is stronger. Conversely, in the middle region of the microchannel, the influence of the electric double layer is less significant, leading to lower velocities compared to the boundary layers.

Figure 2.6 demonstrated to further visualize the secondary flow patterns under the influence of electroosmotic parameters and with or without the rough surface of the microchannel. From the left panel, in Figs. 2.6(a)-2.6(c), we observe the impact of EDL thickness on the secondary flow pat-

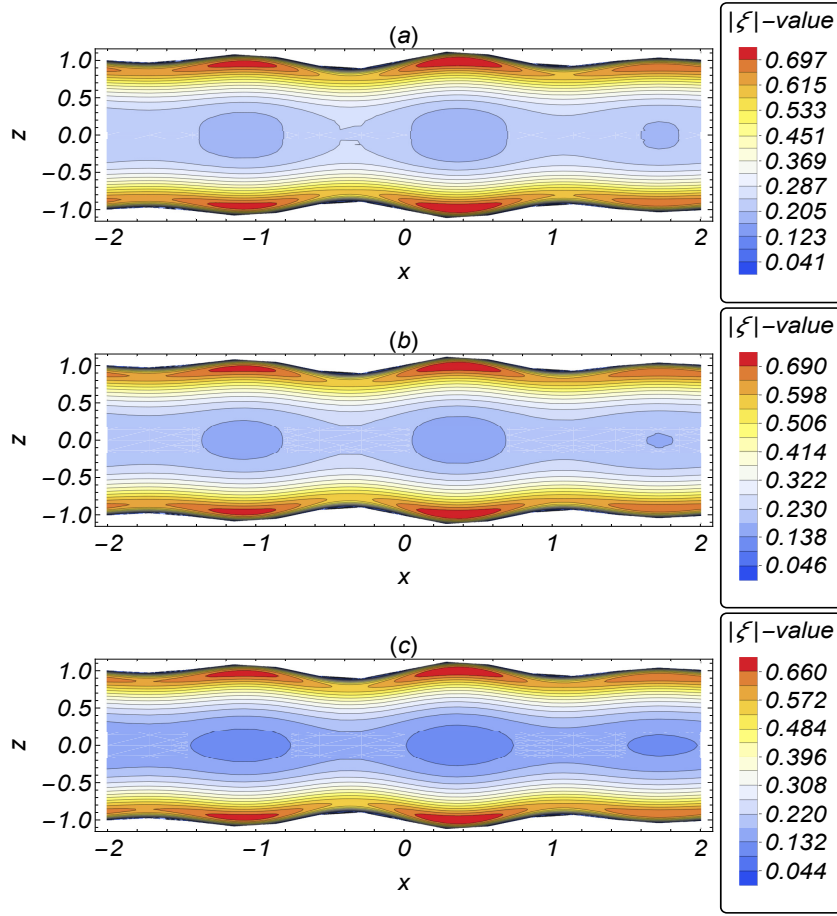


Figure 2.7: Velocity magnitude ($|\xi| = \sqrt{u^2 + v^2}$) contours for (a) $Ha = 0$, (b) $Ha = 1$, (c) $Ha = 2$, when $\kappa = 20$, $\omega = 5$, $t = 2$, $\alpha_1 = 0.05$, $\alpha_2 = 0.04$, $\alpha_3 = 0.03$, $\beta_1 = 5$, $\beta_2 = 4$ and $\beta_3 = 2$. The magnitude of the flow velocity diminishes with the Hartmann number Ha . This scenario is different from the smooth surface channel and without rotation.

terns. When the electric double layer (EDL) thickness is almost overlapping (for $\kappa = 10$), multiple flow circulations occur. As the EDL thickness decreases, meaning the electroosmotic parameter increases, these additional flow circulations vanish, and a strong flow circulation with positive values takes place. This enhancement of secondary flow is attributed to the electric double layer near the solid surfaces. This secondary flow drives the fluid motion towards the walls, resulting in higher velocities in the boundary layers. The presence of surface roughness introduces additional complexities to the flow dynamics within the microchannel. As the roughness parameter α_1 increases, the irregularities on the microchannel surface become more pronounced. These irregularities disrupt the secondary flow patterns, leading to the formation of vortices, which is delineated in Figs. 2.6(d)-2.6(f). When $\alpha_1 = 0$, representing a smooth microchannel, no distinct flow circulation is observed (Fig. 2.6(d)). However, in the presence of roughness of the channel (Figs. 2.6(e)-2.6(f)) the flow circulation becomes stronger. This variation in α_1 induces changes in flow patterns and enhances flow magnitude. The increased irregularity of the microchannel surface due to roughness

alters the flow dynamics, leading to the formation of vortices. This phenomenon underscores the significant role of surface roughness in modifying flow patterns in the microchannels. The formation of vortices can be attributed to the interaction between the fluid flow and the rough surface. This phenomenon is crucial in microfluidic applications as it affects the overall flow behaviour and can impact processes like mixing and particle manipulation within microchannels.

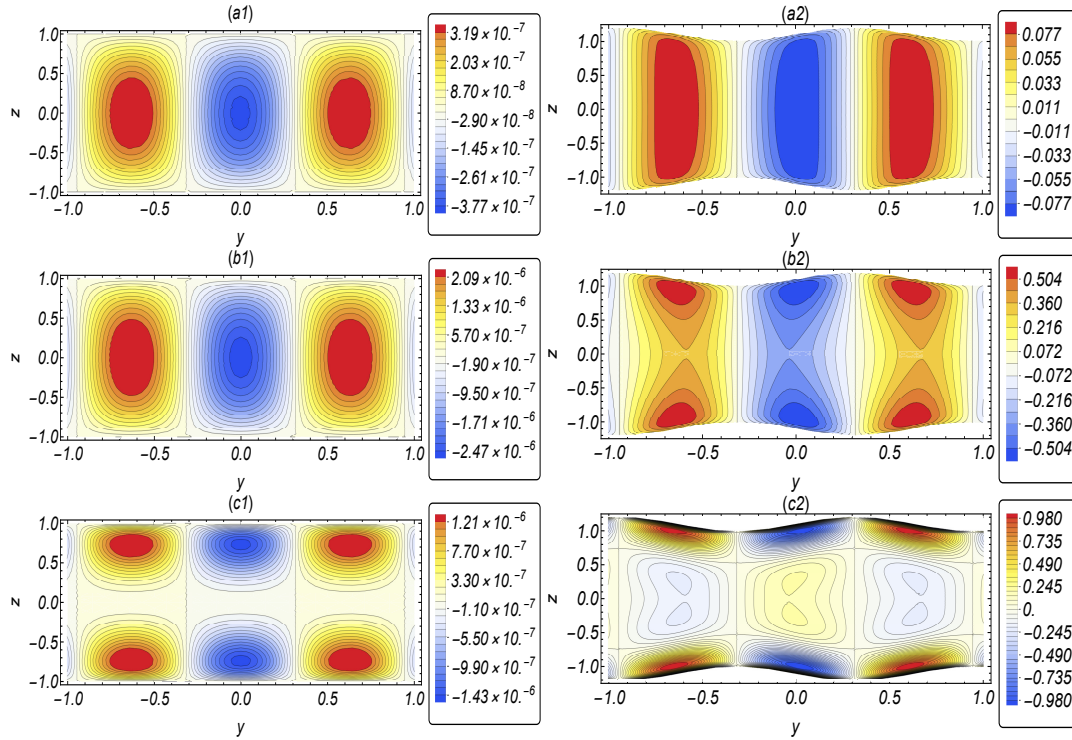


Figure 2.8: Vorticity Contours for (a) $\omega = 0.1$, (b) $\omega = 1$, (c) $\omega = 8$ when $\kappa = 20$, $Ha = 0.5$, $t = 2$, $\alpha_2 = 0.04$, $\alpha_3 = 0.03$, $\beta_1 = 5$, $\beta_2 = 4$ and $\beta_3 = 2$. The left panel figures represent the smooth channel ($\alpha_1 = 0$), while the right panel figures depict the same with an increase in the roughness of the surface ($\alpha_1 = 0.1$).

Figure 2.7 represents the contour plot for velocity magnitude with different Hartmann numbers in the presence of surface roughness and rotation of the channel. As discussed earlier, the maximum velocity at the boundary layers is a result of the rotational effect in the system. As the Hartmann number increases, the strength of the flow circulation decreases. This is because of the Lorentz force that tries to stabilize the flow. The effect of a magnetic field on the flow behaviours is opposite to that of the rotation and electroosmotic parameters. This effect is clearly prominent in Figs. 2.7(a)-2.7(c), where higher velocities are observed near the walls. However, the increment of rotation is seen to have a small reduction in the flow velocity. This reduction can be attributed to the increasing influence of centrifugal forces as the rotation number increases.

Figure 2.8 illustrates the vorticity contours for different rotation rates respectively for smooth and rough surface microchannels. Very clearly we can observe the differences in the formation of vorticity contours between smooth surface and rough surface channels. In the smooth surface channel ($\alpha_1 = 0$), as shown in the left panel (cf. Figs. 2.8(a)-2.8(c)), the vortices primarily exist

in the middle of the channel. The alternative counter-rotating vortices with positive and negative values are observed and transported along the streamwise direction. As the rotation speed increases, the primary vortices split into multiple vortices with less strength and shifted towards the surface of the channel. This is what we expect from the earlier studies. However, in the case of rough surface microchannel as shown in Figs. 2.8(a)-(c) in the right panel, the primary vortices splitted up at lower rotation rates (when $\omega = 1$). From Fig. 2.8(c), we observe that at higher rotation number ($\omega = 8$), the number of vortex formation increases in the case of a rough surface channel than that of a smooth channel. For a smooth microchannel, rotating and counter-rotating vortices are symmetric, while the vortices are symmetric but more irregular and disturbed, spanning the entire rough surface. The shift of vortices towards the boundary layers with increasing rotation and roughness indicates a change in the flow dynamics, likely due to the interaction between the rotational effects and the surface roughness, leading to more complex flow patterns.

2.5.2 Flow rate analysis

Rotationally induced transient secondary flow refers to the additional flow patterns that arise in a fluid system due to the combined effects of rotation and transient conditions. The primary driving force of this secondary flow is the Coriolis force. By examining the angle between the volumetric flow rates in the transverse direction ($q_y(t)$) and the axial direction ($q_x(t)$), one can observe the behaviour of the rotationally induced secondary flow with surface roughness. This angle can be quantified using $\eta(t) = \tan^{-1} \left[\frac{q_y(t)}{q_x(t)} \right]$. The angle $\eta(t)$ at any fixed time t provides insights into the direction and strength of the additional flow patterns generated by the combined effects of rotation and the rough surface conditions. To investigate the impact of ω , κ and Ha on the secondary flow

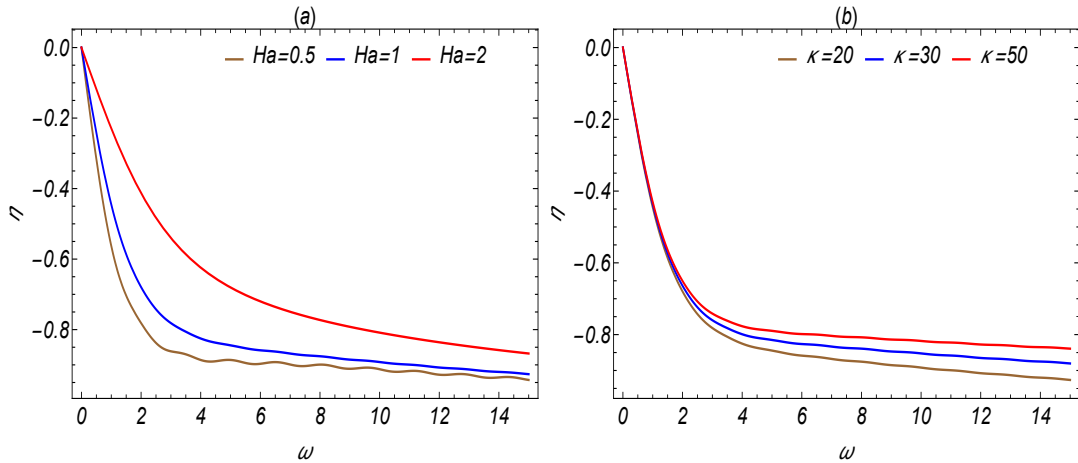


Figure 2.9: The flow rate angle η (radian) versus ω with variation of (a) Hartmann parameter (Ha) for $\kappa = 20$, (b) roughness parameter (α_1) for $Ha = 1$, when $\alpha_1 = 0.025$, $\alpha_2 = 0.04$, $\alpha_3 = 0.01$, $\beta_1 = 5$, $\beta_2 = 10$, $\beta_3 = 2$.

generated by rotation, we analyze the angle $\eta(t)$. Fig. 2.9 illustrates the variation of this angle, providing the relationship between ω , Ha and κ with the resulting secondary flow. Through this

analysis, we learn how these parameters interact and shape the flow patterns. The fluid experiences an electroosmotic force and the Lorentz force resulting from EMHD flow, and the rotation affects the flow velocity field due to the Coriolis force. To fully understand the nature of the flow through a rough surface, it is necessary to consider both factors and their respective magnitudes. Fig. 2.9 clearly demonstrates the substantial impact of (ω) on the oscillatory characteristics exhibited by the flow. As the rotation number (ω) increases, there is a remarkable decrease in the value of the angle η , which serves as compelling evidence for the enhancement of the secondary induced flow. This important fact suggests that higher rotation frequencies exert more influence on secondary flow, leading to intensified fluid motion. This phenomenon is consistent with the findings reported by Chang and Wang [2011]. Fig. 2.9(a) depicts that the applied magnetic field acts as a retarding force, increasing the angle η , which leads to a decrease in the strength of the secondary flow. This effect indicates that the magnetic field can be used to control the oscillatory behaviour of the flow. Fig. 2.9(b) reveals that at lower values of the rotation number ω , the influence of electroosmosis on the flow is minimal, and hence, the angle η remains largely unchanged. However, with an increase in the rotation number ω (beyond $\omega > 2$), the dominance of the Coriolis force becomes more pronounced, resulting in a significant increase in the angle η . This phenomenon implies that higher rotation frequencies have a more pronounced effect on the induced secondary flow.

2.5.3 Analysis of wall shear stress and Poiseuille number

Wall shear stress plays a vital role, impacting flow patterns, secondary flows, and flow separation in a rotating system. It influences the development of boundary layers, transport processes, and mixing characteristics. Wall shear stress also affects drag, resistance, and fluid-structure interactions, making it crucial for engineering design and analysis in rotating channel applications. In microfluidic devices, wall shear stress governs not only the drag and resistance by the fluid particles but also delineates their stability and flow patterns. With the motivation rooted in microfluidic engineering design, the dimensionless wall shear stresses along the rough walls at $z = \pm h$ are derived as follows:

$$\begin{aligned}\tau_u &= \tau_{ux} + i\tau_{uy} = \left[\frac{\partial \xi}{\partial z} \right]_{z=h} \\ &= \frac{\zeta_w \kappa^3 \tanh(\kappa h)}{(Ha^2 - \kappa^2 + 2i\omega)} - \left(\frac{\zeta_w \kappa^2 (H^2 + 2i\omega)}{Ha^2 - \kappa^2 + 2i\omega} \right) \frac{\tanh(h\sqrt{Ha^2 + 2i\omega})}{\sqrt{Ha^2 + 2i\omega}} \\ &\quad - \sum_{n=0}^{\infty} \frac{(1+2n)\pi A_n}{2h} \cos(n\pi) e^{-(2i\omega + Ha^2 + \lambda_n^2)t},\end{aligned}\tag{2.54}$$

$$\begin{aligned}\tau_l &= \tau_{lx} + i\tau_{ly} = \left[\frac{\partial \xi}{\partial z} \right]_{z=-h} \\ &= -\frac{\zeta_w \kappa^3 \tanh(\kappa h)}{(Ha^2 - \kappa^2 + 2i\omega)} + \left(\frac{\zeta_w \kappa^2 (H^2 + 2i\omega)}{Ha^2 - \kappa^2 + 2i\omega} \right) \frac{\tanh(h\sqrt{Ha^2 + 2i\omega})}{\sqrt{Ha^2 + 2i\omega}} \\ &\quad + \sum_{n=0}^{\infty} \frac{(1+2n)\pi A_n}{2h} \cos(n\pi) e^{-(2i\omega + Ha^2 + \lambda_n^2)t}.\end{aligned}\tag{2.55}$$

By decomposing the complex Eqs. (2.54) and (2.55) into their real and imaginary components, we can extract the primary and secondary wall shear stresses acting on the rough walls, attributed to both the primary and secondary flows. This process allows us to compute the numerical values of the dimensionless wall shear stresses, namely τ_{ux} and τ_{uy} , experienced by the upper rough wall ($z = h$) due to these flows. Similarly, we evaluate the wall shear stresses τ_{lx} and τ_{ly} , on the lower rough wall ($z = -h$), resulting from the influence of the primary and secondary flows. Secondary wall shear stress arising from the Coriolis effect in rotating channel flows, distorts primary flow patterns, influencing vortex formation, stability, and flow separation. This secondary shear stress enhances heat and mass transfer, impacting boundary layers and convective processes near channel walls. Fig. 2.10 analyzes the magnitude of wall shear stress ($|\tau| = \sqrt{\tau_{lx}^2 + \tau_{ly}^2}$) along the direction of primary flow for different values of the rotation parameter ω and the Hartmann number Ha . The magnitude of the wall shear stress experiences a diminishing trend with increasing rotation number, as delineated in Fig. 2.10(a). As the rotation number increases, the Coriolis force becomes more significant, causing the flow velocity to decrease. This reduction in the wall shear stress is due to the retardation of flow velocity, as the shear stress is directly proportional to the velocity gradient perpendicular to the flow direction. The magnitude of the wall shear stress has an enhancing nature with increasing Hartmann numbers, as displayed in Fig. 2.10(b). This behaviour is due to the strengthening of the magnetic field, which induces Lorentz force and resists the flow. This distinctive behaviour arises from the interaction between primary and secondary flows, where the wall roughness plays a vital role in shaping these oscillations along the direction of fluid flow.

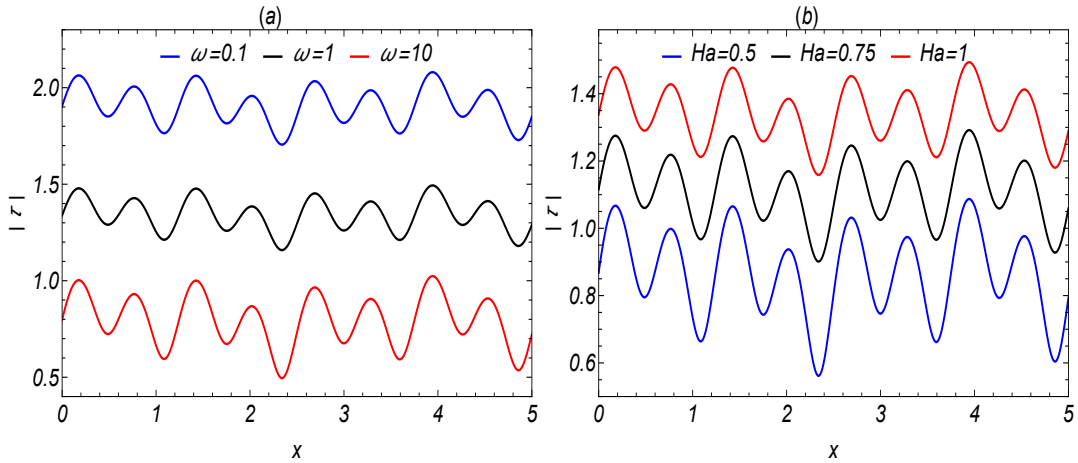


Figure 2.10: Magnitude of Wall shear stress as a function of x with a variation of (a) ω for $Ha = 1$ and (b) Ha for $\omega = 1$, when $\kappa = 20$, $t = 2$, $\alpha_1 = 0.02$, $\alpha_2 = 0.04$, $\alpha_3 = 0.01$, $\beta_1 = 5$, $\beta_2 = 10$, $\beta_3 = 2$.

The Poiseuille number (Po) is a dimensionless parameter which is defined as $Po = fRe$ (cf. Krogstad et al. [2005], Herwig et al. [2008]), where Re is Reynolds number and f is called friction factor expressed as

$$f = \frac{8\bar{\tau}_w}{\rho u_{HS}^2}. \quad (2.56)$$

Here, $\tilde{\tau}_w$ represents the wall shear stress, and u_{HS} is the Helmholtz-Smoluchowski velocity. [Stroh et al. \[2020\]](#) mentioned that the increase of friction factor f with an increase in roughness gives the sign of the increased strength of secondary flow. By using equation (2.55), it is expressed in dimensionless form as

$$f = \frac{8|\tau|}{Re}. \quad (2.57)$$

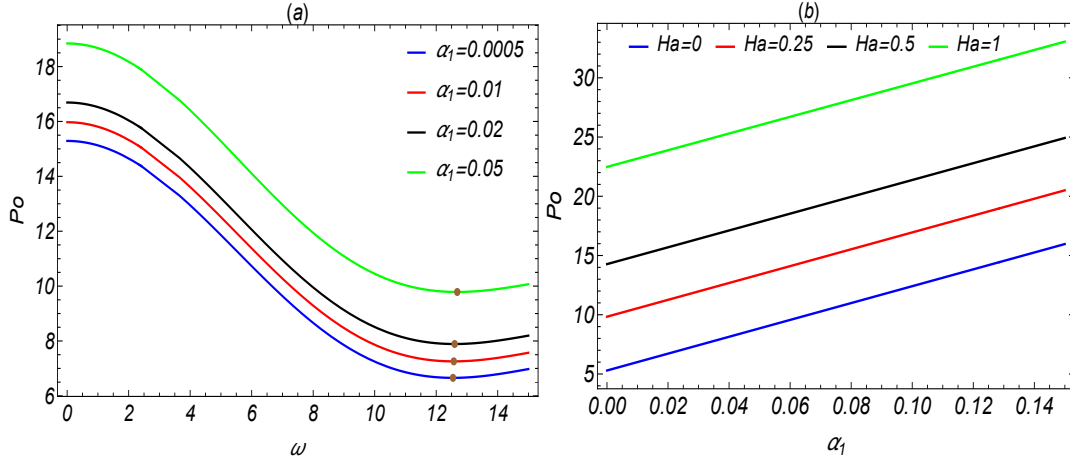


Figure 2.11: Variation in Poiseuille number (Po) as a function of (a) rotation number ω for $Ha = 0.5$, and (b) surface roughness α_1 for $\omega = 5$ when $\kappa = 20$, $t = 2$, $\alpha_2 = 0.04$, $\alpha_3 = 0.01$, $\beta_1 = 5$, $\beta_2 = 10$, $\beta_3 = 2$. The increase in the friction factor f with an increase in roughness indicates a strengthening of the secondary flow ([Stroh et al. \[2020\]](#)). The brown colour marker in the subfigure (a) indicate the minimum point which depends on the roughness of the microchannel.

The Poiseuille number (Po), representing the friction factor intensity, depends on multiple flow-controlling parameters. In this study, we examine how surface roughness, rotation, and electromagnetic forces influence the friction factor. This understanding is crucial for assessing the impact of these factors on flow characteristics, thereby affecting the Poiseuille number and overall flow behaviour in microchannels. [Gamrat et al. \[2008\]](#) reported that the Poiseuille number (Po) is independent of the Reynolds number in the laminar flow regime and measured the Poiseuille number $Po = 24$ for a smooth channel. Figs. 2.11(a) and 2.11(b) demonstrate that an increase in surface roughness enhances the friction factor, resulting in an increase in the Poiseuille number (Po). This occurs because the rough surface of the microchannel increases the wall shear stress, increasing thus the flow friction factor. This result is also supported by the findings of [Herwig et al. \[2008\]](#), who reported that the Po number increases as a function of surface roughness. The increase in rotation number significantly reduces the value of the Poiseuille number (Po), as depicted in Fig. 2.11(a). This reduction occurs because the rotation number diminishes the magnitude of the flow velocity as observed in Fig. 2.7. The presence of system rotation reduces the wall shear stress (cf. Fig. 2.10(a)), thus decreasing the friction factor. From Fig. 2.11(a), it is clear that the minimum value of Po occurs in the range of $12.5 < Po < 12.9$. This implies that for a fixed value of the Hartmann number and electroosmotic parameter, the minimum Poiseuille number Po follows a linear relationship with the roughness amplitude (α_1), which is estimated as $Po = 2.804\alpha_1 + 12.544$. This estimate fits well

2.5. Results and Discussion

within the range of $0 < \alpha_1 < 0.15$. The Poiseuille number increases with the applied magnetic field, defined in terms of the Hartmann number. Electromagnetic forces interact with the flow, altering its velocity distribution and the intensity of shear stress at the wall. This interaction leads to a change in flow behaviour, resulting in an increase in the friction factor, which measures resistance to flow. This phenomenon is important for the interplay between electromagnetic forces, surface roughness, and flow characteristics in microchannels.

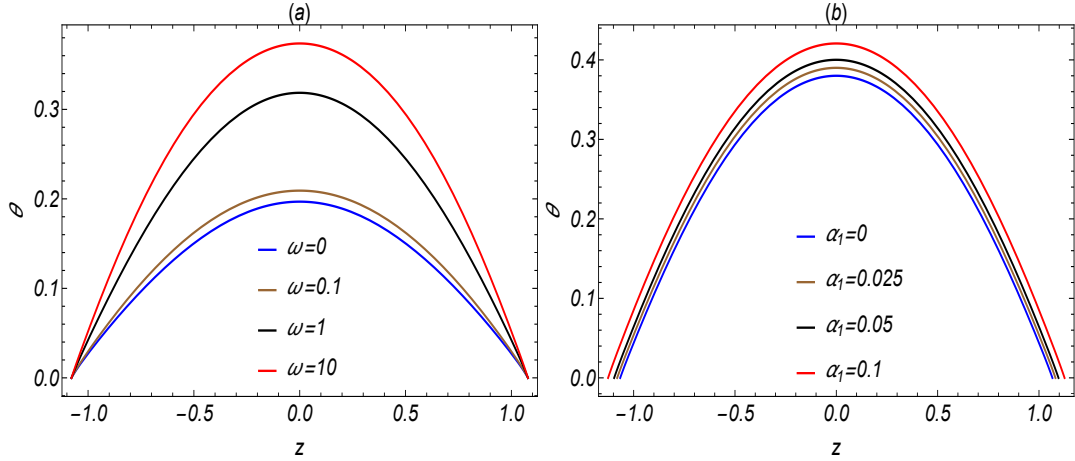


Figure 2.12: Temperature profiles (θ) as a function of z for (a) different ω (for $\alpha_1 = 0.02$) and (b) α_1 (for $\omega = 5$) when $\kappa = 20$, $t = 2$, $Ha = 1$, $Br = 0.01$, $Pe = 5$, $Pr = 5$, $\gamma_j = 0.6$, $\alpha_2 = 0.04$, $\alpha_3 = 0.01$, $\beta_1 = 5$, $\beta_2 = 10$, $\beta_3 = 2$

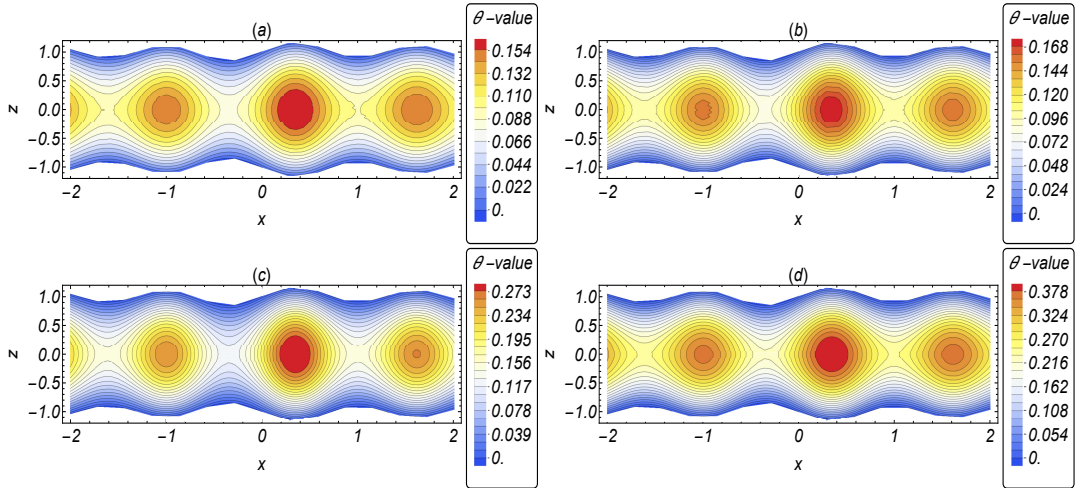


Figure 2.13: Isotherms for (a) $\omega = 0$, (b) $\omega = 0.1$, (c) $\omega = 1$, (d) $\omega = 10$ when $\kappa = 20$, $t = 2$, $Ha = 0.5$, $Br = 0.01$, $Pe = 5$, $Pr = 5$, $\gamma_j = 0.6$, $\alpha_1 = 0.05$, $\alpha_2 = 0.04$, $\alpha_3 = 0.03$, $\beta_1 = 5$, $\beta_2 = 4$, $\beta_3 = 2$

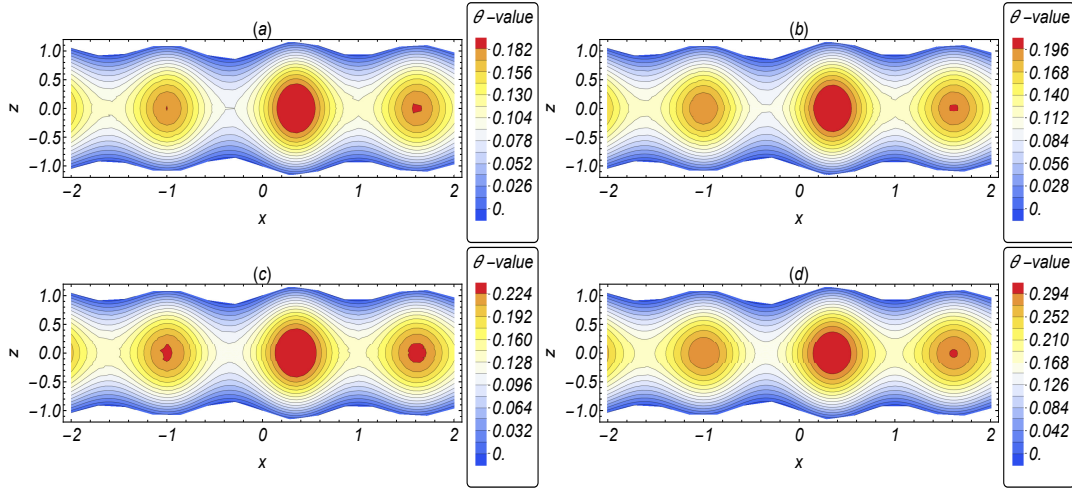


Figure 2.14: Isotherms for (a) $Ha = 0$, (b) $Ha = 0.5$, (c) $Ha = 1$, (d) $Ha = 2$ when $\kappa = 20$, $\omega = 0.5$, $t = 2$, $Br = 0.01$, $Pe = 5$, $Pr = 7$, $\gamma_j = 0.6$, $\alpha_1 = 0.05$, $\alpha_2 = 0.04$, $\alpha_3 = 0.03$, $\beta_1 = 5$, $\beta_2 = 4$, $\beta_3 = 2$.

2.5.4 Temperature distribution

In this section, we present the results pertaining to the rotation-induced temperature profiles, focusing on the thermal aspects of the problem. Fig. 2.12(a) shows the increase in temperature with increasing rotation number, which is attributed to the increase in rotational energy in the system. As the rotation number increases, more energy is imparted to the fluid due to the rotation, leading to higher temperatures. This phenomenon is commonly observed in rotating systems, where the rotational energy is converted into thermal energy, resulting in an increase in temperature. Similarly, the higher roughness parameter increases the temperature, as shown in Fig. 2.12(b). This is because the rough surface of the microchannel disrupts the flow, causing more friction between the fluid and the channel walls. This increased friction leads to a conversion of mechanical energy into heat, increasing the temperature of the fluid. In both cases, the increase in temperature is a result of the additional energy dissipation as a result of the presence of rotation and wall roughness.

Figures 2.13-2.14 represent the contour plot (isotherms) of the temperature distribution with different rotation numbers ω and the Hartmann number Ha . These plots offer a comprehensive view of the evolving thermal characteristics within the system, allowing for a deeper understanding of the temperature distribution. From Fig. 2.13, it is evident that the magnitude of the temperature exhibits a notable increase as the rotation number (ω) increases. This observation highlights the strong influence of rotation on the thermal characteristics of the system. Fig. 2.14 gives the thermal characteristics induced by rotation in the presence of an applied magnetic field. We observe a notable enhancement in the temperature when subjected to an increase in the Hartmann number. This improvement can be attributed to the decreased flow velocity, which promotes the convective transport of thermal energy and enhances heat diffusion from the rough surface of the channel. As a result, the dimensionless temperature rises with higher values of the Hartmann number, as depicted in Figs. 2.14(a)-2.14(d). Higher values of the Hartmann number also lead to increased

flow disturbances, which can be advantageous in microfabrication technology where controlled heat transfer and fluid mixing are desired.

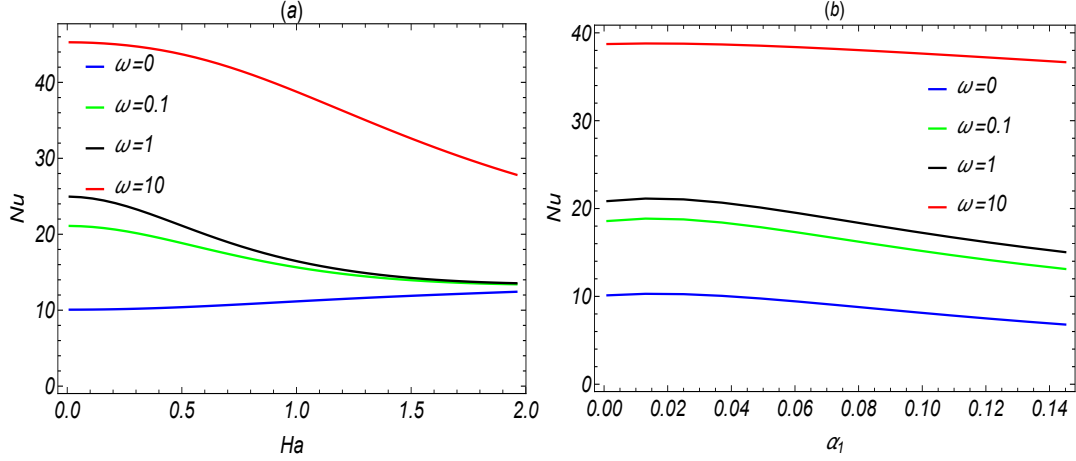


Figure 2.15: The Nusselt number as a function of (a) Hartmann number (Ha) for $\alpha_1 = 0.05$ and (b) roughness amplitude α_1 with variation for different ω respectively, when the other parameters are $\kappa = 20$, $Br = 0.01$, $Pr = 5$, $\gamma_j = 0.6$, $\alpha_2 = 0.04$, $\alpha_3 = 0.01$, $\beta_1 = 5$, $\beta_2 = 10$, $\beta_3 = 2$.

2.5.5 Rate of heat transfer analysis

The Nusselt number serves as a key parameter for assessing the efficiency of the heat transfer rate, representing the effectiveness of energy conversion between the rough microchannel surface and the surrounding fluid. The Nusselt number is determined by numerically calculating the bulk mean temperature, derived from the Eq. (2.45). Figs. 2.15 and 2.16 illustrate for understanding the impact of different parameters on the heat transfer process and the variations of the Nusselt number are investigated with different rotation number (ω), Hartmann number (Ha) and roughness parameter (α_1). Figs. 2.15(a) and 2.15(b) reveal that the rotation number enhances the Nusselt number. Fig. 2.15(b) shows the interaction between system rotation and surface roughness that contributes to this enhancement. This phenomenon can be attributed to rotation-induced secondary flows, which disrupt the thermal boundary layer and facilitate heat transfer. It is worth noting from Fig. 2.15(a) that the Nusselt number decreases as the Hartmann number increases when the system is under rotation. However, in the absence of rotation, the Nusselt number increases with Ha . In the presence of a transverse magnetic field, a gradual increase in the Nusselt number with the Hartmann number is observed, as depicted in Fig. 2.16(a). This behaviour can be attributed to the interplay between the Lorentz force and the induced flow. As the Hartmann number increases, the Lorentz force becomes more dominant, inducing stronger flow patterns that enhance heat transfer, leading to an increase in the Nusselt number. In Fig. 2.16(b), the gradual increase in the Nusselt number suggests a slow increase in heat transfer efficiency. This behaviour arises from the less dominant nature of the electroosmotic effect compared to stronger forces, such as the Lorentz force in the presence of a magnetic field. The surface roughness morphology disrupts the flow of fluid within

microfluidic channels, inducing irregular flow patterns. These disruptions can result in increased energy losses due to flow separation and recirculation. Therefore, reducing energy consumption improves thermal performance in 3D printed surface topography.

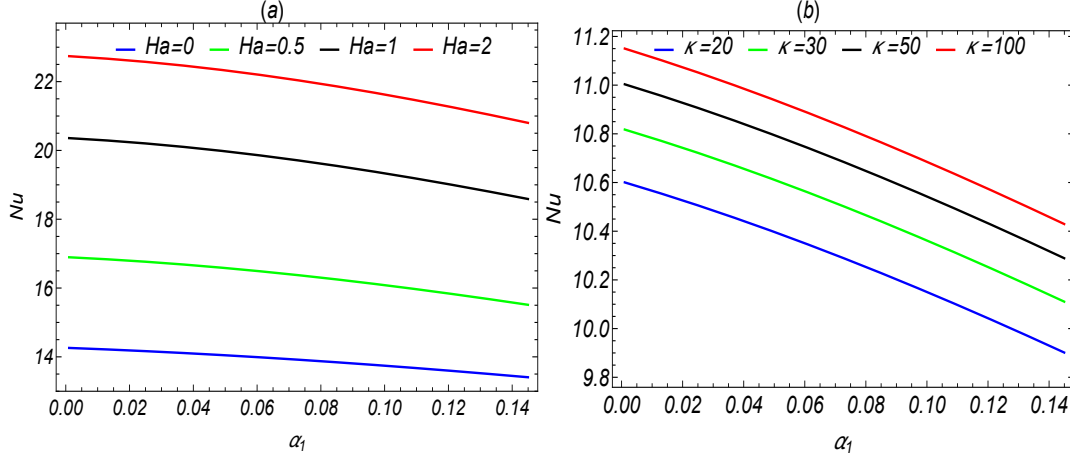


Figure 2.16: The Nusselt number as a function of α_1 with variation of (a) Hartmann number (Ha) and (b) electroosmotic parameter (κ) for $\omega = 1$, $Br = 0.01$, $Pr = 5$, $\gamma_j = 0.6$, $\alpha_2 = 0.04$, $\alpha_3 = 0.01$, $\beta_1 = 5$, $\beta_2 = 10$, $\beta_3 = 2$. The surface roughness reduces the energy consumption of the microfluidic devices in the context of 3D printing technology.

2.5.6 Entropy generation

The volumetric rate of local entropy generation can be determined by using the following expression (Herwig et al. [2008]; Bejan and Kestin [1983])

$$S_D''' = \frac{\mu}{\tilde{T}} \left[2 \left(\frac{\partial \tilde{u}}{\partial \tilde{x}} \right)^2 + \left(\frac{\partial \tilde{u}}{\partial \tilde{z}} \right)^2 + \left(\frac{\partial \tilde{v}}{\partial \tilde{z}} \right)^2 + \left(\frac{\partial \tilde{v}}{\partial \tilde{x}} \right)^2 \right] + \frac{k_{th}}{\tilde{T}^2} \left\{ \left(\frac{\partial \tilde{T}}{\partial \tilde{x}} \right)^2 + \left(\frac{\partial \tilde{T}}{\partial \tilde{z}} \right)^2 \right\} + \frac{\sigma_e}{\tilde{T}} \left\{ E_x^2 + B_0^2 (\tilde{u}^2 + \tilde{v}^2) \right\}, \quad (2.58)$$

where S_D''' represents the total volumetric entropy generation rate per unit volume which is the combination of the fluid flow friction, thermal irreversibility, Joule heating effects, the irreversibility due to the applied magnetic field.

By introducing the following entropy generation constant

$$S_D^0 = k_{th} \left(\frac{\tilde{q}_w \tilde{H}}{k_{th}} \right)^2 / (\tilde{T}_w^2 \tilde{H}^2), \quad (2.59)$$

one can easily obtain the dimensionless volumetric entropy generation, and is given by

$$\begin{aligned}
N_{ent}(x, z, t) &= S_D'''/S_D^0 \\
&= \frac{Br}{\theta \lambda_T^2} \left\{ 2 \left(\frac{\partial u}{\partial x} \right)^2 + \left(\frac{\partial u}{\partial z} \right)^2 + \left(\frac{\partial v}{\partial z} \right)^2 + \left(\frac{\partial v}{\partial x} \right)^2 \right\} \\
&\quad + \frac{1}{\theta^2 \lambda_T^2} \left\{ \left(\frac{\partial \theta}{\partial x} \right)^2 + \left(\frac{\partial \theta}{\partial z} \right)^2 \right\} + \frac{1}{\theta \lambda_T^2} \left\{ \gamma_j + Ha^2(u^2 + v^2) \right\}, \quad (2.60)
\end{aligned}$$

where $\lambda_T = \frac{\tilde{q}_w H / k_{th}}{\bar{T}_w}$ is a dimensionless temperature difference parameter.

Hence, the average entropy generation can be obtained as

$$N_s(t) = \int_0^1 \int_{-h}^h N_{ent}(x, z, t) dz dx. \quad (2.61)$$

The average entropy generation presented in Fig. 2.17, provides a comprehensive view of the thermodynamic behaviour of the flow under varied conditions. Surface roughness plays a crucial role by altering the flow patterns, leading to the formation of more isotherms within the channel. These additional features contribute significantly to the overall entropy production due to increased fluid mixing and internal friction. The inverse relationship between entropy generation and heat transfer emphasizes the impact of fluid dynamics on thermal processes. The electromagnetic interaction with fluid particles enhances heat transfer (see Fig. 2.16(a)) by inducing more vigorous flow patterns. This effect is particularly evident in the reduction of entropy generation with increasing Hartmann number (cf. Fig. 2.17(a)), indicating improved heat transfer efficiency. Again, an increase in the rotation number leads to higher entropy generation. This phenomenon is attributed to the Coriolis force, which causes the formation of additional vortices near the boundary layer. These complex flow structures increase the internal fluid friction, resulting in higher entropy production despite the enhanced heat transfer associated with the increased rotational motion. Similarly, an increase in the electroosmotic parameter also leads to higher entropy generation, as shown in Fig. 2.17(c). The parameter κ influences the electroosmotic effects, which can be used to enhance fluid mixing and increase the entropy generation rate. The entropy generation serves as a measure of the irreversibility of a process. In this case, the increased mixing due to electroosmosis contributes to higher internal irreversibilities within the fluid, leading to a higher entropy generation rate.

2.6 Conclusions

This chapter focused on investigating electromagnetohydrodynamic (EMHD) flow and heat transfer in a rotating rough surface microchannel. We analyzed the effects of secondary flow and surface roughness in a rotating microchannel. Our findings emphasized the crucial role of rotation in thermal energy management for the optimal design of microfluidic devices. The analytical solutions have been obtained using the separation of variable methods. We discussed the friction factor and entropy generation to assess the thermal energy efficiency and system performance. The study reveals that rotation significantly influences the electrokinetic transport of the electrolyte, resulting in

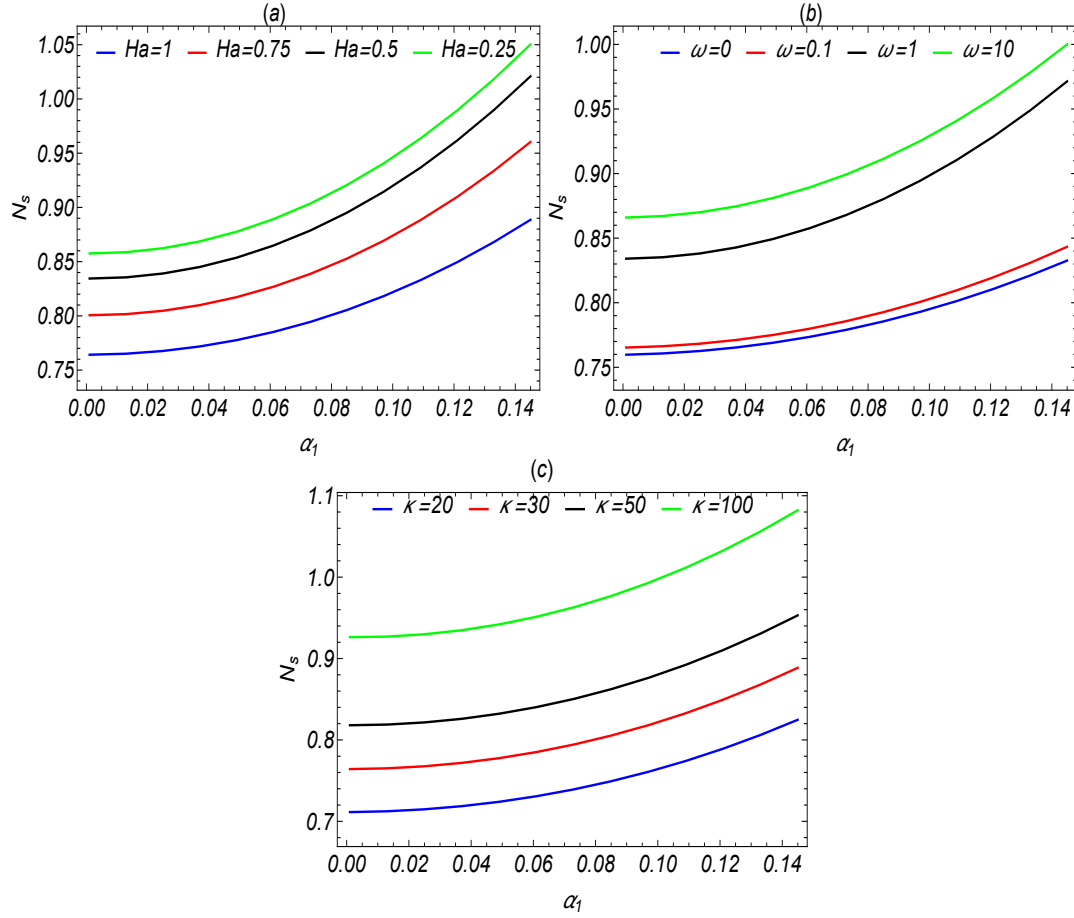


Figure 2.17: Impact of roughness parameter on entropy generation with the variation of (a) Hartmann number (Ha) for $\omega = 1$ and $\kappa = 20$, (b) rotation number (ω) for $\kappa = 20$ and $Ha = 1$, (c) electroosmotic parameter (κ) for $\omega = 1$ and $Ha = 1$, when other parameters are $Br = 0.01$, $Pr = 5$, $\gamma_j = 0.6$, $\alpha_2 = 0.04$, $\alpha_3 = 0.01$, $\beta_1 = 5$, $\beta_2 = 10$, $\beta_3 = 2$, $y = 0.5$, $t = 2$, $z = 0$. Each profile exhibits a nonlinear relationship, which is best represented by a cubic polynomial in α_1 , between entropy generation and surface roughness.

changes in flow patterns and temperature distribution. The surface roughness of the microchannel, along with rotation, both contributed to the increase in temperature. As the rotation rate increases, multiple vorticity contours appear in the rough surface channel compared to the smooth surface channel. At higher rotation rates, we observed two minima in the velocity profiles lead to Taylor dispersion in the transverse direction. This transverse movement contributes to the spreading of liquid and promoting mixing. Rotation-induced secondary flow influences the thermal energy and entropy generation of the system. Therefore, considering rotation is essential in the design and optimization of microfluidic devices to accurately predict and control heat transfer processes. These results may be helpful to engineering researchers to improve thermal performance and enhance control of temperature in micro-heat exchangers, lab-on-a-chip devices and microscale cooling systems.

Appendix

2.A Mathematical expressions in temperature distribution

The following expressions are used to express the solution of $\Theta_1(z)$

$$\phi_1 = (Ha^4 + 4\omega^2)^{1/4} \sin\left(\frac{1}{2} \arg(Ha^2 + 2i\omega)\right), \quad (2.62)$$

$$\phi_2 = (Ha^4 + 4\omega^2)^{1/4} \cos\left(\frac{1}{2} \arg(Ha^2 + 2i\omega)\right), \quad (2.63)$$

$$A_1 = -\frac{4\kappa^2 \omega \cosh(Ha\kappa)}{((Ha^2 - \kappa^2)^2 + 4\omega^2)(1 + \cosh(2Ha\kappa))}, \quad (2.64)$$

$$A_2 = \frac{2\kappa^2 \omega}{(-Ha^2 + \kappa^2)^2 + 4\omega^2}, \quad (2.65)$$

$$A_3 = \frac{16Ha^2(\pi^2 \kappa^2 + HaS(\pi^2 + 4Ha^2 \kappa^2))}{\pi(\pi^2 + 4Ha^2 \kappa^2)(8Ha^2 Ha^2 \pi^2 + \pi^4 + 16Ha^4(Ha^4 + 4\omega^2))}, \quad (2.66)$$

$$A_4 = \frac{2(\sin(Ha\phi_1) \sinh(Ha\phi_2))}{\cos(2Ha\phi_1) + \cosh(2Ha\phi_2)}, \quad (2.67)$$

$$A_5 = \frac{2(\cos(Ha\phi_1) \cosh(Ha\phi_2))}{\cos(2Ha\phi_1) + \cosh(2Ha\phi_2)}, \quad (2.68)$$

$$A_6 = \frac{\kappa^2(Ha^2 - \kappa^2) \operatorname{sech}(Ha\kappa)}{Ha^4 - 2Ha^2 \kappa^2 + \kappa^4 + 4\omega^2}, \quad (2.69)$$

$$\begin{aligned} \Gamma_1(z) = -Br[& \{-(A_2 A_4 \phi_1 + A_2 A_5 \phi_2) \cosh(z\phi_2) \sin(z\phi_1) + A_6 \kappa \sinh(z\kappa) \\ & + (A_1 A_4 \phi_1 - A_2 A_5 \phi_1 + A_2 A_4 \phi_2) \cos(z\phi_1) \sinh(z\phi_2)\}^2], \end{aligned} \quad (2.70)$$

$$\begin{aligned} \Gamma_2(z) = BrHa^2[& \{(A_1 \cosh(z\kappa) + A_2 A_5) \cos(z\phi_1) \cosh(z\phi_2) + A_2 A_4 \sin(z\phi_1) \sinh(z\phi_2)\}^2 \\ & + \{A_6 \cosh(z\kappa) + (A_2 A_4 \cos(z\phi_1) \cosh(z\phi_2) - A_2 A_5 \sin(z\phi_1) \sinh(z\phi_2))\}^2], \end{aligned} \quad (2.71)$$

$$\Gamma(z) = \iint \left\{ \Gamma_1(z) - \Gamma_2(z) \right\} dz dz + \left[\iint \left\{ \Gamma_1(z) - \Gamma_2(z) \right\} dz dz \right]_{\text{at } z=h}. \quad (2.72)$$

3

Two-layer Electroosmotic Flow in a Rough Surface Microchannel

3.1 Introduction

The surface roughness of the microchannel is an important factor in microfabrication technology as it can impact the performance of microfabricated devices. Surface roughness may arise from various factors such as lithography techniques, deposition methods, and manufacturing processes ([Cho et al. \[2013\]](#); [Keramati et al. \[2016\]](#); [Kang and Suh \[2009\]](#)). The impact of roughness in microfabrication technology may affect the performance of microfabricated devices, leading to increased friction, wear, and reduced efficiency. The use of two immiscible fluids in rough microchannels provides a wide range of applications in various fields, including microfluidics, chemical engineering, and materials sciences. The rough surface promotes mixing and interfacial contact between two fluids, enhancing mass transfer rates for efficient liquid-liquid extraction processes. Moreover, the rough surface promotes coalescence and coalescence-induced separation of the two fluids in the liquid-liquid separation process ([Holland et al. \[2002\]](#)). The geometry of the channel plays an important role in the mixing process. A channel with irregular walls or bends can create eddies or vortices that can promote mixing, while a straight channel with smooth walls may require additional mixing devices to achieve the desired level of mixing ([Gepner and Floryan \[2016\]](#)). Thus, it is necessary to control the flow phenomena to manipulate and separate different components of a mixture based on their physical properties and or design of microchannels.

[Gu and Lawrence \[2005\]](#) presented a one-dimensional analytical solution to the fully nonlinear problem of two-layer frictional exchange and made an excellent comparison with the experimental

data. Their study highlighted the importance of interfacial and bottom friction in determining the possible exchange of flow rate. [Lenz and Kumar \[2007\]](#) investigated the steady state behavior of the interface between two immiscible liquids flowing in a channel in which one wall is fixed and the other wall is topographically microstructured. They pointed out that in some cases, interfacial features present in the flow of a single layer of liquid over surfaces with topography can be completely suppressed by large pressure gradient. The effect of free surface on the interfacial instabilities of the gravity-driven flow of two superposed Newtonian liquid layers down an inclined wall is studied by [Gaurav \[2010\]](#) with three distinct interfacial modes, viz., gas-liquid, liquid-liquid, and liquid-solid. Their results showed that surface variation has a stabilizing effect on both gas-liquid and liquid-liquid interfaces in the low-wave number limit when the more viscous liquid layer is near the deformable wall. [Samanta \[2013\]](#) has investigated the effect of surfactant on the interfacial waves in a two-layer channel flow at low to moderate Reynolds numbers to study the linear stability analysis of the flow. [Dubrovina et al. \[2017\]](#) investigated the streamwise pressure-driven flow of two stratified viscous immiscible fluids with different electric properties in a channel having topographically structured walls. In the presence of topography, linearly stable uniform flows become non-uniform spatially periodic steady states and nonlinear structures emerge in the linearly unstable regime. [Mohammadi and Smits \[2017\]](#) performed the stability of the two-layer Couette flow subject to the variations in viscosity ratio, thickness ratio, interfacial tension, and density ratio. They have proposed a new interfacial mode at a low viscosity ratio with different properties and observed that there are no unstable Tollmien-Schlichting waves but the interfacial tension always has a stabilizing effect, while the effects of the density ratio cannot be generalized easily. The buoyant displacement flows of two generalized Newtonian fluids in a 2D channel with wall slip are considered by [Taghavi \[2018\]](#). An experimental investigation on the interfacial instabilities in the dynamics of the interface between two immiscible liquids in a cylindrical container with rotationally oscillating about its axis is carried out by [Piao and Park \[2021\]](#). This work has been focused on the formation of droplets. The impact of wall slip on the stability of a two-layered plane Poiseuille flow through a horizontal and inclined channel are investigated by [Ramakrishnan et al. \[2021\]](#) and [Mishra et al. \[2021\]](#) respectively.

Electroosmosis is characterized as the movement of electrolyte liquid under the influence of an applied electric field. It can be quantified by the electroosmotic mobility depending upon the surface charge density and ionic strength of the electrolyte solution. This phenomenon promotes microfluidics research, particularly in the development of lab-on-chip devices and medical devices ([Stone et al. \[2004\]](#)). A significant amount of research has been conducted on electroosmotic flow (EOF) under magnetic environments in recent years. Because the magnetic field is used to control EOF for enhancing the performance of microfluidic devices in various applications. It is reported that MHD and EMHD have a wide range of applications in micro-fabrication technology ([Jang and Lee \[2000\]](#)), including the development of micro-pumps ([Lemoff and Lee \[2000\]](#); [Huang et al. \[2000\]](#)), micro-mixers ([Erickson and Li \[2002\]](#)), and microreactors ([Renault et al. \[2012\]](#)). These technologies are now increasingly important in the fields of micro-electronics, biomedical engineering, and microfluidic flow ([Eijkel et al. \[2003\]](#); [Nash and Fritsch \[2016\]](#)).

Two-layer flow plays a significant role in the electroosmotic pumping of liquids in various microfluidic systems. The concept of two immiscible fluids of different viscosities and different electrical conductivities have various applications in microreactors, microelectronic cooling systems, micro energy systems etc (Wang et al. [2009]). Su et al. [2013] discussed the transient electroosmotic flow of two immiscible fluids through a slit microchannel. They have focused on the semi-analytical solution of velocity distribution by applying the Laplace transform method and concluded that the velocity magnitude is enhanced with the zeta potential difference at the fluid-fluid interface. An analytical result for electrostatic potential distribution has been obtained by Das and Hardt [2011], wherein they demonstrated that the net electrostatic potential is influenced by the electric double layers and the potential jump at the liquid-liquid interface. Huang et al. [2014] carried out the electroosmotically driven flow of two immiscible fluids, by considering one fluid layer as a non-Newtonian power-law fluid driven by electroosmotic force and the other layer as a Newtonian fluid driven by interfacial shear stress. Demekhin et al. [2016a] studied the stability analysis of two-layer electrolyte fluids in the presence of an electric field. The computed results have been found in good agreement with the experimental data. Electrohydrodynamic instability of two viscous fluids is performed in order to observe droplet formation, mixing, and cooling efficiency in microfluidic systems (Ozen et al. [2006]; Thaokar and Kumaran [2005]). The heat transfer analysis of two-layer electroosmotic flow is carried out by Shit et al. [2016d], wherein they obtained the analytical solutions for velocity and temperature distribution. An almost similar observation is done by considering the hydrodynamic slippage and asymmetric wall heating condition (Banerjee et al. [2022]). They have estimated some critical values for the Brinkman number for which the Nusselt number enhances. Ranjit et al. [2021] performed an electrothermal pumping analysis of the peristaltic flow of two-layer couple stress fluids in an asymmetric microchannel without considering the magnetic field. An experimental investigation of the electroosmotically and pressure-driven flow of two fluids has been performed by Wang et al. [2005]. A comparative study with experimental and theoretical investigation of electroosmotic two-layered flow is studied by Gao et al. [2005] to control the fluid-fluid interface by applying the external electric field. However, the previous investigations are limited to the study of electroosmotic two-layered flow through a smooth narrow confinement. To the best of the authors' knowledge, the analytical investigation of EMHD two-layered flow through a rough surface in two dimensions has not yet been reported in the literature.

It is a very difficult task to solve analytically coupled partial differential equations in two dimensions with electromagnetic effects. In the present analysis, we have explored the analytical solution for the two-layered EMHD flow through a rough microchannel by applying the perturbation technique. By using this analytical approach, we have explored the effect of roughness on the applied potential, EDL potential, EMHD flow and the volumetric flow rate. The boundary layer thickness is also obtained. Furthermore, the present results also have been compared with the previous existing literature.

3.2 Mathematical modeling and solution

3.2.1 Problem description

The physical configuration under consideration of a problem (cf. Fig. 3.1) is a microchannel with the undulated walls $\tilde{y} = \pm \tilde{h}(\tilde{x})$, where $\tilde{h}(\tilde{x})$ is expressed as (Cho et al. [2013])

$$\tilde{h}(\tilde{x}) = H + H \left[\alpha \sin\left(2\pi \frac{\tilde{x}}{H}\right) + \lambda \sin\left(4\pi \frac{\tilde{x}}{H}\right) \right]. \quad (3.1)$$

We denote α and λ as the wave amplitudes of the walls, H is the half-height of the microchannel, which is assumed to be much smaller than the length (L) and width (W) of the microchannel ($H \ll L$ and $H \ll W$). The channel is filled with steady, viscous incompressible fluids with an immiscible interface located at $\tilde{y} = 0$. Two immiscible fluids with different viscosities μ_1 and μ_2 are filled in the upper and lower portion of the microchannel are known as layer-1 ($0 \leq \tilde{y} \leq \tilde{h}(\tilde{x})$) and layer-2 ($-\tilde{h}(\tilde{x}) \leq \tilde{y} \leq 0$) respectively. In addition to the pressure gradient, we assume that the flow is induced by an applied electric field \mathbf{E} that acts along \tilde{z} -direction and an external magnetic field \mathbf{B} is applied along \tilde{y} -direction. Therefore the flow is influenced by the combined effect of electromagnetohydrodynamic force and pressure gradient. When the ion separation takes place towards the undulated surfaces, an electric double layer (EDL) is generated near the solid-fluid interface. The variable zeta potential is imposed at the walls depending on the waviness of the microchannel. However, due to the different fluid flow layers, a zeta potential difference $\delta\zeta$ is formed at the fluid-fluid interface. Further, it is assumed that the rough surface walls are hydrophobic and the corresponding slip length is much smaller than the amplitudes of waviness.

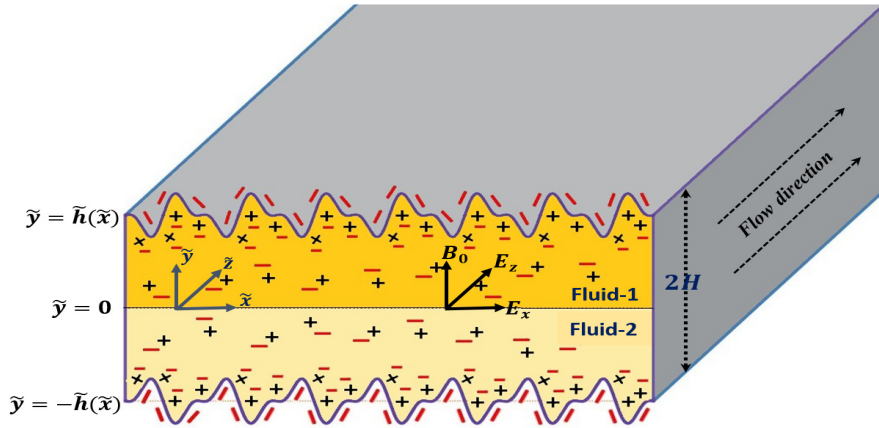


Figure 3.1: Physical Sketch of the problem describing the two-layer EMHD flow in a rough microchannel, whose walls are represented by $\tilde{h}(\tilde{x})$ in which a magnetic field of strength B_0 is applied along \tilde{y} -direction. The upper portion of the channel ($0 \leq \tilde{y} \leq \tilde{h}(\tilde{x})$) is identified as layer-1 and the lower portion of the channel ($-\tilde{h}(\tilde{x}) \leq \tilde{y} \leq 0$) is represented as layer-2.

3.2.2 Governing equation for Potential distribution

The ionized liquid forms an EDL at the solid-liquid interface under the influence of an electroosmotically driven body force. The electrostatic potential ($\tilde{\phi}_i$) for two-layer flow is constituted by the combination of EDL potential ($\tilde{\psi}_i$) and an applied potential ($\tilde{\Phi}_i$) according to [Keramati et al. \[2016\]](#) has the form

$$\tilde{\phi}_i = \tilde{\Phi}_i + \tilde{\psi}_i, \quad i = 1, 2. \quad (3.2)$$

3.2.2.1 Laplace equation for applied potential

An external electric field is defined as $\mathbf{E} = -\nabla\tilde{\phi}_i$, where $\tilde{\phi}_i$ represents the electrostatic potential for both the layers. Since the applied electric potential $\tilde{\Phi}_i$ depends on the wave amplitude of the microchannel, we compute the effects of surface waviness on the applied electric potential $\tilde{\Phi}_i$. The externally applied electric potential $\tilde{\Phi}_i$ satisfy the Laplace's equation ([Kang and Suh \[2009\]](#); [Lei et al. \[2019\]](#)),

$$\tilde{\nabla}^2 \tilde{\Phi}_i = 0, \quad i = 1, 2, \quad \tilde{\nabla}^2 \equiv \frac{\partial^2}{\partial \tilde{x}^2} + \frac{\partial^2}{\partial \tilde{y}^2}. \quad (3.3)$$

By introducing the dimensionless variables $x = \frac{\tilde{x}}{H}$, $y = \frac{\tilde{y}}{H}$ and $\Phi_i = \frac{\tilde{\Phi}_i}{E_0 H}$ in Eq. (3.3), we find

$$\nabla^2 \Phi_i = 0, \quad i = 1, 2, \quad \nabla^2 \equiv \frac{\partial^2}{\partial x^2} + \frac{\partial^2}{\partial y^2}. \quad (3.4)$$

The boundary conditions for Φ_i at the wall of the microchannel can be expressed as (cf. [Lei et al. \[2019\]](#))

$$\frac{\partial \Phi_i}{\partial n} = \nabla \Phi_i \cdot \hat{n}_i = 0, \quad i = 1, 2, \quad (3.5)$$

where \hat{n}_i denotes the unit normal on upper and lower wall of the microchannel respectively, and are given by

$$\hat{n}_1 = \frac{\nabla\{y - (1 + \alpha f(x))\}}{\|\nabla\{y - (1 + \alpha f(x))\}\|}, \quad (3.6)$$

and

$$\hat{n}_2 = \frac{\nabla\{y - (-1 - \alpha f(x))\}}{\|\nabla\{y - (-1 - \alpha f(x))\}\|}. \quad (3.7)$$

In Eqs. (3.6) and (3.7), $f(x) = \sin(2\pi x) + \frac{\lambda}{\alpha} \sin(4\pi x)$.

At the interface of the two-layer fluids, we impose continuity of potential and flux jump condition

$$\Phi_1 = \Phi_2, \quad \text{at } y = 0, \quad (3.8)$$

and

$$\nabla \Phi_1 \cdot \hat{n}_1 - \varepsilon \nabla \Phi_2 \cdot \hat{n}_2 = \bar{\delta}_\Phi(x), \quad \text{at } y = 0, \quad (3.9)$$

where $\varepsilon = \frac{\varepsilon_2}{\varepsilon_1}$ is the permittivity ratio and $\bar{\delta}_\Phi(x) = \delta_\Phi\{\alpha \sin(2\pi x) + \lambda \sin(4\pi x)\}$ ([Banerjee and Nayak \[2019\]](#)) indicates potential flux jump at the fluid-fluid interface.

Since the applied potential distribution depends on the amplitude of the microchannel, we assumed $\Phi_i = \Phi_i(x, y)$. Therefore, the boundary conditions (3.5), (3.8) and (3.9) can be rewritten in the following form:

$$\frac{\partial \Phi_1}{\partial y} - \alpha f'(x) \frac{\partial \Phi_1}{\partial x} = 0, \text{ at } y = 1 + \alpha f(x), \quad (3.10)$$

$$\frac{\partial \Phi_2}{\partial y} + \alpha f'(x) \frac{\partial \Phi_1}{\partial x} = 0, \text{ at } y = -1 - \alpha f(x), \quad (3.11)$$

$$\Phi_1 = \Phi_2, \text{ at } y = 0, \quad (3.12)$$

and

$$\left(\frac{\partial \Phi_1}{\partial y} + \varepsilon \frac{\partial \Phi_2}{\partial y} \right) - \alpha f'(x) \left(\frac{\partial \Phi_1}{\partial x} + \varepsilon \frac{\partial \Phi_2}{\partial x} \right) = \bar{\delta}_\Phi(x), \text{ at } y = 0, \quad (3.13)$$

where $f'(x) = 2\pi[\sin(2\pi x) + 2\frac{\lambda}{\alpha} \sin(4\pi x)]$.

3.2.2.2 Poisson equation for EDL potential

Within the electrical double layer, the net charge densities (ρ_{ei}) for fluid layer-1 and layer-2 are obtained from the Poisson's equation

$$\tilde{\nabla}^2 \tilde{\psi}_i = -\frac{\rho_{ei}}{\varepsilon_i}, \quad i = 1, 2, \quad (3.14)$$

where ε_i indicates the permittivity of the medium. Hence, for the hydrodynamically developed and thermodynamic equilibrium conditions (Sadeghi et al. [2012]), the electrical potential distribution can be obtained by solving Poisson-Boltzmann equations for fluid layer-1 and layer-2 separately. The net charge densities (ρ_{ei}) for fluid layer-1 and layer-2 can be written respectively as (Masliyah and Bhattacharjee [2006])

$$\rho_{ei} = 2n_0 e z_0 \sinh\left(\frac{e z_0}{k_B T_{av}} \tilde{\psi}_i\right), \quad i = 1, 2, \quad (3.15)$$

where n_0 denotes the number of positive and negative ions (in molar unit), e is the charge of electron, z_0 indicates the valance, k_B is the Boltzmann constant, and T_{av} denotes the absolute temperature.

Using the equations (3.14) and (3.15), the Poisson-Boltzmann equations can be expressed as

$$\tilde{\nabla}^2 \tilde{\psi}_i = \frac{2n_0 e z_0}{\varepsilon_i} \sinh\left(\frac{e z_0}{k_B T_{av}} \tilde{\psi}_i\right), \quad i = 1, 2. \quad (3.16)$$

Imposing Debye-Hückle linearization, we have $\sinh\left(\frac{e z_0}{k_B T_{av}} \tilde{\psi}_i\right) \approx \frac{e z_0}{k_B T_{av}} \tilde{\psi}_i$ and hence equation (3.16) has the form

$$\tilde{\nabla}^2 \tilde{\psi}_i = \frac{2n_0 e z_0}{\varepsilon_i} \left(\frac{e z_0}{k_B T_{av}} \tilde{\psi}_i \right), \quad i = 1, 2. \quad (3.17)$$

The appropriate boundary conditions (Qi and Ng [2018]) for the potential distribution $\tilde{\psi}_i$ are set to

$$\tilde{\psi}_1 = \tilde{\zeta}(\tilde{x}) \text{ at } \tilde{y} = \tilde{h}(\tilde{x}), \quad (3.18)$$

$$\tilde{\psi}_2 = \tilde{\zeta}(\tilde{x}) \quad \text{at} \quad \tilde{y} = -\tilde{h}(\tilde{x}), \quad (3.19)$$

where $\pm \tilde{\zeta}(\tilde{x})$ are the scaled zeta potential at the upper and lower walls of the microchannel and $\tilde{\zeta}(\tilde{x}) = \tilde{\zeta}_0 \left\{ 1 + \frac{\alpha}{2} \sin\left(2\pi \frac{\tilde{x}}{H}\right) + \frac{\lambda}{2} \sin\left(4\pi \frac{\tilde{x}}{H}\right) \right\}$ (cf. Banerjee and Nayak [2019]).

Two more boundary conditions are introduced at the interface (at $\tilde{y} = 0$) as follows:

$$\tilde{\psi}_2 - \tilde{\psi}_1 = \tilde{\delta}_\zeta(\tilde{x}) \quad \text{at} \quad \tilde{y} = 0, \quad (3.20)$$

$$\varepsilon_1 \tilde{\nabla} \tilde{\psi}_1 \cdot \hat{n}_1 - \varepsilon_2 \tilde{\nabla} \tilde{\psi}_2 \cdot \hat{n}_2 = -\tilde{Q}_d \quad \text{at} \quad \tilde{y} = 0, \quad (3.21)$$

where \tilde{Q}_d , and $\tilde{\delta}_\zeta(\tilde{x})$ respectively denote the charge jump and zeta potential difference at the interface of two fluids.

Let us introduce the following dimensionless variables and parameters

$$\begin{aligned} y &= \frac{\tilde{y}}{H}, \quad x = \frac{\tilde{x}}{H}, \quad \psi_i = \frac{\tilde{\psi}_i}{\tilde{\zeta}_0}, \quad \zeta(x) = \frac{\tilde{\zeta}(\tilde{x})}{\tilde{\zeta}_0}, \\ \varepsilon &= \frac{\varepsilon_2}{\varepsilon_1}, \quad \delta_\zeta = \frac{\tilde{\delta}_\zeta}{\tilde{\zeta}_0}, \quad Q = \frac{H \tilde{Q}_d}{\varepsilon_1 \tilde{\zeta}_0}, \quad \kappa_i = \frac{H}{\lambda_i^D}. \end{aligned} \quad (3.22)$$

By introducing the above variables and parameters (3.22), equation (3.17) reduces to

$$\nabla^2 \psi_i = \kappa_i^2 \psi_i, \quad i = 1, 2, \quad (3.23)$$

where $\lambda_i^D = (e z_0)^{(-1)} \left(\frac{\varepsilon_i k_B T_{av}}{2 n_0} \right)^{\frac{1}{2}}$ is defined as Debye length and κ_i as the electroosmotic parameter.

Invoking the equation (3.22) into the equations (3.18)-(3.21), dimensionless boundary conditions reduce to,

$$\psi_1 = \zeta(x) \quad \text{at} \quad y = 1 + \alpha f(x), \quad (3.24)$$

$$\psi_2 = \zeta(x) \quad \text{at} \quad y = -1 - \alpha f(x), \quad (3.25)$$

$$\psi_1 - \psi_2 = \delta_\zeta(x) \quad \text{at} \quad y = 0, \quad (3.26)$$

and

$$\left(\frac{\partial \psi_1}{\partial y} + \varepsilon \frac{\partial \psi_2}{\partial y} \right) - \alpha f'(x) \left(\frac{\partial \psi_1}{\partial x} + \varepsilon \frac{\partial \psi_2}{\partial x} \right) = -Q \quad \text{at} \quad y = 0, \quad (3.27)$$

where $\delta_\zeta(x) = \delta_\zeta \{ 1 + \alpha \sin(2\pi x) + \lambda \sin(4\pi x) \}$.

3.2.3 Governing equations for fluid flow

The electrically conducting two-layer fluid model has been considered under the combined influence of electroosmotic body force, Lorentz force and pressure gradient. The conservation of mass and momentum equations for the flow can be expressed as (Su et al. [2013]; Karniadakis et al. [2005])

$$\nabla \cdot \mathbf{v} = 0, \quad (3.28)$$

$$\rho \left[\frac{\partial \mathbf{v}}{\partial t} + (\mathbf{v} \cdot \nabla) \mathbf{v} \right] = -\nabla p + \mu \nabla^2 \mathbf{v} + \rho_e \mathbf{E} + \mathbf{J} \times \mathbf{B}, \quad (3.29)$$

where ρ , p and μ are respectively denote the density, pressure and viscosity of the fluid, \mathbf{v} the velocity vector, \mathbf{E} applied electric field along the \tilde{z} -axis and \mathbf{B} stands for the applied magnetic field along the \tilde{y} -axis. The last two terms indicate the electromagnetohydrodynamic body forces, combination of electroosmotic force ($\rho_e \mathbf{E}$) and the Lorentz force ($\mathbf{J} \times \mathbf{B}$), where $\mathbf{J} = \sigma_e (\mathbf{E} + \mathbf{v} \times \mathbf{B})$ and σ_e represents the electrical conductivity of the electrolyte solution.

For steady, incompressible and viscous fluid flow in a microchannel under low Reynolds number assumption, inertia is ignored, so that the equation (3.29) can be reduced to (Li [2004]; Santiago [2001])

$$-\nabla p + \mu \nabla^2 \mathbf{v} + \rho_e \mathbf{E} + \mathbf{J} \times \mathbf{B} = 0. \quad (3.30)$$

We assumed that the height is significantly smaller in comparison to both the length and width of the microchannel. Due to this significant size difference, the fluid motion becomes largely independent along the width of the microchannel. Therefore, we can confidently assume that the primary flow predominantly occurs along the length of the channel, rendering the other velocity components, especially the vertical and transverse velocities negligible. However, the axial velocity component is influenced by the undulations on the surface of the microchannel. Consequently, we can express the velocity vector $\mathbf{v} = (0, 0, w(x, y))$, where $w(x, y)$ represents the axial velocity component that depends on the waviness of the surface.

Under these assumptions, the momentum equation (3.30) for the two-layer fluid flow with different viscosities in the complex wavy microchannel can be expressed as (Shit et al. [2016d]; Santiago [2001])

$$\mu_i \tilde{\nabla}^2 \tilde{w}_i - \tilde{\nabla} \tilde{p}_i + \rho_{ei} E_z - \sigma_{ei} B_0^2 \tilde{w}_i + \sigma_{ei} B_0 E_{xi} = 0, \quad i = 1, 2, \quad (3.31)$$

where $\tilde{\nabla}^2 \equiv \frac{\partial^2}{\partial \tilde{x}^2} + \frac{\partial^2}{\partial \tilde{y}^2}$. The term $\rho_{ei} E_z$ is the electroosmotic body force term, $\sigma_{ei} B_0^2 w_i$ be the reduced form of the Lorentz force and $\sigma_{ei} B_0 E_{xi}$ is the flow aiding force due to the transverse electric field, μ_i and σ_{ei} are the viscosity and electrical conductivity of the fluids of layer-1 and layer-2 respectively. The electroosmotic body force ($\rho_{ei} E_z$) arises due to the interaction of charged ions with the applied electric field, driving fluid motion in microchannel. Additionally, the flow aiding force ($\sigma_{ei} B_0 E_{xi}$) complements the electroosmotic force, facilitating the fluid transport. These forces crucially depend on the distribution of the applied potential ($\tilde{\psi}_i$) and EDL potential ($\tilde{\psi}_i$), which dictates the strength and direction of the flow.

The velocity slip boundary conditions at the fluid-solid interface are defined as (Shit et al. [2016d]; Banerjee et al. [2022])

$$\tilde{w}_1 + \tilde{\beta}_1 \tilde{\nabla} \tilde{w}_1 \cdot \hat{n}_1 = 0 \quad \text{at} \quad \tilde{y} = \tilde{h}(\tilde{x}), \quad (3.32)$$

$$\tilde{w}_2 - \tilde{\beta}_2 \tilde{\nabla} \tilde{w}_2 \cdot \hat{n}_2 = 0 \quad \text{at} \quad \tilde{y} = -\tilde{h}(\tilde{x}), \quad (3.33)$$

where $\tilde{\beta}_1$ and $\tilde{\beta}_2$ are slip lengths at the respective walls which are assumed such that $\beta_i < \alpha$, $\beta_i < \lambda$.

3.2. Mathematical modeling and solution

The continuity of velocity and viscous stress as a boundary condition at the fluid-fluid interface are formulated as (Shit et al. [2016d]; Banerjee et al. [2022])

$$\tilde{w}_1 = \tilde{w}_2 \quad \text{at} \quad \tilde{y} = 0, \quad (3.34)$$

$$-\mu_1 \tilde{\nabla} \tilde{w}_1 \cdot \hat{n}_1 + \varepsilon_1 E_z \tilde{\nabla} \tilde{\psi}_1 \cdot \hat{n}_1 = -\mu_2 \tilde{\nabla} \tilde{w}_2 \cdot \hat{n}_2 + \varepsilon_2 E_z \tilde{\nabla} \tilde{\psi}_2 \cdot \hat{n}_2 \quad \text{at} \quad \tilde{y} = 0. \quad (3.35)$$

We define the following dimensionless variables and parameters to reduce all the equations in non-dimensional form as

$$\begin{aligned} w_1 &= \frac{\tilde{w}_1}{W_{HS}}, \quad w_2 = \frac{\tilde{w}_2}{W_{HS}}, \quad W_{HS} = \frac{-\varepsilon_1 \tilde{\zeta}_0 E_z}{\mu_1}, \quad P = \frac{(-\partial p_1 / \partial z) H^2}{\mu_1 W_{HS}}, \\ Ha &= B_0 H \sqrt{\frac{\sigma_{e1}}{\mu_1}}, \quad S_1 = \frac{E_{x1} H}{W_{HS}} \sqrt{\frac{\sigma_{e1}}{\mu_1}}, \quad S_2 = \frac{E_{x2} H}{W_{HS}} \sqrt{\frac{\sigma_{e1}}{\mu_1}}, \\ \sigma &= \frac{\sigma_{e2}}{\sigma_{e1}}, \quad \mu = \frac{\mu_2}{\mu_1}, \quad \Gamma = \frac{(-\partial p_2 / \partial z)}{(-\partial p_1 / \partial z)}, \quad \beta_1 = \frac{\tilde{\beta}_1}{H}, \quad \beta_2 = \frac{\tilde{\beta}_2}{H}. \end{aligned} \quad (3.36)$$

where W_{HS} represents Helmholtz-Smoluchowski velocity, P denotes the dimensionless pressure gradient, Ha the Hartmann number, S_i are the strength of transverse electric field along x -direction, β_i are the velocity slip parameters, Γ the pressure gradient ratio, σ the electrical conductivity ratio, and μ indicate the viscosity ratio of layer-2 to layer-1.

Use of equation (3.36) in the momentum equation (3.31) and in the boundary conditions (3.32) to (3.35), we can transform them into the dimensionless form as

$$\nabla^2 w_1 - Ha^2 w_1 + \kappa_1^2 \psi_1 + Ha S_1 + P = 0, \quad (3.37)$$

and

$$\mu \nabla^2 w_2 - \sigma Ha^2 w_2 + \varepsilon \kappa_2^2 \psi_2 + \sigma Ha S_2 + \Gamma P = 0, \quad (3.38)$$

where the electric field strengths S_1 and S_2 depend on the roughness of the microchannel walls.

The corresponding boundary conditions in non-dimensional form are reduce to

$$w_1 + \beta_1 \left\{ \frac{\partial w_1}{\partial y} - \alpha f'(x) \frac{\partial w_1}{\partial x} \right\} = 0 \quad \text{at} \quad y = 1 + \alpha f(x), \quad (3.39)$$

$$w_2 - \beta_2 \left\{ \frac{\partial w_2}{\partial y} - \alpha f'(x) \frac{\partial w_2}{\partial x} \right\} = 0 \quad \text{at} \quad y = -1 - \alpha f(x), \quad (3.40)$$

$$w_1 = w_2 \quad \text{at} \quad y = 0, \quad (3.41)$$

$$\begin{aligned} \frac{\partial w_1}{\partial y} + \frac{\partial \psi_1}{\partial y} - \alpha f'(x) \left(\frac{\partial w_1}{\partial x} + \frac{\partial \psi_1}{\partial x} \right) &= \mu \frac{\partial w_2}{\partial y} + \varepsilon \frac{\partial \psi_2}{\partial y} \\ &\quad - \alpha f'(x) \left(\mu \frac{\partial w_2}{\partial x} + \varepsilon \frac{\partial \psi_2}{\partial x} \right) \quad \text{at} \quad y = 0. \end{aligned} \quad (3.42)$$

3.3 Analytical solution: Perturbation analysis

To gain analytical insights, we have chosen the perturbation technique to solve the aforementioned two-layer microfluidic problem. Drawing from experimental data on the wave amplitude or roughness amplitude (α) observed in glass microchannels (Ren et al. [2011]), it becomes evident that this parameter typically hovers around the order of 0.01, especially in microchannels approximately $10\mu m$ in height. In light of this, we propose that values for the wave amplitude, denoted as α , can be taken as high as 0.05, based on the experimental findings reported by Weilin et al. [2000]. Therefore, we choose α as a perturbation parameter to gain analytical insights into the problem.

3.3.1 Effect of wave amplitude on applied potential

For small value of $\alpha (<< 1)$, we have expanded Φ_i asymptotically (for $i = 1, 2$) in the following form

$$\Phi_1 = \Phi_{10} + \alpha\Phi_{11} + \dots, \quad (3.43)$$

$$\Phi_2 = \Phi_{20} + \alpha\Phi_{21} + \dots. \quad (3.44)$$

Substituting Eqs. (3.43) and (3.44) in Eq. (3.4), one may write system of equations as

$$\nabla^2\Phi_{ij} = 0, \quad i = 1, 2, \text{ and } j = 0, 1, \dots. \quad (3.45)$$

Again substituting Eqs. (3.43) and (3.44) in the dimensionless boundary conditions (3.10)-(3.13), we get

$$\left(\frac{\partial\Phi_{10}}{\partial y} + \alpha \frac{\partial\Phi_{11}}{\partial y} + \dots \right) - \alpha f'(x) \left(\frac{\partial\Phi_{10}}{\partial x} + \alpha \frac{\partial\Phi_{11}}{\partial x} + \dots \right) = 0, \quad \text{at } y = 1 + \alpha f(x), \quad (3.46)$$

$$\left(\frac{\partial\Phi_{20}}{\partial y} + \alpha \frac{\partial\Phi_{21}}{\partial y} + \dots \right) + \alpha f'(x) \left(\frac{\partial\Phi_{20}}{\partial x} + \alpha \frac{\partial\Phi_{21}}{\partial x} + \dots \right) = 0, \quad \text{at } y = -1 - \alpha f(x), \quad (3.47)$$

$$(\Phi_{10} + \alpha\Phi_{11} + \dots) = (\Phi_{20} + \alpha\Phi_{21} + \dots), \quad \text{at } y = 0, \quad (3.48)$$

and

$$\begin{aligned} & \left\{ \left(\frac{\partial\Phi_{10}}{\partial y} + \alpha \frac{\partial\Phi_{11}}{\partial y} + \dots \right) - \varepsilon \left(\frac{\partial\Phi_{20}}{\partial y} + \alpha \frac{\partial\Phi_{21}}{\partial y} + \dots \right) \right\} \\ & - \alpha f'(x) \left\{ \left(\frac{\partial\Phi_{10}}{\partial x} + \alpha \frac{\partial\Phi_{11}}{\partial x} + \dots \right) + \varepsilon \left(\frac{\partial\Phi_{20}}{\partial x} + \alpha \frac{\partial\Phi_{21}}{\partial x} + \dots \right) \right\} \\ & - \alpha f(x) \delta_\Phi = 0, \quad \text{at } y = 0. \end{aligned} \quad (3.49)$$

To obtain the appropriate boundary conditions at $y = \pm 1$ for Eq. (3.45) up to first-order perturbation, let us expand the boundary conditions (3.46) and (3.47) in Taylor series expansions about

$y = 1$ and $y = -1$, respectively. After obtaining the expansions, one may easily write down the following boundary conditions:

$$O(1) : \frac{\partial \Phi_{10}}{\partial y} = 0, \text{ at } y = 1, \quad (3.50)$$

$$\frac{\partial \Phi_{20}}{\partial y} = 0, \text{ at } y = -1, \quad (3.51)$$

$$\Phi_{10} = \Phi_{20}, \text{ at } y = 0, \quad (3.52)$$

$$\frac{\partial \Phi_{10}}{\partial y} - \varepsilon \frac{\partial \Phi_{20}}{\partial y} = 0, \text{ at } y = 0, \quad (3.53)$$

$$O(\alpha) : \frac{\partial \Phi_{11}}{\partial y} + f(x) \frac{\partial^2 \Phi_{10}}{\partial y^2} - f'(x) \frac{\partial \Phi_{10}}{\partial x} = 0, \text{ at } y = 1, \quad (3.54)$$

$$\frac{\partial \Phi_{21}}{\partial y} - f(x) \frac{\partial^2 \Phi_{20}}{\partial y^2} + f'(x) \frac{\partial \Phi_{20}}{\partial x} = 0, \text{ at } y = -1, \quad (3.55)$$

$$\Phi_{11} = \Phi_{21}, \text{ at } y = 0, \quad (3.56)$$

$$\left(\frac{\partial \Phi_{11}}{\partial y} - \varepsilon \frac{\partial \Phi_{21}}{\partial y} \right) - f'(x) \left(\frac{\partial \Phi_{10}}{\partial x} + \varepsilon \frac{\partial \Phi_{20}}{\partial x} \right) = \delta_\Phi f(x), \text{ at } y = 0. \quad (3.57)$$

In order to obtain the solution of Eq. (3.45) for applied potential Φ_i at both layers, we use the corresponding boundary conditions (3.50)-(3.57). It is worthwhile to mention here that when $\alpha = 0$ (unperturbed), then one can retain microchannel with parallel plate. In this case, the normalized applied electric field acts simply along x -direction and the gradient of voltage becomes constant (Chakraborty and Paul [2006]; Lei et al. [2017]). By solving the Eq. (3.45) (for $j = 0$) subject to the boundary conditions (3.50)-(3.53), one can easily notice that the solution of Φ_{10} and Φ_{20} are independent of y . Hence the solution for Φ_{10} and Φ_{20} considering uniqueness upto constant can be written in the form

$$\Phi_{10} = C_1 x, \quad (3.58)$$

$$\Phi_{20} = C_3 x, \quad (3.59)$$

where, C_1 and C_3 are constants to be determined. Furthermore, the solutions of Φ_{11} and Φ_{21} can be evaluated as

$$\Phi_{11} = C_5(x) \cosh(\lambda y) + C_6(x) \sinh(\lambda y), \quad (3.60)$$

$$\Phi_{21} = C_7(x) \cosh(\lambda y) + C_8(x) \sinh(\lambda y), \quad (3.61)$$

The expressions for $C_5(x)$, $C_6(x)$, $C_7(x)$ and $C_8(x)$ are appended in Appendix 3.A.

3.3.2 Effect of wave amplitude on EDL potential

To obtain the analytical solution for the EDL potential (ψ_i), we first need to introduce the asymptotic expansion of ψ_i (for $i = 1, 2$) in the following form

$$\psi_1 = \psi_{10} + \alpha \psi_{11} + \dots, \quad (3.62)$$

$$\psi_2 = \psi_{20} + \alpha \psi_{21} + \dots. \quad (3.63)$$

Substituting (3.62) and (3.63) in Eq. (3.23), one may write

$$(\nabla^2 - \kappa_i^2)\psi_{ij} = 0, \quad i = 1, 2, \text{ and } j = 0, 1, \dots \quad (3.64)$$

Again substituting (3.62) and (3.63) in the dimensionless boundary conditions (3.24)-(3.27) yield

$$(\psi_{10} + \alpha\psi_{11} + \dots) = \zeta(x) \quad \text{at } y = 1 + \alpha f(x), \quad (3.65)$$

$$(\psi_{20} + \alpha\psi_{21} + \dots) = \zeta(x) \quad \text{at } y = -1 - \alpha f(x), \quad (3.66)$$

$$(\psi_{10} - \psi_{20}) + \alpha(\psi_{11} - \psi_{21}) + \dots = \delta_\zeta, \quad \text{at } y = 0, \quad (3.67)$$

and

$$\begin{aligned} & \left\{ \left(\frac{\partial \psi_{10}}{\partial y} + \alpha \frac{\partial \psi_{11}}{\partial y} + \dots \right) - \varepsilon \left(\frac{\partial \psi_{20}}{\partial y} + \alpha \frac{\partial \psi_{21}}{\partial y} + \dots \right) \right\} \\ & - \alpha f'(x) \left\{ \left(\frac{\partial \psi_{10}}{\partial x} + \alpha \frac{\partial \psi_{11}}{\partial x} + \dots \right) + \varepsilon \left(\frac{\partial \psi_{20}}{\partial x} + \alpha \frac{\partial \psi_{21}}{\partial x} + \dots \right) \right\} = -Q, \\ & \text{at } y = 0. \end{aligned} \quad (3.68)$$

The boundary conditions (3.65) and (3.66) are expanded in Taylor series about $y = 1$ and $y = -1$ respectively. Then the Eqs. (3.64) (for $j=0,1$), can be written easily in the following appropriate boundary conditions.

$$O(1) : \quad \frac{\partial \psi_{10}}{\partial y} = 1, \quad \text{at } y = 1, \quad (3.69)$$

$$\frac{\partial \psi_{20}}{\partial y} = 1, \quad \text{at } y = -1, \quad (3.70)$$

$$\psi_{10} - \psi_{20} = \delta_\zeta, \quad \text{at } y = 0, \quad (3.71)$$

$$\frac{\partial \psi_{10}}{\partial y} - \varepsilon \frac{\partial \psi_{20}}{\partial y} = -Q, \quad \text{at } y = 0, \quad (3.72)$$

$$O(\alpha) : \quad \psi_{11} + f(x) \frac{\partial \psi_{10}}{\partial y} = \frac{1}{2} f(x), \quad \text{at } y = 1, \quad (3.73)$$

$$\psi_{21} - f(x) \frac{\partial \psi_{20}}{\partial y} = \frac{1}{2} f(x), \quad \text{at } y = -1, \quad (3.74)$$

$$\psi_{11} - \psi_{21} = \delta_\zeta f(x), \quad \text{at } y = 0, \quad (3.75)$$

$$\left(\frac{\partial \psi_{11}}{\partial y} - \varepsilon \frac{\partial \psi_{21}}{\partial y} \right) - f'(x) \left(\frac{\partial \psi_{10}}{\partial x} + \varepsilon \frac{\partial \psi_{20}}{\partial x} \right) = 0, \quad \text{at } y = 0. \quad (3.76)$$

The solution for the potential distributions for two layer flow are obtained as

$$\psi_{10} = B_1 \cosh(\kappa_1 y) + B_2 \sinh(\kappa_1 y), \quad (3.77)$$

$$\psi_{20} = B_3 \cosh(\kappa_2 y) + B_4 \sinh(\kappa_2 y), \quad (3.78)$$

$$\begin{aligned}\psi_{11} = \frac{1}{B_9} [B_5 \{ \varepsilon \gamma_2 \cosh(\gamma_2) \sinh(\gamma_1 y) + \gamma_1 \cosh(\gamma_1 y) \sinh(\gamma_2) \} \\ + \varepsilon \gamma_2 (B_6 + \delta_\zeta \cosh(\gamma_2)) \sinh(\gamma_1 - \gamma_1 y)] f(x),\end{aligned}\quad (3.79)$$

and

$$\begin{aligned}\psi_{21} = \frac{1}{B_9} [\gamma_1 (B_5 - \delta_\zeta \cosh(\gamma_1)) \sinh(\gamma_2 + \gamma_2 y) \\ + B_6 \{ \varepsilon \gamma_2 \cosh(\gamma_2 y) \sinh(\gamma_1) - \gamma_1 \cosh(\gamma_1) \sinh(\gamma_2 y) \}] f(x),\end{aligned}\quad (3.80)$$

where $\gamma_1 = \sqrt{\kappa_1^2 + \lambda^2}$, $\gamma_2 = \sqrt{\kappa_2^2 + \lambda^2}$ and the expressions for B_1 to B_{10} are given in Appendix 3.B.

3.3.3 Effect of wave amplitude on two-layered flow

In a similar fashion, the perturbation technique is applied to obtain the approximate analytical solution for velocity distribution. To achieve this, we first expand dependent variables asymptotically with a perturbation parameter $\alpha (< 1)$. We write

$$\mathcal{F}_i = \mathcal{F}_{i0} + \alpha \mathcal{F}_{i1} + \dots, \quad j = 0, 1, \quad i = 1, 2, \quad (3.81)$$

where \mathcal{F}_i is used for the variables S_i and w_i . In this context, the strength of the transverse electric field (S_i where $i = 1, 2$), depends on the potential distribution in both layers. It is well-established that insights into the electric field can be obtained by considering the negative gradient of the electric potential. Therefore, expressions for S_i can be easily derived, and the detailed formulations are provided in Appendix 3.C.

Substituting Eq. (3.81) in Eqs. (3.37) and (3.38), we obtain

$$\nabla^2 w_{1j} - Ha^2 w_{1j} + \kappa_1^2 \psi_{1j} + Ha S_{1j} + P = 0, \quad j = 0, 1, \dots \quad (3.82)$$

and

$$\mu \nabla^2 w_{2j} - \sigma Ha^2 w_{2j} + \varepsilon \kappa_2^2 \psi_{2j} + \sigma Ha S_{2j} + \Gamma P = 0, \quad j = 0, 1, \dots \quad (3.83)$$

Further, substituting Eq. (3.81) in the dimensionless boundary conditions (3.39)-(3.42), we constitute the following:

$$\begin{aligned}\left(w_{10} + \alpha w_{11} + \dots \right) + \beta_1 \left\{ \left(\frac{\partial w_{10}}{\partial y} + \alpha \frac{\partial w_{11}}{\partial y} + \dots \right) \right. \\ \left. - \alpha f'(x) \left(\frac{\partial w_{10}}{\partial x} + \alpha \frac{\partial w_{11}}{\partial x} + \dots \right) \right\} = 0 \quad \text{at } y = 1 + \alpha f(x),\end{aligned}\quad (3.84)$$

$$\begin{aligned}\left(w_{20} + \alpha w_{21} + \dots \right) - \beta_2 \left\{ \left(\frac{\partial w_{20}}{\partial y} + \alpha \frac{\partial w_{21}}{\partial y} + \dots \right) \right. \\ \left. + \alpha f'(x) \left(\frac{\partial w_{20}}{\partial x} + \alpha \frac{\partial w_{21}}{\partial x} + \dots \right) \right\} = 0 \quad \text{at } y = -1 - \alpha f(x),\end{aligned}\quad (3.85)$$

$$(w_{20} - w_{10}) + \alpha(w_{21} - w_{11}) + \dots = 0 \quad \text{at } y = 0, \quad (3.86)$$

$$\begin{aligned} & \left(\frac{\partial w_{10}}{\partial y} + \alpha \frac{\partial w_{11}}{\partial y} + \dots \right) + \left(\frac{\partial \psi_{10}}{\partial y} + \alpha \frac{\partial \psi_{11}}{\partial y} + \dots \right) \\ & - \alpha f'(x) \left\{ \left(\frac{\partial w_{10}}{\partial x} + \alpha \frac{\partial w_{11}}{\partial x} + \dots \right) + \left(\frac{\partial \psi_{10}}{\partial x} + \alpha \frac{\partial \psi_{11}}{\partial x} + \dots \right) \right\} \\ & - \mu \left(\frac{\partial w_{20}}{\partial y} + \alpha \frac{\partial w_{21}}{\partial y} + \dots \right) - \varepsilon \left(\frac{\partial \psi_{20}}{\partial y} + \alpha \frac{\partial \psi_{21}}{\partial y} + \dots \right) \\ & + \alpha f'(x) \left\{ \mu \left(\frac{\partial w_{20}}{\partial x} + \alpha \frac{\partial w_{21}}{\partial x} + \dots \right) + \varepsilon \left(\frac{\partial \psi_{20}}{\partial x} + \alpha \frac{\partial \psi_{21}}{\partial x} + \dots \right) \right\} = 0, \\ & \text{at } y = 0. \end{aligned} \quad (3.87)$$

The boundary conditions (3.84) and (3.85) are expanded in Taylor series about $y = 1$ and $y = -1$ respectively, and retain the terms of like powers of α . The boundary conditions for velocity corresponding to zeroth order and first order can be expressed as

$$O(1) : w_{10} + \beta_1 \frac{\partial w_{10}}{\partial y} = 0 \quad \text{at } y = 1, \quad (3.88)$$

$$w_{20} - \beta_2 \frac{\partial w_{20}}{\partial y} = 0 \quad \text{at } y = -1, \quad (3.89)$$

$$w_{10} = w_{20} \quad \text{at } y = 0, \quad (3.90)$$

$$\frac{\partial w_{10}}{\partial y} + \frac{\partial \psi_{10}}{\partial y} = \mu \frac{\partial w_{20}}{\partial y} + \varepsilon \frac{\partial \psi_{20}}{\partial y} \quad \text{at } y = 0. \quad (3.91)$$

$$\begin{aligned} O(\alpha) : w_{11} + \beta_1 \frac{\partial w_{11}}{\partial y} + f(x) \frac{\partial w_{10}}{\partial y} + \beta_1 \left\{ f(x) \frac{\partial^2 w_{10}}{\partial y^2} - f'(x) \frac{\partial w_{10}}{\partial x} \right\} &= 0 \\ \text{at } y = 1, \end{aligned} \quad (3.92)$$

$$\begin{aligned} w_{21} - \beta_2 \frac{\partial w_{21}}{\partial y} - f(x) \frac{\partial w_{20}}{\partial y} + \beta_2 \left\{ f(x) \frac{\partial^2 w_{20}}{\partial y^2} - f'(x) \frac{\partial w_{20}}{\partial x} \right\} &= 0 \\ \text{at } y = -1, \end{aligned} \quad (3.93)$$

$$w_{11} = w_{21} \quad \text{at } y = 0, \quad (3.94)$$

$$\begin{aligned} & \frac{\partial w_{11}}{\partial y} + \frac{\partial \psi_{11}}{\partial y} - f'(x) \left(\frac{\partial w_{10}}{\partial x} + \frac{\partial \psi_{10}}{\partial x} \right) - \mu \frac{\partial w_{21}}{\partial y} - \varepsilon \frac{\partial \psi_{21}}{\partial y} \\ & + f'(x) \left(\mu \frac{\partial w_{20}}{\partial x} + \varepsilon \frac{\partial \psi_{20}}{\partial x} \right) = 0, \quad \text{at } y = 0. \end{aligned} \quad (3.95)$$

The solution of the two-layered flow transport is obtained from equations (3.82) and (3.83) subject to the boundary conditions (3.88)-(3.95) for layer-1 and layer-2 respectively such that

$$\begin{aligned} w_{10} &= A_1 \cosh(Hay) + A_2 \sinh(Hay) + \frac{P + HaS_{10}}{Ha^2} \\ &+ \frac{\kappa_1^2}{(Ha^2 - \kappa_1^2)} \left\{ B_1 \cosh(\kappa_1 y) + B_2 \sinh(\kappa_1 y) \right\}, \end{aligned} \quad (3.96)$$

$$w_{20} = A_3 \cosh\left(Ha\sqrt{\frac{\sigma}{\mu}}y\right) + A_4 \sinh\left(Ha\sqrt{\frac{\sigma}{\mu}}y\right) + \frac{P\Gamma + \sigma Ha S_{20}}{\sigma Ha^2} + \frac{\varepsilon \kappa_2^2}{(\sigma Ha^2 - \mu \kappa_1^2)} \left\{ B_3 \cosh(\kappa_2 y) + B_4 \sinh(\kappa_2 y) \right\}, \quad (3.97)$$

$$w_{11} = \left[A_9 \cosh(\gamma_3 y) + A_{10} \sinh(\gamma_3 y) + \frac{Ha\{F_1(y) + F_2(y)\}}{\gamma_3^2 - \lambda^2} + \frac{(Ha - \kappa_1^2)\psi_{11}}{(\gamma_1^2 - \gamma_3^2)f(x)} \right] f(x) + f'(x) \left[A_{11} \cosh(\gamma_3 y) + A_{12} \sinh(\gamma_3 y) + \frac{Ha}{\gamma_3^2 - \lambda^2} \left\{ F_4(y) + F_5(y) \right\} \right], \quad (3.98)$$

and

$$w_{21} = \left[A_{13} \cosh\left(\frac{\gamma_4 y}{\sqrt{\mu}}\right) + A_{14} \sinh\left(\frac{\gamma_4 y}{\sqrt{\mu}}\right) + \frac{\sigma Ha}{\gamma_4^2 - \lambda^2 \mu} \left\{ F_1(y) + F_6(y) \right\} - \frac{(\sigma Ha - \varepsilon \kappa_2^2)\psi_{21}}{(\gamma_4^2 - \mu \gamma_2^2)} \right] f(x) + \left[A_{15} \cosh\left(\frac{\gamma_4 y}{\sqrt{\mu}}\right) + A_{16} \sinh\left(\frac{\gamma_4 y}{\sqrt{\mu}}\right) + \frac{\sigma Ha}{\gamma_4^2 - \mu \lambda^2} \left\{ F_4(y) - F_5(y) \right\} \right] f'(x). \quad (3.99)$$

In the above equations, $\gamma_3 = \sqrt{Ha^2 + \lambda^2}$, $\gamma_4 = \sqrt{\sigma Ha^2 + \lambda^2}$. However, the expressions for $F_1(y)$, $F_2(y)$, $F_3(y)$, $F_4(y)$, $F_5(y)$, $F_6(y)$ and $F_7(y)$ are provided in Appendix 3.C and the expressions for A_i , ($i = 1, 2, \dots, 16$) are given in Appendix 3.D.

Thus, substituting these expressions in Eq. (3.81), the analytical solution for velocity distribution can be realized.

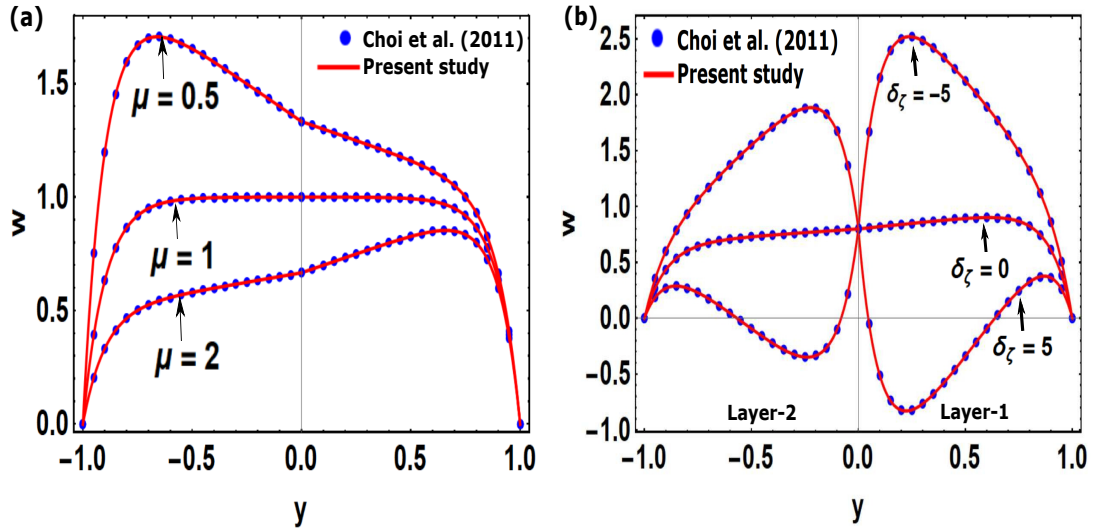


Figure 3.2: Comparison of present velocity profiles with the results of Choi et al. [2011] in limiting case $\varepsilon = 1$, $Q = 0$, $\alpha = \lambda = 0$, $P = 0$, $\beta_1 = 0$, $\beta_2 = 0$, $S_{10} = S_{20} = 0$, and for the same electroosmotic parameters $\kappa_1 = \kappa_2 = 10$, where (a) shows the velocity variation for different values of viscosity ratio μ , and (b) reveals the velocity profiles with varying zeta potential difference δ_ζ at the fluid-fluid interface.

3.4 Validation of Results

To affirm the correctness of the present analytical investigation, we have compared our results with the results of Choi et al. [2011] by setting $\alpha = 0$. Choi et al. [2011] considered the steady electroosmotic flow of two immiscible viscous, Newtonian fluids confined between two parallel plates. Their study focused on the influence of zeta potential and the charge densities across the fluid-fluid interface of two immiscible fluids. But in the present study, we have examined the waviness of the microchannel with the wave amplitudes α and λ . We have incorporated the interfacial potential jump δ_ζ and the viscosity ratio μ . From the analysis of Choi et al. [2011], the velocity distribution for two layers is recovered exactly and the results resembled correctly with the present analysis for $\alpha = 0, P = 0, \beta_1 = 0, \beta_2 = 0, S_{10} = 0, S_{20} = 0, Ha \rightarrow 0$. Choi et al. [2011] pointed out that the velocity profiles are symmetric for equal viscosity ($\mu = 1$) and it represents the electroosmotic flow of a single fluid. But for different viscosities of two fluids, the maximum velocity for two layers occurs in the low viscosity fluid layer. These results also agreed with the present analysis as depicted in Fig. 3.2(a). Further, Fig. 3.2(b) illustrates the velocity profiles with the variation of the interfacial potential jump. Choi et al. [2011] described that when the permittivities and viscosities are identical for two fluids ($\mu = 1, \varepsilon = 1$), then the velocity distribution shows symmetric about $y = 0$ with $\delta_\zeta = 0$. However, for large values of δ_ζ , the flow reversal takes place in the flow region. These results also resembled our observations made in the present analysis. This establishes the correctness of our analysis for two-layer electroosmotic flow in a microchannel. The wave amplitude α , which is the perturbation parameter is chosen such that $O(\alpha^2)$ are neglected and α take values between 0 and 0.05.

We further conducted a comparison of our results by considering the flow of a single fluid through a non-hydrophobic ($\beta_1 = \beta_2 = 0$) microchannel with an undulated wall. The microchannel was devoid of any fluid-fluid interface at $y = 0$. To ensure consistency in our results, we set the following parameters: $\mu = 1, \varepsilon = 1, \sigma = 1, \beta_1 = \beta_2 = 0, Q = 0, \delta_\zeta = 0$. Our computed results revealed a parabolic velocity profile and undulated streamlines in limiting case as illustrated in Figs. 3.3(a)-3.3(c). The disturbances of fluid flow in the microchannel are observed due to the undulation of the channel walls. It may be mentioned here that the streamlines formed by elliptical boluses can be thought of as the microfluidic droplets in the middle region and transported in the forward direction, while exhibiting oscillatory flow near the boundary of the microchannel. Our findings align closely with those reported in theoretical investigation (Tripathi et al. [2017]). This alignment indicates that the observed fluid flow behavior in the undulated microchannel is consistent. We observed from Fig. 3.3(b) that the maximum velocity reaches at the central line of the channel for all Debye length. But there is a significant change near the channel which is due to the formation of EDL and boundary layer. This observation motivated us to focus on the study of boundary layer formation in the context of present developing model.

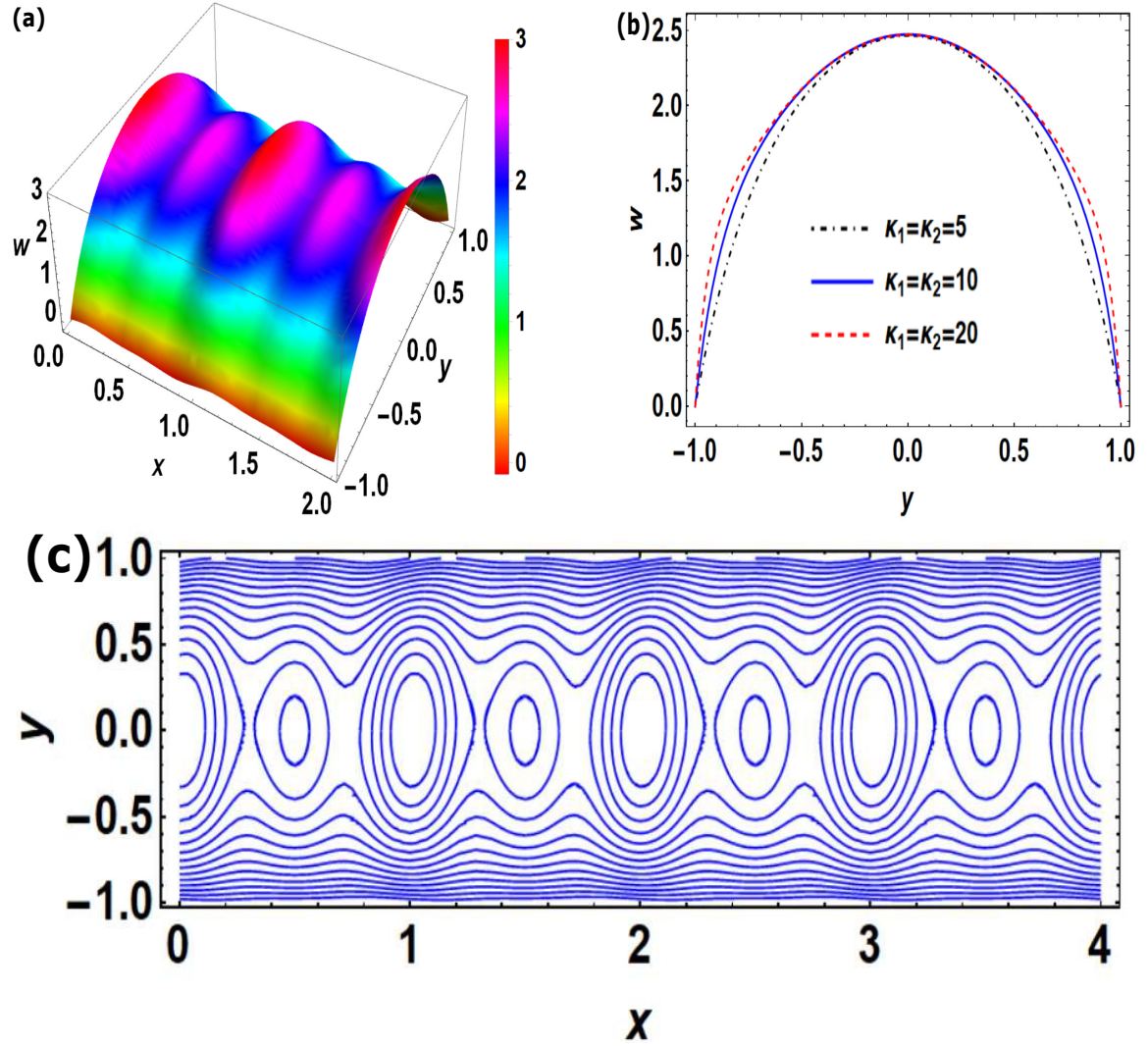


Figure 3.3: (a) 3D Velocity profile, (b) velocity variation for different $\kappa_i (i = 1, 2)$ at $x = 0.5$ and (c) streamlines for single fluid flow through the undulated microchannel for $\alpha = 0.02$, $\lambda = 0.01$, $\mu = 1$, $Ha = 0.5$, $S_{10} = S_{20} = 5$, $\kappa_1 = \kappa_2 = 5$, $P = 1$, $\varepsilon = 1$, $\sigma = 1$, $\beta_1 = \beta_2 = 0$, $Q = 0$, $\delta_\zeta = 0$, which exhibits a symmetric velocity profile and undulated streamlines, without any presence of a hydrophobic solid-fluid interface.

3.5 Results and Discussion

A theoretical study has been performed to observe the two-layer flow transport through a wavy microchannel with hydrophobic surfaces, under an electromagnetic environment. A perturbation technique has been employed to solve the governing equations analytically. To generate the numerical data, we assigned suitable values of pertinent parameters involved in this investigation. Therefore it is mandatory to fix up the ranges of the important parameters. The height of the microchannel (H) is $10 \sim 40\mu m$ (Cho et al. [2013]; Horiuchi and Dutta [2006]; Rana et al. [2022]). The slip lengths are denoted as $\tilde{\beta}_i(i = 1, 2) \sim 0 - 200nm$ (Shit et al. [2016d]; Zhu and Granick [2001]) and therefore, the non-dimensional slip parameters are estimated as $\beta_i(i = 1, 2) \sim 0 - 0.02$. On the basis of the ionic strength of two fluids, the thickness of EDL ($\lambda_i^D(i = 1, 2)$) is treated as $0.25\mu m - 1\mu m$ (Shit et al. [2016d]). Hence, the electroosmotic parameters are taken as $\kappa_i(i = 1, 2) \sim 5 - 20$. The applied Electrical field in the axial direction and the transverse direction are assumed to be $E_{xi}(i = 1, 2) \sim 0 - 2 \times 10^4 V/m$ and $E_z \sim 0 - 2 \times 10^4 V/m$ respectively (Yau et al. [2011]; Reza et al. [2021]). The applied magnetic field is taken as $B_0 \sim 1 - 50T$ (Rana et al. [2022]). The position of the fluid-fluid interface is considered at the origin of the channel (Choi et al. [2011]; Ranjit et al. [2021]). The wall zeta potentials for the microchannel are denoted as $\tilde{\zeta}_0 \sim (-18)mV - (-12.5)mV$ (Banerjee et al. [2022]) and the dimensionless zeta potential ratio is $\delta_\zeta \sim (-0.5) - 0.5$ as in (Shit et al. [2016d]; Banerjee et al. [2022]). The dimensionless charge density jump is taken as $Q = 0.05$ and the dimensionless pressure gradient is $P \sim 0.5 - 2$ according to the study (Shit et al. [2016d]; Banerjee et al. [2022]). Further, the various ratios that have been described in the previous sections are chosen as $\varepsilon \sim 1$, $\sigma \sim 0.5 - 2$, $\mu \sim 0.2 - 5$ and $\Gamma \sim 0.5 - 2$ (cf. Gao et al. [2005]; Shit et al. [2016d]; Banerjee et al. [2022]; Wang et al. [2005]; Gao et al. [2007]).

3.5.1 Two layered electromagnetohydrodynamic flow analysis

In an effort to visualize the influence of electromagnetic effect on the flow characteristics, Figs. 3.4-3.6 are presented for the variation of velocity profiles with different parameters involving slip boundary and undulated surface. The interaction of electrolyte solutions with the hydrophobic surface augments the electroosmotic velocity. But the interaction of magnetic field with the electrolyte solution also needs to be more focused (refer Fig. 3.4). It can be observed that for a fixed location of y , the velocity is increasing with $Ha < 1$, while it is decaying with $Ha \geq 1$ as seen in Figs. 3.4(a) and 3.4(b) respectively. The Hartmann number show a strong dependency as the strength of the applied magnetic field. From the equation (3.31), one can notice that the applied electromagnetic force is the combination of 'flow-aiding' ($\sim \sigma_{ei}E_{xi}B_0$) force and the 'flow-opposing' ($\sim \sigma_{ei}B_0^2\tilde{w}_i$) force. For low Hartmann number ($Ha < 1$) the Lorentz force is dominated by the 'flow aiding' force, as a result the velocity of the flow gets enhanced which is seen in Fig. 3.4(a). However, for higher values of Hartmann number ($Ha \geq 1$) the Lorentz force is acting as a retarding force and in this case, the Lorentz force inhibits the flow opposing force leading to reduction in the flow velocity as seen in Fig. 3.4(b). From both these figures fluid velocity in the layer-2 is higher than the fluid in layer-1. This is because of the effect of zeta potential difference at the fluid-fluid interface. It

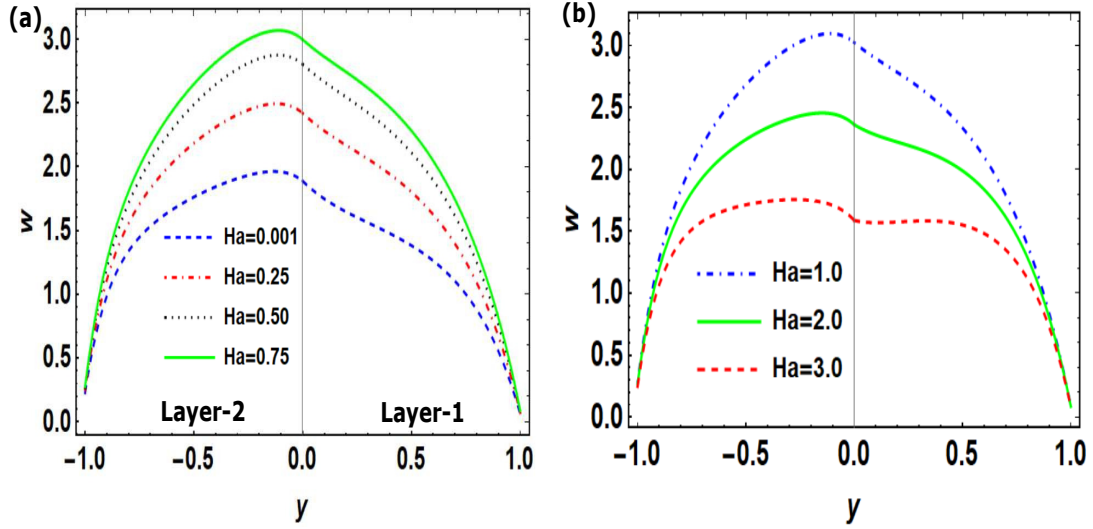


Figure 3.4: Velocity profiles for both fluid layers with variation of Ha for $\varepsilon = 1$, $Q = 0.05$, $\kappa_1 = 5$, $\kappa_2 = 10$, $\alpha = 0.025$, $\lambda = 0.05$, $P = 2$, $\beta_1 = 0.01$, $\beta_2 = 0.02$, $S_{10} = 5$, $S_{20} = 5$, $\mu = 0.7$, $\delta_\zeta = 0.5$, $\delta_\Phi = 0.1$, $\sigma = 1$, $\Gamma = 1$, $x = 0.5$. In the Figure (a), the electric force is stronger than the magnetic force field ($Ha < 1$) for which the axial velocity increases. In Figure (b), the Lorentz force is strong due to higher magnetic field strength ($Ha \geq 1$) than the electric force, results in the decreasing fluid velocity.

enhances the electroosmotic mobility of the electrolytes, resulting in slightly elevation of the flow velocity within the fluid in the layer 2.

Fig. 3.5(a) shows the velocity profiles for different values of viscosity ratio. Since $\mu = \mu_2/\mu_1$, the values $\mu < 1$ correspond to the viscosity of fluid in the layer-2 is lesser than the viscosity of fluid in the layer-1 and for $\mu > 1$, the viscosity is higher in the fluid layer-2. The resistance to flow is large for higher viscosity and thereby velocity reduces with increasing viscous ratio as shown in Fig. 3.5(a). The increase of viscosity ratio produces resistance to flow due to the interaction of fluid molecules and the electrolyte mobile ions. As a result, reduction in electroosmotic mobility is observed. The maximum velocity for two-layer fluids occur in the low viscosity fluid region. Fig. 3.5(b) illustrates the impact of the charge density jump (Q) on the axial velocity. Notably, as the charge density jump increases, the axial velocity experiences a significant decrease in layer-1, whereas it increases in layer-2. The significance of Q in influencing the velocity is likely more pronounced within the fluid-fluid interfacial region, where the charge density jump has a more direct impact on the electrokinetic behavior. The influence of Q near the channel walls is found to be insignificant. Moreover, the velocity reaches its maximum when the charge density jump Q is higher, particularly in the layer characterized by a lower viscosity fluid.

Fig. 3.6(a) shows a monotonic behavior with electric conductivity ratio of the two fluids. Interfacial potential jump δ_ζ is playing an important role in two-layer EMHD flow. The interfacial potential jump affects the EDL potential due to the absorption of ions at the fluid-fluid interface. This sudden change in EDL potential distribution affects the velocity distribution of the flow (Gao

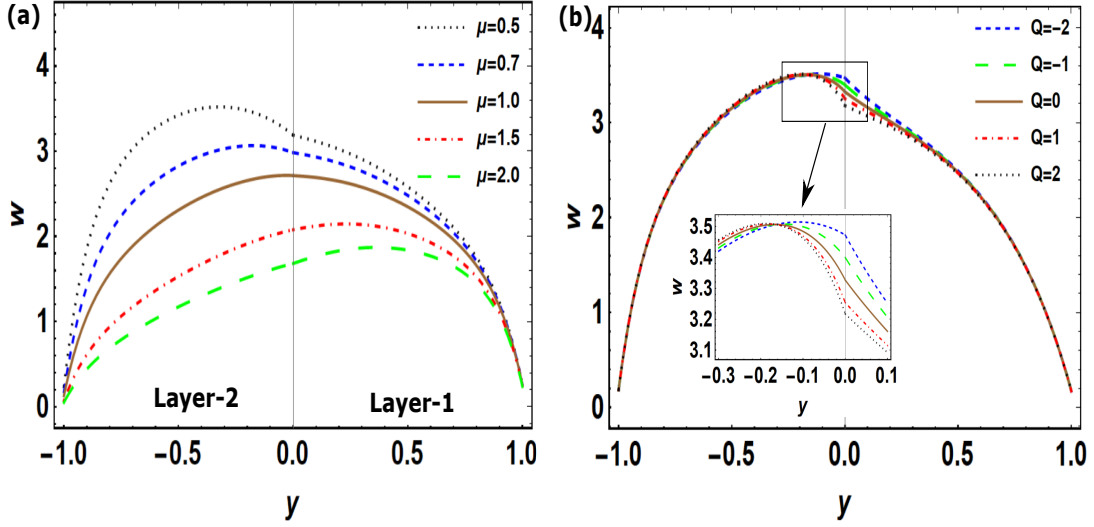


Figure 3.5: Velocity profiles for both fluid layers (a) variation of μ for $Q = 0.05$, (b) variation of Q for $\mu = 0.7$, when $\varepsilon = 1$, $\kappa_1 = 5$, $\kappa_2 = 10$, $Ha = 0.5$, $\alpha = 0.025$, $\lambda = 0.05$, $P = 2$, $\beta_1 = 0.01$, $\beta_2 = 0.02$, $S_{10} = 5$, $S_{20} = 5$, $\delta_\zeta = 0.1z$, $\delta_\Phi = 0.1$, $\sigma = 1$, $x = 0.5$. In Figure (a), the maximum velocity is observed in the fluid layer 2 for $\mu < 1$ due to lesser viscosity, while for $\mu > 1$, the velocity is higher in layer-1 than the layer-2.

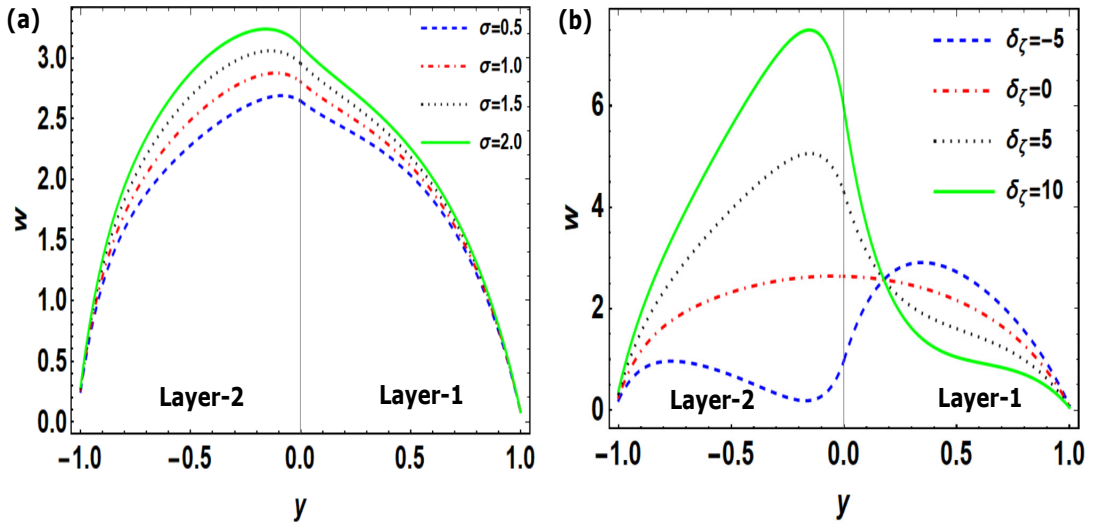


Figure 3.6: Velocity profiles for both fluid layers (a) variation of σ for $\delta_\zeta = 0.1$, (b) variation of δ_ζ for $\sigma = 1$, when $\varepsilon = 1$, $Q = 0.05$, $\kappa_1 = 5$, $\kappa_2 = 10$, $Ha = 0.5$, $\alpha = 0.025$, $\lambda = 0.05$, $P = 2$, $\beta_1 = 0.01$, $\beta_2 = 0.02$, $S_{10} = 5$, $S_{20} = 5$, $\delta_\Phi = 0.1$, $\mu = 0.7$, $\Gamma = 1$, $x = 0.5$.

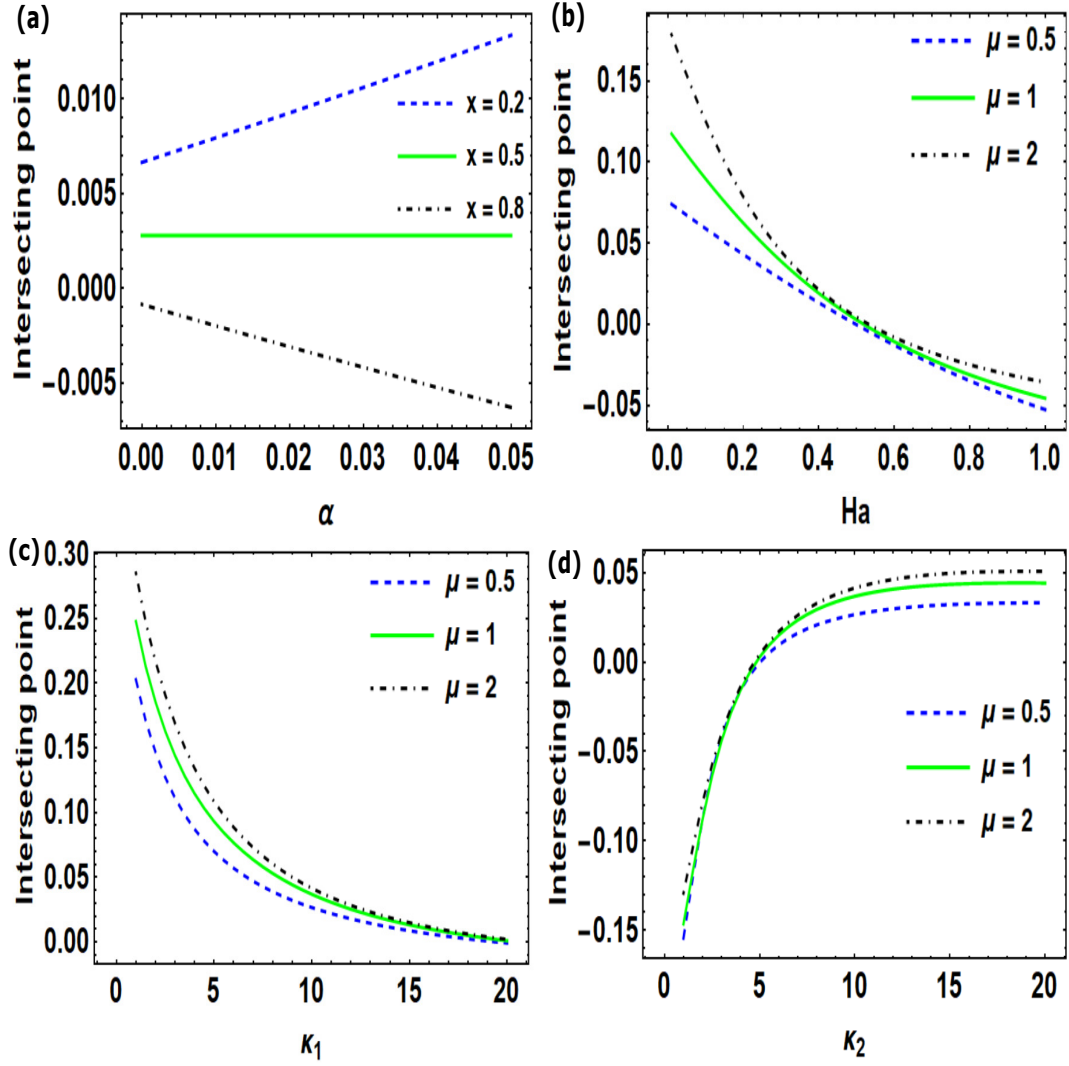


Figure 3.7: Plot for shifting of intersecting point on the y -axis at which the flow behaviour changes for the variation in (a) wave amplitude α and different x location of the rough surface channel (b) Hartmann number Ha and the viscosity ration μ (c) κ_1 and (d) κ_2 when $\varepsilon = 1$, $Q = 0.05$, $P = 1$, $\beta_1 = 0.01$, $\beta_2 = 0.02$, $S_{10} = 5$, $S_{20} = 5$, $\delta_\zeta = 0.1$, $\delta_\Phi = 0.1$, $\sigma = 1$, $\Gamma = 1$. The intersecting point 0 indicates the fluid-fluid interface.

et al. [2005]). Fig. 3.6(b) displays the velocity profiles for different values of δ_ζ . When $\delta_\zeta = 0$, the system exhibits a fully developed velocity profile, characterized by smooth and well-defined flow behavior. However, as δ_ζ deviates from zero, the velocity profiles undergo sudden changes at an intriguing intersecting point. This phenomenon arises due to a significant alteration in the potential distribution, which in turn influences the flow patterns of the charged particles. The absorption of ions at this intersecting point indicates the occurrence of electromagnetic interactions between the two fluids, leading to the observed shifts of intersecting point in the velocity profiles. The precise location of the intersecting point is dependent on various parameters, such as the applied magnetic field, applied electric field and the fluid properties, as depicted in detail in Fig. 3.7. The intersecting point is predominantly manifests either within layer-1 or layer-2, elucidating the intricate interplay between the electromagnetic fields and fluid dynamics. Fig. 3.7(a) shows how the intersecting point varies with different x values, signifying the influence of spatial position on this phenomenon. Furthermore, with an increase in the Hartmann number, Fig. 3.7(b) illustrates a gradual shift of the intersecting point from layer-1 to layer-2, indicating the transition from one flow behavior to another. Fig. 3.7(c) demonstrated a similar pattern for the parameter κ_1 , where smaller values of κ_1 lead to a rapid shifting of the intersecting point. As the value of κ_2 increases, the intersecting point transitions from layer-2 to layer-1. Conversely, for lower values of κ_2 result in a rapid displacement as shown in Fig. 3.7(d). The results presented in Figs. 3.7(a)-3.7(d) offer new findings that may be an interesting fact to the microfluidics researchers.

3.5.2 Streamline analysis

Wall amplitude plays an important role in fluid transport through a microchannel and the corresponding flow disturbance is expected to be more prominent at the boundary than at the middle layers. In this analysis, the two-layered flow transport phenomena through a hydrophobic wavy microchannel with an electromagnetic field effect have been investigated. The surface variation of the wall is associated with two dimensionless parameters α and λ . When $\lambda = 0$, then the microchannel becomes a wavy microchannel, and the variation of λ and α change the structure of the undulated surfaces of the microchannel. The variation of the walls depends on both coordinates x and y , therefore the flow patterns very much depend on the wall undulations of the microchannel.

To visualize the flow pattern in the rough microfluidic channel, the streamlines are plotted in Figs. 3.8-3.10 for different roughness parameter, viscosity ratio and zeta potential jump parameter in both the fluid layers. The streamlines are highly affected by the undulations of the surface. It is noted that the streamlines follow an oscillatory pattern with the variation of the surface of the microchannel. We observe that elliptical boluses or w may call as droplets are formed near the fluid-fluid interface (at $y = 0$). The number and size of the closed streamlines called as fluid bolus are increased with a rise in the values of α as shown in Figs. 3.8(a)-3.8(c). With an increasing values of α clearly impact on the streamlines pattern and thereby on the mixing of two fluids. In this case, bolus sizes are elongated vertically as the fluid experiences abrupt variations along the transverse direction. The formation of the boluses in layer-2 is more prominent than the boluses of fluid in layer-1. This is due to the presence of different fluid properties. The differences in viscosity, density,

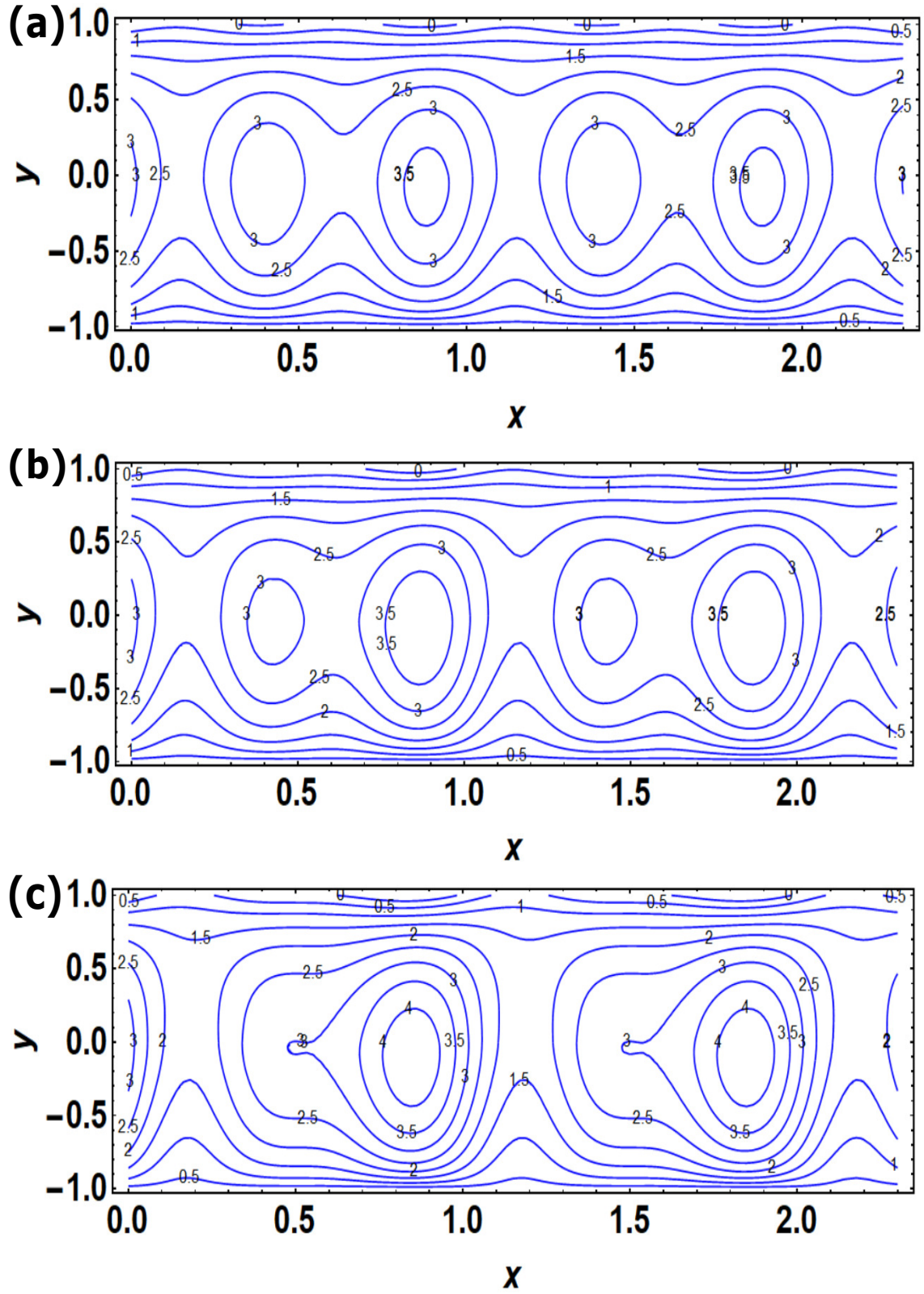


Figure 3.8: Streamlines for both fluid layers with variation of wave amplitude for (a) $\alpha = 0.01$, (b) $\alpha = 0.025$, (c) $\alpha = 0.05$ with $\varepsilon = 1$, $Q = 0.05$, $\kappa_1 = 5$, $\kappa_2 = 10$, $\lambda = 0.025$, $P = 2$, $\beta_1 = 0.02$, $\beta_2 = 0.01$, $S_{10} = 5$, $S_{20} = 5$, $\mu = 1.1$, $\delta_\zeta = 0.1$, $\delta_\Phi = 0.1$, $\sigma = 1$, $\Gamma = 1$. The visualization reveals a captivating oscillatory pattern, with the formation of semi-elliptical boluses near the fluid-fluid interface at $y = 0$.

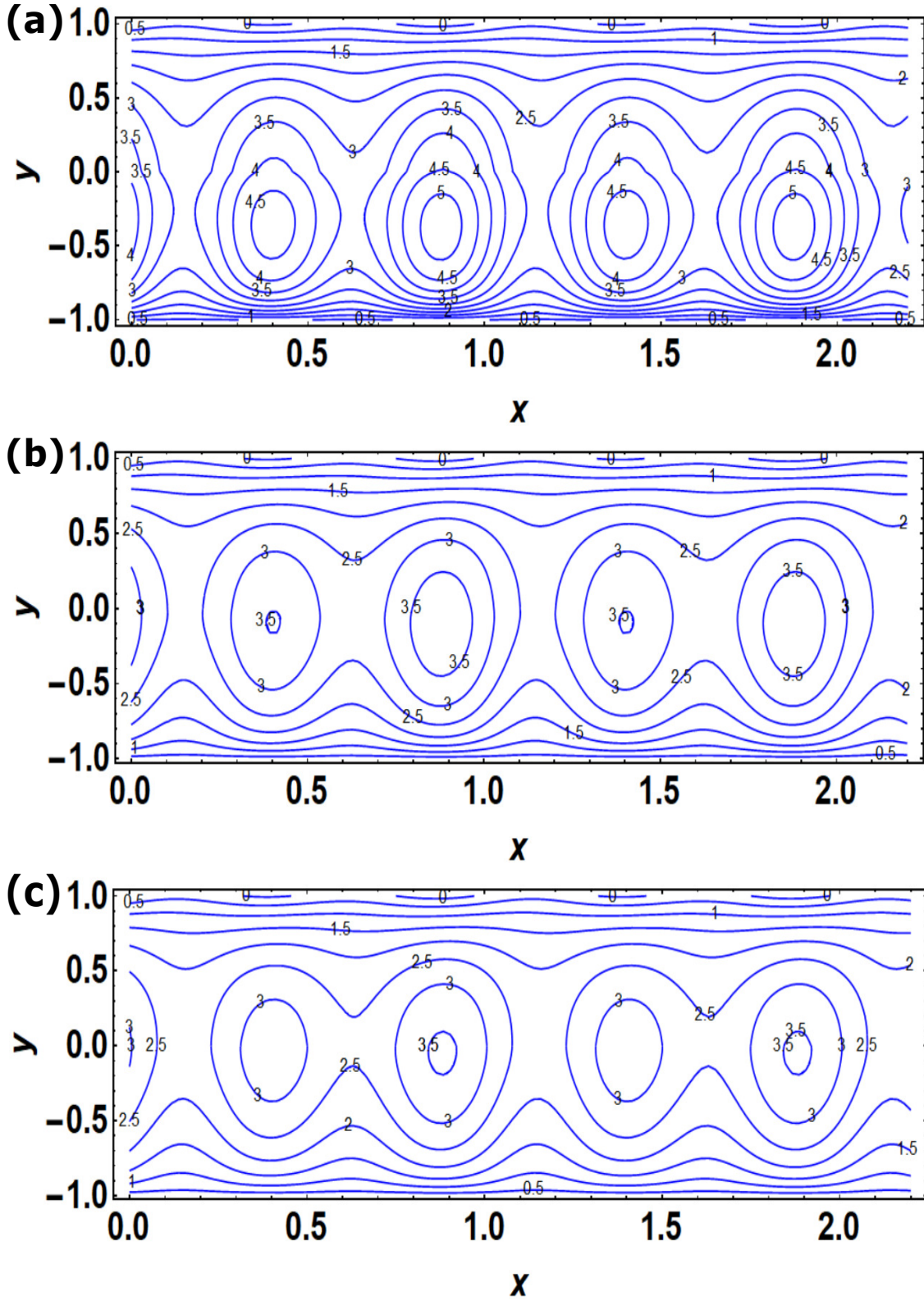


Figure 3.9: Streamlines for both fluid layers with variation of viscosity ratio (a) $\mu = 0.5$, (b) $\mu = 1$, (c) $\mu = 1.2$ for $\varepsilon = 1$, $Q = 0.05$, $\kappa_1 = 5$, $\kappa_2 = 10$, $\alpha = 0.01$, $\lambda = 0.025$, $P = 2$, $\beta_1 = 0.01$, $\beta_2 = 0.02$, $S_{10} = 5$, $S_{20} = 5$, $\delta_\zeta = 0.1$, $\delta_\Phi = 0.1$, $\sigma = 1$, $\Gamma = 1$.

permittivity, and electrical conductivity of two-layer fluid changes the flow patterns and therefore the streamlines are highly impacted. The maximum velocity occurs at the fluid-fluid interfacial layer of the microchannel depending on the waviness. Figs. 3.9(a)-3.9(c) depict almost identical oscillatory behaviour in velocity contours. In this scenario, the interfacial fluid boluses shifted from layer-2 to layer-1 in accordance with the increasing nature of the viscosity ratio. The shape of the boluses also depend on the enhancing nature of the viscosity ratio. It is worthwhile to mention here that the velocity is maximum in layer-2 for $\mu < 1$ and it reaches its peak in layer-1 for $\mu > 1$. Upon comparative analysis, the middle layer attains maximum velocity, particularly notable for low-viscosity fluid.

Figs. 3.10(a)-3.10(c) depict how the interfacial potential jump (δ_ζ) affects streamlines. In Fig. 3.10(b), δ_ζ is zero, the system displays undulating streamlines typical for a microchannel behaviour. However, Figs. 3.10(a) and 3.10(c) show the deviation from $\delta_\zeta = 0$ lead to sudden shift in the velocity distribution and change in the streamlines, featuring distinct boluses. This intriguing phenomenon is a consequence of a substantial alteration in the potential distribution. The change in potential zeta potential jump significantly influences the trajectories and behavior of charged particles within the microchannel, resulting in the modifications of flow patterns. Specifically a negative potential jump ($\delta_\zeta < 0$) indicating a higher potential in layer-1 than that of layer-2, leads to the separation of microfluidic droplets on either side of the liquid-liquid interface. This separation also hinges on the thickness of the electrical double layer, represented by the electroosmotic parameters κ_1 and κ_2 . Fig. 3.10(c) reveals that streamlines are remain parallel in layer-1, while the droplets forms as well in layer-2 due to the combined effects of $\kappa_1 < \kappa_2$ and a positive potential jump ($\delta_\zeta > 0$).

3.5.3 Volumetric flow rate

The volumetric flow rate in the two-layer fluid flow per unit width of the microchannel are defined as q_1 and q_2 for layer-1 and layer-2 respectively. Then the flow rate in the microchannel can be expressed as

$$q(x) = \int_{-1-\alpha f(x)}^{1+\alpha f(x)} w dy = q_1 + q_2, \quad (3.100)$$

where,

$$q_1 = \int_0^{1+\alpha f(x)} w_1 dy \text{ and } q_2 = \int_{-1-\alpha f(x)}^0 w_2 dy. \quad (3.101)$$

Further, we evaluate the mean velocity over one wavelength Λ , of the microchannel for layer-1 and layer-2 are respectively described as

$$Q_1 = \int_0^\Lambda q_1 dx = Q_{10} + \alpha Q_{11}, \quad (3.102)$$

and

$$Q_2 = \int_0^\Lambda q_2 dx = Q_{20} + \alpha Q_{21}. \quad (3.103)$$

The detailed expressions for Q_{10} , Q_{11} , Q_{20} and Q_{21} are given in Appendix 3.E.

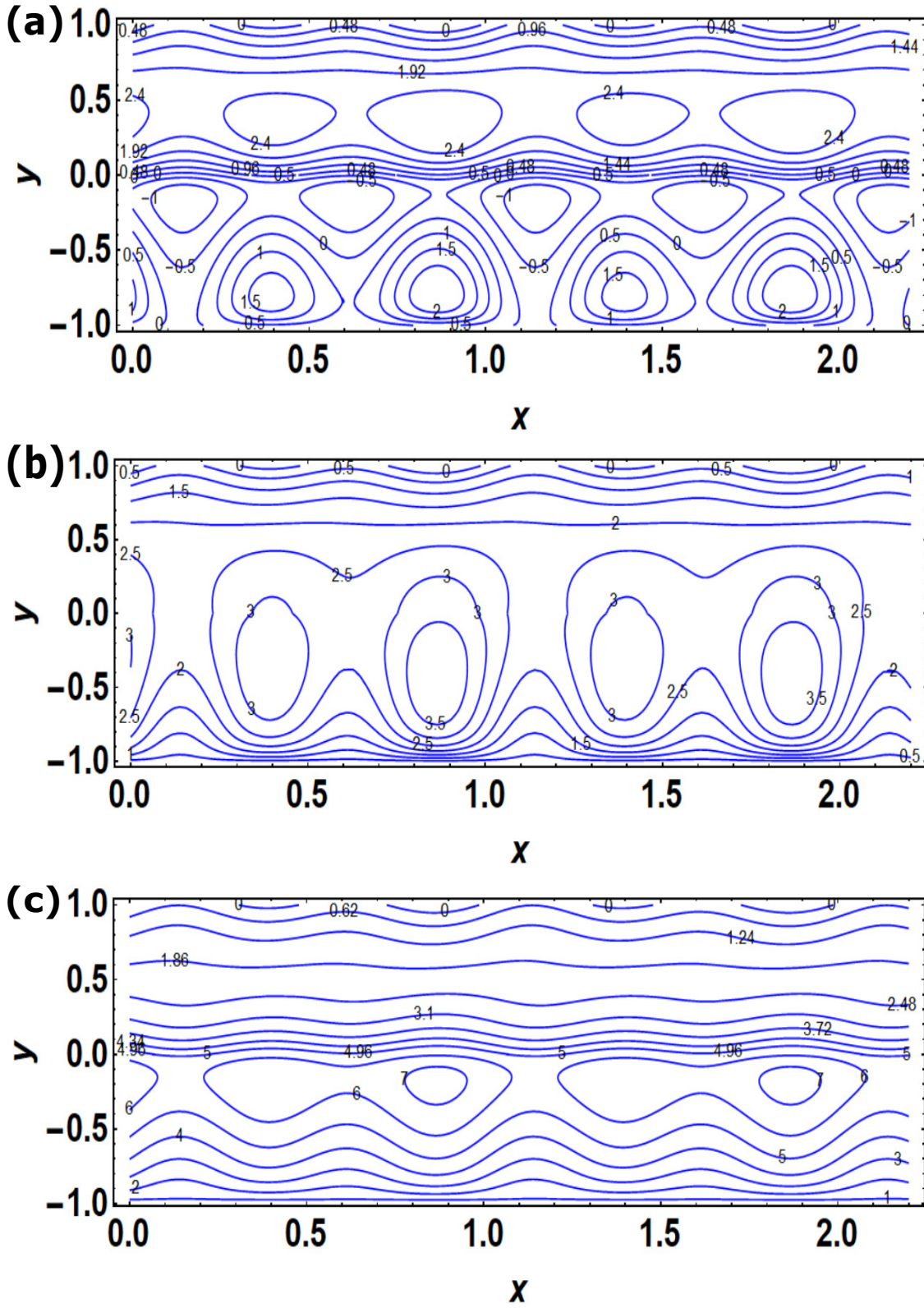


Figure 3.10: Streamlines for both fluid layers with variation of zeta potential difference for (a) $\delta\zeta = -5$ (b) $\delta\zeta = 0$, (c) $\delta\zeta = 5$ with $\varepsilon = 1$, $Q = 0.05$, $\kappa_1 = 5$, $\kappa_2 = 10$, $\alpha = 0.025$, $\lambda = 0.05$, $P = 2$, $\beta_1 = 0.02$, $\beta_2 = 0.01$, $S_{10} = 5$, $S_{20} = 5$, $\mu = 0.7$, $\delta\phi = 0.1$, $\sigma = 1$, $\Gamma = 1$.

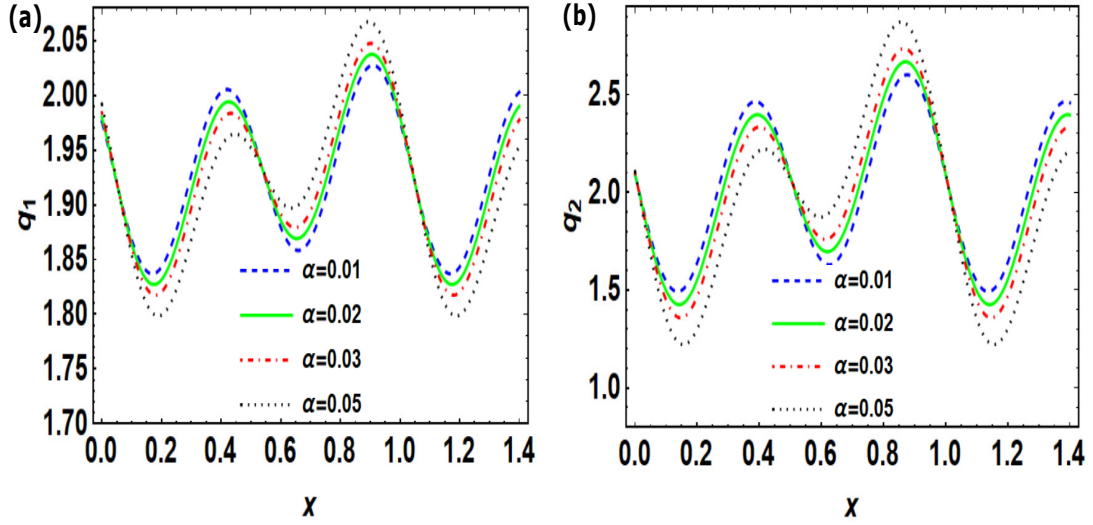


Figure 3.11: Volume flow rates for (a) layer-1 and (b) layer-2 vary with α , considering $\varepsilon = 1$, $Q = 0.05$, $\kappa_1 = 5$, $\kappa_2 = 10$, $Ha = 0.5$, $\lambda = 0.05$, $P = 2$, $\beta_1 = 0.02$, $\beta_2 = 0.01$, $S_{10} = 5$, $S_{20} = 5$, $\mu = 1$, $\delta_\zeta = 0.1$, $\delta_\Phi = 0.1$, $\sigma = 1$, $\Gamma = 1$. In this figure, the oscillating volumetric flow rate in both fluid layers, due to the varying surface, is influenced by wave amplitude α , enhancing flow in part of the microchannel while significantly reducing it in the remaining portion.

The volumetric flow rate for two-layer fluid flow in the microchannel is expressed by the Eq. (3.100) and the mean flow rates Q_1 and Q_2 are expressed in the equations (3.102) and (3.103). In Figs. 3.11-3.13, we have focused on the variations of volumetric flow rate with different pertinent parameters. The varying surface becomes responsible for the oscillating behavior of the volumetric flow rate in both fluid layers. The wave amplitude α enhances the flow rate partly in the microchannel whereas it is reduced significantly on the remaining portion of the microchannel as depicted in Fig. 3.11(a) and 3.11(b). Fig. 3.12 indicates the variation of flow rate with Hartmann number. Increasing the Hartmann number Ha augments the flow rate for both fluids as displayed in Figs. 3.12(a) and 3.12(b). It is noted that the applied magnetic field acts as a retarding force, but it is dominated by the flow-aiding force, which enhances the fluid velocity (see Fig. 3.4(a)). As a result, the volumetric flow rate is increased for both fluid layers. Similar oscillatory volumetric flow rate profiles are shown in Figs. 3.13(a) and 3.13(b), where the control parameter is δ_Φ . Fig. 3.14 shows the enhanced oscillations in the volumetric flow rate in layer-2, as compared to layer-1, can be attributed to the influence of the interfacial effects between the two fluid layers. These interfacial complexities introduce additional flow oscillations in layer 2. As a result, the distinct characteristics of each fluid layer and their interactions account for the disparities in flow oscillations is observed.

In a rough microchannel, the irregularities on the channel surface disrupts the smooth flow, creating additional resistance. This increased resistance hinders the flow velocity of both fluid-1 and fluid-2. So, the surface roughness can significantly affect the mean velocities throughout the channel domain. An increase in roughness (α) restricts the flow velocity in both the fluid layers.

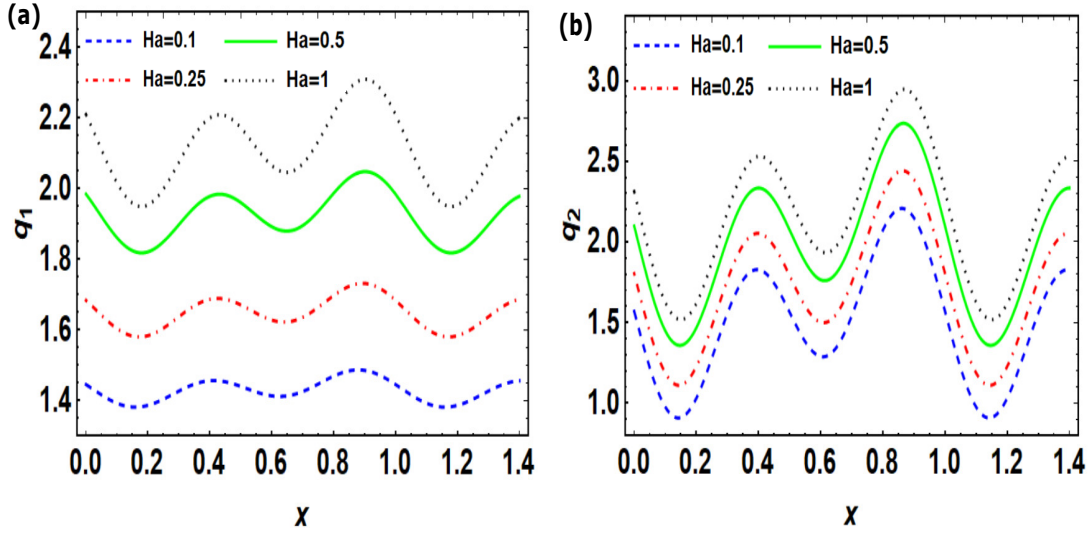


Figure 3.12: Volume flow rates for (a) layer-1 and (b) layer-2 vary with Hartmann number, considering $\varepsilon = 1$, $Q = 0.05$, $\kappa_1 = 5$, $\kappa_2 = 10$, $\alpha = 0.025$, $\lambda = 0.05$, $P = 1$, $\beta_1 = 0.02$, $\beta_2 = 0.01$, $S_{10} = 5$, $S_{20} = 5$, $\mu = 1$, $\delta_\zeta = 0.1$, $\delta_\Phi = 0.1$, $\sigma = 1$, $\Gamma = 1$. This figure indicates that the higher Hartmann numbers (Ha) lead to increased flow rates for both fluids, with the applied magnetic field, initially a retarding force, being overtaken by the flow-aiding force, ultimately enhancing fluid velocity and overall volumetric flow rates.

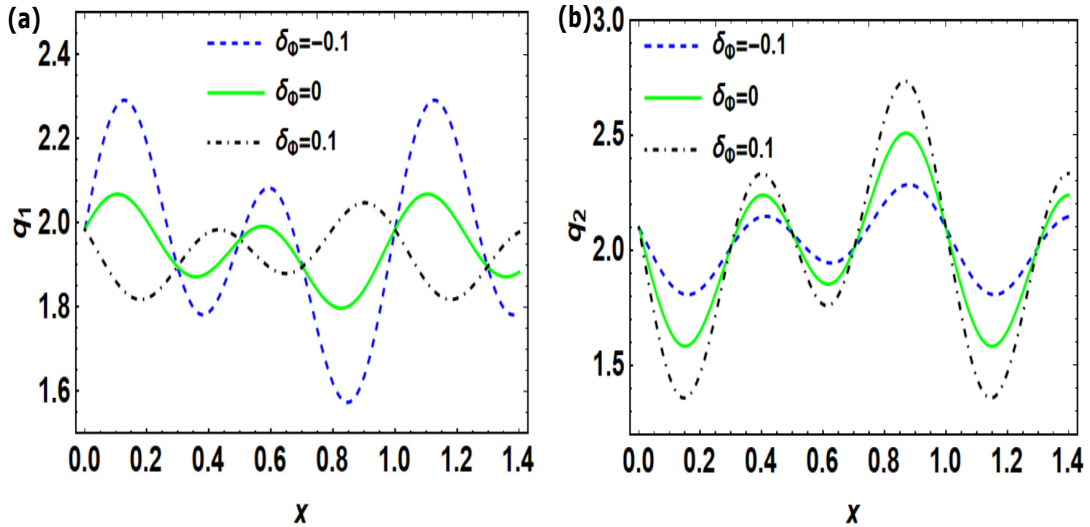


Figure 3.13: Volume flow rates for (a) layer-1 and (b) layer-2 vary with δ_Φ , considering $\varepsilon = 1$, $Q = 0.05$, $\kappa_1 = 5$, $\kappa_2 = 10$, $\alpha = 0.025$, $\lambda = 0.05$, $P = 1$, $\beta_1 = 0.02$, $\beta_2 = 0.01$, $S_{10} = 5$, $S_{20} = 5$, $\mu = 1$, $\delta_\zeta = 0.1$, $Ha = 0.5$, $\sigma = 1$, $\Gamma = 1$.

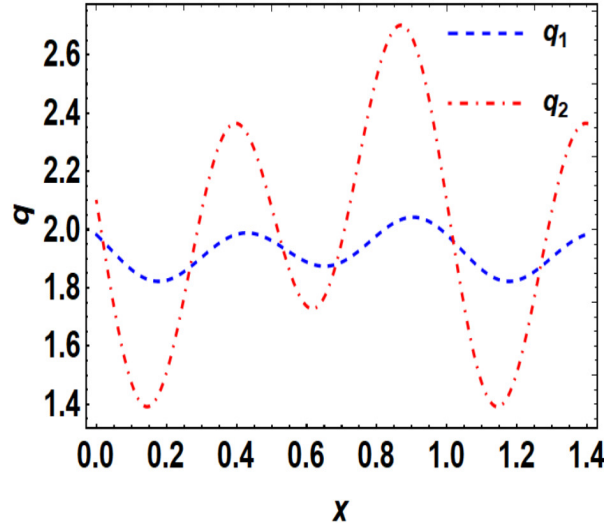


Figure 3.14: Volume flow rate profiles for layer-1 and layer-2 for $\varepsilon = 1$, $Q = 0.05$, $\kappa_1 = 5$, $\kappa_2 = 10$, $\alpha = 0.025$, $\lambda = 0.05$, $P = 1$, $\beta_1 = 0.02$, $\beta_2 = 0.01$, $S_{10} = 5$, $S_{20} = 5$, $\mu = 1$, $\delta_\zeta = 0.1$, $\delta_\Phi = 0.1$, $\sigma = 1$, $\Gamma = 1$.

Further, increasing Hartmann number enhances the strength of the applied magnetic field, which reduces the flow velocity due to the presence of Lorentz force. Therefore the mean velocities for both the fluids are decreased with the roughness (α) and different values of Hartmann number Ha .

3.5.4 Estimation of boundary layer thickness

The boundary layer plays a crucial role in fluid flow in the microchannel, in particular for microchannel with wall roughness. Understanding and accurate prediction of the boundary layer thickness is essential in chemical and biomedical engineering. Boundary layer thickness is defined as the distance from a solid surface to the point where the fluid velocity has reached approximately 99% of the maximum velocity. The thickness of the boundary layer depends on various factors such as the fluid velocity, viscosity, external body forces, and the topography of the surface.

In this investigation, two immiscible electrolytes are considered in a rough microchannel. In this model, two boundary layer thicknesses δ_1 and δ_2 are taken as the distance at which it becomes 99% of the viscous velocity for fluid-1 and fluid-2 respectively. Hence, one may write

$$w_i = 0.99w_{Ei}, \quad i = 1, 2, \quad (3.104)$$

where w_i are the velocities in the viscous region (near wall) and w_{Ei} are the velocities in the non-viscous region (far wall) for fluid-1 and fluid-2. To estimate the boundary layer thickness (δ_i), we use the above relation (3.104) and constructed the following mathematical expressions:

$$w_1|_{y=1+\alpha f(x)-\delta_1} = 0.99w_{E1}|_{y=1+\alpha f(x)-\delta_1}, \quad (3.105)$$

$$w_2|_{y=-1-\alpha f(x)+\delta_2} = 0.99w_{E2}|_{y=-1-\alpha f(x)+\delta_2}, \quad (3.106)$$

where w_{E1} and w_{E2} are the velocity fields corresponding to flow in the non-viscous regions for layer-1 and layer-2 respectively. Hence, by solving equations (3.105) and (3.106), we can obtain the boundary layer thickness for both fluid regions are taken in the form

$$\delta_1 = \delta_1(\alpha, \lambda, \kappa_1, \kappa_2, Ha, P, Q, \delta_\zeta, \delta_\Phi, \beta_1, \beta_2, \mu, \varepsilon, \sigma, \Gamma), \quad (3.107)$$

and

$$\delta_2 = \delta_2(\alpha, \lambda, \kappa_1, \kappa_2, Ha, P, Q, \delta_\zeta, \delta_\Phi, \beta_1, \beta_2, \mu, \varepsilon, \sigma, \Gamma). \quad (3.108)$$

An oscillatory pattern in the boundary layer thickness along the direction of x indicates that the thickness of the boundary layer varies periodically following the geometry of the microchannel wall. This oscillatory behavior can arise from the interactions between the fluid flow and the roughness on the channel wall (see Figs. 3.15 and 3.17). The behavior of the boundary layer thickness in a rough microchannel depends on the presence or absence of a transverse electric field. In the absence of a transverse electric field, the boundary layer thickness at the upper wall and at the lower wall of the undulated microchannel is increased with the increase of Hartmann number as shown in Figs. 3.15(a) and 3.16(a). This is because a higher Hartmann number leads to a stronger Lorentz force that impedes the flow, causing the boundary layer to expand. The roughness of the microchannel walls further enhances this effect by creating additional disruptions and promoting the growth of the boundary layer. However, an opposite trend is observed in the presence of a transverse electric field as displayed in Figs. 3.15(b) and 3.16(b). The presence of the transverse electric field introduces additional forces that interact with the fluid flow, altering the dynamics of the boundary layer. This interaction may lead to a reduction in the boundary layer thickness.

The thickness of the boundary layer is an important parameter that characterizes the region of wall shear stress near the surface. Figs. 3.17(a) and 3.17(b) illustrate the relationship between the boundary layer thickness and the Hartmann number for both rough walls of the microchannel. This behavior can be attributed to the Lorentz forces induced by the magnetic field, which acts to suppress the fluid motion, resulting in thinner boundary layers. Additionally, it is stated that the roughness of the microchannel reduces the boundary layer thickness for both fluid layers. The irregularities created by the rough surface of the microchannel produce thinner boundary layers.

3.6 Concluding remarks

A theoretical investigation on the effect of wall roughness of microchannel on EMHD flow of two immiscible electrolytes is carried out in this chapter, by highlighting the importance of surface roughness in the design and optimization of microfluidic devices. The analytical solution is obtained by employing the perturbation technique to provide insights into the effects of surface roughness on the flow and separation behavior of the two immiscible electrolytes. We observed that surface roughness can significantly affect the electrokinetic transport of the immiscible electrolytes, leading to changes in the flow patterns and the separation efficiency. The increase in wave amplitude does

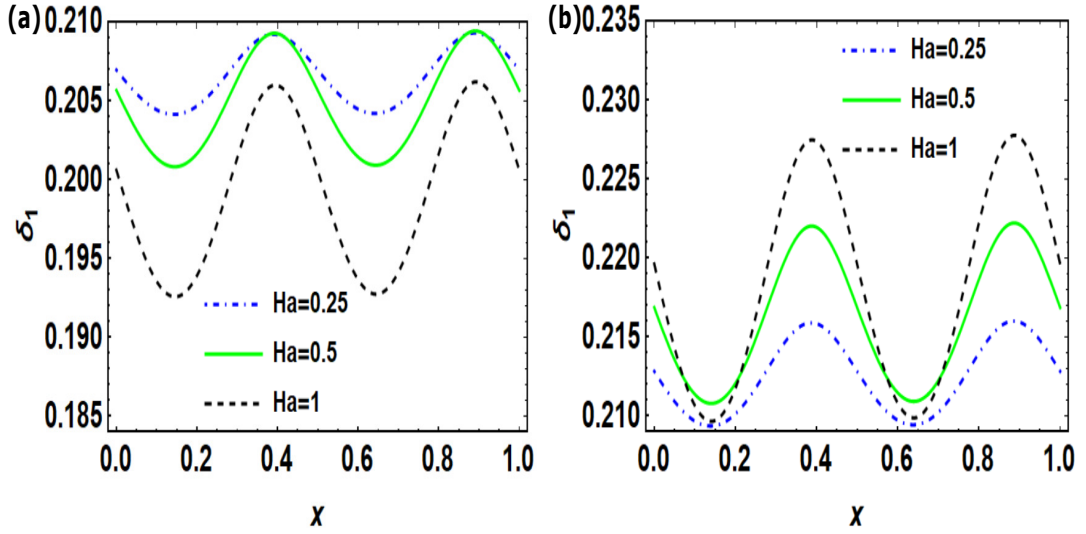


Figure 3.15: Variation of boundary layer thickness at the upper wall for different Hartmann number. Subfigure (a) illustrates the scenario with $S_1 = 0$, while subfigure (b) represents the case with $S_1 = 3$. The parameters for both scenarios include $\varepsilon = 1$, $Q = 0.05$, $\kappa_1 = 5$, $\kappa_2 = 10$, $\alpha = 0.01$, $\lambda = 0.05$, $P = 1$, $\beta_1 = 0.02$, $\beta_2 = 0.01$, $\mu = 1$, $\delta_\zeta = 0.1$, $\delta_\Phi = 0.1$, $\sigma = 1$, $\Gamma = 1$.

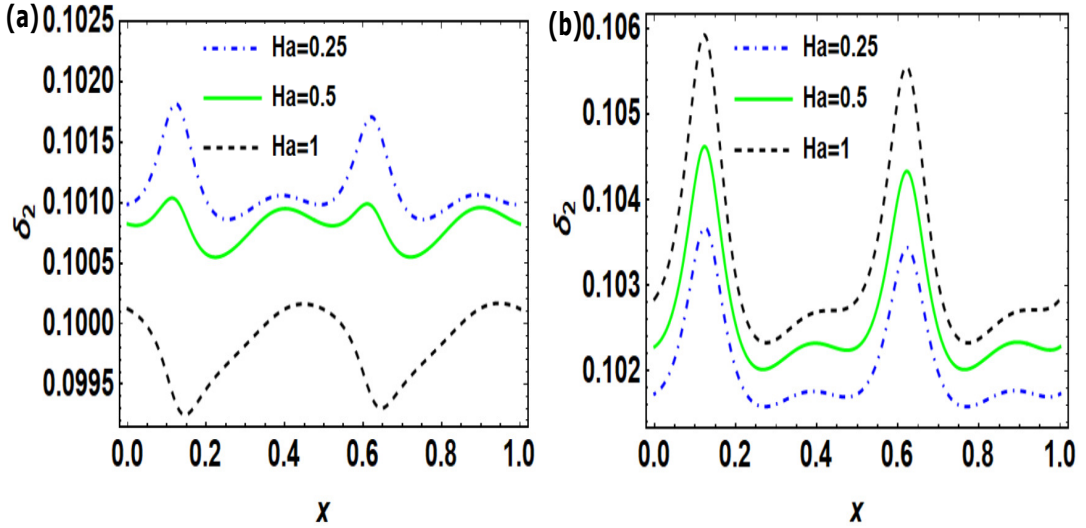


Figure 3.16: Variation of boundary layer thickness at the lower wall for different Hartmann number. Subfigure (a) illustrates the scenario with $S_2 = 0$, while subfigure (b) represents the case with $S_2 = 3$. The parameters for both scenarios include $\varepsilon = 1$, $Q = 0.05$, $\kappa_1 = 5$, $\kappa_2 = 10$, $\lambda = 0.05$, $\alpha = 0.01$, $P = 1$, $\beta_1 = 0.02$, $\beta_2 = 0.01$, $\mu = 1$, $\delta_\zeta = 0.1$, $\delta_\Phi = 0.1$, $\sigma = 1$, $\Gamma = 1$.

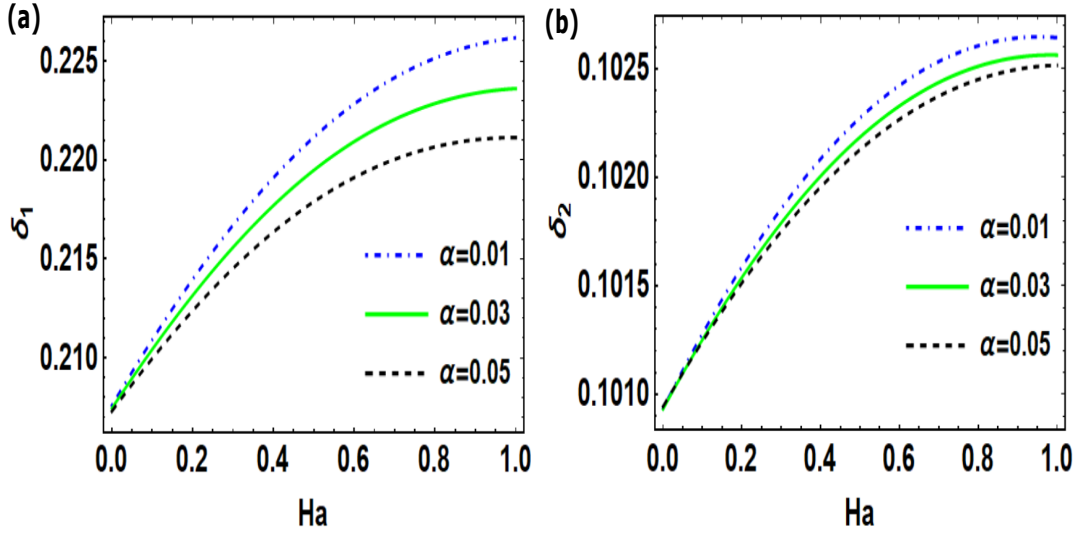


Figure 3.17: Variation of boundary layer thickness (a) at the upper wall and (b) at the lower wall for different roughness parameter (α) and $\varepsilon = 1$, $Q = 0.05$, $\kappa_1 = 5$, $\kappa_2 = 10$, $S_{10} = 3$, $S_{20} = 3$, $\alpha = 0.01$, $\lambda = 0.05$, $P = 1$, $\beta_1 = 0.02$, $\beta_2 = 0.01$, $\mu = 1$, $\delta_\zeta = 0.1$, $\delta_\Phi = 0.1$, $\sigma = 1$, $\Gamma = 1$.

indeed enhance the disturbance of the fluid layers in a microchannel with a rough surface. Specifically, the study found that an increase in α leads to a greater disturbance of fluid flow in layer-1 near the top wall of the rough microchannel. In contrast, fluid in layer-2 exhibits almost similar velocity profiles as the case of a smooth surface, but the fluid layer is more disturbed compared to fluid layer-1. This observation suggests that the effect of roughness on fluid flow is more significant near the solid-liquid interface. Therefore, the roughness of the microchannel walls should be considered in the design and optimization of microfluidic devices that involve the transport of fluids and solutes.

The fluid with a higher zeta potential moves faster than the fluid with a lower zeta potential because of the electroosmotic effect. Therefore, the difference in zeta potential between the two immiscible fluids plays a significant role in determining the velocity profiles of the fluids in the microchannel. The zeta potential difference at the fluid-fluid interface and the slip velocity at the rough surface both contribute to the enhancement of the electroosmotic mobility of the electrolytes.

The velocity profiles of the two fluids are also affected by the zeta potential jump (δ_ζ) at the fluid-fluid interface. The absorption of ions at the interface creates a sudden change in potential distribution and affects the patterns of velocity profiles at the interface. This behavior is attributed to the effect of zeta potential difference at the fluid-fluid interface, which enhances the electroosmotic mobility of the electrolytes and thus increases the flow velocity in layer-2.

For low Hartmann number ($Ha < 1$), the Lorentz force is dominated by the flow-aiding force and enhances the flow velocity. However, for higher values of Hartmann number ($Ha \geq 1$), the Lorentz force acts as a retarding force, preventing the flow-aiding force and viscous force, resulting in a decrease in flow velocity.

The formation of boluses at the fluid-fluid interface is due to the interplay between the elec-

3.6. Concluding remarks

osmotic and magnetohydrodynamic forces. The oscillatory streamlines arise due to the presence of not only the roughness of the walls but also the transverse electric field and the magnetic field. As the roughness amplitude ratio increases, the disturbances in the flow become more profound, leading to the formation of larger boluses. The formation of boluses is an important phenomenon in microfluidics as it can be utilized for mixing and separation of different species in a microchannel.

The thickness of the boundary layer, a crucial parameter describing the flow near a surface, displays periodic variations along a microchannel with a rough wall due to interactions with the roughness elements. These oscillations arise from the interactions between the fluid flow and the roughness of the microchannel.

Appendices

3.A Mathematical expressions in connection with the applied potential

The following expressions for $C_i(x)$'s ($i = 5, 6, 7, 8$), are used in the manuscript text

$$C_5(x) = \frac{1}{\lambda(1+\varepsilon)\sinh(\lambda)} [(C_1 + \varepsilon C_3)f(x) - \{(C_1 + \varepsilon C_3)f'(x) + \delta_\Phi f(x)\} \cosh(\lambda)],$$

$$C_6(x) = \frac{1}{\lambda(1+\varepsilon)} [(C_1 + \varepsilon C_3)f'(x) + \delta_\Phi f(x) + (C_1 - C_3)\varepsilon f(x) \operatorname{sech}(\lambda)],$$

$$C_7(x) = \frac{1}{\lambda(1+\varepsilon)\sinh(\lambda)} [(C_1 + \varepsilon C_3)f(x) - \{(C_1 + \varepsilon C_3)f'(x) + \delta_\Phi f(x)\} \cosh(\lambda)],$$

$$C_8(x) = \frac{1}{\lambda(1+\varepsilon)} [(C_1 - C_3)\varepsilon f(x) \operatorname{sech}(\lambda) - (C_1 + \varepsilon C_3)f'(x) - \delta_\Phi f(x)].$$

3.B Mathematical expressions in connection with the EDL potential

The expressions for B_1 to B_{10} are given by

$$B_1 = \frac{1}{B_{10}\sinh(\kappa_1)} [\sinh(\kappa_2)\{\kappa_1 + Q \sinh(\kappa_1)\} + \varepsilon \kappa_2 \sinh(\kappa_1)\{1 - \delta_\zeta \cosh(\kappa_2)\}],$$

$$B_2 = \frac{1}{B_{10}} [\varepsilon \kappa_2 \cosh(\kappa_2) \operatorname{cosech}(\kappa_1) + \coth(\kappa_1)\{\varepsilon \kappa_2(\delta_\zeta \cosh(\kappa_2) - 1) - Q \sinh(\kappa_2)\}],$$

$$B_3 = \frac{1}{B_{10}\sinh(\kappa_1)} [\sinh(\kappa_1)\{\varepsilon \kappa_2 + Q\} + \kappa_1 \sinh(\kappa_2)\{1 + \delta_\zeta \cosh(\kappa_1)\}],$$

$$B_4 = \frac{1}{B_{10}} [\cosh(\kappa_2)\{Q + \delta_\zeta \kappa_1 \coth(\kappa_1) + \kappa_1 \operatorname{cosech}(\kappa_1)\} - \kappa_1 \coth(\kappa_1)],$$

$$B_5 = -\frac{\kappa_1}{2} \{B_2 \cosh(\kappa_1) + B_1 \sinh(\kappa_1)\},$$

$$B_6 = \frac{3\kappa_2}{2} \{B_4 \cosh(\kappa_2) - B_3 \sinh(\kappa_2)\},$$

$$B_7 = \frac{\varepsilon \gamma_1 \gamma_2 f(x)}{B_9} \{B_5 \cosh(\gamma_2) - \cosh(\gamma_1)(B_6 + \delta_\zeta \cosh(\gamma_2))\},$$

$$B_8 = \frac{\gamma_1 \gamma_2 f(x)}{B_9} \{B_5 \cosh(\gamma_2) - \cosh(\gamma_1)(B_6 + \delta_\zeta \cosh(\gamma_2))\},$$

$$B_9 = \varepsilon \gamma_2 \cosh(\gamma_2) \sinh(\gamma_1) + \gamma_1 \cosh(\gamma_1) \sinh(\gamma_2),$$

$$B_{10} = \varepsilon \kappa_2 \cosh(\kappa_2) + \kappa_1 \coth(\kappa_1) \sinh(\kappa_2).$$

3.C Mathematical expressions in connection with the transverse electric field

By using the relation $\mathbf{E} = -\nabla \tilde{\phi}_i$ and the expansion (3.81), one can easily obtain the expressions for S_i . Here, $S_{10} = C_1$, $S_{20} = C_3$,

$$S_{11} = \{F_1(y) + F_2(y) - F_3(y)\}f(x) + \{F_4(y) + F_5(y)\}f'(x),$$

$$S_{21} = \{F_1(y) + F_6(y) - F_7(y)\}f(x) + \{F_4(y) - F_5(y)\}f'(x).$$

The expressions for $F_1(y)$, $F_2(y)$, $F_3(y)$, $F_4(y)$, $F_5(y)$, $F_6(y)$, $F_7(y)$ are given as follows:

$$F_1(y) = \frac{(C_1 + \varepsilon C_3) - \delta_\Phi \cosh(\lambda)}{(1+\varepsilon)\lambda \sinh(\lambda)} \cosh(\lambda y),$$

$$F_2(y) = \frac{\delta_\Phi + \varepsilon(C_1 - C_3) \operatorname{sech}(\lambda)}{(1+\varepsilon)\lambda} \sinh(\lambda y),$$

$$F_3(y) = \frac{1}{B_9} [B_5 \{\varepsilon \gamma_2 \cosh(\gamma_2) \sinh(\gamma_1 y) + \gamma_1 \cosh(\gamma_1 y) \sinh(\gamma_2)\} + \varepsilon \gamma_2 (B_6 + \delta_\zeta \cosh(\gamma_2)) \sinh(\gamma_1 - \gamma_1 y)],$$

$$F_4(y) = \frac{(C_1 + \varepsilon C_3) \cosh(\lambda)}{(1+\varepsilon)\lambda \sinh(\lambda)} \cosh(\lambda y),$$

$$F_5(y) = \frac{(C_1 + \varepsilon C_3)}{(1+\varepsilon)\lambda} \sinh(\lambda y),$$

$$\begin{aligned}
 F_6(y) &= \frac{(C_1 - C_3) \operatorname{sech}(\lambda) - \delta_\Phi}{(1 + \varepsilon)\lambda} \sinh(\lambda y), \\
 F_7(y) &= \frac{1}{B_9} [\gamma_1 (B_5 - \delta_\zeta \cosh(\gamma_1)) \sinh(\gamma_2 + \gamma_2 y) + B_6 \{ \varepsilon \gamma_2 \cosh(\gamma_2 y) \sinh(\gamma_1) \\
 &\quad - \gamma_1 \cosh(\gamma_1) \sinh(\gamma_2 y) \}].
 \end{aligned}$$

3.D Mathematical expressions in connection with the velocity distribution

The expressions for A_i 's ($i = 1, \dots, 16$) are given as follows:

$$\begin{aligned}
 A_1 &= -\frac{M_2(M_4M_7M_8 - M_5M_9 + M_6M_8) + M_3M_5}{M_1M_5 + M_2M_4M_8}, \\
 A_2 &= -\frac{M_1(M_4M_7M_8 - M_5M_9 + M_6M_8) + M_3M_4M_8}{M_1M_5 + M_2M_4M_8}, \\
 A_3 &= -\frac{M_5(M_3 - M_1M_7) + M_2(M_6M_8 - M_5M_9)}{M_1M_5 + M_2M_4M_8}, \\
 A_4 &= -\frac{M_4(M_2M_9 + M_1M_7 - M_3) + M_1M_6}{M_1M_5 + M_2M_4M_8}, \\
 A_5 &= Ha \{ A_2 \cosh(Ha) + A_1 \sinh(Ha) \} + \frac{\kappa_1^3}{Ha^2 - \kappa_1^2} \{ B_2 \cosh(\kappa_1) + B_1 \sinh(\kappa_1) \}, \\
 A_6 &= Ha^2 \{ A_1 \cosh(Ha) + A_2 \sinh(Ha) \} + \frac{\kappa_1^4}{Ha^2 - \kappa_1^2} \{ B_1 \cosh(\kappa_1) + B_2 \sinh(\kappa_1) \}, \\
 A_7 &= Ha \sqrt{\frac{\sigma}{\mu}} \left\{ A_4 \cosh\left(Ha \sqrt{\frac{\sigma}{\mu}}\right) + A_3 \sinh\left(Ha \sqrt{\frac{\sigma}{\mu}}\right) \right\} \\
 &\quad + \frac{\varepsilon \kappa_2^3}{\sigma Ha^2 - \mu \kappa_2^2} \left\{ B_4 \cosh(\kappa_2) + B_3 \sinh(\kappa_2) \right\}, \\
 A_8 &= Ha^2 \frac{\sigma}{\mu} \left\{ A_3 \cosh\left(Ha \sqrt{\frac{\sigma}{\mu}}\right) + A_4 \sinh\left(Ha \sqrt{\frac{\sigma}{\mu}}\right) \right\} \\
 &\quad + \frac{\varepsilon \kappa_2^4}{\sigma Ha^2 - \mu \kappa_2^2} \left\{ B_3 \cosh(\kappa_2) + B_4 \sinh(\kappa_2) \right\}, \\
 A_9 &= \frac{1}{A_{17}} \{ G_{12}(G_7G_{10} - G_1\gamma_3) - G_{10}\gamma_4\sqrt{\mu}(G_3 + G_{11}G_5) \}, \\
 A_{10} &= \frac{1}{A_{17}} \{ \{ G_9(G_5G_{11} + G_3) - G_1G_{11} \} \gamma_4\sqrt{\mu} - G_{12}G_7G_9 \}, \\
 A_{11} &= \frac{1}{A_{17}} \{ G_{12}(G_{10}G_8 - G_2\gamma_3) - G_{10}\gamma_4\sqrt{\mu}(G_4 + G_{11}G_6) \}, \\
 A_{12} &= \frac{1}{A_{17}} \{ \gamma_4\sqrt{\mu}(G_{11}G_6G_9 + G_4G_9 - G_{11}G_2) + G_{12}G_8G_9 \}, \\
 A_{13} &= \frac{1}{A_{17}} \{ G_{12}(G_{10}G_7 - G_1\gamma_3 + G_5G_9\gamma_3) - G_{10}G_3\gamma_4\sqrt{\mu} \}, \\
 A_{14} &= \frac{1}{A_{17}} \{ G_{10}G_{11}G_7 + \gamma_3(G_3G_9 + G_{11}G_5G_9 - G_1G_{11}) \}, \\
 A_{15} &= \frac{1}{A_{17}} \{ G_{10}(G_{12}G_8 - G_4\gamma_4\sqrt{\mu}) + G_{12}\gamma_3(G_9G_6 - G_2) \}, \\
 A_{16} &= \frac{1}{A_{17}} \{ G_{10}G_{12}G_8 + \gamma_3(G_{11}G_6G_9 + G_4G_9 - G_{11}G_2) \}, \\
 A_{17} &= (G_{12}G_9\gamma_3 + G_{10}G_{11}\gamma_4\sqrt{\mu}), \\
 M_1 &= \cosh(Ha) + \beta_1 Ha \sinh(Ha), \\
 M_2 &= \beta_1 Ha \cosh(Ha) + \sinh(Ha), \\
 M_3 &= \frac{\kappa_1^2}{Ha^2 - \kappa_1^2} \{ (B_1 + \beta_1 B_2 \kappa_1) \cosh(\kappa_1) + (B_2 + \beta_1 B_1 \kappa_1) \sinh(\kappa_1) \} + \frac{Ha S_{10} + P}{Ha^2}, \\
 M_4 &= \cosh\left(Ha \sqrt{\frac{\sigma}{\mu}}\right) + \beta_2 Ha \sqrt{\frac{\sigma}{\mu}} \sinh\left(Ha \sqrt{\frac{\sigma}{\mu}}\right), \\
 M_5 &= -\beta_2 Ha \sqrt{\frac{\sigma}{\mu}} \cosh\left(Ha \sqrt{\frac{\sigma}{\mu}}\right) + \sinh\left(Ha \sqrt{\frac{\sigma}{\mu}}\right), \\
 M_6 &= \frac{\varepsilon \kappa_2^2}{\sigma Ha^2 - \mu \kappa_2^2} \{ (B_3 - \beta_2 B_4 \kappa_2) \cosh(\kappa_2) - (B_4 - \beta_2 B_3 \kappa_2) \sinh(\kappa_2) \} + \frac{\sigma Ha S_{20} + P\Gamma}{\sigma Ha^2}, \\
 M_7 &= \frac{(P + Ha S_{10} - Ha S_{20})\sigma + P\Gamma}{\sigma Ha^2} + \frac{B_1 \kappa_1^2}{Ha^2 - \kappa_1^2} - \frac{B_3 \varepsilon \kappa_2^2}{\sigma Ha^2 - \mu \kappa_2^2}, \\
 M_8 &= -Ha \sqrt{\sigma \mu},
 \end{aligned}$$

$$\begin{aligned}
 M_9 &= Ha^2 \left(\frac{B_2 \kappa_1}{Ha^2 - \kappa_1^2} - \frac{\sigma B_4 \varepsilon \kappa_2}{\sigma Ha^2 - \mu \kappa_2^2} \right), \\
 G_1 &= A_5 + \beta_1 A_6 + \frac{B_5(Ha - \kappa_1^2)}{\gamma_1^2 - \gamma_3^2} + \frac{HaF_1(y)}{\gamma_3^2 - \lambda^2} + \frac{HaF_2(y)}{\gamma_3^2 - \lambda^2} + \beta_1 \left(\frac{Ha\lambda F_2(y)}{\gamma_3^2 - \lambda^2} + \frac{Ha\lambda F_1(y)}{\gamma_3^2 - \lambda^2} \right. \\
 &\quad \left. + \frac{\gamma_1(Ha - \kappa_1^2) \left\{ B_5 \gamma_1 \sinh(\gamma_1) \sinh(\gamma_2) - \varepsilon \gamma_2 [B_6 + \{\delta_\zeta - B_5 \cosh(\gamma_1)\} \cosh(\gamma_2)] \right\}}{(\gamma_1^2 - \gamma_3^2) \{ \varepsilon \gamma_2 \cosh(\gamma_2) \sinh(\gamma_1) + \gamma_1 \cosh(\gamma_1) \sinh(\gamma_2) \}} \right), \\
 G_2 &= \frac{Ha \{F_4(y) + F_5(y)\}}{\gamma_3^2 - \lambda^2} + \beta_1 \frac{Ha\lambda \{F_4(y) + F_5(y)\}}{\gamma_3^2 - \lambda^2}, \\
 G_3 &= \beta_2 A_8 - A_7 - \frac{B_6(\sigma Ha - \varepsilon \kappa_2^2)}{\gamma_4^2 - \mu \gamma_2^2} + \frac{\sigma HaF_1(y)}{\gamma_4^2 - \mu \lambda^2} - \frac{\sigma HaF_6(y)}{\gamma_4^2 - \mu \lambda^2} + \beta_2 \left(\frac{\sigma Ha\lambda F_6(y)}{\gamma_4^2 - \mu \lambda^2} - \frac{\sigma Ha\lambda F_1(y)}{\gamma_4^2 - \mu \lambda^2} \right. \\
 &\quad \left. + \frac{\gamma_2(\sigma Ha - \varepsilon \kappa_2^2) \left\{ B_6 \varepsilon \gamma_2 \sinh(\gamma_1) \sinh(\gamma_2) + \gamma_1 [B_5 + \{\delta_\zeta + B_6 \cosh(\gamma_2)\} \cosh(\gamma_1)] \right\}}{(\gamma_4^2 - \mu \gamma_2^2) \{ \varepsilon \gamma_2 \cosh(\gamma_2) \sinh(\gamma_1) + \gamma_1 \cosh(\gamma_1) \sinh(\gamma_2) \}} \right), \\
 G_4 &= \frac{\sigma Ha \{F_4(y) + F_5(y)\}}{\gamma_4^2 - \mu \lambda^2} + \beta_2 \frac{\sigma Ha\lambda \{F_4(y) + F_5(y)\}}{\gamma_4^2 - \mu \lambda^2}, \\
 G_5 &= \frac{HaF_1(y)}{\gamma_3^2 - \lambda^2} + \frac{(Ha - \kappa_1^2) \left\{ B_5 \gamma_1 \sinh(\gamma_2) + \varepsilon \gamma_2 \sinh(\gamma_1) [B_6 + \delta_\zeta \cosh(\gamma_2)] \right\}}{(\gamma_1^2 - \gamma_3^2) \{ \varepsilon \gamma_2 \cosh(\gamma_2) \sinh(\gamma_1) + \gamma_1 \cosh(\gamma_1) \sinh(\gamma_2) \}} \\
 &\quad - \frac{\sigma HaF_1(y)}{\gamma_4^2 - \mu \lambda^2} + \frac{(\sigma Ha - \varepsilon \kappa_2^2) \left\{ B_6 \varepsilon \gamma_2 \sinh(\gamma_1) + \gamma_1 \sinh(\gamma_2) [B_5 - \delta_\zeta \cosh(\gamma_1)] \right\}}{(\gamma_4^2 - \mu \gamma_2^2) \{ \varepsilon \gamma_2 \cosh(\gamma_2) \sinh(\gamma_1) + \gamma_1 \cosh(\gamma_1) \sinh(\gamma_2) \}}, \\
 G_6 &= \frac{Ha(C_1 + \varepsilon C_3) \cosh(\lambda)}{(1 + \varepsilon) \lambda \sinh(\lambda)} \left\{ \frac{1}{\gamma_3^2 - \lambda^2} - \frac{\sigma}{\gamma_4^2 - \mu \lambda^2} \right\}, \\
 G_7 &= B_7 - \varepsilon B_8 + \frac{Ha\lambda F_2(y)}{\gamma_3^2 - \lambda^2} + \frac{\varepsilon \gamma_1 \gamma_2 (Ha - \kappa_1^2) \left\{ B_5 \cosh(\gamma_2) - \cosh(\gamma_1) [B_6 + \delta_\zeta \cosh(\gamma_2)] \right\}}{(\gamma_1^2 - \gamma_3^2) \{ \varepsilon \gamma_2 \cosh(\gamma_2) \sinh(\gamma_1) + \gamma_1 \cosh(\gamma_1) \sinh(\gamma_2) \}} \\
 &\quad - \mu \left(\frac{\sigma Ha\lambda F_6(y)}{\gamma_4^2 - \mu \lambda^2} + \frac{\gamma_1 \gamma_2 (\sigma Ha - \varepsilon \kappa_2^2) \left\{ -B_5 \cosh(\gamma_2) + \cosh(\gamma_1) [B_5 + \delta_\zeta \cosh(\gamma_2)] \right\}}{(\gamma_4^2 - \mu \gamma_2^2) \{ \varepsilon \gamma_2 \cosh(\gamma_2) \sinh(\gamma_1) + \gamma_1 \cosh(\gamma_1) \sinh(\gamma_2) \}} \right), \\
 G_8 &= \frac{Ha\lambda(C_1 + \varepsilon C_3)}{(1 + \varepsilon) \lambda} \left\{ \frac{1}{\gamma_3^2 - \lambda^2} - \frac{\mu \sigma}{\gamma_4^2 - \mu \lambda^2} \right\}, \\
 G_9 &= \cosh(\gamma_3) + \beta_1 \gamma_3 \sinh(\gamma_3), \\
 G_{10} &= \beta_1 \gamma_3 \cosh(\gamma_3) + \sinh(\gamma_3), \\
 G_{11} &= \cosh\left(\frac{\gamma_4}{\sqrt{\mu}}\right) + \frac{\beta_2 \gamma_4}{\sqrt{\mu}} \sinh\left(\frac{\gamma_4}{\sqrt{\mu}}\right), \\
 G_{12} &= \frac{\beta_2 \gamma_4}{\sqrt{\mu}} \cosh\left(\frac{\gamma_4}{\sqrt{\mu}}\right) + \sinh\left(\frac{\gamma_4}{\sqrt{\mu}}\right).
 \end{aligned}$$

3.E Mathematical expressions for the mean velocity

The expressions for Q_{10} , Q_{11} , Q_{20} and Q_{21} are as follows:

$$\begin{aligned}
 Q_{10} &= \Lambda \left\{ \frac{A_2 \cosh(Ha) + A_1 \sinh(Ha)}{Ha} - \frac{\kappa_1 (B_2 \cosh(\kappa_1) + B_1 \sinh(\kappa_1))}{\kappa^2 - Ha^2} + \frac{P + HaS_{10} - A_2 Ha}{Ha^2} + \frac{B_2 \kappa_1}{\kappa_1^2 - Ha^2} \right\}, \\
 Q_{11} &= \left[\frac{A_{10}(\cosh(\gamma_3) - 1) + A_9 \sinh(\gamma_3)}{\gamma_3} + \frac{HaF_2(y)(\cosh(\lambda) - 1) + HaF_1(y) \sinh(\lambda)}{\gamma_3^2 \lambda - \lambda^3} + A_1 \cosh(Ha) \right. \\
 &\quad \left. + A_2 \sinh(Ha) + \frac{(Ha - \kappa_1^2) \left\{ B_5 \gamma_1 \sinh(\gamma_2) + \varepsilon \gamma_2 \sinh(\gamma_1) [B_6 + \delta_\zeta \cosh(\gamma_2)] \right\}}{(\gamma_1^2 - \gamma_3^2) \{ \varepsilon \gamma_2 \cosh(\gamma_2) \sinh(\gamma_1) + \gamma_1 \cosh(\gamma_1) \sinh(\gamma_2) \}} + \frac{\kappa_1^2 \{ B_1 \cosh(\kappa_1) + B_2 \sinh(\kappa_1) \}}{Ha^2 - \kappa_1^2} \right]
 \end{aligned}$$

3.E. Mathematical expressions for the mean velocity

$$\begin{aligned}
& + \frac{P+HaS_{10}}{Ha^2} \left] \frac{\sin^2(\Lambda\pi)}{\pi} \left(1 + \frac{\lambda}{\alpha} + \frac{\lambda}{\alpha} \cos(2\Lambda\pi)\right) + \left\{ \frac{A_{12}(\cosh(\gamma_3)-1)}{\gamma_3} + \frac{A_{11} \sinh(\gamma_3)}{\gamma_3} \right. \right. \\
& \left. \left. + \frac{Ha\{F_5(y)(\cosh(\lambda)-1)+F_4(y) \sinh(\lambda)\}}{\gamma_3^2 \lambda - \lambda^3} \right\} \left\{ \sin(2\Lambda\pi) + \frac{\lambda}{\alpha} \sin(4\lambda\pi) \right\}, \\
Q_{20} = & \Lambda \left\{ \frac{\varepsilon \kappa_2 \{B_4(1-\cosh(\kappa_2))+B_3 \sinh(\kappa_2)\}}{Ha^2 \sigma - \mu \kappa_2^2} + \frac{A_4 \sqrt{\mu} - A_4 \sqrt{\mu} \cosh\left(\frac{Ha\sqrt{\sigma}}{\sqrt{\mu}}\right) + A_3 \sqrt{\mu} \sinh\left(\frac{Ha\sqrt{\sigma}}{\sqrt{\mu}}\right)}{H\sqrt{\sigma}} \right. \\
& \left. + \frac{\sigma HaS_{20} + P\Gamma}{Ha^2 \sigma} \right\}, \\
Q_{21} = & \left\{ \frac{A_{16} \sqrt{\mu} (1 - \cosh(\frac{\gamma_4}{\sqrt{\mu}}))}{\gamma_4} + \frac{A_{15} \sqrt{\mu} \sinh(\frac{\gamma_4}{\sqrt{\mu}})}{\gamma_4} + \frac{Ha\sigma \{F_5(y)(\cosh(\lambda)-1)+F_4(y) \sinh(\lambda)\}}{\gamma_4^2 \lambda - \lambda^3 \mu} \right\} \left\{ \sin(2\Lambda\pi) + \frac{\lambda}{\alpha} \sin(4\lambda\pi) \right\} + \\
& \left[\frac{A_{14} \sqrt{\mu} (1 - \cosh(\frac{\gamma_4}{\sqrt{\mu}})) + A_{15} \sqrt{\mu} \sinh(\frac{\gamma_4}{\sqrt{\mu}})}{\gamma_4} + \frac{Ha\sigma F_5(y)(\cosh(\lambda)-1) + Ha\sigma F_4(y) \sinh(\lambda)}{\gamma_4^2 \lambda - \lambda^3 \mu} \right. \\
& \left. + \frac{(\sigma Ha - \varepsilon \kappa_2^2) \left\{ B_6 \varepsilon \gamma_2 \sinh(\gamma_1) + \gamma_1 \sinh(\gamma_2) [B_5 - \delta_\zeta \cosh(\gamma_1)] \right\}}{(\gamma_4^2 - \mu \gamma^2) \{ \varepsilon \gamma_2 \cosh(\gamma_2) \sinh(\gamma_1) + \gamma_1 \cosh(\gamma_1) \sinh(\gamma_2) \}} \right] + A_3 \cosh(Ha\sqrt{\sigma/\mu}) \\
& - A_4 \sinh(Ha\sqrt{\sigma/\mu}) + \frac{\varepsilon \kappa_2^2 \{B_3 \cosh(\kappa_2) - B_4 \sinh(\kappa_2)\}}{\sigma Ha^2 - \mu \kappa_2^2} + \frac{P\Gamma + \sigma HaS_{20}}{Ha^2 \sigma} \left] \frac{\sin^2(\Lambda\pi)}{\pi} \left(1 + \frac{\lambda}{\alpha} + \frac{\lambda}{\alpha} \cos(2\Lambda\pi)\right).
\end{aligned}$$

4

EMHD Flow and Heat Transfer in Porous Microchannel with Surface Corrugation

4.1 Introduction

Microfluidic devices are broadly used to develop by modern science and technology. It plays a crucial role in many modern scientific devices which are involved in heat and mass transfer characteristics. It has been used in many modern industrial technology such as transport of chemical species, biomedical devices (Nandy et al. [2008]; Ohno et al. [2008]; Becker and Gartner [2000]; Masliyah and Bhattacharjee [2006]), lab-on-chip devices (Stone et al. [2004]), electro-osmosis micropumps (Nash and Fritsch [2016]), electromagnetohydrodynamic (EMHD) micropumps (Jang and Lee [2000]; Homsy et al. [2005]; Nguyen and Kassegne [2008]; Lemoff and Lee [2000]; Eijkel et al. [2003]; Huang et al. [2000]), heat transfer in micro-electro-mechanical systems (MEMS) and thermal transport of micro-electronic devices.

In EMHD micropump the flow is happened due to the Lorentz force. The interaction between the magnetic and electric fields make a continuous flow in the pump. This research helps to develop some device such as micro coolers, some complex flow phenomena in the fluidic network, mixing and stirring (Shojaeian and Shojaeian [2012]; Bau et al. [2003]; Gao et al. [2005]; Bau et al. [2001]; Gleeson et al. [2004]). EMHD flow in the microchannel has been widely studied by several researchers and also various theoretical and experimental (Das et al. [2012]; Sinha and Shit [2015];

The content of this chapter has been published in European Physical Journal Plus (Springer), 136(5):496, (2021).

Sarkar et al. [2017b]; Wang et al. [2016]; Sarkar et al. [2017a]; Vargas et al. [2017]; Xie and Jian [2017]; Sarkar et al. [2016]) investigations are done by them. The study of EMHD flow of fluid in parallel plate microchannel is done by Chakraborty and Paul [2006]. The thermo-fluidic transport phenomenon is analyzed by Chakraborty et al. [2013]. EMHD flow through a curved rectangular microchannel is performed by Liu et al. [2018]. They also discussed the analytical solutions of the velocity and the rate of entropy generation. EMHD flow transportation analysis is also analyzed by taking different fluids. There are so many researchers are investigated the electromagnetohydrodynamic flow through microchannel by taking Newtonian fluids as well as non-newtonian fluids as a working fluid. Liu and Jian [2019] discussed the electroviscous effects on EMHD flow of maxwell fluid in microchannel. They have obtained the analytical solution and discussed the flow transport characteristics with the influence of the streaming potential and electroviscous effect. Thermal transport phenomenon of nanofluid via parallel plate microchannel with the influence of electromagnetohydrodynamic effects investigated by Zhao et al. [2017].

Flow transport and heat transfer through a saturated porous medium is important in modern science and technology and it has been taken attention of researchers for several decades due to the wide range of the engendering applications, petroleum exploration, electronic component cooling, pressurized water reactors, transpiration cooling, oil recovery, involving porous insulation, heat pipe wicking structures, packed-bed catalytic nuclear reactors, chemical catalytic reactors, thermal insulation processes and even the flow of liquids in various physiological and biological processes. There so many investigations on heat transfer phenomenon through porous medium are provided by researchers. Biswas et al. [2021b] demonstrated the MHD thermal convection flow of hybrid nanofluid for augmenting thermal transport phenomenon through the porous media subject to the non-uniform heating. Unsteady MHD free convectional rotating flow over an exponentially accelerated inclined plate through the saturated porous medium is investigated by Krishna et al. [2020]. They also analyzed the impact of Hall current and ion slip effects on the rotating flow transport with variable temperature and concentration. Ghalambaz et al. [2020] simulated the free convection heat transfer of a suspension of nano-encapsulated phase change materials (NEPCMs) by using the finite volume method and which is discussed in an inclined porous cavity. More recently, the transport phenomena of porous media of microchannel has received much interest due to the conventional applications in the emerging fields of microscale heat transfer. (Karniadakis et al. [2005]; Karniadakis and Beskok [2002]; Nield and Bejan [1999]; Zadeh et al. [2020]) However, porous microchannels are used to fabricate more advanced microfluidic devices in several industries and equipments.

In any conduit, there exists some roughness due to manufacturing. The surface may affect the velocity profile due to the roughness effects in any fluid flow analysis. Last few years some researchers are working on the rough microchannel flow. Buren et al. [2014] worked on the EMHD flow through a corrugated wall micro parallel channel. They are shown that the mean velocity distribution of the rough microchannel is smaller than the smooth microchannel. The Jeffrey fluid through a corrugated micro parallel plate with EMHD effect is investigated by Si and Jain [2015]. The combined effect of EMHD flow in a slightly corrugated wall micro parallel channel is investigated by Ren et al. [2011] and Buren et al. [2017]. Rashid and Nadeem [2019] studied the EMHD

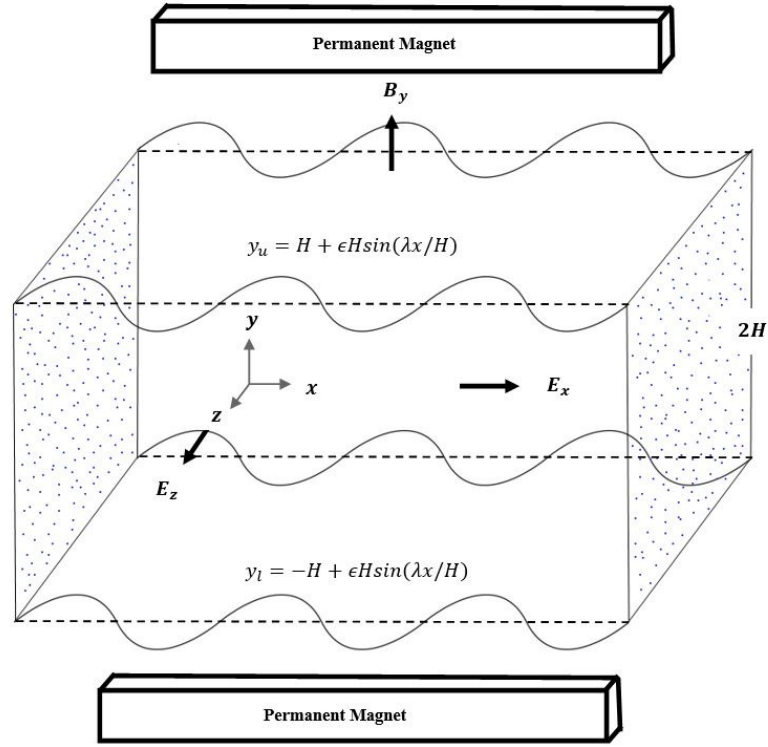


Figure 4.1: Physical Sketch of the problem.

flow of nanofluid through a corrugated wall microchannel. The perturbation technique is used to examine the flow and copper nano-particle is used in the nanofluid. [Rashid et al. \[2018\]](#) investigated the analytical solution of the corrugated wall microchannel flow through a porous medium under EMHD effects. They considered the second-grade fluid as a working fluid and carried out the flow analysis by using the perturbation technique. In all these works they have investigated the flow transport phenomenon they without describing the temperature distribution associated with such flow.

In this chapter, we concentrate to look into the flow transport and thermal characteristics of the fluid with the intergraded influence of electromagnetohydrodynamic effect and constant pressure gradient through a porous medium microchannel with corrugated walls. Both effects are acting independently in on the stress distribution. The impact of combined force due to electric kinematic and eletromagnetic force on flow and temperature distribution in the presence of roughness wall of the microchannel has been investigated and analyzed. In this study, the approximation analytical solutions have been found to examine characteristics on velocity and temperature of the fluid flow in the microchannel with corrugated walls through a porous medium by using the perturbation technique. Further, we examine the effect of roughness of the channel on the flow phenomenon and thermal characteristics.

4.2 Mathematical Model and Problem Description

This paper delineates the thermo-fluidic transport characteristics of a symmetric electrolyte between two fixed corrugated wall (cf. Fig. 4.1) of a porous medium microchannel with a gap height of $2H$, width W ($W \gg 2H$), and length L ($L \gg 2H$), under a combined electromagnetohydrodynamic effects and imposed pressure-gradient. Here we consider EMHD flow of a viscous, incompressible Newtonian fluid with viscosity μ , electrical conductivity σ_e and density ρ . We fixed the origin at the middle of the microchannel with unit base vector (e_x, e_y, e_z) , in the cartesian co-ordinate system. The upper and lower wavy walls are illustrated as

$$y_u = H + \varepsilon H \sin\left(\frac{\lambda x}{H}\right), \quad y_l = -H + \varepsilon H \sin\left(\frac{\lambda x}{H}\right), \quad (4.1)$$

where ε is small amplitude, λ is wave number.

4.3 Electrical potential distribution

In corrugated wall channel, to evaluate the net charge density ρ_e in the EDL, first the EDL potential $\psi = \psi(x, y)$ is determined by solving the Poisson equation $\nabla^2 \psi = -\frac{\rho_e}{\varepsilon}$. Due to symmetry of the electrolytes, the charge density ρ_e and the electric potential ψ are followed the below equation (Masliyah and Bhattacharjee [2006])

$$\rho_e = -\varepsilon \nabla^2 \psi = -2ez_0 n_0 \sinh(ez_0 \psi / k_B T_a), \quad (4.2)$$

where n_0 , e , z_0 , k_B denote ion density, electronic charge, the valance, the Boltzmann constant respectively. Here T_a and ε represent the absolute temperature, the permittivity constant of the solution. Since ψ is small enough, so $(ez_0 \psi / k_B T_a) \ll 1$, the term $\sinh(ez_0 \psi / k_B T_a)$ can be approximated by $(ez_0 \psi / k_B T_a)$.

This principle is known as Debye-Hückle linearization (Masliyah and Bhattacharjee [2006]). After executing this Debye-Hückle linearization, finally we obtain the linearized Poisson equation from (4.2):

$$\nabla^2 \psi = \kappa^2 \psi, \quad (4.3)$$

where $\kappa = ez_0(2n_0/\varepsilon k_B T_a)^{\frac{1}{2}}$ is Debye-Hückle parameter and $1/\kappa$ be the thickness of the EDL. The boundary conditions are

$$\psi = \zeta \text{ at } y = y_u \text{ and } y = y_l. \quad (4.4)$$

Here ζ be the constant zeta potential. We introduce the non-dimensional variables $\psi^* = \psi/\zeta$, $y^* = y/H$, $x^* = x/H$ to make dimensionless the linearized Poisson equation and which becomes

$$\nabla^{*2} \psi^* = \frac{\partial^2 \psi^*}{\partial x^{*2}} + \frac{\partial^2 \psi^*}{\partial y^{*2}} = \omega^2 \psi^*, \quad (4.5)$$

where $\omega = \kappa H$ referred as normalized reciprocal thickness of the EDL that significant the ratio of

half height of microchannel to Debye length ($1/\kappa$). The non-dimensional boundary conditions for the electrical potential equation are as follows:

$$\psi^* = 1 \text{ at } y^* = 1 + \varepsilon \sin(\lambda x^*), \quad (4.6)$$

$$\psi^* = 1 \text{ at } y^* = -1 + \varepsilon \sin(\lambda x^*). \quad (4.7)$$

We investigate an analytic solution in the form of a Poincare type asymptotic expansion for the EDL potential as

$$\psi^*(x^*, y^*) = \psi_0^*(x^*, y^*) + \varepsilon \psi_1^*(x^*, y^*) + \varepsilon^2 \psi_2^*(x^*, y^*) + \dots \quad (4.8)$$

Substituting the above expansion in Eq. (4.5) and equating the terms of like power of ε , the governing equation of the EDL potential can be divided into the following equations:

$$\nabla^{*2} \psi_0^* = \omega^2 \psi_0^*, \quad \nabla^{*2} \psi_1^* = \omega^2 \psi_1^*, \quad \nabla^{*2} \psi_2^* = \omega^2 \psi_2^*, \quad (4.9)$$

where the higher power of the ε have been ignored here. The associated boundary conditions for ψ^* are derived from equation (4.6) and (4.7) by expanding in a Taylor's series and are obtained by:

$$\begin{aligned} \psi^*(x^*, 1 + \varepsilon \sin(\lambda x^*)) &= \psi^*(x^*, 1) + \varepsilon \sin(\lambda x^*) \frac{\partial \psi^*}{\partial y^*}(x^*, 1) \\ &+ \frac{\varepsilon^2}{2} \sin(\lambda x^*) \frac{\partial^2 \psi^*}{\partial y^{*2}}(x^*, 1) + \dots = 1, \end{aligned} \quad (4.10)$$

and

$$\begin{aligned} \psi^*(x^*, -1 + \varepsilon \sin(\lambda x^*)) &= \psi^*(x^*, -1) + \varepsilon \sin(\lambda x^*) \frac{\partial \psi^*}{\partial y^*}(x^*, -1) \\ &+ \frac{\varepsilon^2}{2} \sin(\lambda x^*) \frac{\partial^2 \psi^*}{\partial y^{*2}}(x^*, -1) + \dots = 1. \end{aligned} \quad (4.11)$$

Substituting the Eq. (4.8) into Eq. (4.10) and Eq. (4.11) we get

$$\begin{aligned} \psi_0^*(x^*, 1) &+ \varepsilon [\psi_1^*(x^*, 1) + \sin(\lambda x^*) \frac{\partial \psi_0^*}{\partial y^*}(x^*, 1)] + \varepsilon^2 [\psi_2^*(x^*, 1) \\ &+ \sin(\lambda x^*) \frac{\partial \psi_1^*}{\partial y^*}(x^*, 1) + \frac{\sin^2(\lambda x^*)}{2} \frac{\partial^2 \psi_0^*}{\partial y^{*2}}(x^*, 1)] + \dots = 1, \end{aligned} \quad (4.12)$$

and

$$\begin{aligned} \psi_0^*(x^*, -1) &+ \varepsilon [\psi_1^*(x^*, -1) + \sin(\lambda x^*) \frac{\partial \psi_0^*}{\partial y^*}(x^*, -1)] + \varepsilon^2 [\psi_2^*(x^*, -1) \\ &+ \sin(\lambda x^*) \frac{\partial \psi_1^*}{\partial y^*}(x^*, -1) + \frac{\sin^2(\lambda x^*)}{2} \frac{\partial^2 \psi_0^*}{\partial y^{*2}}(x^*, -1)] + \dots = 1. \end{aligned} \quad (4.13)$$

Equating the terms having the same power of ε from Eqs. (4.12) and (4.13), the boundary conditions

associated with ψ_0^* , ψ_1^* and ψ_2^* are derived as

$$\psi_0^*(x^*, 1) = 1, \quad (4.14)$$

$$\psi_0^*(x^*, -1) = 1, \quad (4.15)$$

$$\psi_1^*(x^*, 1) + \sin(\lambda x^*) \frac{\partial \psi_0^*}{\partial y^*}(x^*, 1) = 0, \quad (4.16)$$

$$\psi_1^*(x^*, -1) + \sin(\lambda x^*) \frac{\partial \psi_0^*}{\partial y^*}(x^*, -1) = 0, \quad (4.17)$$

$$\psi_2^*(x^*, 1) + \sin(\lambda x^*) \frac{\partial \psi_1^*}{\partial y^*}(x^*, 1) + \frac{\sin^2(\lambda x^*)}{2} \frac{\partial^2 \psi_0^*}{\partial y^{*2}}(x^*, 1) = 0, \quad (4.18)$$

$$\psi_2^*(x^*, -1) + \sin(\lambda x^*) \frac{\partial \psi_1^*}{\partial y^*}(x^*, -1) + \frac{\sin^2(\lambda x^*)}{2} \frac{\partial^2 \psi_0^*}{\partial y^{*2}}(x^*, -1) = 0. \quad (4.19)$$

The solution of the Eq. (4.9) subject to the boundary conditions (4.14)-(4.19) yields

$$\psi_0^*(x^*, y^*) = \frac{e^{\omega(1-y^*)}(1 + e^{2\omega y^*})}{1 + e^{2\omega}}, \quad (4.20)$$

$$\psi_1^*(x^*, y^*) = \frac{\omega(1 - e^{2\omega})e^{\sqrt{\omega^2 + \lambda^2}(1-y^*)}(e^{2\sqrt{\omega^2 + \lambda^2}y^*} - 1)}{(1 + e^{2\omega})(e^{2\sqrt{\omega^2 + \lambda^2}} - 1)} \sin(\lambda x^*), \quad (4.21)$$

$$\psi_2^*(x^*, y^*) = \alpha e^{\sqrt{\omega^2 + 4\lambda^2}(1-y^*)}(1 + e^{2\sqrt{\omega^2 + 4\lambda^2}y^*}) \sin(2\lambda x^*), \quad (4.22)$$

$$\text{where } \alpha = \left(\frac{\omega\sqrt{\omega^2 + \lambda^2}(e^{2\omega} - 1)(e^{2\sqrt{\omega^2 + \lambda^2}} + 1)}{(1 + e^{2\omega})(e^{2\sqrt{\omega^2 + \lambda^2}} - 1)} - \frac{\omega^2}{2} \right) \frac{\tan(\lambda)}{2(e^{2\sqrt{\omega^2 + 4\lambda^2}} + 1)}.$$

4.4 Velocity distribution

The governing equation of momentum conservation within a fluid through porous medium in the presence of pressure gradient is given by

$$\frac{D}{Dt}(\rho \mathbf{V}) = -\nabla p + \nabla \cdot (\boldsymbol{\tau}) + \mathbf{b} - \frac{\mu}{k} \mathbf{V}, \quad (4.23)$$

where $\boldsymbol{\tau}$ is the stress tensor, k be the permeability of the porous medium and \mathbf{b} is the body force per unit volume, is given as

$$\mathbf{b} = \rho_e \mathbf{E} + \mathbf{F}, \quad (4.24)$$

ρ_e and \mathbf{E} represent the net electric charge density and applied electric field, respectively. Here, \mathbf{F} denotes the Lorentz force which is created due to interaction of fluid flow and applied magnetic field, is written as

$$\mathbf{F} = \mathbf{J} \times \mathbf{B}, \quad (4.25)$$

where $\mathbf{J} = \sigma_e(\mathbf{E} + \mathbf{V} \times \mathbf{B})$ and σ_e is the electric conductivity of the medium.

4.4. Velocity distribution

The parallel plates are assumed to infinitely long along x -direction and the velocity gradients along the x -direction can be neglected. Since for present geometrical configuration, $W \gg 2H$, the velocity component along the x -direction is approximately equal to zero based on the physical flow situation without loss of generality of the microscale flow. In the paper, we assumed that steady flow occurs in z -direction due to constant pressure gradient along the z -direction and also combine body force due to electro kinetic force and electromagnetic force. So the velocity component along the z -direction is represented by $u = u(x, y)$, depends on x and y and independent of z (Chakraborty and Paul [2006]) and satisfies the following equations (z -component of momentum equations).

$$\mu \left(\frac{\partial^2 u}{\partial x^2} + \frac{\partial^2 u}{\partial y^2} \right) - \frac{\partial p}{\partial z} - \frac{\mu u}{k} + \rho_e E_z + \sigma_e E_x B_y - \sigma_e B_y^2 u = 0. \quad (4.26)$$

The boundary conditions are

$$u = 0 \text{ at } y = y_u \text{ and } y = y_l. \quad (4.27)$$

The following non-dimensional variables are used to make dimensionless the equation (26)

$$x^* = \frac{x}{H}, y^* = \frac{y}{H}, u^* = \frac{u}{U}, \quad (4.28)$$

$$Da = \frac{k}{H^2}, Ha = B_y H \sqrt{\frac{\sigma_e}{\mu}}, P_1 = \frac{(-\frac{\partial p}{\partial z}) H^2}{\mu U}, S = \frac{E_x a}{U} \sqrt{\frac{\sigma_e}{\mu}}. \quad (4.29)$$

Then Eq. (4.26) becomes:

$$\left(\frac{\partial^2 u^*}{\partial x^{*2}} + \frac{\partial^2 u^*}{\partial y^{*2}} \right) - \left(\frac{1}{Da} + Ha^2 \right) u^* + \omega^2 \psi^* + P_1 + HaS = 0, \quad (4.30)$$

where $U = -\frac{\epsilon \zeta E_z}{\mu}$ is denoted as maximum possible electroosmotic velocity which known as the Helmholtz-Smoluchowski velocity. The non-dimensional momentum Eq. (4.30) is subjected to the no-slip boundary conditions which are

$$u^* = 0 \text{ at } y^* = 1 + \epsilon \sin(\lambda x^*), \quad (4.31)$$

$$u^* = 0 \text{ at } y^* = -1 + \epsilon \sin(\lambda x^*). \quad (4.32)$$

It is not so easy to solve the Eq. (4.30) due to term $\omega^2 \psi^*$. To solve easily we use a transformation:

$$u^@ = - \left(\frac{1}{Da} + Ha^2 \right) u^* + \frac{\left(\frac{1}{Da} + Ha^2 \right) \omega^2 \psi^*}{\left(\frac{1}{Da} + Ha^2 - \omega^2 \right)}. \quad (4.33)$$

Using Eqs. (4.33) and (4.5), Eq. (4.30) is reached to the following form:

$$\frac{\partial^2 u^@}{\partial x^{*2}} + \frac{\partial^2 u^@}{\partial y^{*2}} - Qu^@ = P, \quad (4.34)$$

where $Q = \left(\frac{1}{Da} + Ha^2 \right)$ and $P = \left(\frac{1}{Da} + Ha^2 \right) (P_1 + HaS)$.

Then the boundary conditions (4.31) and (4.32) become:

$$u^@ = \frac{Q\omega^2}{Q-\omega^2} \text{ at } y^* = 1 + \varepsilon \sin(\lambda x^*), \quad (4.35)$$

$$u^@ = \frac{Q\omega^2}{Q-\omega^2} \text{ at } y^* = -1 + \varepsilon \sin(\lambda x^*). \quad (4.36)$$

In similar way as for the EDL potential, $u^@$ is dislocated with a Poincare type asymptotic expansion which leads to the following governing equations for $u_0^@, u_1^@$ and $u_2^@$

$$\frac{\partial^2 u_0^@}{\partial x^{*2}} + \frac{\partial^2 u_0^@}{\partial y^{*2}} - Qu_0^@ = P, \quad (4.37)$$

$$\frac{\partial^2 u_1^@}{\partial x^{*2}} + \frac{\partial^2 u_1^@}{\partial y^{*2}} - Qu_1^@ = 0, \quad (4.38)$$

$$\frac{\partial^2 u_2^@}{\partial x^{*2}} + \frac{\partial^2 u_2^@}{\partial y^{*2}} - Qu_2^@ = 0, \quad (4.39)$$

with the suitable boundary conditions expressed as:

$$u_0^@(x^*, 1) = \frac{Q\omega^2}{Q-\omega^2}, \quad (4.40)$$

$$u_0^@(x^*, -1) = \frac{Q\omega^2}{Q-\omega^2}, \quad (4.41)$$

$$u_1^@(x^*, 1) + \sin(\lambda x^*) \frac{\partial u_0^@}{\partial y^*}(x^*, 1) = 0, \quad (4.42)$$

$$u_1^@(x^*, -1) + \sin(\lambda x^*) \frac{\partial u_0^@}{\partial y^*}(x^*, -1) = 0, \quad (4.43)$$

$$u_2^@(x^*, 1) + \sin(\lambda x^*) \frac{\partial u_1^@}{\partial y^*}(x^*, 1) + \frac{\sin^2(\lambda x^*)}{2} \frac{\partial^2 u_0^@}{\partial y^{*2}}(x^*, 1) = 0, \quad (4.44)$$

$$u_2^@(x^*, -1) + \sin(\lambda x^*) \frac{\partial u_1^@}{\partial y^*}(x^*, -1) + \frac{\sin^2(\lambda x^*)}{2} \frac{\partial^2 u_0^@}{\partial y^{*2}}(x^*, -1) = 0. \quad (4.45)$$

Solving Eqs. (4.37)-(4.39) with the boundary conditions (4.40)-(4.45) and one can obtain:

$$u_0^@(x^*, y^*) = \frac{(\frac{P}{Q} + \frac{Q\omega^2}{Q-\omega^2})e^{\sqrt{Q}(1-y^*)}(1 + e^{2\sqrt{Q}y^*})}{1 + e^{2\sqrt{Q}}} - \frac{P}{Q}, \quad (4.46)$$

$$u_1^@(x^*, y^*) = \frac{(P + \frac{Q\omega^2}{Q-\omega^2})(1 - e^{2\sqrt{Q}})e^{\sqrt{Q+\lambda^2}(1-y^*)}(e^{2\sqrt{Q+\lambda^2}y^*} - 1)}{\sqrt{Q}(1 + e^{2\sqrt{Q}})(e^{2\sqrt{Q+\lambda^2}} - 1)} \sin(\lambda x^*), \quad (4.47)$$

$$u_2^@(x^*, y^*) = \beta e^{\sqrt{Q+4\lambda^2}(1-y^*)}(1 + e^{2\sqrt{Q+4\lambda^2}y^*}) \sin(2\lambda x^*), \quad (4.48)$$

4.5. Temperature distribution and Nusselt number

where $\beta = \left\{ \frac{\sqrt{Q+\lambda^2}(P+\frac{Q^2\omega^2}{Q-\omega^2})(e^{2\sqrt{Q}}-1)(e^{2\sqrt{Q+\lambda^2}}+1)}{\sqrt{Q}(1+e^{2\sqrt{Q}})(e^{2\sqrt{Q+\lambda^2}}-1)} - \frac{1}{2}(P+\frac{Q^2\omega^2}{Q-\omega^2}) \right\} \frac{\tan(\lambda)}{2(e^{2\sqrt{Q+4\lambda^2}}+1)}$.

Volume flow rate and mean velocity: The volume flow rate per unit width of the channel is expressed as:

$$\begin{aligned} q(x^*) &= \int_{y_l}^{y_u} u^* dy^* \\ &= \int_{y_l}^{-1} u^* dy^* + \int_{-1}^1 u^* dy^* + \int_1^{y_u} u^* dy^* \\ &= \int_{-1}^1 u_0^* dy^* + \varepsilon \left[\int_{-1}^1 u_1^* dy^* + \sin(\lambda x^*) \{u_0^*(1) - u_0^*(-1)\} \right] \\ &\quad + \varepsilon^2 \left[\int_{-1}^1 u_2^* dy^* + \sin(\lambda x^*) \{u_1^*(x^*, 1) - u_1^*(x^*, -1)\} \right] \\ &\quad + \frac{1}{2} \sin^2(\lambda x^*) \left\{ \frac{du_0^*}{dy^*} \Big|_{y=-1} - \frac{du_0^*}{dy^*} \Big|_{y=1} \right\}. \end{aligned} \quad (4.49)$$

Here the function u^* in the last two integrals are expanded in Taylor's series about $y = \pm 1$ on averaging the one wavelength $[0, \frac{2\pi}{\lambda}]$ of corrugation. Then using Eq. (4.33) and Eqs. (4.46)-(4.49) we can evaluate the mean velocity :

$$u_m^* = \frac{\lambda}{4\pi} \int_0^{\frac{2\pi}{\lambda}} q(x^*) dx^*, \quad (4.50)$$

i.e.

$$u_m^* = \frac{\lambda}{4\pi} \int_0^{\frac{2\pi}{\lambda}} q(x^*) dx^* = u_0^* [1 + \varepsilon^2 \phi + O(\varepsilon^4)], \quad (4.51)$$

where

$$u_0^* = \left\{ \frac{Da(P_1 + HaS)}{1 + Ha^2 Da} - \frac{\{P + (Q - P_1 - HaS)\omega^2\} \tanh(\sqrt{Q})}{Q^{3/2}(Q - \omega^2)} + \frac{\omega \tanh(\omega)}{Q - \omega^2} \right\}, \quad (4.52)$$

$$\phi = \frac{\left\{ \frac{(e^{2\sqrt{Q}}-1)(HaS+P_1)}{(e^{2\sqrt{Q}}+1)\sqrt{Q}} + \frac{(e^{2\sqrt{Q}}-1)\omega^2\sqrt{Q}}{(e^{2\sqrt{Q}}+1)(Q-\omega^2)} + \frac{a\omega^3(e^{2\omega}-1)}{(e^{2\omega}+1)\{Da(\omega^2-Ha^2)-1\}} \right\}}{4 \left\{ \frac{Da(P_1+HaS)}{1+Ha^2Da} - \frac{\{P+(Q-P_1-HaS)\omega^2\} \tanh(\sqrt{Q})}{Q^{3/2}(Q-\omega^2)} + \frac{\omega \tanh(\omega)}{Q-\omega^2} \right\}}. \quad (4.53)$$

4.5 Temperature distribution and Nusselt number

To investigate the thermal transport characteristics associated with combined electromagnetohydrodynamic flows through corrugated microchannel through porous medium is written as:

$$\rho C_P u \frac{\partial T}{\partial z} = k_{Th} \left(\frac{\partial^2 T}{\partial x^2} + \frac{\partial^2 T}{\partial y^2} \right) + S_J, \quad (4.54)$$

where C_P is the specific heat of the liquid at constant pressure, T is the local temperature of the liquid, k_{Th} is the thermal conductivity of the liquid and $S_J = (E_x^2 + E_z^2)/\sigma_e$ is the volumetric

heat generation due to Joule heating effect. Now, for thermally fully developed flow, the classical non-dimensional temperature $T^* = \frac{k_{Th}(T-T_W)}{q_w}$ is invariant of the axial co-ordinate, where T_W is the channel wall temperature, which is constant at the cross section of the channel and q_w is the average inward wall heat flux over the channel. Further, for thermally fully developed flow with constant heat flux, we may write:

$$\frac{\partial T}{\partial z} = \frac{\partial T_W}{\partial z} = \frac{\partial T_b}{\partial z}, \quad (4.55)$$

where T_b is the bulk mean temperature. The overall energy balance on an element control volume can be expressed as:

$$\frac{\partial T_b}{\partial z} = \frac{q_w/H + (E_x^2 + E_z^2)/\sigma_e}{\rho C_p u_{av}}, \quad (4.56)$$

where u_{av} is the average velocity of the channel cross section. So, the non-dimensional energy equation may be written as:

$$\frac{\partial^2 T^*}{\partial x^{*2}} + \frac{\partial^2 T^*}{\partial y^{*2}} = -\frac{Nu}{u_{av}^*} (1 + S_j) u^* + Nu S_j, \quad (4.57)$$

where $S_j = \frac{(E_x^2 + E_z^2)H}{\sigma_e q_w}$, $u_{av}^* = \frac{u_{av}}{U}$.

The supplementary non-dimensional boundary conditions are:

$$T^* = 0 \text{ at } y^* = 1 + \varepsilon \sin(\lambda x^*), \quad (4.58)$$

$$T^* = 0 \text{ at } y^* = -1 + \varepsilon \sin(\lambda x^*). \quad (4.59)$$

To solve the above Eq. (4.57) we use a transformation:

$$T^@ = \frac{Q}{\frac{Nu}{u_{av}^*} (1 + S_j)} T^* + \frac{Q}{Q - \omega^2} \psi^*. \quad (4.60)$$

Using Eqs. (4.60), (4.33) and (4.5), Eq. (4.57) is reduced to the following form:

$$\frac{\partial^2 T^@}{\partial x^{*2}} + \frac{\partial^2 T^@}{\partial y^{*2}} - u^@ = \frac{Q S_j}{\frac{Nu}{u_{av}^*} (1 + S_j)}, \quad (4.61)$$

subject to the boundary conditions

$$T^@ = \frac{Q}{Q - \omega^2} \text{ at } y^* = 1 + \varepsilon \sin(\lambda x^*), \quad (4.62)$$

$$T^@ = \frac{Q}{Q - \omega^2} \text{ at } y^* = -1 + \varepsilon \sin(\lambda x^*). \quad (4.63)$$

Hence, by similar fashion as for the EDL potential, $T^@$ is replaced with a Poincare type asymptotic

expansion leading to the following governing equations for $T_0^@$, $T_1^@$ and $T_2^@$

$$\frac{\partial^2 T_0^@}{\partial x^{*2}} + \frac{\partial^2 T_0^@}{\partial y^{*2}} - u_0^@ = \frac{QS_j}{u_{av}^*(1+S_j)}, \quad (4.64)$$

$$\frac{\partial^2 T_1^@}{\partial x^{*2}} + \frac{\partial^2 T_1^@}{\partial y^{*2}} - u_1^@ = 0, \quad (4.65)$$

$$\frac{\partial^2 T_2^@}{\partial x^{*2}} + \frac{\partial^2 T_2^@}{\partial y^{*2}} - u_2^@ = 0, \quad (4.66)$$

with the relevant boundary conditions which are subjected to:

$$T_0^@(x^*, 1) = \frac{Q}{Q - \omega^2}, \quad (4.67)$$

$$T_0^@(x^*, -1) = \frac{Q}{Q - \omega^2}, \quad (4.68)$$

$$T_1^@(x^*, 1) + \sin(\lambda x^*) \frac{\partial T_0^@}{\partial y^*}(x^*, 1) = 0, \quad (4.69)$$

$$T_1^@(x^*, -1) + \sin(\lambda x^*) \frac{\partial T_0^@}{\partial y^*}(x^*, -1) = 0, \quad (4.70)$$

$$T_2^@(x^*, 1) + \sin(\lambda x^*) \frac{\partial T_1^@}{\partial y^*}(x^*, 1) + \frac{\sin^2(\lambda x^*)}{2} \frac{\partial^2 T_0^@}{\partial y^{*2}}(x^*, 1) = 0, \quad (4.71)$$

$$T_2^@(x^*, -1) + \sin(\lambda x^*) \frac{\partial T_1^@}{\partial y^*}(x^*, -1) + \frac{\sin^2(\lambda x^*)}{2} \frac{\partial^2 T_0^@}{\partial y^{*2}}(x^*, -1) = 0. \quad (4.72)$$

By evaluating Eq. (4.64)-(4.66) with the boundary conditions (4.67)-(4.72), we get:

$$\begin{aligned} T_0^@(x^*, y^*) &= \frac{2 + S_j \{2 + Qu_{av}^*(1 - y^{*2})\}}{2(1 + S_j)} - \frac{P}{Q^2} \\ &+ \frac{(\frac{P}{Q} + \frac{Q\omega^2}{Q - \omega^2}) \{e^{\sqrt{Q}(1-y^*)} + e^{\sqrt{Q}(1+y^*)}\}}{Q(1 + e^{2\sqrt{Q}})}, \end{aligned} \quad (4.73)$$

$$\begin{aligned} T_1^@(x^*, y^*) &= \left\{ \frac{(\frac{P}{Q} + \frac{Q\omega^2}{Q - \omega^2})(1 - e^{2\sqrt{Q}})}{\sqrt{Q}(1 - e^{2\sqrt{Q}})} - \frac{NuQS_j u_{av}^*}{(1 + S_j)} \right\} \frac{\sinh(\lambda y^*) \sin(\lambda x^*)}{\sinh(\lambda)} \\ &+ \sum_{m=0}^{\infty} \sum_{n=0}^{\infty} a_{mn} \sin \frac{(m+1)\pi x^*}{60} \sin(n+1)\pi y^*, \end{aligned} \quad (4.74)$$

$$T_2^@ (x^*, y^*) = G_\beta \frac{\cosh(2\lambda y^*) \sin(2\lambda x^*)}{2 \cos(\lambda) \cosh(2\lambda)} + \sum_{m_1=0}^{\infty} \sum_{n_1=0}^{\infty} A_{m_1 n_1} \sin \frac{(m_1+1)\pi x^*}{60} \sin(n_1+1)\pi y^*, \quad (4.75)$$

where

$$\begin{aligned} a_{mn} &= G_\delta \int_0^{60} \int_0^1 G_\alpha \sin(\lambda x^*) \sinh(\sqrt{Q+\lambda^2} y^*) \sin\left(\frac{(m+1)\pi x^*}{60}\right) \sin((n+1)\pi y^*) dx^* dy^*, \\ A_{m_1 n_1} &= G_\eta \int_0^{60} \int_0^1 G_\gamma \sin(\lambda x^*) \cosh(\sqrt{Q+4\lambda^2} y^*) \sin\left(\frac{(m_1+1)\pi x^*}{60}\right) \sin((n_1+1)\pi y^*) dx^* dy^*, \\ G_\alpha &= \frac{2(P+\frac{Q^2\omega^2}{Q-\omega^2})(1-e^{2\sqrt{Q}})\{\sinh(\sqrt{Q+\lambda^2})+\cos(\sqrt{Q+\lambda^2})\}}{\sqrt{Q}(1+e^{2\sqrt{Q}})(e^{2\sqrt{Q+\lambda^2}}-1)}, \quad G_\beta = -\left[\frac{\partial T_1^@}{\partial y^*}(x^*, 1) + \frac{\sin^2(\lambda x^*)}{2} \frac{\partial^2 T_0^@}{\partial y^{*2}}(x^*, 1)\right]_{x^*=1}, \\ G_\gamma &= 2\beta\{\sinh(\sqrt{Q+\lambda^2}) + \cos(\sqrt{Q+\lambda^2})\}, \\ G_\delta &= -\frac{4}{60\{\frac{(m+1)^2\pi^2}{60^2} + (n+1)^2\pi^2\}}, \quad G_\eta = -\frac{4}{60\{\frac{(m_1+1)^2\pi^2}{60^2} + (n_1+1)^2\pi^2\}}. \end{aligned}$$

After obtaining the the solutions of $T_0^@$, $T_1^@$ and $T_2^@$, it is easy to find the dimensionless temperature distribution $T^* = \frac{Nu(1+S_j)}{Qw_{av}^*}(T^@ - \frac{Q\Psi^*}{Q-\omega^2}) = \theta(say)$.

Nusselt Number: By taking the advantage of the velocity and temperature distribution, the non-dimensional bulk mean temperature can be written as

$$T_b^* = \frac{\int_0^{\frac{2\pi}{\lambda}} \int_{-1+\varepsilon \sin(\lambda x^*)}^{1+\varepsilon \sin(\lambda x^*)} u^* \theta^* dx^* dy^*}{\int_0^{\frac{2\pi}{\lambda}} \int_{-1+\varepsilon \sin(\lambda x^*)}^{1+\varepsilon \sin(\lambda x^*)} u^* dx^* dy^*}, \quad (4.76)$$

where $\theta^* = \frac{(1+S_j)}{Qu_{av}^*}(T^@ - \frac{Q\Psi^*}{Q-\omega^2})$.

The Nusselt number is a dimensionless quantity that measures the rate of energy conversion from the heated wall to the fluid flowing through the micro-channel. Since the walls of the micro-channel are maintained with a constant wall temperature, the flow becomes thermally fully developed. In this situation, the assumption of the Nusselt number is independent of the location of the channel (local Nusselt number assumption is not a good estimation). Thus, we define the Nusselt number (Nu) in terms of the dimensionless bulk temperature T_b^* as (Hadjicostantinou and Simek [2002])

$$Nu = \frac{2hq_w}{k_{Th}(T_w - T_b)} = \frac{-2}{T_b^*}. \quad (4.77)$$

In the above, the temperature difference motivating heat transfer to be that between the wall temperature (T_w), and the convective heat transfer coefficient based on the bulk temperature (T_b).

We use numerical integration techniques to find the Nusselt number.

4.6 Results and Discussion

In this chapter, the heat and flow transport characteristics of the fluid in the porous microchannel with wavy rough walls has been examined. The equations (4.30) subject to the boundary conditions (4.31) and (4.32) and Eq. (4.57) subject to the boundary conditions (4.58) and (4.59) are solved analytically using the perturbation method. To obtain the approximate analytical solutions, all computations are done using the Mathematica program.

Table 4.1: Comparing the numerical values of the volumetric flow rate obtained in Buren et al. [2014] with the results from our investigation, across various Hartmann numbers (Ha)

	Buren et al.	Buren et al.	Present work	Present work
Ha	$q(1)$	$q(60)$	$q(1)$	$q(60)$
0.5	-0.30304	-0.30299	-0.30309	-0.3030
0.75	-0.2722	-0.27223	-0.2722	-0.27227
1	-0.2384	-0.23846	-0.23839	-0.23843
2	-0.1295	-0.1295	-0.12948	-0.1295
5	-0.03201	-0.03205	-0.031996	-0.03201

The numerical validation of this present results with those of Buren et al. [2014] have made in tabular form. The Table-4.1 shows the numerical values of volumetric flow rate at different location of the microchannel for different values of the Hartmann number Ha . For the purpose of comparison we have set $S = 0, \omega = 0, P_1 = 0.5, \varepsilon = 0.25, \lambda = 0.025, Da \rightarrow \infty$ in order to bring both the studies in the same situation.

Table 4.2: Typical values of the physical variables

Physical variables	Values [units]
Characteristic channel length (H)	$40\mu m$
Density of the fluid (ρ)	$1060 kg/m^3$
Charge of the photon (e)	$1.6 \times 10^{-19} Coulomb$
Electrical potential at the wall (ζ)	$-12mV$
Electrical field in axial direction (E_x)	$0 - 2 \times 10^4 V/m$
Electrical field in transverse direction (E_z)	$0 - 2 \times 10^4 V/m$
Applied magnetic field (B_y)	$1 - 50T$
Boltzmann constant (k_B)	$1.38 \times 10^{-23} J/K$
Ion density (n_0)	$1 mol/m^3$
Average absolute temperature (T_a)	$300K$
Initial surface temperature (T_w)	$300K$
Valence of ions (z)	1
Permittivity of the fluid (ε)	$5.3 \times 10^{-10} C/Vm$
Viscosity of the fluid (μ)	$10^{-6} m^2/s$
Permeability of porous media (K)	$0 - 10^{-11} m^2$
Wall heat flux (q_w)	$1000W/m^2$
Electrical conductivity (σ_e)	$10^{-3} - 1.0S/m$
Thermal conductivity (k_{Th})	$0.613W/mK$
Specific heat (c_p)	$3760J/KgK$

It is observed that EMHD flow characteristics represented by dimensionless flow velocity (u^*) and thermal characteristics represented by dimensionless temperature distribution (θ) and the Nusselt number (Nu) depend on the dimensionless physical parameters the wall roughness parame-

ters amplitude (ε), wavenumber (λ), (Darcy Number) porosity parameter (Da), (Hartman Number) applied magnetic field (Ha), Transverse electric field (S). To examine and analyze the effects of wavy roughness and porosity of micro-channel on the electromagnetically driven flow and temperature, the following typical parametric values are used (Ren et al. [2011]; Chakraborty et al. [2013]) : $O(\rho) \sim 1 \times 10^3 - 5.91 \times 10^3 \text{kgm}^{(-3)}$, $O(\mu) \sim 0.001 \text{kgms}^{(-1)}$, $O(B_y) \sim 1 - 50 \text{T}$, $O(E_x) \sim 0 - 10^4 \text{V/m}$, $O(E_z) \sim 0 - 10^4 \text{V/m}$, $O(P_1) \sim 10 \text{Pa/m}$, $O(S_j) \sim (-1) - (-15)$.

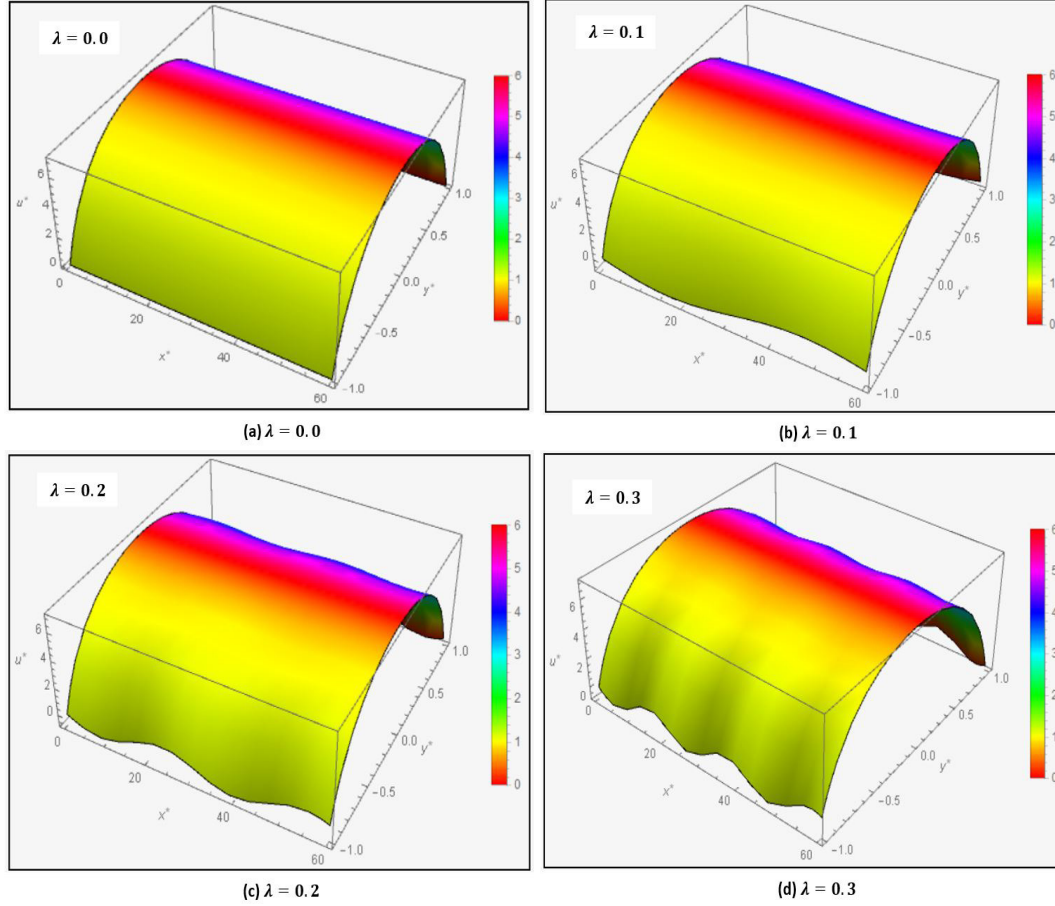


Figure 4.2: Three dimensional velocity distribution for (a) $\lambda = 0$; (b) $\lambda = 0.1$; (c) $\lambda = 0.2$ and (d) $\lambda = 0.3$ with $S = 50$, $Ha = 1$, $\varepsilon = 0.025$, $Da = 0.2$.

Based on the physical properties, the numerical values of various physical quantities have been described in Table-4.2. (Ren et al. [2011]; Chakraborty et al. [2013]; Ranjit and Shit [2017]; Shit et al. [2016b]) For example, in this model, the range of the Hartmann number, Darcy number and joule heating parameter are taken between 0.001 to 5, 0.001 to ∞ and (-15) to (-2) respectively.

4.6.1 Effect of wall roughness on flow velocity

The velocity distributions for 3D variations and contour of the fluid for the different values of nondimensional wavy roughness parameters λ (wavenumber), are displayed in Fig. 4.2 respectively when $S = 50$, $Ha = 1$, $\varepsilon = 0.025$, $Da = 0.2$. It is observed from these figures that velocity

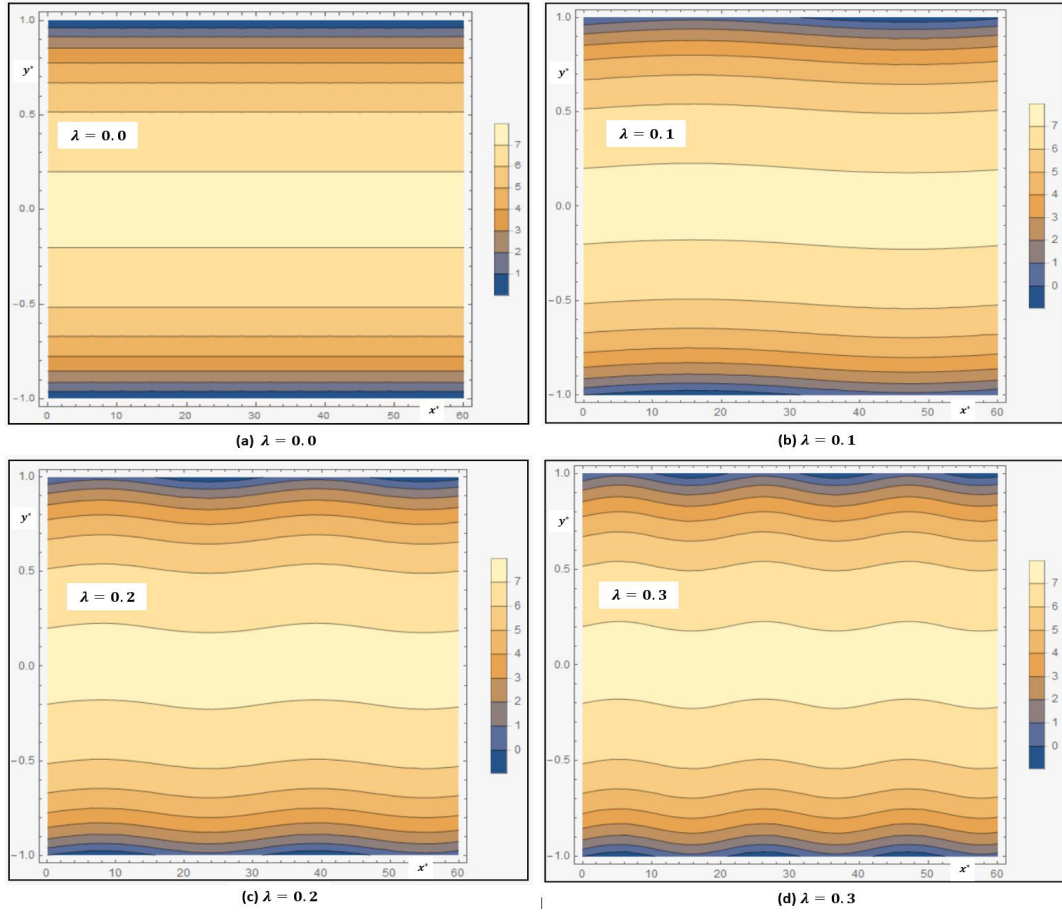


Figure 4.3: Velocity contour for (a) $\lambda = 0$; (b) $\lambda = 0.1$; (c) $\lambda = 0.2$ and (d) $\lambda = 0.3$ with $S = 50$, $Ha = 1$, $\varepsilon = 0.025$, $Da = 0.2$.

distribution is affected by changing the roughness effect in the presence of a magnetic field $Ha = 1$ and transverse electric field $S = 50$. The flow near the wavy surface is disturbed by increasing the value of wavenumber (λ) while velocity in the middle layer is also affected slightly. From Fig 4.2, it is noticed that in the presence of a transverse electric field, the velocity profile becomes parabolic means flow occurs the fully developed. But Fig. 4.3 shows that the nature of the boundary layer has been changed due to changing the value of wavenumber.

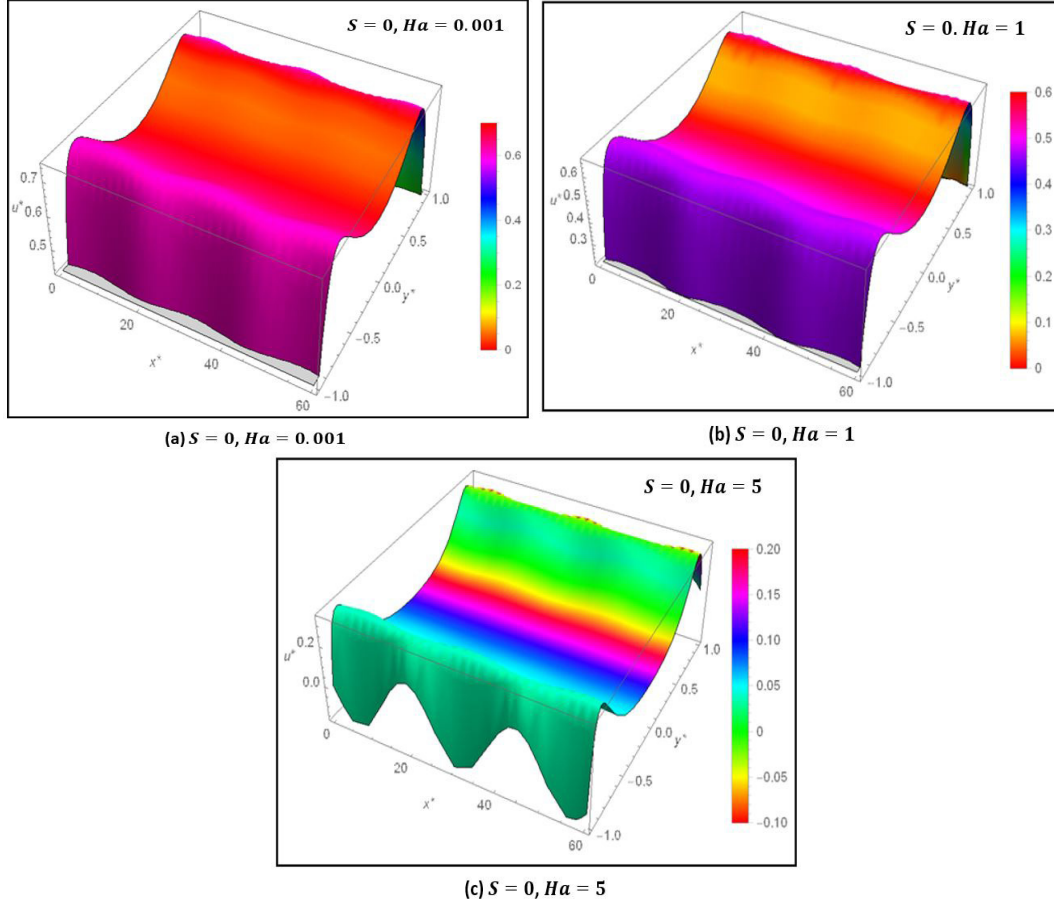


Figure 4.4: Three dimensional Velocity distribution for (a) $Ha = 0.001$, (b) $Ha = 1.0$, (c) $Ha = 5.0$ with $S = 0$, $\omega = 10$, $\varepsilon = 0.025$, $Da = 0.5$, $\lambda = 0.25$.

4.6.2 Effect of electromagnetic field on flow velocity

The magnitude of the applied magnetic field is embodied by the Hartmann number. The influence of the applied transverse magnetic field on the flow velocity is shown in 3D variations and contour plots in the absence of transverse electric field ($S = 0$) in Figs. 4.4-4.5 and the presence of transverse electric field ($S = 25$) in Figs. 4.6-4.7. It must be noted from the momentum transport Eq. (4.26) that the body force due to applied electromagnetic effects has two components which are controlled by an applied transverse magnetic field and transverse electric field, the first one is ‘flow-aiding’ ($\sim \sigma_e E_x B_y$) which combined effect of transverse electric field and magnetic field. But another term

4.6. Results and Discussion

which is ‘flow-opposing’ ($\sim \sigma_e B_y^2 u$), is controlled by the electromagnetic Lorenz force due to the presence of the magnetic field.

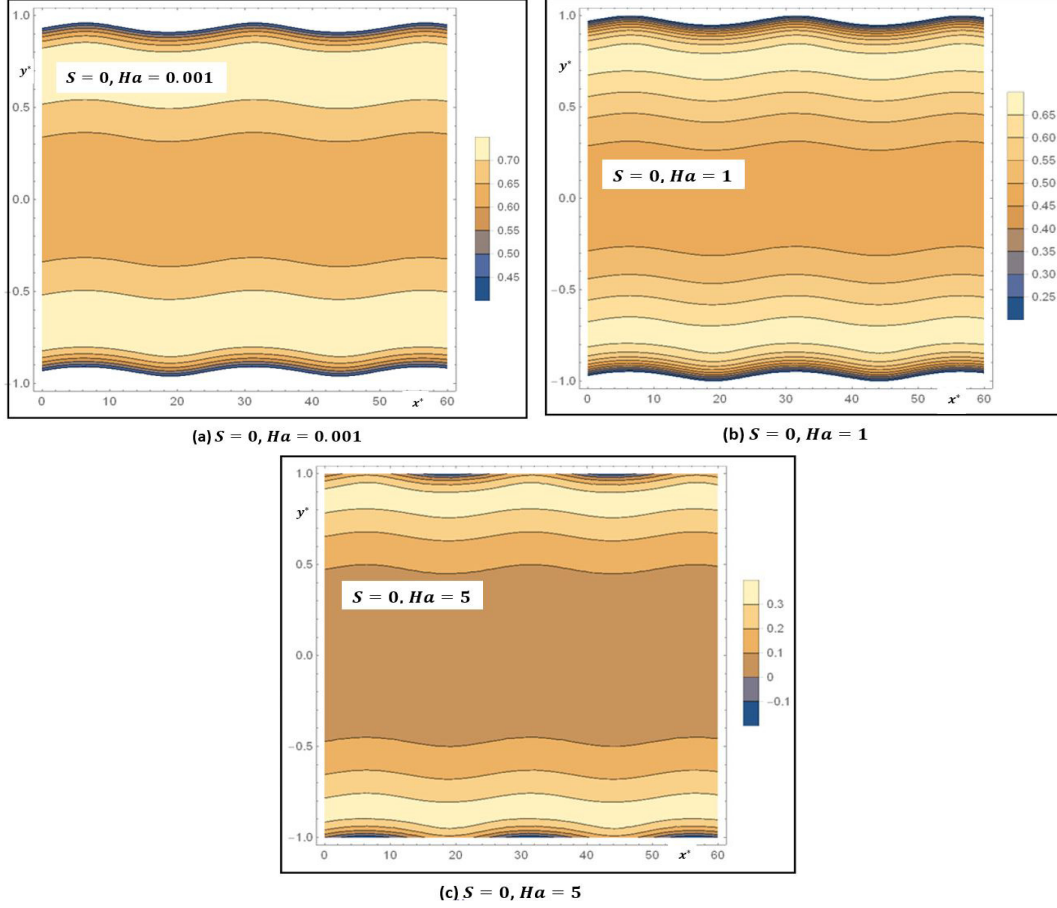


Figure 4.5: Velocity contour plot for (a) $Ha = 0.001$, (b) $Ha = 1.0$, (c) $Ha = 5.0$ with $S = 0$, $\omega = 10$, $\varepsilon = 0.025$, $Da = 0.5$, $\lambda = 0.25$.

By increasing the magnetic field, this Lorenz force enhances the decay of kinetic energy in the absence of the transverse electric field. Figs. 4.4-4.5 show that velocity distribution does not show in parabolic nature in the absence of a transverse electric field. It is noted from these figures that boundary layer thickness is reducing by increasing the magnetic field. The middle layer of fluid is more affected by Lorentz force for the large value of Ha (See Figs. 4.4-4.5). The interesting result is observed in Figs. 4.6-4.7 that in the presence of a transverse electric field ($S = 25$), the velocity distribution is changing towards the parabolic profile by increasing the magnetic field. It can be explained physically that the ‘flow-opposing’ is dominated by ‘flow-aiding’ by increasing the strength of the applied magnetic field. Therefore boundary layer thickness is increasing by increasing the magnetic field in the presence of a transverse electric field. Fig. 4.7 shows that middle layer is becoming straight line as ‘flow-aiding’ has overcome the ‘flow-opposing’ due to the presence of large magnetic effect and middle a layer does not show the effect of wavy roughness of the surface. From this results signify that effect of wavy roughness of a surface can be controlled

by applying suitable strength of magnetic and a transverse field in the presence of electroosmosis force.

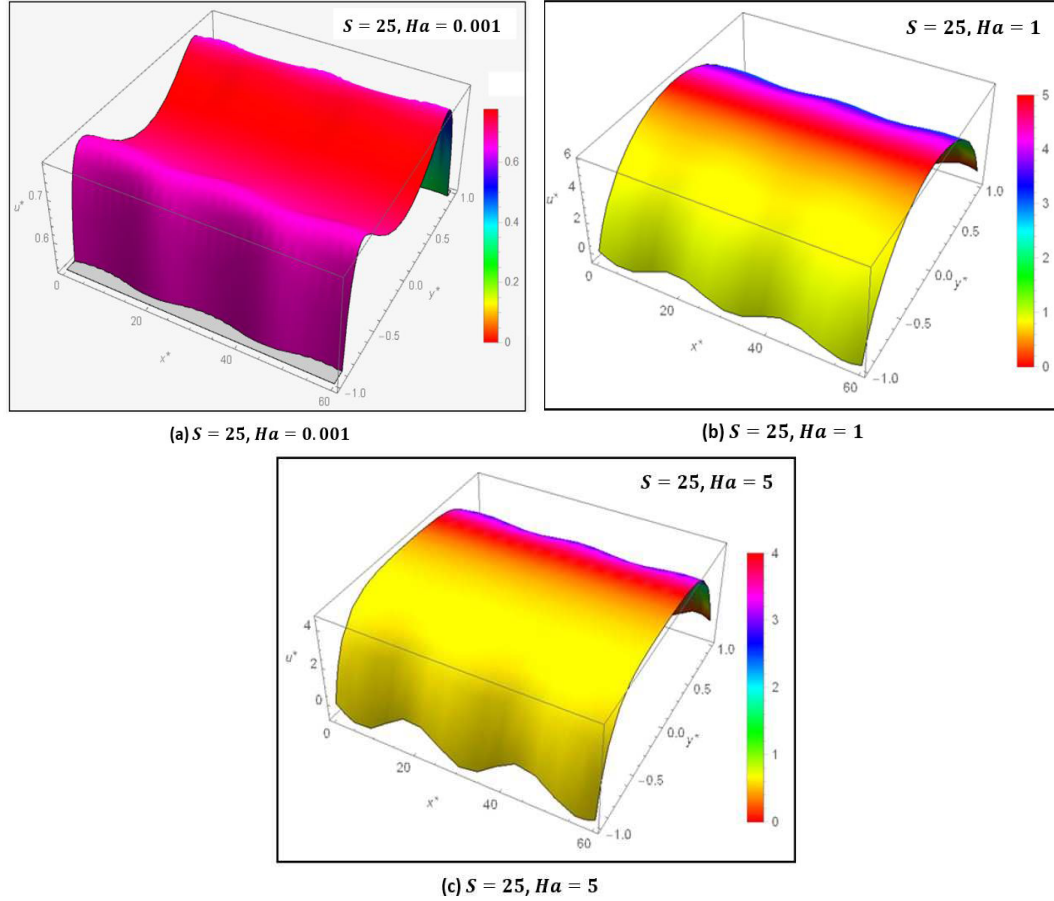


Figure 4.6: Three dimensional Velocity distribution for (a) $Ha = 0.001$, (b) $Ha = 1.0$, (c) $Ha = 5.0$ with $S = 25$, $\omega = 10$, $\varepsilon = 0.025$, $Da = 0.5$, $\lambda = 0.25$.

4.6.3 Effect of porosity on flow velocity

The effect of porosity parameter, Darcy Number (Da) on the velocity distribution represented by 3D velocity and contour profiles are depicted in Figs. 4.8-4.9 when $S = 50$, $Ha = 1$, $\varepsilon = 0.025$, $Da = 0.2$, (a) $\lambda = 0$, (b) $\lambda = 0.1$. The Darcy number is represented by the permeability of the porous medium of the micro-channel. It is observed that in the case of low Darcy number, the flow profile becomes plug flow and the middle layer of the flow does not affect by the wavenumber. But increasing the Darcy number, the permeability of the medium is increasing and the flow is becoming parabolic profile. The middle layer of flow is disturbed by increasing the value of Darcy Number. The boundary layer thickness is also affected by the Darcy number. It is also noted from the 3D velocity profile that when there is no porosity, the maximum velocity occurs in the middle layers of the flow.

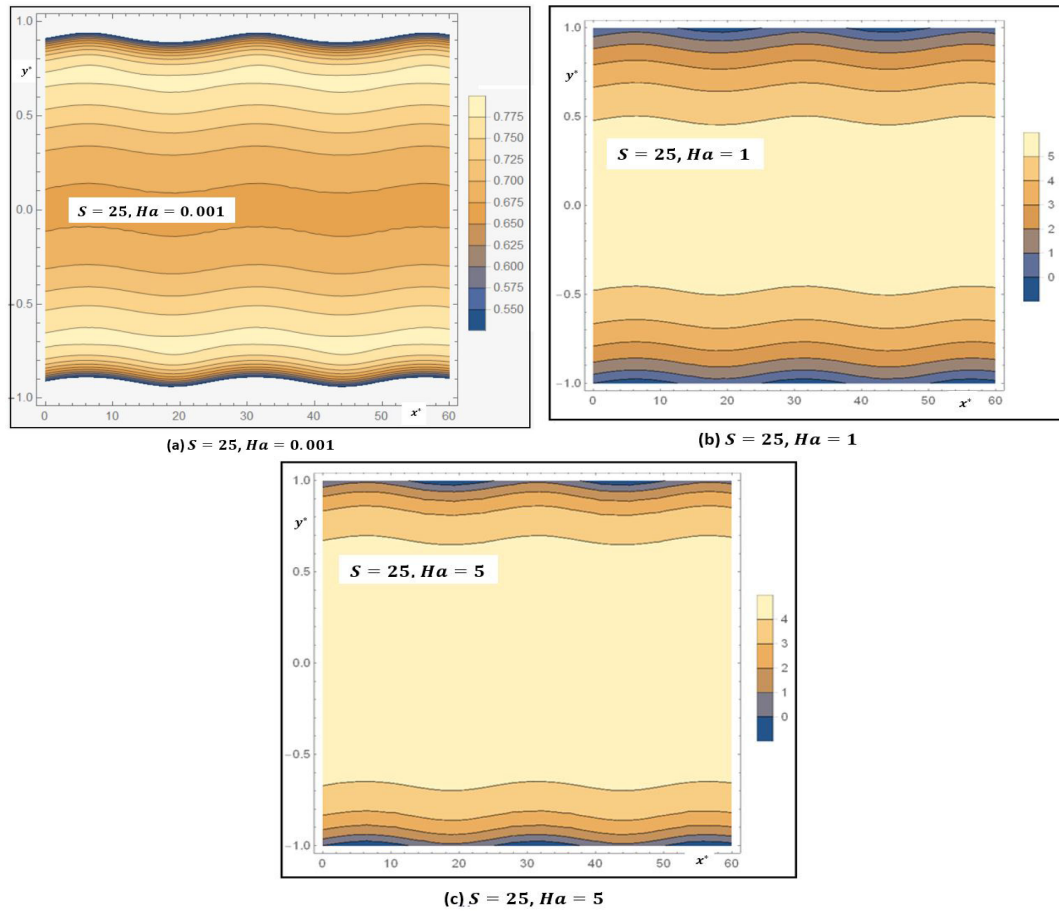


Figure 4.7: Velocity contour plot for (a) $Ha = 0.001$, (b) $Ha = 1.0$, (c) $Ha = 5.0$ with $S = 25$, $\omega = 10$, $\varepsilon = 0.025$, $Da = 0.5$, $\lambda = 0.25$.

4.6.4 Effects on mean velocity

From Eq. (4.51), the leading order perturbations to the mean velocity represented by ϕ has computed and the results have been shown in Figs. 4.10-4.12. The effect of the physical parameters Ha , Da , S and P on ϕ has examined and analyzed its results. It is noticed from Fig. 4.10(a) that in the absence of a transverse electric field, mean velocity is increasing monotonically by increasing the value of applied magnetic field Ha . But in the presence of the transverse electric field, the mean velocity is decreasing with increasing the magnetic field (lower values of Hartmann number) up to some critical value of Ha , then again the mean velocity is increasing by increasing the value of Hartmann number for the fixed other physical parameters $\omega = 10$, $\varepsilon = 0.025$, $\lambda = 0.25$.

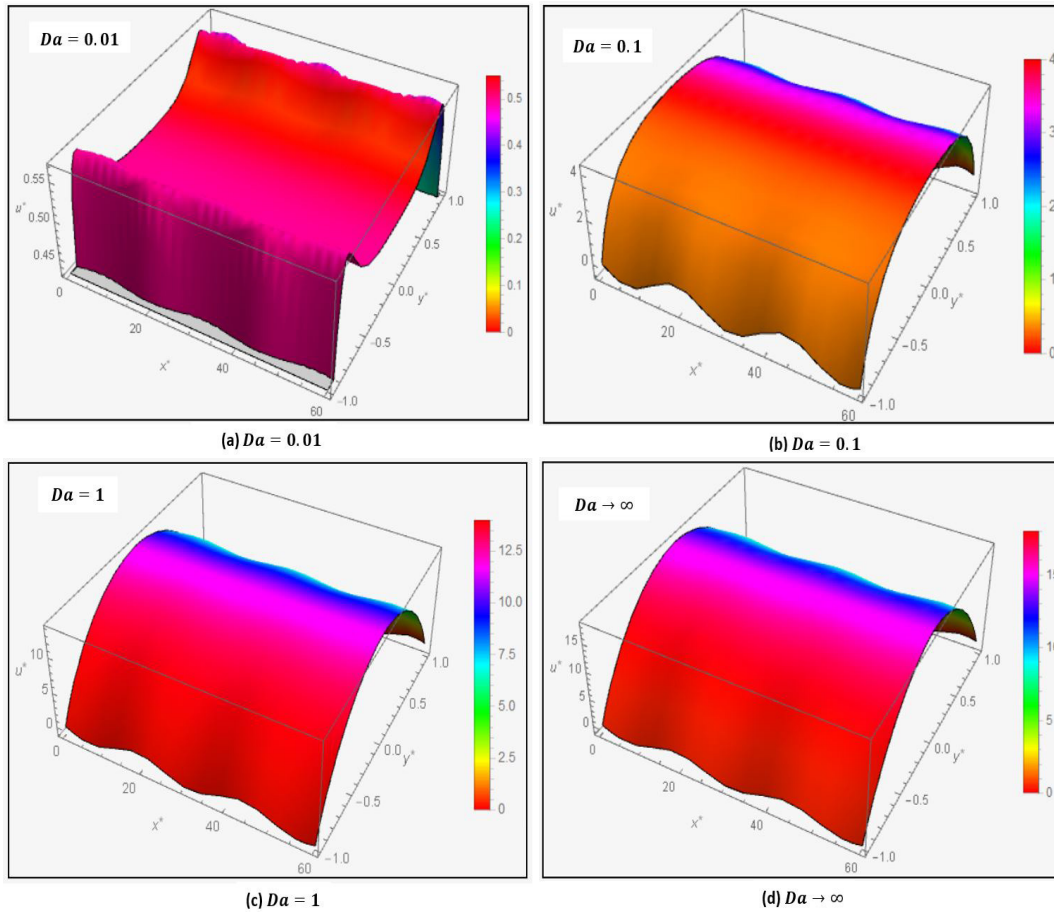


Figure 4.8: Three dimensional velocity distribution for (a) $Da = 0.01$, (b) $Da = 0.1$, (c) $Da = 1$ and (d) $Da \rightarrow \infty$ with $S = 50$, $\omega = 10$, $\varepsilon = 0.025$, $Ha = 1$, $\lambda = 0.25$.

In general, in the absence of a transverse magnetic field, only Lorentz force which is acting on the fluid particle reduces the fluid particle. But due to the electrokinetic force for electroosmosis flow, dominates the Lorentz force and the mean velocity increases with increasing the magnetic field for the constant axial electric field. This result is consistent with the physical phenomenon of electromagnetic and electrokinetic theory. Therefore, in the presence of a transverse magnetic field, aiding flow which occurs at a low magnetic field (less than 1), dominates the flow opposing due to

4.6. Results and Discussion

Lorentz force. But again for the large value of the magnetic field (greater than 1), the combined effect of electromagnetic and electrokinetic causes to increase the mean velocity by increasing the magnetic field.

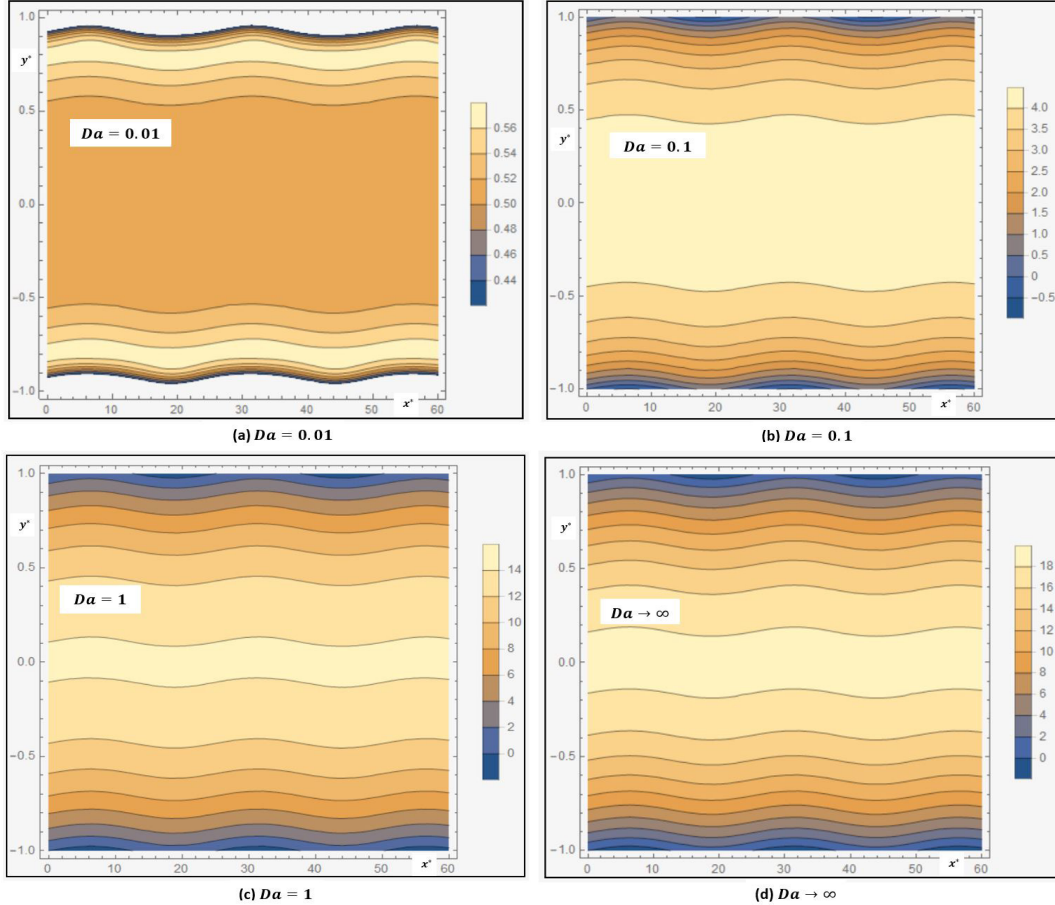


Figure 4.9: Velocity contour plot for (a) $Da = 0.01$, (b) $Da = 0.1$, (c) $Da = 1$ and (d) $Da \rightarrow \infty$ with $S = 50$, $\omega = 10$, $\varepsilon = 0.025$, $Ha = 1$, $\lambda = 0.25$.

It also can be found from Fig. 4.11 that the mean velocity is decreasing with increasing Darcy number (Da) when other all physical parameters are constant at both cases absent or present of a transverse electric field. The porosity of the micro-channel reduces the velocity of fluid flow. So when Darcy number increases the permeability of the porous increases which causes the decrease of the mean velocity of a fluid. In the presence of the transverse electric field, the mean velocity decrease with increasing the negative pressure gradient parameter P_1 (see Fig. 4.11). But when absent of the transverse electric field, the combined effect of electromagnetic and electrokinetic force infer the pressure gradient, and in this case there no effect of a pressure gradient to the mean velocity. It is also interesting to mention that for a small value of the transverse magnetic field, the mean velocity decrease by increasing the transverse electric field up to certain critical value and after that mean velocity is affected by changing the transverse electric field (see Fig. 4.12).

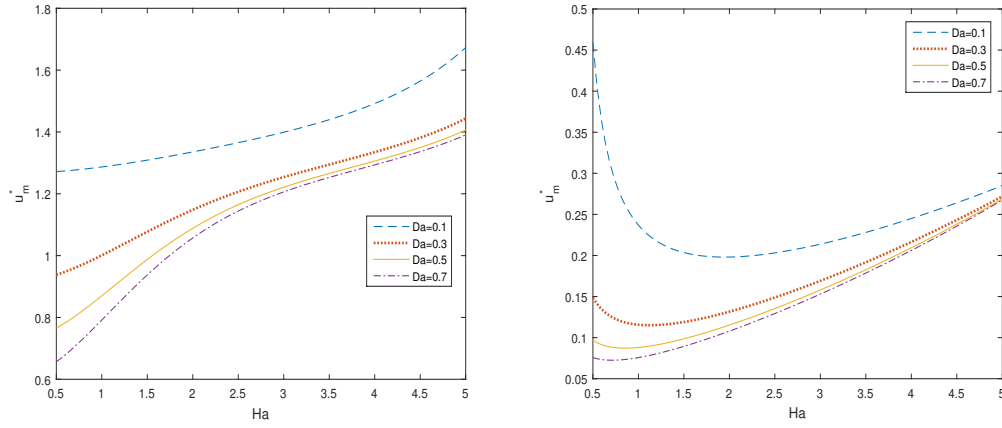


Figure 4.10: Variation of mean velocity with Ha for (a) $S = 0$, (b) $S = 50$. when $\omega = 10$, $\varepsilon = 0.025$, $\lambda = 0.25$.

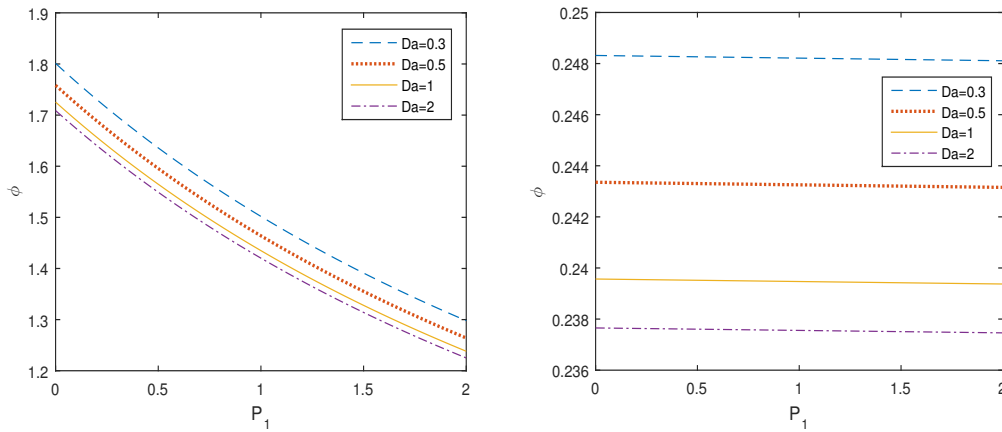


Figure 4.11: Variation of mean velocity with Pressure gradient for different values of Da when $\omega = 10$, $\varepsilon = 0.025$, $\lambda = 0.25$, (a) $S = 50$, (b) $S = 0$

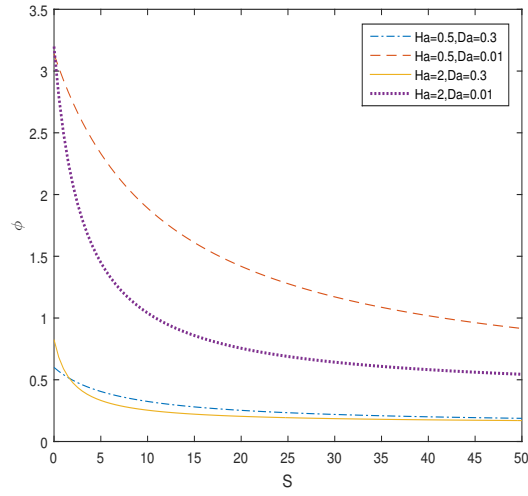


Figure 4.12: Variation of mean velocity with transverse electric field when $\omega = 10$, $\varepsilon = 0.025$, $\lambda = 0.25$.

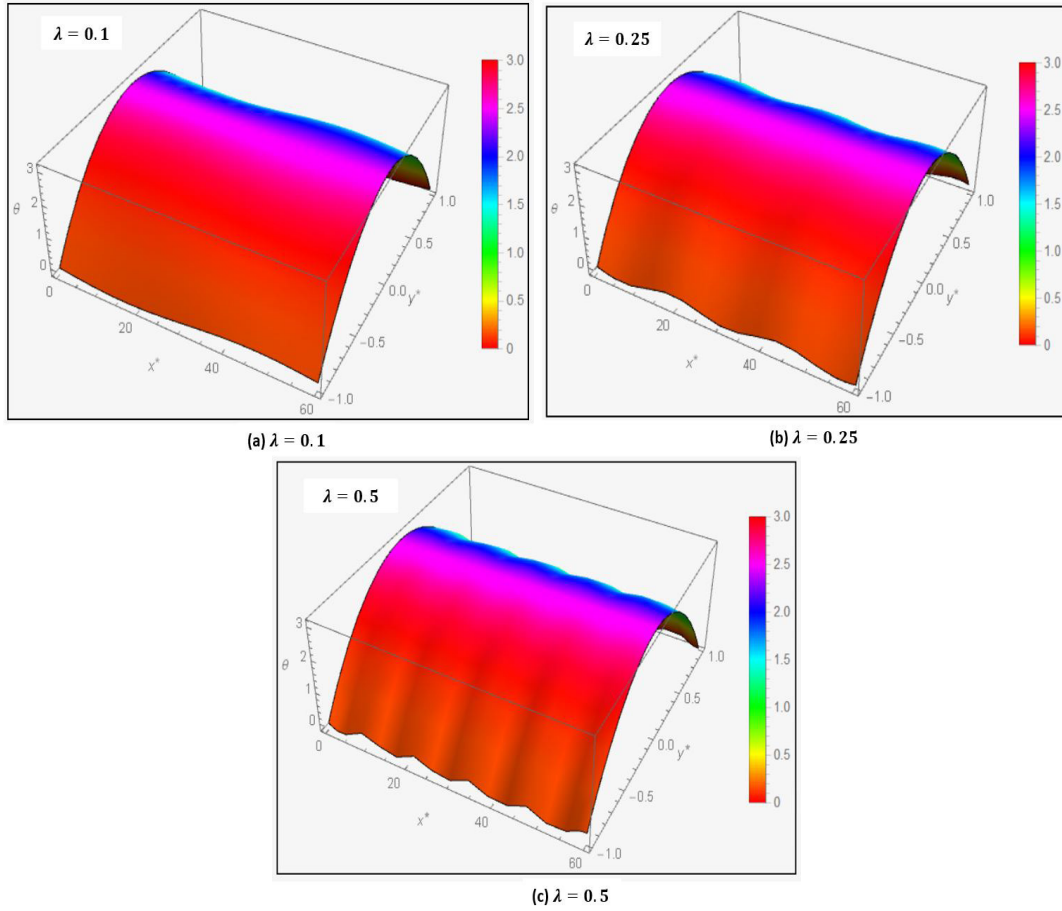


Figure 4.13: Temperature distribution for (a) $\lambda = 0.1$, (b) $\lambda = 0.25$ and (c) $\lambda = 0.5$ when $S = 50$, $\omega = 10$, $\varepsilon = 0.025$, $Da = 0.1$, $Ha = 1$, $S_j = -2$.

4.6.5 EMHD thermal characteristics: temperature variation

Figures 4.13-4.14 depict the 3D and contour plot of temperature distribution for different value wavy roughness parameter wave number (λ) for fixed other physical parameters $S = 50$, $\omega = 10$, $\varepsilon = 0.025$, $Da = 0.1$, $Ha = 1$, $S_j = -2$. It is found that the middle layer of temperature distribution is disturbed by increasing the wavenumber as the velocity near the sure is changing due to change of wave number which leads to diffusion of temperature distrusting from the surface towards the middle of micro-channel. It is also observed from the computation that the temperature of a point is increasing by ceasing the disturbance by changing the wavenumber of the wavy wall surface.

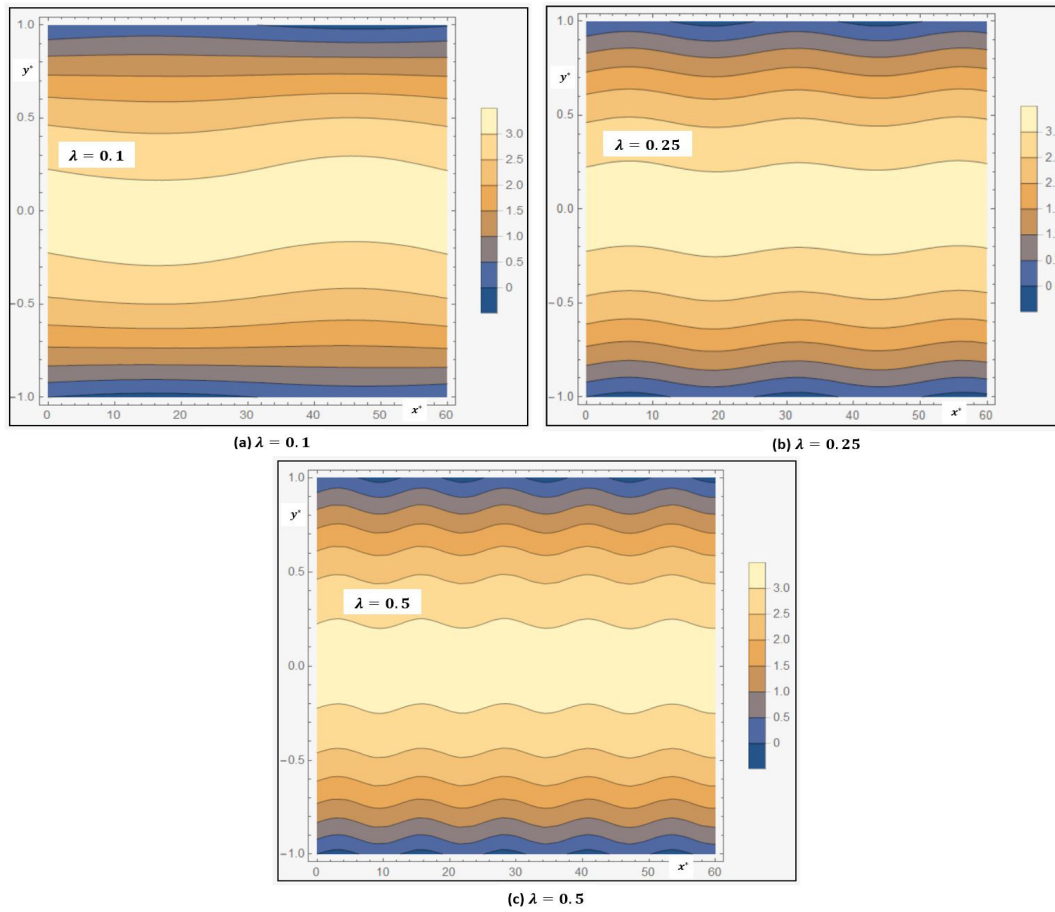


Figure 4.14: Temperature distribution contour for (a) $\lambda = 0.1$, (b) $\lambda = 0.25$ and (c) $\lambda = 0.5$ when $S = 50$, $\omega = 10$, $\varepsilon = 0.025$, $Da = 0.1$, $Ha = 1$, $S_j = -2$.

The effect of the magnetic field in the presence of a transverse electric field on temperature distribution has been displayed in Figs. 4.15-4.16. Due to the Joule heating term, the more energy will be dissipated by increasing the magnetic field which leads to increase temperature by increasing the magnetic field Ha . Combine effect of electromagnetic due to the presence of transverse magnetic and electric field and electrokinetic due to electroosmosis are playing an important role to control the temperature distribution of fluid inside the porous microchannel. It is noticed from the figure from the contour plot (Fig. 4.16) that temperature distribution in the middle of microchemical is

more disturbed by increasing the magnetic field.

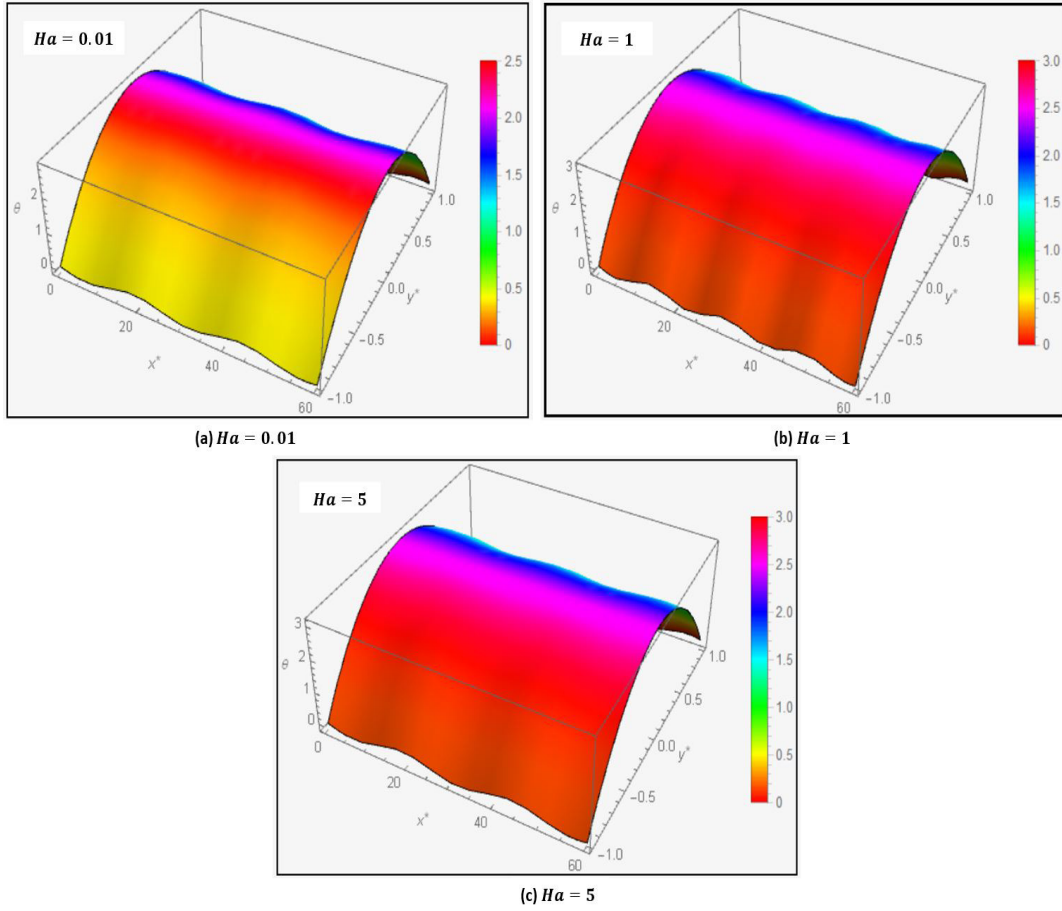


Figure 4.15: Temperature distribution for (a) $Ha = 0.01$, (b) $Ha = 1$ and (c) $Ha = 5$ when $S = 50$, $\omega = 10$, $\varepsilon = 0.025$, $Da = 0.1$, $\lambda = 0.25$, $S_j = -2$.

The effect of Darcy number Da on temperature distribution is shown in Figs. 4.17 and 4.18. The temperature of the fluid is increasing with increasing the Darcy number when other physical parameters are constant. It is interesting to note that in the low Darcy number, the temperature distribution in the middle layer is not uniform as in permeability of the porous medium is small and the temperature is unable to diffusion uniformly in the middle later in the interaction of wavy roughness of surface and porosity. But in the case of large Darcy number, the permeability of the porous medium increases and it leads to making flat temperature distribution the middle layer.

4.6.6 EMHD thermal characteristics: Nusselt number

The heat transfer characteristic of this problem has been focused on the analysis of the variation of the Nussult number for changing the various physical parameter (Fig. 4.19). The relation of convective and conductive heat transfer of the fluid is represented by the Nusselt number. It is observed that changing the amplitude (ε) of the wavy roughness of surface does not affect the rate of heat transfer as we found from our computation that temperature discussion does not affect by the

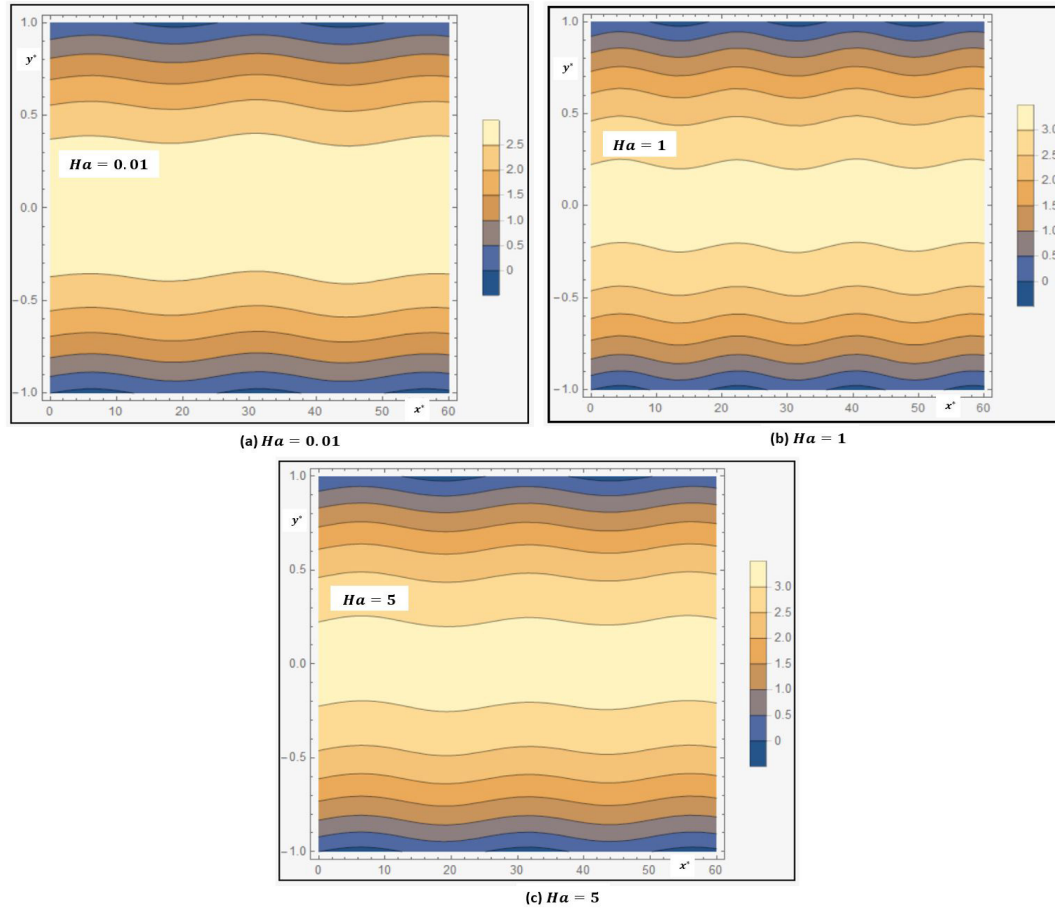


Figure 4.16: Temperature distribution contour for (a) $Ha = 0.01$, (b) $Ha = 1$ and (c) $Ha = 5$ when $S = 50$, $\omega = 10$, $\varepsilon = 0.025$, $Da = 0.1$, $\lambda = 0.25$, $S_j = -2$.

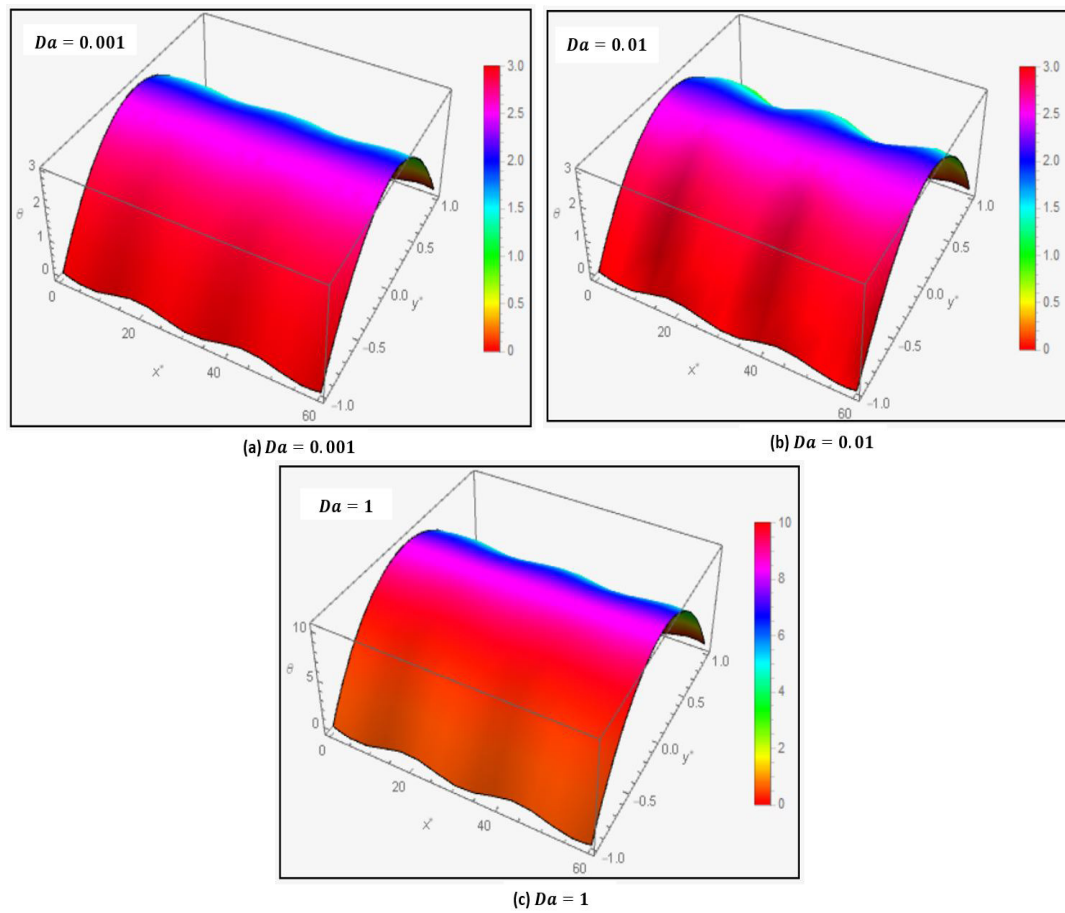


Figure 4.17: Temperature distribution for (a) $Da = 0.001$, (b) $Da = 0.01$ and (c) $Da = 1$ when $S = 50$, $\omega = 10$, $\varepsilon = 0.025$, $Ha = 1$, $\lambda = 0.25$, $S_j = -2$.

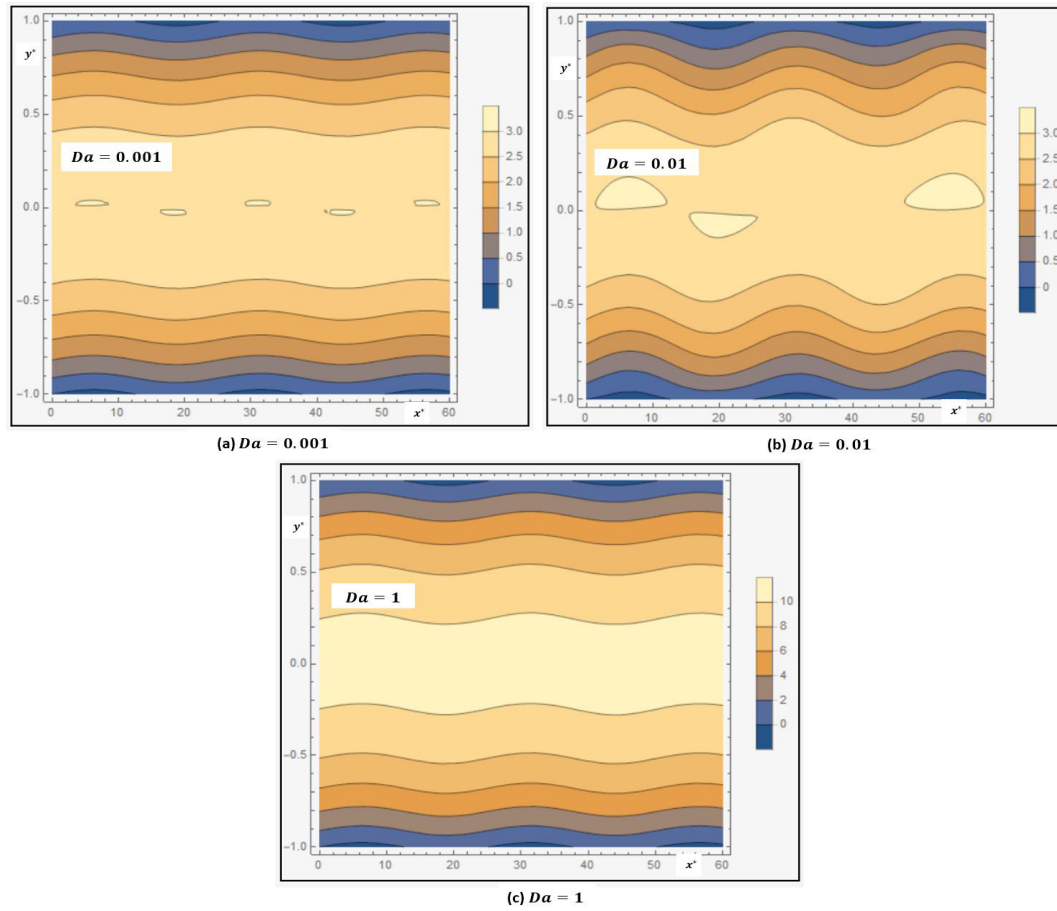


Figure 4.18: Temperature distribution contour for (a) $Da = 0.001$, (b) $Da = 0.01$ and (c) $Da = 1$ when $S = 50$, $\omega = 10$, $\varepsilon = 0.025$, $Ha = 1$, $\lambda = 0.25$, $S_j = -2$.

4.7. Conclusions

ϵ . But it is interesting to note that the transverse electric field controls the rate of heat transfer. From the energy equation, it is observed that the Joule heat is increasing with increases transverse electric field. Therefore the diffusion of temperature becomes more by increasing the transverse electric field and value of Nusselt number decreases. It is found that convective heat transfer is more than the diffusion rate of temperature by increasing the Darcy number. So Nusselt number increases by increasing the Darcy number (see Fig. 4.19(b)). By increasing the magnetic strength, Joule heating which is increases enhances the temperature diffusion rate. But electromagnetic force which becomes more by increasing the magnetic field leads to dominating the temperature dissipation rate. It results in Nusselt number is increasing by increasing the magnetic field.

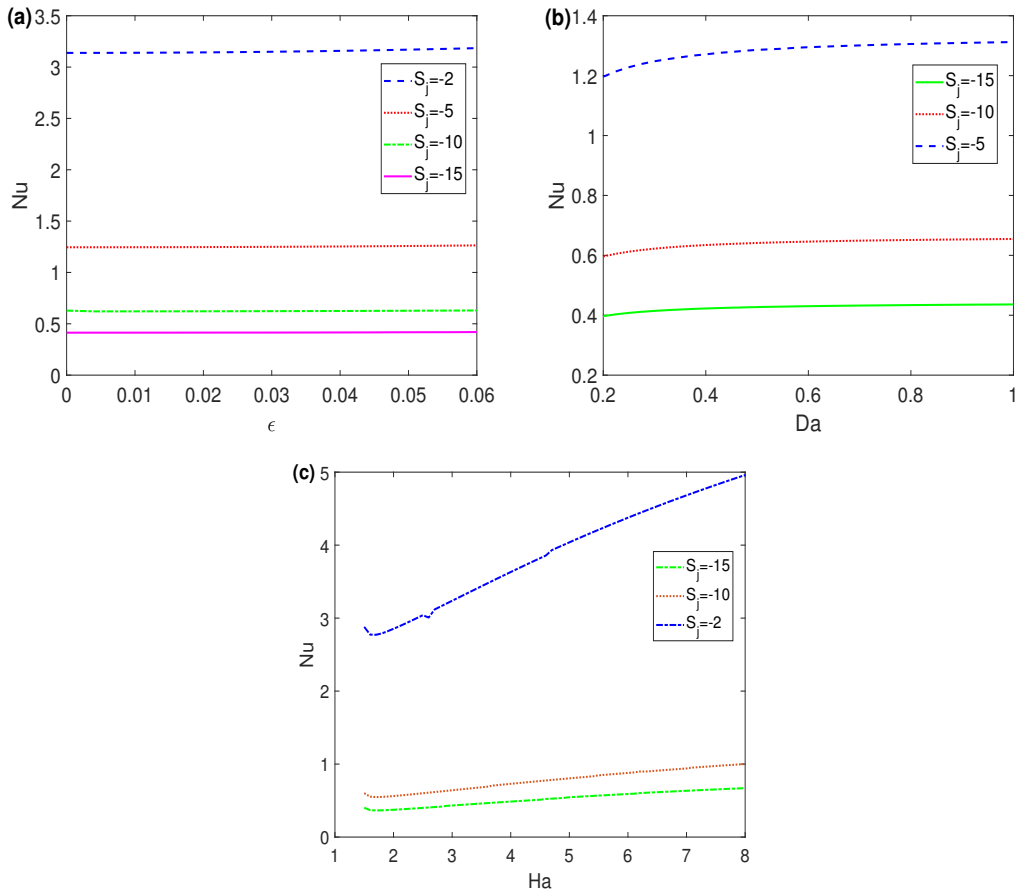


Figure 4.19: Nusselt number with (a) variation of ϵ for $Da = 0.1$, $Ha = 0.5$, (b) Variation Darcy Number Da for $\epsilon = 0.025$, $Ha = 0.5$, (c) Variation Hartmann Number Ha for $\epsilon = 0.025$, $Da = 0.1$, when other parameters are $S = 50$, $\omega = 10$, $\lambda = 0.25$.

4.7 Conclusions

The effect of regular roughness of wall in the presence of united electrokinetic and electromagnetic force with constants pressure gradient on the velocity and temperature of fluid flow in microchannel

has been studied. It is interesting to note that approximation analytical solutions for velocity and temperature of the fluid flow has been derived by using the perturbation technique and analyse its heat transfer characteristics.

In this chapter, the following points are concluded.

- It is noted that fluid flow does not develop fully in the absence of a transverse electric field. But in the presence of a transverse electric field, the flow developed fully by increase the applied magnetic field. The nature of the boundary layer is altered by the effect of changing the value of wavenumber.
- The middle layer of flow is affected by the wavy roughness of the surface in the presence of a low magnetic field. But the nature of middle due to wavy roughness has changed by increase the applied magnetic in the presence and absence of transverse electric field.
- It is observed that the flow becomes plug flow in the case of low Darcy number, and the middle layer of the flow does not affect by the wavenumber. The middle layer of flow is disturbed by increasing the value of Darcy Number and flow is becoming parabolic profile.
- Mean velocity monotonically increasing by increasing the magnetic field in the absence of a transverse magnetic field. But in the presence of a transverse electric field, the nature of mean velocity is reverse at the low magnetic field and large magnetic field. Interaction of electrokinetic force and Lorentz force, the mean velocity increases with increasing the magnetic field for constant axial electric field. The mean velocity of fluid decreases by increasing the Darcy number,
- It is interesting to note that the middle layer of temperature distribution is affected by increasing the wavenumber of the wavy wall surface. By the increasing magnetic field, magnetic diffusion will be more by Joule heating in the increasing magnetic field, as result temperature increases. The temperature of the fluid is increasing with increasing the Darcy number but in the low Darcy number, the temperature distribution in the middle layer is not uniform.
- The amplitude of the wavy roughness of the surface does not affect the rate of heat transfer. But it is interesting to note that transverse electric field controls the rate of heat transfer and the diffusion of temperature becomes more by increasing the transverse electric field and value of Nusselt number decreases. Nusselt number increases by increasing the Darcy number.

5

Surface Roughness on EMHD thermo-fluidic transport in a porous microchannel

5.1 Introduction

Electrokinetic flow in the microchannels has received special attention from researchers in the past years because of their microfluidics applications in the fabrication of lab-chip and medical devices. The theory of electromagnetohydrodynamics (electrokinetic flow in the presence of a magnetic field) is recently a developing topic of research to assess the flow controlling parameters. Several theoretical aspects for observing the flow characteristics in a microchannel with regular surface (Ng [2013]; Wang et al. [2016]; Vargas et al. [2017]) have been modeled to apply widely in biomedical devices (West et al. [2002]; Ohno et al. [2008]), micro-electronic devices (Nandy et al. [2008]; Becker and Gartner [2000]), lab-on-chip devices (Stone et al. [2004]), electro-osmosis micropumps (Arulanandam and Li [2000]; Rahmati et al. [2020]), sample separation (Wu et al. [2010]), magnetohydrodynamic micropump (Jang and Lee [2000]; Nash and Fritsch [2016]), electromagnetohydrodynamic (EMHD) micropumps (Homsy et al. [2005]; Nguyen and Kassegne [2008]; Lemoff and Lee [2000]; Eijkel et al. [2003]; Huang et al. [2000]), specific mixing (Erickson and Li [2002]), and in the micro-electro-mechanical systems (MEMS).

Magnetohydrodynamic (MHD) flow phenomena describes the motion of electrically conducting fluids under the influence of an external magnetic field and several investigators (Mahanthesh

The content of this chapter has been published in *Colloids and Surfaces A: Physicochemical and Engineering Aspects* (Elsevier), 650:129336 (2022).

[2021]; Laughlin [1989]; Mahanthesh [2020]; Rana et al. [2021a]; Rhodes and Smolentsev [2021]; Mackolil and Mahanthesh [2021]; Reza and Rana [2021]; Abdelhameed [2021]) paid their attention to solve various type of problems in multiple disciplines. Also, some researchers are focused on MHD mixed convection flow by considering different type of fluids (Krishna et al. [2021]; Selimefendigil and Chamkha [2020]; Krishna et al. [2020]; Selimefendigil et al. [2020]; Raza et al. [2019]; Alsabery et al. [2019a]). Recently, micro-fabrication technology is very much impelled by magnetohydrodynamics (MHD) (Abdulhameed et al. [2019]; Wang et al. [2020]) and electromagnetohydrodynamics (EMHD) (Reza et al. [2019]) for its wide range of applications. Sarkar et al. [2016] explored the hydro-electric energy conversion in EMHD flow through microchannel to optimize the energy transfer in microfluidic systems. In this study, they presented analytical as well as numerical results to assess overall energy transfer in the microscale systems. Yang et al. [2019] examined the MHD electroosmotic flow and heat transfer performance in the microchannel, wherein they discussed the impact of viscous dissipation, Joule heating and the heat generation due to electromagnetic force on the electrokinetic flow phenomena, and solved the governing equations by the method of separation of variables. Rashid and Nadeem [2019] presented a mathematical model to find the impact of nanoparticles on the EMHD flow through a corrugated microchannel by applying the perturbation method. The impact of waviness on the walls of the microchannel on the velocity and temperature is discussed by them and concluded that an increment of wave number increases the corrugation of the microchannel and thereby changes the flow characteristics. Entropy generation on EMHD flow through porous asymmetric microchannel is studied by Noreen et al. [2021] by taking into account water based nanofluids. They inspired by nano-medicine technology and solved a non-linear mathematical model numerically to discuss the heat transfer rate by considering different nanoparticles. It has been observed that total entropy generation of titania-water nanofluid is lower than copper-water nanofluid and alumina-water nanofluid. The effect of combined EMHD flow in a corrugated microchannel is discussed by Buren et al. [2017], wherein they reported that the flow is disturbed by wall roughness of the channel and the mean velocity is reduced by the wall roughness. Three dimensional surface corrugation on EMHD flow is performed by Li et al. [2019] with two sinusoid functions and obtained the analytical solutions for the governing equations by utilizing the perturbation method. They pointed out that the flow rate can be maximum for increasing the strength of a magnetic field. Ranjit and Shit [2017] estimated the entropy generation of couple stress fluid in a narrow confinement with asymmetric porous surface to develop microfluidic devices in biomedical and industrial technology. They found that the entropy generation is maximum in the middle of the lower and upper portion of the microchannel.

Flow transport and heat transfer in the microchannel with waviness was widely studied numerically (Yang and Liu [2008]; Alsabery et al. [2019b]; Tayebi and Chamkha [2020]; Hitt and McGarry [2004]; Hadigol et al. [2011]) and experimentally with an aim to its extensive applications in cooling system and computational biology (Shit et al. [2016b]; Yang et al. [2021]; Shit et al. [2016c]; Vasista et al. [2021]; Jimenez et al. [2019]; Deng et al. [2021]). Cakir and Akturk [2021] investigated the heat transfer characteristics of nanofluids in a wavy microchannel using the computational techniques. They explored the thermal conductivity efficiency and convective heat transfer coeffi-

cients of nanofluid flow for different Reynolds number and volumetric nanoparticle ratio. A three-dimensional numerical investigation on two phase boiling flow through wavy microchannel has been carried out by [Tiwari and Moharana \[2021\]](#). They compared the results of boiling instability and bubble behavior of single and two phase flow with straight and wavy microchannel. It is concluded that the presence of waviness of the channel, the laminar flow layers and the enhancing effect of convective heat transfer reduce the flow instability. A mathematical model has been proposed by [Saleem et al. \[2021\]](#) to perform peristaltic electroosmotic flow of micropolar Bingham visco-plastic fluid by applying lubrication theory. They observed that the axial velocity of the flow reduces but micro-angular velocity increases with a rise in the electric field strength and remarked that electroosmotic flow helps to control the flow characteristics. [Khan et al. \[2021\]](#) evaluated a numerical simulation on the thermal characteristics of nanofluid using alumina nanoparticles in ANSYS FLU-ENT by focusing cooling performance of straight, wavy, and dual wavy micro-channel. This study shows that dual waviness with a flat base and wavy base showed maximum increase of Nusselt number more than fifty percent when compared with straight channel of equal concentration. An experimental investigation on boiling instability in sinusoidal microchannel is studied by [Ma et al. \[2021\]](#), wherein they observed the pressure and temperature fluctuations of the sinusoidal wavy microchannel with secondary walls (SWSC microchannel). Their experimental investigations reported that the SWSC microchannels can achieve better heat removal performance than the smooth rectangular microchannels. A numerical study on the electroosmotic flow through a microchannel with complex wavy wall has been investigated by [Yau et al. \[2011\]](#). They studied the steady-state electroosmotic flow by comparing with the traditional pressure driven flow and observed the flow recirculations on the pressure driven flow. However, no recirculation on the electroosmotic flow through the microchannel with complex wavy surface is observed. [Cho et al. \[2013\]](#) has performed a numerical investigation on the electroosmosic flow through a complex wavy microchannel by a periodic electric field. In this case, the flow recirculations are generated in the trough region of the wavy walls and the velocity profiles are more sensitive near the wavy surface. An exact solution for electroosmotic flow in wavy microchannel between a plane wall and a sinusoidal wall is investigated by [Xia et al. \[2009\]](#) using boundary integral method by employing the complex functions. They concluded that the electric field has changed due to the waviness of the surface and the recirculation bubbles are found because of the external forces and the geometry of the microchannel. [Kang and Suh \[2009\]](#) analyzed a numerical simulation on electroosmotic flow in microchannel with wavy rough surface. They predicted the flow transport by using the Poisson-Nernst-Planck model and remarked that the ionic-species transport depend on the shape of the rough surface.

Most of the above studies have conducted the electroosmotic flow numerically through microchannels with a complex wavy surface. However, the present chapter performs an analytical study on the flow and heat transfer characteristics of the electrolyte solution through a porous microchannel with a complex wavy rough surface. An approximate analytical solution has been investigated by applying the perturbation technique to observe the velocity and temperature profiles having the complex wavy roughness of the wall of the microchannel. Three-dimensional velocity profiles and temperature distributions along with the volumetric flow rate and heat transfer rate are

presented. The Joule heating effects on the streamline contours and isotherms are observed. The results have been compared between the straight and wavy surface microchannel.

5.2 Problem statement and Mathematical Formulation

This study performs the electromagnetohydrodynamic flow and heat transfer characteristics of a symmetric electrolyte between two fixed complex wavy rough walls of the microchannel. The rough surfaces of the microchannel are kept with a height $2H$, width W ($2H \ll W$), and length L ($2H \ll L$). We assume that steady and fully developed flow of a Newtonian fluid is driven under the combined influence of pressure gradient and electromagnetic force. The channel width W is taken along x -direction and the channel length L is assumed along the z -direction. For the purpose of mathematical modeling, we consider the electromagnetohydrodynamic flow of an incompressible, viscous and Newtonian fluid. We consider the rectangular microchannel with origin at the the middle of the channel (cf. Fig. 5.1). The mathematical expressions for the upper and lower walls of the wavy surfaces (Cho et al. [2013]) are illustrated as

$$\begin{aligned} \tilde{Y}_u(x) &= H + 2H \left[\alpha \sin\left(2\pi \frac{x}{H}\right) + \lambda \sin\left(4\pi \frac{x}{H}\right) \right], \\ &\text{and} \\ \tilde{Y}_l(x) &= -H - 2H \left[\alpha \sin\left(2\pi \frac{x}{H}\right) + \lambda \sin\left(4\pi \frac{x}{H}\right) \right], \end{aligned} \quad (5.1)$$

where α and λ denote the wave amplitudes.

In this investigation, the fluid flow is generated by the applied electric field \mathbf{E} and the applied magnetic field \mathbf{B} , which are applied along z -direction and y -direction respectively. Therefore, the flow is driven by the combined electromagnetohydrodynamic (EMHD) force and pressure gradient along the z -direction.

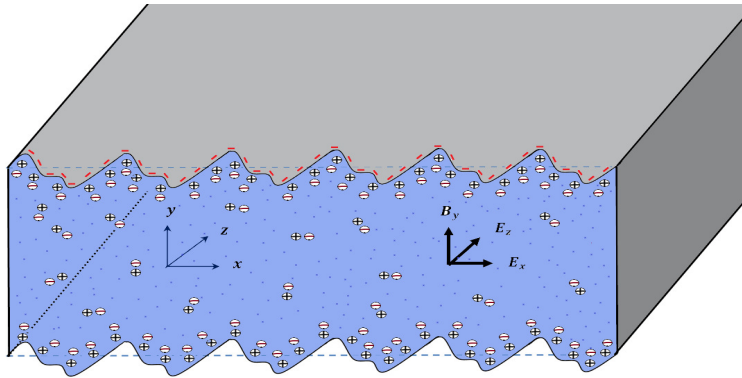


Figure 5.1: Physical Sketch of the problem

5.3 Electrical potential distribution

The ionization of electrolyte solution formulates an electric double layer (EDL) due to electroosmosis. Two layers form the EDL one is the stern layer which is a very thin layer of ions absorbed on the charged surface, and another is the diffuse layer, where the ions take a rapid thermal motion. The thickness of the EDL is typical of the order of a few nanometers, which depends on the concentration of the electrolyte solution.

The electrostatic potential (φ) is constituted by the combination of EDL potential (ψ) and an applied potential (Φ). Therefore, it can be written as (Kang and Suh [2009]; Keramati et al. [2016]; Lei et al. [2019]; Martinez et al. [2016a])

$$\varphi(x, y, z) = \Phi(x, y, z) + \psi(x, y, z). \quad (5.2)$$

5.3.1 The effects of roughness on the applied potential distribution

An external electric field is defined as $\mathbf{E} = -\nabla\varphi$, where φ is the electrostatic potential. In this article, we assumed that the applied electric potential Φ is depends on the wall roughness of the microchannel. Therefore, it is very interesting phenomenon to investigate the effects of surface roughness on the applied electric potential Φ and consequently on the flow characteristics. The externally applied electric potential Φ satisfies the Laplace's equation (Kang and Suh [2009]; Lei et al. [2019]),

$$\nabla^2\Phi = 0. \quad (5.3)$$

By introducing the dimensionless variables $x^* = \frac{x}{H}$, $y^* = \frac{y}{H}$, $z^* = \frac{z}{H}$ and $\Phi^* = \frac{\Phi}{E_z H}$ in Eq. (5.3), we find

$$\nabla^{*2}\Phi^* = 0. \quad (5.4)$$

Similarly, the boundary conditions reduces to (cf. Lei et al. [2019])

$$\frac{\partial\Phi^*}{\partial n} = \nabla^*\Phi^* \cdot \hat{n}_i = 0, \quad i = 1, 2, \quad (5.5)$$

on the rough surface, where \hat{n}_i is the unit normal on upper wall and lower wall of the microchannel respectively, are given by

$$\hat{n}_1 = \frac{\nabla^*\{y^* - (1 + \varepsilon f(x^*))\}}{\|\nabla^*\{y^* - (1 + \varepsilon f(x^*))\}\|}, \quad (5.6)$$

and

$$\hat{n}_2 = \frac{\nabla^*\{y^* - (-1 - \varepsilon f(x^*))\}}{\|\nabla^*\{y^* - (-1 - \varepsilon f(x^*))\}\|}, \quad (5.7)$$

where $f(x^*) = [\sin(2\pi x^*) + R_\alpha \sin(4\pi x^*)]$, $\varepsilon = 2(\lambda/R_\alpha)$, $R_\alpha = \frac{\lambda}{\alpha}$ is the amplitude ratio of the complex wavy rough surface.

Now the boundary conditions take in the following form

$$\frac{\partial\Phi^*}{\partial y^*} - 2\pi\varepsilon\{\cos(2\pi x^*) + 2R_\alpha \cos(4\pi x^*)\}\frac{\partial\Phi^*}{\partial x^*} = 0, \quad \text{at } y^* = 1 + \varepsilon f(x^*), \quad (5.8)$$

and

$$\frac{\partial \Phi^*}{\partial y^*} + 2\pi\epsilon\{\cos(2\pi x^*) + 2R_\alpha \cos(4\pi x^*)\} \frac{\partial \Phi^*}{\partial x^*} = 0, \text{ at } y^* = -1 - \epsilon f(x^*). \quad (5.9)$$

We seek Φ^* in the form of perturbation method that follows

$$\Phi^* = \Phi_0^* + \epsilon \Phi_1^* + \epsilon^2 \Phi_2^* + \dots. \quad (5.10)$$

Substituting (5.10) in Eq. (5.4), one may write

$$\nabla^{*2} \Phi_i^* = 0, \quad i = 0, 1, 2, \dots. \quad (5.11)$$

Again substituting (5.10) in Eqs. (5.8) and (5.9) yield

$$\begin{aligned} \left(\frac{\partial \Phi_0^*}{\partial y^*} + \epsilon \frac{\partial \Phi_1^*}{\partial y^*} + \epsilon^2 \frac{\partial \Phi_2^*}{\partial y^*} + \dots \right) - \epsilon \left\{ 2\pi \cos(2\pi x^*) + 4\pi R_\alpha \cos(4\pi x^*) \right\} \\ \left(\frac{\partial \Phi_0^*}{\partial x^*} + \epsilon \frac{\partial \Phi_1^*}{\partial x^*} + \epsilon^2 \frac{\partial \Phi_2^*}{\partial x^*} + \dots \right) = 0, \text{ at } y^* = 1 + \epsilon f(x^*), \end{aligned} \quad (5.12)$$

and

$$\begin{aligned} \left(\frac{\partial \Phi_0^*}{\partial y^*} + \epsilon \frac{\partial \Phi_1^*}{\partial y^*} + \epsilon^2 \frac{\partial \Phi_2^*}{\partial y^*} + \dots \right) + \epsilon \left\{ 2\pi \cos(2\pi x^*) + 4\pi R_\alpha \cos(4\pi x^*) \right\} \\ \left(\frac{\partial \Phi_0^*}{\partial x^*} + \epsilon \frac{\partial \Phi_1^*}{\partial x^*} + \epsilon^2 \frac{\partial \Phi_2^*}{\partial x^*} + \dots \right) = 0, \text{ at } y^* = -1 - \epsilon f(x^*). \end{aligned} \quad (5.13)$$

The boundary conditions (5.12) and (5.13) are expanded respectively about $y^* = 1$ and $y^* = -1$, and then one may easily write

$$\frac{\partial \Phi_0^*}{\partial y^*} = 0, \text{ at } y^* = 1, \quad (5.14)$$

$$\frac{\partial \Phi_0^*}{\partial y^*} = 0, \text{ at } y^* = -1, \quad (5.15)$$

$$\frac{\partial \Phi_1^*}{\partial y^*} + f(x^*) \frac{\partial^2 \Phi_0^*}{\partial y^{*2}} - \left\{ 2\pi \cos(2\pi x^*) + 4\pi R_\alpha \cos(4\pi x^*) \right\} \frac{\partial \Phi_0^*}{\partial x^*} = 0, \text{ at } y^* = 1, \quad (5.16)$$

$$\frac{\partial \Phi_1^*}{\partial y^*} - f(x^*) \frac{\partial^2 \Phi_0^*}{\partial y^{*2}} + \left\{ 2\pi \cos(2\pi x^*) + 4\pi R_\alpha \cos(4\pi x^*) \right\} \frac{\partial \Phi_0^*}{\partial x^*} = 0, \text{ at } y^* = -1, \quad (5.17)$$

$$\begin{aligned} \frac{\partial \Phi_2^*}{\partial y^*} + f(x^*) \frac{\partial^2 \Phi_1^*}{\partial y^{*2}} + \frac{1}{2} \{f(x^*)\}^2 \frac{\partial^3 \Phi_0^*}{\partial y^{*3}} - \left\{ 2\pi \cos(2\pi x^*) + 4\pi R_\alpha \cos(4\pi x^*) \right\} \\ \left\{ \frac{\partial \Phi_1^*}{\partial x^*} + f(x^*) \frac{\partial^2 \Phi_0^*}{\partial x^* \partial y^*} \right\} = 0, \text{ at } y^* = 1, \end{aligned} \quad (5.18)$$

$$\begin{aligned} \frac{\partial \Phi_2^*}{\partial y^*} - f(x^*) \frac{\partial^2 \Phi_1^*}{\partial y^{*2}} + \frac{1}{2} \{f(x^*)\}^2 \frac{\partial^3 \Phi_0^*}{\partial y^{*3}} + \left\{ 2\pi \cos(2\pi x^*) + 4\pi R_\alpha \cos(4\pi x^*) \right\} \\ \left\{ \frac{\partial \Phi_1^*}{\partial x^*} - f(x^*) \frac{\partial^2 \Phi_0^*}{\partial x^* \partial y^*} \right\} = 0, \text{ at } y^* = -1. \end{aligned} \quad (5.19)$$

In order to obtain the solution of applied potential Φ^* , we have to solve the Eq. (5.11) with the linked boundary conditions (5.14)-(5.19). It is worthwhile to mention here that when $\varepsilon = 0$ (unperturbed), then there is no roughness in the microchannel. In this case, the normalized applied electric field acts simply in z - and x -directions and the gradient of voltage should be constant in the x -direction as well as in z -direction. By solving Eq. (5.11) (for $i = 0$) subject to the boundary conditions (5.14) and (5.15), one can easily notice that the solution of Φ_0^* is independent of y^* . Hence the solution of Φ_0^* can be written as

$$\Phi_0^* = C_1 x^* + C_2 z^* + C_3, \quad (5.20)$$

where, C_1 , C_2 and C_3 are constants. Furthermore, the solutions of Φ_1^* and Φ_2^* can be evaluated as

$$\Phi_1^* = -C_1 \left\{ 2\pi \cos(2\pi x^*) + 4\pi R_\alpha \cos(4\pi x^*) \right\} \frac{\cosh(\lambda y^*)}{\cosh(\lambda)}, \quad (5.21)$$

$$\begin{aligned} \Phi_2^* = C_1 \left\{ 2\pi \cos(2\pi x^*) + 4\pi R_\alpha \cos(4\pi x^*) \right\} \left\{ \lambda^2 \{f(x^*)\}^2 - 4\pi^2 \cos(2\pi x^*) \right. \\ \left. - 16\pi^2 R_\alpha \cos(4\pi x^*) \right\} \frac{\cosh(2\lambda y^*)}{\cosh(2\lambda)}. \end{aligned} \quad (5.22)$$

5.3.2 The effects of roughness on the EDL potential distribution

We obtain the net charge density ρ_e within the electrical double layer from the Poisson equation $\nabla^2 \psi = -\frac{\rho_e}{\varepsilon}$. In general, the Nernst-Planck equations describe the relation between electrostatic potential and electric charge density. However, the electric charge density is described by the Boltzmann equation for the hydrodynamically developed and thermodynamic equilibrium conditions (Sadeghi et al. [2012]). Utilizing this Boltzmann equation, the electric charge density for the electrolytes acquainted with the relation between the electric potential ψ and the charge density ρ_e , which is described as follows (Masliyah and Bhattacharjee [2006]):

$$\rho_e = 2ez_0 n_0 \sinh\left(\frac{ez_0 \psi}{k_B T_{av}}\right), \quad (5.23)$$

where n_0 is the ion density (in molar unit), e is the electron charge, z_0 is the valance, k_B is the Boltzmann constant, and T_{av} is the absolute temperature, ε denoted permittivity constant. $\left(\frac{ez_0 \psi}{k_B T_{av}}\right) \ll 1$ as ψ is significantly small. Thus by Dybye-Hückel linearization principle (Masliyah and Bhattacharjee [2006]), the term $\sinh\left(\frac{ez_0 \psi}{k_B T_{av}}\right)$ can be approximated to $\left(\frac{ez_0 \psi}{k_B T_{av}}\right)$. Hence, substituting the net charge density expression into the Poisson equation, then the Poisson equation reduces to the

Poisson-Boltzmann equation which can be written in the following linearized form:

$$\nabla^2 \psi = \kappa^2 \psi, \quad (5.24)$$

where $\kappa = e z_0 (2n_0 / \epsilon k_B T_{av})^{1/2}$ is defined as the Debye-Hückel parameter. The EDL thickness is represented by $1/\kappa$. The boundary conditions for potential distribution are taken as (Qi and Ng [2018])

$$\begin{aligned} \psi &= \tilde{\zeta}_c(x) \text{ at } y = \tilde{Y}_u, \\ \psi &= \tilde{\zeta}_c(x) \text{ at } y = \tilde{Y}_l, \end{aligned} \quad (5.25)$$

where $\tilde{\zeta}_c(x) = \tilde{\zeta}_0 \left\{ 1 + \alpha \sin\left(2\pi \frac{x}{H}\right) + \lambda \sin\left(4\pi \frac{x}{H}\right) \right\}$ is the scaled surface potential (Banerjee and Nayak [2019]) and $\tilde{\zeta}_0$ is the constant zeta potential. By introducing dimensionless variables $\psi^* = \frac{\psi}{\tilde{\zeta}_0}$, $\zeta^*(x^*) = \frac{\tilde{\zeta}_c(x)}{\tilde{\zeta}_0}$, $x^* = \frac{x}{H}$, $y^* = \frac{y}{H}$, the Poisson-Boltzmann equation with linear form can be written as

$$\nabla^{*2} \psi^* = \frac{\partial^2 \psi^*}{\partial x^{*2}} + \frac{\partial^2 \psi^*}{\partial y^{*2}} = \omega^2 \psi^*, \quad (5.26)$$

in which $\omega = \kappa H$ is defined as the electroosmotic parameter. We set the following boundary conditions for the EDL potential,

$$\psi^* = \zeta^*(x^*) \text{ at } y^* = 1 + \epsilon f(x^*), \quad (5.27)$$

$$\psi^* = \zeta^*(x^*) \text{ at } y^* = -1 - \epsilon f(x^*), \quad (5.28)$$

where $\zeta^*(x^*) = 1 + \alpha \sin(2\pi x^*) + \lambda \sin(4\pi x^*)$. The analytical solution of the EDL potential can be obtained by expanding

$$\psi^*(x^*, y^*) = \psi_0^{\otimes}(x^*, y^*) + \epsilon \psi_1^{\otimes}(x^*, y^*) + \epsilon^2 \psi_2^{\otimes}(x^*, y^*) + \dots \quad (5.29)$$

By replacing the asymptotic expansion in the dimensionless linearized potential distribution equation (5.26) and separating the electric potentials, we obtain the following equations

$$\begin{aligned} \nabla^{*2} \psi_0^{\otimes} &= \omega^2 \psi_0^{\otimes}, \\ \nabla^{*2} \psi_1^{\otimes} &= \omega^2 \psi_1^{\otimes}, \\ \nabla^{*2} \psi_2^{\otimes} &= \omega^2 \psi_2^{\otimes}. \end{aligned} \quad (5.30)$$

The boundary conditions reduce to

$$\begin{aligned} \psi^*(x^*, 1 + \epsilon f(x^*)) &= \psi^*(x^*, 1) + \epsilon f(x^*) \frac{\partial \psi^*}{\partial y^*}(x^*, 1) + \\ &\epsilon^2 \frac{(f(x^*))^2}{2} \frac{\partial^2 \psi^*}{\partial y^{*2}}(x^*, 1) + \dots = \zeta^*(x^*), \end{aligned} \quad (5.31)$$

and

$$\begin{aligned}\psi^*(x^*, -1 - \varepsilon f(x^*)) &= \psi^*(x^*, -1) - \varepsilon f(x^*) \frac{\partial \psi^*}{\partial y^*}(x^*, -1) \\ &+ \varepsilon^2 \frac{(f(x^*))^2}{2} \frac{\partial^2 \psi^*}{\partial y^{*2}}(x^*, -1) + \dots = \zeta^*(x^*).\end{aligned}\quad (5.32)$$

Substituting the Eq. (5.29) into the Eqs. (5.31) and (5.32) yielding

$$\begin{aligned}\psi_0^\oplus(x^*, 1) + \varepsilon \left[\psi_1^\oplus(x^*, 1) + f(x^*) \frac{\partial \psi_0^\oplus}{\partial y^*}(x^*, 1) \right] &+ \varepsilon^2 \left[\psi_2^\oplus(x^*, 1) \right. \\ &+ \left. f(x^*) \frac{\partial \psi_1^\oplus}{\partial y^*}(x^*, 1) + \frac{(f(x^*))^2}{2} \frac{\partial^2 \psi_0^\oplus}{\partial y^{*2}}(x^*, 1) \right] + \dots = \zeta^*(x^*),\end{aligned}\quad (5.33)$$

and

$$\begin{aligned}\psi_0^\oplus(x^*, -1) + \varepsilon \left[\psi_1^\oplus(x^*, -1) - f(x^*) \frac{\partial \psi_0^\oplus}{\partial y^*}(x^*, -1) \right] &+ \varepsilon^2 \left[\psi_2^\oplus(x^*, -1) \right. \\ &- \left. f(x^*) \frac{\partial \psi_1^\oplus}{\partial y^*}(x^*, -1) + \frac{(f(x^*))^2}{2} \frac{\partial^2 \psi_0^\oplus}{\partial y^{*2}}(x^*, -1) \right] + \dots = \zeta^*(x^*).\end{aligned}\quad (5.34)$$

The boundary conditions linked with ψ_0^\oplus , ψ_1^\oplus and ψ_2^\oplus derived from the above two equations (5.33) and (5.34) are respectively written as

$$\psi_0^\oplus(x^*, 1) = 1, \quad (5.35)$$

$$\psi_0^\oplus(x^*, -1) = 1, \quad (5.36)$$

$$\psi_1^\oplus(x^*, 1) + f(x^*) \frac{\partial \psi_0^\oplus}{\partial y^*}(x^*, 1) = g(x^*), \quad (5.37)$$

$$\psi_1^\oplus(x^*, -1) - f(x^*) \frac{\partial \psi_0^\oplus}{\partial y^*}(x^*, -1) = g(x^*), \quad (5.38)$$

$$\psi_2^\oplus(x^*, 1) + f(x^*) \frac{\partial \psi_1^\oplus}{\partial y^*}(x^*, 1) + \frac{(f(x^*))^2}{2} \frac{\partial^2 \psi_0^\oplus}{\partial y^{*2}}(x^*, 1) = 0, \quad (5.39)$$

$$\psi_2^\oplus(x^*, -1) - f(x^*) \frac{\partial \psi_1^\oplus}{\partial y^*}(x^*, -1) + \frac{(f(x^*))^2}{2} \frac{\partial^2 \psi_0^\oplus}{\partial y^{*2}}(x^*, -1) = 0, \quad (5.40)$$

where $g(x^*) = \frac{1}{2}f(x^*)$. The analytical solution for the potential distribution within the EDL of the complex wavy rough microchannel is obtained by solving the the Eq. (5.30) linked with the boundary conditions (5.35)-(5.40), and gives

$$\psi_0^\oplus(x^*, y^*) = \frac{\cosh(\omega y^*)}{\cosh(\omega)}, \quad (5.41)$$

$$\psi_1^\oplus(x^*, y^*) = \left\{ g(x^*) - \omega \tanh(\omega) f(x^*) \right\} \frac{\cosh(\sqrt{\omega^2 + \lambda^2} y^*)}{\cosh(\sqrt{\omega^2 + \lambda^2})}, \quad (5.42)$$

$$\psi_2^{\otimes}(x^*, y^*) = \left[\left\{ \omega \tanh(\omega) f(x^*) - g(x^*) \right\} \sqrt{\omega^2 + \lambda^2} \tanh(\sqrt{\omega^2 + \lambda^2}) - \frac{\omega^2}{2} f(x^*) \right] \frac{\cosh(\sqrt{\omega^2 + 4\lambda^2} y^*)}{\cosh(\sqrt{\omega^2 + 4\lambda^2})} f(x^*). \quad (5.43)$$

For the special case of $\varepsilon = 0$, the electric potential distribution reduces to $\psi^* = \frac{\cosh(\omega y^*)}{\cosh(\omega)}$, which is consistent for the rectangular microchannel (Chakraborty and Paul [2006]) with regular surface.

5.4 Velocity distribution

Owing to the assumptions of the present study, the governing equation (Lei et al. [2019]; Reza et al. [2021]) for a laminar flow through the porous medium can be expressed as

$$\rho \left[\frac{\partial \mathbf{U}}{\partial t} + (\mathbf{U} \cdot \nabla) \mathbf{U} \right] = -\nabla p + \mu \nabla^2 \mathbf{U} - \frac{\mu}{K} \mathbf{U} + \rho_e \left(-\nabla \Phi - \nabla \psi \right) + \mathbf{F}, \quad (5.44)$$

where μ is the fluid viscosity, σ_e the electrical conductivity, ρ the density, K indicates the permeability of the porous medium and last term of equation (44) represents the body force per unit volume, \mathbf{E} is the applied electric field, ρ_e denotes the net electric charge density and the Lorentz force \mathbf{F} can be expressed as

$$\mathbf{F} = \mathbf{J} \times \mathbf{B}, \quad (5.45)$$

where $\mathbf{J} = \sigma_e(\mathbf{E} + \mathbf{U} \times \mathbf{B})$ and σ_e indicates the electrical conductivity of the electrolyte solution.

We assumed that the velocity gradients along the x -direction can be neglected because $W \gg 2H$. The velocity component along the x -direction is approximately equal to zero, based on the physical flow situation of the microscale flow. Further, we assume that the flow is steady and the flow is driven by the constant pressure gradient along the z -direction. The present physical situation assumes that the flow is purely along z -direction. The order of length scale of microchannel along z -direction is more than the dimension of along y -direction. Hence the velocity component takes in the form $w = w(x, y)$. The momentum equation (z -component) of this problem is simplified as

$$\mu \left(\frac{\partial^2 w}{\partial x^2} + \frac{\partial^2 w}{\partial y^2} \right) - \frac{\partial p}{\partial z} - \frac{\mu w}{K} + \rho_e E_z + \sigma_e E_x B_y - \sigma_e B_y^2 w = 0, \quad (5.46)$$

where the electric field components depend on the roughness of the microchannel. These electric field components are computed from the relation of electric field and electrostatic potential ϕ (from Eq. (5.2)) is defined as (Lei et al. [2019])

$$\mathbf{E} = -\nabla \Phi - \nabla \psi. \quad (5.47)$$

It is noted that when $\varepsilon = 0$, the microchannel has no roughness and thereby the electric field component E_x becomes constant.

5.4. Velocity distribution

We set the boundary conditions at wall as

$$\begin{aligned} w &= 0 \quad \text{at } y = \tilde{Y}_u, \\ w &= 0 \quad \text{at } y = \tilde{Y}_l. \end{aligned} \quad (5.48)$$

The following variables and parameters are employed to establish dimensionless form of the Eq. (5.46):

$$x^* = \frac{x}{H}, \quad y^* = \frac{y}{H}, \quad w^* = \frac{w}{W_e}, \quad (5.49)$$

$$Da = \frac{K}{H^2}, \quad Ha = B_y H \sqrt{\frac{\sigma_e}{\mu}}, \quad P_1 = \frac{(-\frac{\partial p}{\partial z})H^2}{\mu W_e}, \quad S = \frac{E_{00}H}{W_e} \sqrt{\frac{\sigma_e}{\mu}}. \quad (5.50)$$

Use of (5.49) and (5.50) in the Eq. (5.46) yields

$$\begin{aligned} &\left(\frac{\partial^2 w^*}{\partial x^{*2}} + \frac{\partial^2 w^*}{\partial y^{*2}} \right) - \left(\frac{1}{Da} + Ha^2 \right) w^* + \omega^2 \psi^* + P_1 + HaS \left\{ 1 \right. \\ &\left. + \varepsilon \left(v_1(x^*) \cosh(\sqrt{\omega^2 + \lambda^2} y^*) + v_2(x^*) \cosh(\lambda y^*) \right) + O(\varepsilon^2) \right\} = 0, \end{aligned} \quad (5.51)$$

where $W_e = -\frac{\varepsilon \tilde{\zeta}_0 E_z}{\mu}$ is defined as the well-known Helmholtz-Smoluchowski velocity, Da the Darcy number, Ha the Hartmann number.

$$\begin{aligned} v_1(x^*) &= \frac{\pi \tanh(\omega)}{\cosh(\sqrt{\omega^2 + \lambda^2})} [2\omega \{ \cos(2\pi x^*) + 2R_\alpha \cos(4\pi x^*) \} - \cos(2\pi x^*) - 2\cos(4\pi x^*)], \\ v_2(x^*) &= \frac{-1}{\cosh(\lambda)} \{ 4\pi^2 \cos(2\pi x^*) + 16\pi^2 R_\alpha \cos(4\pi x^*) \}. \end{aligned}$$

Now the dimensionless Eq. (5.51) can be solved together with the no-slip boundary conditions which are expressed as

$$w^* = 0 \quad \text{at } y^* = 1 + \varepsilon f(x^*), \quad (5.52)$$

$$w^* = 0 \quad \text{at } y^* = -1 - \varepsilon f(x^*). \quad (5.53)$$

It is quite complicated to solve the Eq. (5.51) because of the presence of the term $\omega^2 \psi^*$. However, to solve the equation effortlessly, the following transformation is applied:

$$w^@ = - \left(\frac{1}{Da} + Ha^2 \right) w^* + \frac{(\frac{1}{Da} + Ha^2) \omega^2 \psi^*}{(\frac{1}{Da} + Ha^2 - \omega^2)}. \quad (5.54)$$

Applying the transformation (5.54) to the Eqs. (5.51) and (5.26), we obtain

$$\begin{aligned} \frac{\partial^2 w^@}{\partial x^{*2}} + \frac{\partial^2 w^@}{\partial y^{*2}} - Q w^@ &= P + HaS Q \left\{ \varepsilon \left(v_1(x^*) \cosh(\sqrt{\omega^2 + \lambda^2} y^*) \right. \right. \\ &\left. \left. + v_2(x^*) \cosh(\lambda y^*) \right) + O(\varepsilon^2) \right\}, \end{aligned} \quad (5.55)$$

where $Q = \left(\frac{1}{Da} + Ha^2 \right)$ and $P = \left(\frac{1}{Da} + Ha^2 \right) (P_1 + HaS)$.

Then the appropriate boundary conditions becomes:

$$w^@ = \frac{Q\omega^2}{Q - \omega^2} \text{ at } y^* = 1 + \varepsilon f(x^*), \quad (5.56)$$

$$w^@ = \frac{Q\omega^2}{Q - \omega^2} \text{ at } y^* = -1 - \varepsilon f(x^*). \quad (5.57)$$

In a similar fashion as for potential distribution, the governing equations for velocity distribution $w^@$ is luxated with the asymptotic expansion, which conducts as

$$\frac{\partial^2 w_0^@}{\partial x^{*2}} + \frac{\partial^2 w_0^@}{\partial y^{*2}} - Qw_0^@ = P, \quad (5.58)$$

$$\frac{\partial^2 w_1^@}{\partial x^{*2}} + \frac{\partial^2 w_1^@}{\partial y^{*2}} - Qw_1^@ = HaSQ\{v_1(x^*) \cosh(y^* \sqrt{\omega^2 + \lambda^2}) + v_2(x^*) \cosh(\lambda y^*)\}, \quad (5.59)$$

$$\frac{\partial^2 w_2^@}{\partial x^{*2}} + \frac{\partial^2 w_2^@}{\partial y^{*2}} - Qw_2^@ = 0, \quad (5.60)$$

and the boundary conditions are reduced to

$$w_0^@(x^*, 1) = \frac{Q\omega^2}{Q - \omega^2}, \quad (5.61)$$

$$w_0^@(x^*, -1) = \frac{Q\omega^2}{Q - \omega^2}, \quad (5.62)$$

$$w_1^@(x^*, 1) + f(x^*) \frac{\partial w_0^@}{\partial y^*}(x^*, 1) = 0, \quad (5.63)$$

$$w_1^@(x^*, -1) - f(x^*) \frac{\partial w_0^@}{\partial y^*}(x^*, -1) = 0, \quad (5.64)$$

$$w_2^@(x^*, 1) + f(x^*) \frac{\partial w_1^@}{\partial y^*}(x^*, 1) + \frac{(f(x^*))^2}{2} \frac{\partial^2 w_0^@}{\partial y^{*2}}(x^*, 1) = 0, \quad (5.65)$$

$$w_2^@(x^*, -1) - f(x^*) \frac{\partial w_1^@}{\partial y^*}(x^*, -1) + \frac{(f(x^*))^2}{2} \frac{\partial^2 w_0^@}{\partial y^{*2}}(x^*, -1) = 0. \quad (5.66)$$

Now, one can easily obtain the velocity distribution by solving the Eqs. (5.58)-(5.60) subjected to the boundary conditions (5.61)-(5.66) and it is given by

$$w_0^@(x^*, y^*) = \frac{\{PQ + (Q^2 - P)\omega^2\} \cosh(\sqrt{Q}y^*)}{Q(Q - \omega^2) \cosh(\sqrt{Q})} - \frac{P}{Q}, \quad (5.67)$$

$$w_1^@ (x^*, y^*) = -\frac{\{PQ + (Q^2 - P)\omega^2\} \tanh(\sqrt{Q}) \cosh(\sqrt{Q + \lambda^2} y^*)}{\sqrt{Q}(Q - \omega^2) \cosh(\sqrt{Q + \lambda^2})} f(x^*) + \sum_{m=0}^{\infty} \sum_{n=0}^{\infty} b_{mn} \sin \frac{(m+1)\pi x^*}{6} \sin(n+1)\pi y^*, \quad (5.68)$$

$$w_2^@ (x^*, y^*) = \{\beta(f(x^*))^2 - v_3(x^*)f(x^*)\} \frac{\cosh(\sqrt{Q + 4\lambda^2} y^*)}{\cosh(\sqrt{Q + 4\lambda^2})}, \quad (5.69)$$

$$\text{where } \beta = \frac{\sqrt{Q + \lambda^2} \{PQ + (Q^2 - P)\omega^2\} \tanh(\sqrt{Q}) \tanh(\sqrt{Q + \lambda^2})}{\sqrt{Q}(Q - \omega^2)} - \frac{\{PQ + (Q^2 - P)\omega^2\}}{(Q - \omega^2)},$$

$$v_3(x^*) = \frac{\partial}{\partial y^*} \left[\sum_{m=0}^{\infty} \sum_{n=0}^{\infty} b_{mn} \sin \frac{(m+1)\pi x^*}{6} \sin(n+1)\pi y^* \right]_{At y^*=1},$$

$$b_{mn} = \frac{-4}{6\{\frac{(m+1)^2\pi^2}{6^2} + (n+1)^2\pi^2\}} \int_0^6 \int_0^1 \left[HaSQ \left\{ v_1(x^*) \cosh(\sqrt{\omega^2 + \lambda^2} y^*) + v_2(x^*) \cosh(\lambda y^*) \right\} \sin\left(\frac{(m+1)\pi x^*}{6}\right) \sin((n+1)\pi y^*) \right] dx^* dy^*.$$

For the special case of $\varepsilon = 0$ and $Da \rightarrow \infty$, the velocity distribution reduces to $w^* = \frac{HaS+P_1}{Ha^2} \{1 - \frac{\cosh(Hay^*)}{\cosh(Ha)}\} - \frac{\omega^2}{Ha^2 - \omega^2} \{\frac{\cosh(Hay^*)}{\cosh(Ha)} - \frac{\cosh(\omega y^*)}{\cosh(\omega)}\}$, which is consistent for the rectangular microchannel ([Chakraborty and Paul \[2006\]](#)).

The volumetric flow rate per unit width of the complex wavy rough microchannel is expressed as

$$q(x^*) = \int_{-1-\varepsilon f(x^*)}^{1+\varepsilon f(x^*)} w^* dy^* = \int_{-1}^1 w^* dy^* + \int_1^{1+\varepsilon f(x^*)} w^* dy^* + \int_{-1-\varepsilon f(x^*)}^{-1} w^* dy^* = \int_{-1}^1 w_0^{\otimes} dy^* + \varepsilon \left[\int_{-1}^1 w_1^{\otimes} dy^* + f(x^*) \{w_0^{\otimes}(1) - w_0^{\otimes}(-1)\} \right] + \varepsilon^2 \left[\int_{-1}^1 w_2^{\otimes} dy^* + f(x^*) \{w_1^{\otimes}(x^*, 1) - w_1^{\otimes}(x^*, -1)\} + \frac{(f(x^*))^2}{2} \left\{ \frac{dw_0^{\otimes}}{dy^*} \Big|_{y=1} - \frac{dw_0^{\otimes}}{dy^*} \Big|_{y=-1} \right\} \right]. \quad (5.70)$$

Using the Eq. (5.54) in the Eqs. (5.67)-(5.69) one can evaluate the mean velocity over six wave lengths (entire width of the channel) as

$$w_m^{\otimes} = \int_0^6 q(x^*) dx^* = \phi_0 [1 + \varepsilon^2 \phi_m + O(\varepsilon^4)], \quad (5.71)$$

where

$$\phi_0 = \frac{6}{Q^2(Q - \omega^2)} \{2P(Q - \omega^2) + 2Q^2\omega \tanh(\omega) - \frac{2}{\sqrt{Q}}(PQ - P\omega^2 + Q^2\omega^2) \tanh(\sqrt{Q})\},$$

and

$$\phi_m = \sqrt{Q} \left[\frac{(1+R_\alpha^2) \tanh(\sqrt{Q^2+4\lambda^2})(PQ - P\omega^2 + Q^2\omega^2)}{\sqrt{Q^2+4\lambda^2}} \left\{ \sqrt{Q} - 2\sqrt{Q^2 + \lambda^2} \tanh(\sqrt{Q}) \tanh(\sqrt{Q^2 + \lambda^2}) \right\} + \frac{Q^2\omega^2 \tanh(\sqrt{4\lambda^2 + \omega^2})}{\sqrt{4\lambda^2 + \omega^2}} \left\{ \omega^2(1 + R_\alpha) - 2\sqrt{\lambda^2 + \omega^2} \left(\omega(1 + R_\alpha) \tanh(\omega) - 1 \right) \tanh(\sqrt{\lambda^2 + \omega^2}) \right\} \right] / \left[2P(Q - \omega^2) + 2Q^2\omega \tanh(\omega) \right]$$

$$- \frac{2}{\sqrt{Q}}(PQ - P\omega^2 + Q^2\omega^2) \tanh(\sqrt{Q}) \Big].$$

The expression ϕ_0 is the volumetric flow rate of a smooth microchannel with no waviness and ϕ_m is defined as a waviness function, which describes the impact of waviness on the total volumetric flow rate (w_m^*) of the microchannel with complex wavy roughness.

5.5 Thermal behaviour

Thermal energy equation linked with combined electromagnetohydrodynamic flows via a poriferous microchannel is taken as (Reza et al. [2021])

$$\rho C_P w \frac{\partial T}{\partial z} = k_{Th} \left(\frac{\partial^2 T}{\partial x^2} + \frac{\partial^2 T}{\partial y^2} \right) + \Upsilon_1 + \Upsilon_2, \quad (5.72)$$

where C_P , T , k_{Th} are the specific heat, local temperature of the liquid and thermal conductivity respectively and $\Upsilon_1 = \mu \{ (\frac{\partial w}{\partial y})^2 + (\frac{\partial w}{\partial x})^2 + \frac{w^2}{K} \}$ contributes the different viscous dissipation effects which basically a combination of the frictional heating at the channel wall and the internal heating inside the porous medium and $\Upsilon_2 = \sigma_e \{ E_z^2 + B_y^2 w^2 - 2E_x B_y w \}$ indicates the heat generation with the interaction of external body forces.

Now, for the analysis of thermal behavior, the dimensionless temperature $T^* = \frac{h(T - T_W)}{q_w}$ is considered invariant and wall temperature is denoted by T_W . The dimensionless temperature T^* is coupled with stipulated uniform surround heat flux (Bejan [2006]). Here the wall heat flux is defined as $q_w = h(T_W - T_b)$. Under the assumption of constant heat flux, we consider

$$\frac{\partial T}{\partial z} = \frac{\partial T_W}{\partial z} = \frac{\partial T_b}{\partial z}, \quad (5.73)$$

where T_b represents the mean bulk temperature. The final energy proportion on an elementary control volume is composed as

$$\begin{aligned} \frac{\partial T_b}{\partial z} = \frac{1}{\rho C_P w_{av}} \{ & q_w / H + \sigma_e E_z^2 + \frac{\mu W_e^2}{H^2} (\Gamma_1 + \Gamma_2 + \frac{\Gamma_3}{K}) \\ & + \sigma_e (W_e^2 B_y^2 \Gamma_3 - 2E_x B_y W_e \Gamma_4) \}, \end{aligned} \quad (5.74)$$

where w_{av} is the average velocity of the complex wavy microchannel in cross section and

$$\begin{aligned} \Gamma_1 &= \int_0^6 \int_{-1-\varepsilon f(x^*)}^{1+\varepsilon f(x^*)} (\frac{\partial w^*}{\partial y^*})^2 dx^* dy^*, \quad \Gamma_2 = \int_0^6 \int_{-1-\varepsilon f(x^*)}^{1+\varepsilon f(x^*)} (\frac{\partial w^*}{\partial x^*})^2 dx^* dy^*, \\ \Gamma_3 &= \int_0^6 \int_{-1-\varepsilon f(x^*)}^{1+\varepsilon f(x^*)} (w^*)^2 dx^* dy^*, \quad \Gamma_4 = \int_0^6 \int_{-1-\varepsilon f(x^*)}^{1+\varepsilon f(x^*)} w^* dx^* dy^*. \end{aligned}$$

The dimensionless energy equation can be expressed as

$$\begin{aligned} \frac{\partial^2 T^*}{\partial x^{*2}} + \frac{\partial^2 T^*}{\partial y^{*2}} = \frac{Nu}{w_{av}^{\otimes}} \left[1 + S_j + Br \left\{ \Gamma_1 + \Gamma_2 + \left(Ha^2 + \frac{1}{Da} \right) \Gamma_3 - 2HaS \left(1 \right. \right. \right. \\ \left. \left. \left. + \varepsilon v_1(x^*) \cosh(\sqrt{\omega^2 + \lambda^2} y^*) + \varepsilon v_2(x^*) \cosh(\lambda y^*) + O(\varepsilon^2) \right) \Gamma_4 \right\} \right] w^* \\ - Nu \left[Br \left\{ \left(\frac{\partial w^*}{\partial y^*} \right)^2 + \left(\frac{\partial w^*}{\partial x^*} \right)^2 + \left(Ha^2 + \frac{1}{Da} \right) w^{*2} - 2HaS \left(1 \right. \right. \right. \\ \left. \left. \left. + \varepsilon v_1(x^*) \cosh(\sqrt{\omega^2 + \lambda^2} y^*) + \varepsilon v_2(x^*) \cosh(\lambda y^*) + O(\varepsilon^2) \right) w^* \right\} + S_j \right]. \end{aligned} \quad (5.75)$$

The suitable dimensionless boundary conditions reduced to

$$T^* = 0 \text{ at } y^* = 1 + \varepsilon f(x^*) \text{ at constant wall temperature } T_W, \quad (5.76)$$

$$T^* = 0 \text{ at } y^* = -1 - \varepsilon f(x^*) \text{ at constant wall temperature } T_W. \quad (5.77)$$

The non-dimensional energy Eq. (5.75) without dissipation (i.e. for $Br = 0$) may be described as follows

$$\frac{\partial^2 T^*}{\partial x^{*2}} + \frac{\partial^2 T^*}{\partial y^{*2}} = \frac{Nu}{w_{av}^{\otimes}} (1 + S_j) w^* - Nu S_j, \quad (5.78)$$

where $S_j = \frac{\sigma_c E_z^2 H}{q_w}$, $w_{av}^{\otimes} = \frac{w_{av}}{W_e}$ and the boundary conditions (5.76) and (5.77) are reduced as

$$T^* = 0 \text{ at } y^* = 1 + \varepsilon f(x^*), \quad (5.79)$$

$$T^* = 0 \text{ at } y^* = -1 - \varepsilon f(x^*). \quad (5.80)$$

We solve the above dimensionless energy Eq. (5.75) by utilizing the numerical methods and for without dissipation case, the energy Eq. (5.78) is solved analytically by applying the perturbation technique.

To evaluate the above Eq. (5.78), we use the following transformation

$$T^@ = \frac{Q w_{av}^{\otimes}}{Nu(1 + S_j)} T^* + \frac{Q}{Q - \omega^2} \psi^*. \quad (5.81)$$

Multiplying with $\frac{Q w_{av}^{\otimes}}{Nu(1 + S_j)}$ and $\frac{Q}{(Q - \omega^2)}$ to the Eqs. (5.78) and (5.26) respectively and adding them. By applying the transformation (5.81), the Eq. (5.78) can be rewritten as

$$\frac{\partial^2 T^@}{\partial x^{*2}} + \frac{\partial^2 T^@}{\partial y^{*2}} - w^@ + \frac{Q S_j w_{av}^{\otimes}}{(1 + S_j)} = 0, \quad (5.82)$$

With the following boundary conditions

$$T^@ = \frac{Q}{Q - \omega^2} \text{ at } y^* = 1 + \varepsilon f(x^*), \quad (5.83)$$

$$T^@ = \frac{Q}{Q - \omega^2} \text{ at } y^* = -1 - \varepsilon f(x^*). \quad (5.84)$$

In a similar fashion as in potential distribution, the governing equations for temperature distribution $T^@$ is luxated with the asymptotic expansion, which yields

$$\frac{\partial^2 T_0^@}{\partial x^{*2}} + \frac{\partial^2 T_0^@}{\partial y^{*2}} - w_0^@ + \frac{QS_j w_{av}^@}{(1 + S_j)} = 0, \quad (5.85)$$

$$\frac{\partial^2 T_1^@}{\partial x^{*2}} + \frac{\partial^2 T_1^@}{\partial y^{*2}} - w_1^@ = 0, \quad (5.86)$$

$$\frac{\partial^2 T_2^@}{\partial x^{*2}} + \frac{\partial^2 T_2^@}{\partial y^{*2}} - w_2^@ = 0, \quad (5.87)$$

with the associated boundary conditions described by

$$T_0^@(x^*, 1) = \frac{Q}{Q - \omega^2}, \quad (5.88)$$

$$T_0^@(x^*, -1) = \frac{Q}{Q - \omega^2}, \quad (5.89)$$

$$T_1^@(x^*, 1) + f(x^*) \frac{\partial T_0^@}{\partial y^*}(x^*, 1) = 0, \quad (5.90)$$

$$T_1^@(x^*, -1) - f(x^*) \frac{\partial T_0^@}{\partial y^*}(x^*, -1) = 0, \quad (5.91)$$

$$T_2^@(x^*, 1) + f(x^*) \frac{\partial T_1^@}{\partial y^*}(x^*, 1) + \frac{(f(x^*))^2}{2} \frac{\partial^2 T_0^@}{\partial y^{*2}}(x^*, 1) = 0, \quad (5.92)$$

$$T_2^@(x^*, -1) - f(x^*) \frac{\partial T_1^@}{\partial y^*}(x^*, -1) + \frac{(f(x^*))^2}{2} \frac{\partial^2 T_0^@}{\partial y^{*2}}(x^*, -1) = 0. \quad (5.93)$$

We obtain the temperature distribution by solving the Eqs. (5.85)-(5.87) subjected to the appropriate boundary conditions (5.88)-(5.93) and it is given by

$$T_0^@(x^*, y^*) = \frac{G_1 \cosh(\sqrt{Q} y^*)}{Q} + \frac{G_2 y^{*2}}{2} + \frac{Q}{Q - \omega^2} - \left\{ \frac{G_1 \cosh(\sqrt{Q})}{Q} + \frac{G_2}{2} \right\}, \quad (5.94)$$

$$T_1^@(x^*, y^*) = -\frac{f(x^*)}{\cosh(\lambda) \cos(\lambda)} \left\{ \frac{G_1 \sinh(\sqrt{Q})}{\sqrt{Q}} + G_2 \right\} \cosh(\lambda y^*) \cos(\lambda x^*) \\ + \sum_{m=0}^{\infty} \sum_{n=0}^{\infty} a_{mn} \sin \frac{(m+1)\pi x^*}{6} \sin(n+1)\pi y^*, \quad (5.95)$$

$$T_2^@(x^*, y^*) = -\frac{\cosh(2\lambda y^*) \cos(2\lambda x^*)}{\cosh(2\lambda) \cos(2\lambda)} \left\{ (G_5 \cos(\lambda x^*) + \frac{G_4}{2}) \{f(x^*)\}^2 \right. \\ \left. - v_4(x^*) f(x^*) \right\} + \sum_{m_1=0}^{\infty} \sum_{n_1=0}^{\infty} A_{m_1 n_1} \sin \frac{(m_1+1)\pi x^*}{6} \sin(n_1+1)\pi y^*, \quad (5.96)$$

where,

$$G_1 = \frac{\{PQ + (Q^2 - P)\omega^2\}}{Q(Q - \omega^2) \cosh(\sqrt{Q})},$$

$$G_2 = -\frac{QS_j w_{av}^{\otimes}}{(1 + S_j)} - \frac{P}{Q},$$

$$G_3 = -\frac{\{PQ + (Q^2 - P)\omega^2\} \tanh(\sqrt{Q})}{\sqrt{Q}(Q - \omega^2) \cosh(\sqrt{Q + \lambda^2})},$$

$$G_4 = G_1 \cosh(\sqrt{Q}) + G_2,$$

$$G_5 = \frac{\lambda \tanh(\lambda)}{\cos(\lambda)} \left\{ \frac{G_1 \sinh(\sqrt{Q})}{\sqrt{Q}} + G_2 \right\},$$

$$G_6 = \frac{\beta}{\cosh(\sqrt{Q + 4\lambda^2})},$$

$$a_{mn} = \frac{-4}{6\left\{\frac{(m+1)^2\pi^2}{6^2} + (n+1)^2\pi^2\right\}} \int_0^6 \int_0^1 \left[G_3 f(x^*) \cosh(\sqrt{Q + \lambda^2} y^*) \right. \\ \left. + \sum_{m=0}^{\infty} \sum_{n=0}^{\infty} b_{mn} \sin\left(\frac{(m+1)\pi x^*}{6}\right) \sin(n+1)\pi y^* \sin\left(\frac{(m+1)\pi x^*}{6}\right) \sin((n+1)\pi y^*) \right] dx^* dy^*,$$

$$v_4(x^*) = \frac{\partial}{\partial y^*} \left[\sum_{m=0}^{\infty} \sum_{n=0}^{\infty} a_{mn} \sin\left(\frac{(m+1)\pi x^*}{6}\right) \sin(n+1)\pi y^* \right]_{At y^*=1},$$

$$A_{m_1 n_1} = \frac{-4}{6\left\{\frac{(m_1+1)^2\pi^2}{6^2} + (n_1+1)^2\pi^2\right\}} \int_0^6 \int_0^1 \left[\left\{ G_6 \{f(x^*)\}^2 \right. \right. \\ \left. \left. - \frac{v_3(x^*) f(x^*)}{\cosh(\sqrt{Q + 4\lambda^2})} \right\} \cosh(\sqrt{Q + 4\lambda^2} y^*) \sin\left(\frac{(m_1+1)\pi x^*}{6}\right) \sin((n_1+1)\pi y^*) \right] dx^* dy^*.$$

Nusselt Number: The significance of Nusselt number is concreted by a non-dimensional quantity which measures the rate of heat transfer. The dimensionless bulk mean temperature (T_b^{\otimes}) can be defined as

$$T_b^{\otimes} = \frac{\int_0^6 \int_{-1-\varepsilon f(x^*)}^{1+\varepsilon f(x^*)} w^* \theta^{\otimes} dx^* dy^*}{\int_0^6 \int_{-1-\varepsilon f(x^*)}^{1+\varepsilon f(x^*)} w^* dx^* dy^*}, \quad (5.97)$$

where $\theta^{\otimes} = \frac{(1+S_j)}{Q w_{av}^{\otimes}} (T^{\otimes} - \frac{Q \psi^*}{Q - \omega^2})$.

The rate of heat transfer at the wall of the complex wavy rough microchannel is described in the form of the Nusselt number which is expressed as

$$Nu = \frac{2hq_w}{k_{Th}(T_W - T_b)} = \frac{-2}{T_b^{\otimes}}. \quad (5.98)$$

5.6 Results and Discussion

An analytical investigation has been conducted to observe the flow transport and heat transfer characteristics through a porous microchannel with complex wavy roughness. The governing equations of the thermo-fluidic transport are evaluated analytically by employing the perturbation technique. Once the velocity and temperature distributions are determined, the numerical solution to the Nusselt number has been evaluated. To perform the numerical solution, the dimensionless parameters have been estimated on the basis of the physical properties described in Table-5.1 (Yau et al. [2011]; Cho et al. [2013]; Hooman [2008]; Rana et al. [2021b]; Reza et al. [2021]). For example, when $H = 10\mu m$ and $K = 10^{-11}$, then $Da=0.1$ and when $H = 40\mu m$, $B_y = 50T$, $\sigma_e = 1.0S/m$ then

Table 5.1: The values of the physical parameters

Characteristic feature	Values
Channel length (H)	$10 - 40\mu m$
Charge of the photon (e)	$1.6 \times 10^{-19} \text{Coulomb}$
Density of the fluid (ρ)	1060kg/m^3
Electrical field in axial direction (E_x)	$0 - 2 \times 10^4 \text{V/m}$
Surface Electrical potential (ζ)	-12mV
Transversal Electrical field (E_z)	$0 - 2 \times 10^4 \text{V/m}$
Applied magnetic field (B_y)	$1 - 50 \text{T}$
Boltzmann constant (k_B)	$1.38 \times 10^{-23} \text{J/K}$
Ion density (n_0)	1mol/m^3
Mean absolute temperature (T_{av})	300K
Wall temperature (T_w)	300K
Valence of ions (z)	1
Fluid Permittivity (ϵ)	$5.3 \times 10^{-10} \text{C/Vm}$
Viscosity of the fluid (μ)	$10^{-6} \text{m}^2/\text{s}$
Permeability of porous media (K)	$0 - 10^{-11} \text{m}^2$
Wall heat flux (q_w)	1000W/m^2
Electrical conductivity (σ_e)	$10^{-3} - 1.0 \text{S/m}$
Thermal conductivity (k_{Th})	0.613W/mK
Specific heat (c_p)	3760J/KgK

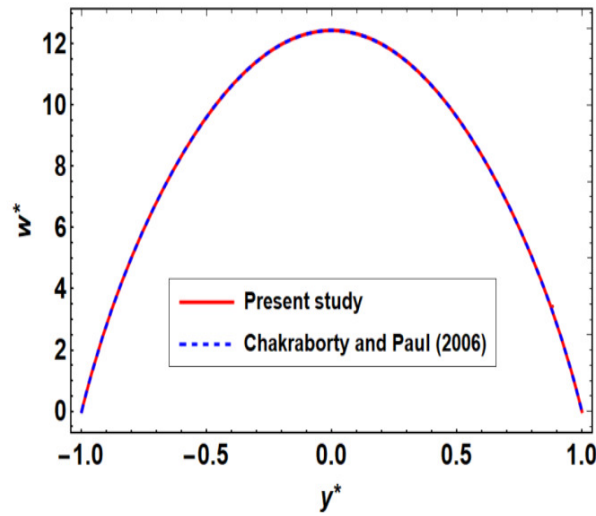


Figure 5.2: Comparison of velocity profile with Chakraborty and Paul [2006] for $\omega = 10$, $S = 50$, $P_1 = 0.5$, $Ha = 0.5$, $\epsilon = 0.0$, $Da \rightarrow \infty$.

$Ha = 2$ etc. In this analytical model, the Hartmann number, Joule heating parameter, and the Darcy number are taken in the ranges 0.01 to 2, (-15) to (-2), and 0.0006 to 0.1 respectively.

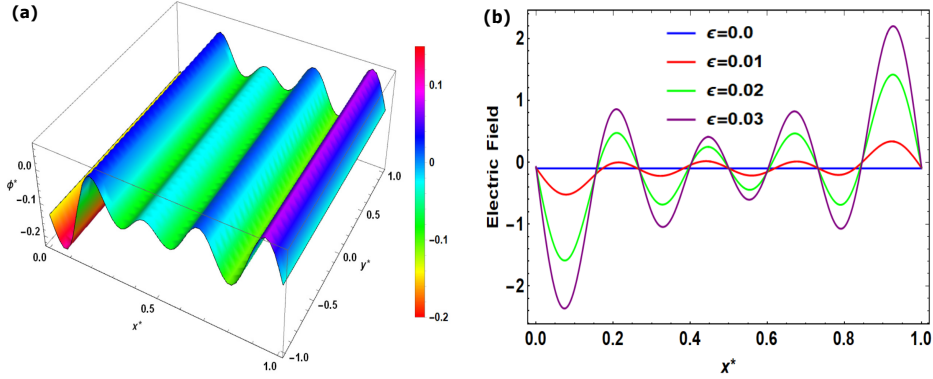


Figure 5.3: (a) 3D plot for applied electrical potential distribution when $\varepsilon = 0.025$, $R_\alpha = 0.7$, (b) variation of applied electric field at the rough wall for different ε when $\omega = 10$, $y^* = 0.5$, $R_\alpha = 0.7$.

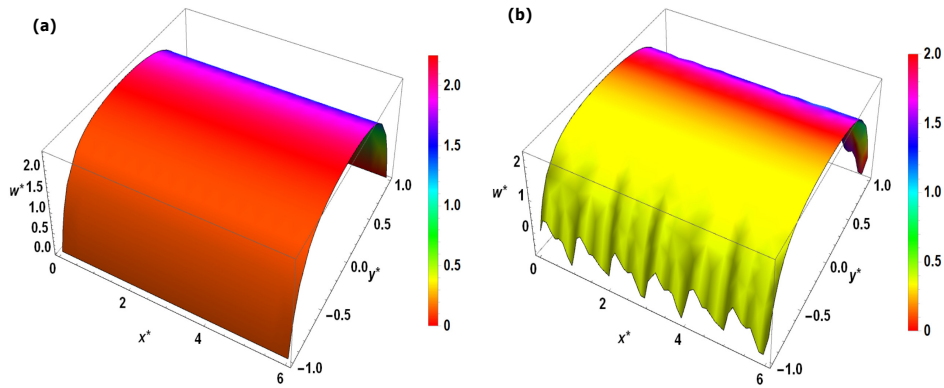


Figure 5.4: Comparison of 3D velocity profiles for $\omega = 10$, $S = 50$, $P_1 = 0.5$, $Ha = 0.5$, $R_\alpha = 0.7$, $Da = 0.03$, (a) $\varepsilon = 0.0$ (smooth microchannel); (b) $\varepsilon = 0.025$.

5.6.1 Validation of the result

To validate the analytical solution of the present model, the outcomes for the velocity profiles have been compared with the rectangular microchannel corresponding to the analytical work of [Chakraborty and Paul \[2006\]](#). Fig. 5.2 compares the analytical results between the present work and the results of rectangular microchannel ([Chakraborty and Paul \[2006\]](#)). When $\varepsilon = 0$ and $Da \rightarrow \infty$, then the present study becomes a smooth rectangular microchannel and a better agreement exists between the present results and the results of the rectangular microchannel ([Chakraborty and Paul \[2006\]](#)). Thus, the validity of this analytical model for the flow within the complex wavy microchannel through the porous media is approved.

5.6.2 Analysis of electric field on rough surface

The electric field plays an important role in electroosmotic flow through the rough surface microchannel. It depends on the electrostatic potential (ϕ), which is combined with applied electric potential (Φ) and EDL potential (ψ). Since the applied electric potential (Φ) and EDL potential (ψ) both are perturbed by the influence of surface roughness with a small amplitude ε of wavy surface roughness. The disturbance in the applied electric potential (Φ) due to changes in the surface roughness is represented in Fig. 5.3(a). The visualization of three-dimensional waviness in the dimensionless applied electric potential (Φ^*) is presented. It may be noted that the total electrical potential distribution gets disturbed due to the roughness of the surface. This implies that the applied electric field depends on the roughness amplitude of the rough (wavy) microchannel. We can easily visualize this phenomenon from Fig. 5.3(b). For $\varepsilon \neq 0$, the electric field strength becomes uneven profiles, as shown in Fig. 5.3(b), and similar types of oscillations are also delineated against the x axis. The increment of perturbation parameter (amplitude of roughness) (ε) increases the strength of the electric field in some regions, whereas in some other regions, it is being diminished significantly.

5.6.3 Analysis of flow transport characteristics

Fig. 5.4 represents the comparison of results between a rough microchannel and a smooth microchannel. In this study, $\varepsilon = 0$ implies the smooth surface of the microchannel. Fig. 5.4(a) shows the three-dimensional velocity profile for a smooth microchannel with porous medium and it becomes a parabolic velocity profiles with no disturbance near the boundary walls. But, when the value of ε increases, there exist some roughness (waviness) on the surface, as a result the three-dimensional velocity profile generates a disturbance (waviness) of the flow characteristics near the rough surface, is delineated in Fig. 5.4(b).

The three-dimensional velocity profiles and contour plots for different wavy amplitude ratio (R_α) are presented in Figs. 5.5-5.6 indicate the impact of the complex wavy roughness on the flow characteristics respectively. The amplitude of the waviness (roughness) of the microchannel is generated by the wave amplitude ratio R_α , such that an increment of R_α induces the increase of the roughness, which is physically conducted as flow resistance. To comprehend the influence of the complex wavy roughness, one can say that R_α is the ratio of two wave amplitudes that determines the change of the complex wavy surface. The diversity of velocity profiles is affected by the variation of the roughness of the surface under the action of a magnetic field for which $Ha = 0.5$ and the lateral electric field $S = 50$ are delineated in Figs. 5.5(a)-5.5(d). The flow patterns at the boundary layers have been changed due to the variation of the wall roughness. The influence of the roughness of the wall makes the disturbance on the boundary layers of the flow which are shown in Figs. 5.6(a)-5.6(d). When $R_\alpha = 0$, then it becomes the wavy microchannel and the recirculations are observed in the boundary layers as displayed in Fig. 5.6(a). However, an increment of the wall roughness makes up for more recirculations on the boundary layers as depicted in Figs. 5.6(b)-5.6(d). The closed streamlines (bolus) are generated near the boundary layers of the flow for

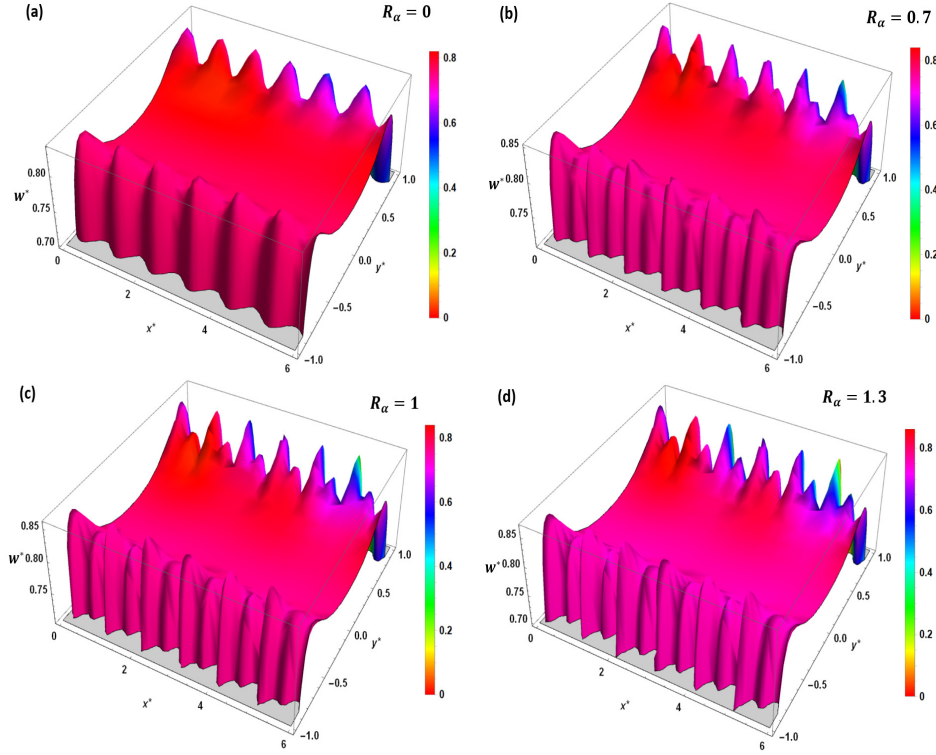


Figure 5.5: 3D velocity profiles for $\omega = 10$, $S = 50$, $P_1 = 0.5$, $Ha = 0.5$, $\varepsilon = 0.025$, $Da = 0.03$, (a) $R_\alpha = 0$; (b) $R_\alpha = 0.7$; (c) $R_\alpha = 1$ and (d) $R_\alpha = 1.3$.

$R_\alpha = 0$. Furthermore, the intensification of the formulation of boluses near the boundary layers has enhancing effect with the increase of wave amplitude ratio (R_α). The internal small boluses are generated in the alternate large boluses across the boundary layers of the microchannel as represented by Figs. 5.6(b)-5.6(d).

The significance of the Hartmann number embodies the strength of the magnitude of the applied magnetic field. The impact of applied magnetic field strength on the three-dimensional velocity profiles is delineated in Figs. 5.7(a)-5.7(d) respectively. It can be observed from the governing flow transport Eq. (5.46) that there are two body force components due to the applied electromagnetic forces, one is 'flow-aiding' ($\sim \sigma_e E_x B_y$) and the other is 'flow-opposing' ($\sim \sigma_e B_y^2 w$). As we recall that the Hartmann number indicates the ratio between the applied magnetic field and the viscous force which measures the strength of two relative forces. On the other hand, the flow aiding force is controlled by the strength of the transverse electric field and applied magnetic field. The improvement of the Hartmann number gives a hint of the increment of Lorentz force which dominates the strength of the viscous force. Figs. 5.7(a)-5.7(d) depict that due to the combined effect of electromagnetic field, the velocity profiles increase with an increase of Hartmann number (Ha), and the velocity profiles are changing towards the fully developed velocity profile by enhancing the magnitude of the applied magnetic field. The improvement of the Hartmann number is acting as a retarding force, on the other hand, the flow aiding force suppressed the Lorentz force, therefore the flow velocity increases. For low Hartmann number, the recirculations have occurred in the bound-

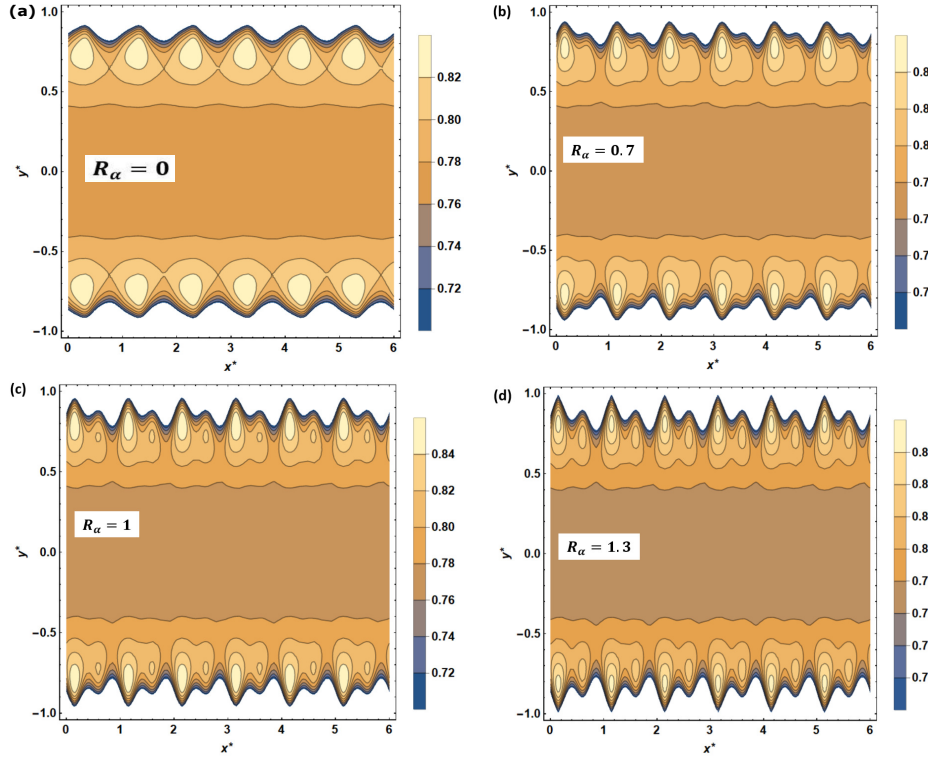


Figure 5.6: Contour plot for velocity profiles for $\omega = 10$, $S = 50$, $P_1 = 0.5$, $Ha = 0.5$, $\varepsilon = 0.025$, $Da = 0.03$, (a) $R_\alpha = 0$; (b) $R_\alpha = 0.7$; (c) $R_\alpha = 1$ and (d) $R_\alpha = 1.3$.

ary layers. Also, there are formulated boluses near the boundary layers of the microchannel for low Hartmann number. While there are no recirculations as well as no boluses formation within the boundary layers for large Hartmann number. The axial velocity increases and becomes fully developed with the increase of the Hartmann number as indicated in Fig. 5.8(a). These phenomena generate because the transverse electric field exerts the flow-aiding force, which dominates the Lorentz force.

The exploration of the flow transport through the porous medium is one of the most important parts of this investigation. The graphical interpretation of the flow field under the influence of the porosity parameter (Darcy number) is illustrated by three-dimensional velocity profiles as shown in Figs. 5.9(a)-5.9(d). The significance of Darcy number embodies the permeability of the porous medium. Therefore, the higher Darcy number means the permeability is high, which implies that the resistance is very low to the flow transport through the porous medium. However, the expansion of the axial flow profiles is displayed in Fig. 5.8(b) and it can be observed that the flow profiles become parabolic for higher Darcy number. The increasing effect of permeability enhances the three-dimensional velocity profiles, whereas for low Darcy number the velocity profile is not fully developed as depicted in Fig. 5.9. The middle layers of the flow do not affect by the wave amplitude ratio and the flow is attained the maximum velocity in its middle layers. There are no recirculations on the boundary layers for higher permeability, are presented in Figs. 5.9(b), 5.9(c) and 5.9(d). For low Darcy number, (for low permeability in the porous medium), the recirculations by the

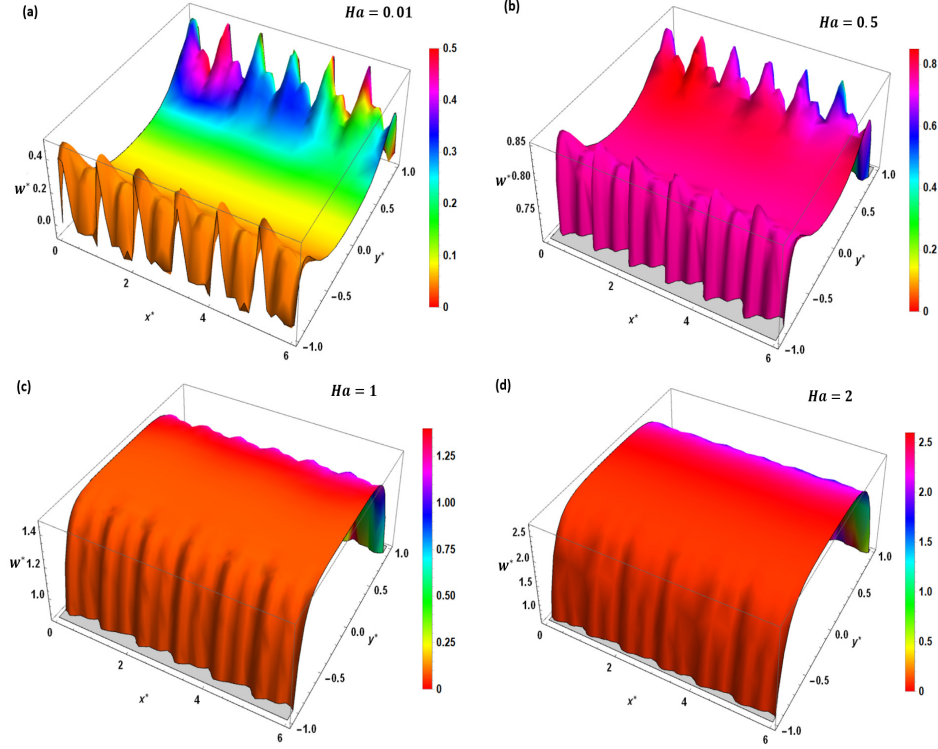


Figure 5.7: 3D velocity profiles for $\omega = 10$, $S = 50$, $P_1 = 0.5$, $Da = 0.03$, $\varepsilon = 0.025$, $R_\alpha = 0.7$, (a) $Ha = 0.01$; (b) $Ha = 0.5$; (c) $Ha = 1$ and (d) $Ha = 2$.

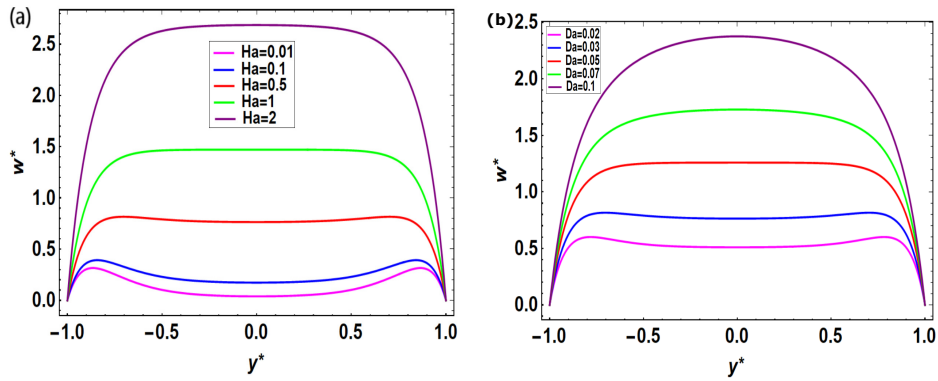


Figure 5.8: Axial velocity profiles in complex wavy microchannel for different (a) Hartmann number and (b) Darcy number when $\omega = 10$, $S = 50$, $P_1 = 0.5$, $x^* = 0.5$, $\varepsilon = 0.025$, $R_\alpha = 0.7$.

velocity contours are formed within the boundary layers. Furthermore, the formation of velocity contours near the boundary layers is illustrated by a low Darcy number and some internal boluses are generated in the central zone across the microchannel.

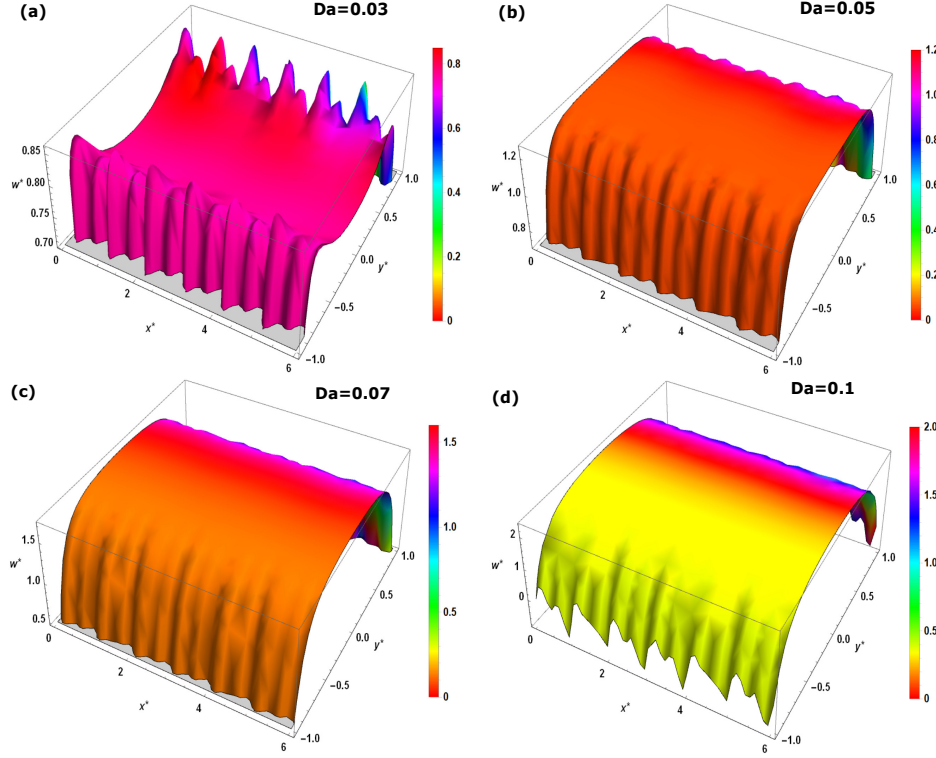


Figure 5.9: 3D velocity profiles for $\omega = 10$, $S = 50$, $P_1 = 0.5$, $Ha = 0.5$, $\varepsilon = 0.025$, $R_\alpha = 0.7$, (a) $Da = 0.03$; (b) $Da = 0.05$; (c) $Da = 0.07$ and (d) $Da = 0.1$.

In this investigation, the streamlines are represented graphically in Fig. 5.10. The variations for the flow streamlines with different wave amplitude ratio (R_α) within the complex wavy microchannel are illustrated in this figure. The symmetric recirculations are observed in the boundary layers for $R_\alpha = 0$ as displayed in Fig. 5.10(a). The enhancement of the wall roughness makes up for more recirculations on the boundary layers as delineated in the Figs. 5.10(b)-5.10(d) and the recirculations become asymmetric due to the complex wavy roughness. Some boluses are generated near the boundary layer of the flow domain and the intensification of the formulation of boluses near the boundary layers is enhanced with the increase of wave amplitude ratio (R_α). The diversity in the velocity profiles has been demonstrated through the streamlines near the boundary layers due to the complex wavy roughness. As the surface roughness enhances, the flow velocity is causing more resistance. As a result, more recirculations are generated with the boluses across the microchannel.

5.6.4 Analysis of volumetric flow rate

The volume flow rate in the complex wavy microchannel is expressed by the Eq. (5.71) and it is demonstrated through the waviness function ϕ_m . Therefore, to understand the volumetric flow rate

5.6. Results and Discussion

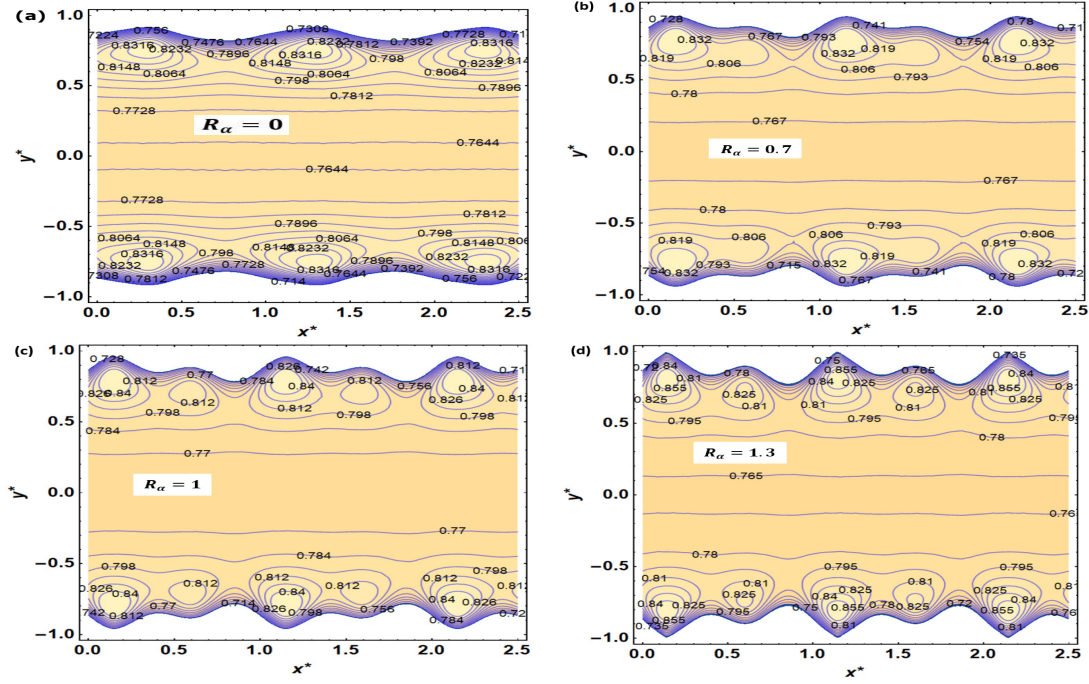


Figure 5.10: Stream line plots for $\omega = 10$, $S = 50$, $P_1 = 0.5$, $Ha = 0.5$, $\varepsilon = 0.025$, $Da = 0.03$, (a) $R_\alpha = 0$; (b) $R_\alpha = 0.7$; (c) $R_\alpha = 1$ and (d) $R_\alpha = 1.3$.

through the complex wavy microchannel, we focused on the variation of the waviness function (ϕ_m) with other pertinent parameters.

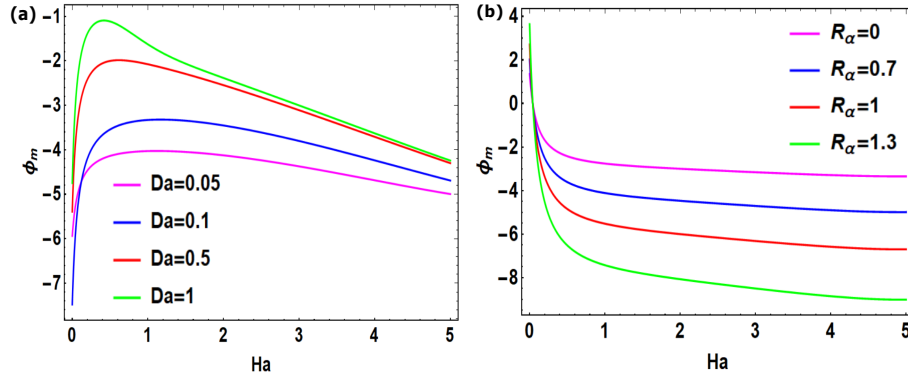


Figure 5.11: Variation of ϕ_m with Ha for (a) different values of Da and (b) different values of R_α with $\omega = 10$, $S = 50$, $P_1 = 0.5$.

The variations of ϕ_m with different values of Hartmann number, Darcy number, and wave amplitude ratio are depicted in Figs. 5.11, 5.12 and 5.13 respectively. The variations of ϕ_m are not monotonic with the increasing value of applied magnetic field strength, which is shown in Fig. 5.11. But, Fig. 5.11(a) deals with the variation of waviness function (ϕ_m) against Hartmann number (Ha) for different values of Darcy number (Da). The function ϕ_m enhances with an increase in the Darcy number. Thus the volumetric flow rate is increased with the variation of the Darcy number because the function ϕ_m is negative. But the variation of waviness function (ϕ_m) against

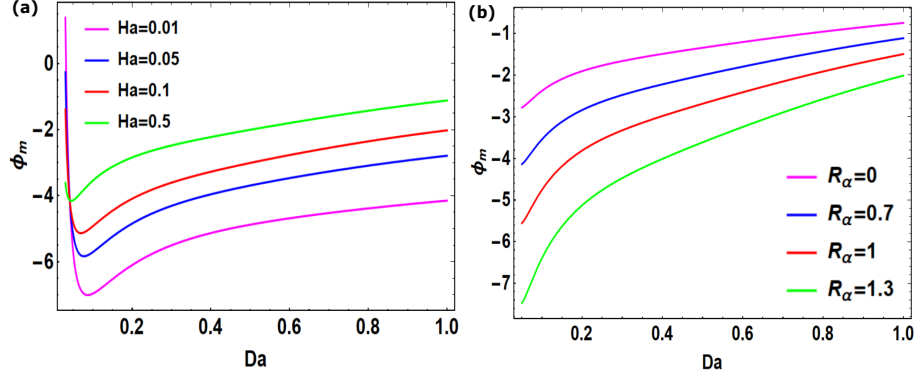


Figure 5.12: Variation of ϕ_m with Da for (a) different values of Ha and (b) different values of R_α with $\omega = 10$, $S = 50$, $P_1 = 0.5$.

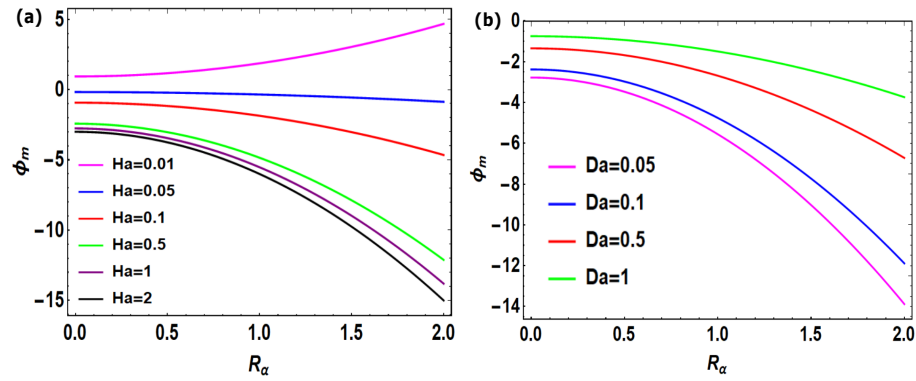


Figure 5.13: Variation of ϕ_m with R_α for (a) different values of Ha and (b) different values of Da with $\omega = 10$, $S = 50$, $P_1 = 0.5$.

Hartmann number (Ha) for different values of R_α decreases as displayed in Fig. 5.11(b). It can be observed that the increment of roughness reduces the function values of ϕ_m because of the flow resistance in the presence of roughness of a complex wavy surface. The variation of ϕ_m with Darcy number is plotted in Fig. 5.12 with different values of Hartmann number and R_α respectively. It is noticed from both the figures that the variation of waviness function (ϕ_m) increases monotonically with the increases of Darcy number. The waviness function (ϕ_m) is enhanced with the increase of the applied magnetic field as shown in Fig. 5.12(a). Due to the applied electromagnetic forces, the volumetric flow rate is increased for the higher permeability of the porous medium. But the impact of roughness reduces the function values of waviness function (ϕ_m) as shown in Fig. 5.12(b). This fact lies in the roughness of the complex wavy surface resisting the flow velocity, and therefore the volumetric flow rate through the complex wavy rough surface is diminished with the enhancement of the permeability of the porous medium. Fig. 5.13 reveals the impact of roughness on the waviness function (ϕ_m) with different Hartmann numbers and Darcy number respectively. The roughness of the complex wavy surface resists the flow velocity and therefore, the function ϕ_m is monotonically decreased with the increment of the wave amplitude ratio R_α except for the very low Hartmann number. The function ϕ_m is decreased for the increase of Hartmann number (Fig. 5.13(a)) but it is decreased for the increase of Darcy number (Fig. 5.13(b)). Thus, the volumetric flow rate through the microchannel is reduced due to the resistance of the complex wavy rough surface.

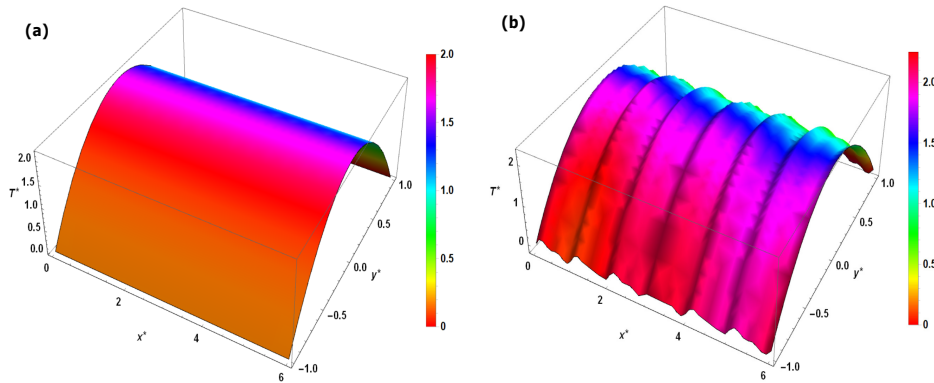


Figure 5.14: Comparison of 3D temperature profiles for $\omega = 10$, $S = 50$, $P_1 = 0.5$, $Da = 0.1$, $R_\alpha = 0.7$, $S_j = -2$, (a) $\epsilon = 0.0$ (smooth microchannel); (b) $\epsilon = 0.025$.

5.6.5 Analysis of thermal characteristics

Heat transfer plays an important role in thermo-fluidic transport phenomena in the presence of a rough surface microchannel. It generates chaotic temperature differences in the boundary layers of the flow transport through the rough surface microchannel. To visualize these temperature profiles between a rough and smooth surface microchannel, we have illustrated them in Fig. 5.14. It is observed that a parabolic temperature profile is generated for the smooth microchannel as displayed in Fig. 5.14(a), while a significant disturbance occurs for the rough microchannel as shown in Fig.

5.14(b). Also, the waviness generates in the temperature profile due to the roughness throughout the microchannel.

The contour plots of temperature (called isotherms) for different wavy amplitude ratio (R_α) are shown in Figs. 5.15(a)-5.15(d), indicate the impact of the complex wavy roughness on the thermal transport characteristics respectively. It is described that the roughness of the complex wavy microchannel gets disturbed in the dimensionless temperature. It is slightly higher near the rough surface with the increment of wavy amplitude ratio (R_α). The disturbance in the dimensionless temperature is delineated very clearly by the contour plots, near to the complex wavy rough surface of the microchannel. More disturbances are observed in the roughness region of the microchannel and the dimensionless temperature is slightly lower for the wavy microchannel ($R_\alpha = 0$) as shown in Fig. 5.15(a). Some symmetric boluses are formed in the middle layers across the microchannel for $R_\alpha = 0$ (see Fig. 5.15(a)), but with the enhancement of wavy amplitude ratio (R_α) generated asymmetric boluses (temperature disturbances) in the middle layers throughout the complex wavy microchannel which is displayed in Fig. 5.15(b)-5.15(d).

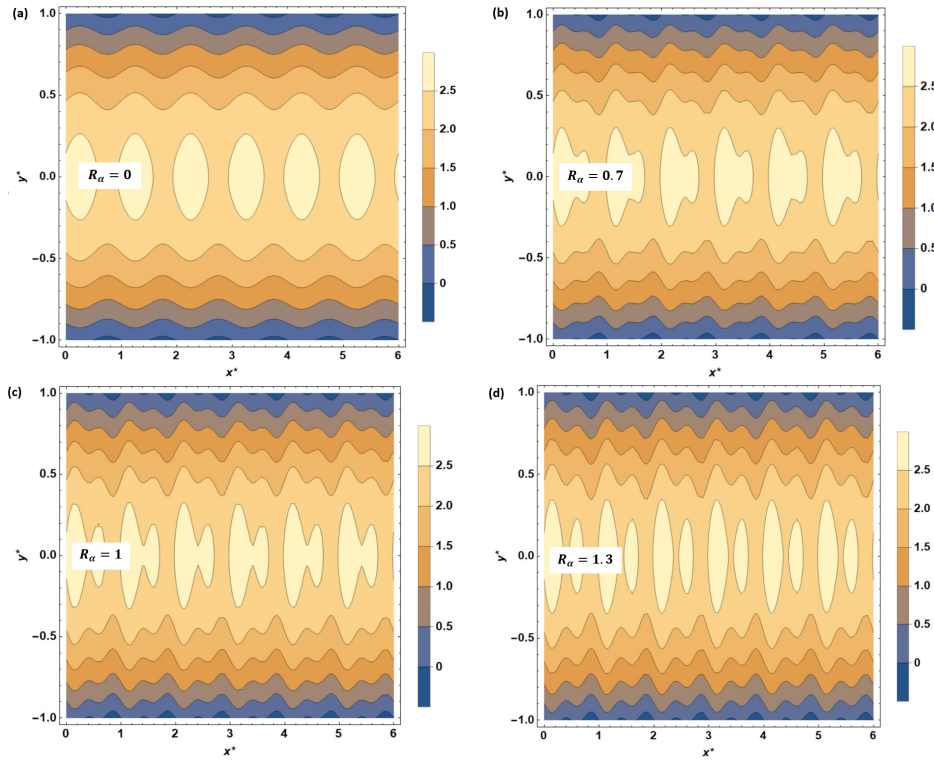


Figure 5.15: Contour plot for temperature profiles for $\omega = 10$, $S = 50$, $P_1 = 0.5$, $Ha = 0.5$, $\varepsilon = 0.025$, $Da = 0.03$, $S_j = -2$, (a) $R_\alpha = 0$; (b) $R_\alpha = 0.7$; (c) $R_\alpha = 1$ and (d) $R_\alpha = 1.3$

To observe the thermal characteristics due to the effect of an applied magnetic field, the contour plots for different Hartmann number are depicted in Fig. 5.16. In the presence of transverse electric field ($S = 50$), and an increment of the strength of the applied magnetic field, as embodied by enhancement of Hartmann number, subsists a significant reduction in the temperature profiles, as displayed in Fig. 5.16(a)-5.16(d). The apprehensible enhancement of flow velocity (see Fig.

5.7) with the increases in Hartmann number, enhances the transport of advective thermal energy and diffusive heat transfer from the rough surface of the channel. As a result, the dimensionless temperature rises with the increase of Ha , delineated in Figs. 5.16(a)-5.16(d). The disturbances are generated near the rough surface with the increases in Hartmann number and the intensification of the formulation of isotherms is shown in the middle portion of the channel. For higher values of Hartmann number ($Ha \geq 1$), more disturbances are generated, which may be useful in the micro-fabrication technology.

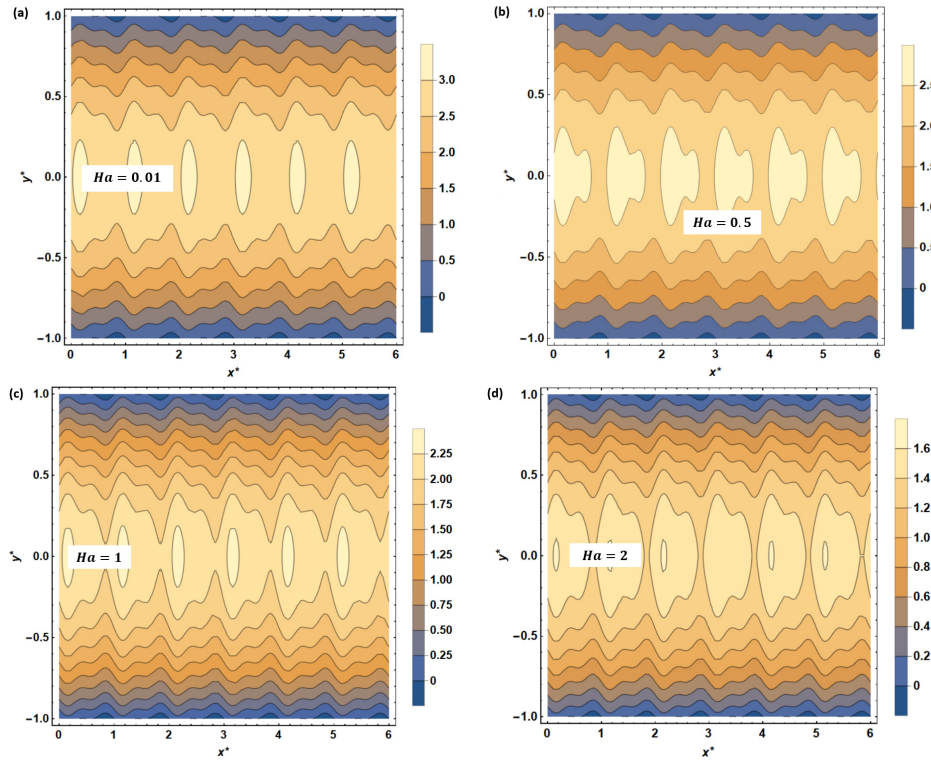


Figure 5.16: Contour plot for temperature profiles for $\omega = 10$, $S = 50$, $P_1 = 0.5$, $Da = 0.03$, $\varepsilon = 0.025$, $R_\alpha = 0.7$, $S_j = -2$, (a) $Ha = 0.01$; (b) $Ha = 0.5$; (c) $Ha = 1$ and (d) $Ha = 2$

Fig. 5.17 depicts the graphical interpretation of the three-dimensional temperature profiles for different Darcy number (Da) in the complex wavy microchannel and the influence of the porosity parameter (Darcy number) on the temperature profiles is described very briefly. The increasing effect of permeability of the porous medium generates very disturbing temperature profiles as depicted in Figs. 5.17(a)-5.17(d). The enhancing trend of permeability of the porous medium reduces temperature profiles. For lower values of Darcy number, the viscous resistance is higher and therefore the chaotic advection of thermal energy is improved, as a result, the overall temperature distribution on the complex wavy rough surface is reduced. The permeability of the porous medium generates the parabolic temperature profiles for $Da < 1$. These figures delineate that the isotherm contours are formed in the middle layers across the microchannel.

The variations of temperature contour plots for different Joule heating effect (S_j) are represented in Fig. 5.18, which indicates the impact of heat generation on the thermal transport characteristics.

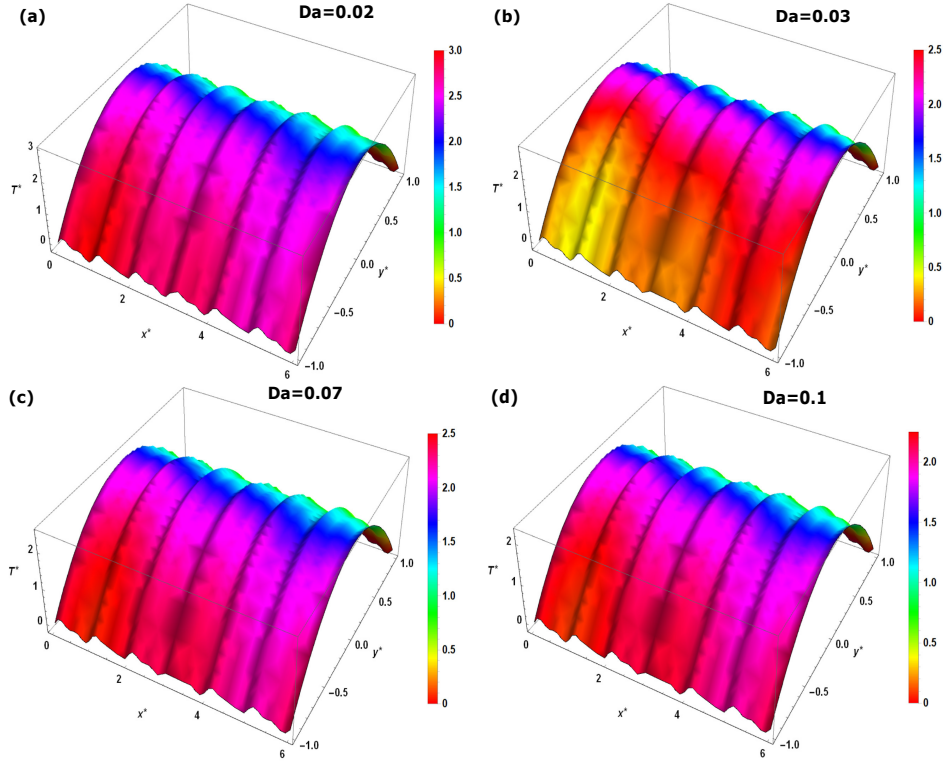


Figure 5.17: 3D temperature profiles for $\omega = 10$, $S = 50$, $P_1 = 0.5$, $\varepsilon = 0.025$, $R_\alpha = 0.7$, $S_j = -2$, (a) $Da = 0.02$; (b) $Da = 0.03$; (c) $Da = 0.07$ and (d) $Da = 0.1$.

It can be observed that the temperature profiles are enhanced with the increase of Joule heating parameters but when there is no Joule heating effect, then the temperature becomes lower. The patterns on the temperature profiles at the boundary layers have been changed due to the variation of the wall roughness. The influence of the Joule heating effect significantly produces the disturbance in the temperature distribution.

The impact of viscous dissipation plays a very important role during the electrothermal flow through the rough surface microchannel. The mechanical energy is generated due to the employment of shear stress on the adjacent fluid layers which is transfigured into heat is called viscous dissipation. In this study, the viscous dissipation function is the combination of frictional heating at the surface and internal heating in the porous medium, which is expressed by the Darcy term. After making it dimensionless, the dissipation function is controlled by the parameters viz., Brinkman number (Br) and Darcy number (Da), as shown in Eq. (5.75). When $Br = 0$, then there is no influence of viscous dissipation; when $Da \rightarrow \infty$, it represents that the Darcy term in dissipation function has no contribution, this implies that the only frictional heating at the surface of the microchannel is acting as dissipation function for $Da \rightarrow \infty$.

The axial temperature profiles for different values of Brinkman number are displayed in Fig. 5.19(a). It can be observed that the axial temperature profiles are parabolic in nature and the increment of the Brinkman number enhances the axial temperature profiles. The significance of the Brinkman number embodies the ratio between viscous dissipation and the transportation of heat due

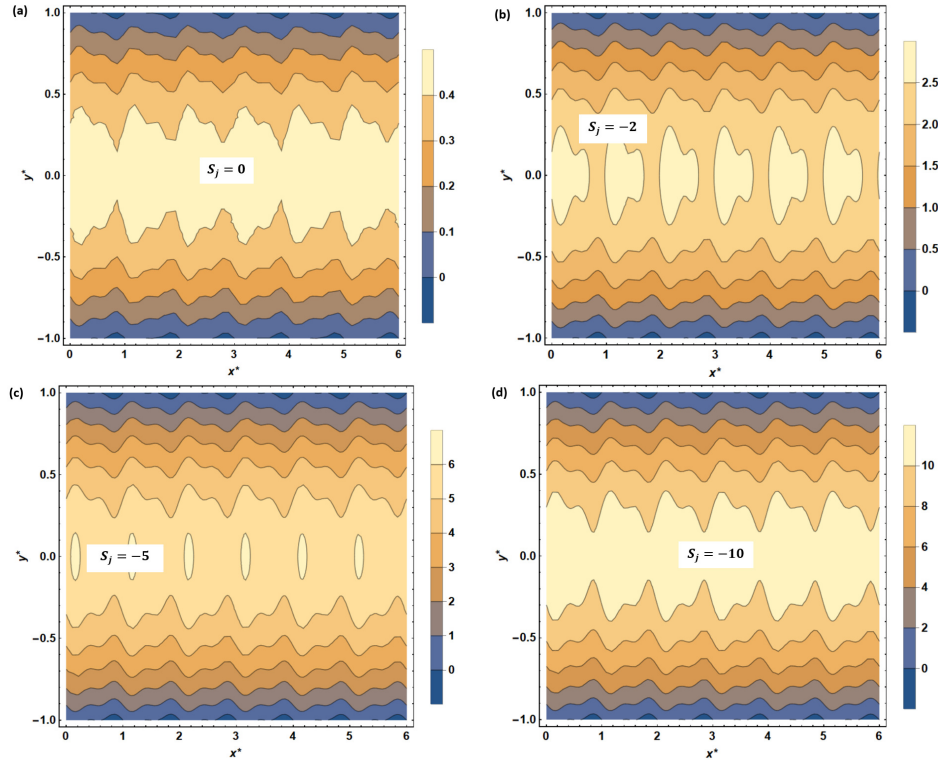


Figure 5.18: Contour plot for temperature profiles for $\omega = 10$, $S = 50$, $P_1 = 0.5$, $Ha = 0.5$, $\varepsilon = 0.025$, $R_\alpha = 0.7$, $Da = 0.03$, (a) $S_j = 0$; (b) $S_j = -2$; (c) $S_j = -5$ and (d) $S_j = -10$.

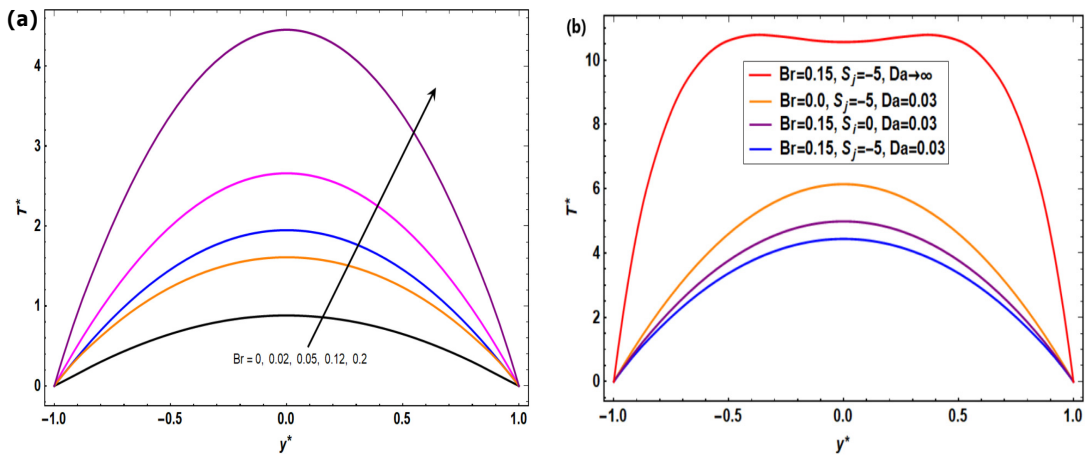


Figure 5.19: Axial Temperature profiles in complex wavy microchannel for different (a) Brinkman number (Br), (b) comparison of axial temperature profiles with dissipation and joule heating effects for $\omega = 10$, $S = 50$, $P_1 = 0.5$, $Ha = 0.5$, $\varepsilon = 0.025$, $R_\alpha = 0.7$, $x^* = 0.5$

to the conduction of molecules of the electrolyte solution. Thus, the higher values of the Brinkman number mean the heat conduction is slower than the heat produced by viscous dissipation and as a result, the temperature rises which is represented in Fig. 5.19(a). The comparison of axial temperature profiles with the impact of dissipation and Joule heating is delineated in Fig. 5.19(b). In this figure one can easily observe the changes in temperature profiles due to the different viscous dissipation effects and Joule heating. The temperature profiles are parabolic except when there is no effect of internal heating due to porous medium ($Da \rightarrow \infty$) and it becomes higher than other profiles for $Da \rightarrow \infty$. This implies that the presence of a porous medium in the complex wavy microchannel reduces the temperature, which is shown in Fig. 5.19(b).

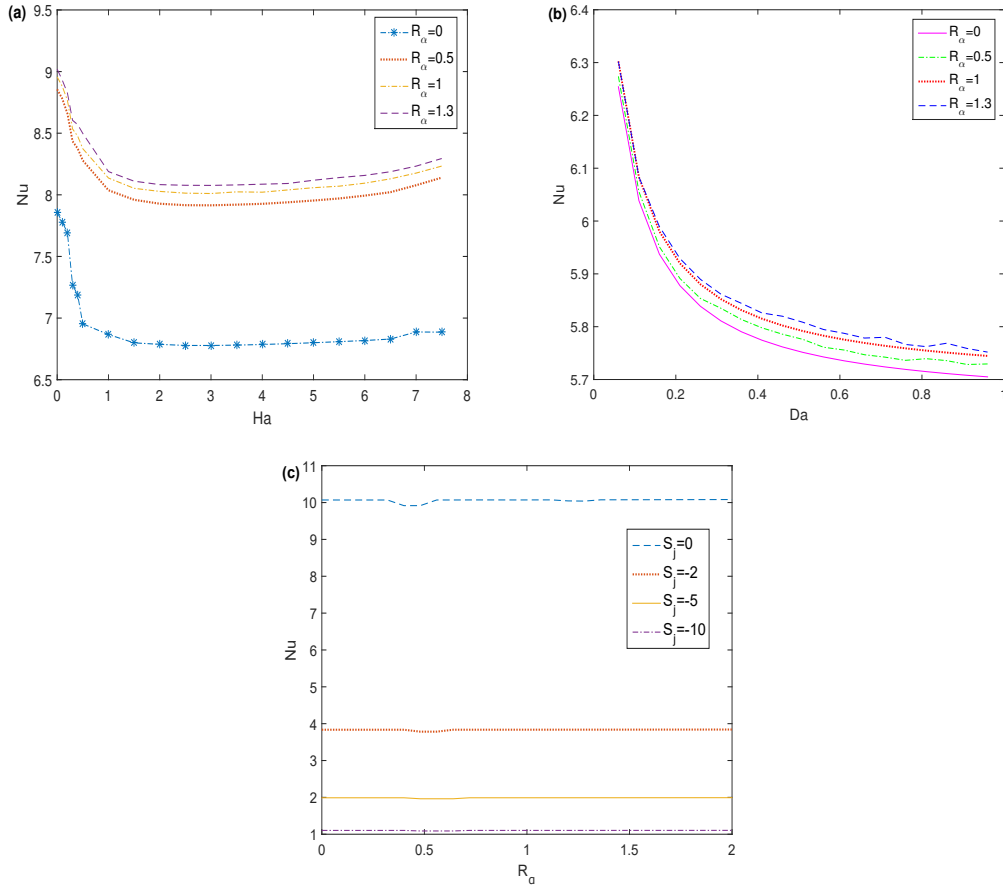


Figure 5.20: Variation of Nusselt number with (a) Hartmann number, (b) Darcy number for different values of R_α and $\omega = 10$, $S = 50$, $P_1 = 0.5$, $\varepsilon = 0.025$, $S_j = -2$, (c) Variation of Nusselt number with wave amplitude ratio (R_α) for different values of joule heating parameter and $\omega = 10$, $S = 50$, $P_1 = 0.5$, $\varepsilon = 0.025$, $Ha = 1$, $Da = 0.03$.

5.6.6 Analysis of heat transfer rate: Nusselt number

In this study, the significance of the Nusselt number embodies the rate of heat transfer that measures the rate of energy conversion from the surface of the microchannel to the fluid domain. The Nus-

selt number is calculated by applying the bulk mean temperature, which is calculated numerically from Eq. (5.97). The variation of Nusselt number for different other parameters such as Hartmann number (Ha), Darcy number (Da), and wave amplitude ratio (R_α) are delineated graphically in the Figs. 5.20(a), 5.20(b) and 5.20(c) respectively. The Nusselt number is gradually decreased with the improvement of the strength of the applied magnetic field, which is displayed in Fig. 5.20(a). A rapid reduction is shown in the Nusselt number profiles with the enhancement of permeability of the porous medium as depicted in Fig. 5.20(b). The enhancing trend of the roughness of the complex wavy microchannel improves the Nusselt number with increasing nature of magnetic field strength (See Fig. 5.20(a)) but it reduces the Nusselt number with the augmentation of permeability of the porous medium as represented in Fig. 5.20(b). From Fig. 5.20(c), we observed that the increase of the Joule heating parameter causes a decrease in the Nusselt number.

5.7 Conclusions

The impact of complex wavy roughness on the electromagnetohydrodynamic (EMHD) flow transport and thermal characteristics through a porous microchannel have been investigated. The governing equations of the thermo-fluidic transport are solved analytically by employing the perturbation technique. Different values of wave amplitude with respect to the roughness of the microchannel are considered in this performance. The changes in the flow patterns and the disturbance on the temperature profiles due to the effects of roughness are discussed briefly. The impact of the applied magnetic field, electric field and Joule heating are discussed on the thermo-fluidic transport through the complex wavy microchannel with a porous medium. Further, the influence of roughness on the rate of heat transfer is also performed. The surface roughness produces disturbance in the flow and heat transfer in the microchannel. The disturbances in the flow phenomena may have significant contributions to the separation process. Due to the enhancement of the applied magnetic field, the velocity profiles increase and it becomes fully developed under the action of a transverse electric field. The middle layer of the flow is not affected by the wave amplitude and there is an only disturbance on the boundary layers of the flow due to the resistance of the roughness of the complex wavy surface. The high permeability of the porous medium generates the parabolic velocity profiles but the volumetric flow rate is diminished for the high permeability of the porous medium with the enhancing nature of roughness. Also, the roughness of the complex wavy surface resists the volume flow rate of the microchannel. The temperature profiles are always parabolic for $Da < 1$. The roughness of the surface enhances the Nusselt number.

6

Role of Anisotropic Permeability on EMHD Heat Transfer in a Rough Microchannel

6.1 Introduction

Microfluidic technologies have been developed to offer a host of performance benefits in the modern scientific world. Various contemporary microfluidic devices are manufactured to enhance microchannel flow structures, thermal performance, and fast reaction responses. These devices are widely used in designing various microelectromechanical systems, such as microturbines (Soares [2015]), MHD micropumps (Jang and Lee [2000]; Nash and Fritsch [2016]), EMHD micropumps (Nguyen and Kassegne [2008]; Lemoff and Lee [2000]), and fuel cells (Soares [2015]), among others. Furthermore, there are numerous applications of porous microchannels in energy, pharmaceutical, and biomedical fields. These applications are commonly employed in microreactors (Renault et al. [2012]) and micro-heat exchanger technology (Jiang et al. [2018]). Moreover, these technologies are found in the field of photocatalytic water purification (Zhang et al. [2021a]), tissue engineering (Mehta and Linderman [2006]), cell growth technology, hydrogen production (Chen et al. [2011]), and fuel cells (Zhang et al. [2021b]; Krewer et al. [2007]; Oliveira et al. [2010]), among others. Recently, researchers have paid attention to nanofluids due to their potential for heat transfer applications (Avramenko et al. [2018]) in various conventional fluids, such as engine oil and water, containing nanoscale metallic particles (Sheikholeslami et al. [2013]; Uddin et al.

The content of this chapter has been published in Chinese Journal of Physics (Elsevier), 88:537-556 (2024).

[2013]; Sheikholeslami et al. [2014]; Mahian et al. [2013]). Several authors (Mohammed et al. [2011]; Mahian et al. [2014]; Ho et al. [2014]; Kherbeet et al. [2014]) have reported relevant works in microchannels by considering nanofluids. It is fascinating to note that nanofluids in micro heat exchangers enhance the cooling rate of water-based systems (Avramenko et al. [2019]; Mohammed et al. [2011]; Salman et al. [2013]).

Due to certain limitations in manufacturing technology, microfluidic channels exhibit surface roughness. As this roughness can alter flow patterns, researchers have focused on studying wavy microchannels (Rana et al. [2021b]; Reza et al. [2021]) and rough microchannels (Rana et al. [2022]; Keramati et al. [2016]). To optimize energy transfer in microfluidic systems, Sarkar et al. [2016] investigated energy conversion in EMHD flow through microchannels, considering hydroelectric phenomena. They provided analytical and numerical results of governing equations to assess overall energy transfer in microscale systems. Rashid and Nadeem [2019] employed a mathematical model of EMHD flow to explore nanoparticle effects on flow transport through a microchannel with corrugated walls. The influence of wall waviness on velocity and temperature was examined, revealing that increasing the wave number enhances microchannel corrugation, thereby altering flow characteristics. Yang et al. [2019] studied MHD electroosmotic flow and heat transfer in microchannels, analyzing effects like viscous dissipation, Joule heating, and electromagnetic force on electrokinetic flow. They employed variable separation methods to solve governing equations. Noreen et al. [2021] investigated entropy generation in EMHD flow through porous asymmetric microchannel using water-based nanofluids. Inspired by nanomedicine technology, where in they solved a non-linear mathematical model to discuss heat transfer rates with various nanoparticles. Total entropy generation of titania-water nanofluid was found to be lower than that of copper-water and alumina-water nanofluids. Li et al. [2019] introduced three-dimensional surface corrugation to EMHD flow using two sinusoidal functions, obtaining analytical solutions for governing equations via the perturbation method. They concluded that flow rate can be maximized by increasing magnetic field strength. Buren et al. [2017] examined the combined effect of EMHD flow in a corrugated microchannel, revealing that channel wall roughness disrupts flow and reduces mean velocity. Ranjit and Shit [2017] calculated entropy generation of two stress fluids in close confinement with an asymmetric porous surface, aiming to develop microfluidic devices for biomedical and industrial use. They observed highest entropy generation in the middle portion of the upper and lower portion of the microchannel.

Flow transport and heat transfer within porous media hold fundamental significance in various advanced technologies, encompassing oil recovery, powder metallurgy, transpiration cooling, drying processes, and agricultural engineering, among others. Nield and Bejan [2006] have dedicated their efforts to both numerical and experimental studies on flow patterns within porous channels. Marzougui et al. [2021] investigated mixed convection flow and heat transport within a channel subjected to a uniform magnetic field. They employed the generalized Brinkman-extended Darcy model with the Boussinesq approximation, utilizing COMSOL Multiphysics for computation. Alhajaj et al. [2020] validated their hybrid nanofluidic flow and heat transport through a porous channel by comparing experimental results and numerical simulations. Degan et al. [2016]

delved into radiation-mixed convection flow within a vertical channel containing an anisotropic porous medium. They analytically solved the generalized Brinkman-extended Darcy model with no-slip boundary conditions, revealing the influence of thermal radiation and anisotropic permeability on thermo-fluidic motion. Neffah et al. [2018] explored the thermo-fluidic transport of non-Newtonian power-law fluid in an anisotropic porous channel under the influence of chemical reactions. Analyzing the linear stability of horizontally flowing fluid within an anisotropic porous medium, Malashetty et al. [2005] achieved excellent agreement between exact and asymptotic solutions. They explored the effects of thermal non-equilibrium and anisotropic porous medium permeability on the onset of convection. Kameswaran et al. [2016] numerically analyzed the melting effect on mixed convection flow over a variable permeability vertical plate. By transforming governing equations into nonlinear ordinary differential equations through similarity transformations, they found that the rate of heat transfer and radiative heat transfer are both enhanced by the melting effect. Degan et al. [2002] presented an exact solution for fully developed forced convection flow within a horizontal channel featuring an anisotropic porous medium. It is reported that heat transfer rate relies on porous matrix orientation, with permeability ratio and angle influencing thermal convection in the anisotropic porous channel. Zhou et al. [2022] discussed electrochemical reactions in microreactor flow through an anisotropic porous microchannel. They numerically simulated three-dimensional flow fields under low pressure, optimizing the anisotropic porous media.

Despite the aforementioned motivating literature, no prior work has been conducted on wavy microchannel with anisotropic porous medium. This research delves into the steady, incompressible, viscous nanofluid flow within an anisotropic porous microchannel featuring wavy walls. Electromagnetic phenomena and pressure gradients are influential factors in this study. The research aims to decipher nanofluidic EMHD flow behavior and heat transfer under the sway of anisotropic permeability and electromagnetic conditions. Mathematically modeling the flow problem facilitates visualization of thermo-fluidic analysis, with numerical solutions for governing equations. The research expounds on the effects of anisotropic permeability and porous medium permeability angle on thermo-fluidic transport, alongside detailing the implications of diverse viscous dissipation and Joule heating due to electric and magnetic field interaction. Furthermore, this chapter presents an analytical solution for validation against numerical findings.

6.2 Mathematical formulation and problem description

This chapter delineated the flow transport characteristics of a symmetric electrolyte solution through a wavy microchannel with a porous medium under combined electro-magnetohydrodynamic effects and imposed pressure-gradient. The channel walls are considered as wavy surface geometry (Fig. 6.1), which can be modeled by considering a wavy wall of the form: $h_w(x) = H - \lambda_a \cos^2(\pi x/L)$, in which λ_a and L denote the amplitude and the characteristic length of the microchannel respectively. In contrast, $2H$ denotes the constant height of the microchannel. It also assumes that the microchannel width (W) and length is much greater than the channel height ($L \gg W \gg 2H$). The electrolyte solution generates an EDL near the boundary wall, and the induced electric field

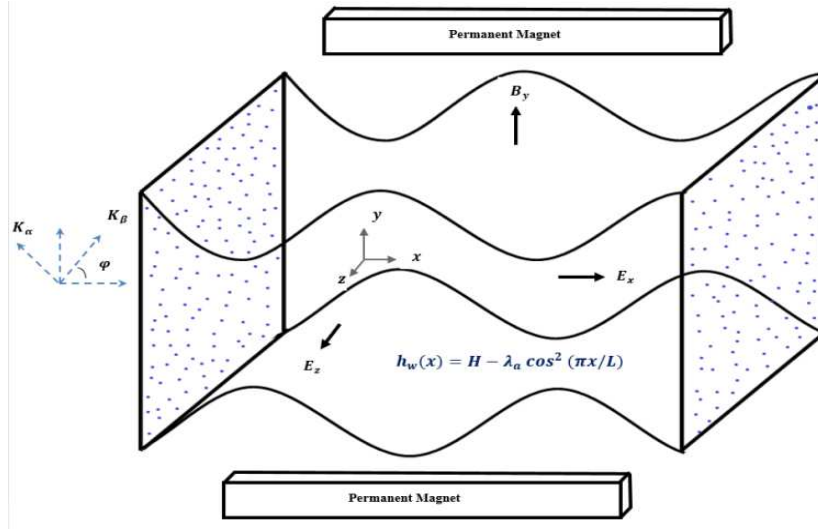


Figure 6.1: Physical sketch of the problem

in x -direction creates an electroosmotic flow. Also, the applied magnetic field is induced in y -direction. A constant heat flux q_w is imposed on the impermeable wall of the microchannel. The electroosmotic force is generated by the applied electric field component E_x , due to the EDL near the microchannel wall, which is directed opposite to the fluid motion. The total system is subjected to an applied magnetic field B_y perpendicular to the fluid flow direction and E_z is imposed as an external transverse electric field in z -direction. The microchannel is filled with an anisotropic porous material, in which the impenetrable walls are at $y = \pm h_w$. Assumed that the flow is steady and fully developed. The permeabilities along the two principle axis are K_α, K_β respectively, which are assumed to be constants. The orientation angle (anisotropic angle) φ is defined as the angle between the horizontal direction and the principal axis with permeability K_β .

In this investigation, nanofluid is considered where blood is taken as a base fluid, and Fe_3O_4 is taken as a nanoparticle. As per the requirement of various bio-medical applications and lab-on-chip applications, this nanofluid is considered. The thermophysical properties of the nanofluid are shown in the Table-6.1.

Table 6.1: Thermo-physical properties of nanofluid

Physical property	Base fluid	Nanoparticle (Fe_3O_4)
ρ ($kg.m^{-3}$)	1.08×10^3	5.2×10^{-3}
c_p ($J.kg^{-1}.K^{-1}$)	3.5×10^3	670
k ($W.m^{-1}.K^{-1}$)	0.59	6
σ ($S.m^{-1}$)	0.6	2.5×10^4
ϵ ($F.m^{-1}$)	2.03×10^{-7}	80

The governing equations for the corresponding mass conservation, momentum conservation,

energy and nanoparticle volume fraction can be expressed as (Rana et al. [2021b]; Avramenko and Shevchuk [2022]; Rana et al. [2022]):

$$\nabla \cdot \mathbf{U} = 0, \quad (6.1)$$

$$\rho_{eff}(\mathbf{U} \cdot \nabla)\mathbf{U} = -\nabla p + \mu_{eff}\nabla^2\mathbf{U} - \frac{\mu_{eff}}{K}\mathbf{U} - \frac{C_F\rho_{eff}}{\sqrt{K}}|\mathbf{U}|\mathbf{U} + \mathbf{b}, \quad (6.2)$$

$$\begin{aligned} (\rho c_p)_{eff}(\mathbf{U} \cdot \nabla)T &= k_{eff}\nabla^2T + \frac{\mathbf{J} \cdot \mathbf{J}}{\sigma_{eff}} + \mu_{eff}(\nabla\mathbf{U} + \nabla\mathbf{U}^T) \cdot \nabla\mathbf{U} \\ &+ (\rho c_p)_p \left(D_B \nabla T \cdot \nabla \Phi_p + \frac{D_T}{T} \nabla T \cdot \nabla T \right), \end{aligned} \quad (6.3)$$

$$(\mathbf{U} \cdot \nabla)\Phi_p = D_B \nabla^2\Phi_p + \frac{D_T}{T} \nabla^2T, \quad (6.4)$$

where \mathbf{U} is velocity vector, T represents the temperature, Φ_p denotes the volume fraction of nanoparticles, p stands for the pressure, C_F represents the inertial coefficient, D_B denotes the effective Brownian diffusion coefficient, D_T take into account the effective thermophoresis coefficient, which influences the nanoparticle mass transfer in the nanofluid, μ_{eff} corresponds to the effective viscosity and ρ_{eff} signifies the effective density, $(\rho c_p)_{eff}$ indicates effective heat capacitance and k_{eff} stands for effective thermal conductivity of the nanofluid.

The net body force \mathbf{b} in Eq. (6.2) due to the combined EMHD effect is given by:

$$\mathbf{b} = \rho_e \mathbf{E} + \mathbf{F}, \quad (6.5)$$

where ρ_e be the net charge density. The body fore is essentially contributed by the applied electric field \mathbf{E} and the Lorentz force \mathbf{F} due to the applied magnetic field. Here, $\mathbf{F} = \mathbf{J} \times \mathbf{B}$, where \mathbf{J} is the current density and \mathbf{B} is the magnetic field. In the present study, it is assumed that the applied magnetic field is sufficiently strong. The current density and the Lorentz force both are affected by the Hall current. By considering hall current, the current density \mathbf{J} may be written as:

$$\mathbf{J} + \frac{\sigma_{eff}}{en_e}(\mathbf{J} \times \mathbf{B}) = \sigma_{eff}(\mathbf{E} + \mathbf{U} \times \mathbf{B}), \quad (6.6)$$

where e be the fundamental charge of an electron, n_e is the number density of free electrons and σ_{eff} is called the effective electric conductivity of nanofluid.

In the preceding Eq. (6.2), K corresponds to the permeability of the porous medium. The permeability is second order tensor because the porous medium is anisotropic. Hence, the permeability tensor is defined as:

$$K = \begin{bmatrix} K_\alpha \sin^2 \varphi + K_\beta \cos^2 \varphi & (K_\beta - K_\alpha) \sin \varphi \cos \varphi \\ (K_\beta - K_\alpha) \sin \varphi \cos \varphi & K_\alpha \cos^2 \varphi + K_\beta \sin^2 \varphi \end{bmatrix}. \quad (6.7)$$

At the microchannel wall ($y = h_w$), we assume velocity slip, temperature slip, and nanoparticle volume fraction slip. These assumptions are based on the slip boundary condition, driven by the

necessity to precisely capture the intricate interaction of fluid dynamics, temperature gradients, and nanoparticle distribution at the channel's surface. These conditions align with the slip boundary condition, which can be expressed as follows:

$$\mathbf{U} + \beta_s \nabla \mathbf{U} \cdot \hat{n} = 0; \quad T + \tau_s \nabla T = 0; \quad \Phi_p + \delta_s \nabla \Phi_p = 0 \quad \text{at } y = h_w. \quad (6.8)$$

where β_s is called slip length, τ_s is the height of the temperature jump, δ_s represents the slip effect on volume fraction.

In the middle layers of the flow ($y = 0$), continuity is assumed, leading to the application of boundary conditions for velocity, temperature, and the volume fraction of nanoparticles. These conditions are crucial for upholding the conservation of mass, heat, and nanoparticle volume fraction within the flow and can be expressed as follows:

$$\nabla \cdot \mathbf{U} = 0; \quad \nabla T = 0; \quad \nabla \Phi_p = 0 \quad \text{at } y = 0. \quad (6.9)$$

6.2.1 Flow transport phenomena

In microfluidic transport the flow transport happens very slowly and usually it is a unidirectional flow. Therefore in this case, the velocities in y -direction and z -direction are assumed to be negligibly small, which approximate i.e. $v \approx 0, w \approx 0$. So, the flow is fully developed along x -direction which gives $u = u(y)$. Then, under the assumptions the simplified form of the mass conservation and momentum conservation equations (6.1) and (6.2) through the anisotropic porous medium within the EDL is written as:

$$\frac{du}{dx} = 0, \quad (6.10)$$

$$\frac{dp}{dx} + \frac{a_p^* \mu_{eff}}{K_\alpha} u + \frac{C_F \rho_{eff} b_p^*}{\sqrt{K_\alpha}} u^2 - \mu_{eff} \frac{d^2 u}{dy^2} = \rho_e E_x - \frac{\sigma_{eff} B_y^2 u}{1 + m_{eff}^2} + \frac{\sigma_{eff} B_y E_z}{1 + m_{eff}^2}, \quad (6.11)$$

$$\frac{c_p^* \mu_{eff} u}{K_\alpha} + \frac{\rho_{eff} C_F d_p^* u^2}{\sqrt{K_\alpha}} + \frac{dp}{dy} = 0, \quad (6.12)$$

where $a_p^* = \sin^2(\varphi) + K^* \cos^2(\varphi)$, $b_p^* = \sin^2(\varphi) + \sqrt{K^*} \cos^2(\varphi)$, $c_p^* = (1 - K^*) \sin(\varphi) \cos(\varphi)$, and $d_p^* = (1 - \sqrt{K^*}) \sin(\varphi) \cos(\varphi)$ are the parameters which are characterizing the anisotropy property of the porous medium and $K^* = K_\alpha / K_\beta$ is called the anisotropic permeability ratio, $m_{eff} = \sigma_{eff} B_y / (en_e)$ denotes the effective Hall parameter for the nanofluid. It is well known to all that no-slip boundary condition is not valid for physiological flow of blood through heart valves and arteries, thin films and rarefied fluid motion.

The relevant boundary conditions for velocity distribution are derived from (6.8) and (6.9) as follows:

$$\frac{du}{dy} = 0 \quad \text{at } y = 0 \quad \text{and} \quad u + \beta_s \frac{du}{dy} = 0 \quad \text{at } y = h_w. \quad (6.13)$$

If $\beta_s = 0$, then the interfacial slip boundary condition truncates to no-slip boundary condition.

Using Eq. (6.10) in Eq. (6.11) and Eq. (6.12) we get

$$\frac{\partial}{\partial x} \left(\frac{dp}{dx} \right) = 0 \text{ and } \frac{\partial}{\partial x} \left(\frac{dp}{dy} \right) = 0, \quad (6.14)$$

i.e.,

$$\frac{\partial}{\partial x} \left(\frac{dp}{dx} \right) = 0 \text{ and } \frac{\partial}{\partial y} \left(\frac{dp}{dx} \right) = 0. \quad (6.15)$$

Therefore, it follows from Eq. (6.14) and Eq. (6.15) that $\frac{dp}{dx} = \text{constant}$. So, the pressure gradient becomes constant along the x -direction.

To determine an explicit form of the net charge density ρ_e that appears in Eq. (6.11), one have to express the electric double layer phenomenon. It is well known that the EDL is formed near to the wall when the electrolyte solution is in contact with dielectric walls of the microchannel. Then the relation between electrical potential ψ and the net charge density ρ_e is constructed by the following Poisson equation

$$\nabla^2 \psi = \frac{\rho_e}{\epsilon_{eff}}, \quad (6.16)$$

where ϵ_{eff} is called effective permittivity of the nanofluid.

Further, assume that the wall zeta potential is a varying zeta potential (Banerjee and Nayak [2019]) near the microchannel wall, which can be expressed as $\psi_w(x) = \psi_0 \{1 - \frac{\lambda_a}{H} \cos^2(\pi x/L)\}$ and ψ_0 is the constant zeta potential, which is very small $|\psi_0| \leq 25mV$. By using Debye-Hückel approximation, the net charge densities of ions transformed into the unit volume of fluid as $n^\pm = n_0(1 \mp ez_0\psi/k_B T_a)$, which reduces the Eq. (6.16) as

$$\frac{\epsilon_{eff}}{\epsilon_f} \frac{d^2 \psi}{dy^2} = \kappa^2 \psi, \quad (6.17)$$

where $\kappa = ez_0(2n_0/\epsilon_f k_B T_a)^{\frac{1}{2}}$ where n_0 is the ion density(in molar unit), e is the electronic charge, z_0 is the valance, k_B is the Boltzmann constant, and T_a is the absolute temperature. Here ω is called the normalized reciprocal thickness of the EDL which representing the ratio of half height of microchannel to Debye length (i.e. $1/\kappa$) and κ is Dybye-Hückle parameter and $1/\kappa$ be the thickness of the EDL. To make dimensionless the following non-dimensional quantities are introduced:

$$\psi^* = \psi/\psi_0, \quad \psi_w^*(x^*) = \psi_w(x)/\psi_0, \quad y^* = y/H, \quad x^* = x/L, \quad h = h_w/H. \quad (6.18)$$

Then Eq. (6.17) reduces to the following form:

$$\epsilon(\phi_p) \frac{d^2 \psi^*}{dy^{*2}} = \omega^2 \psi^*, \quad (6.19)$$

where $\omega = \kappa H$ is called electroosmotic parameter and $\epsilon(\phi_p)$ is defined by the following relation

(Chakraborty and Roy [2008]):

$$\varepsilon(\phi_p) = \frac{\varepsilon_{eff}}{\varepsilon_f} = 1 + \frac{2(\varepsilon_p - \varepsilon_f)\phi_p}{(\varepsilon_p + 2\varepsilon_f) - \phi_p(\varepsilon_p - \varepsilon_f)}, \quad (6.20)$$

where ε_p and ε_f are the permittivities of the nano particles and the base fluid respectively.

The non-dimensional boundary conditions for the electrical potential equation are as follows:

$$\frac{d\psi^*}{dy^*} = 0 \text{ at } y^* = 0 \text{ and } \psi^* = \psi_w^* \text{ at } y^* = h = 1 - \lambda \cos^2(\pi x^*), \quad (6.21)$$

where $\lambda = \lambda_a/H$ is called the dimensionless amplitude of the wavy channel.

Further, one may write the mathematical expression of net charge density as follows:

$$\rho_e = -\varepsilon_f \kappa^2 \psi. \quad (6.22)$$

To make the equations dimensionless, the following non dimensional quantities are introduced:

$$\begin{aligned} u^* &= \frac{u}{U_{HS}}, \quad P^* = \frac{(\partial p / \partial x)H}{L}, \quad U_{HS} = \frac{\varepsilon_f \psi_w E_x}{\mu_f}, \\ p^* &= \frac{p}{\rho_f U_{HS}^2}, \quad Re = \frac{\rho_f U_{HS} H}{\mu_f}, \quad F = \frac{\rho_f C_F U_{HS} H}{\mu_f}, \\ Da &= \frac{K_a}{H^2}, \quad Ha = B_y H \sqrt{\frac{\sigma_f}{\mu_f}}, \quad S = \frac{E_z H}{U_{HS}} \sqrt{\frac{\sigma_f}{\mu_f}}. \end{aligned} \quad (6.23)$$

Hence Eq. (6.11) and (6.12) reduce to the following non-dimensional form:

$$\begin{aligned} &\mu(\phi_p) \left(\frac{d^2 u^*}{dy^{*2}} \right) - \left\{ \sigma(\phi_p) \left(\frac{Ha^2}{1 + m_{eff}^2} \right) + \mu(\phi_p) \left(\frac{a_p^*}{Da} \right) \right\} u^* \\ &- \rho(\phi_p) \left(\frac{b_p^* F}{\sqrt{Da}} \right) u^{*2} + \frac{\omega^2 \psi^*}{\varepsilon(\phi_p)} + \sigma(\phi_p) \left(\frac{HaS}{1 + m_{eff}^2} \right) = P^* Re, \end{aligned} \quad (6.24)$$

$$\mu(\phi_p) \left(\frac{c_p^*}{Da Re} \right) u^* + \rho(\phi_p) \left(\frac{d_p^* F}{Re \sqrt{Da}} \right) u^{*2} + \frac{dp^*}{dy^*} = 0, \quad (6.25)$$

where U_{HS} is the Helmholtz-Smoluchowski velocity with characteristic electric field strength E_x , Da represents the Darcy number, Ha represents the Hartmann number which is indicating the strength of the applied magnetic field B_y , F is the Forchhemier number which indicates non-dimensional inertial parameter, S represents the strength of the transverse electric field E_z . $m = \sigma_f B_y / (en_e)$ denotes the Hall parameter, $m_{eff} = m \sigma(\phi_p)$ and Re is the Reynolds number. $\mu(\phi_p)$, $\sigma(\phi_p)$, $\rho(\phi_p)$ are connected to the thermo-physical properties of nanofluid that can be expressed as (Xuan and Li [2003]; Yu and Choi [2003]; Avramenko and Shevchuk [2022]) :

$$\mu(\phi_p) = \frac{\mu_{eff}}{\mu_f} = \frac{1}{(1 - \phi_p)^{2.5}}, \quad (6.26)$$

$$\rho(\phi_p) = \frac{\rho_{eff}}{\rho_f} = \phi_p \frac{\rho_p}{\rho_f} + (1 - \phi_p), \quad (6.27)$$

$$\sigma(\phi_p) = \frac{\sigma_{eff}}{\sigma_f} = 1 + \frac{3(\sigma_p - \sigma_f)\phi_p}{(\sigma_p + 2\sigma_f) - (\sigma_p - \sigma_f)\phi_p}, \quad (6.28)$$

where ϕ_p is the nanoparticle volume fraction, μ_f be the viscosity of the base fluid, ρ_p is the density of the nanoparticles, ρ_f is the density of the base fluid, σ_f and σ_p denote the electric conductivity of the base fluids and nanoparticles respectively.

After non-dimensionalization, the boundary conditions reduce to

$$\frac{du^*}{dy^*} = 0 \text{ at } y^* = 0 \text{ and } u^* + \beta \frac{du^*}{dy^*} = 0 \text{ at } y^* = h, \quad (6.29)$$

in which $\beta = \beta_s/H$ indicates the slip parameter.

6.2.2 Thermal transport phenomena

The energy distribution during nanofluid flow through the porous microchannel with wavy wall is presented by considering the velocity distribution, along with volumetric heat generation due to body force and energy dissipation factor. In view of all the above considerations, the governing Eq. (6.3) for thermal energy is found to be expressed by

$$(\rho c_p)_{eff} u \frac{\partial T}{\partial x} = k_{eff} \left(\frac{\partial^2 T}{\partial x^2} + \frac{\partial^2 T}{\partial y^2} \right) + Q_v + Q_h + Q_d, \quad (6.30)$$

where $Q_v = \mu_{eff} \left\{ \left(\frac{du}{dy} \right)^2 + \frac{a_p^* u^2}{K} \right\} + \frac{b_p^* C_F \rho_{eff}}{\sqrt{K}} u^3$, contributes the different viscous dissipation effects which basically a combination of the internal heating inside the porous medium which is defined by Darcy term, the frictional heating at the channel wall defined by Al-Hadhrami term and the non-linear drag power defined by Forchheimer term respectively, $Q_h = \frac{\sigma_{eff}}{(1+m_{eff}^2)} (E_x^2 + B_y^2 u^2 - 2E_z B_y u)$ indicates the volumetric heat generation due to external body forces and $Q_d = (\rho c_p)_p \left\{ D_B \frac{dT}{dy} \frac{d\phi_p}{dy} + \frac{D_T}{T} \left(\frac{dT}{dy} \right)^2 \right\}$ contributes the different diffusion effects which basically a combination of the Brownian diffusion and thermophoretic diffusion. Hence, the boundary conditions for temperature distribution from (3.32) and (3.33) can be summarized as follows:

$$\begin{aligned} \frac{\partial T}{\partial y} &= 0 \text{ at } y = 0, \\ T + \tau_s \frac{\partial T}{\partial y} &= 0 \text{ at } y = h_w, \end{aligned} \quad (6.31)$$

where $q_w = h_f(T_w - T_b)$ accounts the applied heat flux throughout the entire wavy wall of the microchannel, T_w represents the wall temperature, T_b stands the bulk mean temperature.

Further, for thermally developed flow under imposed constant wall heat flux, one may write

$\frac{dT_w}{dx} = \frac{dT_b}{dx} = \frac{\partial T}{\partial x} = \text{constant}$, so that $\frac{\partial^2 T}{\partial x^2} = 0$. Under these consideration Eq. (6.30) can be rewritten as follows:

$$(\rho c_p)_{eff} u \frac{dT_b}{dx} = k_{eff} \frac{d^2 T}{dy^2} + Q_v + Q_h + Q_d. \quad (6.32)$$

In order to calculate the bulk mean temperature gradient, let us apply the overall energy balance on Eq. (6.32). Hence, the overall energy balance of an elementary control volume of the fluid with the length of duct dx gives the following expression:

$$(\rho c_p)_{eff} h_w u_m \frac{\partial T_b}{\partial x} = q_w + \int_0^{h_w} Q_v dy + \int_0^{h_w} Q_h dy + \int_0^{h_w} Q_d dy. \quad (6.33)$$

From the above expression (6.33), the bulk mean temperature gradient in the thermally developed situation yields

$$\frac{dT_b}{dx} = \frac{\Upsilon_1}{(\rho c_p)_{eff}} = \Upsilon_2(\text{say}), \quad (6.34)$$

where $\Upsilon_1 = \frac{1}{h_w u_m} \{q_w + \mu_{eff}(\beta_3 + \frac{a_p^* \beta_1}{K}) + \frac{b_p^* C_F \rho_{eff} \beta_2}{\sqrt{K}} + \frac{\sigma_{eff}}{(1+m_{eff}^2)}(E_x^2 + B_y^2 \beta_1 - 2E_z B_y u_m)\}$, $u_m = \int_0^{h_w} u dy$, $\beta_1 = \int_0^{h_w} u^2 dy$, $\beta_2 = \int_0^{h_w} u^3 dy$, $\beta_3 = \int_0^{h_w} (\frac{du}{dy})^2 dy$.

By introducing the dimensionless temperature, $T^* = \frac{k_f(T-T_w)}{q_w H}$ and using Eq. (6.34) in Eq. (6.32), one may obtain the dimensionless energy equation as follows:

$$\begin{aligned} k(\phi_p) \frac{\partial^2 T^*}{\partial^2 y^*} = & \xi(\phi_p) Pe \Upsilon u^* - \mu(\phi_p) \left\{ \left(\frac{du^*}{dy^*} \right)^2 + \frac{a_p^* u^{*2}}{Da} \right\} Br \\ & - \rho(\phi_p) \left(\frac{b_p^* Br F}{\sqrt{Da}} \right) u^{*3} + N_B \frac{dT^*}{dy^*} \frac{d\phi_p}{dy^*} + N_t \left(\frac{dT^*}{dy^*} \right)^2 \\ & - \frac{\sigma(\phi_p)}{(1+m_{eff}^2)} \left(Br H a^2 u^{*2} - 2 H a S B r u^* + \gamma_j \right), \end{aligned} \quad (6.35)$$

where $k(\phi_p) = \frac{k_{eff}}{k_f}$, $\xi(\phi_p) = \frac{(\rho c_p)_{eff}}{(\rho c_p)_f}$, $\Upsilon = \frac{k_f \Upsilon_2}{q_w}$ is the ratio of heat generation due to the interaction of the applied electric field and magnetic field to heat conduction, $Pe = \frac{(\rho c_p)_f u_{HS} H}{k_f}$ is called Peclet number, $Br = \frac{u_{HS}^2 \mu_f}{H q_w}$ is the Brinkman number which describes the ratio of heat produced by viscous dissipation and heat transport by molecular conduction, $N_B = \frac{\tau_{pf} D_B (\Phi_w - \Phi_\infty)}{\alpha_f}$ indicates Brownian motion parameter and $N_t = \frac{\tau_{pf} q_w}{\alpha_f H} \left(\frac{D_T}{T_\infty} \right)$ denotes the thermophoresis parameter, $\tau_{pf} = (\rho c_p)_p / (\rho c_p)_f$, $\alpha_f = k_f / (\rho c_p)_f$ and $\gamma_j = \frac{\sigma_f E_x^2 H}{q_w}$ is the measure of the joule heating due to heat conduction. $k(\phi_p)$ and $\xi(\phi_p)$ are connected to the nanfluid properties which can be expressed as (Xuan and Li [2003]; Yu and Choi [2003]; Avramenko and Shevchuk [2022])

$$k(\phi_p) = \frac{(\rho c_p)_{eff}}{(\rho c_p)_f} = \phi_p \frac{(\rho c_p)_p}{(\rho c_p)_f} + (1 - \phi_p), \quad (6.36)$$

$$\xi(\phi_p) = \frac{k_{eff}}{k_f} = \frac{k_p + 2k_f + 2(k_p - k_f)(1 + v_n)^3 \phi_p}{k_p + 2k_f - 2(k_p - k_f)(1 + v_n)^3 \phi_p}, \quad (6.37)$$

where $(\rho c_p)_p$ and $(\rho c_p)_f$ denote the heat capacitance of the nanoparticles and the base fluid respectively, k_p and k_f represent the thermal conductivities of nanoparticle and the base fluid respectively, v_n is the ratio between the thickness of the nanolayer and the radius of the nanoparticle, which is a non-dimensional quantity.

The dimensionless boundary condition together with the temperature jump condition given by

$$\begin{aligned} \frac{\partial T^*}{\partial y^*} &= 0 \text{ at } y^* = 0, \\ T^* + \tau \frac{\partial T^*}{\partial y^*} &= 0 \text{ at } y^* = h. \end{aligned} \quad (6.38)$$

in which $\tau = \tau_s/H$ is a measure of temperature slip.

Once we determine the temperature distribution and velocity distribution, the non-dimensional bulk temperature can be obtained by the following expression:

$$T_b^* = \frac{\int_0^h u^* T^* dy^*}{\int_0^h u^* dy^*} = \frac{k_f(T_b - T_w)}{q_w H}. \quad (6.39)$$

In thermal transport phenomenon an important heat transfer parameter can be expressed as Nusselt number Nu , which illustrates the rate of heat transfer and can be defined as:

$$Nu = \frac{H q_w}{k_{eff}(T_w - T_b)} = -\frac{k_f}{k_{eff}} \frac{1}{T_b^*}. \quad (6.40)$$

6.2.3 Mass transfer phenomena

Within microchannel flow, the mass transfer in the direction of flow is negligibly small when compared to the substantial mass transfer occurring across the channel. In this setting, convective term of Eq. (6.4) play a minor role in the direction of flow, while mass transfer across the channel, possibly driven by diffusion. Taking into account all the factors discussed above, the governing equation for mass transfer is formulated as

$$D_B \frac{\partial^2 \Phi_p}{\partial y^2} + \frac{D_T}{T_\infty} \frac{\partial^2 T}{\partial y^2} = 0, \quad (6.41)$$

where T_∞ is the temperature outside the boundary layer. The boundary conditions can be expressed as (cf. [Raza et al. \[2016\]](#))

$$\begin{aligned} \frac{\partial \Phi_p}{\partial y} &= 0 \text{ at } y = 0, \\ \Phi_p + \delta_s \frac{\partial \Phi_p}{\partial y} &= 0 \text{ at } y = h_w. \end{aligned} \quad (6.42)$$

By introducing the dimensionless volume fraction, $\phi_p = (\Phi_p - \Phi_w)/(\Phi_w - \Phi_\infty)$ in Eq. (6.41), one may obtain the dimensionless mass transfer equation as follows:

$$N_B \frac{\partial^2 \phi_p}{\partial y^{*2}} + N_t \frac{\partial^2 T^*}{\partial y^{*2}} = 0. \quad (6.43)$$

The dimensionless boundary conditions are given by

$$\begin{aligned} \frac{\partial \phi_p}{\partial y^*} &= 0 \text{ at } y^* = 0, \\ \phi_p + \delta \frac{\partial \phi_p}{\partial y^*} &= 0 \text{ at } y^* = h, \end{aligned} \quad (6.44)$$

where $\delta = \delta_s/H$ represents the slip effect on volume fraction.

6.3 Results and Discussion

In this section, we present numerical results for velocity distribution (u^*), temperature distribution (T^*), and the volume fraction of nanoparticles (ϕ_p). We addressed the nonlinear equations that define these distributions, specifically Eqs. (6.24), (6.35), and (6.43). The solution was achieved using the Runge-Kutta method, with adherence to the respective boundary conditions given by Eqs. (6.29), (6.38), and (6.44). Additionally, we determined the Nusselt number through a numerical integration method. To ensure appropriate results, pertinent parameters involved in this investigation are assigned suitable set of values. The height of the microchannel (H) is $100 - 200 \mu m$ with wave amplitude $\lambda_a \sim 0 - 0.1$ for wavy surface (Rana et al. [2022]; Buren et al. [2017]). Based on the ionic strength of the electrolyte solution, the thickness of the EDL (κ) is considered as $0.25 \mu m - 1 \mu m$ (Keramati et al. [2016]; Buren et al. [2017]). Hence, the electroosmotic parameter is taken as $\kappa \sim 5 - 20$. The applied Electrical field in the axial direction and the transverse direction are considered as $E_x \sim 0 - 2 \times 10^4 V/m$ and $E_y \sim 0 - 2 \times 10^4 V/m$ respectively (Rana et al. [2022]; Buren et al. [2017]). The applied magnetic field is taken as $B_y \sim 1 - 50 T$ (Rana et al. [2022]), where the range of the Hartmann number is in a wide range from $Ha \sim 0 - 5$. In fact, the range of Hartmann number is very small for microfluidic flow (Rana et al. [2022]). The wall zeta potential for the rough microchannel is taken as $\psi_0 \sim (-18)mV - (-12.5)mV$ (Banerjee and Nayak [2019]). The range of permeability values for the porous microchannel, which extends from 0 to $10^{-11} m^2$ (Rana et al. [2022]; Karmakar and Rajasekhar [2016]), corresponds to a spectrum of Darcy numbers (Da) that varies from 0 to 1. Due to the constant heat flux $q_w = 1500 W/m^2$, the range of joule heating parameter is $\gamma_j \sim 1 - 10$ (Banerjee and Nayak [2019]). When the channel height is taken in the range $100 - 200 \mu m$ and the range of Brinkman number $Br \sim 0 - 1$, which are taken from the existing literature (Rana et al. [2022]). The values for both the Brownian diffusion and thermophoretic diffusion parameters are maintained at low levels, ranging from 0 to 1 (Avramenko and Shevchuk [2022]; Niazi and Xu [2020]).

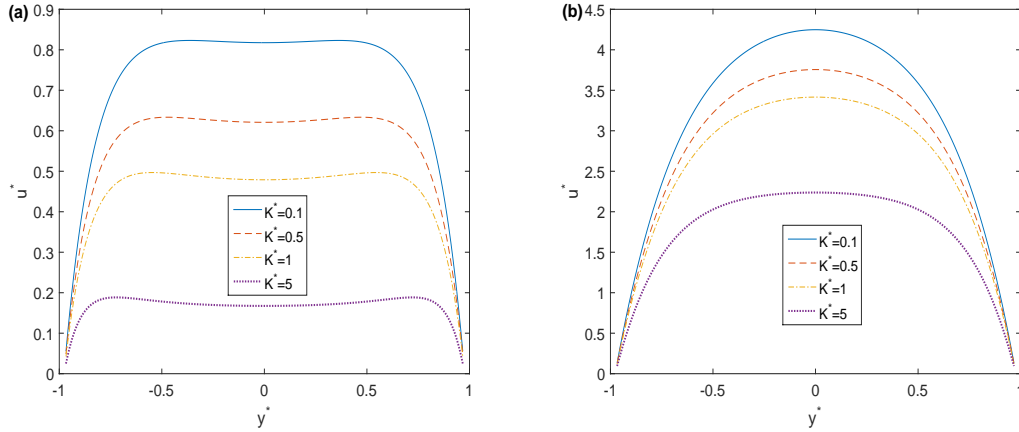


Figure 6.2: Velocity profiles for different anisotropic permeability ratio and (a) $Da = 0.02$, (b) $Da = 0.5$ with $\omega = 4$, $S = 50$, $P^* = 0.5$, $Ha = 1$, $F = 1$, $m = 1$, $\varphi = \pi/4$, $\beta = 0.01$, $\lambda = 0.05$.

6.3.1 Electromagnetohydrodynamic flow analysis

The velocity profiles is displayed in Fig. 6.2 for different anisotropic permeability ratio. The anisotropic nature of the porous medium characterized by $a_p^* = \sin^2(\varphi) + K^* \cos^2(\varphi)$, depends on K^* and the permeability angle φ which resisted the flow through the porous layers. Fig. 6.2(a) delineated the velocity profiles for various permeability ratios (K^*) and a fixed value of $Da = 0.02$ corresponding to the fluid velocity in an anisotropic porous medium given by Eq. (6.24). The permeability ratio $K^* < 1$ indicates $K_\alpha < K_\beta$ and $K^* > 1$ implies $K_\alpha > K_\beta$ for a fixed Darcy number. It can be observed from Fig. 6.2(a) that the enhancement of permeability ratio ($K^* = K_\alpha/K_\beta$) reduces the permeability K_β , which decreases the velocity of the flow. The flow becomes fully developed for $Da = 0.5$, and the velocity is reduced with the increment of permeability ratio (K^*) as depicted in Fig. 6.2(b). Furthermore, the flow experienced resistance due to the augmentation of the anisotropic permeability ratio. So the flow becomes slower. It may be noticed that a large Darcy number generates parabolic velocity profiles, and the velocity becomes maximum at the centerline of the microchannel. Still, the velocity profiles are not parabolic for a low Darcy number.

The impact of anisotropic permeability angle (φ) on the velocity distribution within the porous microchannel is displayed in Fig. 6.3. The enhancing nature of permeability angle (φ) reduces the velocity of the flow, as delineated in Figs. 6.3(a)-6.3(b). Fully developed and parabolic velocity profiles are shown in Fig. 6.3(b) for $Da = 0.5$, but it is not illustrative for the low Darcy number, which is depicted in Fig. 6.3(a). So, the improvement of permeability angle (φ) resists the flow velocity; as a result, the motion of the fluid is diminished. It can be observed that the velocity is maximum for permeability angle $\varphi = \pi/2$, and it becomes minimum for permeability angle $\varphi = 0$. For $\varphi = 0$ and $K^* < 1$, the permeability along the flow direction is enhanced. But $\varphi = \pi/2$ and $K^* < 1$ correspond to a reduced flow direction permeability. Hence, the variation of φ generates the diversity in the velocity profiles, and it attains the maximum value at $\varphi = 0$ and minimum value at $\varphi = \pi/2$.

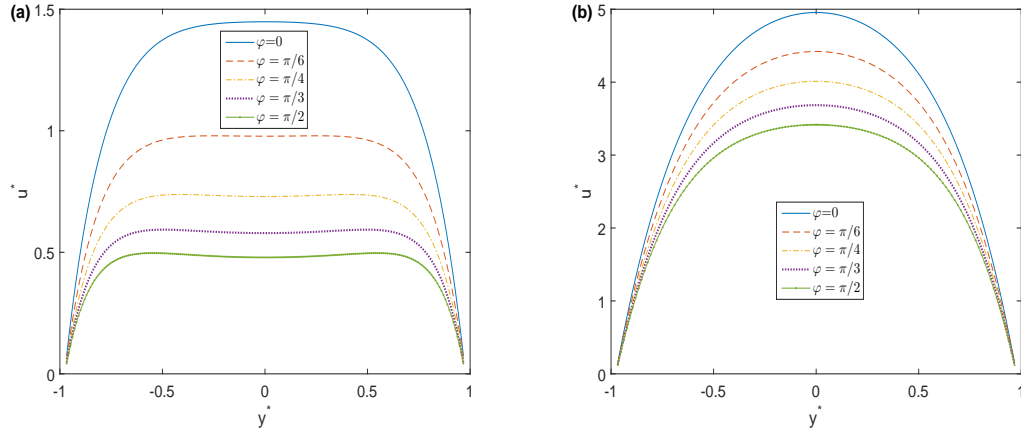


Figure 6.3: Velocity profiles for different permeability angle and (a) $Da = 0.02$, (b) $Da = 0.5$ with $\omega = 4$, $S = 50$, $P^* = 0.5$, $Ha = 1$, $F = 1$, $m = 1$, $K^* = 0.25$, $\beta = 0.01$, $\lambda = 0.05$.

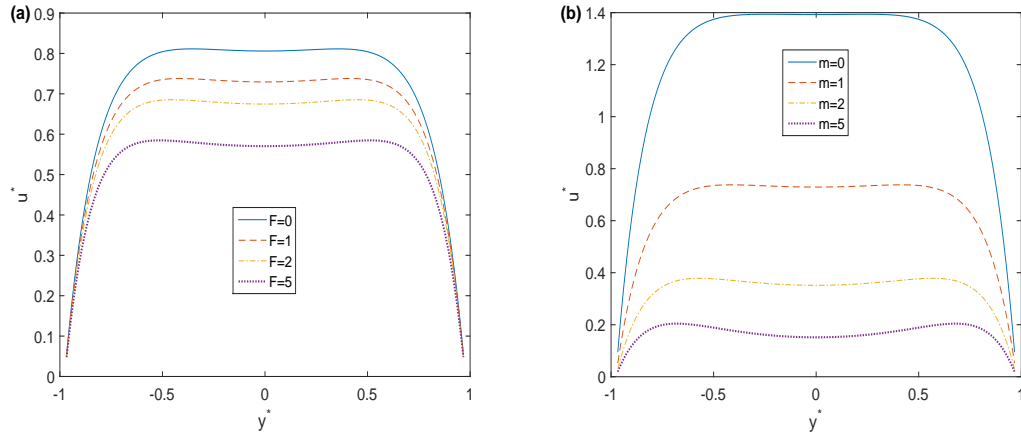


Figure 6.4: Velocity profiles for different (a) Forchheimer parameter and (b) Hall parameter with $\omega = 4$, $S = 50$, $P^* = 0.5$, $Ha = 1$, $\varphi = \pi/4$, $K^* = 0.25$, $Da = 0.02$, $\beta = 0.01$, $\lambda = 0.05$.

The influence of Forchheimer inertial parameter (F) on the velocity distribution is shown in Fig. 6.4(a). The Forchheimer inertial parameter physically significance embodies the strength of inertial coefficient in the porous medium. The magnitude of velocity profiles decrease with the enhancing nature of Forchheimer inertial parameter (F) for the fixed values of other pertinent parameters. The inertial coefficient in the porous medium acts as a drag force, reducing the velocity for the low Darcy number. However, the larger inertia and low Darcy number indicate the slug flow behavior, and the flow velocity magnitude is flattened in the middle region of the microchannel. Furthermore, without inertial dragging force ($F = 0$), the velocity of the flow becomes maximum as depicted in Fig. 6.4(a).

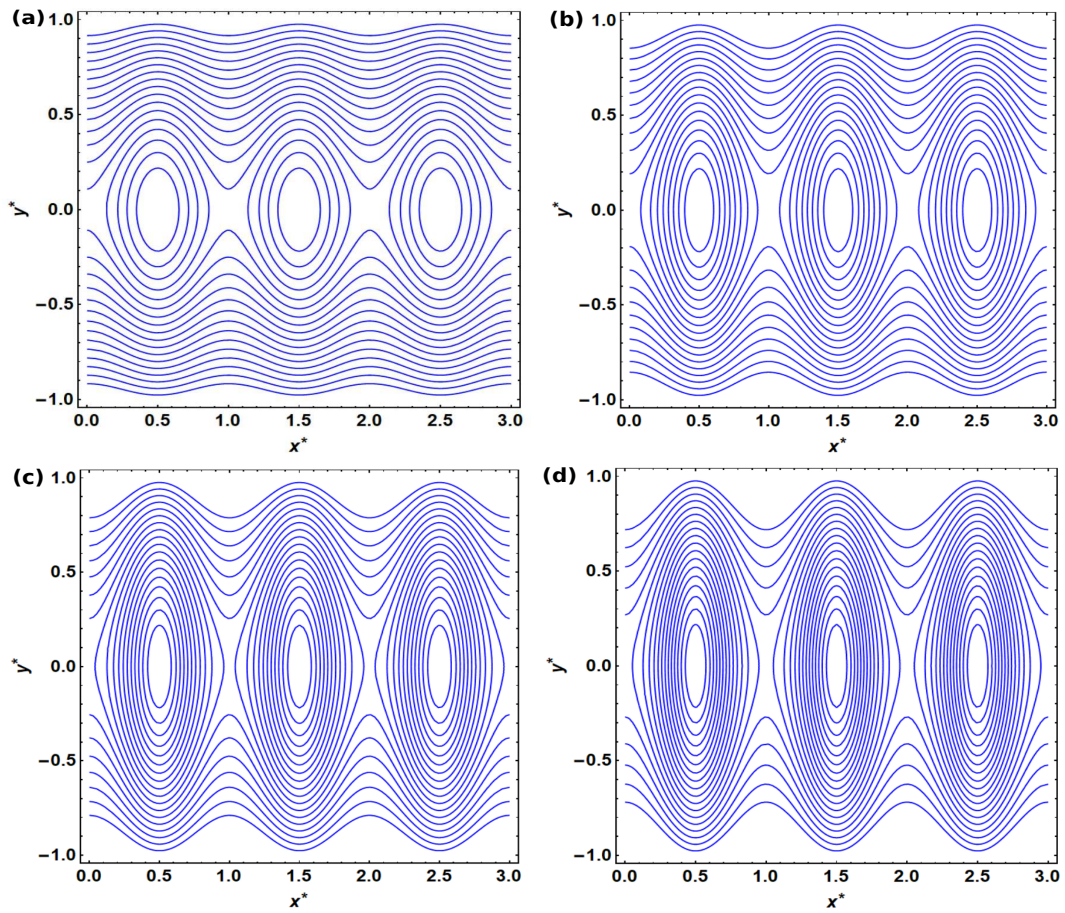


Figure 6.5: Streamline plots for $\omega = 10$, $S = 50$, $P^* = 0.5$, $Ha = 1$, $F = 1$, $m = 1$, $\varphi = \pi/4$, $K^* = 0.5$, $Da = 0.02$, $\beta = 0.01$, (a) $\lambda = 0.05$; (b) $\lambda = 0.1$; (c) $\lambda = 0.15$ and (d) $\lambda = 0.2$.

The presence of electric potential along the conducting material and the applied magnetic field along the transverse direction generates an additional electric current called Hall current. The impact of Hall parameter (m) on the EMHD flow velocity is delineated in Fig. 6.4(b). This figure depicted that the velocity is decreased with the increment of the Hall parameter. The term $\frac{\sigma_{eff}}{1+m_{eff}^2}(B_y E_z - B_y^2 u)$ in Eq. (6.11) depends on electromagnetic force, Hall current, transverse electric field and effective electric conductivity of Fe_3O_4 nanoparticles. The enhancing nature of Hall

parameter decreases the effective conductivity $\frac{\sigma_{eff}}{1+m_{eff}^2}$. The electric conductivity of Fe_3O_4 nanoparticles and the retarding effect of electromagnetic force reduces the flow velocity as the Hall parameter is enhanced. Furthermore, the velocity becomes maximum in the middle region for $m = 0$.

The streamlines are displayed in Fig. 6.5 to visualize the flow velocity patterns through the wavy microchannel. The variations of the streamlines for different wave amplitude (λ) in the wavy microchannel are shown in this figure. It is visible that the streamlines depend on the waviness of the microchannel, which means it depends on the wave amplitude of the wavy microchannel because the waviness of the microchannel changes the pattern of streamlines as depicted in Figs. 6.5(a)-6.5(d). It can be observed that the wavy surface of the microchannel generates wavy streamlines near boundary layers and symmetric recirculations in the middle layers. The increment of the wave amplitude (λ) increases the waviness of the microchannel; as a result, the waviness makes up more symmetric recirculations in the middle layers, as delineated in Figs. 6.5(a)-6.5(d). Furthermore, some circular boluses are formed in the intermediate layers of the flow, as shown in Fig. 6.5(a). Still, the boluses become elliptical with the enhancement of the waviness of the surface, as delineated in Figs. 6.5(b)-6.5(d).

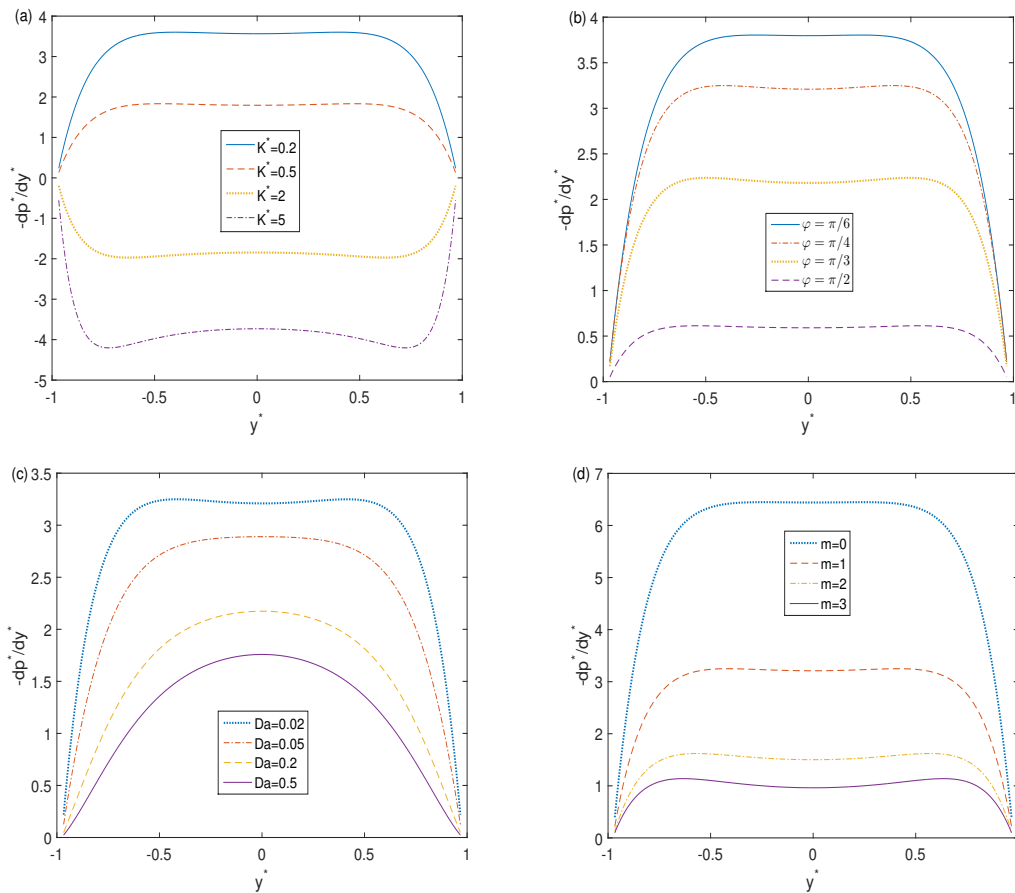


Figure 6.6: Variation of vertical pressure gradient for different (a) anisotropic permeability ratio, (b) permeability angle (c) Darcy number and (d) Hall parameter with $\omega = 4$, $S = 50$, $P^* = 0.5$, $Ha = 1$, $F = 1$, $\beta = 0.01$, $\lambda = 0.05$.

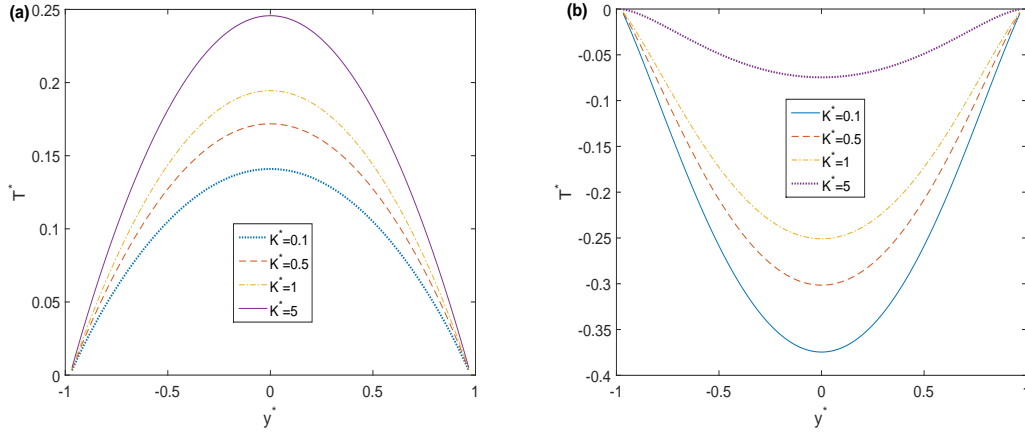


Figure 6.7: Temperature profiles for different anisotropic permeability ratio and (a) $Da = 0.02$, (b) $Da = 0.5$ with $\omega = 4$, $S = 50$, $P^* = 0.5$, $Ha = 1$, $F = 1$, $m = 1$, $\varphi = \pi/4$, $\phi_p = 0.04$, $\beta = 0.01$, $Br = 0.004$, $\gamma_j = 0.6$, $\lambda = 0.05$, $N_B = 0.1$, $N_t = 0.1$.

6.3.2 Pressure gradient analysis

The vertical pressure gradient ($-\partial p^*/\partial y^*$) is plotted in Figs. 6.6(a)-6.6(d) with variation of anisotropic permeability ratio (K^*), permeability angle (φ), Darcy number (Da) and Hall parameter (m) respectively. Fig. 6.6(a) depicts that the vertical pressure gradient decreases with the increases of the anisotropic permeability ratio for $K^* < 1$. But the opposite phenomenon is shown for $K^* > 1$. The enhancement of permeability angle (φ) reduces the vertical pressure gradient ($-\partial p^*/\partial y^*$) as shown in Fig. 6.6(b). For large permeability angle (φ), the anisotropic parameter enhances as a result, the vertical pressure gradient decreases. Fig. 6.6(c) depicts the decrement of vertical pressure gradient with the enhancement of Darcy number. Also, it can be noticed that the vertical pressure gradient profile for large Darcy number becomes parabolic and is diminished for higher porous medium. A reduction in the vertical pressure gradient profiles is displayed in Fig. 6.6(d) with an increment of the Hall parameter. Furthermore, the vertical pressure gradient is maximum for $m = 0$.

6.3.3 Thermal characteristics analysis

The non-dimensional temperature indicates the difference between the fluid temperature inside the porous microchannel and the temperature of the impenetrable wall. The temperature distribution profiles for the variation of anisotropic permeability ratio (K^*) are shown in Fig. 6.7 for fixed values of other parameters. The temperature profile increases (in the positive direction) with the increment of K^* for $Da = 0.02$, as depicted in Fig. 6.7(a). The characterization of the anisotropic porous medium is $\alpha_p^* = \sin^2(\varphi) + K^* \cos^2(\varphi)$, which depends on the permeability angle φ and K^* . As a result, the fluid in porous layers gains temperature due to the internal heat generation inside the anisotropic porous medium. But, the temperature profiles decrease (in the negative direction) with the increment of K^* for $Da = 0.5$, as depicted in Fig. 6.7(b). Furthermore, due to symmetry, the

temperature profiles become maximum at the middle layers of the flow for low Darcy numbers.

The influence of anisotropic permeability angle (φ) on the temperature distribution within the porous microchannel is displayed in Fig. 6.8. The enhancing nature of permeability angle (φ) enhances (in the positive direction) the temperature distribution as delineated in Fig. 6.8(a). The increment of permeability angle (φ) resists the velocity of the flow (see Fig. 6.3(a)), as a result, the temperature is enhanced due to internal heating in the porous microchannel. But, the temperature profiles are reduced (in the negative direction) with the increment of φ for $Da = 0.5$ as depicted in Fig. 6.8(b). It can be noticed from Fig. 6.8(a) that the temperature is maximum for permeability angle $\varphi = \pi/2$, and it becomes minimum for permeability angle $\varphi = 0$ for low Darcy number. Hence, the variation of φ generates the diversity in the temperature profiles due to the variation of the Darcy number.

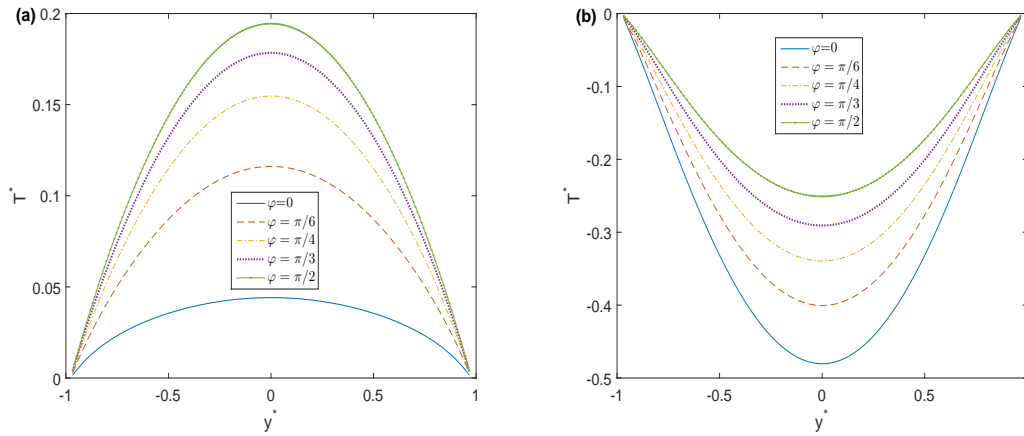


Figure 6.8: Temperature profiles for different permeability angle and (a) $Da = 0.02$, (b) $Da = 0.5$ with $\omega = 4$, $S = 50$, $P^* = 0.5$, $Ha = 1$, $F = 1$, $m = 1$, $K^* = 0.25$, $\phi_p = 0.04$, $\beta = 0.01$, $Br = 0.004$, $\gamma_j = 0.6$, $\lambda = 0.05$, $N_B = 0.1$, $N_t = 0.1$.

The influence of Forchhemier inertial parameter (F) on the temperature distribution is depicted in Fig. 6.9(a). The dimensionless temperature profiles are increased with the enhancing nature of Forchheimer inertial parameter (F) for the fixed values of other parameters. The inertial coefficient in the porous medium creates frictional heating in the porous microchannel for a low Darcy number. Therefore the dimensionless temperature increases. However, the larger inertia and low Darcy number indicate enhancing temperature behavior, and it becomes maximum in the middle region of the microchannel. Furthermore, the temperature of the flow becomes minimum for no inertial effect, as depicted in Fig. 6.9(a).

The influence of Hall parameter (m) on the dimensionless temperature is displayed in Fig. 6.9(b) for other fixed parameters and low Darcy number ($Da = 0.02$). The temperature increases with the increment of the Hall parameter. The retarding effect of electromagnetic body force reduces the flow velocity and generates heat due to the interaction of the applied magnetic field and the electric field. Therefore the dimensionless temperature is enhanced. Furthermore, the temperature becomes maximum in the middle region and minimum for $m = 0$.

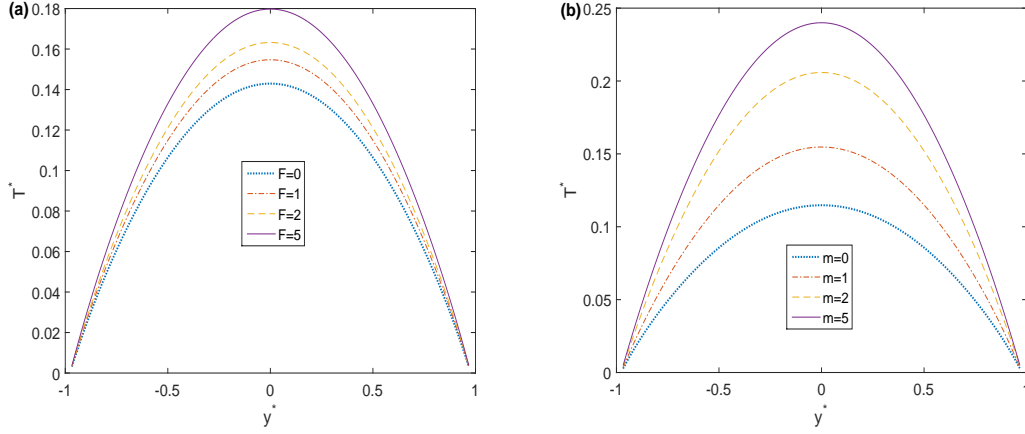


Figure 6.9: Temperature profiles for different (a) Forchemmier parameter and (b) Hall parameter with $\omega = 4$, $S = 50$, $P^* = 0.5$, $Ha = 1$, $K^* = 0.25$, $\varphi = \pi/4$, $\phi_p = 0.04$, $\beta = 0.01$, $Br = 0.004$, $\gamma_j = 0.6$, $\lambda = 0.05$, $N_B = 0.1$, $N_t = 0.1$.

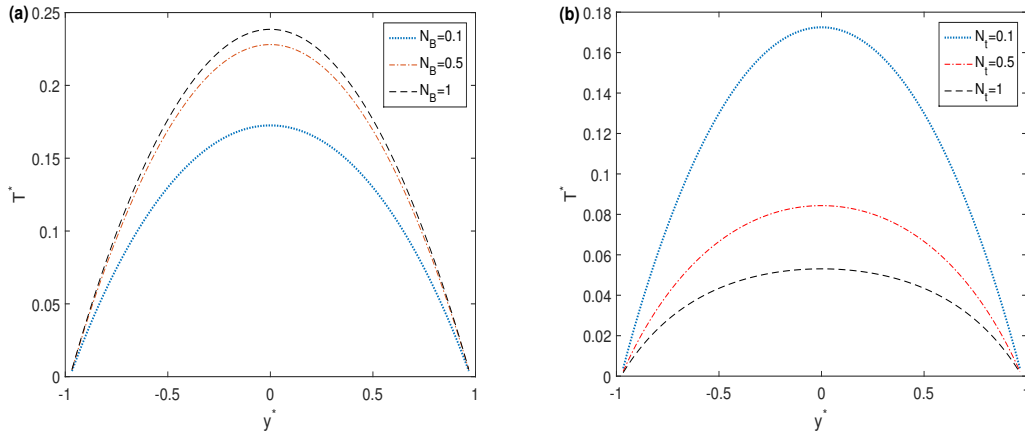


Figure 6.10: Temperature profiles for different (a) Brownian motion parameter and (b) thermophoresis parameter with $\omega = 4$, $S = 50$, $P^* = 0.5$, $K^* = 0.25$, $\varphi = \pi/4$, $\beta = 0.01$, $Br = 0.004$, $\gamma_j = 0.6$, $\lambda = 0.05$.

The significant impact of the Brownian motion parameter (N_B) and the thermophoresis parameter (N_t) on the dimensionless temperature is visually presented in Figs. 6.10(a) and 6.10(b) respectively. The Brownian motion parameter (N_B) exerts its effect by enhancing the thermal energy transfer within the nanofluid. As it increases, the vigorous random motion of nanoparticles significantly elevates the temperature. In contrast, the thermophoresis parameter (N_t) represents the thermophoretic migration of particles induced by temperature gradients. When (N_t) increases, the thermophoretic effect intensifies, leading to particle motion that opposes temperature rise as clearly seen in Fig. 6.10(b). This behavior results in a reduction in temperature, reminiscent of the cooling effect observed when particles move against temperature gradients. These results provide a clear understanding of how the interplay between Brownian motion and thermophoresis influences temperature changes within nanofluids for this problem. Brownian motion contributes to heating, while thermophoresis acts as a cooling mechanism by causing particles to move against temperature gradients. These insights are valuable for understanding and controlling the thermal behavior of nanofluids in various applications.

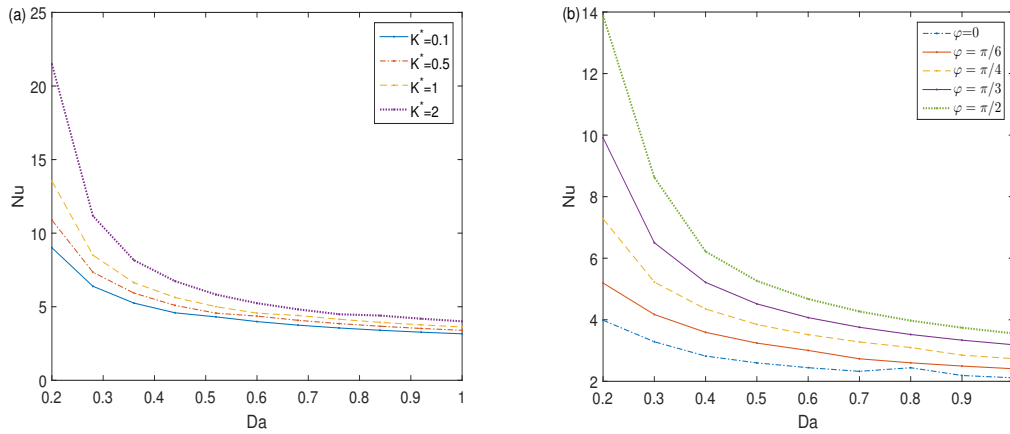


Figure 6.11: Variation of Nusselt number for different (a) anisotropic permeability ratio and (b) permeability angle with $\omega = 4$, $S = 50$, $P^* = 0.5$, $Ha = 1$, $K^* = 0.25$, $\beta = 0.01$, $Br = 0.004$, $\gamma_j = 0.6$, $\lambda = 0.05$.

6.3.4 Rate of heat transfer analysis

The rate of heat transfer, a non-dimensional quantity, is embodied as the Nusselt number. It characterizes the energy conversion rate from the heated impermeable wall to the fluid flowing through the porous microchannel. It is evaluated numerically by calculating the non-dimensional bulk mean temperature from Eq. (6.39). The graphical interpretation for the Nusselt number with the variation of other parameters is discussed in Figs. 6.11-6.14.

The increment of the Darcy number gradually decreases the Nusselt number, as shown in Fig. 6.11. It can be observed from both figures that the Nusselt number becomes the maximum low Darcy number. Fig. 6.11(a) depicts that the enhancing nature of anisotropic permeability ratio (K^*)

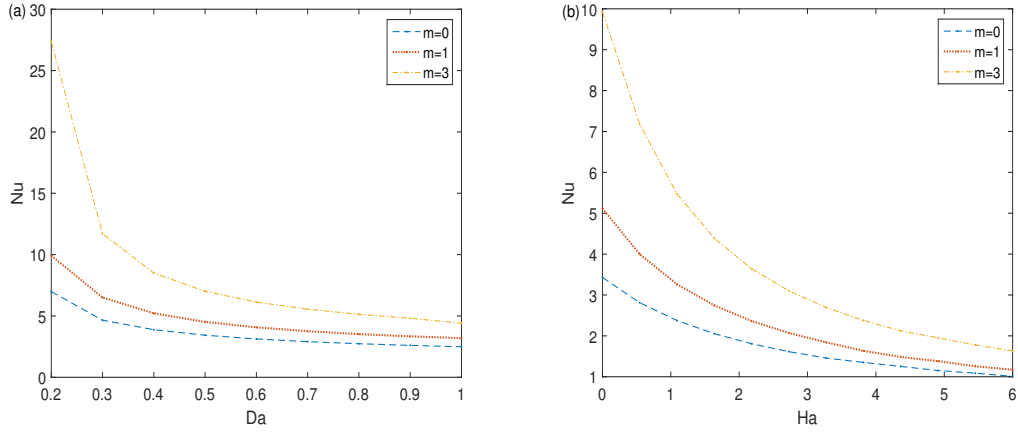


Figure 6.12: Influence of Hall parameter on Nusselt number with (a) Darcy number and (b) Hartmann number with $\omega = 4$, $S = 50$, $P^* = 0.5$, $K^* = 0.25$, $\varphi = \pi/3$, $\beta = 0.01$, $Br = 0.004$, $\gamma_j = 0.6$, $\lambda = 0.05$.

increases the Nusselt number with the increase of Darcy number. It can be observed that Nusselt number becomes the maximum at low Darcy number. The increment of permeability angle (φ) enhances the Nusselt number with the increases of Darcy number, as delineated in Fig. 6.11(b). Furthermore, the Nusselt number becomes maximum for $\varphi = \pi/2$ and low Darcy number, and it is minimum for $\varphi = 0$ and large Darcy number.

The influence of the Hall parameter on the Nusselt number is displayed in Fig. 6.12. It can be noticed from Figs. 6.12(a) and 6.12(b) that the Nusselt number decreases gradually with the increment of Darcy number as well as the Hartmann number. Also, the heat transfer rate increases due to the increasing of the Hall parameter. The presence of the Hall parameter due to an applied external magnetic field improved the heat transfer rate. Further, one may be noticed that for both figures, the Nusselt number is minimum for $m = 0$.

The enhancement of Forchhemmer inertia parameter (F) increases the Nusselt number, as shown in Fig. 6.13. Fig. 6.13(a) depicts that the increment of anisotropic permeability ratio (K^*) increases the Nusselt number with the increase of Forchhemmer inertia parameter. The increment of permeability angle (φ) enhances the rate of heat transfer with the increases of the Forchhemmer inertia parameter, as delineated in Fig. 6.13(b). Furthermore, the Nusselt number becomes maximum in a high inertial environment with $\varphi = \pi/2$, and it is minimum in a low inertial environment with $\varphi = 0$.

Temperature is influenced by viscous dissipation, which is characterized by the Brinkman number, and it plays an essential role in the cooling and heating processes. The combined impact of thermal slip and viscous dissipation has been demonstrated in Fig. 6.14(a). Due to the viscous dissipation, the Nusselt number decreases with an enhancing thermal slip parameter. As the thermal slip increases, the heat conduction due to Darcy dissipation and frictional heating due to inertial parameter reduces the Nusselt number. Similarly, the enhancing thermal slip improves the heat transfer rate with the increment of joule heating, as depicted in Fig. 6.14(b). Due to the heat generation, the

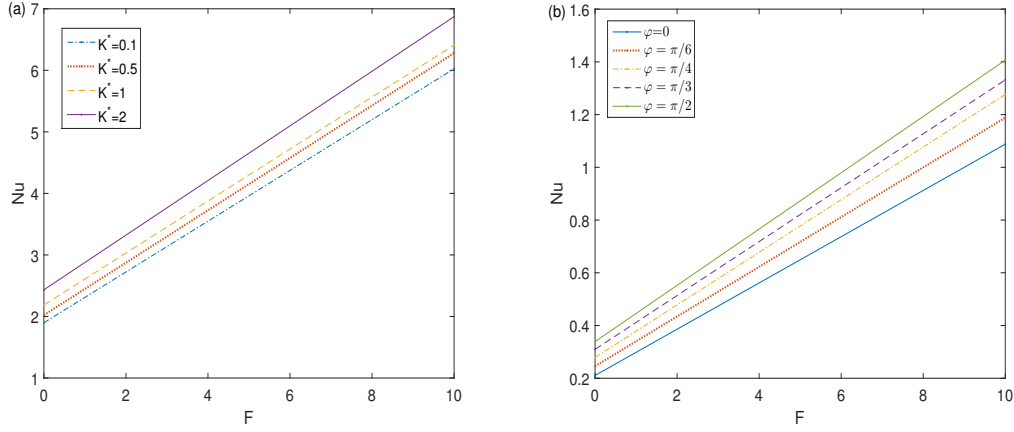


Figure 6.13: Variation of Nusselt number with Forchhemmer inertia parameter for different (a) anisotropic permeability ratio and (b) permeability angle with $\omega = 4$, $S = 50$, $P^* = 0.5$, $Ha = 1$, $\beta = 0.01$, $Br = 0.004$, $\gamma_j = 0.6$, $\lambda = 0.05$.

increment of Joule heating enhances the temperature.

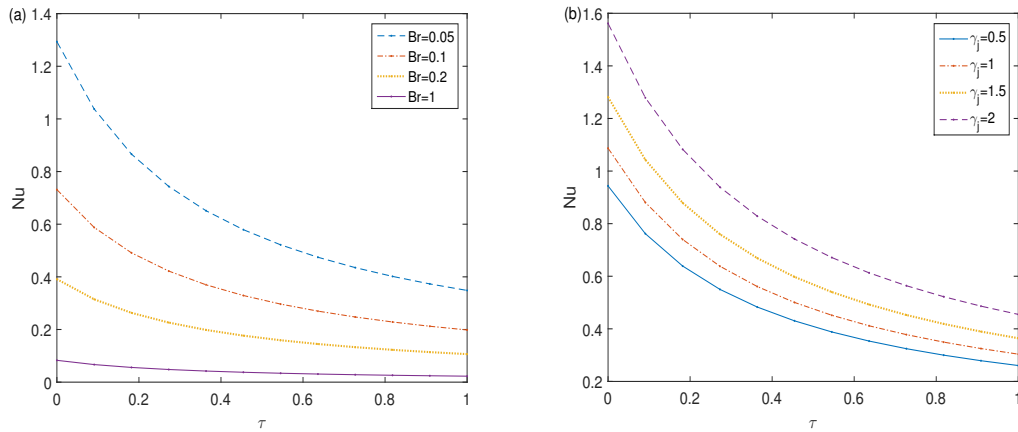


Figure 6.14: Variation of Nusselt number with temperature slip for different (a) Brinkmann number and (b) joule heating parameter with $\omega = 4$, $S = 50$, $P^* = 0.5$, $Ha = 1$, $K^* = 0.25$, $\varphi = \pi/3$, $\beta = 0.01$, $\lambda = 0.05$.

6.3.5 Volume fraction analysis

Integrating nanoparticles into porous microfluidic systems contribute a new dimension of complexity, opening the door to innovative applications like improved drug delivery and advanced filtration technologies. The interaction of nanoparticles within anisotropic porous structures significantly influences fluid dynamics and mass transport. This challenge underscores the necessity to explore how the nanoparticle volume fraction impacts electromagnetic-hydrodynamic (EMHD) flow within anisotropic porous microchannels.

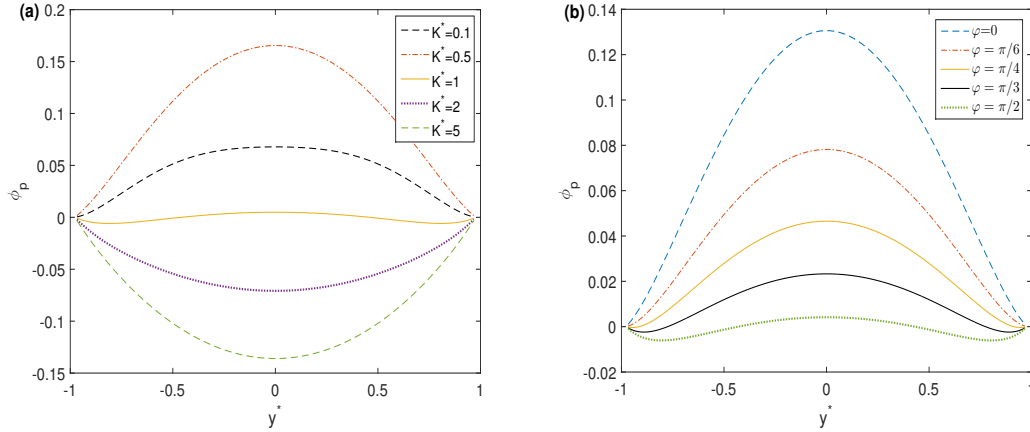


Figure 6.15: Volume fraction profiles of nanoparticle for different (a) anisotropic ratio and (b) anisotropic angle with $\omega = 4$, $S = 50$, $P^* = 0.5$, $Ha = 1$, $Da = 0.2$, $\beta = 0.01$, $Br = 0.004$, $\gamma_j = 0.6$, $\lambda = 0.05$, $N_B = 0.1$, $N_t = 0.1$.

In this section, our aim is to visualize nanoparticle volume fraction profiles and investigate their dependencies on various relevant parameters, as illustrated in Figs. 6.15 and 6.16. In Fig. 6.15(a), we present nanoparticle volume fraction profiles while varying the anisotropic permeability ratio (K^*), while keeping other parameters constant. When $K^* < 1$, the volume fraction of nanoparticles exhibits an upward trend (in the positive direction), as depicted in Fig. 6.15(a). This behavior results from enhanced nanoparticle infiltration into the porous medium, driven by the lower anisotropic permeability ratio. Conversely, when K^* exceeds or equals 1 ($K^* \geq 1$), we observe a decrease in nanoparticle volume fraction (in the negative direction), as also shown in Fig. 6.15(a). This reduction can be attributed to the restricted entry of nanoparticles into the porous medium due to higher anisotropic permeability. Understanding these variations in nanoparticle distribution is fundamental to comprehending the physics of fluid-particle interactions within anisotropic porous structures. Fig. 6.15(b) illustrates how the anisotropic permeability angle (φ) influences nanoparticle volume fraction within the porous microchannel. An increasing permeability angle (φ) results in a reduction in nanoparticle volume fraction, as depicted in Fig. 6.15(b). This effect can be attributed to the enhanced permeability along the preferred direction, allowing fewer nanoparticles to be retained within the porous medium.

Moving to Fig. 6.16(a), nanoparticle volume fraction profiles are presented as the Hartmann number varies, with all other parameters held constant. The influence of Ha on nanoparticle concentration is intriguing, driven by the intricate interplay of physical forces. For $Ha \geq 1$, an increase in nanoparticle volume fraction is observed due to a transverse electric field that acts as a flow-enhancing force, boosting fluid velocity and increasing nanoparticle entrainment. In contrast, for Ha less than 1, a decrease in nanoparticle volume fraction is evident as the magnetic field takes on a flow-retarding role, reducing fluid velocity and resulting in lower nanoparticle concentration. The increase in the thermophoresis parameter (N_t) results in a decrease in nanoparticle volume fraction, as shown in Fig. 6.16(b). This phenomenon is driven by thermophoresis, where nanoparti-

cles migrate away from temperature gradients, redistributing them and reducing their concentration in such regions. Understanding this effect is crucial for applications involving precise control of nanoparticle distribution in response to temperature variations.

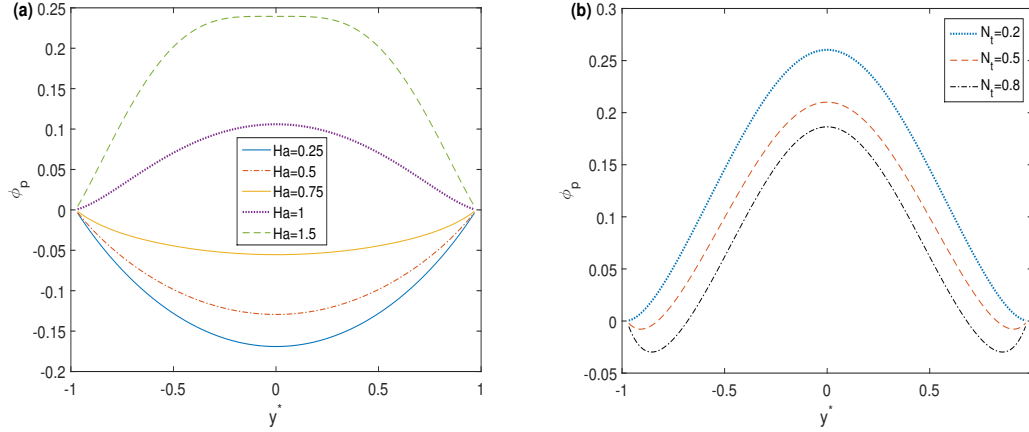


Figure 6.16: Volume fraction profiles of nanoparticle for different (a) Hartmann number and (b) thermophoresis parameter with $\omega = 4$, $S = 50$, $P^* = 0.5$, $K^* = 2$, $\varphi = \pi/4$, $\beta = 0.01$, $Br = 0.004$, $\gamma_j = 0.6$, $\lambda = 0.05$, $N_B = 0.1$.

6.4 Asymptotic analysis for velocity distribution in a nano-particle free context

For asymptotic solution, we investigate the analytical solution in the form of a Poincare type asymptotic expansion for the flow velocity. For nanoparticle free context, the Eq. (6.24) is reduced to

$$\frac{d^2 u^*}{dy^{*2}} - \left(\frac{Ha^2}{1+m^2} + \frac{a_p^*}{Da} \right) u^* - \frac{b_p^* F}{\sqrt{Da}} u^{*2} + \omega^2 \psi^* + \frac{HaS}{1+m^2} = P^* Re. \quad (6.45)$$

6.4.1 Case-I: For large Darcy number

For the large value of Darcy number, (when $Da \gg 1$), that means $\varepsilon \ll 1$, where $\varepsilon = 1/\sqrt{Da}$. We look for an asymptotic expansion of the velocity distribution of the flow which is described as follows:

$$u^* = u_0^* + \varepsilon u_1^* + \varepsilon^2 u_2^* + \dots \quad (6.46)$$

After substituting the Eq. (6.46) into the Eq. (6.45) and separating at each order of ε one can easily find the analytical solution. The results up to the second order are presented as follows:

$$u_0^* = 2\Gamma_1 \cosh(A_2 y^*) + A_3 \cosh(a_5 y^*) + A_4, \quad (6.47)$$

$$u_1^* = 2\Gamma_2 \cosh(A_2 y^*) + \frac{a_3}{6} \left\{ 6\Gamma_1 \cosh(A_2 y^*) \left(\frac{A_4}{A_2^2} + \frac{4A_3 \cosh(a_5 y^*)}{4A_2^2 - a_5^2} \right) \right\} \\ + \frac{a_3}{2} \left[\frac{4A_3 A_4 \cosh(a_5 y^*)}{A_2^2 - a_5^2} + \frac{A_3^2 \cosh(2a_5 y^*)}{A_2^2 - 4a_5^2} + \frac{1}{A_2^2} \left\{ 4\Gamma_1^2 + A_3^2 + 2A_4^2 \right. \right. \\ \left. \left. + 4\Gamma_1 A_2 \sinh(A_2 y^*) \left(\frac{4A_2^2 A_3 \sinh(a_5 y^*)}{a_5^3 - 4A_2^2 a_5} - A_4 y^* \right) \right\} \right], \quad (6.48)$$

$$u_2^* = 2\Gamma_4 \cosh(A_2 y^*) + \Gamma_3 F(y^*). \quad (6.49)$$

The expressions for $a_2, a_3, a_4, a_5, a_6, A_2, A_3, A_4, \Gamma_1, \Gamma_2, \Gamma_3, \Gamma_4$ and $F(y^*)$ are given in Appendix 6.A.

6.4.2 Case-II: For small Darcy number

For sufficiently small value of Darcy number, we have $Da \ll 1$. That means $1/\varepsilon \ll 1$, where $\varepsilon^2 = 1/Da$. Thus, Eq. (6.45) can be described as follows:

$$\frac{1}{\varepsilon^2} \left(\frac{d^2 u^*}{dy^{*2}} \right) - \frac{1}{\varepsilon^2} \left\{ \left(\frac{Ha^2}{1+m^2} \right) u^* + a_p^* \varepsilon^2 u^* \right\} - \frac{1}{\varepsilon} b_p^* F u^{*2} \\ + \frac{1}{\varepsilon^2} \left\{ \omega^2 \psi^* + \left(\frac{HaS}{1+m^2} \right) - P^* Re \right\} = 0. \quad (6.50)$$

To obtain the solution of the velocity distribution for low Darcy number, we use the method of stretching (Nayfeh [2008]). The boundary layers are located near the wavy wall, i.e. $y^* = h$. Therefore, according to Bush (Bush [1992]), one can easily find the outer solution for the regions which is far away from the wall. Hence the outer solution can be written as

$$u^{*out} = \frac{a_6}{a_p^* \varepsilon^2}. \quad (6.51)$$

Further, the inner solution can be evaluated by applying the stretched variable, which is defined as

$$\eta = (1 - y^*) \varepsilon. \quad (6.52)$$

After neglecting the smaller terms, the corresponding momentum equation for the inner region yields

$$\frac{d^2 u^{*in}}{d\eta^2} - A_1^2 u^{*in} = 0. \quad (6.53)$$

We have applied the Prandtl's matching principle (Bush [1992]) to find the composite solution, which can be expressed as follows:

$$u^{*comp} = u^{*out} + u^{*in} - (u^{*in})^{out}. \quad (6.54)$$

Hence, the composite solution for the momentum equation can be written as

$$u^* = u^{*comp} = \frac{a_6}{a_p^* \epsilon^2} \left[1 - \frac{2e^{-A_1(h-1)\epsilon}}{1 + A_1\beta\epsilon} \left\{ A_1\beta\epsilon \cosh\left(A_1(h-y^*)\epsilon\right) + \sinh\left(A_1(h-y^*)\epsilon\right) \right\} \right]. \quad (6.55)$$

The expressions for a_6 and A_1 are given in Appendix 6.A.

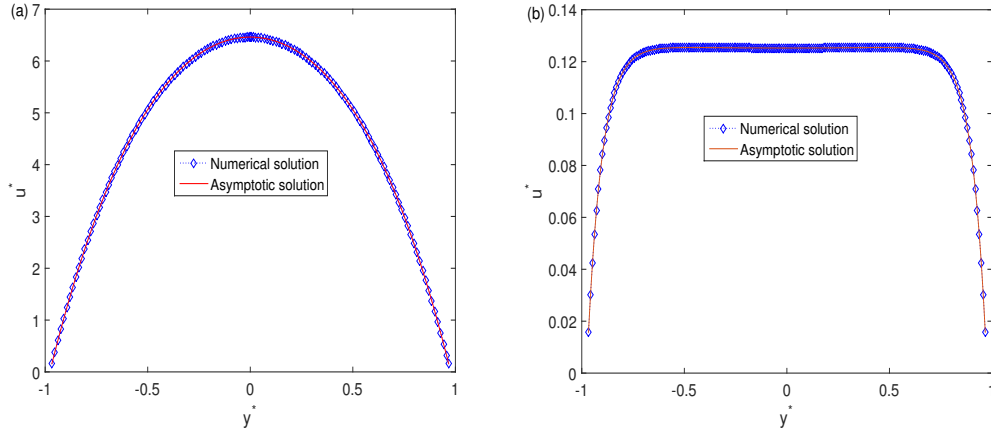


Figure 6.17: Velocity profiles for (a) $Da = 10$ (large Darcy number case) (b) $Da = 5 \times 10^{-3}$ (small Darcy number case) with $F = 1$, $S = 50$, $P^* = 0.5$, $Ha = 1$, $\varphi = \pi/4$, $K^* = 1$, $\beta = 0.01$, $\lambda = 0.05$.

The above explanation plays a significant role in the numerous applications of high/low permeable porous medium. So many scientific applications can be executed in extremely beneficial cases such as large and small Darcy numbers (Barletta and Rees [2019]; Karmakar and Rajasekhar [2017]). High-permeable porous mediums are popularly used in refrigerators, computer cabinets, thermal insulating devices, etc. (Calmidi and Mahajan [2000]; Kaviany and Mittal [1987]). Similarly, the low absorbent porous medium is utilized in microporous medium (Bau and Torrance [1982]) to improve the cold plate devices for the application of thermo-fluidic transport. These motivational applications are inspired to analyze the cases for high and low Darcy numbers.

We have compared our numerical results with the asymptotically computed results, and it can be observed from Fig. 6.17 that there is a good agreement between the asymptotic and numerical results of the velocity profiles. Fig. 6.17(a) delineates the results for large Darcy numbers. It can be observed that the velocity profile becomes fully developed and parabolic in the microchannel, which is matchable to the plane-Poiseuille flow. But for a low Darcy number, the velocity profile is not parabolic, as displayed in Fig. 6.17(b). Also, one may observe a flat velocity profile towards the center of the microchannel for a low Darcy number. This type of velocity profile is analogous to the slug flow.

6.5 Conclusions

In summary, our mathematical model has successfully explained the complexities of fully developed nanofluidic flow and heat transfer within an anisotropic porous microchannel featuring a wavy wall geometry. This intricate flow is notably shaped by externally applied electric and magnetic fields, as well as pressure gradients. By employing the Brinkmann extended Darcy model to account for the Forchheimer inertial effect, we have captured a comprehensive view of the behavior of the system.

Our investigation has unveiled several key findings. The anisotropic permeability of the porous medium significantly influences velocity and temperature profiles. The angle of permeability further adds diversity to these profiles, thus playing a crucial role. The presence of Forchheimer inertial effects leads to frictional heating, fostering slug flow behavior for low Darcy numbers. The retardation caused by electromagnetic forces and the Hall current collectively diminishes flow velocity, leading to the formation of boluses within the midsection of the microchannel due to the presence of waviness.

Furthermore, our asymptotic velocity distribution aligns well with the numerical result, particularly demonstrating its reliability for low Darcy numbers. The heat transfer rate showcases substantial variation contingent on anisotropic permeability shifts. The behavior of the Nusselt number is noteworthy, reaching a maximum at low Darcy numbers with $\varphi = \pi/2$ and a minimum in environments characterized by low inertia ($\varphi = 0$).

The anisotropic permeability ratio (K^*) significantly affects nanoparticle distribution. A ratio K^* less than 1 increases nanoparticle volume fraction, while a ratio K^* greater than and equal to 1 decreases it. The Hartmann number (Ha) influences nanoparticle concentration. The concentration increases when the values of Ha greater than or equal to 1 and decreases when the values of Ha less than 1. An increase in the thermophoresis parameter (N_t) reduces nanoparticle volume fraction by causing nanoparticles to migrate away from temperature gradients. These findings have practical implications for nanoparticle distribution control.

In practical terms, these insights stand as valuable design tools for thermo-fluidic transport applications involving anisotropic porous media. They find direct applicability in crafting advanced microfluidic systems, encompassing microreactors and heat exchangers. Moreover, the implications extend to global entropy generation, aiding in optimizing operational conditions for nanofluidic devices. Particularly, electromagnetic interactions come to the fore in the context of MHD micropumps and EMHD micropumps.

Appendix

6.A Mathematical expressions connected with the asymptotic solution for velocity distribution

The expressions for Γ_j , A_j , ($j = 1, 2, 3, 4$), a_i ($i = 2, 3, \dots, 6$) and $F(y^*)$ which are appeared in equations (6.47)-(6.49) are given as follows

$$\begin{aligned} \Gamma_1 &= -\frac{1}{(1+\sqrt{a_2}\beta)e^{A_2h}+(1-\sqrt{a_2}\beta)e^{-A_2}} \left\{ A_4 + \frac{a_5(\cosh(a_5h)+a_5\beta \sinh(a_5h))}{a_2-a_5^2} \right\}, \\ \Gamma_2 &= \frac{a_3}{12(\cosh(A_2h)+A_2\beta \sin(A_2h))} \left[\frac{4\Gamma_1^2 \cosh(2A_2h)}{A_2^2} + \frac{12A_3A_4 \cosh(a_5h)}{A_2^2-a_5^2} + \frac{3A_3^2 \cosh(2a_5h)}{A_2^2-4a_5^2} \right. \\ &\quad + \frac{6\Gamma_1A_4(2h+\beta) \sinh(A_2h)}{A_2} + \frac{24\Gamma_1A_2A_3\beta \cosh(a_5h) \sinh(A_2h)}{4A_2^2-a_5^2} + \frac{12A_4A_3a_5\beta \sinh(a_5h)}{-A_2^2+a_5^2} + \frac{8\Gamma_1^2\beta \sinh(2A_2h)}{A_2} \\ &\quad + \frac{48\Gamma_1A_2A_3 \sinh(a_5h) \sinh(A_2h)}{-4A_2^2a_5-a_5^3} - \frac{3(4\Gamma_1^2+A_3^2+2A_4^2)}{A_2^2} + \frac{6\Gamma_1 \cosh(A_2h)}{4A_2^2a_5-A_2^2a_5^3} \left\{ 4A_2^2A_3(\beta(\sinh(a_5h)(2A_2^2-a_5^2) \right. \\ &\quad \left. - a_5 \cosh(a_5h))) - A_4a_5(a_5^2-4A_2^2)(2A_2^2h\beta-1) \right\} - \frac{6A_3^2a_5\beta \sinh(2a_5h)}{A_2^2-4a_5^2} \left. \right], \\ \Gamma_3 &= \left\{ 12a_1^2A_2^4a_5^2(A_2-2a_5)^2(A_2-a_5)^2(a_5-2A_2)^2(A_2+a_5)^2(2A_2+a_5)^2(A_2+2a_5)^2(9A_2^6-82A_2^2a_5^2+ \right. \\ &\quad \left. 9a_5^4) \right\}^{-1}, \Gamma_4 = \frac{-F(h)-\beta F'(h)}{2\Gamma_3 \cosh(A_2h)+A_2\beta \sinh(A_2h)}, A_1 = \sqrt{a_p^*}, A_2 = \sqrt{a_2}, A_3 = \frac{a_4}{a_2-a_5^2}, A_4 = \frac{a_6}{a_2}, a_2 = \left(\frac{Ha^2}{1+m^2} \right), \\ a_3 &= b_p^*F, a_4 = \frac{\psi_w^*\omega^2}{\cosh(a_5h)}, a_5 = \omega, a_6 = \left(\frac{HaS}{1+m^2} \right) - P^*Re, \\ F(y^*) &= -12(4A_2^4a_5-17A_2^2a_5^3+4a_5^5)^2(91A_2^4a_5^2-91A_2^2a_5^4-9A_2^6+9a_5^6)[a_3\{a_3A_4a_5^2(6\Gamma_1^2 \\ &\quad +A_3^2+2A_4^2)-a_3A_4A_2^2(6\Gamma_1^2+3A_3^2+2A_4^2)-4\Gamma_1A_2^2(A_2+a_5)(A_2-a_5)\Gamma_2\}+a_1A_2^2A_4(a_5^2 \\ &\quad -A_2^2)a_p^*]-6A_2^4a_3^2A_3^2(36A_2^8-373A_2^6a_5^2+455A_2^4a_5^4-127A_2^2a_5^6+9a_5^8)\{6A_4a_5^2(4A_2^4-13A_2^2a_5^2 \\ &\quad +3a_5^4)+\Gamma_1 \cosh(A_2y^*)(6A_2^6-26A_2^4a_5^2+31A_2^2a_5^4+36a_5^6) \cosh(2a_5y^*)\}-6A_2^4a_3^2A_3^2(9A_2^4 \\ &\quad -37A_2^2a_5^2+4a_5^4)(4A_2^4a_5-5A_2^2a_5^3+a_5^5)^2 \cosh(3a_5y^*)+2A_2^2A_3a_5^2(A_2^4-13A_2^2a_5^2 \\ &\quad +36a_5^4) \cosh(a_5y^*)(36A_2^4-13A_2^2a_5^2+a_5^4)\{-3a_3^3(48A_2^6\Gamma_1^2+12A_2^6A_3^2+48A_2^6A_4^2) \\ &\quad -A_2^4(248\Gamma_1^2+47A_2^3+220A_4^2)a_5^2+A_2^2(232\Gamma_1^2+43A_2^3+116A_4^2)a_5^4-8(4\Gamma_1^2+A_2^3+2A_4^2)a_5^6\} \\ &\quad -6a_3^3A_2^2a_p^*(4A_2^6-21A_2^4a_5^2+21A_2^2a_5^4-4a_5^6)-12a_3(9A_2^6-46A_2^4a_5^2+41A_2^2a_5^4-4a_5^6) \\ &\quad \{ \Gamma_1a_3A_4(36A_2^4-25A_2^2a_5^2+a_5^4)+2A_2^2(4A_2^4-5A_2^2a_5^2+a_5^4)\Gamma_2\} \cosh(A_2y^*)+8\Gamma_1a_3^2(4A_2^6-21A_2^4a_5^2 \\ &\quad +21A_2^2a_5^4-4a_5^6)\{ \Gamma_1(54A_2^4+5A_2^2a_5^2+a_5^4) \cosh(2A_2y^*)+3A_2A_4y^*(9A_2^4-10A_2^2a_5^2+a_5^4) \sinh(A_2y^*)\} \\ &\quad +2(A_2^4a_5-5A_2^2a_5^3+4a_5^5)^2(36A_2^6-337A_2^4a_5^2+118A_2^2a_5^4-9a_5^6)[(a_3\{10\Gamma_1a_3(a_5^2 \\ &\quad -4A_2^2)+6A_2^2A_4(a_5^2-4A_2^2)\Gamma_2+3\Gamma_1a_3((A_3^2+4A_4^2)a_5^2-8A_2^4A_4y^{*2}+2A_2^2(A_4^2a_5^2y^{*2}-8A_4^2 \\ &\quad -3A_2^3))\}+3\Gamma_1A_2^2a_p^*(a_5^2-4A_2^2)) \cosh(A_2y^*)-4\Gamma_1a_3(a_5^2-4A_2^2)(3\Gamma_1a_3A_4 \\ &\quad +2A_2^2\Gamma_2) \cosh(2A_2y^*)+\Gamma_1^3a_3^2(a_5^2-4A_2^2) \cosh(3A_2y^*)+2A_2y^*[a_3\{ \Gamma_1a_3(40A_2^2\Gamma_1^2+18A_2^2A_3^2 \\ &\quad +48A_2^2A_4^2)-\Gamma_1a_3(10\Gamma_1^2+3A_2^3+12A_4^2)a_5^2\}-6A_2^2A_4\Gamma_1a_3(a_5^2-4A_2^2)\Gamma_2-3A_2^2\Gamma_1a_p^*(a_5^2 \\ &\quad -4A_2^2)] \sinh(A_2y^*)+8A_2a_3^2\Gamma_1^2A_4(a_5^2-4A_2^2)y^* \sinh(2A_2y^*)]+16A_2^3a_3A_3a_5(A_2^2-4a_5^2)(A_2^4 \\ &\quad -10A_2^2a_5^2+9a_5^4)[6\Gamma_1A_2a_3A_4(49A_2^4a_5^2-36A_2^6-14A_2^2a_5^4+a_5^6)y^* \cosh(A_2y^*)+3(9A_2^2 \\ &\quad -a_5^2)\{ \Gamma_1a_3A_4(28A_2^4-15A_2^2a_5^2-a_5^4)+2A_2^2(4A_2^4-5A_2^2a_5^2+a_5^4)\Gamma_2\} \sinh(A_2y^*) \\ &\quad +4\Gamma_1^2a_3(-11A_2^4a_5^2-36A_2^6+A_2^2a_5^4+a_5^6) \sinh(2A_2y^*)]+30\Gamma_1A_2^5A_3^2A_3^2(A_2 \\ &\quad -3a_5)(A_2-2a_5)(A_2-a_5)(2A_2-a_5)(3A_2-a_5)a_5(A_2+a_5)(2A_2+a_5)(3A_2+a_5)(A_2 \\ &\quad +2a_5)(A_2+3a_5)(2A_2^2-5a_5^2) \sinh(2a_5y^*) \sinh(A_2y^*)]. \end{aligned}$$

7

Electroosmotic flow in anisotropic porous microtube with rough surface

7.1 Introduction

Microfluidic systems have revolutionized various fields, from biomedicine to chemical analysis, offering precise fluid manipulation at a microscale level ([Sim et al. \[2017\]](#); [Koh et al. \[2016\]](#); [Middlemiss et al. \[2016\]](#); [Triantafyllou et al. \[2016\]](#); [Liang et al. \[2017\]](#); [Rodrigo et al. \[2018\]](#)). Central to these systems is the concept of electro-osmotic (EO) pumping ([Ajdari \[1996\]](#); [Schrell et al. \[2016\]](#); [Nam et al. \[2015\]](#)), a mechanism that propels fluids through microchannels without the need for traditional pumps. In EO pumping, the interaction between an electric field and the charged surface of a microchannel induces a flow of liquid. This phenomenon occurs due to the formation of an electric double layer (EDL) near the charged surface, which exerts a force on the fluid. By applying an external electric field, researchers can control the direction and rate of fluid flow within the microchannels, enabling precise and efficient fluid manipulation.

In practical channels, surface irregularities arise from manufacturing processes or the presence of substances like macromolecules. These irregularities can significantly influence laminar flow. Conduits exhibit varying degrees of surface roughness, influenced by manufacturing methods. Surface conditions can profoundly affect flow characteristics, underscoring the importance of accounting for roughness in fluid flow analysis. This is especially crucial in microflows, where wall effects become increasingly significant as the flow cross-section decreases. Motivated by these factors, researchers have investigated the impact of roughness on electroosmotic flow. [Shu et al. \[2010\]](#) investigated the electroosmotic flow through a wavy microchannel to understand the rela-

tionship between the electric potential and the wall waviness. Using the Ritz method, they found that flow enhancement increases with greater surface corrugation. [Martinez et al. \[2016b\]](#) conducted an asymptotic analysis on the electroosmotic flow of a Phan-Thien-Tanner fluid in a wavy-walled microchannel using the domain perturbation method. [Chang et al. \[2016b\]](#) developed a mathematical model for electroosmotic flow through a microchannel, considering three-dimensional waviness. They observed that mean velocity in the rough channel can exceed that in a smooth channel. [Yoshida et al. \[2016\]](#) used a Lattice Boltzmann simulation to investigate electroosmotic flow between two undulated surfaces, noting that variations in channel width reduce flow rates compared to straight channels. [Arcos et al. \[2018\]](#) explored the dispersion coefficient of a passive solute in a viscoelastic fluid under steady-state pure electro-osmotic flow (EOF), using the simplified Phan-Thien-Tanner model to model fluid rheology. They determined that the dispersion coefficient is primarily influenced by the Deborah number and the ratio of the half-height of the microchannel to the Debye length.

Another emerging technology in microfluidics is electro-magnetohydrodynamic (EMHD) pumping ([Homsy et al. \[2005\]](#); [Nguyen and Kassegne \[2008\]](#); [Lemoff and Lee \[2000\]](#); [Eijkel et al. \[2003\]](#); [Huang et al. \[2000\]](#)), which utilizes the combined effects of electromagnetic fields and fluid dynamics to drive fluid flow. EMHD pumping offers advantages such as non-contact operation and high efficiency, making it ideal for various microfluidic applications. The operation of an Electromagnetohydrodynamic (EMHD) micropump relies on the Lorentz force, a consequence of the interaction between magnetic and electric fields, to induce a continuous flow within the device. This technology is pivotal for the development of micro-coolers and plays a crucial role in understanding complex flow phenomena within fluidic networks, such as mixing and stirring ([Erickson and Li \[2002\]](#); [Stone et al. \[2004\]](#)). [Buren et al. \[2017\]](#) discussed the impact of combined EMHD flow in a corrugated microchannel, noting that wall roughness disrupts the flow and reduces the mean velocity. [Li et al. \[2019\]](#) investigated three-dimensional surface corrugations on EMHD flow using sinusoidal functions, obtaining analytical solutions for the governing equations through perturbation methods. They suggested that increasing the strength of a magnetic field could maximize the flow rate. [Noreen et al. \[2021\]](#) explored entropy generation in EMHD flow through porous asymmetric microchannels using water-based nanofluids, inspired by nanomedicine technology. They numerically solved a nonlinear mathematical model to analyze heat transfer rates with different nanoparticles. [Reza et al. \[2021\]](#) presented a mathematical model for the thermal transport of EMHD flow in a wavy microchannel with a porous medium. [Rana et al. \[2022\]](#) investigated a complex wavy rough microchannel, noting that surface roughness affects the electric potential, and the interaction between roughness and the porous medium reduces the EMHD flow rate. More recently, [Rana et al. \[2024\]](#) conducted a numerical investigation involving an anisotropic porous microchannel with a wavy surface. They found that anisotropic permeability significantly influences flow transport and heat transfer, with the presence of anisotropy enhancing the heat transfer rate in the porous medium.

From the literature review, it is evident that most studies have focused on rough microchannels, yet the tube shape is more practical for designing microfluidic systems. Few works have explored rough microtubes. [Keramati et al. \[2016\]](#) developed an analytical model for the thermo-fluidic

transport of electroosmotic flow in rough microtubes, noting that the heat transfer rate decreases with increasing joule heating. [Chang et al. \[2016a\]](#) discussed electroosmotic flow analytically by employing perturbation techniques and considering sinusoidal roughness on the microtube surface. They found that the impact of roughness on the electroosmotic flow (EOF) rate becomes more pronounced as the nondimensional electrokinetic width increases. [Lei et al. \[2019\]](#) investigated electroosmotic flow through a bumpy microtube using the boundary perturbation method. They examined the effects of roughness on electroosmotic pumping and predicted the impact of roughness levels on pumping efficiency.

Despite the significant research highlighted earlier, there is still a gap in the literature regarding anisotropic porous microtube with rough surface. The present study aims to expand our research by focusing on analytical solutions for steady Electromagnetohydrodynamic (EMHD) pumping flow in a rough microtube filled with an anisotropic porous medium. Compared to EMHD flow through rough microchannels, microtubes are more practical for microfluidic applications. This study explores the effects of surface roughness in the azimuthal direction on EMHD pumping in the presence of an anisotropic porous medium, considering a wide range of geometrical and physical parameters. To achieve this, we employ a combination of boundary perturbations to obtain analytical solutions for the governing equations. We assume that the charge distribution of the electrolyte is governed by the Poisson-Boltzmann equation, linearized under the Debye-Hückel Approximation. The motion of the electrolyte solution follows the Navier-Stokes equation, considering the assumptions at low Reynolds numbers. Specifically, we focus on surface roughness with amplitudes smaller than 0.1. Additionally, we provide further analysis to demonstrate how the theoretical results can be used to model the level of tube roughness and how the pumping flow is influenced by the anisotropic permeability.

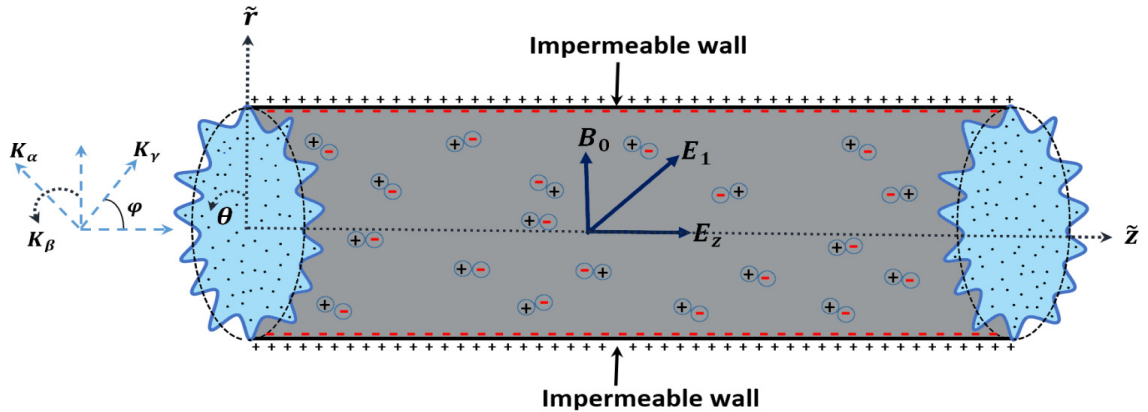


Figure 7.1: The schematic diagram depicts a rough microtube, with the rough surface represented by $\tilde{r} = \tilde{r}_w$, incorporating the effects of surface roughness in the azimuthal direction. Flow occurs in the axial direction \tilde{z} , and the tube contains an anisotropic porous medium with permeabilities $K_\alpha, K_\beta, K_\gamma$ along the principal axes, as well as an anisotropic angle φ . A uniform magnetic field of strength B_0 is applied along the radial direction of the flow, while an electric field of strength E_z is imposed along the axial direction, and a transverse electric field is applied along the azimuthal direction.

7.2 Mathematical modeling of the Problem

7.2.1 Problem description

A cylindrical microtube with an anisotropic porous medium is considered which is bounded by the sinusoidal wavy impermeable wall. The geometry of the problem is shown in Fig. 7.1 and the impermeable wavy wall is described as (Keramati et al. [2016])

$$\tilde{r}_w = R \left\{ 1 + \varepsilon \sin \left(\frac{2\pi}{\lambda} \theta \right) \right\}, \quad (7.1)$$

where R is the mean radius of the microtube, λ denotes the wave length in the axial direction and ε stands for the relative roughness of the corrugated microtube. The steady, laminar, hydrodynamically and thermally fully developed flow of an incompressible, viscous, Newtonian fluid is considered. The polar cylindrical coordinate system $(\tilde{r}, \theta, \tilde{z})$ is introduced to describe the flow. The flow is assumed in the \tilde{z} -direction. The permeability along the principal axes are $K_\alpha, K_\beta, K_\gamma$ respectively, where $K_i (i = \alpha, \beta, \gamma)$ denote the permeability constants. The anisotropy characteristics is measured by the anisotropic permeability of the porous medium. The magnetic field and the electric field are applied in the radial and the axial direction respectively.

7.2.2 Governing equations

This physical model illustrates the electromagnetohydrodynamic (EMHD) flow through a rough microtube with anisotropic porous medium. The flow is influenced by the magnetic field \mathbf{B} and the electric field \mathbf{E} , which are applied in the radial and the axial direction respectively. The applied electric potential $\tilde{\Phi}$ satisfies the Laplace's equation (Kang and Suh [2009]; Lei et al. [2019]).

$$\tilde{\nabla}^2 \tilde{\Phi} = 0. \quad (7.2)$$

Here $\tilde{\nabla}^2 \equiv \frac{\partial^2}{\partial \tilde{r}^2} + \frac{1}{\tilde{r}} \frac{\partial}{\partial \tilde{r}} + \frac{1}{\tilde{r}^2} \frac{\partial^2}{\partial \theta^2} + \frac{\partial^2}{\partial \tilde{z}^2}$.

The presence of an electric field creates an electric double layer (EDL) in the electrolyte solution near the solid and fluid interface. EDL consist two layers where one is stern layer and another is diffuse layer. The charge density ρ_e within the EDL follows the Boltzmann distribution and the EDL potential $\tilde{\psi}$ satisfies the Poisson Boltzmann equation (Arcos et al. [2018]; Kleinstreuer [2013])

$$\rho_e = -\varepsilon \tilde{\nabla}^2 \tilde{\psi} = -2n_0 e z_0 \sinh \left(\frac{e z_0 \tilde{\psi}}{k_B T_{av}} \right). \quad (7.3)$$

Here ε denotes the electrical permittivity of the medium, n_0 indicates the concentration of bulk electrolyte solution, e is the charge of the proton, z_0 denotes the valance, k_B is called Boltzmann constant and T_{av} is the average temperature. Further, a wall zeta potential $\tilde{\zeta}$ is imposed in the rough surface of the microtube (Joly et al. [2014]).

Since, the wall zeta potential is very small compared to the thermal voltage, which implies that $\frac{e z_0 \tilde{\zeta}}{k_B T_{av}} \ll 1$. Therefore with the Dybye-Hückle linearization the term $\sinh \left(\frac{e z_0 \tilde{\psi}}{k_B T_{av}} \right)$ is approximated

to $\frac{ez_0\tilde{\psi}}{k_B T_{av}}$ and the Eq. (7.3) can be linearized as follows:

$$\tilde{\nabla}^2 \tilde{\psi} = -\frac{\rho_e}{\varepsilon} = \frac{2n_0 e^2 z_0^2}{\varepsilon k_B T_{av}} \tilde{\psi} = \kappa^2 \tilde{\psi}. \quad (7.4)$$

Here $\kappa^{-1} = \sqrt{\frac{\varepsilon k_B T_{av}}{2n_0 e^2 z_0^2}}$ is called Debye length (Arcos et al. [2018]).

From the assumptions, the flow is viscous and incompressible. So, we have the governing equations for continuity and the momentum are as follows: (Lei et al. [2019]; Rana et al. [2022])

$$\tilde{\nabla} \cdot \tilde{\mathbf{U}} = 0, \quad (7.5)$$

$$\rho \left[\frac{\partial \tilde{\mathbf{U}}}{\partial t} + (\tilde{\mathbf{U}} \cdot \tilde{\nabla}) \tilde{\mathbf{U}} \right] = -\tilde{\nabla} \tilde{p} + \mu_e \tilde{\nabla}^2 \tilde{\mathbf{U}} - \frac{\mu_f}{\tilde{\mathbf{K}}} \tilde{\mathbf{U}} + \rho_e \mathbf{E} + \mathbf{F}, \quad (7.6)$$

where $\tilde{\nabla} \equiv \frac{\partial}{\partial \tilde{r}} + \frac{1}{\tilde{r}} \frac{\partial}{\partial \theta} + \frac{\partial}{\partial \tilde{z}}$, $\tilde{\nabla}^2 \equiv \frac{\partial^2}{\partial \tilde{r}^2} + \frac{1}{\tilde{r}} \frac{\partial}{\partial \tilde{r}} + \frac{1}{\tilde{r}^2} \frac{\partial^2}{\partial \theta^2} + \frac{\partial^2}{\partial \tilde{z}^2}$, ρ , \tilde{p} , μ_e and μ_f are denoted as density, pressure, effective viscosity inside the porous medium and dynamic viscosity of the fluid. $\tilde{\mathbf{U}} = (\tilde{u}, \tilde{v}, \tilde{w})$ is the velocity vector. The last two terms indicate the electromagnetohydrodynamic body force which is a combination of electroosmotic force ($\rho_e \mathbf{E}$) and Lorentz force ($\mathbf{J} \times \mathbf{B}$), where $\mathbf{J} = \sigma_e (\mathbf{E} + \tilde{\mathbf{U}} \times \mathbf{B})$ and σ_e suggests the electrical conductivity of the electrolyte solution. Here $\tilde{\mathbf{K}}$ corresponds to the permeability of the porous medium. Owing to the assumption, the porous medium is anisotropic and it is a third order tensor described by

$$\tilde{\mathbf{K}} = \begin{bmatrix} K_\alpha \cos^2 \varphi + K_\gamma \sin^2 \varphi & 0 & (K_\gamma - K_\alpha) \sin \varphi \cos \varphi \\ 0 & K_\beta & 0 \\ (K_\gamma - K_\alpha) \sin \varphi \cos \varphi & 0 & K_\gamma \cos^2 \varphi + K_\alpha \sin^2 \varphi \end{bmatrix}, \quad (7.7)$$

where φ is the anisotropic angle.

Theorem 1 (Horn and Johnson [2013]) *A Hermitian matrix is positive definite if and only if all of its eigenvalues are positive.*

It is obvious that the $\tilde{\mathbf{K}}$ is symmetric and the eigenvalues are K_α , K_β and K_γ . Since K_α , K_β , $K_\gamma > 0$, by theorem 1, $\tilde{\mathbf{K}}$ is positive definite. Hence $\tilde{\mathbf{K}}^{-1}$ exists and it is positive definite and unique.

Based on the physical phenomena of microscale system, it is assumed that the velocity gradient is only along the axial direction of the microtube because the mean radius is very very smaller than the length of the microtube. So, we can assume that the flow is purely along the axial direction of the rough microtube for this present problem. Hence the velocity components can be written as $\tilde{\mathbf{U}} = (0, 0, \tilde{u})$, where \tilde{u} is the function of \tilde{r} and θ only. So, the momentum Eq. (7.6) is normalized as

$$-\frac{\partial \tilde{p}}{\partial \tilde{r}} - \frac{\mu_f \gamma_2}{K_\alpha} \tilde{u} = 0, \quad (7.8)$$

$$-\frac{\partial \tilde{p}}{\partial \theta} = 0, \quad (7.9)$$

$$-\frac{\partial \tilde{p}}{\partial \tilde{z}} + \mu_e \tilde{\nabla}^2 \tilde{u} - \frac{\mu_f \gamma_1}{K_\alpha} \tilde{u} + \rho_e E_z - \sigma_e B_0^2 \tilde{u} + \sigma_e B_0 E_1 = 0. \quad (7.10)$$

Here $\gamma_1 = K \cos^2 \varphi + \sin^2 \varphi$, $\gamma_2 = (K - 1) \cos \varphi \sin \varphi$ and $K = \frac{K_\alpha}{K_\gamma}$ denotes the anisotropic permeability ratio. E_z and E_1 are electric field components along the axial and transverse directions respectively. These electric field components are calculated from the relation $\mathbf{E} = -\tilde{\nabla} \tilde{\Phi} - \tilde{\nabla} \tilde{\psi}$ (Lei et al. [2019]). It can be observed from the equations (7.8)-(7.10) that the pressure gradient is independent of θ . So, equations (7.8) and (7.9) yield

$$\frac{\partial}{\partial \tilde{z}} \left(\frac{\partial \tilde{p}}{\partial \tilde{r}} \right) = 0 \text{ and } \frac{\partial}{\partial \tilde{z}} \left(\frac{\partial \tilde{p}}{\partial \theta} \right) = 0. \quad (7.11)$$

Again, from Eq. (7.10), one can write

$$\frac{\partial}{\partial \tilde{z}} \left(\frac{\partial \tilde{p}}{\partial \tilde{z}} \right) = 0. \quad (7.12)$$

Hence, one may write that $\frac{\partial \tilde{p}}{\partial \tilde{z}} = \text{constant} = -G$ (say).

Here, the mean radius of the microtube is R , which is considered as reference characteristic length so that $\nabla^2 \equiv R^2 \tilde{\nabla}^2$ and $\nabla^2 \equiv \frac{\partial^2}{\partial r^2} + \frac{1}{r} \frac{\partial}{\partial r} + \frac{1}{r^2} \frac{\partial^2}{\partial \theta^2} + \frac{\partial^2}{\partial z^2}$. Making dimensionless all the physical variables as follows: $\Phi = \tilde{\Phi}/(E_0 R)$, $\psi = \tilde{\psi}/(E_0 R)$, $\zeta = \tilde{\zeta}/(E_0 R)$, $\mathbf{U} = \tilde{\mathbf{U}}/\mathbf{u}_{hs}$, where $\mathbf{u}_{hs} = -(\epsilon \tilde{\zeta} E_z)/\mu_f$ is called Helmholtz-Smoluchowski velocity and E_0 indicates the strength of the applied electric field (Rana et al. [2022]; Lei et al. [2019]). So, the Laplace Eq. (7.2) for applied potential becomes

$$\nabla^2 \Phi = 0, \quad (7.13)$$

subjected to the boundary condition at the rough surface of the microtube

$$\frac{\partial \Phi}{\partial n} = \nabla \Phi \cdot \mathbf{n} = 0, \quad (7.14)$$

where \mathbf{n} is the unit normal on the inner surface of the microtube. The linearized Poisson Boltzmann Eq. (7.4) can be written as

$$\nabla^2 \psi = \omega^2 \psi, \quad (7.15)$$

with $\psi = \zeta$ at the boundary of the microtube. Here $\zeta = \tilde{\zeta}/(E_0 R)$ is the dimensionless wall zeta potential and $\omega = \kappa R$, denotes the dimensionless electrokinetic width. This investigation is influenced by the electrokinetic width ω , which is the ratio of the mean radius of the rough microtube to the Debye length κ^{-1} . The dimensionless form of the continuity equation becomes

$$\nabla \cdot \mathbf{U} = 0. \quad (7.16)$$

Eq. (7.10) is normalized as

$$\mu \nabla^2 u - \left(Ha^2 + \frac{\gamma_1}{Da} \right) u + \frac{\omega^2 \psi}{\zeta} + HaS + P = 0, \quad (7.17)$$

where $\mu = \mu_e/\mu_f$ denotes the viscosity ratio, $Ha = B_0 R \sqrt{\sigma_e/\mu_f}$ is Hartmann number which indicates the strength of the applied magnetic field, $Da = K_\alpha/R^2$ is Darcy number, $S = (E_1 R/\mathbf{u}_{hs}) \sqrt{\sigma_e/\mu_f}$ is the strength of lateral electric field which depends on the roughness of the microtube and $P = (GR^2)/(\mu_f \mathbf{u}_{hs})$ is the dimensionless (constant) pressure gradient along the axial direction.

The purpose of the present study is to investigate the EMHD flow in the porous microtube with rough wall, where the roughness of the wall is modeled by Eq. (7.1). Divided by the mean radius R , the dimensionless form of the rough wall is given by

$$r_w = \frac{\tilde{r}_w}{R} = 1 + \varepsilon \sin(M\theta), \quad (7.18)$$

where $M = 2\pi/\lambda$ denotes the wave number of corrugation.

Let us establish a clear definition for the roughness term denoted as ε . Drawing from experimental data regarding the roughness amplitude (ε) observed in glass microchannels (Ren et al. [2011]), one can ascertain that this parameter tends to hover around the order of 0.01, especially when dealing with microchannels of approximately $10\mu m$ in radius. It is worth noting that microchannel heat sinks predominantly constructed from silicon often exhibit notably rough surfaces. In light of this, we posit that values for the roughness parameter, denoted as ε could potentially reach as high as 0.1, drawing insights from the experimental findings reported by Weilin et al. [2000].

It is worth highlighting numerical values of several parameters that validate the approximations we have employed. Firstly, we note the proton charge (e) equal to $1.609 \times 10^{-19}C$ and the Boltzmann constant (k_B) equal to $1.381 \times 10^{-23}m^2kg s^{-2}K^{-1}$. At a temperature (T_{av}) of $298K$, the thermal voltage ($k_B T_{av}/e$) amounts to $25.6mV$ (millivolts). Consequently, the Debye-Huckel approximation remains valid when the absolute zeta potential ($|\tilde{\zeta}|$) is significantly smaller than $25.6mV$, denoted as ($|\tilde{\zeta}|/(k_B T_{av}/e) \ll 1$). Secondly, within the domain of capillary electrophoresis applications, the parameter ω typically spans a range between 1 and 100, while the Debye length (κ^{-1}) characterizing the electric double layer (EDL) extends from 1 to $100nm$ (Kumar and Crittenden [2013]; Probststein [2003]; Kortschot et al. [2014]). These phenomena occur within microtubes featuring widths on the order of $100nm$ to $1\mu m$. The pursuit of lower ω values steers us toward narrower microtubes or a reduction in bulk concentration (n_0). Our selection of the permeability for the porous microtube in the range of $0 - 10^{-11}m^2$ (Rana et al. [2022]) corresponds to Darcy numbers (Da) varying between 0 and 1. It is noteworthy that surface roughness typically exhibits a range between 0.1 and $10nm$ (Chkhalo et al. [2017]; Schiotz and Jacobsen [2017]). This variation implies that geometric roughness ε may fluctuate within the range of 0.01 to 0.1. For instance, in this context, we assume the average radius of the microtube (R) is $100nm - 20\mu m$. Furthermore, we consider the scenario of low Reynolds numbers ($Re = \rho \mathbf{u}_{hs} R/\mu$), exemplified by Blood with concentration of $3.9mol m^{-3}$. At $T_{av} = 298K$, the electric permittivity of the electrolyte is $\varepsilon = 6.6405 \times 10^{-10}C^2 N^{-1}m^{-2}$. The mass density (ρ) and dynamic viscosity (μ) of Blood are approximately $\rho = 1060kg m^{-3}$ and $\mu = 4 \times 10^{-3}Pas$, respectively (Majee et al. [2021]). By taking numerical values such as $\tilde{\zeta} = -0.2mV - 2mV$ and $E_z = 2 \times 10^5V$ (Rana et al. [2022]; Kortschot et al. [2014]), along with the data mentioned earlier, we can calculate \mathbf{u}_{hs} to be either $6.6 \times 10^{-3}ms^{-1}$ or

$-6.6 \times 10^{-2} ms^{-1}$. The transverse electrical field is assumed to range from $E_1 = 0 - 3 \times 10^3 V/m$ (Reza et al. [2021]; Rana et al. [2022]), which modulates the strength of the transverse electric field within the interval 0 to 10. Simultaneously, the applied magnetic field is considered to be in the vicinity of $B_0 \sim 1 - 2 \times 10^4 T$ (Rana et al. [2022]), resulting in a corresponding range of Hartmann numbers spanning from 0 to 2. Consequently, the Reynolds numbers (Re) remain substantially below 1, affirming the soundness of our established model within a reasonable range of physical parameters.

7.3 Perturbation analysis due to roughness

7.3.1 Effect of roughness on the applied electric field

Surface roughness plays an important role for applied electric field and it modifies the applied potential ϕ near the rough surface of the microtube. To understand the influence of roughness, we solve Eq. (7.13) subject to the boundary condition (7.14) at the rough wall of the microtube. The unit normal \mathbf{n} on the rough wall is expressed as

$$\mathbf{n} = \frac{\nabla\{r - 1 - \varepsilon \sin(M\theta)\}}{\|\nabla\{r - 1 - \varepsilon \sin(M\theta)\}\|} = \frac{1 - \frac{\varepsilon M}{r} \cos(M\theta)}{\sqrt{1 + \frac{\varepsilon^2 M^2}{r^2} \cos^2(M\theta)}}. \quad (7.19)$$

Hence, the boundary condition (7.14) becomes

$$\frac{\partial \Phi}{\partial r} - \frac{\varepsilon M}{r^2} \cos(M\theta) \frac{\partial \Phi}{\partial \theta} = 0, \text{ at } r = 1 + \varepsilon \sin(M\theta). \quad (7.20)$$

For perturbation analysis of applied electric potential Φ , we seek Φ in the following form of perturbation

$$\Phi = \Phi_0 + \varepsilon \Phi_1 + \varepsilon^2 \Phi_2 + \dots. \quad (7.21)$$

Substituting (7.21) in (7.13), then one may write

$$\nabla^2 \Phi_i = 0, \quad i = 0, 1, 2, 3, \dots. \quad (7.22)$$

Again, substituting (7.21) in (7.20), then the boundary condition becomes

$$\left(\frac{\partial \Phi_0}{\partial r} + \varepsilon \frac{\partial \Phi_1}{\partial r} + \varepsilon^2 \frac{\partial \Phi_2}{\partial r} + \dots \right) - \frac{\varepsilon M}{r^2} \cos(M\theta) \left(\frac{\partial \Phi}{\partial \theta} + \varepsilon \frac{\partial \Phi}{\partial \theta} + \varepsilon^2 \frac{\partial \Phi}{\partial \theta} + \dots \right) = 0, \text{ at } r = 1 + \varepsilon \sin(M\theta). \quad (7.23)$$

The boundary condition (7.23) can be expanded about $r = 1$ as follows

$$\begin{aligned} & \left\{ \frac{\partial \Phi_0}{\partial r} + \varepsilon \sin(M\theta) \frac{\partial^2 \Phi_0}{\partial r^2} + \varepsilon^2 \frac{\sin^2(M\theta)}{2} \frac{\partial^3 \Phi_0}{\partial r^3} + \dots \right\} \\ & + \left\{ \varepsilon \frac{\partial \Phi_1}{\partial r} + \varepsilon^2 \sin(M\theta) \frac{\partial^2 \Phi_1}{\partial r^2} + \dots \right\} + \left\{ \varepsilon^2 \frac{\partial^2 \Phi_2}{\partial r^2} + \dots \right\} \\ & - M \cos(M\theta) \left\{ \varepsilon \frac{\partial \Phi_0}{\partial \theta} + \varepsilon^2 \sin(M\theta) \frac{\partial^2 \Phi_0}{\partial r \partial \theta} + \dots \right\} \\ & - M \cos(M\theta) \left\{ \varepsilon^2 \frac{\partial \Phi_1}{\partial \theta} + \dots \right\} + \dots = 0, \text{ at } r = 1. \end{aligned} \quad (7.24)$$

From Eq. (7.24), one can easily collect the terms for the same power of ε , which gives the separate boundary condition for various order of Φ_i . Then, one may ready to solve for Φ_i at various order.

1. Zeroth order

It is worthwhile to mention that when $\varepsilon = 0$ (unperturbed), then the flow is passing through the smooth microtube. That means there is no roughness in the microtube. Therefore, the normalized applied electric field acts simply in axial direction and the gradient of voltage should be constant in the axial direction. So, one can simply write $E_z/E_0 = -\nabla \Phi_0 = e_z$, where e_z is the unit vector in the z -direction. Hence the solution of Φ_0 can be written as (Lei et al. [2019])

$$\Phi_0 = -z. \quad (7.25)$$

2. First order

For first order solution of Φ_1 , we have to solve Eq. (7.22) for $i = 1$, subject to the following boundary condition which is obtained from Eq. (7.24),

$$\frac{\partial \Phi_1}{\partial r} = -\sin(M\theta) \frac{\partial^2 \Phi_0}{\partial r^2} + M \cos(M\theta) \frac{\partial \Phi_0}{\partial \theta}, \text{ at } r = 1. \quad (7.26)$$

Then, the solution of Φ_1 is given by

$$\Phi_1 = -r^{-M} \cos(M\theta). \quad (7.27)$$

3. Second order

Similarly, for second order solution of Φ_2 , we have to solve Eq. (7.22) for $i = 2$, subject to the following boundary condition which is obtained from Eq. (7.24),

$$\begin{aligned} & \frac{\partial \Phi_2}{\partial r} = -\sin(M\theta) \frac{\partial^2 \Phi_1}{\partial r^2} - \frac{\sin^2(M\theta)}{2} \frac{\partial^3 \Phi_0}{\partial r^3} \\ & + M \cos(M\theta) \left\{ \frac{\partial \Phi_1}{\partial \theta} + \sin(M\theta) \frac{\partial^2 \Phi_0}{\partial r \partial \theta} \right\}, \text{ at } r = 1. \end{aligned} \quad (7.28)$$

Then, the solution of Φ_2 is given by

$$\Phi_2 = -\frac{1}{2} \left(M + \frac{1}{2} \right) r^{-2M} \sin(2M\theta). \quad (7.29)$$

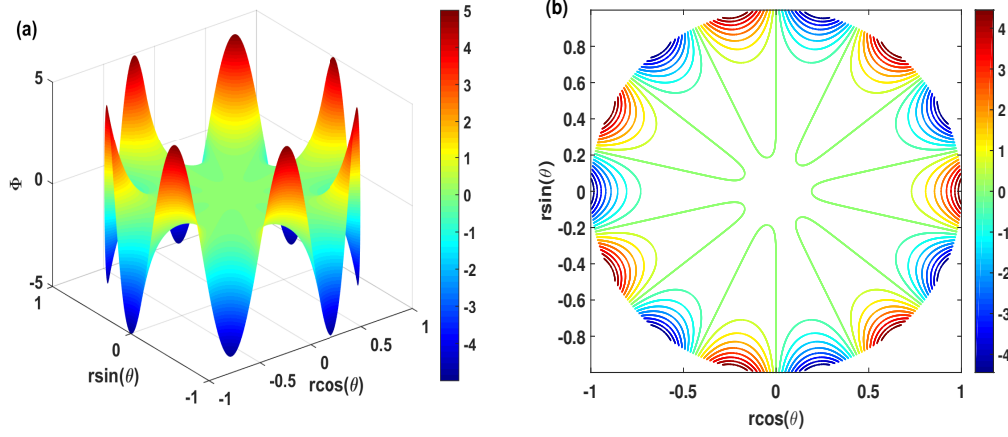


Figure 7.2: (a) Applied potential (Φ) profile produced by applied electric field for $M = 7, \varepsilon = 0.01$. (b) Contour for Φ .

Figs. 7.2(a) and 7.2(b) provide visual representations of how the applied electric potential (Φ) is distributed in the immediate vicinity of the rough wall of the microtube. It can be observed that the disturbances or fluctuations in electric potential are notably more prominent and exhibit oscillatory behavior near the rough wall. This phenomenon can be attributed to the interaction between the electric field and the irregularities in the rough surface. These findings are consistent with the existing literature, particularly the work conducted by [Lei et al. \[2019\]](#).

7.3.2 Effect of roughness on Potential Distribution and Electric Double Layer

Surface roughness plays an important role in determining of ion distribution of electrolyte solution within the electric double layer (EDL). To understand the impact of roughness, we solve Eq. (7.15) for EDL potential ψ with $\psi = \zeta$ at the wall of the rough microtube and reducing in the center of the microtube. Likewise, one may perturb the EDL potential ψ in series of ε as follows:

$$\psi = \psi_0 + \varepsilon \psi_1 + \varepsilon^2 \psi_2 + \dots. \quad (7.30)$$

Substituting Eq. (7.30) in Eq. (7.15), then one may write

$$\nabla^2 \psi_i = \omega^2 \psi_i, \quad i = 0, 1, 2, \dots. \quad (7.31)$$

Now, the boundary condition $\psi = \zeta$ on the wall $r = 1 + \varepsilon \sin(M\theta)$ can be Taylor expanded about $r = 1$, then

$$\psi + \varepsilon \sin(M\theta) \frac{\partial \psi}{\partial r} + \frac{\varepsilon^2 \sin^2(M\theta)}{2} \frac{\partial^2 \psi}{\partial r^2} + \dots = \zeta, \quad \text{at } r = 1. \quad (7.32)$$

Substituting (7.30) in (7.32) and collecting the terms for the same power of ε , which gives the separate boundary condition for various order of ψ_i , which are described as follows:

$$\psi_0 = \zeta, \text{ at } r = 1, \quad (7.33)$$

$$\psi_1 + \sin(M\theta) \frac{\partial \psi_0}{\partial r} = 0, \text{ at } r = 1, \quad (7.34)$$

$$\psi_2 + \sin(M\theta) \frac{\partial \psi_1}{\partial r} + \frac{\sin^2(M\theta)}{2} \frac{\partial^2 \psi_0}{\partial r^2} = 0, \text{ at } r = 1. \quad (7.35)$$

Now, one can easily solve the Eq. (7.31) subjected to the boundary conditions (7.33)-(7.35) for ψ_i at various orders.

1. Zeroth order

It is obvious that when $\varepsilon = 0$ (unperturbed), then the flow is passing through the smooth microtube. That means one have to calculate the EDL potential for a smooth microtube. Then Eq. (7.31) (for $i = 0$) subject to the boundary condition (7.33) yields the following solution for ψ_0

$$\psi_0 = \frac{\zeta I_0(\omega r)}{I_0(\omega)}. \quad (7.36)$$

2. First order

For first order solution of ψ_1 , we have to solve Eq. (7.31) for $i = 1$, subject to the following boundary condition which is obtained from Eq. (7.34) by using (7.36),

$$\psi_1 = -\sin(M\theta) \frac{\zeta \omega I_1(\omega)}{I_0(\omega)}, \text{ at } r = 1. \quad (7.37)$$

Now, by solving Eq. (7.31) for $i = 1$, subject to the boundary condition (7.37), the solution for ψ_1 can be obtained as

$$\psi_1 = -\frac{\zeta \omega I_1(\omega)}{I_M(\omega) I_0(\omega)} I_M(\omega r) \sin(M\theta). \quad (7.38)$$

3. Second order

Similarly, for second order solution of ψ_2 , we have to solve Eq. (7.31) for $i = 2$, subject to the following boundary condition which is obtained from Eq. (7.35) with the help of (7.36) and (7.38),

$$\psi_2 = \{1 - \cos(2M\theta)\} \alpha_1, \text{ at } r = 1. \quad (7.39)$$

where $\alpha_1 = \frac{\zeta \omega^2 I_1(\omega) \{I_{M-1}(\omega) + I_{M+1}(\omega)\}}{4 I_M(\omega) I_0(\omega)} - \frac{\zeta \omega^2 \{I_0(\omega) + I_2(\omega)\}}{8 I_0(\omega)}$. Now, by solving Eq. (7.31) for $i = 2$, subject to the boundary condition (7.39), the solution for ψ_2 can be obtained as

$$\psi_2 = \alpha_1 \frac{I_0(\omega r)}{I_0(\omega)} - \alpha_1 \frac{I_{2M}(\omega r)}{I_{2M}(\omega)} \cos(2M\theta). \quad (7.40)$$

Figs. 7.3(a) and 7.3(b) offer graphical representations of the Electric Double Layer (EDL) potential (ψ) distribution within the immediate vicinity of the rough wall of the microtube. These visualizations unveil a fascinating observation: the EDL potential exhibits significant disturbances

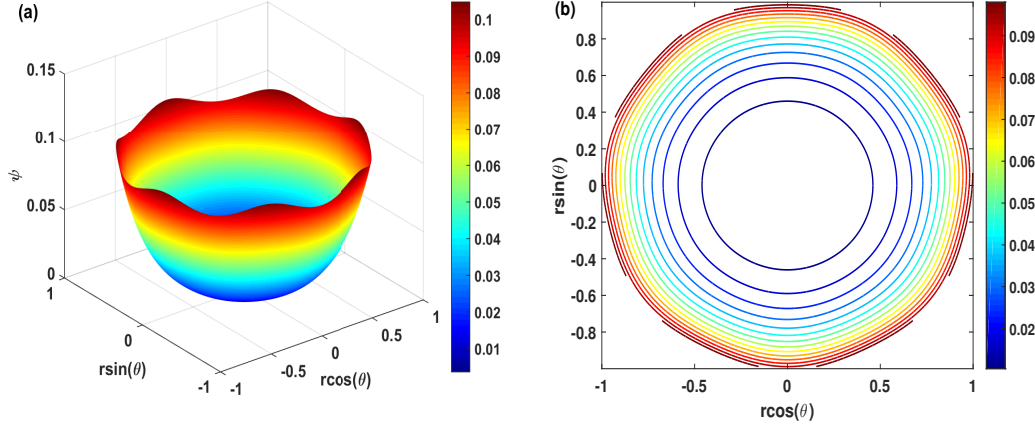


Figure 7.3: (a) EDL potential (ψ) profile for $\omega = 5, M = 7, \varepsilon = 0.01, \zeta = 0.1$. (b) Contour for ψ .

and a characteristic wavy pattern near the rough wall. This intriguing behavior arises from the complex interplay between the distribution of ions in the vicinity and the surface irregularities of the wall. These findings closely align with the pioneering work of [Lei et al. \[2019\]](#).

7.3.3 Effect of roughness on EMHD flow

The flow distribution through the rough microtube with electromagnetic environment is the major subject of this present investigation. To understand the flow transport we have to solve the Eq. (7.17) with the help of applied potential and EDL potential which are already determined in Section 7.3.1 and 7.3.2. We find the perturbation solution for the velocity distribution by solving Eq. (7.17) subject to the no slip boundary condition $u = 0$ on the rough wall of the microtube and the flow velocity is always finite ($u \neq \infty$) at $r = 0$. To solve the Eq. (7.17) effortlessly, we use the following relation such that

$$\chi = \frac{\frac{1}{\mu} \left(Ha^2 + \frac{\gamma_1}{Da} \right) \omega^2 \psi}{\frac{1}{\mu} \left(Ha^2 + \frac{\gamma_1}{Da} \right) - \omega^2} - u \left(Ha^2 + \frac{\gamma_1}{Da} \right) \zeta. \quad (7.41)$$

Using the relation (7.41) in Eq. (7.15) and (7.17), one can easily obtain as

$$\mu \nabla^2 \chi - \left(Ha^2 + \frac{\gamma_1}{Da} \right) \chi - \left(Ha^2 + \frac{\gamma_1}{Da} \right) (HaS + P) = 0. \quad (7.42)$$

Substituting the relation (7.41), the no-slip boundary condition becomes

$$\chi = \frac{\frac{1}{\mu} \left(Ha^2 + \frac{\gamma_1}{Da} \right) \omega^2 \zeta}{\frac{1}{\mu} \left(Ha^2 + \frac{\gamma_1}{Da} \right) - \omega^2} \text{ at } r = 1 + \varepsilon \sin(M\theta), \quad (7.43)$$

$$\chi \neq \infty \text{ at } r = 0. \quad (7.44)$$

Now, we introduce the asymptotic expansion of χ and S in the perturbed series of ε ,

$$\chi = \chi_0 + \varepsilon \chi_1 + \varepsilon^2 \chi_2 + \cdots, \quad (7.45)$$

$$S = S_0 + \varepsilon S_1 + \varepsilon^2 S_2 + \cdots. \quad (7.46)$$

Here the strength of lateral electric field (S) depends on the roughness of the microtube and it depends on the electric field component (E_1) on the transverse direction of the flow. One can easily obtain the expressions for $S_i (i = 0, 1, 2, \dots)$ by using the relation $\mathbf{E} = -(\tilde{\nabla}\tilde{\Phi} + \tilde{\nabla}\tilde{\Psi})$, which are obtained as

$$S_1 = S_0 \left\{ -Mr^{-M-1} \sin(M\theta) - \frac{M\omega\zeta^2 I_1(\omega)}{I_0(\omega)I_M(\omega)} I_M(\omega r) \cos(M\theta) \right\}, \quad (7.47)$$

$$S_2 = S_0 \left\{ -M(M + \frac{1}{2})r^{-2M-1} \cos(2M\theta) - 2M\zeta\alpha_1 \frac{I_{2M}(\omega r)}{I_{2M}(\omega)} \sin(2M\theta) \right\}, \quad (7.48)$$

where $S_0 = (E_0 R / \mathbf{u}_{hs}) \sqrt{\sigma_e / \mu_f}$ is called the constant strength of lateral electric field. For unperturbed case ($\varepsilon = 0$), that means if there is no roughness on the microtube, then $S = S_0$.

Substituting (7.45) and (7.46) in (7.42) yields the following equations at different order of ε

$$\mu \nabla^2 \chi_i - \left(Ha^2 + \frac{\gamma_1}{Da} \right) \chi_i - \left(Ha^2 + \frac{\gamma_1}{Da} \right) (Ha S_i + P) = 0, \quad (7.49)$$

where $i = 0, 1, 2, \dots$, with the boundary conditions (7.43) and (7.44). The boundary condition (7.43) can be Taylor expanded about $r = 1$, then

$$\chi + \varepsilon \sin(M\theta) \frac{\partial \chi}{\partial r} + \frac{\varepsilon^2 \sin^2(M\theta)}{2} \frac{\partial^2 \chi}{\partial r^2} + \cdots = \alpha_2, \text{ at } r = 1, \quad (7.50)$$

where $\alpha_2 = \left\{ \frac{1}{\mu} \left(Ha^2 + \frac{\gamma_1}{Da} \right) \omega^2 \zeta \right\} / \left\{ \frac{1}{\mu} \left(Ha^2 + \frac{\gamma_1}{Da} \right) - \omega^2 \right\}$. Substituting Eq. (7.45) in Eq. (7.50) and collecting the terms for the same power of ε , which gives the separate boundary condition for various order of χ_i , which are described as follows:

$$\chi_0 = \alpha_2, \text{ at } r = 1, \quad (7.51)$$

$$\chi_1 + \sin(M\theta) \frac{\partial \chi_0}{\partial r} = 0, \text{ at } r = 1, \quad (7.52)$$

$$\chi_2 + \sin(M\theta) \frac{\partial \chi_1}{\partial r} + \frac{\sin^2(M\theta)}{2} \frac{\partial^2 \chi_0}{\partial r^2} = 0, \text{ at } r = 1, \quad (7.53)$$

and $\chi_i (i = 0, 1, 2, \dots)$ are finite at $r = 0$. Now, one can easily solve the Eq. (7.49) subjected to the boundary conditions (7.51)-(7.53) for χ_i at various orders.

1. Zeroth order

At zeroth order ($\varepsilon = 0$), it is obvious that the flow is passing through the smooth microtube. That means it is the simple case of EMHD flow through a smooth microtube with porous medium. Therefore we have to calculate the velocity distribution for a smooth microtube. Then Eq. (7.49)

(for $i = 0$) subject to the boundary condition (7.51) yields the following solution for χ_0

$$\chi_0 = \frac{(\alpha_2 + P + HaS_0)I_0\left(\sqrt{\frac{1}{\mu}(Ha^2 + \frac{\gamma_1}{Da})}r\right)}{I_0\left(\sqrt{\frac{1}{\mu}(Ha^2 + \frac{\gamma_1}{Da})}\right)}. \quad (7.54)$$

2. First order

For first order solution of χ_1 , we have to solve Eq. (7.49) for $i = 1$, subject to the following boundary condition which is obtained from Eq. (7.52) by using (7.54),

$$\chi_1 = -\alpha_3 \sin(M\theta), \text{ at } r = 1, \quad (7.55)$$

where $\alpha_3 = \left(\sqrt{\frac{1}{\mu}(Ha^2 + \frac{\gamma_1}{Da})}\right) \frac{I_1\left(\sqrt{\frac{1}{\mu}(Ha^2 + \frac{\gamma_1}{Da})}\right)}{I_0\left(\sqrt{\frac{1}{\mu}(Ha^2 + \frac{\gamma_1}{Da})}\right)}(\alpha_2 + P + HaS_0)$ and χ_1 is finite at $r = 0$. Now,

by solving Eq. (7.49) for $i = 1$, subject to the boundary condition (7.55), the solution for χ_1 can be obtained as

$$\begin{aligned} \chi_1 = & -\frac{\alpha_3 I_M\left(\sqrt{\frac{1}{\mu}(Ha^2 + \frac{\gamma_1}{Da})}r\right)}{I_M\left(\sqrt{\frac{1}{\mu}(Ha^2 + \frac{\gamma_1}{Da})}\right)} \sin(M\theta) \\ & + \sum_{m=0}^{\infty} \sum_{n=0}^{\infty} \left[a_{mn} \sin\{(m+1)\pi r\} \sin\left\{\frac{(n+1)}{2}\theta\right\} \right], \end{aligned} \quad (7.56)$$

where

$$a_{mn} = \frac{-\frac{4HaS_0}{\mu}(Ha^2 + \frac{\gamma_1}{Da})}{2\pi\{(m+1)^2\pi^2 + \frac{(n+1)^2}{4}\}} \int_0^1 \int_0^{2\pi} \left[F_1(r, \theta) \sin\{(m+1)\pi r\} \sin\left\{\frac{(n+1)}{2}\theta\right\} \right] dr d\theta,$$

$$F_1(r, \theta) = Mr^{-M-1} \sin(M\theta) + \frac{M\omega \zeta^2 I_1(\omega)}{I_0(\omega) I_M(\omega)} I_M(\omega r) \cos(M\theta) \Big\}.$$

3. Second order

Similarly, for second order solution of χ_2 , we have to solve Eq. (7.49) for $i = 2$, subject to the following boundary condition which is obtained from Eq. (7.53) with the help of Eq. (7.54) and Eq. (7.56),

$$\begin{aligned} \chi_2 = & \sum_{m=0}^{\infty} \sum_{n=0}^{\infty} \left[\alpha_6 a_{mn} \left\{ \cos\left(\frac{n+1-2M}{2}\theta\right) - \cos\left(\frac{n+1+2M}{2}\theta\right) \right\} \right] \\ & + \alpha_5 \left\{ 1 - \cos(2M\theta) \right\}, \text{ at } r = 1. \end{aligned} \quad (7.57)$$

where

$$\alpha_4 = \frac{\alpha_3 \sqrt{\frac{1}{\mu}(Ha^2 + \frac{\gamma_1}{Da})}}{2I_M\left(\sqrt{\frac{1}{\mu}(Ha^2 + \frac{\gamma_1}{Da})}\right)} \left\{ I_{M+1}\left(\sqrt{\frac{1}{\mu}(Ha^2 + \frac{\gamma_1}{Da})}\right) + I_{M-1}\left(\sqrt{\frac{1}{\mu}(Ha^2 + \frac{\gamma_1}{Da})}\right) \right\},$$

$$\alpha_5 = \frac{\alpha_4}{2} - \left(P + HaS_0 + \alpha_2 \right) \left\{ \frac{1}{\mu} (Ha^2 + \frac{\gamma_1}{Da})^2 \right\} \frac{I_0 \left(\sqrt{\frac{1}{\mu} (Ha^2 + \frac{\gamma_1}{Da})} \right) + I_2 \left(\sqrt{\frac{1}{\mu} (Ha^2 + \frac{\gamma_1}{Da})} \right)}{8I_0 \left(\sqrt{\frac{1}{\mu} (Ha^2 + \frac{\gamma_1}{Da})} \right)},$$

$$\alpha_6 = \frac{1}{2}(m+1)\pi \cos\{(m+1)\pi\}.$$

Now, by solving Eq. (7.49) for $i = 2$, subject to the boundary condition (7.57), the solution for χ_2 can be obtained as

$$\begin{aligned} \chi_2 = & \alpha_5 \frac{I_0 \left(\sqrt{\frac{1}{\mu} (Ha^2 + \frac{\gamma_1}{Da})} r \right)}{I_0 \left(\sqrt{\frac{1}{\mu} (Ha^2 + \frac{\gamma_1}{Da})} \right)} - \alpha_5 \frac{I_{2M} \left(\sqrt{\frac{1}{\mu} (Ha^2 + \frac{\gamma_1}{Da})} r \right)}{I_{2M} \left(\sqrt{\frac{1}{\mu} (Ha^2 + \frac{\gamma_1}{Da})} \right)} \cos(2M\theta) \\ & + \sum_{m=0}^{\infty} \sum_{n=0}^{\infty} \left[\alpha_6 a_{mn} \frac{I_{\frac{n+1-2M}{2}} \left(\sqrt{\frac{1}{\mu} (Ha^2 + \frac{\gamma_1}{Da})} r \right)}{I_{\frac{n+1-2M}{2}} \left(\sqrt{\frac{1}{\mu} (Ha^2 + \frac{\gamma_1}{Da})} \right)} \cos \left(\frac{n+1-2M}{2} \theta \right) \right] \\ & - \sum_{m=0}^{\infty} \sum_{n=0}^{\infty} \left[\alpha_6 a_{mn} \frac{I_{\frac{n+1+2M}{2}} \left(\sqrt{\frac{1}{\mu} (Ha^2 + \frac{\gamma_1}{Da})} r \right)}{I_{\frac{n+1+2M}{2}} \left(\sqrt{\frac{1}{\mu} (Ha^2 + \frac{\gamma_1}{Da})} \right)} \cos \left(\frac{n+1+2M}{2} \theta \right) \right] \\ & + \sum_{m=0}^{\infty} \sum_{n=0}^{\infty} \left[A_{mn} \sin\{(m+1)\pi r\} \sin \left\{ \frac{(n+1)}{2} \theta \right\} \right], \end{aligned} \quad (7.58)$$

where

$$A_{mn} = \frac{-\frac{4HaS_0}{\mu} (Ha^2 + \frac{\gamma_1}{Da})}{2\pi \{ (m+1)^2 \pi^2 + \frac{(n+1)^2}{4} \}} \int_0^1 \int_0^{2\pi} \left[F_2(r, \theta) \sin\{(m+1)\pi r\} \sin \left\{ \frac{(n+1)}{2} \theta \right\} \right] dr d\theta,$$

$$F_2(r, \theta) = \left\{ -M(M + \frac{1}{2}) r^{-2M-1} \cos(2M\theta) - 2M\zeta \alpha_1 \frac{I_{2M}(\omega r)}{I_{2M}(\omega)} \sin(2M\theta) \right\}.$$

7.3.4 EMHD pumping rate

The EMHD pumping rate in a rough microtube under can be influenced by various factors, including the geometry of the tube, the applied electric field. For this case, the EMHD pumping rate can be expressed as

$$Q = \int_0^{1+\varepsilon \sin(M\theta)} u(r, \theta) r dr = \int_0^{1+\varepsilon \sin(M\theta)} \{u_0 + \varepsilon u_1 + \varepsilon^2 u_2 + \dots\} r dr. \quad (7.59)$$

We look for $Q = Q_0 + \varepsilon Q_1 + \varepsilon^2 Q_2 + \dots$. Let the microtube is smooth, i.e. $\varepsilon = 0$, then the zeroth order of EMHD pumping rate is obtained as

$$Q_0 = \int_0^1 u_0 r dr. \quad (7.60)$$

By utilizing Leibniz's theorem on Eq. (7.59), the ensuing expression can be derived as

$$\begin{aligned}\frac{dQ}{d\varepsilon} &= \frac{d}{d\varepsilon} \left[\int_0^{1+\varepsilon \sin(M\theta)} (u_0 + \varepsilon u_1 + \varepsilon^2 u_2 + \cdots) r dr \right] \\ &= \left[\int_0^{1+\varepsilon \sin(M\theta)} (u_1 + 2\varepsilon u_2 + \cdots) r dr \right. \\ &\quad \left. + \sin(M\theta)(u_0 + \varepsilon u_1 + \varepsilon^2 u_2 + \cdots) r \right]_{\text{at } r=1+\varepsilon \sin(M\theta)}.\end{aligned}\quad (7.61)$$

Again, let $\varepsilon = 0$, and one can easily obtain the first order of EMHD pumping rate from Eq. (7.61) as

$$Q_1 = \left[\int_0^1 u_1 r dr + \sin(M\theta) u_0(1) \right] = 0. \quad (7.62)$$

Similarly, by utilizing Leibniz's theorem on Eq. (7.61), the ensuing expression can be derived as

$$\begin{aligned}\frac{d^2 Q}{d\varepsilon^2} &= \frac{d}{d\varepsilon} \left[\int_0^{1+\varepsilon \sin(M\theta)} (u_1 + 2\varepsilon u_2 + \cdots) r dr \right. \\ &\quad \left. + \sin(M\theta)(u_0 + \varepsilon u_1 + \varepsilon^2 u_2 + \cdots) r \right]_{\text{at } r=1+\varepsilon \sin(M\theta)} \\ &= \left[\int_0^{1+\varepsilon \sin(M\theta)} (2u_2 + \cdots) r dr \right. \\ &\quad \left. + \sin(M\theta)(u_1 + 2\varepsilon u_2 + \cdots) r \right]_{\text{at } r=1+\varepsilon \sin(M\theta)} \\ &\quad \left. + \sin(M\theta)(u_1 + 2\varepsilon u_2 + \cdots) r \right]_{\text{at } r=1+\varepsilon \sin(M\theta)} \\ &= \left[\int_0^{1+\varepsilon \sin(M\theta)} (2u_2 + \cdots) r dr \right. \\ &\quad \left. + 2\sin(M\theta)(u_1 + 2\varepsilon u_2 + \cdots) r \right]_{\text{at } r=1+\varepsilon \sin(M\theta)}.\end{aligned}\quad (7.63)$$

Assuming $\varepsilon = 0$, the second-order EMHD pumping rate can be readily obtained from Eq. (7.63) as

$$Q_2 = 2 \left[\int_0^1 u_2 r dr + \sin(M\theta) u_1(1) \right]. \quad (7.64)$$

Hence, the EMHD pumping rate Q can be expanded as

$$\begin{aligned}
 Q &= Q_0 + \varepsilon Q_1 + \varepsilon^2 Q_2 + \dots \\
 &= \left[\int_0^1 u_0 r dr + 2\varepsilon^2 \left\{ \int_0^1 u_2 r dr + \sin(M\theta) u_1(1) \right\} \right] \\
 &= \left[\frac{Da}{(DaHa^2 + \gamma_1)\zeta} \left\{ \frac{1}{2}(P + HaS_0) + \frac{(DaHa^2 + \gamma_1)\zeta \omega I_1(\omega)}{\{\gamma_1 + Da(Ha^2 - \mu\omega^2)\}I_0(\omega)} \right. \right. \\
 &\quad \left. \left. - \frac{(\alpha_2 + P + HaS_0)I_1\left(\sqrt{\frac{1}{\mu}(Ha^2 + \frac{\gamma_1}{Da})}\right)}{I_0\left(\sqrt{\frac{1}{\mu}(Ha^2 + \frac{\gamma_1}{Da})}\right)} \right\} + \varepsilon^2 \left\{ 2 \int_0^1 u_2 r dr \right. \right. \\
 &\quad \left. \left. + \frac{2Da \sin^2(M\theta)}{(DaHa^2 + \gamma_1)\zeta} \left(\alpha_3 - \frac{(DaHa^2 + \gamma_1)\zeta \omega^3 I_1(\omega)}{\{\gamma_1 + Da(Ha^2 - \mu\omega^2)\}I_0(\omega)} \right) \right\} \right] \quad (7.65)
 \end{aligned}$$

Thus, the alteration in the EMHD pumping rate occurs at the second order of ε , which is a composite of two components. These components make the most significant contributions to the EMHD pumping rate in the presence of surface roughness. The first component emerges from the second order velocity, while the second component results from the interaction with the first order velocity component.

The mean pumping rate characterizes the average rate of fluid movement within a rough microtube. In this research, key factors influencing mean pumping behavior are the EMHD effect, microtube surface roughness, and the anisotropic permeability of the surrounding porous medium. To compute the mean pumping rate, integration of the volumetric flow rate is required, expressed as:

$$U_m = M \int_0^{2\pi/M} Q d\theta = U_{m0} \{1 - \varepsilon^2 \eta\}, \quad (7.66)$$

where

$$\begin{aligned}
 U_{m0} &= \frac{2\pi Da}{(DaHa^2 + \gamma_1)\zeta} \left\{ \frac{1}{2}(P + HaS_0) + \frac{(DaHa^2 + \gamma_1)\zeta \omega I_1(\omega)}{\{\gamma_1 + Da(Ha^2 - \mu\omega^2)\}I_0(\omega)} \right\} \\
 &\quad - \frac{2\pi Da(\alpha_2 + P + HaS_0)I_1\left(\sqrt{\frac{1}{\mu}(Ha^2 + \frac{\gamma_1}{Da})}\right)}{(DaHa^2 + \gamma_1)\zeta I_0\left(\sqrt{\frac{1}{\mu}(Ha^2 + \frac{\gamma_1}{Da})}\right)}, \quad \eta = \eta_1 + \eta_2, \\
 \eta_1 &= -\frac{2\pi Da}{U_{m0}(DaHa^2 + \gamma_1)\zeta} \left(\alpha_3 - \frac{(DaHa^2 + \gamma_1)\zeta \omega^3 I_1(\omega)}{\{\gamma_1 + Da(Ha^2 - \mu\omega^2)\}I_0(\omega)} \right), \\
 \eta_2 &= -\frac{2M}{U_{m0}} \int_0^{2\pi/M} \int_0^1 u_2 r dr d\theta.
 \end{aligned}$$

In this context, U_{m0} represents the mean pumping rate of EMHD flow in a smooth microtube, encompassing the Helmholtz-Smoluchowski rate. The symbol η signifies the net effect of the mean pumping rate attributed to the EMHD effect, particularly concerning second-order contributions in ε . Here, η can be divided into two components, denoted as η_1 and η_2 , which are primarily influenced by the EMHD effect and the anisotropic permeability of the porous medium. The mathematical expression for the mean pumping rate, considering the influence of the EMHD effect within an anisotropic porous medium, constitutes the main outcome of this study. The subsequent section is dedicated to providing a comprehensive interpretation of this result across various physical aspects.

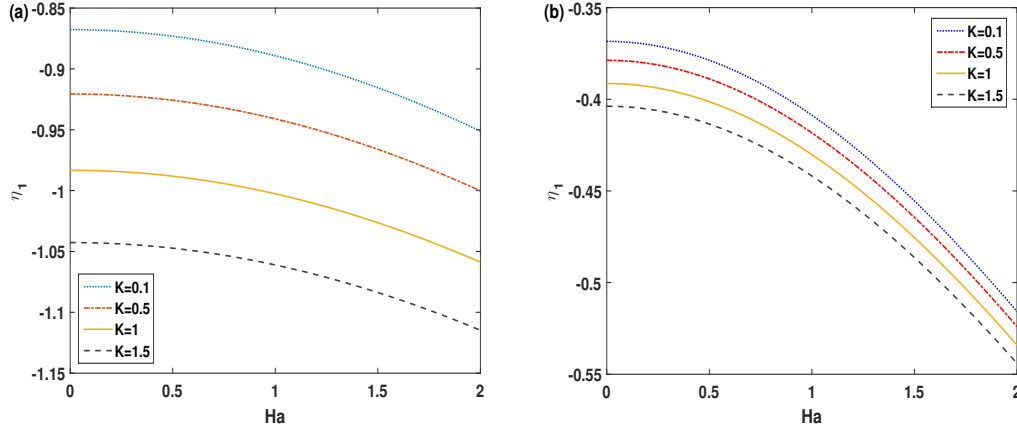


Figure 7.4: Plot for η_1 versus Ha in the absence of transverse electric field ($S = 0$) for two different Darcy number: (a) $Da = 0.04$ and (b) $Da = 0.4$ with $\omega = 10, M = 8, \zeta = 0.1, \mu = 0.5, P = 1, \varphi = \pi/3$.

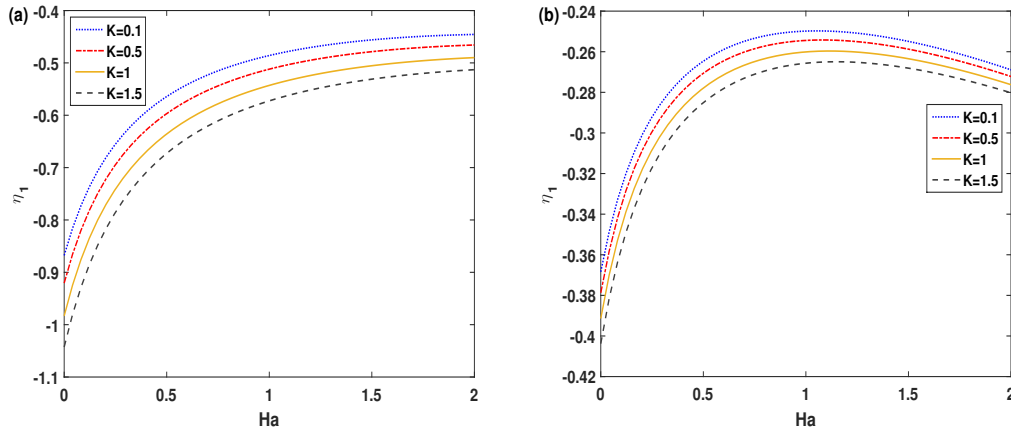


Figure 7.5: Plot for η_1 versus Ha in the presence of transverse electric field ($S = 5$) for two different Darcy number: (a) $Da = 0.04$ and (b) $Da = 0.4$ with $\omega = 10, M = 8, \zeta = 0.1, \mu = 0.5, P = 1, \varphi = \pi/3$.

7.4 Results and Discussions

7.4.1 Variability in η and its influence on EMHD pumping rate

This section explores the impact of anisotropic permeability ratio (K), anisotropic angle (φ), Darcy number (Da), wave numbers (M) and Hartmann number (Ha) on the net effect (η). Our analysis will commence by assessing how η_1 responds to variations in K , φ , Da , M and Ha , followed by an exploration of the impact of these parameters on η_2 .

It is evident from Figs. 7.4-7.7 that η_1 consistently maintains a negative value with small variations attributed to the external body forces and the resistance force due to the porous medium. It is important to note that we are examining two cases in this context: one involving the presence of a transverse electric field ($S = 5$) and the other in its absence ($S = 0$). For $S = 0$ and $Da = 0.04$, η_1 decreases with increasing Ha , with a more pronounced reduction for $Da = 0.4$, as depicted in Figs. 7.4(a)-7.4(b). The amplifying effect of anisotropic permeability ratio (K) results a reduction of η_1 for $S = 0$. However, when $S = 5$, a rapid enhancement is observed at the low Hartmann number and it is decreased for higher Darcy number ($Da = 0.4$) and $Ha > 1$ as shown in Figs. 7.5(a)-7.5(b). It is noteworthy that in this scenario, the transverse electric field component acts as a flow-aiding force on the EMHD velocity of the flow, leading to a minor alteration in η_1 for low permeable medium. This modification is primarily driven by the influence of the first-order velocity component on the flow behavior. A similar pattern emerges when examining the behavior of η_1 as we vary the anisotropic angle (φ), as depicted in Figs. 7.6 and 7.7. The most substantial alteration in η_1 occurs in scenarios involving low-permeability media at $\varphi = 0$. The parameter $\gamma_1 = K \cos^2 \varphi + \sin^2 \varphi$ governs the anisotropy of the porous medium. Consequently, when $\varphi = 0$, radial permeability is effectively non-existent. With an increase in φ , permeability in both horizontal and radial directions rises, resulting in a diminishing change in η_1 , as illustrated in Figs. 7.6 and 7.7. In short, a fascinating finding is that when η_1 varies more, the EMHD pumping rate increases. This connection exists because η_1 is mainly driven by the first-order velocity generated by the roughness of the microtube. The alteration in the EMHD pumping rate is influenced by both electromagnetic and resistance forces due to anisotropic permeability.

Figs. 7.8 and 7.9 illustrate the changes in η_2 as a function of the Hartmann number (Ha) under different values of K , considering both $S = 0$ and $S = 5$, respectively. For $S = 0$ and $Da = 0.04$, η_2 increases with rising Ha , exhibiting a more pronounced enhancement for $Da = 0.4$ and $Ha > 1$, as illustrated in Figs. 7.8(a)-7.8(b). The amplifying effect of anisotropic permeability ratio (K) results in an augmentation of η_2 for $S = 0$. However, an interesting observation emerges for $Da = 0.4$ with $Ha < 1$, where η_2 experiences a reduction, as depicted in Fig. 7.8(b). It is noteworthy that η_2 have more sophisticated dependence on Da , K and S . In the presence of a transverse electric field ($S = 5$), Figs. 7.9(a) and 7.9(b) reveal that η_2 decreases with the increasing Hartmann number. This decrease is more rapid for $Da = 0.4$, suggesting a distinct response to the transverse electric field. Additionally, the increment of anisotropic permeability ratio (K) enhances η_2 for low Darcy number ($Da = 0.04$), while for higher Darcy number ($Da = 0.4$), it leads to a decrease in η_2 . The changes in η_2 are more pronounced for low Darcy number compared to higher Darcy number in

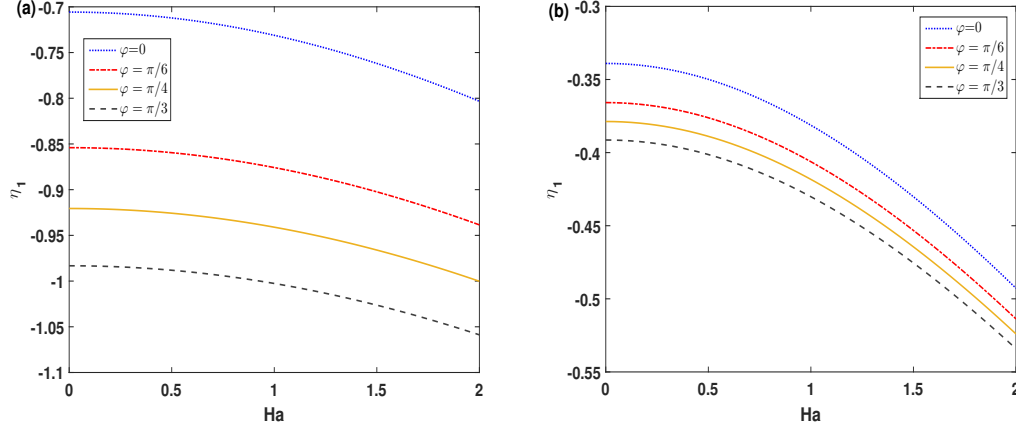


Figure 7.6: Plot for η_1 versus Ha in the absence of transverse electric field ($S = 0$) for two different Darcy number: (a) $Da = 0.04$ and (b) $Da = 0.4$ with $\omega = 10, M = 8, \zeta = 0.1, K = 0.5, \mu = 0.5, P = 1$.

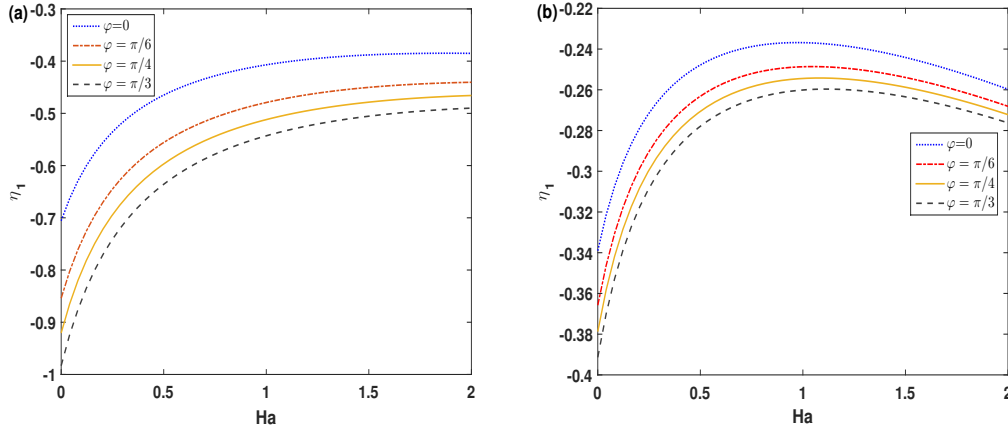


Figure 7.7: Plot for η_1 versus Ha in the presence of transverse electric field ($S = 5$) for two different Darcy number: (a) $Da = 0.04$ and (b) $Da = 0.4$ with $\omega = 10, M = 8, \zeta = 0.1, K = 0.5, \mu = 0.5, P = 1$.

7.4. Results and Discussions

both cases, with or without the presence of a transverse electric field. This indicates that a low Darcy number corresponds to a higher resistance force, resulting in slower flow due to the porosity of the microtube. On the other hand, a high Darcy number implies a more permeable medium, leading to lower resistance forces and influencing faster flow within the porous medium. Consequently, in the presence of a transverse electric field ($S \neq 0$), the variation in η_2 is more significant for $K > 1$ and $Ha < 1$ with a low permeable medium. In the absence of a transverse electric field ($S = 0$), the variation in η_2 is more notable for $K > 1$ and $Ha > 1$ with a low permeable medium.

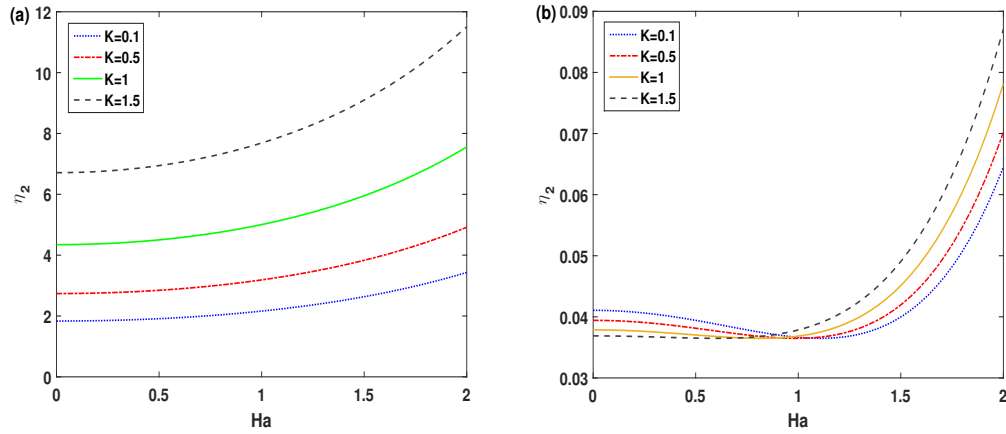


Figure 7.8: Plot of η_2 as a function of Ha in the absence of a transverse electric field ($S = 0$) for two different values of Darcy number: (a) $Da = 0.04$ and (b) $Da = 0.4$. The other parameter values used for these simulations are $\omega = 10, M = 8, \zeta = 0.1, \mu = 0.5, P = 1, \varphi = \pi/3$.

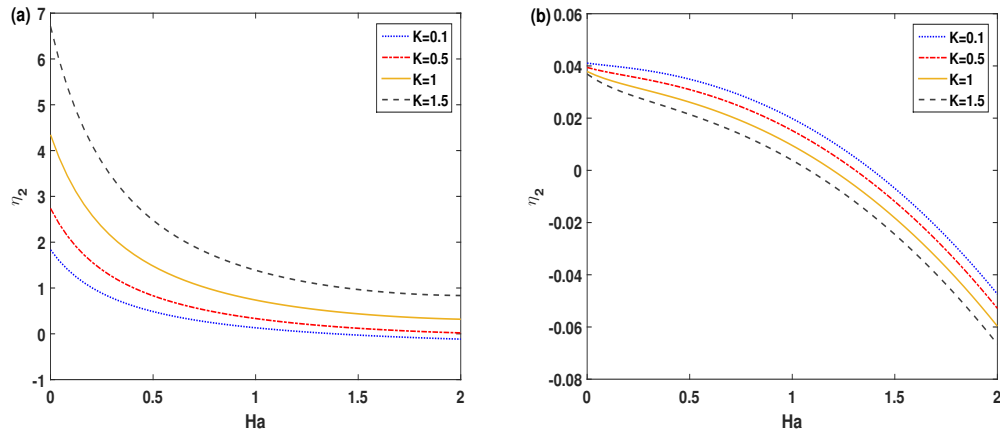


Figure 7.9: Plot of η_2 as a function of Ha in the presence of a transverse electric field ($S = 5$) for two different values of Darcy number: (a) $Da = 0.04$ and (b) $Da = 0.4$. The other parameter values used for these simulations are $\omega = 10, M = 8, \zeta = 0.1, \mu = 0.5, P = 1, \varphi = \pi/3$.

A similar pattern emerges when examining the behavior of η_2 as we vary the anisotropic angle (φ), as depicted in Figs. 7.10 and 7.11. The most substantial alteration in η_2 occurs in scenarios

involving low-permeability media at $\varphi = 0$. The parameter $\gamma_1 = K \cos^2 \varphi + \sin^2 \varphi$ governs the anisotropy of the porous medium. Consequently, when $\varphi = 0$, radial permeability is effectively non-existent. With an increase in φ , permeability in both horizontal and radial directions rises, resulting in an enhancing change in η_2 for low Darcy number $Da = 0.04$, as illustrated in Fig. 7.10(a). However, it has a diminishing change for $Ha < 1$ and a rapid increment for $Ha > 1$, as illustrated in Fig. 7.10(b). In the presence of a transverse electric field, almost similar phenomena occur, which is delineated in Figs. 7.11(a)-7.11(b). From both figures, it is clear that the changes of η_2 are minimum for $\varphi = 0$, at a low Darcy number $Da = 0.04$, but it is maximum for $\varphi = 0$, at a large Darcy number $Da = 0.4$ with $Ha < 1$.

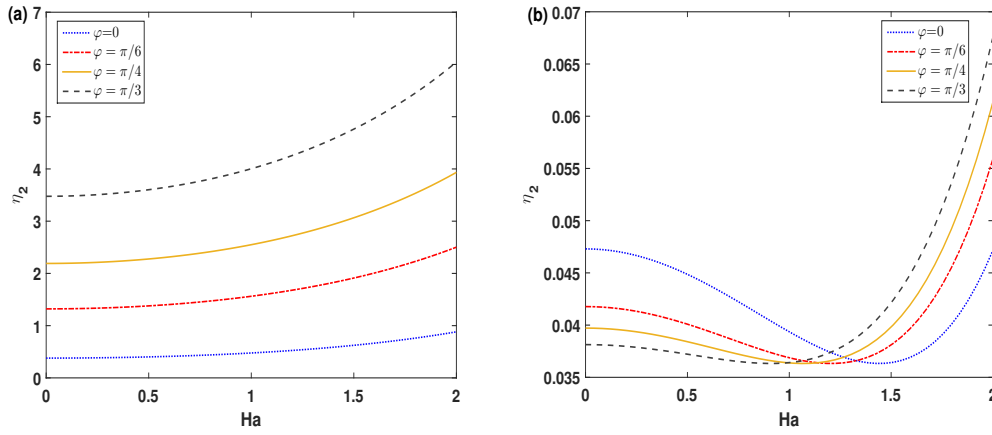


Figure 7.10: Plot of η_2 as a function of Ha in the absence of a transverse electric field ($S = 0$) for two different values of Darcy number: (a) $Da = 0.04$ and (b) $Da = 0.4$. The other parameter values used for these simulations are $\omega = 10, M = 8, \zeta = 0.1, K = 0.5, \mu = 0.5, P = 1$.

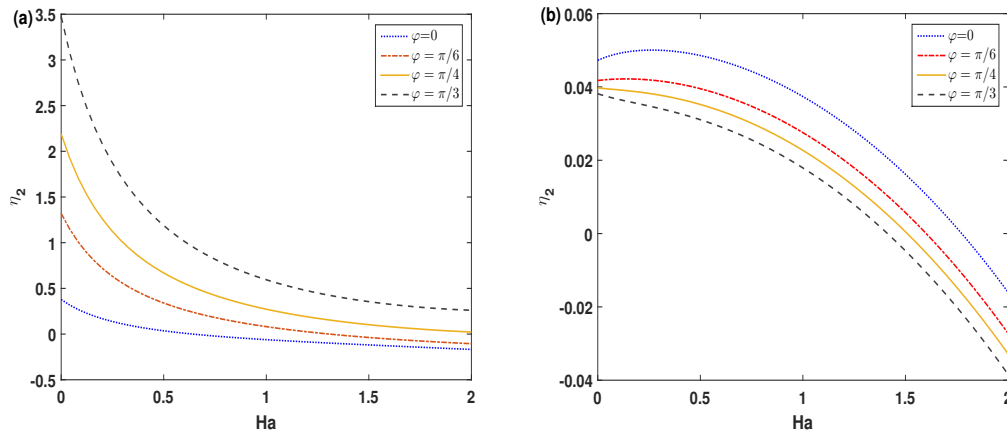


Figure 7.11: Plot of η_2 as a function of Ha in the presence of a transverse electric field ($S = 5$) for two different values of Darcy number: (a) $Da = 0.04$ and (b) $Da = 0.4$. The other parameter values used for these simulations are $\omega = 10, M = 8, \zeta = 0.1, K = 0.5, \mu = 0.5, P = 1$.

In short, a fascinating finding is that when η_2 varies more, the EMHD pumping rate increases. This connection exists because η_2 is mainly driven by the second-order velocity generated by the roughness of the microtube. The alteration in the EMHD pumping rate is influenced by both electromagnetic and resistance forces due to anisotropic permeability. Here permeability is varying with an anisotropic angle (φ), which affects the change in η_2 , as well as the pumping rate. It can be clear that the pumping rate is enhancing in the absence of a transverse electric field ($S = 0$) with less resistance force due to the porous medium ($Da = 0.4$).

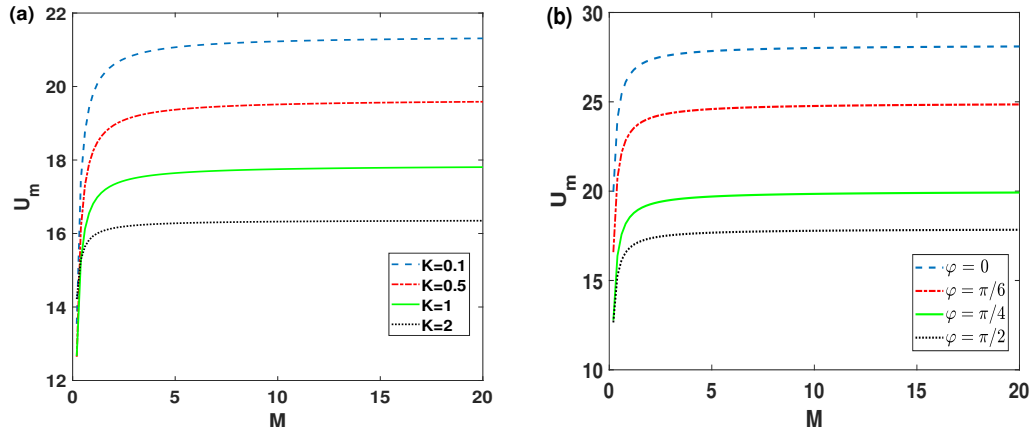


Figure 7.12: Plot of U_m as a function of M for different values of (a) anisotropic permeability ratio (K) and (b) anisotropic angle (φ). The other parameter values used for these simulations are $\omega = 10$, $M = 8$, $\zeta = 0.1$, $S = 5$, $\mu = 0.5$, $P = 1$, $\varepsilon = 0.02$.

The mean pumping rate (U_m) shows a slight influence from the number of corrugations (M), as depicted in Fig. 7.12. However, it exhibits a diminishing trend with increasing permeability ratio (K) and anisotropic angle (φ), as illustrated in Fig. 7.12(a) and 7.12(b) respectively. Fig. 7.12(a) highlights the significant role played by the permeability along the radial direction (K_α) and the axial direction (K_γ) in determining the mean pumping rate of the flow. An increase in the anisotropic permeability ratio leads to greater resistance force from the porous medium along both the radial and axial directions of the microtube, resulting in a reduction in the mean velocity of the flow. Furthermore, it is noteworthy that the pumping rate attains its maximal value at low levels of porous medium. This behavior suggests that as the influence of porous medium increases, the flow experiences greater resistance, leading to a decrease in the mean pumping rate. Fig. 7.12(b) demonstrates a similar trend for the increasing anisotropic angle (φ). Notably, the pumping rate peaks at $\varphi = 0$. This occurrence is rooted in the condition $\gamma_1 = K$ associated with $\varphi = 0$, indicating the absence of permeability along the axial direction and a constant permeability along this direction. Consequently, the pumping rate reaches its maximum compared to other angles, as depicted in Fig. 7.12(b). As the anisotropic angle increases, both the permeability along the radial and axial directions become active. This heightened permeability leads to increased resistance within the flow, consequently reducing the pumping rate. This trend underscores the significance of considering the directional permeability in microfluidic systems, as even slight changes in the anisotropic angle can

significantly impact flow dynamics and pumping efficiency.

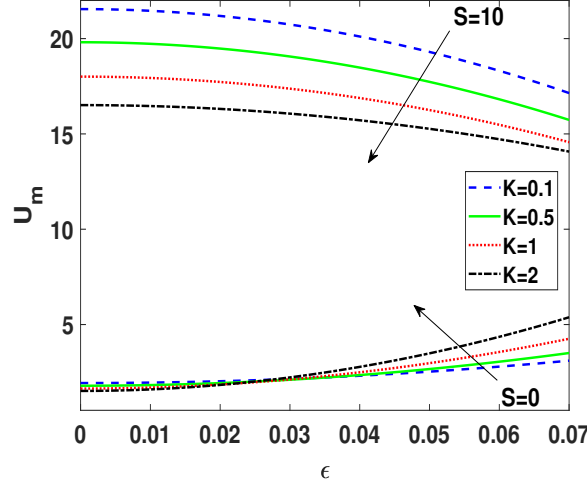


Figure 7.13: Plot of U_m as a function of ϵ for $\omega = 10$, $M = 8$, $\zeta = 0.1$, $K = 0.5$, $\varphi = \pi/4$, $\mu = 0.5$, $P = 1$.

The influence of surface roughness (ϵ) on the mean pumping rate (U_m) is illustrated in Fig. 7.13. An increase in roughness amplitude (ϵ) enhances the mean flow rate for $S = 0$, but this enhancement is diminished for $S = 10$. In the absence of a transverse electric field ($S = 0$), surface roughness can modify the boundary layer near the microtube wall, reducing its thickness and increasing the pumping rate. However, in the presence of a transverse electric field ($S = 10$) reduces the pumping rate. Additionally, an increase in the anisotropic permeability ratio reduces the pumping rate, as the permeability along the axial and radial directions acts as a resistance force. This trend also holds for low roughness amplitudes in the absence of transverse electric field ($S = 0$). However, for $\epsilon > 0.03$, (Fig. 7.13) an interesting phenomenon occurs: the interaction between the permeability along both radial and axial directions and the roughness of the microtube actually enhances the mean pumping rate for $S = 0$.

The anisotropic permeability of the porous medium and surface roughness significantly influence the EMHD pumping rate, as discussed previously. To illustrate this, we compare the EMHD pumping rates in a smooth microtube ($\epsilon = 0$) and a rough microtube ($\epsilon = 0.02$), as summarized in Table-7.1 and Table-7.2. From the tables, we can visualize the comparison between the EMHD pumping rates in a rough microtube ($\epsilon = 0.02$) and a smooth microtube ($\epsilon = 0$). Here, U_m and U_{m0} represent the mean EMHD pumping rates for the rough and smooth microtubes respectively. The tables include the calculation for M_R , which assesses the modification of the EMHD pumping rate due to surface roughness and is given by $\{(U_m - U_{m0})/U_{m0}\} \times 100$. Table 7.1 provides a detailed comparison of the EMHD pumping rates in both rough ($\epsilon = 0.02$) and smooth ($\epsilon = 0$) microtubes across various anisotropic permeability ratios ($K = 0.1, 0.5, 1, 1.5$), considering a fixed anisotropic angle ($\varphi = \pi/3$). The table shows that for a low Darcy number $Da = 0.04$, the rough microtube exhibits a slight increase in the pumping rate compared to the smooth microtube across

Table 7.1: Comparison between EMHD pumping rate in the rough microtube ($\varepsilon = 0.02$) and the smooth microtube ($\varepsilon = 0$) across different anisotropic permeability ratio ($K = 0.1, 0.5, 1, 1.5$) and $M = 8$, $\zeta = 0.1$, $\omega = 10$, $Ha = 0.25$, $\mu = 0.5$, $P = 1$, $S = 5$, $\varphi = \pi/3$. Here U_m and U_{m0} represent the respective mean EMHD pumping rates respectively. $\mathbf{M_R}$ assesses how much the surface roughness of the microtube modifies the EMHD pumping rate and is determined by $\mathbf{M_R} = \{(U_m - U_{m0})/U_{m0}\} \times 100$. It is crucial to understand that corresponds to an enhancement in the EMHD pumping rate, while a negative value signifies a reduction.

	K	U_{m0}	U_m	$\mathbf{M_R}$
$Da = 0.04$	0.1	3.6379	3.6992	0.0168%
	0.5	3.1356	3.4705	0.0467%
	1	2.9891	3.2742	0.0954%
	1.5	2.7245	3.1643	0.1614%
$Da = 0.4$	0.1	14.0067	13.0127	-0.0710%
	0.5	13.3847	12.4389	-0.0707%
	1	12.6857	11.7947	-0.0702%
	1.5	12.0608	11.2193	-0.0698%

all anisotropic permeability ratios. For instance, at $K = 0.5$, the pumping rate increases by approximately 0.0467%. This indicates that surface roughness can have a minor enhancing effect on pumping performance under these conditions. Conversely, at a higher Darcy number $Da = 0.4$, the rough microtube shows a slight decrease in the pumping rate compared to the smooth microtube across all anisotropic permeability ratios. For example, at $K = 1.5$, the pumping rate decreases by approximately 0.0698%. This suggests that at higher Darcy numbers, the influence of surface roughness on pumping performance becomes slightly detrimental.

Table 7.2 compares the EMHD pumping rates in a rough microtube ($\varepsilon = 0.02$) with those in a smooth microtube ($\varepsilon = 0$) across different anisotropic angles ($\varphi = 0, \pi/6, \pi/4, \pi/3, \pi/2$) with a fixed anisotropic permeability ratio $K = 0.5$. For $Da = 0.04$ with different anisotropic angle φ , the M_R values range from -0.0372% to 0.0954%, indicating slight variations in the pumping rate due to surface roughness. Similarly, for $Da = 0.4$ with different anisotropic angle φ , the M_R values range from -0.0717% to -0.0702%, indicating minimal impact of surface roughness on the pumping rate. These findings suggest that surface roughness has a noticeable impact on the EMHD pumping rate in microtubes, with the effect varying depending on the anisotropic angle and low Darcy number. Within the given large value of Darcy number, the surface roughness of the microtube has a negligible effect on the EMHD pumping rate compared to low Darcy number case.

7.4.2 Flow reversal and bolus formation: surface roughness and anisotropic permeability perspectives

The velocity contours for different roughness amplitudes (ε) in Fig. 7.14 provide important insights into the flow behavior in a microtube. For a smooth microtube ($\varepsilon = 0$) shown in Fig. 7.14(a), there

Table 7.2: Comparison between EMHD pumping rate in the rough microtube ($\varepsilon = 0.02$) and the smooth microtube ($\varepsilon = 0$) across different anisotropic angle ($\varphi = 0, \pi/6, \pi/4, \pi/3, \pi/2$) and $M = 8$, $\zeta = 0.1$, $\omega = 10$, $Ha = 0.25$, $\mu = 0.5$, $P = 1$, $S = 5$, $K = 0.5$. Here U_m and U_{m0} represent the respective mean EMHD pumping rates respectively. $\mathbf{M_R}$ assesses how much the surface roughness of the microtube modifies the EMHD pumping rate and is determined by $\mathbf{M_R} = \{(U_m - U_{m0})/U_{m0}\} \times 100$. It is crucial to understand that corresponds to an enhancement in the EMHD pumping rate, while a negative value signifies a reduction.

	φ	U_{m0}	U_m	$\mathbf{M_R}$
$Da = 0.04$	0	5.0206	4.8338	-0.0372%
	$\pi/6$	4.2725	4.2004	-0.0169%
	$\pi/4$	3.7293	3.7680	0.0104%
	$\pi/3$	3.3156	3.4705	0.0467%
	$\pi/2$	2.9891	3.2742	0.0954%
$Da = 0.4$	0	16.0903	14.9373	-0.0717%
	$\pi/6$	15.0661	13.9907	-0.0714%
	$\pi/4$	14.1721	13.1652	-0.0710%
	$\pi/3$	13.3847	12.4389	-0.0707%
	$\pi/2$	12.6857	11.7947	-0.0702%

are no disturbances in the velocity contour. Near the wall, the velocity is minimal due to the no-slip condition, and the flow is not fully developed due to the presence of the porous medium, which introduces resistance and slows down the flow. As surface roughness is introduced (Fig. 7.14(b)-7.14(d)), the flow pattern becomes more complex, and reverse flow occurs due to the presence of roughness. The presence of roughness elements disrupts the flow, leading to the formation of eddies and vortices. These disturbances are more pronounced as the roughness amplitude increases, as seen in Fig. 7.14(c) and 7.14(d). The roughness elements create regions of low velocity and high velocity gradients near the walls, contributing to increased mixing in microfluidic systems. The formation of boluses or recirculation zones near the boundary layers, particularly evident in Fig. 7.14(c) and 7.14(d), further demonstrates the influence of surface roughness on flow dynamics. These boluses result from the interaction between the roughness elements and the flow, leading to localized regions of reversed or stagnant flow. The number and size of these boluses are influenced by the number of corrugations (M) on the microtube surface.

The impact of anisotropic permeability ratio (K) on the velocity contours, as shown in Fig. 7.15, reveals intricate flow behavior in microtubes. The influence of anisotropic permeability introduces varying resistance forces along the radial and axial directions of the microtube, significantly affecting flow velocity. As discussed earlier in Fig. 7.14, the presence of surface roughness induces recirculation zones near the boundary layers and the formation of boluses. However, Fig. 7.15(a)-7.15(d) highlights that the pattern of these boluses is altered by the anisotropic permeability ratio (K). The increase in anisotropic permeability ratio (K) leads to a more complex flow pattern, characterized by the formation of numerous small boluses for $K = 5$ in Fig. 7.15(d). This phenomenon

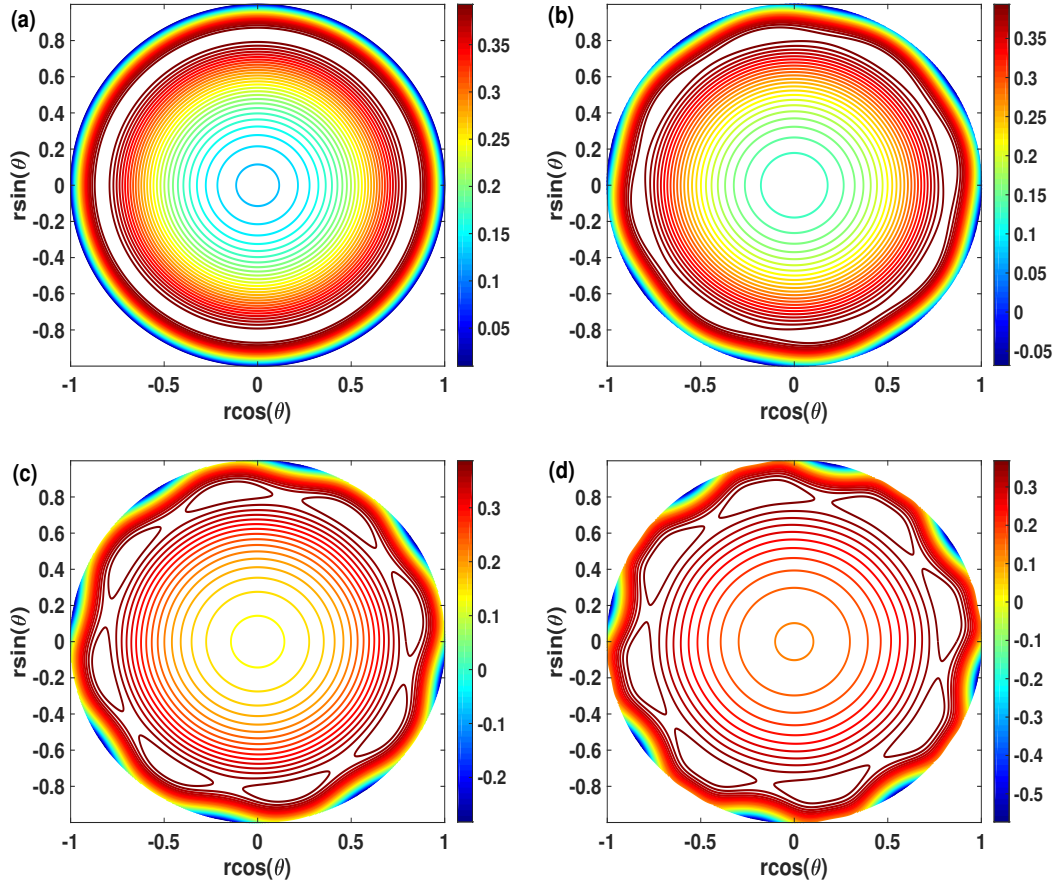


Figure 7.14: Velocity contours for different ε for $Ha = 0.5, S = 5, Da = 0.03, \omega = 10, M = 8, \zeta = 0.1, \mu = 1, P = 1, K = 0.5, \varphi = \pi/4$. (a) $\varepsilon = 0.0$, (b) $\varepsilon = 0.01$, (c) $\varepsilon = 0.03$, (d) $\varepsilon = 0.05$.

occurs because higher anisotropic permeability introduces uneven resistance forces, causing the flow to break up into smaller eddies and boluses.

7.4.3 Radial Pressure gradient

The radial pressure gradient is a critical parameter as it directly influences flow behavior and efficiency of the rough microtube with anisotropic porous medium. Understanding the factors that contribute to the radial pressure gradient, such as surface roughness and anisotropic permeability, is crucial for optimizing the design and performance of microfluidic devices. This parameter plays a significant role in determining the overall pressure requirements. The pressure gradient along the radial direction can be expressed in a dimensionless form as follows, using Eq. (7.8):

$$-Re \frac{\partial p}{\partial r} = \frac{\gamma}{Da} u, \quad (7.67)$$

where $Re = \frac{\rho_f u_{HS} R}{\mu_f}$ is called the Reynolds number.

By integrating along with the range of $r \in [0, 1 + \varepsilon \sin(M\theta)]$ and $\theta \in [0, 2\pi/M]$, one can easily

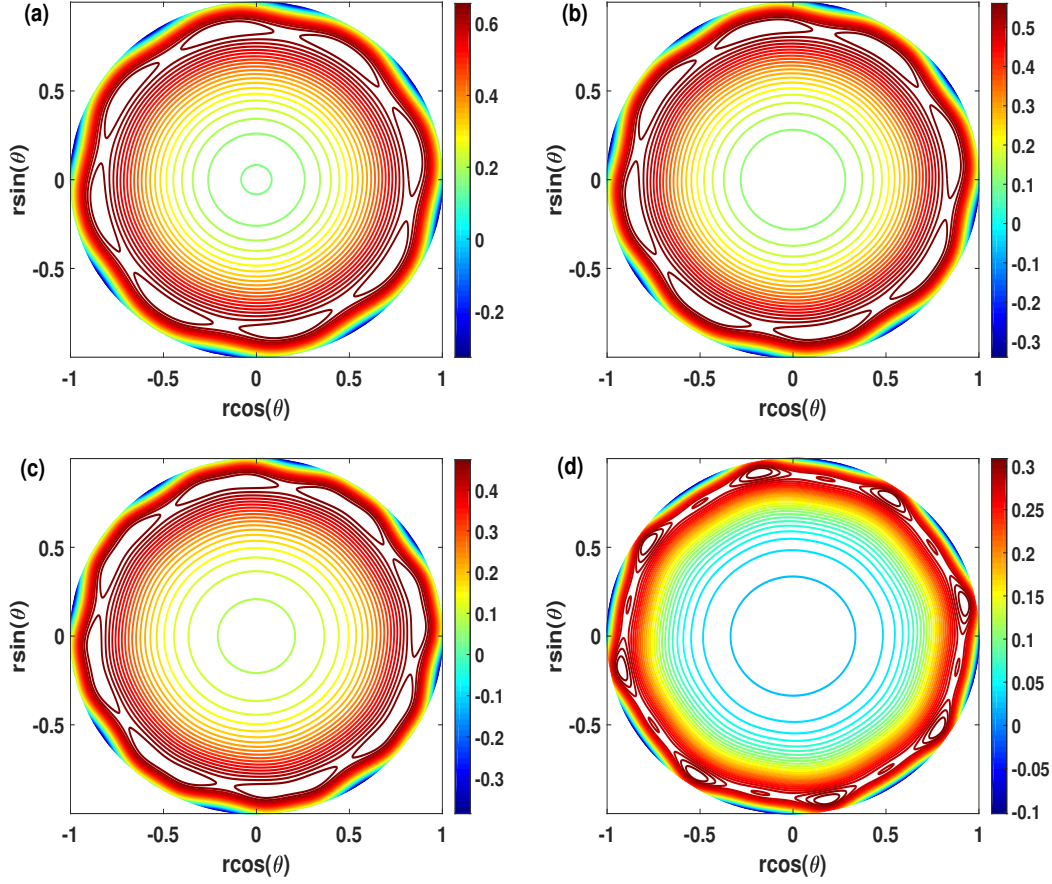


Figure 7.15: Velocity contour plots for different K for $\varepsilon = 0.02$, $S = 5$, $Da = 0.03$, $\omega = 10$, $M = 8$, $\zeta = 0.1$, $\mu = 0.5$, $P = 1$, $\varphi = \pi/3$. (a) $K = 0.1$, (b) $K = 0.5$, (c) $K = 1$, (d) $K = 5$.

calculate the average pressure distribution along the radial direction, which can be obtained as

$$\Delta p = - \int_0^{1+\varepsilon \sin(M\theta)} \int_0^{2\pi/M} \frac{\partial p}{\partial r} dr d\theta = \frac{\gamma_2}{ReDa} \int_0^{1+\varepsilon \sin(M\theta)} \int_0^{2\pi/M} u dr d\theta. \quad (7.68)$$

The radial pressure gradient Δp is illustrated in Figs. 7.16(a)-7.16(c), showing variations in the anisotropic permeability ratio (K), Darcy number (Da), and Hartmann number (Ha) respectively. In Fig. 7.16(a), it is observed that the radial pressure gradient decreases with an increase in the anisotropic permeability ratio for $K < 1$. However, the opposite trend is observed for $K > 1$. This behavior can be attributed to the impact of anisotropic permeability on flow resistance. For $K = 1$, which implies that $\gamma_2 = 0$, the porous medium becomes isotropic and the radial pressure gradient is zero. This indicates that the pressure is constant along the radial direction for an isotropic porous medium. Specifically, when $K < 1$, the flow experiences greater resistance along the radial direction, leading to a decrease in the pressure gradient. Conversely, for $K > 1$, the increased permeability along the radial direction reduces resistance, resulting in an increase in the pressure gradient. The reduction in the radial pressure gradient with an increase in the Darcy number can

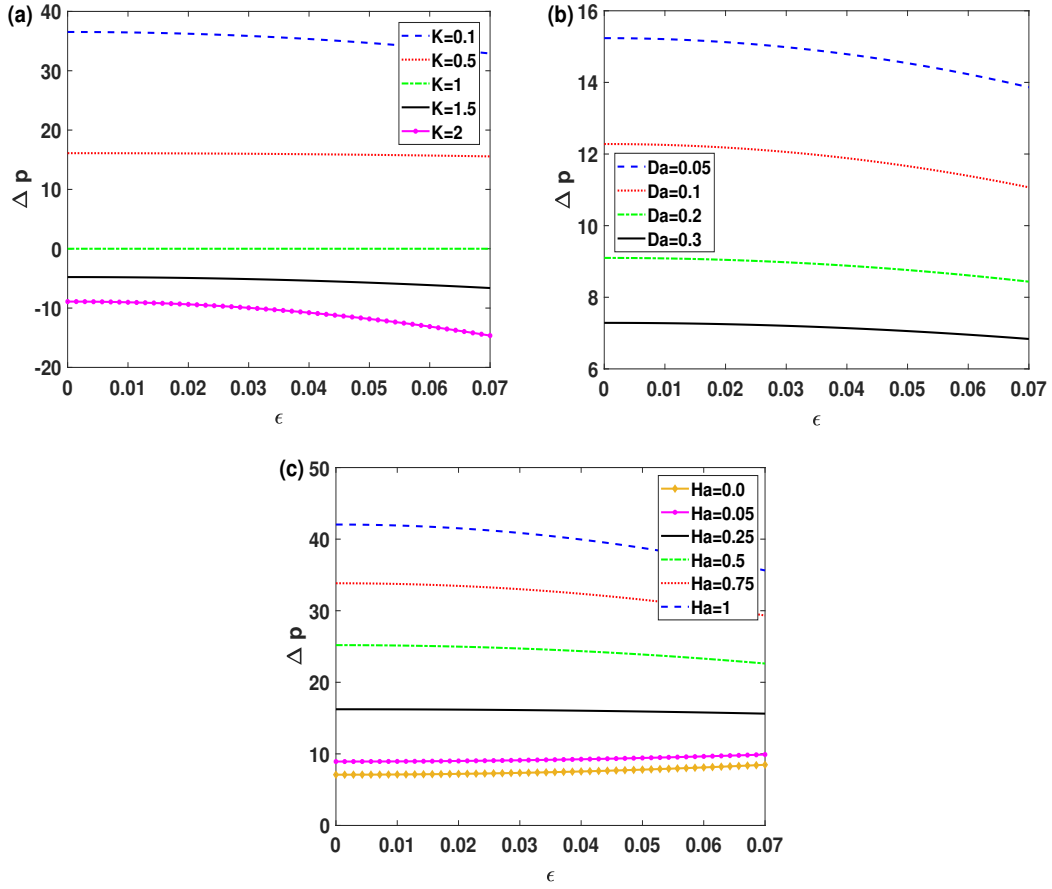


Figure 7.16: Pressure distribution along radial direction for different (a) anisotropic permeability ratio (K), (b) Darcy number (Da), (c) Hartmann number (Ha), where the other parameters are $S = 5$, $\omega = 10$, $M = 8$, $\zeta = 0.1$, $\mu = 0.5$, $P = 1$, $\varphi = \pi/3$.

be attributed to the nature of the Darcy velocity, which is delineated in Fig. 7.16(b). As the Darcy number increases, the Darcy velocity increases, indicating that the flow is less affected by the resistance of the porous medium. This means that a higher Darcy number corresponds to a more open and less restrictive flow path through the porous medium, leading to a reduced pressure gradient along the radial direction. The increase in the Hartmann number (Ha) corresponds to an increase in the radial pressure gradient, as shown in Fig. 7.16(c). This phenomenon is attributed to the presence of a magnetic field, which creates a retarding force known as the Lorentz force. The Lorentz force acts on the fluid, inducing resistance to its flow. As a result, the fluid encounters greater difficulty in moving along the radial direction within the microtube. Consequently, this increased resistance leads to a higher pressure gradient along the radial direction, as the fluid must overcome greater forces to flow through the microtube.

The decrease in the pressure gradient along the radial direction with the enhancement of microtube roughness, as observed in Fig. 7.16, is primarily due to the increased surface area and roughness-induced disruptions in the flow, leading to higher frictional losses and a reduction in the

overall pressure gradient. However, for low Hartmann numbers $Ha < 0.5$ (Fig. 7.16(c)), the effect of the magnetic field becomes more pronounced. The magnetic field interacts with the electric current induced by the flow, resulting in a Lorentz force that acts to reduce the effective resistance to flow, particularly in smoother tubes. This effect can counterbalance the increase in resistance caused by surface roughness, leading to a less significant decrease in the pressure gradient for low Hartmann numbers compared to higher values.

7.4.4 Wall shear stress distribution

At this point, it would be beneficial to derive the analytical expression for the dimensionless wall shear stress. From the Eq. (7.17), one can write the local dimensionless shear stress $\tau = \mu \frac{\partial u}{\partial r}$, the local dimensionless wall shear stress τ_w can be expressed as follows:

$$\begin{aligned} \tau_w = \tau \Big|_{r=1+\varepsilon \sin(M\theta)} &= \tau \Big|_{r=1} + \varepsilon \sin(M\theta) \frac{\partial \tau}{\partial r} \Big|_{r=1} + \frac{\varepsilon^2 \sin^2(M\theta)}{2} \frac{\partial^2 \tau}{\partial r^2} \Big|_{r=1} \\ &= \mu \left[\frac{\partial u_0}{\partial r} + \varepsilon \left\{ \frac{\partial u_1}{\partial r} + \sin(M\theta) \frac{\partial^2 u_0}{\partial r^2} \right\} \right. \\ &\quad \left. + \varepsilon^2 \left\{ \frac{\partial u_2}{\partial r} + \sin(M\theta) \frac{\partial^2 u_1}{\partial r^2} + \frac{\sin^2(M\theta)}{2} \frac{\partial^3 u_0}{\partial r^3} \right\} \right] \Big|_{r=1}. \end{aligned} \quad (7.69)$$

The average wall shear stress (τ_{avg}) along the element domain $0 \leq \theta \leq 2\pi/M$ can be obtained as

$$\tau_{avg} = \frac{2M}{\mathcal{P}} \int_0^{2\pi/M} \tau_w d\theta, \quad (7.70)$$

where \mathcal{P} is the average circumference of the rough microtube, which can be expressed as

$$\mathcal{P} = \int_{circumference} \sqrt{r_w^2 + dr_w^2} = M \int_0^{2\pi/M} \sqrt{r_w^2 + \frac{dr_w^2}{d\theta}} d\theta. \quad (7.71)$$

For the small value of ε , one can easily get the approximate expression for \mathcal{P} , which is as follows

$$\mathcal{P} \approx \frac{\pi}{32} (64 + 16M^2\varepsilon^2 + 4M^2\varepsilon^4 - 3M^4\varepsilon^4). \quad (7.72)$$

By using Eqs. (7.70) and (7.72), the average friction factor can be calculated from the relation $f = \tilde{\tau}_{avg} / (\frac{1}{2}\rho_f u_{HS}^2)$ as (Song et al. [2018])

$$fRe = \frac{128M}{\pi(64 + 16M^2\varepsilon^2 + 4M^2\varepsilon^4 - 3M^4\varepsilon^4)} \int_0^{2\pi/M} \tau_w d\theta. \quad (7.73)$$

Alternatively, when the microtube is smooth ($\varepsilon = 0$), the friction factor can be determined as follows:

$$(fRe)_{sm} = \frac{2\mu M}{\pi} \left\{ \frac{Da\omega^3 I_1(\omega)}{\{\gamma_1 + Da(Ha^2 - \mu\omega^2)\}I_0(\omega)} - \frac{(\alpha_2 + P + HaS_0)I_1\left(\sqrt{\frac{1}{\mu}(Ha^2 + \frac{\gamma_1}{Da})}\right)}{\zeta\mu\sqrt{\frac{1}{\mu}(Ha^2 + \frac{\gamma_1}{Da})}I_0\left(\sqrt{\frac{1}{\mu}(Ha^2 + \frac{\gamma_1}{Da})}\right)} \right\}. \quad (7.74)$$

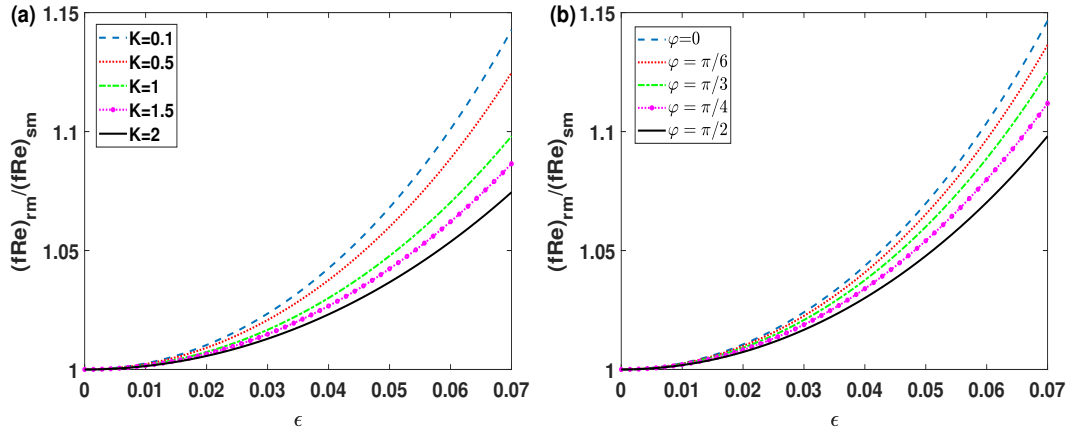


Figure 7.17: Friction factor for different (a) anisotropic permeability ratio (K) and (b) anisotropic angle (φ), where the other parameters are $S = 5$, $\omega = 10$, $M = 8$, $Ha = 1$, $Da = 0.03$, $\zeta = 0.1$, $\mu = 0.5$, $P = 1$, $\varphi = \pi/3$.

The increase in roughness enhances the friction factor ratio $(fRe)_{rm}/(fRe)_{sm}$ between a rough microtube and a smooth microtube due to the increased surface area and irregularities of the rough surface, as shown in Fig. 7.17. This roughness disrupts the flow, creating eddies and vortices, which increase the frictional resistance of the fluid flow. Additionally, the roughness elements create regions of low velocity and high velocity gradients near the walls, leading to increased viscous losses and, consequently, a higher friction factor compared to a smooth microtube. The increment of anisotropic permeability ratio (K) reduces the friction factor ratio, as displayed in Fig. 7.17(a), due to the nature of flow resistance in porous media. Anisotropic permeability introduces varying resistance forces along the radial and axial directions of the microtube, affecting the flow dynamics. When the anisotropic permeability ratio is increased, the resistance to flow along both directions also increases. This increased resistance leads to higher frictional losses, resulting in a lower friction factor ratio compared to scenarios with lower anisotropic permeability ratios. The increment of the anisotropic angle (φ) reduces the friction factor ratio, as displayed in Fig. 7.17(b), due to changes in the flow patterns induced by the anisotropic angle. When φ is increased, the permeability along the radial and axial directions becomes more different, leading to a more anisotropic flow. This altered flow pattern introduces additional resistance forces, increasing the overall frictional losses and reducing the friction factor ratio. For $\varphi = 0$, the friction factor is maximum because the porous medium becomes isotropic, meaning that the permeability is the same in all directions.

In this scenario, the flow encounters uniform resistance along both the radial and axial directions, leading to higher overall resistance and a higher friction factor compared to situations where the permeability is anisotropic.

7.5 Conclusions

This chapter presents a theoretical analysis of electromagnetohydrodynamic (EMHD) pumping in a fluid-saturated anisotropic porous microtube with a rough surface. The effects of roughness amplitude (ϵ) and azimuthal wave number (M) are investigated under the influence of an applied magnetic field and anisotropic porous medium. The analysis, which considers the Debye-Huckel approximation for the electric double layer (EDL) potential and viscous flow for the EMHD pumping, is conducted up to second order in ϵ . The main result of the study is a second-order expression describing the impact of surface roughness on the EMHD pumping rate. The analysis highlights the significant role played by the geometrical roughness (ϵ) and anisotropic permeability ratio (K) in determining the pumping rate. The study concludes with key findings, emphasizing that the second-order effect of surface roughness on the EMHD pumping rate depends on parameters such as K , ϕ , ϵ , and Ha . The analysis is limited to $\epsilon \leq 0.1$, and the main results are summarized below.

The impact of corrugations on the mean pumping rate in a microtube is slight, suggesting that while corrugations may influence flow dynamics to some extent, their effect on overall pumping efficiency is relatively minor compared to other factors such as permeability ratio and anisotropic angle.

The impact of the anisotropic ratio and angle is more pronounced, as an increase in the anisotropic permeability ratio leads to greater resistance force from the porous medium along both the radial and axial directions of the microtube. This results in a reduction in the mean velocity of the flow and, consequently, a decrease in the mean pumping rate. Similarly, as the anisotropic angle increases, both the permeability along the radial and axial directions become active, leading to increased resistance within the flow and a reduction in the pumping rate.

Surface roughness in microtubes alters flow behavior, creating vortices that enhance mixing. It increases velocity gradients near walls, promoting reverse flow and bolus formation. The number and size of boluses depend on the roughness amplitude and the number of corrugations on the microtube surface.

Anisotropic permeability ratio significantly influences the flow patterns in microtubes, introducing varying resistance forces along different directions. The combination of surface roughness and anisotropic permeability leads to complex flow patterns, including the formation of smaller eddies and boluses.

Anisotropic permeability impacts radial pressure gradients, decreasing for $K < 1$ due to increased resistance along the radial direction, and increasing for $K > 1$ as higher permeability reduces resistance. Higher Darcy numbers reduce pressure gradients by allowing flow to overcome porous medium resistance more easily. Elevated Hartmann numbers increase pressure gradients due to the resisting Lorentz force, which makes fluid movement along the radial direction more difficult.

The roughness increase boosts the friction factor ratio between rough and smooth microtubes, raising viscous losses. Conversely, higher anisotropic permeability reduces this ratio by upping resistance forces in various directions, while increasing the anisotropic angle lowers it by inducing more anisotropic flows, both leading to higher losses.

These results highlight the complex interplay between flow dynamics and porous medium characteristics in microfluidic systems. By understanding how anisotropic permeability and angle impact pumping rates, researchers and engineers can make informed decisions in device design to enhance efficiency. This knowledge is crucial for developing microfluidic systems tailored to specific applications, such as drug delivery or lab-on-a-chip technologies, where precise control over fluid flow is essential.

8

Conclusions and Future scope of work

8.1 Major contributions and conclusions

In this thesis, we have investigated the impact of surface roughness on electroosmotic flow and heat transfer within microchannels and microtubes. Our focus includes the complex interactions among magnetic fields, rotating system, and porous media with surface roughness, examining their combined effects on electroosmotic flow across various chapters. The manufacturing process of microfluidic devices naturally introduces roughness to the microchannels and microtubes, highlighting the important role of roughness on flow velocity and heat transfer, especially when interacting with external forces such as magnetic fields, electric fields, porous media, and system rotation. Here, we aim to summarize key findings regarding the impact of surface roughness and its interactions with these external forces, as explored in this thesis:

- ✿ The electromagnetohydrodynamic (EMHD) flow and heat transfer in a rotating rough surface microchannel, including the effects of secondary flow and surface roughness, is investigated. Rotation is found to have clear impact on thermal energy management for microfluidic device design. It is evident that rotation significantly influences electrokinetic transport, altering flow patterns and temperature distribution. Surface roughness, combined with rotation, increases temperature, with higher rotation rates leading to more counter-rotating vortices in rough surface channels. Understanding these interactions is vital for optimizing microfluidic devices and improving thermal performance in various applications (see **Chapter 2**).
- ✿ The impact of wall roughness on EMHD flow of two immiscible electrolytes in a microchannel, emphasizing its significance in device design is examined. The results indicate substan-

tial alterations in electrokinetic transport, leading to changes in flow patterns and separation efficiency. Increased wave amplitude amplifies fluid layer disturbance, particularly near the solid-liquid interface. Zeta potential difference significantly influences flow velocities, with higher zeta potential correlating with faster fluid movement. The study underscores the critical role of surface roughness in microfluidic device design and optimization for efficient fluid and solute transport (see **Chapter 3**).

- ✿ The impact of wall roughness on fluid flow and heat transfer in a microchannel under combined electrokinetic and electromagnetic forces with a constant pressure gradient is studied. Key findings include the influence of the transverse electric field on flow development and the effect of the magnetic field on magnetic diffusion and temperature distribution. Additionally, the study highlights the role of the Darcy number in affecting flow characteristics and temperature profiles. The results suggest that the middle layer of temperature distribution is particularly sensitive to changes in the wavenumber of the wavy wall surface. Moreover, the study emphasizes the importance of the transverse electric field in controlling heat transfer rates and Nusselt numbers, with implications for optimizing microfluidic devices (see **Chapter 4**).
- ✿ The influence of complex wavy roughness on electromagnetohydrodynamic (EMHD) flow and thermal characteristics in a porous microchannel is investigated. The results show that surface roughness affects flow and heat transfer, influencing separation processes. Higher magnetic fields increase velocity profiles, while electric fields lead to fully developed flow. The roughness mainly affects boundary layers, with porous medium permeability affecting flow and heat transfer rates. Temperature profiles are parabolic for low Darcy numbers, with roughness enhancing Nusselt numbers (see **Chapter 5**).
- ✿ The nanofluidic flow and heat transfer in an anisotropic porous microchannel with a wavy wall, under the influence of external electric and magnetic fields is studied. Key findings include the significant impact of anisotropic permeability and its angle on velocity and temperature profiles, as well as the influence of Forchheimer effects on frictional heating and slug flow behavior. The reliability of the model was demonstrated through alignment with numerical results, particularly for low Darcy numbers. Practical implications include the design of advanced microfluidic systems such as microreactors and heat exchangers, and optimization of operational conditions for nanofluidic devices, especially in electromagnetic micropump applications.(see **Chapter 6**).
- ✿ The flow phenomena of electromagnetohydrodynamic (EMHD) pumping in an anisotropic porous microtube with a rough surface is examined. Key findings reveal that while surface roughness has a slight impact on mean pumping rates, the anisotropic ratio and angle significantly affect flow resistance forces and, consequently, the pumping rate. Surface roughness induces flow disturbances, creating eddies and vortices that enhance mixing and promote bolus formation. Anisotropic permeability influences flow by introducing varying resistance

forces along different directions, leading to uncommon flow patterns with smaller eddies and boluses. Furthermore, an increase in roughness amplifies the friction factor ratio between rough and smooth microtubes, resulting in higher viscous losses. These insights underscore the intricate relationship between surface roughness, anisotropic permeability, and flow behavior in microfluidic systems, offering valuable guidance for designing efficient microfluidic devices (see **Chapter 7**).

8.2 Future scope of study

In this thesis, the focus is on the periodic roughness of microchannel and microtube surfaces to visualize the impact of rough surfaces on flow dynamics. Microtubes are considered more realistic than microchannels for designing advanced microfluidic and lab-on-chip devices. Due to limitations in manufacturing processes, random roughness on microtubes is more realistic. This thesis acknowledges this limitation and suggests that future research could consider microtubes with random roughness to achieve more realistic results. Therefore, this thesis addresses this gap by proposing a mathematical model and providing a sketch of a microtube with random roughness, aiming to encourage future research in this direction for more realistic and applicable results.

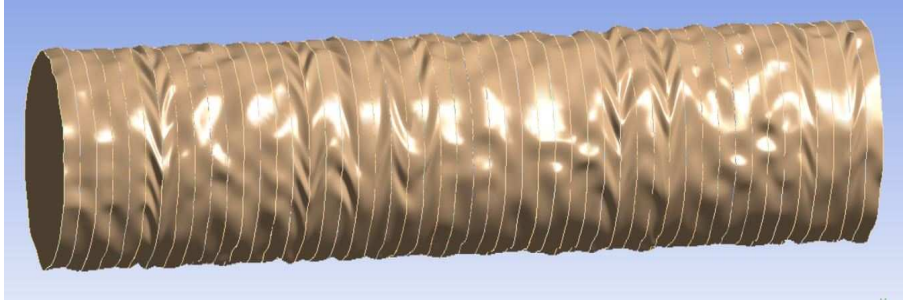


Figure 8.1: Microtube with random roughness

8.2.1 Microtube with random roughness

Random roughness can be formed by using the bottom-up approach which is displayed in Fig. 8.1 in a cylindrical coordinate system (r, θ, z) . Here N points $x_{ij}(r_i, \theta_i, z_j)$, $N = i \times j$ are assumed in the space. To specify the roughness of the model, we only consider the randomness of the radius of the microtube by fixing the spacing S_θ^* and S_z^* for the points at the coordinates θ and z respectively. Hence the points on the z -plane can be written as:

$$r_i = R^* + H^* N_k^*, \quad i = 1, 2, \dots, 360/S_\theta^*, \quad k = i + 360(j-1)/S_\theta^*, \quad (8.1)$$

$$\theta_{i+1} = \theta_i + S_\theta^*, \quad i = 1, 2, \dots, 360/S_\theta^*, \quad \theta_1 = 0. \quad (8.2)$$

Also, the z coordinates for those points can be expressed as:

$$z_{j+1} = z_j + S_z^*, j = 1, 2, \dots, L^*/S_z^*, z_1 = 0, \quad (8.3)$$

where R^* is the radius of the microtube, H^* is the roughness height and L^* is length of the microtube. Here N_k^* are the random numbers which are illustrated the randomness of the surface roughness. The random numbers are originated by using a statistical approach and these are generated by a Gaussian function with a mean value m and a standard deviation σ , which can be constructed as:

$$f(N_k^*) = \frac{1}{\sigma\sqrt{2\pi}} e^{-\frac{(N_k^* - m)^2}{2\sigma^2}}, \quad (8.4)$$

where $f(N_k^*)$ is the probability density function for N_k^* . Here we choose $m = 0, \sigma = 1/3$.

The surface of the rough microtube is shown in Fig. 8.1. In this analysis, the inner diameter D^* is used as a hydraulic diameter of the rough microtube. The mean diameter of the rough microtube can be expressed as:

$$\tilde{D} = D^* + 2H^* \text{mean}(N_k^*) = D^* + 2H^* m^*. \quad (8.5)$$

References

- Abdelhameed, T. N. (2021). Entropy generation analysis for MHD flow of water past an accelerated plate. *Sci. Rep.*, 11:11964.
- Abdulhameed, M., Muhammad, M. M., Gital, A. Y., Yakubu, D. G., and Khan, I. (2019). Effect of fractional derivatives on transient MHD flow and radiative heat transfer in a micro-parallel channel at high zeta potentials. *Phys. A: Stat. Mech. Appl.*, 519:42–71.
- Abhimanyu, P., Kaushik, P., Mondal, P. K., and Chakraborty, S. (2016). Transiencies in rotational electro-hydrodynamics microflows of a viscoelastic fluid under electrical double layer phenomena. *J. Non-Newtonian Fluid Mech.*, 231:56–67.
- Ajdari, A. (1996). Generation of transverse fluid currents and forces by an electric field: Electro-osmosis on charge-modulated and undulated surfaces. *Phys. Rev. E*, 53(5):4996–5005.
- Al-Hadhrani, A., Elliott, L., and Ingham, D. (2003). A new model for viscous dissipation across a range of permeability values. *Transp. Porous Media*, 53:117–122.
- Alhajaj, Z., Bayomy, A. M., Saghir, M. Z., and Rahman, M. M. (2020). Flow of nanofluid and hybrid fluid in porous channels: Experimental and numerical approach. *Int. J. Thermofluids.*, 1-2:100016.
- Alizadeh, A., Hsu, W.-L., Wang, M., and Daiguji, H. (2021). Electroosmotic flow: From microfluidics to nanofluidics. *Electrophoresis*, 42:834–868.
- Alsabery, A. I., Ismael, M. A., Chamkha, A. J., and Hashim, I. (2019a). Effects of two-phase nanofluid model on MHD mixed convection in a lid-driven cavity in the presence of conductive inner block and corner heater. *J. Therm. Anal. Calorim.*, 135:729–750.
- Alsabery, A. I., Mohebbi, R., Chamkha, A. J., and Hashim, I. (2019b). Effect of local thermal non-equilibrium model on natural convection in a nanofluid-filled wavy-walled porous cavity containing inner solid cylinder. *Chem. Eng. Sci.*, 201(29):247–263.
- Aoki, N. and Mae, K. (2006). Effects of channel geometry on mixing performance of micromixers using collision of fluid segments. *Chem. Eng. J.*, 118(3):189–197.
- Arcos, J. C., Mendez, F., Bautista, E. G., and Bautista, O. (2018). Dispersion coefficient in an electro-osmotic flow of a viscoelastic fluid through a microchannel with a slowly varying wall zeta potential. *J. Fluid Mech.*, 839:348–386.

- Arshavsky-Graham, S. and Segal, E. (2020). Lab-on-a-chip devices for point-of-care medical diagnostics. In Bahnemann, J. and Grünberger, A., editors, *Microfluidics in Biotechnology*, volume 179 of *Advances in Biochemical Engineering/Biotechnology*. Springer, Cham.
- Arulanandam, S. and Li, D. (2000). Liquid transport in rectangular microchannels by electroosmotic pumping. *Colloids Surf. A: Physicochem. Eng. Asp.*, 161:89–102.
- Asghar, Z., Ali, N., Waqas, M., and Javed, M. A. (2020). An implicit finite difference analysis of magnetic swimmers propelling through non-newtonian liquid in a complex wavy channel. *Comput. Math. with Appl.*, 79:2189–2202.
- Avramenko, A. A., Kovetska, Y. Y., Shevchuk, I. V., et al. (2018). Mixed convection in vertical flat and circular porous microchannels. *Transp. Porous Med.*, 124:919–941.
- Avramenko, A. A., Kovetska, Y. Y., Shevchuk, I. V., et al. (2019). Heat transfer in porous microchannels with second-order slipping boundary conditions. *Transp. Porous Med.*, 129:673–699.
- Avramenko, A. A. and Shevchuk, I. V. (2022). *Modelling of Convective Heat and Mass Transfer in Nanofluids with and without Boiling and Condensation*. Springer Nature.
- Avramenko, A. A., Tyrinov, A. I., Shevchuk, I. V., Dmitrenko, N. P., Kravchuk, A. V., and Shevchuk, V. I. (2017). Mixed convection in a vertical circular microchannel. *Int. J. Therm. Sci.*, 121:1–12.
- Balasubramanian, S., Kaushik, P., and Mondal, P. K. (2020). Dynamics of viscoelastic fluid in a rotating soft microchannel. *Phys. Fluids*, 32(11200):3.
- Banerjee, A. and Nayak, A. K. (2019). Influence of varying zeta potential on non-newtonian flow mixing in a wavy patterned microchannel. *J. Non-Newt. Fluid Mech.*, 269:17–27.
- Banerjee, D., Pati, S., and Biswas, P. (2022). Analytical study of two-layered mixed electro-osmotic and pressure-driven flow and heat transfer in a microchannel with hydrodynamic slippage and asymmetric wall heating. *Phys. Fluids*, 34:032013.
- Barletta, A. and Rees, D. (2019). On the onset of convection in a highly permeable vertical porous layer with open boundaries. *Phys. Fluids*, 31:074106.
- Bau, H. H. and Torrance, K. (1982). Boiling in low-permeability porous materials. *Int. J. Heat Mass Transf.*, 25:45–55.
- Bau, H. H., Zhong, J., and Yi, M. (2001). A minute magneto hydro dynamic (MHD) mixer. *Sens. Actuators B: Chem.*, 79:207–215.
- Bau, H. H., Zhu, J., Qian, S., and Xiang, Y. (2003). A magnetohydrodynamically controlled fluidic network. *Sens. Actuators B: Chem.*, 88:205–216.

References

- Becker, H. and Gartner, C. (2000). Polymer microfabrication methods for microfluidic analytical applications. *Electrophoresis*, 21:12–26.
- Bejan, A. (2006). *Convection Heat Transfer*. John Wiley, India, fourth edition.
- Bejan, A. and Kestin, J. (1983). Entropy generation through heat and fluid flow. *ASME. J. Appl. Mech*, 50(2):475.
- Bird, R. B., Stewart, W. E., and Lightfoot, E. N. (2002). Transport phenomena. *Appl. Mech. Rev.*
- Biswas, N., Manna, N. K., and Chamkha, A. J. (2021a). Effects of half-sinusoidal nonuniform heating during MHD thermal convection in cu–al₂o₃/water hybrid nanofluid saturated with porous media. *J. Therm. Anal. Calorim.*, 143:1665–1688.
- Biswas, N., Sarkar, U. K., Chamkha, A. J., and Manna, N. (2021b). Magneto-hydrodynamic thermal convection of cu–al₂o₃/water hybrid nanofluid saturated with porous media subjected to half-sinusoidal nonuniform heating. *J. Therm. Anal. Calorim.*, 143:1727–1753.
- Bruus, H. (2008). *Theoretical Microfluidics*. Oxford Master Series in Physics. Oxford University Press.
- Buren, M., Jain, Y., Chang, L., Li, F., and Liu, Q. (2017). Combined electromagnetohydrodynamic flow in a microparallel channel with slightly corrugated walls. *Fluid Dyn. Res.*, 49:025517.
- Buren, M., Jian, Y., and Chang, L. (2014). Electromagnetohydrodynamic flow through a microparallel channel with corrugated walls. *J. Phys. D: Appl. Phys*, 47:425501.
- Bush, A. W. (1992). *Perturbation methods for Engineers and Scientists*. CRC Press, Boca Raton.
- Cakir, M. T. and Akturk, D. (2021). Numerical investigation of heat transfer performance in laminar flow of nanofluids in the wavy micro-channel. *J. Polytech.*, pages 1–1.
- Calmidi, V. and Mahajan, R. (2000). Forced convection in high porosity metal foams. *J. Heat Transf.*, 122:557–565.
- Chakraborty, R., Dey, R., and Chakraborty, S. (2013). Thermal characteristics of electromagnetohydrodynamic flows in narrow channels with viscous dissipation and joule heating under constant wall heat flux. *Int. J. Heat Mass Transf.*, 67:1151–1162.
- Chakraborty, S. (2010). *Microfluidics and Microfabrication*. Springer New York, NY.
- Chakraborty, S. and Paul, D. (2006). Microchannel flow control through a combined electromagnetohydrodynamic transport. *J Phys D: Appl Phys.*, 39:5364–5371.
- Chakraborty, S. and Roy, S. (2008). Thermally developing electroosmotic transport of nanofluids in microchannels. *Microfluid. Nanofluid.*, 4:501–511.

- Chang, C. C. and Wang, C. Y. (2011). Rotating electro-osmotic flow over a plate or between two plates. *Phys. Rev. E*, 84(5):056320.
- Chang, L., Jian, Y., Buren, M., Liu, Q., and Sun, Y. (2016a). Electroosmotic flow through a micro-tube with sinusoidal roughness. *J. Mol. Liq.*, 220:258–264.
- Chang, L., Jian, Y., Buren, M., and Sun, Y. (2016b). Electroosmotic flow through a microparallel channel with 3d wall roughness. *Electrophoresis*, 37:482–492.
- Chapman, D. L. (1913). A contribution to the theory of electrocapillarity. *Lond. Edinb. Dublin Philos. Mag. J. Sci.*, 25:475–481.
- Chen, X., Li, T., Zeng, H., Hu, Z., and Fu, B. (2016). Numerical and experimental investigation on micromixers with serpentine microchannels. *Int. J. Heat Mass Transf.*, 98:131–140.
- Chen, Y., Zhang, C., Wu, R., and Shi, M. (2011). Methanol steam reforming in microreactor with constructal tree-shaped network. *J. Power Sour.*, 196(15):6366–6373.
- Chkhalo, N. I., Mikhailenko, M. S., MilKov, A. V., Pestov, A. E., Polkovnikov, V. N., Salashchenko, N. N., Strulya, I. L., Zorina, M. V., and Zuev, S. Y. (2017). Effect of ion beam etching on the surface roughness of bare and silicon covered beryllium films. *Surf. Coat. Technol.*, 311:351–356.
- Cho, C. C., Chen, C., and Chen, C. K. (2013). Charecteristics of transient electroosmotic flow in microchannels with complex wavy surface and periodic time varing electric field. *J. Fluids Eng*, 135:21301–1.
- Choi, W. S., Sharma, A., Qian, S., Lim, G., and Joo, S. W. (2011). On steady two-fluid electroosmotic flow with full interfacial electrostatics. *J. Colloid Interface Sci.*, 357:521–526.
- Darcy, H. P. G. (1856). *Les Fontaines Publiques de la Ville de Dijon*. Victor Dalmont, Paris.
- Das, S., Chakraborty, S., and Mitra, S. K. (2012). Magnetohydrodynamics in narrow fluidic channels in presence of spatially non-uniform magnetic fields: framework for combinedmagnetohydrodynamic and magnetophoretic particle transport. *Microfluid. Nanofluid.*, 13:799–807.
- Das, S. and Hardt, S. (2011). Electric-double-layer potential distribution in multiplelayer immiscible electrolytes. *Phys. Rev. E*, 84(2):022502.
- Das, S., Vanarse, V. B., and Bandyopadhyay, D. (2024). Electroosmotic micromixing in physico-chemically patterned microchannels. *Ind. Eng. Chem. Res.*, 63:5312–5325.
- Degan, G., Akowanou, C., Fagbemi, L., and Zinsalo, J. M. (2016). Hydrodynamic anisotropy effects on radiation-mixed convection interaction in a vertical porous channel. *Appl. Mathem., Sci. Res. Publish.*, 7(1):22–39.
- Degan, G., Zohoun, S., and Vasseur, P. (2002). Forced convection in horizontal porous channels with hydrodynamic anisotropy. *Int. J. Heat Mass Transf.*, 45(15):3181–3188.

- Demekhin, E. A., Ganchenko, G. S., Navarkar, A., and Amiroudine, S. (2016a). The stability of two layer dielectric-electrolyte micro-flow subjected to an external electric field. *Phys. Fluids*, 28(9):092003.
- Demekhin, E. A., Ganchenko, G. S., Navarkar, A., and Amiroudine, S. (2016b). The stability of two-layer dielectric-electrolyte micro-flow subjected to an external electric field. *Phys. Fluids*, 28(9):092003.
- Deng, S., Xiao, T., and Wu, S. (2021). Two-layer combined electroosmotic and pressure-driven flow of power-law fluids in a circular microcapillary. *Colloids Surf. A: Physicochem. Eng. Asp.*, 610:125727.
- Dubrovina, E., Craster, R., and Papageorgiou, D. (2017). Two-layer electrified pressure-driven flow in topographically structured channels. *J. Fluid Mech.*, 814:222–248.
- Eijkel, J. C. T., Daltonb, C., Haydenb, C. J., Burtb, J. P. H., and Manz, A. (2003). A circular ac magnetohydrodynamic micropump for chromatographic applications. *Sens. Actuators B: Chem.*, 92:215–221.
- Erickson, D. and Li, D. (2002). Influence of surface heterogeneity on electrokinetically driven microfluidic mixing. *Langmuir*, 18(5):1883–1892.
- Gamrat, G., Favre-Marinet, M., Leperson, S., Baviere, R., and Ayela, F. (2008). An experimental study and modelling of roughness effects on laminar flow in microchannels. *J. Fluid Mech.*, 594:399–423.
- Ganchenko, G. S., Demekhin, E. A., Mayur, M., and Amiroudine, S. (2015). Electrokinetic instability of liquid micro- and nanofilms with a mobile charge. *Phys. Fluids*, 27:062002.
- Gandharva, S. and Kaushik, P. (2022). Transient electro-osmotic flow in rotating soft microchannel. *Phys. Fluids*, 34:082023.
- Gao, Y., Wang, C., Wong, N. T. N., Yang, C., Nguyen, N. T., and Ooi, K. T. (2007). Electroosmotic control of the interface position of two-liquid flow through a microchannel. *J. Micromech. Microeng.*, 17(2):358.
- Gao, Y., Wong, T. N., Yang, C., and Ooi, K. T. (2005). Two-fluid electroosmotic flow in microchannels. *J. Colloid Interface Sci.*, 284(1):306–314.
- Gao, Z., Zheng, D., Bai, J., Shang, X., and Li, P. (2023). A numerical investigation of wavy microchannels with secondary branches under non-uniform heating. *Phys. Fluids*, 35:023610.
- Gaurav, S. V. (2010). Role of wall deformability on interfacial instabilities in gravity-driven two-layer flow with a free surface. *Phys. Fluids*, 22:094103.
- Gepner, S. and Floryan, J. (2016). Flow dynamics and enhanced mixing in a converging-diverging channel. *J. Fluid Mech.*, 807:167–204.

- Ghalambaz, M., Mehryan, S. A. M., Zahmatkesh, I., and Chamkha, A. (2020). Free convection heat transfer analysis of a suspension of nano-encapsulated phase change materials (necpm) in an inclined porous cavity. *Int. J. Therm. Sci.*, 157:106503.
- Gheshlaghi, B., Nazaripoor, H., Kumar, A., and Sadrzadeh, M. (2016). Analytical solution for transient electroosmotic flow in a rotating microchannel. *RSC Adv*, 6(21):17632–17641.
- Gleeson, J. P., Roche, O. M., West, J., and Gelb, A. (2004). Modeling annular micromixers. *SIAM J Appl Math*, 64:1294–1310.
- Gloss, D. and Herwig, H. (2009). Microchannel roughness effects: A close-up view. *Heat Transf. Eng.*, 30(1-2):62–69.
- Gouy, M. (1910). Sur la constitution de la charge électrique à la surface d'un electrolyte. *J. Phys. Theor. Appl.*, 9:457–468.
- Gu, L. and Lawrence, G. A. (2005). Analytical solution for maximal frictional two-layer exchange flow. *J. Fluid Mech.*, 543:1–17.
- Gupta, A. S., Misra, J. C., Reza, M., and Soundalgekar, V. M. (2003). Flow in the ekman layer on an oscillating porous plate. *Acta Mech.*, 165:1–16.
- Hadigol, M., Nosrati, R., and Raisee, M. (2011). Numerical analysis of mixed electroosmotic/pressure driven flow of power-law fluids in microchannels and micropumps. *Colloids Surf. A: Physicochem. Eng. Asp.*, 374(1):142–153.
- Hadjiconstantinou, N. G. and Simek, O. (2002). Constant-wall-temperature nusselt number in micro and nano-channels. *ASME. J. Heat Transfer.*, 124(2):356–364.
- Hall, P. (2020). An instability mechanism for channel flows in the presence of wall roughness. *J. Fluid Mech.*, 899:R2.
- Helmholtz, H. V. (1879). Studien über electrische grenzsichten. *Ann. Phys.*, 243:337–382.
- Herwig, H., Gloss, D., and Wenterodt, T. (2008). A new approach to understanding and modelling the influence of wall roughness on friction factors for pipe and channel flows. *J. Fluid Mech.*, 613:35–53.
- Herwig, H., Gloss, D., and Wenterodt, T. (2010). Flow in channels with rough walls-old and new concepts. *Heat Transf. Eng.*, 31(8):658–665.
- Hitt, D. L. and McGarry, M. (2004). Numerical simulations of laminar mixing surfaces in pulsatile microchannel flows. *Math. Comput. Simul.*, 65(4):399–416.
- Ho, C. J., Chung, Y. N., and Lai, C. M. (2014). Thermal performance of al₂o₃/water nanofluid in a natural circulation loop with a mini-channel heat sink and heat source. *Energy Convers. Manage.*, 87:848–858.

References

- Holland, D. M., Rosales, R. R., Stefanica, D., and Tabak, E. G. (2002). Internal hydraulic jumps and mixing in two-layer flows. *J. Fluid Mech.*, 470:63–83.
- Homsy, A., Koster, S., Eijkel, J. C. T., Berg, A. V. D., Lucklum, F., Verpoorte, E., and Rooij, N. F. D. (2005). High current density DC magnetohydrodynamic (MHD) micropump. *Lab Chip*, 5:466–471.
- Hooman, K. (2008). Heat and fluid flow in a rectangular microchannel filled with a porous medium. *Int. J. Heat Mass Transf.*, 51:5804–5810.
- Horiuchi, K. and Dutta, P. (2004). Joule heating effects in electroosmotically driven microchannel flows. *Int. J. Heat Mass Transf.*, 47(14-16):3085–3095.
- Horiuchi, K. and Dutta, P. (2006). Heat transfer characteristics of mixed electroosmotic and pressure driven micro-flows. *JSME Int. J. Ser. B*, 49(3):812–819.
- Horn, R. A. and Johnson, C. R. (2013). *Matrix Analysis*. Cambridge University Press, second edition.
- Hsieh, S.-S., Huang, C.-F., and Pan, J.-S. (2021). Low reynolds numbers convective heat transfer in single/two-phase roughened microchannels. *Appl. Ther. Eng.*, 198:117468.
- Huang, L., Wang, W., Murphy, M. C., Lian, K., and Ling, Z. G. (2000). Liga fabrication and test of a dc type magnetohydrodynamic (MHD) micropump. *Microsyst. Technol.*, 6:84–97.
- Huang, Y., Li, H., and Wong, T. N. (2014). Two immiscible layers of electro-osmotic driven flow with a layer of conducting non-newtonian fluid. *Int. J. Heat Mass Transf.*, 74:368–375.
- Jalali, M., Khoshnood, A., and Alam, M. (2015). Microswimmer-induced chaotic mixing. *J. Fluid Mech.*, 779:669–683.
- Jang, J. and Lee, S. S. (2000). Theoretical and experimental study of MHD (magnetohydrodynamic) micropump. *Sens. Actuators A*, 80:84–97.
- Jian, Y. (2015). Transient MHD heat transfer and entropy generation in a microparallel channel combined with pressure and electroosmotic effects. *Int. J. Heat Mass Transf.*, 89:193–205.
- Jiang, P. X., Fan, M. H., Si, G. S., and Ren, Z. P. (2018). Thermal-hydraulic performance of small scale micro-channel and porous-media heat-exchangers. *Int. J. Heat Mass Transf.*, 119:52–64.
- Jimenez, E., Escandon, J., Mendez, F., and Bautista, O. (2019). Combined viscoelectric and steric effects on the electroosmotic flow in nano/microchannels with heterogeneous zeta potentials. *Colloids Surf. A: Physicochem. Eng. Asp.*, 577:347–359.
- Joly, L., Detcheverry, F., and Biance, A. L. (2014). Anomalous ζ potential in foam films. *Phys. Rev. Lett.*, 113:088301.

- Kameswaran, P. K., Hemalatha, K., and Madhavi, M. (2016). Melting effect on convective heat transfer from a vertical plate embedded in a non-darcy porous medium with variable permeability. *Adv. Powder Technol.*, 27(2):417–425.
- Kandlikar, S. G. (2003). Microchannels and minichannels—history, terminology, classification and current research needs. In *Abstracts of First International Conference on Microchannels and Minichannels*, Rochester, New York, USA.
- Kang, S. and Suh, Y. K. (2009). Numerical analysis on electroosmotic flows in a microchannel with rectangle-waved surface roughness using the poisson-nernst-planck model. *Microfluid. Nanofluid.*, 6:461–477.
- Kar, S., McWhorter, S., Ford, S. M., and Soper, S. A. (1998). Piezoelectric mechanical pump with nanoliter per minute pulse-free flow delivery for pressure pumping in micro-channels. *Analyst*, 123:1435–1441.
- Karmakar, T. and Rajasekhar, G. P. (2016). Effect of anisotropic permeability on fluid flow through composite porous channel. *J. Eng. Mathem.*, 100:33–51.
- Karmakar, T. and Rajasekhar, G. P. (2017). A note on flow reversal in a wavy channel filled with anisotropic porous material. *Proc. R. Soc. A Mathem. Phys. Eng. Sci.*, 473:1–18.
- Karniadakis, G. and Beskok, A. (2002). Micro flows: Fundamentals and simulation. *Appl. Mech. Rev.*, 55(4):B76.
- Karniadakis, G., Beskok, A., and Aluru, N. (2005). *MicroFlows and Nanoflows - Fundamentals and Simulation*. Springer, New York, NY, USA.
- Kaushik, P., Shyam, S., and Mondal, P. K. (2022). Mixing in small scale fluidic systems swayed by rotationality effects. *Phys. Fluids*, 34:062008.
- Kaviany, M. and Mittal, M. (1987). Natural convection heat transfer from a vertical plate to high permeability porous media: An experiment and an approximate solution. *Int. J. Heat Mass Transf.*, 30:967–977.
- Keramati, H., Sadeghi, A., Saidi, M. H., and Chakraborty, S. (2016). Analytical solutions for thermo-fluidic transport in electroosmotic flow through rough microtubes. *Int. J. Heat Mass Trans.*, 92:244–251.
- Khan, M. Z. U., Younis, M. Y., Akram, N., Akbar, B., Rajput, U. A., Bhutta, R. A., Uddin, E., Jamil, M. A., Marquez, F. P. G., and Zahid, F. B. (2021). Investigation of heat transfer in wavy and dual wavy micro-channel heat sink using alumina nanoparticles. *Case Stud. Therm. Eng.*, 28:101515.
- Kherbeet, A. S., Mohammed, H. A., Salman, B. H., Ahmed, H. E., and Alawi, O. A. (2014). Experimental and numerical study of nanofluid flow and heat transfer over microscale backward-facing step. *Int. J. Heat Mass Transf.*, 79:858–867.

- Kleinstreuer, C. (2013). *Microfluidics and Nanofluidics: Theory and Selected Applications*. Wiley.
- Koh, A., Kang, D., Xue, Y., Lee, S., Pielak, R. M., Kim, J., Hwang, T., Min, S., Banks, A., Bastien, P., Manco, M. C., Wang, L., Ammann, K. R., Jang, K. I., Won, P., Han, S., Ghaffari, R., Paik, U., Slepian, M. J., Balooch, G., Huang, Y., and Rogers, J. A. (2016). A soft, wearable microfluidic device for the capture, storage, and colorimetric sensing of sweat. *Sci. Transl. Med.*, 8(366):366ra165.
- Kortschot, R. J., Philipse, A. P., and Erne, B. H. (2014). Debye length dependence of the anomalous dynamics of ionic double layers in a parallel plate capacitor. *J. Phys. Chem. C*, 118:11584–11592.
- Krewer, U., Pfafferoth, M., Kamat, A., Menendez, D. F., and Sundmacher, K. (2007). Hydrodynamic characterisation and modelling of anode flow fields of direct methanol fuel cells. *Chem. Eng. J.*, 126(2-3):87–102.
- Krishna, M. V., Ahamad, N. A., and Chamkha, A. J. (2020). Hall and ion slip effects on unsteady MHD free convective rotating flow through a saturated porous medium over an exponential accelerated plate. *Alex. Eng. J.*, 59(2):565–577.
- Krishna, M. V., Ahamad, N. A., and Chamkha, A. J. (2021). Hall and ion slip impacts on unsteady MHD convective rotating flow of heat generating/absorbing second grade fluid. *Alex. Eng. J.*, 60(1):845–858.
- Krogstad, P. A., Andersson, H. I., Bakken, O. M., and Ashrafiyan, A. (2005). An experimental and numerical study of channel flow with rough walls. *J. Fluid Mech.*, 530:327–352.
- Kumar, B. and Crittenden, S. R. (2013). Stern potential and debye length measurements in dilute ionic solutions with electrostatic force microscopy. *Nanotechnology*, 24:435701.
- Kumar, D., Gaikwad, H., Kaushik, P., and Mondal, P. (2023). Swirl driven solute mixing in narrow cylindrical channel. *Phys. Fluids*, 35:063604.
- Kurzthaler, C. K., Chase, D. L., and Stone, H. A. (2024). Surface corrugation induces helical near-surface flows and transport in microfluidic channels. *J. Fluid. Mech.*, 982:A31.
- Lade, R. K., Hippchen, E. J., Macosko, C. W., and Francis, L. F. (2017). Dynamics of capillary-driven flow in 3d printed open microchannels. *Langmuir*, 33:2949–2964.
- Laughlin, D. R. (1989). A magnetohydrodynamic angular motion sensor for anthropomorphic test device instrumentation. *SAE Int. J. Passeng. Cars - Mech. Syst.*, 98(6):1648–1682.
- Lei, J. C., Chang, C. C., and Wang, C. Y. (2019). Electro-osmotic pumping through a bumpy microtube: Boundary perturbation and detection of roughness. *Phys. Fluids*, 31:012001.
- Lei, J. C., Chen, Y. S., Chang, C. C., and Wang, C. Y. (2017). Analysis of electro-osmotic flow over a slightly bumpy plate. *Phys. Fluids*, 29(12200):5.

- Lemoff, A. V. and Lee, A. P. (2000). An ac magnetohydrodynamic micropump. *Sens. Actuators B: Chem*, 63:178–185.
- Lenz, R. D. and Kumar, S. (2007). Steady two-layer flow in a topographically patterned channel. *Phys. Fluids*, 19(10210):3.
- Leung, W. W. F. and Ren, Y. (2014). Scale-up on mixing in rotating microchannel under subcritical and supercritical operating modes. *Int. J. Heat Mass Transf.*, 77:157–172.
- Li, D. (2004). *Electrokinetics in Microfluidics*. Elsevier, Amsterdam.
- Li, F., Jian, Y., Buren, M., and Long, C. (2019). Effects of three-dimensional surface corrugations on electromagnetohydrodynamic flow through microchannel. *Chin. J. Phys.*, 60:345–361.
- Liang, F., Guo, Y., Hou, S., and Quan, Q. (2017). Photonic-plasmonic hybrid single molecule nanosensor measures the effect of fluorescent labels on dna protein dynamics. *Sci. Adv.*, 3(5):e1602991.
- Liu, Y. and Jian, Y. (2019). Electroviscous effect on electromagnetohydrodynamic flows of maxwell fluids in parallel plate microchannels. *Appl. Math. Mech.*, 40:1457–1470.
- Liu, Y., Jian, Y., and Tan, W. (2018). Entropy generation of electromagnetohydrodynamic (EMHD) flow in a curved rectangular microchannel. *Int. J. Heat Mass Transf.*, 127:901–913.
- Liu, Y., Li, J., and Smits, A. J. (2019). Roughness effects in laminar channel flow. *J. Fluid Mech.*, 876:1129–1145.
- Ma, D. D., Tang, Y. X., and Xia, G. D. (2021). Experimental investigation of flow boiling performance in sinusoidal wavy microchannels with secondary channels. *Appl. Therm. Eng.*, 199:117502.
- Maadi, M. and Golmarz, T. P. (2014). Investigation of mixing and simulation of an electroosmotic micromixer. *J. Mech. Sci. Technol.*, 28(8):3223–3230.
- Mackolil, J. and Mahanthesh, B. (2021). Inclined magnetic field and nanoparticle aggregation effects on thermal marangoni convection in nanoliquid: A sensitivity analysis. *Chin. J. Phys.*, 69:24–37.
- Madana, V. S. T. and Ali, B. A. (2020). Numerical investigation of engulfment flow at low reynolds numbers in a t-shaped microchannel. *Phys. Fluids*, 32(7):072005.
- Mahanthesh, B. (2020). *Statistical and Exact Analysis of MHD Flow Due to Hybrid Nanoparticles Suspended in C₂H₆O₂-H₂O Hybrid Base Fluid*, *Mathematical Methods in Engineering and Applied Sciences*. CRC Press pp. 44.
- Mahanthesh, B. (2021). Flow and heat transport of nanomaterial with quadratic radiative heat flux and aggregation kinematics of nanoparticles. *Int. Commun. Heat Mass Transf.*, 127(10552):1.

References

- Mahian, O., Kianifar, A., Kleinstreuer, C., Al-Nimr, M. A., Pop, I., and Sahin, A. Z. (2013). A review of entropy generation in nanofluid flow. *Int. J. Heat Mass Transf.*, 65:514–532.
- Mahian, O., Kianifar, A., Sahin, A. Z., and Wongwises, S. (2014). Performance analysis of a minichannel-based solar collector using different nanofluids. *Energy Convers. Manage.*, 88:129–138.
- Majee, S., Maiti, S., Shit, G., and Maiti, D. (2021). Spatio-temporal evolution of magnetohydrodynamic blood flow and heat dynamics through a porous medium in a wavy-walled artery. *Comput. Biol. Med.*, 135:104595.
- Malashetty, M. S., Shivakumara, I. S., and Kulkarni, S. (2005). The onset of convection in an anisotropic porous layer using a thermal non-equilibrium model. *Transp. Porous Med.*, 60:199–215.
- Martinez, L., Bautista, O., Escandon, J., and Mendez, F. (2016a). Electro-osmotic flow of a phan-thien-tanner fluid in a wavy-wall microchannel. *Colloids Surf. A: Physicochem. Eng. Asp.*, 498(2):7–19.
- Martinez, L., Bautista, O., Escandon, J., and Mendez, F. (2016b). Electro-osmotic flow of a phan-thien-tanner fluid in a wavy-wall microchannel. *Colloids Surf. A: Physicochem. Eng. Asp.*, 498:7–19.
- Marzougui, S., Bouabid, M., Oudina, F. M., Hamdeh, N. A., Magherbi, M., and Ramesh, K. (2021). A computational analysis of heat transport irreversibility phenomenon in a magnetized porous channel. *Int. J. Numer. Methods Heat Fluid Flow*, 31(7):2197–2222.
- Masliyah, J. H. and Bhattacharjee, S. (2006). *"Electrokinetic and colloid transport phenomena"*. John Wiley, Hoboken.
- Mautner, T. (2004). Application of the synthetic jet concept to low reynolds number biosensor microfluidic flows for enhanced mixing: a numerical study using the lattice boltzmann method. *Biosens. Bioelectron.*, 19(11):1409–1419.
- Mehboudi, A. and Yeom, J. (2019). Experimental and theoretical investigation of a low-reynolds-number flow through deformable shallow microchannels with ultra-low height-to-width aspect ratios. *Microfluid Nanofluid*, 23:66.
- Mehta, K. and Linderman, J. J. (2006). Model-based analysis and design of a microchannel reactor for tissue engineering. *Biotechnol. Bioeng.*, 94(3):596–609.
- Middlemiss, R. P., Samarelli, A., Paul, D. J., Hough, J., Rowan, S., and Hammond, G. D. (2016). Measurement of the earth tides with a mems gravimeter. *Nature*, 531(7596):614–617.
- Milne-Thomson, L. M. et al. (1949). *Theoretical hydrodynamics*, volume 8. Macmillan London.

- Mishra, H., Roy, A., and Vengadesan, S. (2021). Stability of two-layer flows past slippery surfaces. ii. inclined channels. *Phys. Fluids*, 33:084113.
- Mohammadi, A. and Smits, A. (2017). Linear stability of two-layer couette flows. *J. Fluid Mech.*, 826:128–157.
- Mohammed, H. A., Bhaskaran, G., Shuaib, N. H., and Saidur, R. (2011). Heat transfer and fluid flow characteristics in microchannels heat exchanger using nanofluids: a review. *Renew. Sustain. Energy Rev.*, 15:1502–1512.
- Nadarajah, P., Mohamed, K., Abdullah, J., and Devarajan, M. (2024). Thermal and hydraulic performance of al alloy-based 3d printed triangular microchannel heat sink governed by rough walls with graphene and alumina nanofluids as working liquid. *J. Micromech. Microeng.*, 34:035004.
- Nam, S., Cho, I., Heo, J., Lim, G., Bazant, M. Z., Moon, D. J., Sung, G. Y., and Kim, S. J. (2015). Experimental verification of overlimiting current by surface conduction and electro-osmotic flow in microchannels. *Phys. Rev. Lett.*, 114(11):114501.
- Nandy, K., Chaudhuri, S., Ganguly, R., and Puri, I. K. (2008). Analytical model for the magnetophoretic capture of magnetic spheres in microfluidic devices. *J. Magn. Magn. Mater.*, 320(7):1398–1405.
- Nash, C. K. and Fritsch, I. (2016). Poly(3,4-ethylenedioxythiophene)-modified electrodes for microfluidics pumping with redox-magnetohydrodynamics: improving compatibility for broader applications by eliminating addition of redox species to solution. *Anal. Chem.*, 88:1601–1609.
- Navier, C. L. M. H. (1823). Memoire sur les du mouvement des. *Mem Acad. Sci. Inst. France*, 1(6):414–416.
- Nayfeh, A. H. (2008). *Perturbation Methods*. John Wiley and Sons.
- Neffah, Z., Kahalerras, H., and Fersadou, B. (2018). Heat and mass transfer of a non-newtonian fluid flow in an anisotropic porous channel with chemical surface reaction. *Fluid Dynam. Mater. Process.*, 14(1):39–56.
- Ng, C. (2013). Combined pressure-driven and electroosmotic flow of casson fluid through a slit microchannel. *J. Non-Newt. Fluid Mech.*, 198:1–9.
- Ng, C. O. and Qi, C. (2015). Electro-osmotic flow in a rotating rectangular microchannel. *Proc. R. Soc. A*, 471(20150):200.
- Nguyen, B. and Kassegne, S. K. (2008). High-current density dc magnetohydrodynamics micropump with bubble isolation and release system. *Microfluid. Nanofluid.*, 5:383–393.
- Niazi, M. D. K. and Xu, H. (2020). Modelling two-layer nanofluid flow in a micro-channel with electro-osmotic effects by means of buongiorno's model. *Appl. Math. Mech.*, 41(1):83–104.

References

- Nield, D. (2002). Modelling fluid flow in saturated porous media and at interfaces. In Ingham, D. and Pop, I., editors, *Transport Phenomena in Porous Media II*, pages 1–19. Pergamon, London.
- Nield, D. A. and Bejan, A. (1999). *Convection in Porous Media*. Springer, New York, NY, USA.
- Nield, D. A. and Bejan, A. (2006). *Convection in Porous Medium*,. Springer, New York.
- Nimmagadda, R. and Venkatasubbaiah, K. (2017). Experimental and multiphase analysis of nanofluids on the conjugate performance of micro-channel at low reynolds numbers. *Heat Mass Transf.*, 53:2099–2115.
- Noreen, S., Waheed, S., Lu, D. C., and Hussanan, A. (2021). Entropy generation in electromagnetohydrodynamic water based three nano fluids via porous asymmetric microchannel. *Eur. J. Mech. B/Fluids.*, 85:458–466.
- Ohno, K., Tachikawa, K., and Manz, A. (2008). Microfluidics: applications for analytical purposes in chemistry and biochemistry. *Electrophoresis*, 29:4443–4453.
- Oliveira, V., Rangel, C., and Pinto, A. (2010). Effect of anode and cathode flow field design on the performance of a direct methanol fuel cell. *Chem. Eng. J.*, 157(1):174–180.
- Othman, M. I. (2004). Electrohydrodynamic instability of a rotating layer of a viscoelastic fluid heated from below. *Z. Angew. Math. Phys.*, 55:468–482.
- Ozen, O., Aubry, N., Papageorgiou, D. T., and Petropoulos, P. G. (2006). Electrohydrodynamic linear stability of two immiscible fluids in channel flow. *Electrochim. Acta*, 51(25):5316–5323.
- Piao, L. and Park, H. (2021). Interfacial instability for droplet formation in two-layer immiscible liquids under rotational oscillation. *J. Fluid Mech.*, 924:A32.
- Probstein, R. F. (2003). *Physicochemical Hydrodynamics: An Introduction*. Wiley, New York, 2nd edition.
- Qi, C. and Ng, C. (2018). Electroosmotic flow of a two-layer fluid in a slit channel with gradually varying wall shape and zeta potential. *Int. J. Heat Mass Transf.*, 119:52–64.
- Rahmati, A. R., Khorasanizadeh, H., and Arabyarmohammadi, M. R. (2020). Application of lattice boltzmann method to simulate a pressure-affected electroosmotic pump with hydrophobic thermally-jumped walls and temperature-sensitive operating fluid. *Math. Comput. Simul.*, 181:284–297.
- Ramakrishnan, V., Mushthaq, R., Roy, A., and Vengadesan, S. (2021). Stability of two-layer flows past slippery surfaces. i. horizontal channels. *Phys. Fluids*, 33:084112.
- Rana, A., Mishra, D., Reza, M., and Mondal, H. S. (2021a). Electromagnetohydrodynamic flow transport of two layer fluids through a microchannel with interfacial slip at fluid-solid interface. *J. Phys.: Conf. Ser.*, 1849:012017.

- Rana, A., Reza, M., and Shit, G. C. (2024). Effects of anisotropic permeability on EMHD nanofluid flow and heat transfer in porous microchannel with wavy rough walls. *Chin. J. Phys.*, 88:537–556.
- Rana, A., Shit, G. C., and Reza, M. (2021b). Patterned hydrodynamic slip flow control and thermal transport in a wavy microchannel through porous medium with combined electromagnetohydrodynamic effect. *J. Phys. Conf. Ser.*, 1849:012016.
- Rana, A., Shit, G. C., and Reza, M. (2022). Electromagnetohydrodynamic thermo-fluidic transport in a porous microchannel with wall roughness. *Colloids Surf. A: Physicochem. Eng. Asp.*, 650:12933.
- Ranjit, N. K. and Shit, G. C. (2017). Joule heating effects on electromagnetohydrodynamic flow through a peristaltically induced micro-channel with different zeta potential and wall slip,. *Phys. A: Stat. Mech. Appl.*, 482:458–476.
- Ranjit, N. K., Shit, G. C., and Tripathi, D. (2021). Electrothermal analysis in two-layered couple stress fluid flow in an asymmetric microchannel via peristaltic pumping. *J. Therm. Anal. Calorim.*, 144:1325–1342.
- Rashid, M. M. and Nadeem, S. (2019). EMHD flow through microchannels with corrugated walls in the presence of nanofluid. *Can. J. Phys.*, 97(7):701–720.
- Rashid, M. M., Shahzadi, I., and Nadeem, S. (2018). Corrugated walls analysis in microchannels through porous medium under electromagnetohydrodynamic (EMHD) effects. *Results Phys.*, 9:171–182.
- Raza, J., Oudina, F. M., and Chamkha, A. J. (2019). Magnetohydrodynamic flow of molybdenum disulfide nanofluid in a channel with shape effects. *Multidiscip. Model Mater. Struct.*, 15(4):737–757.
- Raza, J., Rohni, A. M., Omar, Z., and Awais, M. (2016). Heat and mass transfer analysis of MHD nanofluid flow in a rotating channel with slip effects. *J. Mol. Liq.*, 219:703–708.
- Ren, J., Ganapathysubramanian, B., and Sundararajan, S. (2011). Experimental analysis of the surface roughness evolution of etched glass for micro/nanofluidic devices. *J. Micromech. Microeng.*, 21(2):025012.
- Renault, C., Colin, S., Orioux, S., Cognet, P., and Tzedakis, T. (2012). Optimal design of multichannel microreactor for uniform residence time distribution. *Microsyst. Technol.*, 18(2):1432–1858.
- Reuss, F. F. (1809). Su run nouvel effet de l'électricité galvanique. *Mem. Soc. Imp. Natur. Moscou*, 2:327–337.
- Reynolds, O. (1883). An experimental investigation of the circumstances which determine whether the motion of water shall be direct or sinuous, and of the law of resistance in parallel channels. *Phil. Trans. R. Soc.*, 174:935–982.

References

- Reza, M. and Rana, A. (2021). Thermo-fluidic transport of electromagnetohydrodynamic flow of sodium alginate based casson nano fluid passing through a porous microtube under the effect of streaming potential. *Int. J. Eng. Tech. (UAE)*, 10(1):38–45.
- Reza, M., Rana, A., and Patra, R. (2019). Thermal characteristics of a casson fluid in microchannel through porous medium with an interfacial slip with combined electromagnetohydrodynamic effect. *ISHMT Dig. Lib.*, pages 959–964.
- Reza, M., Rana, A., and Shit, G. C. (2021). Thermo-fluidic transport of electromagnetohydrodynamic flow in a corrugated porous medium microchannel. *Eur. Phys. J. Plus*, 136:496.
- Rhodes, T. and Smolentsev, S. (2021). Pressure drop in a prototypical 3d magnetohydrodynamic flow across contraction of a fusion blanket manifold. *J. Nucl. Sci. Tech.*, 58(8):908–917.
- Rodrigo, D., Tittl, A., Ait-Bouziad, N., John-Herpin, A., Limaj, O., Kelly, C., Yoo, D., Wittenberg, N. J., Oh, S. H., Lashuel, H. A., and Altug, H. (2018). Resolving molecule-specific information in dynamic lipid membrane processes with multi-resonant infrared metasurfaces. *Nat. Commun.*, 9(1):2160.
- Ruo, A. C., Chang, M. H., and Chen, F. (2010). Effect of rotation on the electrohydrodynamic instability of a fluid layer with an electrical conductivity gradient. *Phys. Fluids*, 22:024102.
- Sadeghi, A., Veisi, H., Saidi, M. H., and Chakraborty, S. (2012). Graetz problem extended to mixed electroosmotically and pressure-driven flow. *J. Thermophys. Heat Trans.*, 26(1):123–133.
- Saleem, A., Kiani, M. N., Nadeem, S., Akhtar, S., Ghalambaz, M., and Issakhov, A. (2021). Electroosmotically driven flow of micropolar bingham viscoplastic fluid in a wavy microchannel: application of computational biology stomach anatomy. *Comput. Methods Biomech. Biomed. Eng.*, 24(3):289–298.
- Salman, B. H., Mohammed, H. A., Munisamy, K. M., and Kherbeet, A. S. (2013). Characteristics of heat transfer and fluid flow in microtube and microchannel using conventional fluids and nanofluids: a review. *Renew. Sustain. Energy Rev.*, 28:848–880.
- Samanta, A. (2013). Effect of surfactant on two-layer channel flow. *J. Fluid Mech.*, 735:519–552.
- Santiago, J. G. (2001). Electroosmotic flows in microchannels with finite inertial and pressure forces. *Anal. Chem.*, 73:2353–2365.
- Sarkar, S., Ganguly, S., and Chakraborty, S. (2017a). Influence of combined electromagnetohydrodynamics on microchannel flow with electrokinetic effect and interfacial slip. *Microfluid. Nanofluid.*, 21(3):1–16.
- Sarkar, S., Ganguly, S., and Dutta, P. (2016). Thermally developing combined magnetohydrodynamic and electrokinetic transport in narrow confinements with interfacial slip. *Int. J. Heat Mass Transf.*, 100:451–463.

- Sarkar, S., Ganguly, S., and Dutta, P. (2017b). Electrokinetically induced thermofluidic transport of power-law fluids under the influence of superimposed magnetic field. *Chem. Eng.Sci*, 171:391–403.
- Schiotz, J. and Jacobsen, K. W. (2017). Nanocrystalline metals: Roughness in flatland. *Nat. Mater.*, 16(11):1059–1060.
- Schrell, A. M., Mukhitov, N., Yi, L., Wang, X., and Roper, M. G. (2016). Microfluidic devices for the measurement of cellular secretion. *Annu. Rev. Anal. Chem.*, 9:249–269.
- Selimefendigil, F. and Chamkha, A. J. (2020). MHD mixed convection of nanofluid in a three-dimensional vented cavity with surface corrugation and inner rotating cylinder. *Int J. Numer. Methods Heat Fluid Flow*, 30(4):1637–1660.
- Selimefendigil, F., Oztop, H. F., and Chamkha, A. J. (2020). Role of magnetic field on forced convection of nanofluid in a branching channel. *Int. J. Numer. Methods Heat Fluid Flow*, 30(4):1755–1772.
- Sengupta, S., Ghosh, S., Saha, S., and Chakraborty, S. (2019). Rotational instabilities in microchannel flows. *Phys. Fluids*, 31:054101.
- Sheikholeslami, M., Gorji-Bandpy, M., and Ganji, D. D. (2014). Lattice boltzmann method for MHD natural convection heat transfer using nanofluid. *Powder Technol.*, 254:82–93.
- Sheikholeslami, M., Gorji-Bandpy, M., Ganji, D. D., and Soleimani, S. (2013). Effect of a magnetic field on natural convection in an inclined half-annulus enclosure filled with cu-water nanofluid using cvfem. *Adv. Powder Technol.*, 24:980–991.
- Shit, G. C., Mondal, A., Sinha, A., and Kundu, P. (2016a). Effects of slip velocity on rotating electroosmotic flow in a slowly varying micro-channel. *Colloids Surf. A Physicochem. Eng. Asp.*, 489:249–255.
- Shit, G. C., Mondal, A., Sinha, A., and Kundu, P. K. (2016b). Electro-osmotic flow of power-law fluid and heat transfer in a micro-channel with effects of joule heating and thermal radiation. *Phys. A: Stat. Mech. Appl.*, 462:1040–1057.
- Shit, G. C., Mondal, A., Sinha, A., and Kundu, P. K. (2016c). Electro-osmotically driven MHD flow and heat transfer in micro-channel. *Phys. A: Stat. Mech. Appl.*, 449:437–454.
- Shit, G. C., Mondal, A., Sinha, A., and Kundu, P. K. (2016d). Two-layer electro-osmotic flow and heat transfer in a hydrophobic micro-channel with fluid-solid interfacial slip and zeta potential difference. *Colloids Surf. A: Physicochem. Eng. Asp.*, 506:535–549.
- Shojaeian, M. and Shojaeian, M. (2012). Analytical solution of mixed electromagnetic/pressure driven gaseous flows in microchannel. *Microfluid. Nanofluid.*, 12:553–564.

References

- Shu, Y. C., Chang, C. C., Chen, Y. S., and Wang, C. Y. (2010). Electro-osmotic flow in a wavy microchannel: Coherence between the electric potential and the wall shape function. *Phys. Fluids*, 22:082001.
- Si, D. and Jain, Y. (2015). Electromagnetohydrodynamic (EMHD) micropump of jeffrey fluid through two parallel microchannels with corrugated walls. *J. Phys. D: Appl. Phys.*, 48:085501.
- Sim, G. D., Krogstad, J. A., Reddy, K. M., Xie, K. Y., Valentino, G. M., Weihs, T. P., and Hemker, K. J. (2017). Nanotwinned metal mems films with unprecedented strength and stability. *Sci. Adv.*, 3(6):e1700685.
- Sinha, A. and Shit, G. C. (2015). Electromagnetohydrodynamic flow of blood and heat transfer in a capillary with thermal radiation. *J. Magn. Magn. Mater.*, 378:143–151.
- Smoluchowski, M. V. (1921). *Handbuch der Elektrizität und des Magnetismus. Band II.* Barth-Verl. Leipz.
- Soares, C. (2015). *Microturbines, Fuel Cells, and Hybrid Systems, Gas Turbines.* A Handbook of Air, Land and Sea Applications. Butterworth-Heinemann, second edition.
- Sochol, R. D., Lu, A., Lei, J., Iwai, K., Lee, L. P., and Lin, L. (2014). Microfluidic bead-based diodes with targeted circular microchannels for low reynolds number applications. *Lab Chip*, 14:1585–1594.
- Song, S., Yang, X., Xin, F., and Lu, T. J. (2018). Modeling of surface roughness effects on stokes flow in circular pipes. *Phys. Fluids*, 30:023604.
- Stern, O. (1924). Zur theorie der elektrolytischen doppelschicht. *Z. Für Elektrochem. Und Angew. Phys. Chem.*, 30:508–516.
- Stokes, G. G. (1845). *Trans. camb. phil. soc.* 8:287–305.
- Stone, H. A., Stroock, A. D., and Ajdari, A. (2004). Engineering flows in small devices: Microfluidics toward a lab-on-a-chip. *Annu. Rev. Fluid Mech.*, 36:381–411.
- Stroh, A., Schaefer, K., Frohnepfel, B., and Forooghi, P. (2020). Rearrangement of secondary flow over spanwise heterogeneous roughness. *J. Fluid. Mech.*, 885:R5.
- Stroock, A. D., Dertinger, S. K. W., Ajdari, A., Mezi, I., Stone, H. A., and Whitesides, G. M. (2002). Chaotic mixer for microchannels. *Science*, 295(5555):647–651.
- Su, J., Jian, Y., Chang, L., and Liu, Q. (2013). Transient electro-osmotic and pressure driven flows of two-layer fluids through a slit microchannel. *Acta Mech. Sin.*, 29(4):534–542.
- Sun, R., Hu, W., Jiao, B., and Qi, C. (2019). Heat transfer characteristics and entropy generation of electroosmotic flow in a rotating rectangular microchannel. *Int. J. Therm. Sci.*, 140:238–254.

- Taghavi, S. M. (2018). A two-layer model for buoyant displacement flows in a channel with wall slip. *J. Fluid Mech.*, 852:602–640.
- Takashima, M. (1976). The effect of rotation on electrohydrodynamic instability. *Can. J. Phys.*, 54:342–347.
- Tayebi, T. and Chamkha, A. J. (2020). Magnetohydrodynamic natural convection heat transfer of hybrid nanofluid in a square enclosure in the presence of a wavy circular conductive cylinder. *J. Ther. Sci. Eng. Appl.*, 12(3):031009.
- Thaokar, R. M. and Kumaran, V. (2005). Electrohydrodynamic instability of the interface between two fluids confined in a channel. *Phys. Fluids*, 17(8):084104.
- Tiwari, N. and Moharana, M. K. (2021). Conjugate effect on flow boiling instability in wavy microchannel. *Int. J. Heat Mass Transf.*, 166:120791.
- Triantafyllou, M. S., Weymouth, G. D., and Miao, J. (2016). Biomimetic survival hydrodynamics and flow sensing. *Annu. Rev. Fluid Mech.*, 48:1–24.
- Tripathi, D., Jhorar, R., Beg, O. A., and Kadir, A. (2017). Electro-magneto-hydrodynamic peristaltic pumping of couple stress biofluids through a complex wavy micro-channel. *J. Mol. Liq.*, 236:358–367.
- Tripathi, D., Sharma, A., and Beg, O. A. (2018). Joule heating and buoyancy effects in electro-osmotic peristaltic transport of aqueous nanofluids through a microchannel with complex wave propagation. *Adv. Powder Technol.*, 29:639–653.
- Uddin, M. J., Yusoff, N. H. M., Beg, O. A., and Ismail, A. I. (2013). Lie group analysis and numerical solutions for non-newtonian nanofluid flow in a porous medium with internal heat generation. *Phys. Scr.*, 87:1–14.
- Vargas, C., Arcos, J., Bautista, O., and Mendez, F. (2017). Hydrodynamic dispersion in a combined magnetohydrodynamic-electroosmotic driven flow through a microchannel with slowly varying wall zeta potentials. *Phys. Fluids*, 29:092002.
- Vasista, K. N., Mehta, S. K., Pati, S., and Sarkar, S. (2021). Electroosmotic flow of viscoelastic fluid through a microchannel with slip-dependent zeta potential. *Phys. Fluids*, 33:12311.
- Verma, M. and Kumaran, V. (2013). A multifold reduction in the transition reynolds number, and ultra-fast mixing, in a micro-channel due to a dynamical instability induced by a soft wall. *J. Fluid Mech.*, 727:407–455.
- Waheed, S., Cabot, J. M., Macdonald, N. P., Lewis, T., Guijt, R. M., Paull, B., and Breadmore, M. C. (2016). 3d printed microfluidic devices: enablers and barriers. *Lab Chip*, 16:1993.

References

- Wang, C., Gao, Y., Nguyen, N. T., Wong, T. N., Yang, C., and Ooi, K. T. (2005). Interface control of pressure-driven two-fluid flow in microchannels using electroosmosis. *J. Micromech. Microeng.*, 15(12):2289.
- Wang, L., Jian, Y., Liu, Q., Li, F., and Chang, L. (2016). Electromagnetohydrodynamic flow and heat transfer of third grade fluids between two micro-parallel plates. *Colloids Surf. A: Physicochem. Eng. Aspects*, 494:87–97.
- Wang, X., Cheng, C., Wang, S., and Liu, S. (2009). Electroosmotic pumps and their applications in microfluidic systems. *Microfluid. Nanofluid.*, 6(2):145–162.
- Wang, X., Xu, H., and Qi, H. (2020). Transient magnetohydrodynamic flow and heat transfer of fractional oldroyd-b fluids in a microchannel with slip boundary condition. *Phys. Fluids*, 32(4):10310.
- Weilin, Q., Mohiuddin Mala, G., and Dongqing, L. (2000). Pressure-driven water flows in trapezoidal silicon microchannels. *Int. J. Heat Mass Transf.*, 43(3):353–364.
- West, J., Karamata, B., Lillis, B., Gleeson, J. P., and Alderman, J. K. (2002). Application of magnetohydrodynamic actuation to continuous flow chemistry. *Lab Chip*, 2:224–230.
- Winter, H. H. (1977). Viscous dissipation in shear flows of molten polymers. In Hartnett, J. P. and Irvine, T. F., editors, *Advances in Heat Transfer*, volume 13, pages 205–267. Elsevier.
- Wu, Z. Q., Cao, X. D., Chen, L., Zhang, J. R., Xia, X. H., Fang, Q., and Chen, H. Y. (2010). Study on the influence of cross-sectional area and zeta potential on separation for hybrid-chip-based capillary electrophoresis using 3d simulations. *Electrophoresis*, 31:3665–3674.
- Xia, Z., Mei, R., Sheplak, M., and Fan, Z. H. (2009). Electroosmotically driven creeping flows in a wavy microchannel. *Microfluid. Nanofluid.*, 6:37–52.
- Xie, Z. and Jian, Y. (2017). Rotating electromagnetohydrodynamic flow of power-law fluids through a microparallel channel. *Colloids Surf. A: Physicochem. Eng. Asp.*, 529:334–345.
- Xie, Z. Y. and Jian, Y. J. (2014). Rotating electroosmotic flow of power-law fluids at high zeta potentials. *Colloids Surf. A: Physicochem. Eng. Asp.*, 461:231–239.
- Xuan, Y. and Li, Q. (2003). Investigation on convective heat transfer and flow features of nanofluids. *ASME J. Heat Transf.*, 125:151–155.
- Yang, C., Jian, Y., Xie, Z., and Li, F. (2019). Heat transfer characteristics of magnetohydrodynamic electroosmotic flow in a rectangular microchannel. *Eur. J. Mech. B/Fluids*, 74:180–190.
- Yang, C. and Li, D. (1997). Electrokinetic effects on pressure-driven liquid flows in rectangular microchannels. *J. Colloid Interface Sci.*, 194(1):95–107.

- Yang, D. and Liu, Y. (2008). Numerical simulation of electroosmotic flow in microchannels with sinusoidal roughness. *Colloids Surf. A: Physicochem. Eng. Asp.*, 328(1):28–33.
- Yang, R. J., Fu, L. M., and Lin, Y. C. (2001). Electroosmotic flow in microchannels. *J. Colloid Interface Sci.*, 239:98–105.
- Yang, X., Wang, S., Zhao, M., and Xiao, Y. (2021). Electroosmotic flow of maxwell fluid in a microchannel of isosceles right triangular cross section. *Phys. Fluids*, 33(3):12311.
- Yau, H., Wang, C., Cho, C. C., and Chen, C. (2011). A numerical investigation into electroosmotic flow in microchannels with complex wavy surfaces. *Sci. Therm.*, 15(1):S87–S94.
- Yoshida, H., Kinjo, T., and Washizu, H. (2016). Analysis of electro-osmotic flow in a microchannel with undulated surfaces. *Comput. Fluids*, 124:237–245.
- Yu, W. and Choi, S. U. S. (2003). The role of interfacial layers in the enhanced thermal conductivity of nanofluids: a renovated maxwell model. *J. Nanopart. Res.*, 5:167–171.
- Yu, W., Tao, J., Yu, X., Zhao, S., Tu, S.-T., and Liu, H. (2017). A microreactor with superhydrophobic pt-al₂o₃ catalyst coating concerning oxidation of hydrogen off-gas from fuel cell. *Appl. Energy*, 185(Part 2):1233–1244.
- Zadeh, S. M. H., Mehryan, S., Ghalambaz, M., Ghodrat, M., Young, J., and Chamkha, A. (2020). Hybrid thermal performance enhancement of a circular latent heat storage system by utilizing partially filled copper foam and cu/go nano-additives. *Energy*, 213:118761.
- Zhang, K., Wang, H., Yao, K., He, G., Zhou, Z., and Sun, D. (2020). Surface roughness improvement of 3d printed microchannel. *J. Micromech. Microeng.*, 30:065003.
- Zhang, M., Yang, Y., An, X., and Hou, L. A. (2021a). A critical review of g – c₃n₄-based photocatalytic membrane for water purification. *Chem. Eng. J.*, page 128663.
- Zhang, Y., Tao, Y., and Shao, J. (2021b). Application of porous materials for the flow field in polymer electrolyte membrane fuel cells. *J. Power Sour.*, 492:229664.
- Zhao, G. P., Jian, Y. J., and Li, F. Q. (2017). Electromagnetohydrodynamic flow and heat transfer of nanofluid in a parallel plate microchannel. *J. Mech.*, 33(1):115–124.
- Zhou, Y., Lohan, D. J., Zhou, F., Nomura, T., and Dede, E. M. (2022). Inverse design of microreactor flow fields through anisotropic porous media optimization and dehomogenization. *Chem. Eng. J.*, 435:13458.
- Zhu, Y. and Granick, S. (2001). Rate-dependent slip of newtonian liquid at smooth surfaces, *phys. Rev. Lett.*, 87(9):096105.

List of Publications

1. **A. Rana**, M. Reza, G. C. Shit, (2024) Effects of Anisotropic Permeability on EMHD Nanofluid Flow and Heat Transfer in Porous Microchannels with Wavy Rough Walls, *Chinese Journal of Physics (Elsevier)*, 88: 537-556, (SCI, IF: 5).
DOI: <https://doi.org/10.1016/j.cjph.2023.11.013>.
2. **A. Rana**, M. Reza, G. C. Shit, (2023) Influence of surface roughness on electroosmotic flow through corrugated micropipe, *AIP Conference Proceedings*, 2728:030010 (SCOPUS).
DOI: <https://doi.org/10.1063/5.0143019>.
3. **A. Rana**, M. Reza, G. C. Shit, (2022) Electromagnetohydrodynamic thermo-fluidic transport in a porous microchannel with wall roughness, *Colloids and Surfaces A: Physicochemical and Engineering Aspects (Elsevier)*, 650:129336, (SCI, IF: 5.518).
DOI: <http://dx.doi.org/10.1016/j.colsurfa.2022.129336>.
4. **A. Rana**, G. C. Shit, M. Reza, (2021) Patterned hydrodynamic slip flow control and thermal transport in a wavy microchannel through porous medium with combined Electromagnetohydrodynamic effect, *Journal of Physics: Conference Series (IOP)*, 1849:012016 (SCOPUS).
DOI: <http://dx.doi.org/10.1088/1742-6596/1849/1/012016>.
5. M. Reza, **A. Rana**, G. C. Shit, (2021) Thermo-fluidic transport of electromagnetohydrodynamic flow in a corrugated porous medium microchannel, *European Physical Journal Plus (Springer)*, 136(5):496 (SCI, IF: 3.758).
DOI: <http://dx.doi.org/10.1140/epjp/s13360-021-01505-w>.

Preprints/Manuscripts Under Preparation

1. **A. Rana**, M. Reza, G. C. Shit, G.P. Raja Sekhar, (2024) Electromagnetohydrodynamic flow of two immiscible electrolytes through a undulating hydrophobic microchannel.
2. **A. Rana**, M. Reza, G. C. Shit, K. S. Drese, (2024) Electromagnetohydrodynamic flow and thermal performance in a rotating rough surface microchannel, submitted in Physics of Fluid.
3. **A. Rana**, M. Reza, G. C. Shit, (2024) Electromagnetohydrodynamic pumping flow in a fluid saturated anisotropic porous microtube with rough surface.

Conferences & Workshops

1. Presented a paper entitled "Electroosmotic flow transport of nanofluid through porous microchannel in presence of magnetic field" at the **1st International Conference on Applied Engineering and Natural Sciences (ICAENS)** held at **Konya Teknik Üniversitesi, Turkey** during November 1-3, 2021 (online).
2. Presented a paper entitled "Influence of surface roughness on electroosmotic flow through corrugated micropipe" at the **3rd National Conference on Recent Advancement in Physical Sciences, (NCRAPS)** held at **National Institute of Technology, Uttarakhand** during December 19-20, 2021.
3. Participated in the workshop on **Physics of Fluids: Methods and Applications** organized at **GITAM Deemed to be University, Hyderabad** during June 28-30, 2022.
4. Presented a paper entitled "A numerical study on electromagnetohydrodynamic flow and heat transfer of power-law fluid in porous microchannel" at the **1st International Conference on Scientific and Academic Research (ICSAR)** held at **Konya Teknik Üniversitesi, Turkey** during December 10-13, 2022 (online).
5. Participated to the online Lecture Series on "Nonlinear Dynamics and Applications" organized by the Department of Mathematics, **Indian Institute of Technology Indore, INDIA**, during February 13-16, 2023.
6. Presented a paper entitled "Two layered electromagnetohydrodynamic flow through a rough microchannel" at the **National Conference on Mathematics: Various Aspects in Society (NCMVAS)** held at **Jadavpur University, India** during March 13-14, 2023.
7. Participated in the workshop on **Physics of Fluids: Methods and Applications** organized at **GITAM Deemed to be University, Hyderabad** during June 19-21, 2023.
8. Presented a paper entitled "Rotation induced transient heat transfer analysis of EMHD flow in a microchannel with sinusoidal roughness" at the **International Conference on Recent Advances in Fluid Mechanics and Nanoelectronics (ICRAFMN)** held at **Manipal Institute of Technology, Bengaluru** during July 12-14, 2023.

Gopal Ch. Shit
5-6-2024
Dr. Gopal Chandra Shit
Professor
Department of Mathematics
Jadavpur University
Kolkata - 700 032. (India)

Anilendu Rana
05.06.2024